

Neurovascular  
Malformation Solutions

Ischemic Stroke  
and Carotid Artery  
Disease Solutions

# Performance Based Solutions

For more information or a product demonstration,  
contact your local MicroVention representative:



**MicroVention, Inc.**  
**Worldwide Headquarters**  
1311 Valencia Avenue  
Tustin, CA 92780 USA  
MicroVention UK Limited  
MicroVention Europe, S.A.R.L.  
MicroVention Deutschland GmbH

PH +1.714.247.8000

PH +44 (0) 191 258 6777

PH +33 (1) 39 21 77 46

PH +49 211 210 798-0

## FLEXIBLE ANEURYSM TREATMENT

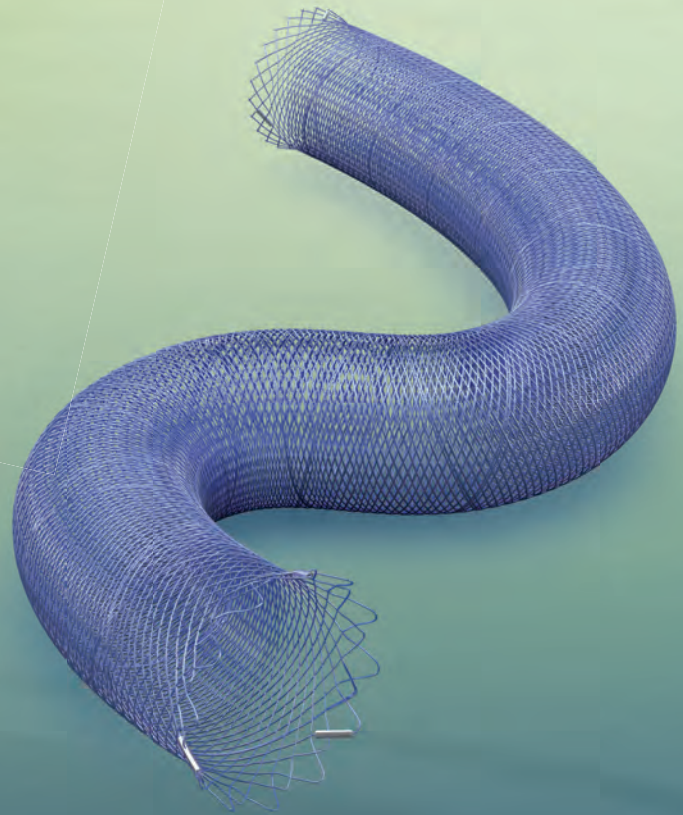


### DERIVO<sup>®</sup> Embolisation Device

- Unique x-ray visibility
- BlueXide<sup>®</sup> surface
- Repositionable up to 70 – 90 %

### ACCLINO<sup>®</sup> flex Stent

- For microcatheters with 0.017" ID (Ø 3.5 and 4.5 mm) and 0.021" ID (Ø 6.5 mm)
- Repositionable up to 90 %

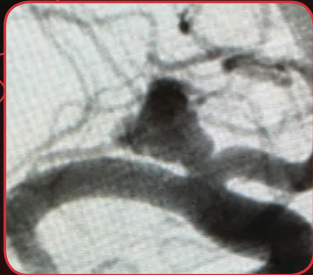


Not for sale within the territory of the United States

# BARRICADE™ COIL SYSTEM

## COILS THAT PERFORM

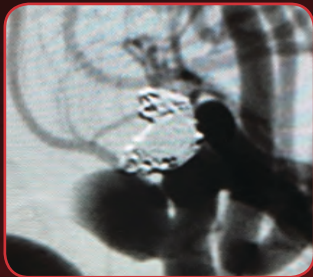
Treatment and 10 Month Follow-up of Right ICA Terminus Aneurysm and Left Pcom Aneurysm



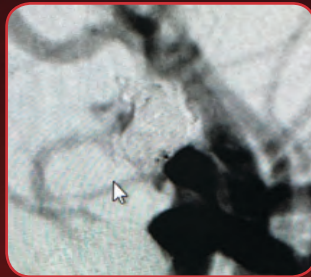
PRE-TREATMENT RIGHT ICA



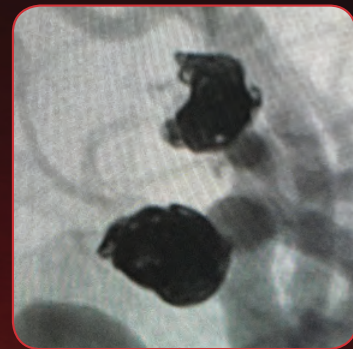
POST-TREATMENT RIGHT ICA



PRE-TREATMENT LEFT PCOM



POST-TREATMENT LEFT PCOM



10 MONTH FOLLOW-UP

“The Barricade Coil System provided great versatility in treating these two aneurysms with diverse morphologies. I am impressed with the stable and complete occlusion of both aneurysms at follow-up.”

-Timothy Malisch, M.D.

## COILS THAT SAVE \$

BARRICADE  
COILS  
SAVED  
\$6,710\*

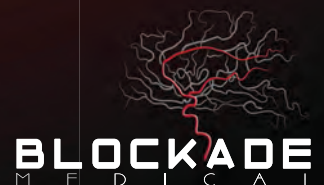
Images courtesy of Timothy Malisch, M.D.

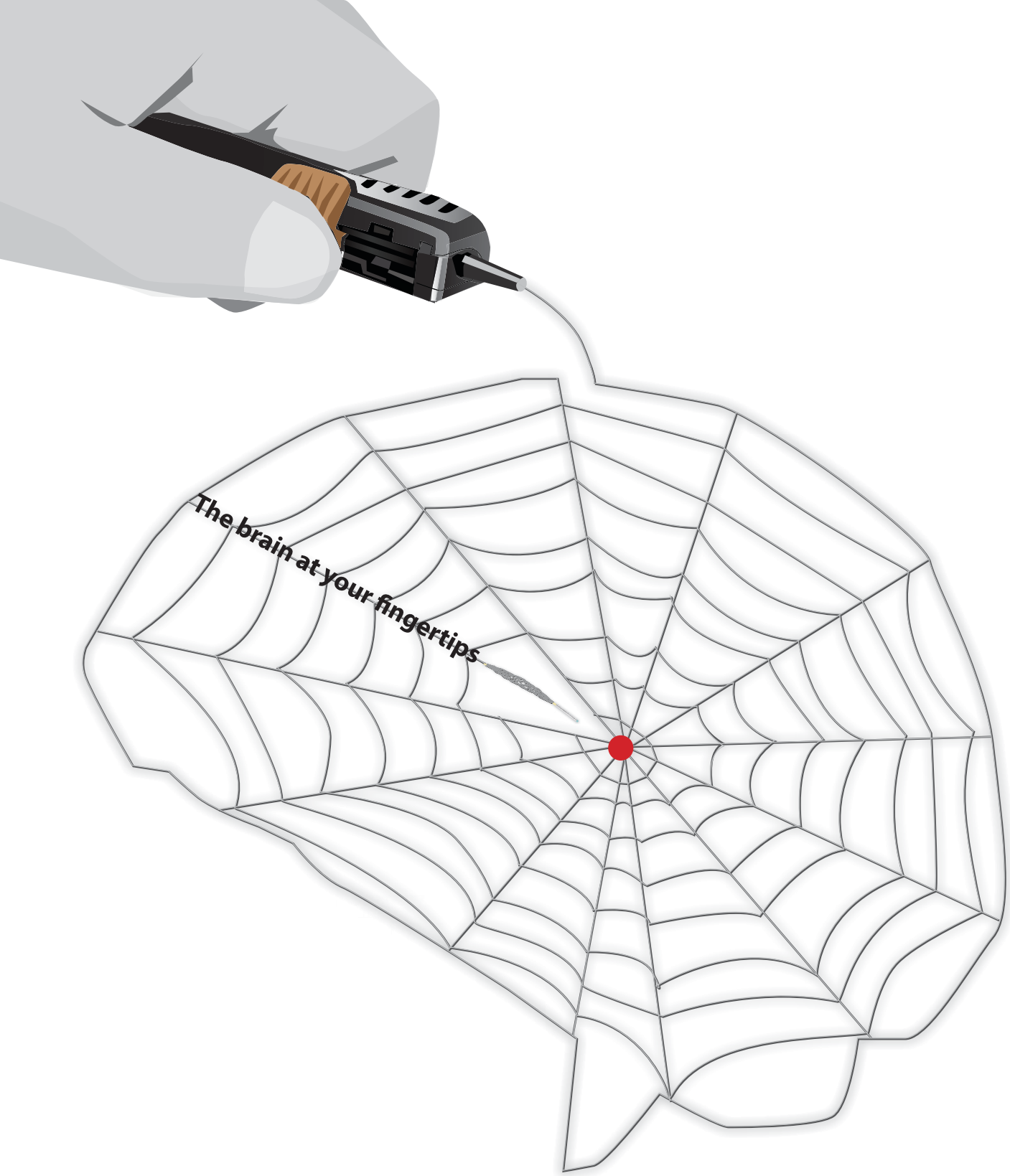
\* Estimated savings in this case, data on file.

The Barricade Coil System is intended for the endovascular embolization of intracranial aneurysms and other neurovascular abnormalities such as arteriovenous malformations and arteriovenous fistulae. The System is also intended for vascular occlusion of blood vessels within the neurovascular system to permanently obstruct blood flow to an aneurysm or other vascular malformation and for arterial and venous embolizations in the peripheral vasculature. Refer to the instructions for use for complete product information.

18 TECHNOLOGY DRIVE #169, IRVINE CA 92618 | p: 949.788.1443 | f: 949.788.1444  
[WWW.BLOCKADEMEDICAL.COM](http://WWW.BLOCKADEMEDICAL.COM)

MKTG-060 Rev. A





The brain at your fingertips

 **Rapid Medical**

[www.rapid-medical.com](http://www.rapid-medical.com) > tigertriever

## Smooth and stable.

Target Detachable Coils deliver consistently smooth deployment and exceptional microcatheter stability. Designed to work seamlessly together for framing, filling and finishing. Target Coils deliver the high performance you demand.

For more information, please visit [www.strykerneurovascular.com/Target](http://www.strykerneurovascular.com/Target) or contact your local Stryker Neurovascular sales representative.



**Target**<sup>®</sup>  
DETACHABLE COILS

# The Foundation of the ASNR Symposium 2017: *Discovery and Didactics* April 22-23, 2017

## ASNR 55<sup>th</sup> Annual Meeting: *Diagnosis and Delivery* April 24-27, 2017



Long Beach Convention & Entertainment Center  
© Long Beach Convention & Visitors Bureau

**Jacqueline A. Bello, MD, FACR**  
**ASNR 2017 Program Chair/President-Elect**  
*Programming developed in cooperation with and appreciation of the...*

**American Society of Functional Neuroradiology (ASFNR)**  
Kirk M. Welker, MD

**American Society of Head and Neck Radiology (ASHNR)**  
Rebecca S. Cornelius, MD, FACR

**American Society of Pediatric Neuroradiology (ASPNR)**  
Susan Palasis, MD

**American Society of Spine Radiology (ASSR)**  
Joshua A. Hirsch, MD, FACR, FSIR

**Society of NeuroInterventional Surgery (SNIS)**  
Blaise W. Baxter, MD

**American Society of Neuroradiology (ASNR)  
Health Policy Committee**  
Robert M. Barr, MD, FACR

**Computer Sciences & Informatics (CSI) Committee**  
John L. Go, MD, FACR

**Research Scientist Committee**  
Dikoma C. Shungu, PhD and Timothy, P.L. Roberts, PhD

**The International Hydrocephalus Imaging Working Group (IHIWG)/CSF Flow Group**  
William G. Bradley, Jr., MD, PhD, Harold L. Rekate, MD  
and Bryn A. Martin, PhD

**Abstract Deadline: Friday, December 9, 2016**  
Please visit [2017.asnr.org](http://2017.asnr.org) for more information



### ASNR 55<sup>th</sup> Annual Meeting

c/o American Society of Neuroradiology  
800 Enterprise Drive, Suite 205 • Oak Brook, Illinois 60523-4216  
Phone: 630-574-0220 • Fax: 630-574-0661 • [2017.asnr.org](http://2017.asnr.org)



ASFNR ASHNR ASPNR ASSR SNIS

THE FOUNDATION OF THE ASNR



**Come to the beach!** Please join us in Long Beach, California, April 22-27, 2017, for the 55<sup>th</sup> Annual Meeting of the ASNR. Known for its 5.5 miles of Pacific Ocean waterfront, this southern California beach resort boasts a blend of city sophistication and seaside serenity. ASNR is delighted to provide a “4D” focus for this meeting, as depicted by our meeting logo: **Discovery and Didactics** for The Foundation of the ASNR Symposium 2017: **Diagnosis and Delivery** for the ensuing Annual Meeting Program.

Centered on Discovery and Didactics, the symposium will feature sessions on “What’s New?” in the role neuroimaging plays defining CNS disease mechanisms and how to best prepare for “What’s Next?” for our subspecialty in terms of training, teaching, and leading the process of lifelong learning. The annual meeting programming will address best practices in Diagnosis and Delivery, as we strive to provide value, promote quality in better health and care and consider cost. Our discussions will consider how to navigate the changing landscape of healthcare reform and reimbursement as subspecialists in a field that is changing at an equally “fast forward” pace!



Hyatt Regency Long Beach  
© Hyatt Regency Long Beach



Westin Long Beach  
© The Westin Long Beach

# CALL FOR AJNR EDITORIAL FELLOWSHIP CANDIDATES

ASNR and AJNR are pleased once again to join efforts with other imaging-related journals that have training programs on editorial aspects of publishing for trainees or junior staff (3–5 years after training), including Radiology (Olmsted fellowship), AJR (Figley and Rogers fellowships), JACR (Bruce J. Hillman fellowship), and Radiologia.

## 2017 Candidate Information and Requirements

### GOALS

- Increase interest in “editorial” and publication-related activities in younger individuals.
- Increase understanding and participation in the AJNR review process.
- Incorporate into AJNR’s Editorial Board younger individuals who have previous experience in the review and publication process.
- Fill a specific need in neuroradiology not offered by other similar fellowships.
- Increase the relationship between “new” generation of neuroradiologists and more established individuals.
- Increase visibility of AJNR among younger neuroradiologists.

### ACTIVITIES OF THE FELLOWSHIP

- Serve as Editorial Fellow for one year. This individual will be listed on the masthead as such.
- Review at least one manuscript per month for 12 months. Evaluate all review articles submitted to AJNR.
- Learn how electronic manuscript review systems work.
- Be involved in the final decision of selected manuscripts together with the Editor-in-Chief.
- Participate in all monthly Senior Editor telephone conference calls.
- Participate in all meetings of the Editors and Publications Committee during the annual meetings of ASNR and RSNA as per candidate’s availability. The Foundation of the ASNR will provide \$2000 funding for this activity.
- Evaluate progress and adjust program to specific needs in annual meeting or telephone conference with the Editor-in-Chief.
- Embark on an editorial scientific or bibliometric project that will lead to the submission of an article to AJNR or another appropriate journal as determined by the Editor-in-Chief. This project will be presented by the Editorial Fellow at the ASNR annual meeting.
- Serve as liaison between AJNR and ASNR’s Young Professionals Network and the 3 YPs appointed to AJNR as special consultants. Participate in meetings and telephone calls with this group. Design one electronic survey/year, polling the group regarding readership attitudes and wishes.
- Recruit trainees as reviewers as determined by the Editor-in-Chief.
- Participate in Web improvement projects.
- Serve as Guest Editor for an issue of AJNR’s News Digest with a timely topic.

### QUALIFICATIONS

- Be a fellow in neuroradiology from North America, including Canada (this may be extended to include other countries).
- Be a junior faculty neuroradiology member (< 3 years) in either an academic or private environment.
- Be an “in-training” or member of ASNR in any other category.

### APPLICATION

- Include a short letter of intent with statement of goals and desired research project. CV must be included.
- Include a letter of recommendation from the Division Chief or fellowship program director. A statement of protected time to perform the functions outlined is desirable.
- Applications will be evaluated by AJNR’s Senior Editors and the Chair of the Publications Committee prior to the ASNR meeting. The name of the selected individual will be announced at the meeting.
- Applications should be received by March 1, 2017 and sent to Ms. Karen Halm, AJNR Managing Editor, electronically at [khalm@asnr.org](mailto:khalm@asnr.org).

### Official Journal:

American Society of Neuroradiology  
American Society of Functional Neuroradiology  
American Society of Head and Neck Radiology  
American Society of Pediatric Neuroradiology  
American Society of Spine Radiology

### EDITOR-IN-CHIEF

**Jeffrey S. Ross, MD**

Professor of Radiology, Department of Radiology,  
Mayo Clinic College of Medicine, Phoenix, AZ

### SENIOR EDITORS

**Harry J. Cloft, MD, PhD**

Professor of Radiology and Neurosurgery,  
Department of Radiology, Mayo Clinic College of  
Medicine, Rochester, MN

**Thierry A.G.M. Huisman, MD**

Professor of Radiology, Pediatrics, Neurology, and  
Neurosurgery, Chairman, Department of Imaging  
and Imaging Science, Johns Hopkins Bayview,  
Director, Pediatric Radiology and Pediatric  
Neuroradiology, Johns Hopkins Hospital,  
Baltimore, MD

**C.D. Phillips, MD, FACR**

Professor of Radiology, Weill Cornell Medical  
College, Director of Head and Neck Imaging,  
New York-Presbyterian Hospital, New York, NY

**Pamela W. Schaefer, MD**

Clinical Director of MRI and Associate Director of  
Neuroradiology, Massachusetts General Hospital,  
Boston, Massachusetts, Associate Professor,  
Radiology, Harvard Medical School, Cambridge, MA

**Charles M. Strother, MD**

Professor of Radiology, Emeritus, University of  
Wisconsin, Madison, WI

**Jody Tanabe, MD**

Professor of Radiology and Psychiatry,  
Chief of Neuroradiology,  
University of Colorado, Denver, CO

### STATISTICAL SENIOR EDITOR

**Bryan A. Comstock, MS**

Senior Biostatistician,  
Department of Biostatistics,  
University of Washington, Seattle, WA

### EDITORIAL BOARD

Ashley H. Aiken, *Atlanta, GA*  
Lea M. Alhilali, *Phoenix, AZ*  
John D. Barr, *Dallas, TX*  
Ari Blitz, *Baltimore, MD*  
Barton F. Branstetter IV, *Pittsburgh, PA*  
Jonathan L. Brisman, *Lake Success, NY*  
Julie Bykowski, *San Diego, CA*  
Keith Cauley, *Danville, PA*  
Asim F. Choudhri, *Memphis, TN*  
Alessandro Cianfoni, *Lugano, Switzerland*  
J. Matthew Debnam, *Houston, TX*  
Seena Dehkharghani, *New York, NY*  
Colin Derdeyn, *Iowa City, IA*  
Rahul S. Desikan, *San Francisco, CA*  
Yonghong Ding, *Rochester, MN*  
Clifford J. Eskey, *Hanover, NH*  
Saeed Fakhran, *Phoenix, AZ*  
Massimo Filippi, *Milan, Italy*  
Allan J. Fox, *Toronto, Ontario, Canada*  
Wende N. Gibbs, *Los Angeles, CA*  
Christine M. Glastonbury, *San Francisco, CA*  
John L. Go, *Los Angeles, CA*  
Allison Grayev, *Madison, WI*  
Brent Griffith, *Detroit, MI*  
Wan-Yuo Guo, *Taipei, Taiwan*  
Ajay Gupta, *New York, NY*  
Rakesh K. Gupta, *Lucknow, India*  
Lotfi Hacein-Bey, *Sacramento, CA*  
Christopher P. Hess, *San Francisco, CA*  
Andrei Holodny, *New York, NY*  
Benjamin Huang, *Chapel Hill, NC*  
George J. Hunter, *Boston, MA*  
Mahesh V. Jayaraman, *Providence, RI*  
Valerie Jewells, *Chapel Hill, NC*  
Christof Karmonik, *Houston, TX*  
Timothy J. Kaufmann, *Rochester, MN*  
Hillary R. Kelly, *Boston, MA*  
Toshibumi Kinoshita, *Akita, Japan*  
Kenneth F. Layton, *Dallas, TX*  
Michael M. Lell, *Nürnberg, Germany*  
Michael Lev, *Boston, MA*  
Karl-Olof Lovblad, *Geneva, Switzerland*  
Franklin A. Marden, *Chicago, IL*  
M. Gisele Matheus, *Charleston, SC*  
Joseph C. McGowan, *Merion Station, PA*  
Stephan Meckel, *Freiburg, Germany*  
Christopher J. Moran, *St. Louis, MO*  
Takahisa Mori, *Kamakura City, Japan*  
Suresh Mukherji, *Ann Arbor, MI*  
Amanda Murphy, *Toronto, Ontario, Canada*  
Alexander J. Nemeth, *Chicago, IL*  
Sasan Partovi, *Cleveland, OH*  
Laurent Pierot, *Reims, France*  
Jay J. Pillai, *Baltimore, MD*  
Whitney B. Pope, *Los Angeles, CA*

Andrea Poretti, *Baltimore, MD*  
M. Judith Donovan Post, *Miami, FL*  
Tina Young Poussaint, *Boston, MA*  
Joana Ramalho, *Lisbon, Portugal*  
Otto Rapalino, *Boston, MA*  
Álex Rovira-Cañellas, *Barcelona, Spain*  
Paul M. Ruggieri, *Cleveland, OH*  
Zoran Rumboldt, *Rovinj-Rovigno, Croatia*  
Amit M. Saindane, *Atlanta, GA*  
Erin Simon Schwartz, *Philadelphia, PA*  
Lubdha M. Shah, *Salt Lake City, UT*  
Aseem Sharma, *St. Louis, MO*  
J. Keith Smith, *Chapel Hill, NC*  
Maria Vittoria Spampinato, *Charleston, SC*  
Gordon K. Sze, *New Haven, CT*  
Krishnamoorthy Thamburaj, *Hershey, PA*  
Cheng Hong Toh, *Taipei, Taiwan*  
Thomas A. Tomsick, *Cincinnati, OH*  
Aquila S. Turk, *Charleston, SC*  
Willem Jan van Rooij, *Tilburg, Netherlands*  
Arastoo Vossough, *Philadelphia, PA*  
Elysa Widjaja, *Toronto, Ontario, Canada*  
Max Wintermark, *Stanford, CA*  
Ronald L. Wolf, *Philadelphia, PA*  
Kei Yamada, *Kyoto, Japan*  
Carlos Zamora, *Chapel Hill, NC*

### EDITORIAL FELLOW

Daniel S. Chow, *San Francisco, CA*

### SPECIAL CONSULTANTS TO THE EDITOR

#### AJNR Blog Editor

Neil Lall, *Denver, CO*

#### Case of the Month Editor

Nicholas Stence, *Aurora, CO*

#### Case of the Week Editors

Juan Pablo Cruz, *Santiago, Chile*  
Sapna Rawal, *Toronto, Ontario, Canada*

#### Classic Case Editor

Sandy Cheng-Yu Chen, *Taipei, Taiwan*

#### Facebook Editor

Peter Yi Shen, *Sacramento, CA*

#### Health Care and Socioeconomics Editor

Pina C. Sanelli, *New York, NY*

#### Physics Editor

Greg Zaharchuk, *Stanford, CA*

#### Podcast Editor

Yvonne Lui, *New York, NY*

#### Twitter Editor

Ryan Fitzgerald, *Little Rock, AR*

### YOUNG PROFESSIONALS ADVISORY COMMITTEE

Asim K. Bag, *Birmingham, AL*  
Anna E. Nidecker, *Sacramento, CA*  
Peter Yi Shen, *Sacramento, CA*

Founding Editor  
Juan M. Taveras

Editors Emeriti  
Mauricio Castillo, Robert I. Grossman,  
Michael S. Huckman, Robert M. Quencer

Managing Editor  
Karen Halm

Assistant Managing Editor  
Laura Wilhelm

Executive Director, ASNR  
James B. Gantenberg

Director of Communications, ASNR  
Angelo Artemakis



# INTRODUCING FULLY AUTOMATED STROKE APPLICATIONS



## ZERO CLICK

Calculation of infarct  
penumbra & mismatch

## AUTOMATED STROKE REPORT

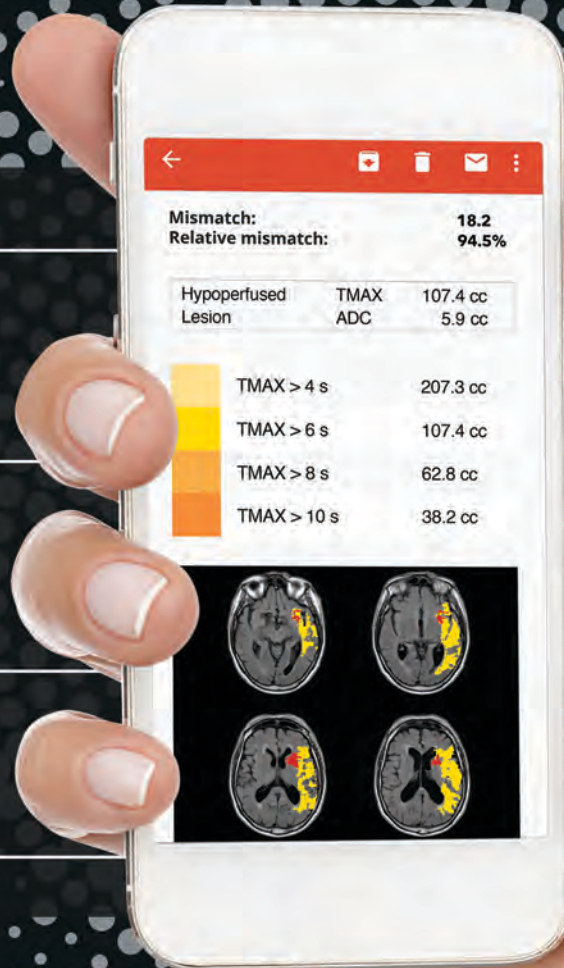
(MRI & CT) by email

## VENDOR-NEUTRAL

& easy integration  
into IT systems

Ask for a free trial

[www.olea-medical.com](http://www.olea-medical.com)



“ Innovation is in our DNA. ”

\* FDA cleared



Improved diagnosis for life™



# Simplify the MOC Process

# CMEgateway.org



# Manage your CME Credits Online

## It's Easy and Free!

Log on to CME Gateway to:

- View or print reports of your CME credits from multiple societies from a single access point.
- Print an aggregated report or certificate from each participating organization.
- Link to SAMs and other tools to help with maintenance of certification.

## American Board of Radiology (ABR) participation!

By activating ABR in your organizational profile, your MOC-fulfilling CME and SAM credits can be transferred to your own personalized database on the ABR Web site.

## Sign Up Today!

go to [CMEgateway.org](http://CMEgateway.org)

### Available to Members of Participating Societies

- |  |  |
|--|--|
| American Board of Radiology (ABR)  | Radiological Society of North America (RSNA) |
| American College of Radiology (ACR)  | Society of Interventional Radiology (SIR)    |
| American Roentgen Ray Society (ARRS)   | SNM  |
| American Society of Neuroradiology (ASNR)  | The Society for Pediatric Radiology (SPR)    |
| Commission on Accreditation of Medical Physics Educational Programs, Inc. (CAMPEP) |  |



### Statement of Ownership, Management, and Circulation (Requester Publications Only)

1. Publication Title <b>American Journal of Neuroradiology</b>	2. Publication Number 0 1 9 5 6 1 0 8	3. Filing Date 10/1/2016
4. Issue Frequency Monthly	5. Number of Issues Published Annually 12	6. Annual Subscription Price (if any) \$390
7. Complete Mailing Address of Known Office of Publication (Not printer) (Street, city, county, state, and ZIP+4®) 800 Enterprise Drive, Suite 205, Oak Brook, IL 60523		Contact Person Karen Halm Telephone (include area code) 630/750-8628 x238
8. Complete Mailing Address of Headquarters or General Business Office of Publisher (Not printer) 800 Enterprise Drive, Suite 205, Oak Brook, IL 60523		
9. Full Names and Complete Mailing Addresses of Publisher, Editor, and Managing Editor (Do not leave blank)		
Publisher (Name and complete mailing address) American Society of Neuroradiology, 800 Enterprise Drive, Suite 205, Oak Brook, IL 60523		
Editor (Name and complete mailing address) Jeffrey S. Ross, 800 Enterprise Drive, Suite 205, Oak Brook, IL 60523		
Managing Editor (Name and complete mailing address) Karen E. Halm, 800 Enterprise Drive, Suite 205, Oak Brook, IL 60523		
10. Owner (Do not leave blank. If the publication is owned by a corporation, give the name and address of the corporation immediately followed by the names and addresses of all stockholders owning or holding 1 percent or more of the total amount of stock. If not owned by a corporation, give the names and addresses of the individual owners. If owned by a partnership or other unincorporated firm, give its name and address as well as those of each individual owner. If the publication is published by a nonprofit organization, give its name and address.)		
Full Name	Complete Mailing Address	
American Society of Neuroradiology	800 Enterprise Drive, Suite 205, Oak Brook, IL 60523	
11. Known Bondholders, Mortgagees, and Other Security Holders Owning or Holding 1 Percent or More of Total Amount of Bonds, Mortgages, or Other Securities. If none, check box <input type="checkbox"/> None		
Full Name	Complete Mailing Address	
12. Tax Status (For completion by nonprofit organizations authorized to mail at nonprofit rates) (Check one) The purpose, function, and nonprofit status of this organization and the exempt status for federal income tax purposes: <input checked="" type="checkbox"/> Has Not Changed During Preceding 12 Months <input type="checkbox"/> Has Changed During Preceding 12 Months (Publisher must submit explanation of change with this statement)		

PS Form 3526-R, July 2014 (Page 1 of 4 (See instructions page 4)) PSN: 7530-09-000-8955 PRIVACY NOTICE: See our privacy policy on [www.usps.com](http://www.usps.com).

13. Publication Title American Journal of Neuroradiology	14. Issue Date for Circulation Data Below 9/9/2016	
15. Extent and Nature of Circulation		
a. Total Number of Copies (Net press run)	3826	3752
b. Legitimate Paid and/or Requested Distribution (By mail and outside the mail)	2846	2910
(1) Outside County Paid/Requested Mail Subscriptions stated on PS Form 3541 (include direct written request from recipient, telemarketing, and internet requests from recipient, paid subscriptions including nominal rate subscriptions, employer requests, advertiser's proof copies, and exchange copies.)		
(2) In-County Paid/Requested Mail Subscriptions stated on PS Form 3541 (include direct written request from recipient, telemarketing, and internet requests from recipient, paid subscriptions including nominal rate subscriptions, employer requests, advertiser's proof copies, and exchange copies.)	0	0
(3) Sales Through Dealers and Carriers, Street Vendors, Counter Sales, and Other Paid or Requested Distribution Outside USPS®	541	522
(4) Requested Copies Distributed by Other Mail Classes Through the USPS (e.g., First-Class Mail®)	0	0
c. Total Paid and/or Requested Circulation (Sum of 15b (1), (2), (3), and (4))	3387	3432
d. Non-Requested Distribution (By mail and outside the mail)	0	0
(1) Outside County Nonrequested Copies Stated on PS Form 3541 (include sample copies, requests over 3 years old, requests induced by a premium, bulk sales and requests including association requests, names obtained from business directories, lists, and other sources)	0	0
(2) In-County Nonrequested Copies Stated on PS Form 3541 (include sample copies, requests over 3 years old, requests induced by a premium, bulk sales and requests including association requests, names obtained from business directories, lists, and other sources)	0	0
(3) Nonrequested Copies Distributed Through the USPS by Other Classes of Mail (e.g., First-Class Mail, nonrequested copies mailed in excess of 10% limit mailed at Standard Mail® or Package Services rates)	0	0
(4) Nonrequested Copies Distributed Outside the Mail (include pickup stands, trade shows, showrooms, and other sources)	37	25
e. Total Nonrequested Distribution (Sum of 15d (1), (2), (3) and (4))	37	25
f. Total Distribution (Sum of 15c and e)	3424	3457
g. Copies not Distributed (See instructions to Publishers #4, (page #3))	402	295
h. Total (Sum of 15f and g)	3826	3752
i. Percent Paid and/or Requested Circulation (15c divided by 15f times 100)	98.9	99.2

\* If you are claiming electronic copies, go to line 16 on page 3. If you are not claiming electronic copies, skip to line 17 on page 3.

16. Electronic Copy Circulation	Average No. Copies Each Issue During Preceding 12 Months	No. Copies of Single Issue Published Nearest to Filing Date
a. Requested and Paid Electronic Copies		
b. Total Requested and Paid Print Copies (Line 15c) + Requested/Paid Electronic Copies		
c. Total Requested Copy Distribution (Line 15f) + Requested/Paid Electronic Copies (Line 16a)		
d. Percent Paid and/or Requested Circulation (Both Print & Electronic Copies) (16b divided by 15c x 100)		

I certify that 65% of all my distributed copies (electronic and print) are legitimate requests or paid copies.

17. Publication of Statement of Ownership for a Requester Publication is required and will be printed in the November issue of this publication.

18. Signature and Title of Editor, Publisher, Business Manager, or Owner  
  
 Date: 10/1/2016

I certify that all information furnished on this form is true and complete. I understand that anyone who furnishes false or misleading information on this form or who omits material or information requested on the form may be subject to criminal sanctions (including fines and imprisonment) and/or civil sanctions (including civil penalties).

## Trevo® XP ProVue Retrievers

See package insert for complete indications, complications, warnings, and instructions for use.

### INDICATIONS FOR USE

- The Trevo Retriever is indicated for use to restore blood flow in the neurovasculature by removing thrombus for the treatment of acute ischemic stroke to reduce disability in patients with a persistent, proximal anterior circulation, large vessel occlusion, and smaller core infarcts who have first received intravenous tissue plasminogen activator (IV t-PA). Endovascular therapy with the device should start within 6 hours of symptom onset.
- The Trevo Retriever is indicated to restore blood flow in the neurovasculature by removing thrombus in patients experiencing ischemic stroke within 8 hours of symptom onset. Patients who are ineligible for intravenous tissue plasminogen activator (IV t-PA) or who fail IV t-PA therapy are candidates for treatment.

### COMPLICATIONS

Procedures requiring percutaneous catheter introduction should not be attempted by physicians unfamiliar with possible complications which may occur during or after the procedure. Possible complications include, but are not limited to, the following: air embolism; hematoma or hemorrhage at puncture site; infection; distal embolization; pain/headache; vessel spasm, thrombosis, dissection, or perforation; emboli; acute occlusion; ischemia; intracranial hemorrhage; false aneurysm formation; neurological deficits including stroke; and death.

### COMPATIBILITY

3x20mm retrievers are compatible with Trevo® Pro 14 Microcatheters (REF 90231) and Trevo® Pro 18 Microcatheters (REF 90238). 4x20mm retrievers are compatible with Trevo® Pro 18 Microcatheters (REF 90238). 4x30mm retrievers are compatible with Excelsior® XT-27® Microcatheters (150cm x 6cm straight REF 275081) and Trevo® Pro 18 Microcatheters (REF 90238). 6x25mm Retrievers are compatible with Excelsior® XT-27® Microcatheters (150cm x 6cm straight REF 275081). Compatibility of the Retriever with other microcatheters has not been established. Performance of the Retriever device may be impacted if a different microcatheter is used.

Balloon Guide Catheters (such as Merci® Balloon Guide Catheter and FlowGate® Balloon Guide Catheter) are recommended for use during thrombus removal procedures.

Retrievers are compatible with the Abbott Vascular DOC® Guide Wire Extension (REF 22260).

Retrievers are compatible with Boston Scientific RHV (Ref 421242).

### SPECIFIC WARNINGS FOR INDICATION 1

- The safety and effectiveness of the Trevo Retrievers in reducing disability has not been established in patients with large core infarcts (i.e., ASPECTS  $\leq 7$ ). There may be increased risks, such as intracerebral hemorrhage, in these patients.
- The safety and effectiveness of the Trevo Retrievers in reducing disability has not been established or evaluated in patients with occlusions in the posterior circulation (e.g., basilar or vertebral arteries) or for more distal occlusions in the anterior circulation.

### WARNINGS APPLIED TO BOTH INDICATIONS

- Administration of IV t-PA should be within the FDA-approved window (within 3 hours of stroke symptom onset).
- Contents supplied STERILE, using an ethylene oxide (EO) process. Nonpyrogenic.
- To reduce risk of vessel damage, adhere to the following recommendations:
  - Take care to appropriately size Retriever to vessel diameter at intended site of deployment.
  - Do not perform more than six (6) retrieval attempts in same vessel using Retriever devices.
  - Maintain Retriever position in vessel when removing or exchanging Microcatheter.
- To reduce risk of kinking/fracture, adhere to the following recommendations:
  - Immediately after unsheathing Retriever, position Microcatheter tip marker just proximal to shaped section. Maintain Microcatheter tip marker just proximal to shaped section of Retriever during manipulation and withdrawal.
  - Do not rotate or torque Retriever.
  - Use caution when passing Retriever through stented arteries.
- Do not resterilize and reuse. Structural integrity and/or function may be impaired by reuse or cleaning.
- The Retriever is a delicate instrument and should be handled carefully. Before use and when possible during procedure, inspect device carefully for damage. Do not use a device that shows signs of damage. Damage may prevent device from functioning and may cause complications.

- Do not advance or withdraw Retriever against resistance or significant vasospasm. Moving or torquing device against resistance or significant vasospasm may result in damage to vessel or device. Assess cause of resistance using fluoroscopy and if needed resheat the device to withdraw.
- If Retriever is difficult to withdraw from the vessel, do not torque Retriever. Advance Microcatheter distally, gently pull Retriever back into Microcatheter, and remove Retriever and Microcatheter as a unit. If undue resistance is met when withdrawing the Retriever into the Microcatheter, consider extending the Retriever using the Abbott Vascular DOC guidewire extension (REF 22260) so that the Microcatheter can be exchanged for a larger diameter catheter such as a DAC® catheter. Gently withdraw the Retriever into the larger diameter catheter.
- Administer anti-coagulation and anti-platelet medications per standard institutional guidelines.

### PRECAUTIONS

- Prescription only – device restricted to use by or on order of a physician.
- Store in cool, dry, dark place.
- Do not use open or damaged packages.
- Use by “Use By” date.
- Exposure to temperatures above 54°C (130°F) may damage device and accessories. Do not autoclave.
- Do not expose Retriever to solvents.
- Use Retriever in conjunction with fluoroscopic visualization and proper anti-coagulation agents.
- To prevent thrombus formation and contrast media crystal formation, maintain a constant infusion of appropriate flush solution between guide catheter and Microcatheter and between Microcatheter and Retriever or guidewire.
- Do not attach a torque device to the shaped proximal end of DOC® Compatible Retriever. Damage may occur, preventing ability to attach DOC® Guide Wire Extension.



**Concentric Medical**  
301 East Evelyn Avenue  
Mountain View, CA 94041

**Stryker Neurovascular**  
47900 Bayside Parkway  
Fremont, CA 94538

[strykerneurovascular.com](http://strykerneurovascular.com)

Date of Release: SEP/2016

EX\_EN\_US

Copyright © 2016 Stryker  
NV00018973.AB

## Target® Detachable Coil

See package insert for complete indications, contraindications, warnings and instructions for use.

### INTENDED USE / INDICATIONS FOR USE

Target Detachable Coils are intended to endovascularly obstruct or occlude blood flow in vascular abnormalities of the neurovascular and peripheral vessels.

Target Detachable Coils are indicated for endovascular embolization of:

- Intracranial aneurysms
- Other neurovascular abnormalities such as arteriovenous malformations and arteriovenous fistulae
- Arterial and venous embolizations in the peripheral vasculature

### CONTRAINDICATIONS

None known.

### POTENTIAL ADVERSE EVENTS

Potential complications include, but are not limited to: allergic reaction, aneurysm perforation and rupture, arrhythmia, death, edema, embolus, headache, hemorrhage, infection, ischemia, neurological/intracranial sequelae, post-embolization syndrome (fever, increased white blood cell count, discomfort), TIA/stroke, vasospasm, vessel occlusion or closure, vessel perforation, dissection, trauma or damage, vessel rupture, vessel thrombosis. Other procedural complications including but not limited to: anesthetic and contrast media risks, hypotension, hypertension, access site complications.

### WARNINGS

- Contents supplied STERILE using an ethylene oxide (EO) process. Do not use if sterile barrier is damaged. If damage is found, call your Stryker Neurovascular representative.
- For single use only. Do not reuse, reprocess or resterilize. Reuse, reprocessing or resterilization may compromise the structural integrity of the device and/or lead to device failure which, in turn, may result in patient injury, illness or death. Reuse, reprocessing or resterilization may also create a risk of contamination of the device and/or cause patient infection or cross-infection, including, but not limited to, the transmission of infectious disease(s) from one patient to another. Contamination of the device may lead to injury, illness or death of the patient.

- After use, dispose of product and packaging in accordance with hospital, administrative and/or local government policy.

- This device should only be used by physicians who have received appropriate training in interventional neuroradiology or interventional radiology and preclinical training on the use of this device as established by Stryker Neurovascular.**

- Patients with hypersensitivity to 316LVM stainless steel may suffer an allergic reaction to this implant.
- MR temperature testing was not conducted in peripheral vasculature, arteriovenous malformations or fistulae models.
- The safety and performance characteristics of the Target Detachable Coil System (Target Detachable Coils, InZone Detachment Systems, delivery systems and accessories) have not been demonstrated with other manufacturer's devices (whether coils, coil delivery devices, coil detachment systems, catheters, guidewires, and/or other accessories). Due to the potential incompatibility of non Stryker Neurovascular devices with the Target Detachable Coil System, the use of other manufacturer's device(s) with the Target Detachable Coil System is not recommended.
- To reduce risk of coil migration, the diameter of the first and second coil should never be less than the width of the ostium.
- In order to achieve optimal performance of the Target Detachable Coil System and to reduce the risk of thromboembolic complications, it is critical that a continuous infusion of appropriate flush solution be maintained between a) the femoral sheath and guiding catheter, b) the 2-tip microcatheter and guiding catheters, and c) the 2-tip microcatheter and Stryker Neurovascular guidewire and delivery wire. Continuous flush also reduces the potential for thrombus formation on, and crystallization of infusate around, the detachment zone of the Target Detachable Coil.
- Do not use the product after the “Use By” date specified on the package.
- Reuse of the flush port/dispenser coil or use with any coil other than the original coil may result in contamination of, or damage to, the coil.
- Utilization of damaged coils may affect coil delivery to, and stability inside, the vessel or aneurysm, possibly resulting in coil migration and/or stretching.
- The fluoro-saver marker is designed for use with a Rotating Hemostatic Valve (RHV). If used without an RHV, the distal end of the coil may be beyond the alignment marker when the fluoro-saver marker reaches the microcatheter hub.

- If the fluoro-saver marker is not visible, do not advance the coil without fluoroscopy.
- Do not rotate delivery wire during or after delivery of the coil. Rotating the Target Detachable Coil delivery wire may result in a stretched coil or premature detachment of the coil from the delivery wire, which could result in coil migration.
- Verify there is no coil loop protrusion into the parent vessel after coil placement and prior to coil detachment. Coil loop protrusion after coil placement may result in thromboembolic events if the coil is detached.
- Verify there is no movement of the coil after coil placement and prior to coil detachment. Movement of the coil after coil placement may indicate that the coil could migrate once it is detached.
- Failure to properly close the RHV compression fitting over the delivery wire before attaching the InZone® Detachment System could result in coil movement, aneurysm rupture or vessel perforation.
- Verify repeatedly that the distal shaft of the catheter is not under stress before detaching the Target Detachable Coil. Axial compression or tension forces could be stored in the 2-tip microcatheter causing the tip to move during coil delivery. Microcatheter tip movement could cause the aneurysm or vessel to rupture.
- Advancing the delivery wire beyond the microcatheter tip once the coil has been detached involves risk of aneurysm or vessel perforation.
- The long term effect of this product on extravascular tissues has not been established so care should be taken to retain this device in the intravascular space.

Damaged delivery wires may cause detachment failures, vessel injury or unpredictable distal tip response during coil deployment. If a delivery wire is damaged at any point during the procedure, do not attempt to straighten or otherwise repair it. Do not proceed with deployment or detachment. Remove the entire coil and replace with undamaged product.

- After use, dispose of product and packaging in accordance with hospital, administrative and/or local government policy.

### CAUTIONS / PRECAUTIONS

- Federal Law (USA) restricts this device to sale by or on the order of a physician.
- Besides the number of InZone Detachment System units needed to complete the case, there must be an extra InZone Detachment System unit as back up.

- Removing the delivery wire without grasping the introducer sheath and delivery wire together may result in the detachable coil sliding out of the introducer sheath.
- Failure to remove the introducer sheath after inserting the delivery wire into the RHV of the microcatheter will interrupt normal infusion of flush solution and allow back flow of blood into the microcatheter.
- Some low level overhead light near or adjacent to the patient is required to visualize the fluoro-saver marker; monitor light alone will not allow sufficient visualization of the fluoro-saver marker.
- Advance and retract the Target Detachable Coil carefully and smoothly without excessive force. If unusual friction is noticed, slowly withdraw the Target Detachable Coil and examine for damage. If damage is present, remove and use a new Target Detachable Coil. If friction or resistance is still noted, carefully remove the Target Detachable Coil and microcatheter and examine the microcatheter for damage.
- If it is necessary to reposition the Target Detachable Coil, verify under fluoroscopy that the coil moves with a one-to-one motion. If the coil does not move with a one-to-one motion or movement is difficult, the coil may have stretched and could possibly migrate or break. Gently remove both the coil and microcatheter and replace with new devices.
- Increased detachment times may occur when:
  - Other embolic agents are present.
  - Delivery wire and microcatheter markers are not properly aligned.
  - Thrombus is present on the coil detachment zone.
- Do not use detachment systems other than the InZone Detachment System.
- Increased detachment times may occur when delivery wire and microcatheter markers are not properly aligned.
- Do not use detachment systems other than the InZone Detachment System.



**Stryker Neurovascular**  
47900 Bayside Parkway  
Fremont, CA 94538

[strykerneurovascular.com](http://strykerneurovascular.com)

Date of Release: MAR/2016

EX\_EN\_US

Copyright © 2016 Stryker  
NV00018669.AB



**MicroVention®**  
**TERUMO**

*Leading the Way  
in Neuroendovascular Therapy*

Aneurysm  
Therapy Solutions

**A 360-Degree Approach to**

**microvention.com**

MICROVENTION is a registered trademark of MicroVention, Inc. Refer to Instructions for Use for additional information.  
© 2016 MicroVention, Inc. 08/16

**NEW**

# Indication for Trevo<sup>®</sup> Retrievers

A New Standard of Care in Stroke



**FIRST**

mechanical thrombectomy device  
indicated to reduce disability in stroke.\*

**FIRST**

new treatment indication for  
stroke in 20 years.

## Trevo XP


PROVUE RETRIEVER

Success accelerated.

\*The Trevo Retriever is indicated for use to restore blood flow in the neurovasculature by removing thrombus for the treatment of acute ischemic stroke to reduce disability in patients with a persistent, proximal anterior circulation, large vessel occlusion, and smaller core infarcts who have first received intravenous tissue plasminogen activator (IV t-PA). Endovascular therapy with the device should start within 6 hours of symptom onset.



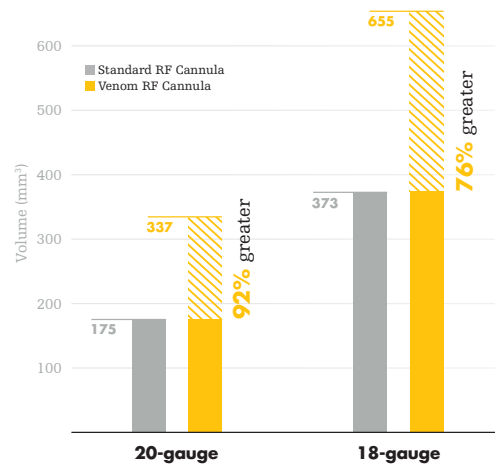
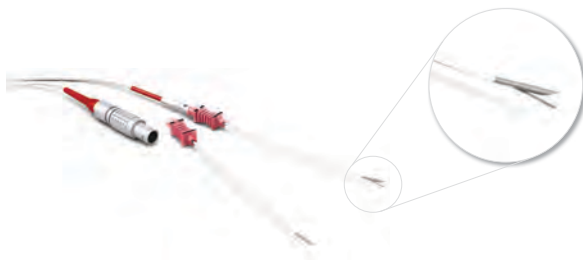
stryker



With the acquisition of the CareFusion vertebral compression fracture (VCF) portfolio from BD (Becton, Dickinson and Company), **Stryker has the most comprehensive and least invasive portfolio** of VCF treatment options

## Celebrating two years of **excellence**

An elegant, cost effective approach to large lesions. The **Venom Cannula and Electrode combination** celebrates **two years of excellence** in helping you achieve larger RF lesions<sup>1</sup> to treat your patients suffering from chronic pain.



Stryker Corporation or its divisions or other corporate affiliated entities own, use or have applied for the following trademark: Venom. All other trademarks are trademarks of their respective owners or holders.

The information presented in this overview is intended to demonstrate the breadth of Stryker product offerings. Always refer to the package insert, product label and/or user instructions before using any Stryker product. Products may not be available in all markets. Product availability is subject to the regulatory or medical practices that govern individual markets. Please contact your Stryker representative if you have questions about the availability of Stryker products in your area.

<sup>1</sup> Effect of the Stryker Venom Cannula and Venom Electrode combination on Lesion Size and Anesthesia Delivery During Radiofrequency Ablation Stryker Instruments, 4100 East Milham Avenue, Kalamazoo, Michigan 49001.

[strykerIVS.com](http://strykerIVS.com)

1000-025-340 Rev C

NOVEMBER 2016

**AJNR**

VOLUME 37 • PP 1965-2178

# AJNR

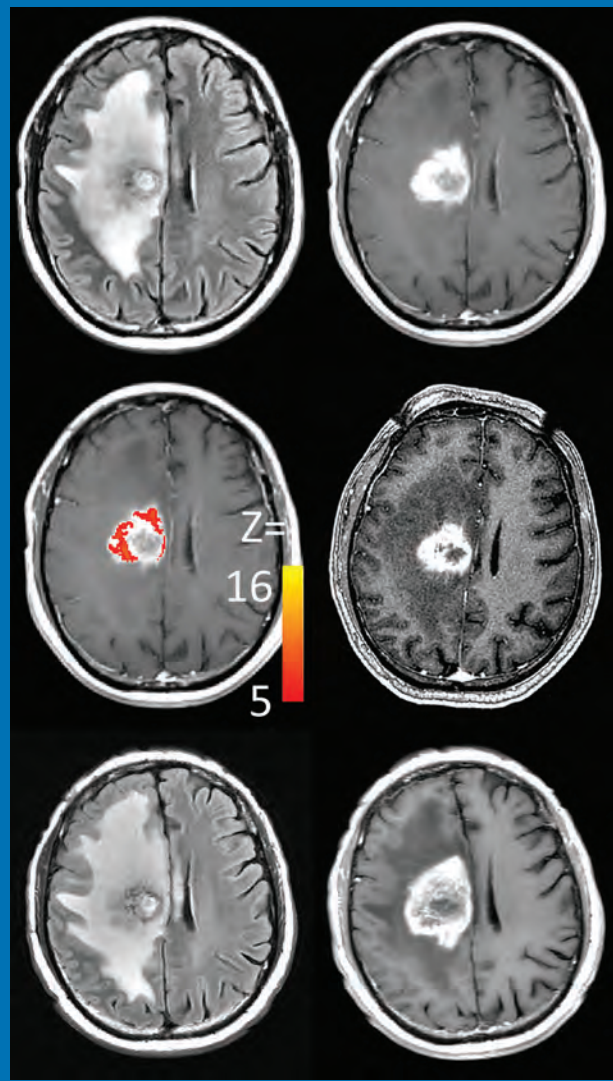
## AMERICAN JOURNAL OF NEURORADIOLOGY

NOVEMBER 2016  
VOLUME 37  
NUMBER 11  
WWW.AJNR.ORG

THE JOURNAL OF DIAGNOSTIC AND  
INTERVENTIONAL NEURORADIOLOGY

Biomarkers to predict response to bevacizumab in recurrent gliomas  
Geographic differences in endovascular treatment of aneurysms  
Imaging features of lacrimal sac and nasolacrimal duct tumors

Official Journal ASNR • ASFNR • ASHNR • ASPNR • ASSR





# AJNR

## AMERICAN JOURNAL OF NEURORADIOLOGY

NOVEMBER 2016  
VOLUME 37  
NUMBER 11  
WWW.AJNR.ORG

Publication Preview at [www.ajnr.org](http://www.ajnr.org) features articles released in advance of print. Visit [www.ajnrblog.org](http://www.ajnrblog.org) to comment on AJNR content and chat with colleagues and AJNR's News Digest at <http://ajnrdigest.org> to read the stories behind the latest research in neuroimaging.

1965 **PERSPECTIVES** *J.S. Ross*

### REVIEW ARTICLE

-  1966 **Aneurysms Associated with Brain Arteriovenous Malformations** **ADULT BRAIN**  
*S.K. Rammos, et al.*










### HEALTH CARE REFORM VIGNETTE

- 1972 **Current Procedural Terminology: History, Structure, and Relationship to Valuation for the Neuroradiologist** *T.M. Leslie-Mazwi, et al.*

### PRACTICE PERSPECTIVES

- 1977 **Comparing Preliminary and Final Neuroradiology Reports: What Factors Determine the Differences?** *K. Stankiewicz, et al.*

### GENERAL CONTENTS

-   1983 **Bidirectional Changes in Anisotropy Are Associated with Outcomes in Mild Traumatic Brain Injury** **ADULT BRAIN**  
*S.B. Strauss, et al.*
- 1992 **Image Quality Required for the Diagnosis of Skull Fractures Using Head CT: A Comparison of Conventional and Improved Reconstruction Kernels** **ADULT BRAIN**  
*S. Takagi, et al.*
- 1996 **Optimized, Minimal Specific Absorption Rate MRI for High-Resolution Imaging in Patients with Implanted Deep Brain Stimulation Electrodes** **ADULT BRAIN**  
*A.M. Franceschi, et al.*
- 2001 **Commentary Regarding Off-Label Scanning of MR Conditional Devices** *M.S. Brown*
-    2003 **Early Biomarkers from Conventional and Delayed-Contrast MRI to Predict the Response to Bevacizumab in Recurrent High-Grade Gliomas** **ADULT BRAIN**  
*D. Daniels, et al.*
-  2010 **Diffusion-Weighted Imaging for Predicting and Monitoring Primary Central Nervous System Lymphoma Treatment Response** **ADULT BRAIN**  
*W.-Y. Huang, et al.*
-    2019 **A Simple Automated Method for Detecting Recurrence in High-Grade Glioma** **ADULT BRAIN**  
*T.K. Yanagihara, et al.*

AJNR (Am J Neuroradiol ISSN 0195–6108) is a journal published monthly, owned and published by the American Society of Neuroradiology (ASNR), 800 Enterprise Drive, Suite 205, Oak Brook, IL 60523. Annual dues for the ASNR include \$170.00 for journal subscription. The journal is printed by Cadmus Journal Services, 5457 Twin Knolls Road, Suite 200, Columbia, MD 21045; Periodicals postage paid at Oak Brook, IL and additional mailing offices. Printed in the U.S.A. POSTMASTER: Please send address changes to American Journal of Neuroradiology, P.O. Box 3000, Denville, NJ 07834, U.S.A. Subscription rates: nonmember \$390 (\$460 foreign) print and online, \$310 online only; institutions \$450 (\$520 foreign) print and basic online, \$895 (\$960 foreign) print and extended online, \$370 online only (basic), extended online \$805; single copies are \$35 each (\$40 foreign). Indexed by PubMed/Medline, BIOSIS Previews, Current Contents (Clinical Medicine and Life Sciences), EMBASE, Google Scholar, HighWire Press, Q-Sensei, RefSeek, Science Citation Index, and SCI Expanded. Copyright © American Society of Neuroradiology.

	2026	Diagnostic Performance of Routine Brain MRI Sequences for Dural Venous Sinus Thrombosis <i>D. Patel, et al.</i>	ADULT BRAIN
	2033	Three-Territory DWI Acute Infarcts: Diagnostic Value in Cancer-Associated Hypercoagulation Stroke (Trousseau Syndrome) <i>P.F. Finelli, et al.</i>	ADULT BRAIN
★	2037	Comparison of CTA- and DSA-Based Collateral Flow Assessment in Patients with Anterior Circulation Stroke <i>I.G.H. Jansen, et al.</i>	ADULT BRAIN
☰	2043	A Semiautomatic Method for Multiple Sclerosis Lesion Segmentation on Dual-Echo MR Imaging: Application in a Multicenter Context <i>L. Storelli, et al.</i>	ADULT BRAIN
🔑	2050	Ataxia Severity Correlates with White Matter Degeneration in Spinocerebellar Ataxia Type 7 <i>C.R. Hernandez-Castillo, et al.</i>	ADULT BRAIN
	2055	Geographic Differences in Endovascular Treatment and Retreatment of Cerebral Aneurysms <i>A.S. Turk, et al.</i>	INTERVENTIONAL
	2060	Prophylactic Antiplatelet Medication in Endovascular Treatment of Intracranial Aneurysms: Low-Dose Prasugrel versus Clopidogrel <i>E.J. Ha, et al.</i>	INTERVENTIONAL
★	2066	Mechanical Thrombectomy in Patients with Acute Ischemic Stroke and Lower NIHSS Scores: Recanalization Rates, Periprocedural Complications, and Clinical Outcome <i>J. Pfaff, et al.</i>	INTERVENTIONAL
🔑	2072	Effect of Intracranial Atherosclerotic Disease on Endovascular Treatment for Patients with Acute Vertebrobasilar Occlusion <i>Y.W. Kim, et al.</i>	INTERVENTIONAL
🔑	2079	Virtual-versus-Real Implantation of Flow Diverters: Clinical Potential and Influence of Vascular Geometry <i>P. Bouillot, et al.</i>	INTERVENTIONAL
🔑 ☰ 🗒	2087	Wall Apposition Is a Key Factor for Aneurysm Occlusion after Flow Diversion: A Histologic Evaluation in 41 Rabbits <i>A. Rouchaud, et al.</i>	INTERVENTIONAL
🖋	2092	Vitamin D and Vulnerable Carotid Plaque <i>J.S. McNally, et al.</i>	EXTRACRANIAL VASCULAR
🔑	2100	Validation of a Hemodynamic Model for the Study of the Cerebral Venous Outflow System Using MR Imaging and Echo-Color Doppler Data <i>G. Gadda, et al.</i>	EXTRACRANIAL VASCULAR
🔑 ☰	2110	DTI Analysis of Presbycusis Using Voxel-Based Analysis <i>W. Ma, et al.</i>	FUNCTIONAL
🔑 ☰ 🗒	2115	Disrupted Brain Connectivity Patterns in Patients with Type 2 Diabetes <i>Y. Cui, et al.</i>	FUNCTIONAL
	2123	Orbital Fat Volumetry and Water Fraction Measurements Using T2-Weighted FSE-IDEAL Imaging in Patients with Thyroid-Associated Orbitopathy <i>Y. Kaichi, et al.</i>	HEAD & NECK
☰	2129	Migration of Bone Wax into the Sigmoid Sinus after Posterior Fossa Surgery <i>K. Byrns, et al.</i>	HEAD & NECK
🖋	2134	Imaging Features of Malignant Lacrimal Sac and Nasolacrimal Duct Tumors <i>V.A. Kumar, et al.</i>	HEAD & NECK
☰	2138	Is Hypoglossal Nerve Palsy Caused by Craniocervical Junction Degenerative Disease an Underrecognized Entity? <i>S.M. Weindling, et al.</i>	HEAD & NECK
	2144	Variability of Cerebral Deep Venous System in Preterm and Term Neonates Evaluated on MR SWI Venography <i>D. Tortora, et al.</i>	PEDIATRICS
🔑	2150	Diffusion Tensor Imaging of the Normal Cervical and Thoracic Pediatric Spinal Cord <i>S. Saksena, et al.</i>	PEDIATRICS
	2158	3D MR Neurography of the Lumbosacral Plexus: Obtaining Optimal Images for Selective Longitudinal Nerve Depiction <i>G. Cho Sims, et al.</i>	PERIPHERAL NERVOUS SYSTEM



2163

**Cervical Spinal Cord DTI Is Improved by Reduced FOV with Specific Balance between the Number of Diffusion Gradient Directions and Averages** *A. Crombe, et al.*

SPINE

2171

**Dorsal Lumbar Disc Migrations with Lateral and Ventral Epidural Extension on Axial MRI: A Case Series and Review of the Literature**

SPINE

*M.M. Zarrabian, et al.*

2178

**35 YEARS AGO IN AJNR**

**ONLINE FEATURES**

**LETTERS**

E71

**Embryologic Anatomic Variations: Challenges in Intra-Arterial Chemotherapy for Intraocular Retinoblastoma** *C. Paruthi, et al.*

E73

**Reply** *S. Bracco, et al.*

E74

**Regarding “Endovascular Treatment of Very Small Intracranial Aneurysms: Meta-Analysis”** *X. Wu, et al.*

E76

**Reply** *W. Brinjikji, et al.*

E77

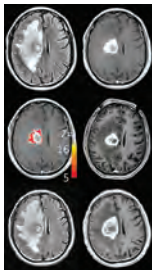
**The Utility of Molecular Imaging for Investigating Patients with Visual Hallucinations** *S. Clifford, et al.*

E79

**Reply** *T.T. Winton-Brown, et al.*

**BOOK REVIEWS** *R.M. Quencer, Section Editor*

Please visit [www.ajnrblog.org](http://www.ajnrblog.org) to read and comment on Book Reviews.



FLAIR and contrast-enhanced T1WI (*top*) show initial lesion and area at risk as defined by the multiparametric subtraction map (*middle left*). That region was not included in the initial treatment plan (*middle right*). Progression is obvious by day 35 (*bottom*).



Indicates Editor's Choices selection



Indicates Fellows' Journal Club selection



Indicates open access to non-subscribers at [www.ajnr.org](http://www.ajnr.org)



Indicates article with supplemental on-line table



Indicates article with supplemental on-line photo



Indicates article with supplemental on-line video



Evidence-Based Medicine Level 1



Evidence-Based Medicine Level 2



The Horsehead Nebula (Barnard 33) is located in the constellation of Orion, which is prominent in the winter sky from the northern hemisphere. The nebula was first described in 1888 by Scottish astronomer Williamina Fleming on a telescope photogrammetry plate made by W.H. Pickering. Despite its distinctive shape and universal recognition due to the Hubble Telescope images, it remains a very difficult visual object for amateur astronomers because it is a dark emission nebula. This RGB image was obtained with a series of 5-minute exposures on a 106-mm Takahashi FSQ telescope based in Australia with a FLI Microline CCD camera (total acquisition time of 3 hours, 45 minutes). Postprocessing was done with Pixinsight and Photoshop.

*Jeffrey S. Ross, Mayo Clinic, Phoenix, Arizona*

# Aneurysms Associated with Brain Arteriovenous Malformations

S.K. Rammos, B. Gardenghi, C. Bortolotti, H.J. Cloft, and G. Lanzino



## ABSTRACT

**SUMMARY:** Brain arteriovenous malformations are frequently associated with the presence of intracranial aneurysms at a higher-than-expected incidence based on the frequency of each lesion individually. The identification of intracranial aneurysms in association with AVMs has increased due to improvement in diagnostic techniques, particularly 3D and superselective conventional angiography. Intracranial aneurysms may confer a higher risk of hemorrhage at presentation and of rehemorrhage in patients with AVMs and therefore may be associated with a more unfavorable natural history. The association of AVMs and intracranial aneurysms poses important therapeutic challenges for practicing neurosurgeons, neurologists, and neurointerventional radiologists. In this report, we review the classification and radiology of AVM-associated intracranial aneurysms and discuss their clinical significance and implications for treatment.

**ABBREVIATION:** IA = intracranial aneurysm

**B**rain arteriovenous malformations are an important cause of intracranial hemorrhage, especially in young individuals, and are associated with increased morbidity and mortality. AVMs are frequently associated with the presence of intracranial aneurysms (IAs) at a higher incidence compared with the anticipated frequency of each lesion individually. Reported rates of IA identification in association with AVMs have increased due to improvement in diagnostic techniques, particularly 3D and superselective conventional angiography. Intracranial aneurysms may confer a higher risk of hemorrhage at presentation and of rehemorrhage in patients with AVMs and therefore may be associated with a more unfavorable natural history.<sup>1-6</sup> In this report, we review the classification and radiology of AVM-associated IAs and discuss their clinical significance and implications for treatment.

## Classification

A clear classification scheme and standardized nomenclature of the different IAs encountered in association with AVMs is of paramount importance to guide treatment decision-making. Loca-

tion, underlying hemodynamic features, and histopathology have all been used to classify IAs associated with AVMs. None of the already described classification schemes are widely accepted. Ideally, a classification scheme based on the anatomic and pathophysiologic relationship of the IA to the AVM could have predictive value for the risk of hemorrhage and the potential impact of hemodynamic changes resulting from AVM treatment. Such a system could then evolve, taking into consideration contemporary microsurgical, endovascular, and radiosurgical treatment modalities (Fig 1).

Aneurysms and aneurysm-like dilations can be divided in reference to the AVM nidus into extranidal and intranidal. Extranidal aneurysms are located on the wall of feeding arteries (arterial aneurysms) or on draining veins (venous varices) proximal (prenidal) and distal (postnidal) to the AVM nidus, respectively. Intranidal aneurysms are, by definition, located within the boundaries of the nidus and are angiographically opacified before substantial venous filling has occurred.<sup>7</sup> Given that pathologic specimens of resected AVM nidi consist of a conglomerate of venous tangles and loops, implicating that venous drainage begins at the level of the nidus, intranidal aneurysms are de facto venous.<sup>8</sup>

Arterial aneurysms may be present on vessels that are not AVM feeders (unrelated aneurysms) or arise from vessels that play a role in the perfusion of the nidus and, as such, are hemodynamically related to the AVM (flow-related aneurysms). Flow-related arterial aneurysms can occur at a considerable distance from the nidus (proximal flow-related aneurysms) or originate from feeding vessels in close proximity to the nidus (distal flow-

From the Department of Neurosurgery (S.K.R.), Arkansas Neuroscience Institute, Little Rock, Arkansas; Institute of Neurosurgery (B.G.), University Hospital of Verona, Verona, Italy; Department of Neurosurgery (C.B.), Istituto Di Ricovero e Cura a Carattere Scientifico, Institute of Neurological Science of Bologna, Bologna, Italy; and Departments of Radiology (H.J.C., G.L.) and Neurosurgery (G.L.), Mayo Clinic, Rochester, Minnesota.

Please address correspondence to Giuseppe Lanzino, MD, Mayo Clinic, 200 First St, Rochester, MN 55905; e-mail: Giuseppe.Lanzino@mayo.edu

Indicates open access to non-subscribers at [www.ajnr.org](http://www.ajnr.org)

<http://dx.doi.org/10.3174/ajnr.A4869>

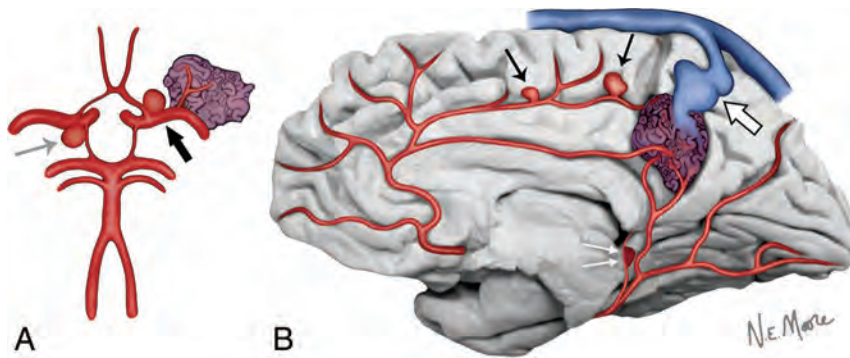


**FIG 1.** In this circle of Willis figure model (A), an AVM nidus in relation to a branch of the left middle cerebral artery is noted. At the left internal carotid artery bifurcation, a hemodynamically relevant aneurysm is located proximal to the feeding pedicle of the AVM nidus (proximal flow-related aneurysm) (black arrow). An unrelated aneurysm, with no hemodynamic connection to the AVM nidus, is present at the right posterior communicating artery origin (gray arrow). In this midsagittal view of the brain (B), distal flow-related aneurysms are seen to originate from the feeding arterial pedicles of the AVM nidus (black arrows). Arterial pseudoaneurysms are thought to be the result of the rupture of thin-walled small perforating arteries that supply the AVM and result from the unclotted portion of the hematoma still in communication with the vessel lumen and are very close to the ependymal surface (double white arrows). Finally, venous varices represent irregular, usually circumferential, enlargements of the venous outflow tract of the AVM nidus (large white arrow).

related aneurysms). According to the classification of Redekop et al<sup>7</sup> of arterial AVM-associated intracranial aneurysms, flow-related aneurysms should be considered proximal if they are located on the supraclinoid internal carotid artery, the circle of Willis, the middle cerebral artery, up to and including the primary bifurcation, the anterior cerebral artery, up to and including the anterior communicating artery, or the vertebrobasilar trunk. All flow-related aneurysms located distal to the aforementioned bifurcation points are considered distal. While proximal flow-related aneurysms predominantly occur at bifurcations, similar to isolated saccular aneurysms, distal flow-related aneurysms frequently occur along the course of the feeding artery pedicle, not related to bifurcations, and may exhibit irregular shapes and a wide neck.<sup>7</sup>

The term “venous aneurysm” is, in fact, inaccurate because the wall differs histologically from the arterial aneurysm wall; therefore, the term “venous varices” is preferred. A constellation of venous abnormalities has recently been described due to the use of superselective angiography, including fusiform (circumferential) and narrow-neck (similar morphologically to saccular aneurysms) variceal enlargements.<sup>8</sup>

Garcia-Monaco et al in 1993<sup>9</sup> first described the presence of pseudoaneurysms occurring in AVMs. Arterial pseudoaneurysms most commonly originate from small perforating arteries or choroïdal branches in proximity to the ependymal surface. The location of arterial pseudoaneurysms indicates the exact point of rupture and represents a weak point of the wall of the vessel. Pseudoaneurysms may therefore show progressive enlargement on repeat angiography. However, spontaneous regression of such pseudoaneurysms has been observed (Fig 2). Arterial pseudoaneurysms may have an irregular shape, and their formation may be the end result of dissection and dynamic vessel remodeling, as underlined by the presence of persistent filling defects and stenoses.<sup>9</sup>

The real impact of intranidal aneurysms on the hemorrhagic presentation is difficult to verify. The AVM nidus is a complex

arrangement of pouches, fistulas, and interconnected circuitry. When an operation is performed shortly after a hemorrhage, venous pseudoaneurysms are encountered as areas of venous dilations, partially filled with thrombus, and indicate the site of rupture at the venous side of shunting.

### Pathogenesis and Demographics

The pathogenesis of IAs in the setting of AVMs is not fully understood. Development of IAs may be related to hemodynamic factors dictated by the presence of shunting in the AVM nidus. This theory is supported by the observation that most aneurysms are located on proximal arteries hemodynamically connected to the AVM nidus. Furthermore, prenidial aneurysms are more frequently encountered in high-flow AVMs and increase in incidence with increasing patient age, a finding that

suggests that their nature may be acquired and their formation, the result of the long-term effects of increased flow requirements. Similarly, it is common for prenidial IAs to regress after AVM obliteration.<sup>6</sup>

Only a fraction of patients with AVMs have IAs; therefore, their formation is postulated to be the result of a complex interaction of flow-related factors, host-specific characteristics, and genetic predisposition.<sup>7</sup> In particular, infratentorial AVMs have been shown to have a higher incidence of associated IAs, hemorrhagic presentation, and unfavorable outcomes.<sup>3,4</sup> In a recent study, AVMs supplied by the posterior circulation, of which 72% were perfusing supratentorial malformations, were found to be more commonly associated with IAs. This finding was suggested to be the result of the interaction between the increased hemodynamic stress due to the presence of the malformation itself and greater peak systolic pressure within the vertebrobasilar system, compared with the anterior circulation.<sup>10</sup> Furthermore, in a comparison of AVM supplying arteries with and without IAs, feeder artery diameter was found to be smaller in feeders with aneurysms, despite similarly high flows on quantitative MR angiography. Arteriovenous malformation feeders with IAs may therefore represent a subgroup in which vessel remodeling cannot compensate for increased blood flow.<sup>11</sup>

On the contrary, in a study that quantified transit times through the AVM nidus as a surrogate of altered hemodynamics, investigators did not find an association of IAs with alterations in AVM hemodynamics. Only a history of prior hemorrhage was shown to correlate with abnormal transit times, leading the authors to conclude that the hemorrhage itself may cause hemodynamic changes and not the other way around. Most interesting, changes in AVM hemodynamics were found to persist long after hemorrhage and did not decrease with time.<sup>12</sup>

The reported incidence of IAs associated with AVMs varies considerably among different studies (2.7%–58%).<sup>13</sup> In a recent meta-analysis on the natural history of brain AVMs, the incidence

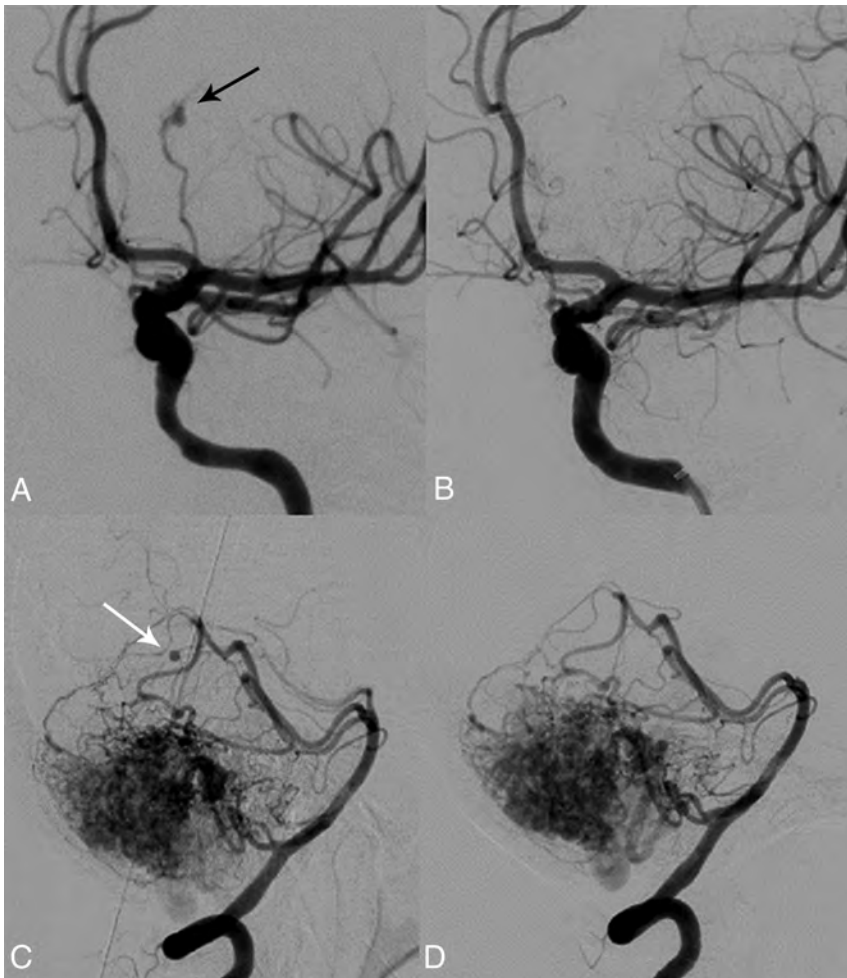


**FIG 2.** A 46-year-old woman with loss of consciousness and right hemiparesis due to an intracerebral hemorrhage in the left thalamus. Conventional angiography (oblique view) reveals a pseudoaneurysm (*black arrow*) of a left posterior communicating artery branch that was treated with *N*-butyl cyanoacrylate embolization (A). Complete pseudoaneurysm obliteration after endovascular treatment was achieved (B). Spontaneous regression of a pseudoaneurysm (*white arrow*) associated with a branch of the right superior cerebellar artery is noted in a 74-year-old woman with subarachnoid hemorrhage centered in the right ambient cistern (C and D).

of IAs was reported to be 18%.<sup>14</sup> A higher incidence of IAs in infratentorial AVMs has also been described.<sup>6,15,16</sup> Discrepancies in the actual incidence are likely multifactorial, including patient population, use of superselective angiography, and the inclusion of intranidal aneurysms.<sup>17</sup> Intranidal aneurysms may, in fact, be visualized during embolization procedures as nidus obliteration progresses. In fact, according to one study, the interrater reliability for the diagnosis of coexisting aneurysms in patients with AVMs was only 40%.<sup>18</sup> Finally, in the prospective A Randomized Trial of Unruptured Brain AVMs (ARUBA) involving 39 clinical sites in 9 countries, the incidence of AVM-associated (defined as flow-related and located on an AVM feeding artery or intranidal) and unrelated IAs was 16.1% and 4.9%, respectively, in a series of 223 patients with treated and untreated unruptured AVMs.<sup>19</sup>

#### Natural History

In ARUBA, the spontaneous annual hemorrhage rate of previously unruptured AVMs was found to be 2.2%.<sup>19</sup> Earlier reports

similarly estimated the risk of rupture at 3% per year, while the rehemorrhage rate was 6%–15% for the first year, and thereafter, it approximated the risk of hemorrhage of previously unruptured AVMs.<sup>14,20</sup>

It is commonly cited that the presence of IAs in patients with AVMs is associated with an increased risk of hemorrhage.<sup>4,6,7,14,21–23</sup> In their meta-analysis, Gross and Du<sup>14</sup> calculated that the presence of IAs increased the risk of hemorrhagic presentation by a factor of 1.8. Unrelated aneurysms, because they seem to be randomly associated with AVMs, exhibit a risk of hemorrhage similar to that of saccular aneurysms in the general population, and their presence does not appear to affect the risk of hemorrhage from the AVM. Certain authors have suggested that prenidal aneurysms are more likely to present with hemorrhage compared with intranidal aneurysms,<sup>7,20</sup> while others have found that distal flow-related and intranidal aneurysms that are immediately adjacent to the site of arteriovenous shunting may be more prone to rupture, given the higher flow, pressure, and shear stress on the vessel wall.<sup>8</sup> Finally, the presence of venous ectasia has been found to be inversely related to the risk of hemorrhage, probably reflecting a protective adaptive mechanism that may become more prevalent in older patients.<sup>24</sup>

In a landmark study of patients with unruptured AVMs seen at the Mayo Clinic between 1974 and 1985, the risk of hemorrhage among patients with a coexisting, originally unruptured AVM

and IA was 7% at 1 year compared with 3% among those with an AVM alone. This higher risk of hemorrhage persisted at 5 years in patients with AVMs and IAs (7%/year) compared with patients with isolated AVMs (1.7%/year).<sup>2</sup>

On the contrary, the independent association between coexisting IAs in patients with AVMs and presentation with hemorrhage, compared in 2 tertiary referral centers in the United States, was found to differ significantly. Despite sharing remarkably similar AVM features, initial presentation with intracerebral hemorrhage was associated with a coexisting aneurysm in one center, but not in the other. In fact, an opposite trend was noted in the latter center, where an IA associated with the AVM was less likely to be detected in patients initially presenting with intracerebral hemorrhage. This finding underscores the limitations of drawing conclusions from referral-based studies and suggests the potential pitfall of including aneurysm presence in AVM risk-stratification models for patient management and clinical trials.<sup>25</sup>

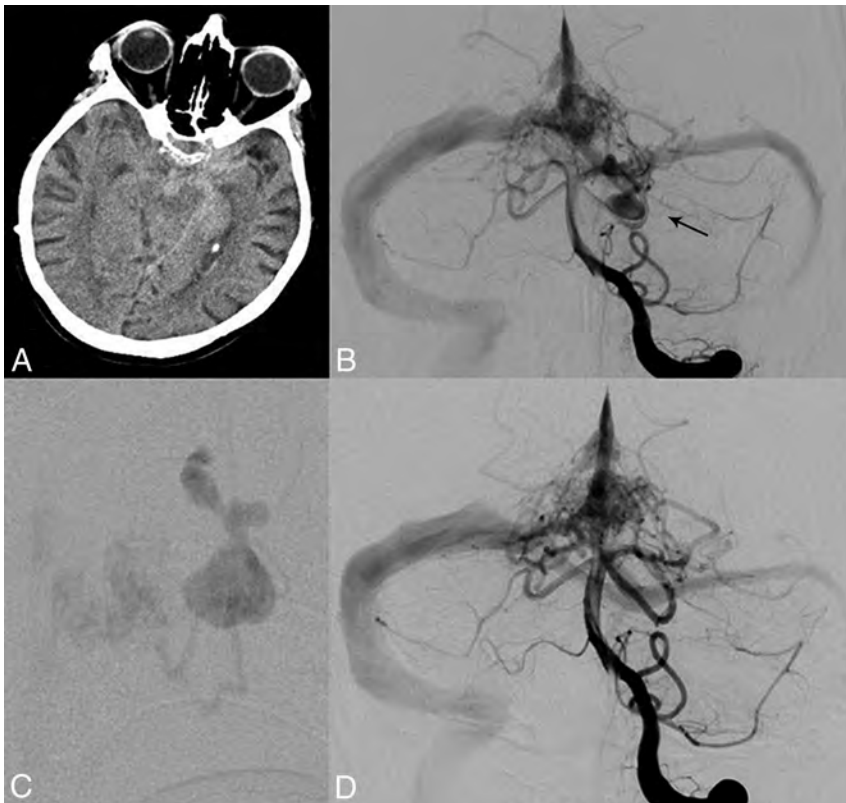


**FIG 3.** A 70-year-old man with subarachnoid hemorrhage centered in the prepontine cistern (A). Left vertebral artery angiography (anteroposterior view) reveals an AVM of the region of the torcula and a large irregular aneurysm of the left superior cerebellar artery (B and C). The presence of isolated subarachnoid hemorrhage suggests the aneurysm as the source of hemorrhage. The aneurysm was treated selectively with *N*-butyl cyanoacrylate embolization as noted on postprocedural angiography (anteroposterior view) (D), while the treatment of the AVM nidus was deferred.

### Treatment

No consensus currently exists on the treatment of IAs associated with AVMs. While strong evidence may be lacking, advances in microsurgery, endovascular technology and technique, and radiosurgery have expanded the availability of treatment options. Treatment options need to be weighed to optimize the risk-to-benefit profile of the intervention based on the expertise and experience of the institution and treating physicians. Reported AVM treatment complication rates are not negligible for surgery (29%; range, 1.5%–54%), endovascular treatment (25%; range, 7.6%–55%), and radiosurgery (13%; range, 0%–63%) as observed in a systematic review of ruptured and unruptured AVMs<sup>26</sup> and in the ARUBA study of previously unruptured AVMs (30.7% complication rate for all treatment modalities).<sup>19</sup>

Any consideration of the treatment of IAs associated with AVMs needs to establish the exact site of rupture in the event of hemorrhagic presentation. The anatomic relationship of IAs and the AVM nidus should be carefully considered when treatment plans are considered. It is of utmost importance to understand whether the source of hemorrhage is the AVM nidus or the IA itself. The diagnosis is made on the basis of clinical experience and inference, and it becomes clearer the farther the hemorrhage is spatially related to the nidus on the head CT scan obtained at presentation.<sup>17</sup> Correlations can then be made with angiographic

studies, including superselective injections. Subarachnoid hemorrhage without associated intracerebral hemorrhage strongly implicates the IA as the possible source of the bleed (Fig 3). Similarly, the presence of a focal hematoma adjacent to the IA with secondary extension to the subarachnoid space implicates the IA as the source of rupture. In the presence of intracerebral hemorrhage with or without SAH, the identification of the hemorrhage epicenter in relation to the nidal angioarchitecture may offer clues to the source of hemorrhage, and dynamic CT performed in the angiography suite may further elucidate the spatial relationship between IAs associated with AVMs and the hemorrhage.<sup>27</sup>

If the IA is considered the source of hemorrhage, then the aneurysm should be treated as early as safely possible following the same treatment criteria for isolated saccular arterial aneurysms. If the aneurysm is located in proximity to the AVM and the AVM itself can be resected surgically, both lesions should be treated simultaneously in a single operation. Proximal flow-related aneurysms should be treated with either surgical or endovascular modalities, depending on their location, morphology, and operator experience.<sup>6,13,28</sup> Treatment of the associated AVM may be postponed for a

later time and can be either surgical, endovascular, radiosurgical, or even conservative (Fig 4). In cases in which the bleeding source is an associated aneurysm and AVM treatment is not indicated, endovascular or surgical closure of the aneurysm alone should be pursued. However, a high rate of aneurysm recurrence has been noted in endovascularly treated IAs without definitive nidal obliteration.<sup>6</sup>

If the source of the hemorrhage is a pseudoaneurysm arising from a small perforating branch, then either prompt treatment or close imaging follow-up should be pursued. Pseudoaneurysms lack a true wall and often display a “dynamic course” in the acute phase with early expansion and rerupture or even spontaneous regression. If the pseudoaneurysm is treated, the AVM can then be treated electively later because the source of hemorrhage has been secured. Endovascular techniques offer a particular advantage when intravascular access can be safely achieved in the vicinity of the pseudoaneurysm, given that most pseudoaneurysms are located on perforating arteries, which can be difficult to reach with an operation.

If the source of hemorrhage has been determined to arise from the AVM or from an intranidal aneurysm, then treatment may not be urgent because the risk of early rerupture is relatively low unless impaired venous outflow of the nidus is present. The lesion can be managed conservatively initially, and an an-



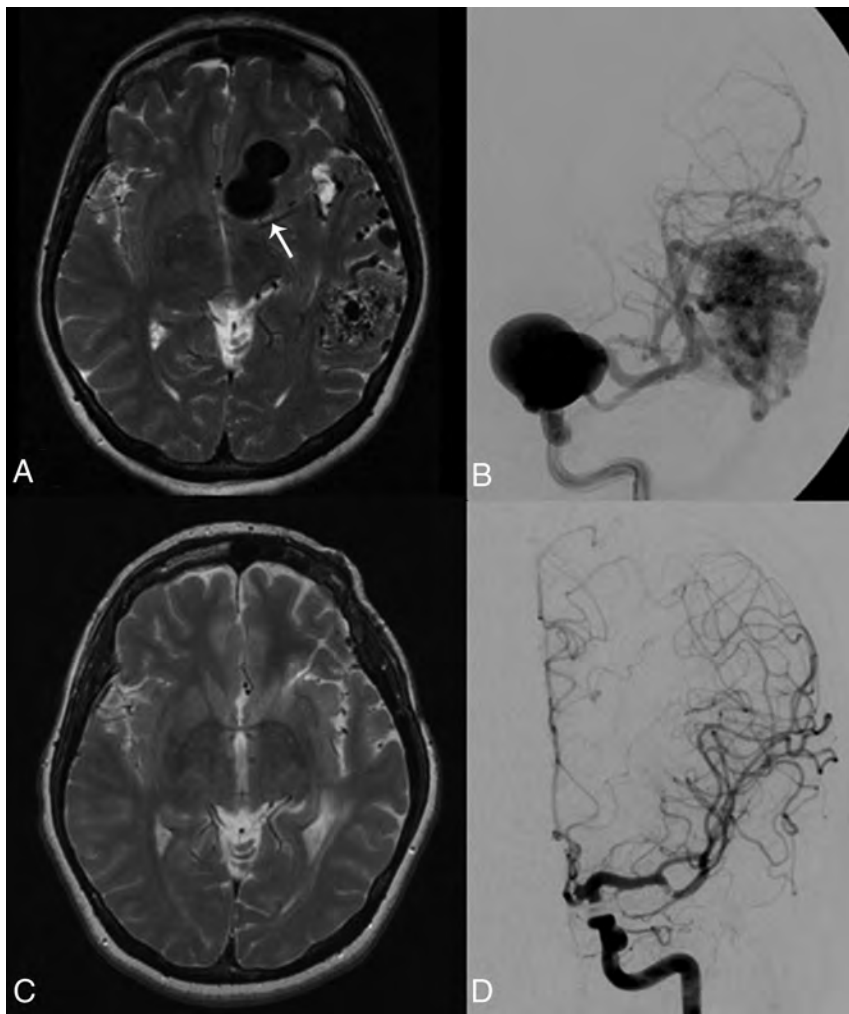


**FIG 4.** A 42-year-old woman who lost consciousness while dancing. MR imaging (T2 axial) reveals a large flow void suggestive of a giant left aneurysm (*arrow*) and an associated left temporal lobe AVM (A). Conventional angiography (anteroposterior projection) confirmed a giant left ICA aneurysm and the left temporal AVM (B). The aneurysm was treated with surgical clipping, and the patient underwent stereotactic radiosurgery for the AVM. Follow-up MR imaging (T2 axial) (C) and conventional angiography (D) 6 years later show complete exclusion of the aneurysm and obliteration of the AVM.

giogram can be obtained after 4–6 weeks. Then, if the balance between the risks of any intended procedure and the risk of the natural history of the lesion are favorable, the management of the AVM and the intranidal aneurysm can proceed as an elective case. Preoperative embolization that targets high-flow fistulas and associated prenidial and intranidal IAs before definitive surgery is a valid option, though its effectiveness has not been firmly established. It is unknown at present whether the strategy of palliative embolization of the nidus/feeding pedicle supplying a segment of the AVM harboring an intranidal aneurysm indeed protects the patient from recurrent hemorrhage.<sup>29</sup>

The treatment goal of associated IAs in patients with unruptured AVMs follows concepts similar to those applied to the treatment of unruptured incidental aneurysms in general. However, it has been shown that distal flow-related aneurysms may decrease in size or even disappear after treatment of the AVM. In a study on the course of untreated aneurysms associated with

AVMs after definitive AVM treatment, 80% of distal flow-related aneurysms regressed after complete AVM occlusion. There were no episodes of SAH from a flow-related aneurysm after AVM obliteration after a follow-up of 7.4 years. On the other hand, of 23 proximal flow-related aneurysms, 78.3% were unchanged, 17.4% were smaller, and only 4.3% were angiographically obliterated after AVM treatment.<sup>7</sup> Because distal flow-related IAs are likely to regress or decrease in size after complete AVM treatment, conservative management of small distal aneurysms may be considered if the AVM is treated. Furthermore, the rate of hemorrhage after radiosurgery in patients with associated IAs may be significantly increased (28% at 5 years versus 2.6%); therefore, endovascular or microsurgical treatment of IAs should be considered in patients whose AVM nidus is targeted with radiosurgery.<sup>30</sup>

## CONCLUSIONS

Aneurysms associated with intracranial AVMs may confer an increased risk of hemorrhagic presentation. Treatment decisions are based primarily on clinical presentation and the relationship of the IA to the AVM nidus.<sup>27</sup> In a hemorrhagic clinical presentation, it is critical to establish the source of hemorrhage. If a prenidial aneurysm is considered the source of the hemorrhage, then it should be treated in an expedited fashion, following the same treatment criteria for isolated ruptured saccular aneurysms,

with either surgical or endovascular modalities. If the source of the hemorrhage is suspected to arise within the AVM nidus, however, treatment can be delayed because the risk of early rehemorrhage from a ruptured AVM is relatively low as long as there is no severe venous outflow obstruction restricting nidal drainage. In cases in which the source of the hemorrhage is a pseudoaneurysm arising from a small perforating branch, either prompt treatment or close imaging follow-up should be pursued. Treatment of associated IAs in most patients with unruptured AVMs should follow the same principles applied to isolated unruptured aneurysms in the general population. Distal flow-related aneurysms have been shown to regress after definitive AVM treatment; thus, conservative management of small distal flow-related aneurysms may be considered after definitive AVM treatment.

Disclosures: Giuseppe Lanzino—UNRELATED: Consultancy: Covidien/Medtronic.\*  
\*Money paid to the institution.

## REFERENCES

1. Stapf C, Mohr JP, Pile-Spellman J, et al. **Concurrent arterial aneurysms in brain arteriovenous malformations with haemorrhagic presentation.** *J Neurol Neurosurg Psychiatry* 2002;73:294–98 CrossRef Medline
2. Brown RD Jr, Wiebers DO, Forbes GS. **Unruptured intracranial aneurysms and arteriovenous malformations: frequency of intracranial hemorrhage and relationship of lesions.** *J Neurosurg* 1990;73:859–63 CrossRef Medline
3. Abla AA, Nelson J, Rutledge WC, et al. **The natural history of AVM hemorrhage in the posterior fossa: comparison of hematoma volumes and neurological outcomes in patients with ruptured infra- and supratentorial AVMs.** *Neurosurg Focus* 2014;37:E6 CrossRef Medline
4. da Costa L, Thines L, Dehdashti AR, et al. **Management and clinical outcome of posterior fossa arteriovenous malformations: report on a single-centre 15-year experience.** *J Neurol Neurosurg Psychiatry* 2009;80:376–79 Medline
5. Gross BA, Ropper AE, Du R. **Vascular complications of stereotactic radiosurgery for arteriovenous malformations.** *Clin Neurol Neurosurg* 2013;115:713–17 CrossRef Medline
6. Platz J, Berkefeld J, Singer OC, et al. **Frequency, risk of hemorrhage and treatment considerations for cerebral arteriovenous malformations with associated aneurysms.** *Acta Neurochir (Wien)* 2014;156:2025–34 CrossRef Medline
7. Redekop G, Terbrugge K, Montanera W, et al. **Arterial aneurysms associated with cerebral arteriovenous malformations: classification, incidence, and risk of hemorrhage.** *J Neurosurg* 1998;89:539–46 CrossRef Medline
8. D'Aliberti G, Talamonti G, Cenzato M, et al. **Arterial and venous aneurysms associated with arteriovenous malformations.** *World Neurosurg* 2015;83:188–96 CrossRef Medline
9. Garcia-Monaco R, Rodesch G, Alvarez H, et al. **Pseudoaneurysms within ruptured intracranial arteriovenous malformations: diagnosis and early endovascular management.** *AJNR Am J Neuroradiol* 1993;14:315–21 Medline
10. Morgan MK, Alsahli K, Wiedmann M, et al. **Factors associated with proximal intracranial aneurysms to brain arteriovenous malformations: a prospective cohort study.** *Neurosurgery* 2016;78:787–92 CrossRef Medline
11. Shakur SF, Amin-Hanjani S, Mostafa H, et al. **Hemodynamic characteristics of cerebral arteriovenous malformation feeder vessels with and without aneurysms.** *Stroke* 2015;46:1997–99 CrossRef Medline
12. Illies T, Forkert ND, Saering D, et al. **Persistent hemodynamic changes in ruptured brain arteriovenous malformations.** *Stroke* 2012;43:2910–15 CrossRef Medline
13. Flores BC, Klinger DR, Rickert KL, et al. **Management of intracranial aneurysms associated with arteriovenous malformations.** *Neurosurg Focus* 2014;37:E11 CrossRef Medline
14. Gross BA, Du R. **Natural history of cerebral arteriovenous malformations: a meta-analysis.** *J Neurosurg* 2013;118:437–43 CrossRef Medline
15. Westphal M, Grzyska U. **Clinical significance of pedicle aneurysms on feeding vessels, especially those located in infratentorial arteriovenous malformations.** *J Neurosurg* 2000;92:995–1001 CrossRef Medline
16. Lv X, Li Y, Yang X, et al. **Characteristics of arteriovenous malformations associated with cerebral aneurysms.** *World Neurosurg* 2011;76:288–91 CrossRef Medline
17. Kim EJ, Halim AX, Dowd CF, et al. **The relationship of coexisting extranidal aneurysms to intracranial hemorrhage in patients harboring brain arteriovenous malformations.** *Neurosurgery* 2004;54:1349–57; discussion 1357–58 CrossRef Medline
18. Al-Shahi R, Pal N, Lewis SC, et al; AVM Observer Agreement Study Group. **Observer agreement in the angiographic assessment of arteriovenous malformations of the brain.** *Stroke* 2002;33:1501–08 CrossRef Medline
19. Mohr JP, Parides MK, Stapf C, et al; international ARUBA investigators. **Medical management with or without interventional therapy for unruptured brain arteriovenous malformations (ARUBA): a multicentre, non-blinded, randomised trial.** *Lancet* 2014;383:614–21 CrossRef Medline
20. Elhammady MS, Aziz-Sultan MA, Heros RC. **The management of cerebral arteriovenous malformations associated with aneurysms.** *World Neurosurg* 2013;80:e123–29 CrossRef Medline
21. Marks MP, Lane B, Steinberg GK, et al. **Hemorrhage in intracerebral arteriovenous malformations: angiographic determinants.** *Radiology* 1990;176:807–13 CrossRef Medline
22. Thompson RC, Steinberg GK, Levy RP, et al. **The management of patients with arteriovenous malformations and associated intracranial aneurysms.** *Neurosurgery* 1998;43:202–11; discussion 211–12 CrossRef Medline
23. Turjman F, Massoud TF, Vinuela F, et al. **Aneurysms related to cerebral arteriovenous malformations: superselective angiographic assessment in 58 patients.** *AJNR Am J Neuroradiol* 1994;15:1601–05 Medline
24. Hettis SW, Cooke DL, Nelson J, et al. **Influence of patient age on angioarchitecture of brain arteriovenous malformations.** *AJNR Am J Neuroradiol* 2014;35:1376–80 CrossRef Medline
25. Halim AX, Singh V, Johnston SC, et al; UCSF BAVM Study Project. **Brain Arteriovenous Malformation. Characteristics of brain arteriovenous malformations with coexisting aneurysms: a comparison of two referral centers.** *Stroke* 2002;33:675–79 CrossRef Medline
26. van Beijnum J, van der Worp HB, Buis DR, et al. **Treatment of brain arteriovenous malformations: a systematic review and meta-analysis.** *JAMA* 2011;306:2011–19 CrossRef Medline
27. Gardenghi B, Bortolotti C, Lanzino G. **Aneurysms associated with arteriovenous malformations.** *Contemp Neurosurg* 2014;36:1–6 CrossRef
28. Pötin M, Ross IB, Weill A, et al. **Intracranial arterial aneurysms associated with arteriovenous malformations: endovascular treatment.** *Radiology* 2001;220:506–13 CrossRef Medline
29. Crowley RW, Ducruet AF, McDougall CG, et al. **Endovascular advances for brain arteriovenous malformations.** *Neurosurgery* 2014;74(suppl 1):S74–82 CrossRef Medline
30. Kano H, Kondziolka D, Flickinger JC, et al. **Aneurysms increase the risk of rebleeding after stereotactic radiosurgery for hemorrhagic arteriovenous malformations.** *Stroke* 2012;43:2586–91 CrossRef Medline

# Current Procedural Terminology: History, Structure, and Relationship to Valuation for the Neuroradiologist

 T.M. Leslie-Mazwi,  J.A. Bello,  R. Tu,  G.N. Nicola,  W.D. Donovan,  R.M. Barr, and  J.A. Hirsch

## ABSTRACT

**SUMMARY:** The year 1965 was critical for US health care policy. In that year, Medicare was created as part of the Social Security Act under President Lyndon B. Johnson after several earlier attempts by Presidents Franklin Roosevelt and Harry Truman. In 1966, the American Medical Association first published a set of standard terms and descriptors to document medical procedures, known as Current Procedural Terminology, or CPT. Fifty years later, though providers have certainly heard the term “CPT code,” most would benefit from an enhanced understanding of the historical basis, current structure, and relationship to valuation of Current Procedural Terminology. This article will highlight this evolution, particularly as it relates to neuroradiology.

**ABBREVIATIONS:** AMA = American Medical Association; ASNR = American Society of Neuroradiology; CMS = Centers for Medicare and Medicaid Services; CPT = Current Procedural Terminology; RUC = AMA/Specialty Society Relative Value Scale Update Committee; RVU = relative value units

President Lyndon B. Johnson’s “Great Society” programs included the creation of Medicare in 1965, which, among its many facets, highlighted the need for efficient and effective determination of physician reimbursement. Consistent and accurate reimbursement requires a common language of medical procedures. The American Medical Association (AMA) plays a unique and sometimes underappreciated physician-centric role in the determination of provider reimbursement. In 1965, the AMA recognized the need for common language and helped create the Current Procedural Terminology (CPT) system to describe medical services and procedures.

The first edition of CPT was published in 1966 and, for the most part, was focused on surgery. As a result, neuroradiology had little representative coding. At that time, 4-digit codes were used. The second edition, published in 1970, expanded each code to 5 digits, with the 70000–79999 code series representing radiology. In the mid- and late 1970s, the third and fourth editions of CPT were released. Not surprisingly, each version was progres-

sively more detailed, in line with the increasingly complex health care system. This evolution has continued since. In 1983, the predecessor of the Centers for Medicare and Medicaid Services (CMS) merged CPT into the Healthcare Common Procedure Coding System, which historically had performed a similar function to CPT. Just as the International Classification of Diseases published by the World Health Organization maintains an updated classification of medical conditions, CPT maintains an updated classification of medical procedures.<sup>1-3</sup>

Thirty years after the creation of the CPT system, the Kennedy-Kassebaum Act, better known as the Health Insurance Portability and Accountability Act of 1996, pushed the legacy of CPT forward.<sup>4</sup> That legislation required the Department of Health and Human Services to set up standards for the electronic transaction of health care information, including code sets.

As a result of the Health Insurance Portability and Accountability Act, the AMA decided to take a detailed look at the CPT system to determine whether the then-30-year-old system was staying relevant. This analysis resulted in the establishment of the CPT-5 project. CPT was expanded very meaningfully with new nomenclature that included tracking new procedures and services. In addition, specific reporting measures that could be used in performance-based payment were built into CPT. With the expansion that resulted from the Health Insurance Portability and Accountability Act, the CMS opted to formally incorporate CPT codes in Medicare claims processing. In 2000, CPT became the national coding standard for reporting medical services and procedures.<sup>5</sup> The AMA continues to recognize the importance of maintaining an updated and relevant CPT coding system and

Received April 2, 2016; accepted after revision May 9.

From the Neuroendovascular Program (T.M.L.-M., J.A.H.), Massachusetts General Hospital, Boston, Massachusetts; Montefiore Medical Center (J.A.B.), Albert Einstein College of Medicine, Bronx, New York; Progressive Radiology (R.T.), The George Washington University, Falls Church, Virginia; Hackensack University Medical Center (G.N.N.), Hackensack, New Jersey; Norwich Diagnostic Imaging Associates (W.D.D.), Norwich, Connecticut; and Mecklenburg Radiology Associates P.A. (R.M.B.), Charlotte, North Carolina.

Please address correspondence to Thabele M. Leslie-Mazwi, Neuroendovascular Program, Massachusetts General Hospital, Harvard Medical School, Boston, MA 02114; e-mail: tleslie-mazwi@mgh.harvard.edu; @JoshuaAHirsch

<http://dx.doi.org/10.3174/ajnr.A4863>

does so through resolutions in its House of Delegates, active physician involvement in systematic review of existing codes, retirement of obsolete codes, and authorship of new codes to reflect changes and innovations in medical practice. The CPT codebook remains a living document that undergoes annual updates. For example, the 2016 edition offers over 350 code changes, 140 of which are new, 134 revised, and 93 deleted.<sup>6</sup> Therefore, CPT is a critical component in the provision of health care in 2016 and into the future.

### **CPT COMMITTEE CONSTRUCT**

There are 2 key committees that constitute what is commonly thought of as “CPT”: the CPT Editorial Panel and the CPT Advisory Committee. The CPT Editorial Panel presides over the development of new and revised codes and is important in the maintenance of code sets.<sup>7</sup> This panel includes physicians and a variety of other stakeholders, including representatives from CMS. The CPT Editorial Panel meets 3 times per year. In contrast, the CPT Advisory Committee comprises representatives of constituent societies from the AMA House of Delegates. This is the mechanism through which the American Society of Neuroradiology (ASNR) is represented. The Advisory Committee assists the CPT Editorial Panel by proposing code set changes and, crucially, by providing insights into coding proposals submitted by other interested stakeholders (eg, other societies, insurance carriers, and industry vendors).<sup>7</sup>

### **CPT CODE CATEGORIES**

The extensive codes in the CPT are divided into 3 categories. Category I codes constitute the CPT codes common in clinical practice. These codes require US Food and Drug Administration approval for any drugs or devices, must have demonstrated clinical efficacy supported by the peer-reviewed literature, and must be commonly practiced by multiple physicians in the United States. Category II codes are used to report quality performance initiatives and are designed to simplify participation in quality measures by diminishing administrative burdens such as medical record review. Category II codes cannot substitute for Category I codes. They are designed to facilitate data collection, tracking of performance measures, and compliance with state or federal law, but are not to be used for coding services or procedures that are ultimately billed. In keeping with the explosive increase in Physician Quality Reporting System measures, the number of category II codes is increasing.<sup>8</sup> Category III codes were created in 2001 to track new or experimental procedures and technologies. These temporary codes are characterized with an alphanumeric descriptor (eg, 3456T). Data accumulated by these tracking codes can aid in the US Food and Drug Administration approval process. Category III codes do not need to meet the evidentiary basis that Category I codes require. Category III codes are not assigned a professional work value, and payment for these services, if any, is at the discretion of Medicare and private payers. Category III codes are by definition temporary and are only approved for a 5-year period; this can be extended once. If warranted by experimental evidence, a Category III code can be converted into a Category I code before the expiration of the initial or renewal term. If the procedure has not been proved effective by that point, the code is allowed to

expire. The advisors and panel members use standard, rigorous protocols for determining medical evidence. CT perfusion imaging is an example of a current Category III code.<sup>9,10</sup>

### **RELATIONSHIP TO THE AMA/SPECIALTY SOCIETY RELATIVE VALUE SCALE UPDATE COMMITTEE**

Medicare has gone through multiple iterations to arrive at its current payment methodology. During the administration of President George H.W. Bush, as a result of the Omnibus Budget Reconciliation Act of 1989, CMS started to use a system of relative value units (RVUs) to calculate the cost for providing physician work, which evolved into the framework of a resource-based relative value scale.<sup>11</sup> The AMA recruited physician input into that system. In 1992, the AMA/Specialty Society Relative Value Scale Update Committee (RUC) was convened. Codes that are established through CPT are then reviewed and debated at the RUC, which recommends suggested RVUs to CMS. Through the American College of Radiology, the radiology community has benefited from continuous representation at the RUC since this committee's inception. The ASNR gained a seat in the AMA House of Delegates in 1996 and has actively participated in the CPT and RUC meetings since then. Continued participation requires that a sufficient percentage of ASNR members maintain active AMA membership.<sup>12-14</sup>

### **RELATIVITY ASSESSMENT WORKGROUP**

The RUC began its work in the early 1990s recommending relative values for CPT codes. Explicit in its charter was that a review of the entire resource-based relative value scale needed to be performed every 5 years. After the third such review in 2007, an ongoing review process was created at the urging of CMS. The “Five-Year Review Committee” was renamed the “Relativity Assessment Workgroup.” Triggers leading to review of “potentially misvalued” codes varied; some of the screening criteria included increasing utilization of a code; change in site of service; change in the physician specialty reporting the code; or CPT codes whose valuation lacked a verifiable data trail.<sup>15</sup>

A Relativity Assessment Workgroup screen for “Codes Performed Together” has been particularly noteworthy for radiologists because many procedures had historically been reported by using a granular, building-block method known as component coding. The underlying premise of this screen is that CPT codes, which are typically reported together on a single Medicare patient on the same day of service (ie, CT abdomen and CT pelvis), may have efficiencies that should be accounted for in determining overall relative value. This screen has expanded in importance and scope over time. Whereas the original filter was set at codes reported together 95% of the time, it is now triggered when codes are performed together more than 50% of the time.<sup>16</sup>

CMS embraced the work of the Relativity Assessment Workgroup with the creation of its own screening processes for “potentially misvalued” codes; for instance, naming codes with high total expenditure. These screens frequently have targeted radiology, given the high technical component costs of advanced imaging such as PET, MR imaging, and CT. A new list of screened codes is published every July in the Medicare Physician Fee Schedule Proposed Rule as part of CMS's annual rulemaking process. Regard-

less of why a code is “caught” by a screen or whose screen “caught” the code (Relativity Assessment Workgroup or CMS), the specialty societies are obligated to respond to the inquiry and formulate a strategy for proving appropriate valuation of both technical and professional components of procedures.

### **WHAT HAPPENS WHEN A CPT CODE IS CAUGHT BY A RELATIVITY ASSESSMENT WORKGROUP SCREEN OR DEEMED POTENTIALLY MISVALUED BY CMS?**

Once a code has been labeled as potentially misvalued, specialty societies declaring an interest in establishing an RVU for the procedure are given the opportunity to provide evidence that the code values captured by the screen should remain untouched (ie, that they are valued appropriately or because a confounding factor would create downstream consequences if the code or code family were revised or revalued). If those arguments fail to convince the Relativity Assessment Workgroup or CMS, the next course of action is either revaluing the services via survey or revision of the CPT nomenclature or code structure (often via “bundling” of multiple discrete codes into more complex, comprehensive codes) via referral back to CPT.

CMS recognizes that these various filtering screens could lead to rank-order anomalies within groups of related codes. This has led to the loose concept of code families, which the AMA and CMS have mostly left to the specialty societies to define. The code family concept is a protective mechanism to prevent rank-order anomalies from occurring when valuing or revaluing a service. Because the various screens described above may flag some but not all procedures in a family, CMS mandates that all codes in a family that relate to the code picked up in the screen or codes that are newly created must be analyzed together. An option specialty societies can choose to take is recommending that a code or family be referred back to CPT—in other words, taking the codes off the RUC table for the time being, allowing the specialty societies to revise the code structure and definitions—before presenting them to the RUC for valuation. The ASNR actively represents neuroradiology interests (from the esoteric to the mundane) at CPT. It is noteworthy but not widely appreciated that ASNR involvement in the CPT and RUC processes is dependent upon threshold membership in the AMA.

We will explore how the changes to the CPT occur through several real-life examples below.

### **EXAMPLES OF RECENT ASNR CODING EFFORTS**

#### ***Carotid Angiography: Procedure Codes Were Bundled with Radiologic Supervision and Interpretation Codes***

In 2010, numerous codes related to carotid and cerebral angiography—the procedural codes describing catheterization and injection and the codes describing radiologic supervision and interpretation codes—were identified via the Codes Performed Together Screen. Per above, the entire family of codes needed to be revised to prevent possible rank-order anomalies. The new code bundle needed to include both the procedural and interpretive components. The CPT Editorial Panel, with input from multiple constituent societies, including ASNR, approved a new series of codes for these services in 2012. These new codes, which bundled the procedure codes with the supervision and interpre-

tion codes, then were sent to the RUC for valuation recommendations.<sup>17</sup>

This code-bundling process resulted in a significant drop in RVUs and, therefore, physician reimbursement, beginning in January 2013. For example: a single vessel-selective diagnostic angiogram of the right internal carotid artery would have a CMS value of 7.60 RVUs in 2012 with standard component coding (including typical reductions for second and subsequent procedures); the single bundled code for that procedure and interpretation has been valued at 6.50 RVUs since 2013, a reduction of 15%. A standard 4-vessel angiogram previously valued at 18.22 RVUs is now 14.25 RVUs, a reduction of 22%.<sup>17</sup>

The negative impact of code bundling on diagnostic radiology was probably most severely felt when bundled codes for CT of abdomen and CT of pelvis were mandated by CMS, also based on the Codes Performed Together Screen. Using the intravenous contrast-enhanced procedures for this example (74160 and 72193), the 2 codes separately reported in 2011 and before were valued at 2.42 RVUs; the combined code 74177 is valued at 1.82 RVUs, a reduction of 25%.

Although beyond the scope of this article, practice expense reimbursement is also affected by code bundling, mainly because of reductions in room times, technologist labor, and nurse labor.

#### ***Myelography: Procedure Code Was Bundled with Radiologic Supervision and Interpretation Codes***

Another classic procedure performed by neuroradiologists was caught in the Codes Performed Together Screen because of the near-universal association between injection and supervision and interpretation codes. ASNR and the American College of Radiology revised the code set and presented the new bundled codes (as well as the original stand-alone codes) to the RUC for valuation. CPT 2015 introduced 4 new bundled codes for myelography in the setting of the same physician performing the injection, supervising the procedure, and interpreting the images. If separate providers perform the procedure and do the interpretation, then the nonbundled original codes are used; hence, the existing codes were maintained (ironically adding more codes to the myelography code set).

It is important to emphasize that the CPT descriptor for myelography includes a thorough radiographic (plain film) examination of the spine after intrathecal injection of iodinated contrast media, involving assessment of static structures, such as the spinal canal and each exit foramen, and real-time assessment of contrast injection and its flow dynamics under direct visualization.<sup>18</sup> It is not appropriate to code for a formal myelogram when x-ray imaging is simply used to document the intrathecal location of needle placement and contrast injection.

Coincidentally, in the same year that ASNR was revising the myelography code set and presenting it to the RUC, the National Correct Coding Committee proposed adding an edit that would deny billing of postmyelography CT on the same day as a radiographic myelogram, independent of the number of providers. CMS raised concerns that myelography and CT with intrathecal contrast media were duplicative procedures. Stakeholders led by the neuroradiology subspecialty societies provided clarification to CMS, which was accepted, and the edit was not pursued further

## Examples of comparative code terminology from various coding sources<sup>20,21</sup>

Source	Vertebroplasty (Injection Only)	Vertebral Augmentation (Injection and Mechanical Device)
ACR	Vertebroplasty, acrylic vertebroplasty	Balloon kyphoplasty, balloon-assisted vertebroplasty
AMA CPT	Percutaneous vertebroplasty	Percutaneous vertebroplasty augmentation including cavity creation using mechanical devices, kyphoplasty
FDA	Vertebroplasty	Kyphoplasty
CMS	Vertebroplasty	Kyphoplasty

**Note:**—ACR indicates American College of Radiology; FDA, US Food and Drug Administration.

beyond adding the -59 modifier when CT of the spine with contrast media is used with the myelography codes.<sup>18</sup>

### **Vertebral Augmentation: Procedure Code Was Bundled with Radiologic Supervision and Interpretation Codes**

Similar to myelography, the effects of bundling extended to the vertebral augmentation code family. The CPT/RUC Joint Workgroup recommended that the injection and interpretation codes for vertebroplasty and vertebral augmentation or sacral augmentation (sacroplasty) be bundled. In February 2014, the CPT Editorial Panel replaced the 8 Category I codes with 6 new comprehensive codes to bundle injection and imaging guidance/interpretation: 22510–22512 for vertebroplasty (cervicothoracic, lumbosacral, and each additional level) and 22513–22515 for kyphoplasty (thoracic, lumbar, and each additional level).

The sacral procedures that were previously coded as Category III codes (0200–01T) were revised to be included under lumbosacral vertebroplasty. Similarly, cervical vertebroplasty was revised to be coded as cervicothoracic. The language used in these procedures can be confusing for coders (Table), and we provide in the reference list a CPT Assistant article with language to help clarify the differences and provide historical context.<sup>19</sup>

### **Scoliosis Plain Film Series: Code Revision and Code Bundling**

The family of scoliosis plain film codes was identified as inconsistent with other plain film codes; some were descriptive of the views, whereas others were defined by the number of views. To reduce confusion, the codes were revised in October 2014 so that the scoliosis code family is now entirely defined by the number of views obtained: 1 view; 2 or 3 views; 4 or 5 views; and 6 or more views (72801, -82, -83, and -84, respectively). This standardized hierarchy and nomenclature is now in step with most other radiography code descriptors.<sup>20</sup>

### **Fetal MR Imaging: Creation of a New Code**

Historically, imaging of the fetus was reported by using an unlisted code or the pelvic MR imaging codes 72195–72197. After an e-mail from a member of the Society of Pediatric Radiology to the AMA, advisors from the ASNR, American College of Radiology, American Roentgen Ray Society, and Society of Pediatric Radiology jointly crafted a new coding proposal for fetal MR imaging to the CPT Editorial Panel in February 2015. The new fetal MR codes—“Magnetic resonance (eg, proton) imaging, fetal, including placental and maternal pelvic imaging when performed; single or first gestation” (74712) and an add-on code: “Magnetic resonance (eg, proton) imaging, fetal, including placental and maternal pelvic imaging when performed; each additional gestation (List separately in addition to code for primary procedure)” (74713)—were accepted into the CPT canon.

Having a discrete CPT code for fetal MR imaging allows members of specialty societies to articulate the differences in physician work and technical expense relative to standard pelvic MR imaging. While presenting to the RUC in April 2015, the societies’ advisors explained that unlike routine pelvic MR imaging, fetal MR imaging is complicated by continuous patient movement, complex anatomy, and intrinsic multiorgan evaluation.<sup>20</sup>

## **DOWNSTREAM CONSEQUENCES OF NEW OR REVISED CPT CODES**

Radiologic societies are cognizant of the downstream effect code revisions and code bundling has on the radiology community. Code bundling not only leads to revisions in Medicare payments, but also requires renegotiation of private insurance contracts. Occasionally, the new bundled service, which by default lacks the granularity of the individual parent codes, may not fully capture how a service is performed in the community. The less granular bundled code can lead to unintended confusion and inequities in the reported cost to perform the procedure.

A recent example of this confusion and lack of granularity is represented by a multiyear project to bundle conscious sedation and anesthesia services into a base procedure (ie, interventional radiology procedure, colonoscopy, etc), where the same physician performing the base procedure typically performs sedation. CMS and the RUC define “typical” as occurring greater than 50% of the time. If a service such as conscious sedation is typical, then it should not be billed separately and should be bundled into the base code being billed by the physician performing the procedure. Unfortunately, the loss of granularity makes it very difficult to bill anesthesia services or conscious sedation in atypical situations or when an anesthesiologist is required. It also leads to inequities in what was paid for when providing conscious sedation or anesthesia services, depending on what the base procedure code was and not on the actual service. This confusion has led to a new multiyear project of unbundling conscious sedation and anesthesia services from all previous base codes. This project provides an example of the unintended consequences and potential harms of bundling.

Developing or revising CPT codes not only requires substantial effort to accurately and appropriately define and categorize medical procedures, but also involves significant strategic considerations, diplomacy, and collaboration. Because code development at the CPT Editorial Panel leads directly to discussions of valuation at the RUC, it is important that the structure of new and revised medical procedure codes appropriately captures the imaging work performed by radiologists and neuroradiologists as part of those procedures. Different specialty societies may view the work of imaging differently in areas where overlap could exist, such as intraoperative MR imaging, functional MR imaging, and

carotid stent placement, or in non-neurologic codes such as CT colonography or coronary CTA. Accurately describing procedures in a way that fully captures the work of image guidance or interpretation and that allows for rapid technologic progress is a team effort and requires an open-minded, collaborative approach.

## CONCLUSIONS

CPT began 50 years ago as an effort to accurately report what was largely a group of surgical services and bill for them more precisely. The CPT system has grown in scope over the years and has seen variable granularity, reflecting the innovations of new procedures, changes in legacy technology, and retirement of obsolete approaches. More recent pressures have come in the form of bundling and code revisions by CMS and the AMA's RUC. An understanding of the CPT coding history and current direction is important as providers navigate these new waters of health care reimbursement.

Disclosures: Jacqueline Bello—*OTHER RELATIONSHIPS*: serves as the ASNR's Assistant Specialty Advisor to the CPT Panel (as described in the article). Joshua Hirsch—*UNRELATED*: Consultancy: Medtronic. Comments: interventional spine, Codman Neurovascular. Comments: Data Safety and Monitoring Board work.

## REFERENCES

1. Thorwarth WT Jr. **CPT: an open system that describes all that you do.** *J Am Coll Radiol* 2008;5:555–60 CrossRef Medline
2. Thorwarth WT Jr. **From concept to CPT code to compensation: how the payment system works.** *J Am Coll Radiol* 2004;1:48–53 CrossRef Medline
3. Hirsch JA, Leslie-Mazwi TM, Nicola GN, et al. **Current procedural terminology; a primer.** *J Neurointerv Surg* 2015;7:309–12 CrossRef Medline
4. HIPAA for Professionals. Services UDoHaH. <http://www.hhs.gov/hipaa/for-professionals/index.html>. Accessed March 17, 2016
5. CPT Process - How a Code Becomes a Code. American Medical Association. <http://www.ama-assn.org/ama/pub/physician-resources/solutions-managing-your-practice/coding-billing-insurance/cpt/cpt-process-faq/code-becomes-cpt.page>. Accessed March 15, 2015
6. 2016 AMA CPT Professional Edition Book. American Medical Association. [https://www.aapc.com/medical-coding-books/2016/2016-cpt-book.aspx?gclid=CO2y\\_cXUy8sCFYy2gQodPYwIog](https://www.aapc.com/medical-coding-books/2016/2016-cpt-book.aspx?gclid=CO2y_cXUy8sCFYy2gQodPYwIog). Accessed March 17, 2016
7. CPT - Current Procedural Terminology. American Medical Association. <http://www.ama-assn.org/ama/pub/physician-resources/solutions-managing-your-practice/coding-billing-insurance/cpt/cpt-editorial-panel.page>. Accessed March 15, 2016
8. CPT - Category II Codes. American Medical Association. <http://www.ama-assn.org/ama/pub/physician-resources/solutions-managing-your-practice/coding-billing-insurance/cpt/about-cpt/category-ii-codes.page>. Accessed March 15, 2016
9. Hirsch JA, Schaefer PW, Romero JM, et al. **Comparative effectiveness research.** *AJNR Am J Neuroradiol* 2014;35:1677–80 CrossRef Medline
10. CPT - Category III Codes. American Medical Association. <http://www.ama-assn.org/ama/pub/physician-resources/solutions-managing-your-practice/coding-billing-insurance/cpt/about-cpt/category-iii-codes.page>. Accessed March 15, 2016
11. Manchikanti L, Singh V, Caraway DL, et al. **Medicare physician payment systems: impact of 2011 schedule on interventional pain management.** *Pain Physician* 2011;14:E5–E33 Medline
12. Hirsch JA, Silva E, 3rd, Nicola GN, et al. **The RUC: a primer for neurointerventionalists.** *J Neurointerv Surg* 2014;6:61–64 CrossRef Medline
13. The RVS Update Committee. American Medical Association. <http://www.ama-assn.org/ama/pub/physician-resources/solutions-managing-your-practice/coding-billing-insurance/medicare/the-resource-based-relative-value-scale/the-rvs-update-committee.page>. Accessed March 15, 2016
14. Donovan WD. **The resource-based relative value scale and neuroradiology: ASNR's history at the RUC.** *Neuroimaging Clin N Am* 2012;22:421–36 CrossRef Medline
15. Silva E 3rd. **New codes from a new source: the rolling five-year review.** *J Am Coll Radiol* 2010;7:10–12 CrossRef Medline
16. Hirsch JA, Donovan WD, Leslie-Mazwi TM, et al. **Component coding and the neurointerventionalist: a tale with an end.** *J Neurointerv Surg* 2013;5:615–19 CrossRef Medline
17. Donovan WD, Leslie-Mazwi TM, Silva E 3rd, et al. **Diagnostic carotid and cerebral angiography: a historical summary of the evolving changes in coding and reimbursement in a complex procedure family.** *J Neurointerv Surg* 2014;6:712–17 CrossRef Medline
18. Chokshi FH, Tu RK, Nicola GN, et al. **Myelography CPT coding updates: effects of 4 new codes and unintended consequences.** *AJNR Am J Neuroradiol* 2016;37:997–99 CrossRef Medline
19. License for Use of Physicians' Current Procedural Terminology, Fourth Edition (CPT). Services CfMaM. <http://www.cms.gov/medicare-coverage-database/details/lcd-details.aspx>. Accessed March 15, 2016
20. American Medical Association. *2016 AMA CPT® Professional Edition Book*. Chicago: American Medical Association; 2016
21. American Medical Association. *Coding Update: Percutaneous Vertebroplasty and Vertebral Augmentation. Vol 1*. Chicago: American Medical Association; 2015

# Comparing Preliminary and Final Neuroradiology Reports: What Factors Determine the Differences?

 K. Stankiewicz,  M. Cohen,  M. Carone,  G. Sevinc,  P.G. Nagy,  J.S. Lewin,  D.M. Yousem, and  L.S. Babiarz

## ABSTRACT

**BACKGROUND AND PURPOSE:** Trainees' interpretations of neuroradiologic studies are finalized by faculty neuroradiologists. We aimed to identify the factors that determine the degree to which the preliminary reports are modified.

**MATERIALS AND METHODS:** The character length of the preliminary and final reports and the percentage character change between the 2 reports were determined for neuroradiology reports composed during November 2012 to October 2013. Examination time, critical finding flag, missed critical finding flag, trainee level, faculty experience, imaging technique, and native-versus-non-native speaker status of the reader were collected. Multivariable linear regression models were used to evaluate the association between mean percentage character change and the various factors.

**RESULTS:** Of 34,661 reports, 2322 (6.7%) were read by radiology residents year 1; 4429 (12.8%), by radiology residents year 2; 3663 (10.6%), by radiology residents year 3; 2249 (6.5%), by radiology residents year 4; and 21,998 (63.5%), by fellows. The overall mean percentage character change was 14.8% (range, 0%–701.8%; median, 6.6%). Mean percentage character change increased for a missed critical finding (+41.6%,  $P < .0001$ ), critical finding flag (+1.8%,  $P < .001$ ), MR imaging studies (+3.6%,  $P < .001$ ), and non-native trainees (+4.2%,  $P = .018$ ). Compared with radiology residents year 1, radiology residents year 2 (−5.4%,  $P = .002$ ), radiology residents year 3 (−5.9%,  $P = .002$ ), radiology residents year 4 (−8.2%,  $P < .001$ ), and fellows (−8.7%;  $P < .001$ ) had a decreased mean percentage character change. Senior faculty had a lower mean percentage character change (−6.88%,  $P < .001$ ). Examination time and non-native faculty did not affect mean percentage character change.

**CONCLUSIONS:** A missed critical finding, critical finding flag, MR imaging technique, trainee level, faculty experience level, and non-native-trainee status are associated with a higher degree of modification of a preliminary report. Understanding the factors that influence the extent of report revisions could improve the quality of report generation and trainee education.

**ABBREVIATIONS:** CF = critical finding; M = modified; PCC = percentage character change; R1 = radiology resident year 1; R2 = radiology resident year 2; R3 = radiology resident year 3; R4 = radiology resident year 4

Understanding the prevalence, causes, and types of discrepancies and errors in examination interpretation is a critical step in improving the quality of radiology reports. In an academic setting, discrepancies and errors can result from nonuniform training levels of residents and fellows. However, even the “ex-

perts” err, and a prior study found a 2.0% clinically significant discrepancy rate among academic neuroradiologists.<sup>1</sup> A number of factors can affect the accuracy of radiology reports. One variable of interest at teaching hospitals is the effect of the involvement of trainees on discrepancies in radiology reports. Researchers have found that compared with studies read by faculty alone, the rate of clinically significant detection or interpretation error was 26% higher when studies were initially reviewed by residents, and it was 8% lower when the studies were initially interpreted by fellows.<sup>2</sup> These findings suggest that perhaps faculty placed too much trust in resident interpretations, which led to a higher rate of discrepancies, while on the other hand, having a second experienced neuroradiology fellow look at a case can help in reducing the error rate.<sup>2</sup>

In our academic setting, preliminary reports initially created by trainees are subsequently reviewed and finalized by faculty or staff. The changes made to preliminary reports are a valuable teaching tool for trainees because clear and accurate report writ-

Received February 18, 2016; accepted after revision May 16.

From The Russell H. Morgan Department of Radiology and Radiological Sciences (K.S., M. Cohen, G.S., P.G.N., J.S.L., D.M.Y., L.S.B.), Johns Hopkins Medical Institutions, Baltimore, Maryland; and Department of Biostatistics, University of Washington (M. Carone), Seattle, Washington.

Paper previously presented at: Annual Meeting of the American Society of Neuroradiology and the Foundation of the ASNR Symposium, May 17–22, 2014; Montreal, Quebec, Canada.

Please address correspondence to David M. Yousem, MD, The Russell H. Morgan Department of Radiology and Radiological Sciences, Johns Hopkins Medical Institutions, 600 N Wolfe St, Phipps B-100F, Baltimore, MD 21287; e-mail: dyousem1@jhu.edu

<http://dx.doi.org/10.3174/ajnr.A4897>



ing is a critical skill for a radiologist.<sup>3</sup> Recently, computer-based tools have been created to help trainees compare the changes between preliminary and final reports to improve their clinical skills and to facilitate their learning. Sharpe et al<sup>4</sup> described the implementation of a Radiology Report Comparator, which allows trainees to view a merged preliminary/final report with all the insertions and deletions highlighted in “tracking” mode. Surrey et al<sup>5</sup> proposed using the Levenshtein percentage or percentage character change (PCC) between preliminary and final reports as a quantitative method of indirectly assessing the quality of preliminary reports and trainee performance. The Levenshtein percentage, a metric used in computer science, compares 2 texts by calculating the total number of single-character changes between the 2 documents, divided by the total character count in the final text.<sup>5</sup>

In this study, we analyzed preliminary neuroradiology reports dictated by trainees and the subsequent finalized reports revised by our faculty. We set out to identify the factors that determine the degree to which the preliminary reports are modified by faculty for residents and fellows, for daytime and nighttime shifts, and for CT and MR imaging examinations. We hypothesized that study complexity, lack of experience (for both trainee and faculty), and perhaps limited language skills (native-versus-non-native speaker) would result in a greater number of corrections.

## MATERIALS AND METHODS

In accordance with the Health Insurance Portability and Accountability Act, our institutional review board reviewed and approved the protocol for this retrospective study and waived the requirement for informed consent.

### Study Sample

Using our electronic medical records and Radiology Information System, we identified all neuroradiology reports generated at our institution between November 1, 2012, and October 31, 2013 (12 consecutive months). Neuroradiology reports by faculty only were excluded. At our institution, 80% of all neuroradiology studies are interpreted by trainees and faculty, and 20% are interpreted by faculty alone. Similar to individuals at other academic medical centers, our trainees, residents, and fellows create preliminary reports that are subsequently reviewed and, if necessary, revised by our faculty. Our entire faculty is neuroradiology fellowship-trained. Because preliminary reports are released into the electronic medical records and are viewable by the referring clinicians, if a significant change is made to the preliminary report, the final report is marked with an electronic flag (M), for modified. At our institution, the ordering or current provider is not automatically alerted to the change, but rather, our faculty or trainee (after discussing the changes with the faculty) communicates directly with the primary clinical team.

Per recommendation of the American College of Radiology and The Joint Commission, our trainees and faculty verbally communicate with the primary clinical team about neuroradiologic abnormal findings that may have immediate impact on patient care. At our institution, a predetermined list of 17 critical findings has been developed, which includes new hemorrhage, new stroke, new/increasing mass, increasing intracranial pressure, new/worsening herniation, new/worsening hydrocephalus,

misplaced/malfunctioning surgical hardware, infection, child abuse, vascular abnormality, new cord compression, new cord infarction, new spinal instability, congenital variations altering surgical approach, acute fracture, and globe/retina/optic nerve compromise. All neuroradiology reports containing a critical finding (CF) are electronically marked with a Flag (C) for ease of identification and documentation.

We have 10 residents and 9 neuroradiology fellows per year. Each year on July 1, the trainee graduates to a higher residency level or fellowship. Because our 12 consecutive months of reports encompasses that transition date, the same trainee may have been designated as a radiology resident year 1 (R1), year 2 (R2), year 3 (R3), or year 4 (R4) and neuroradiology fellow, depending on when the examination was performed.

Our faculty on staff was subdivided into junior, intermediate, and senior faculty based on <3, 3 years but <7 years, and >7 years of experience in practice after fellowship.

For each trainee and faculty member, the native-versus-non-native English-speaker status was recorded. We defined a non-English speaker as an individual who did not enter an English-speaking educational system until high school.

For examinations performed at the same time and involving consecutive body parts, such as CT of the cervical, thoracic, and lumbar spine or CT of the head and maxillofacial region, frequently, our trainee and faculty member dictate a single report, which is then attached to each individual study accession number. We avoided analyzing duplicate reports by including only the reports that had images attached to them. In our Radiology Information System, a complete set of images from an examination can only be attached to a single report, regardless of how many accession numbers (Current Procedural Terminology codes) are linked to that report.

At our institution, trainees are under direct faculty supervision during daytime hours (7 AM to 11 PM Monday through Friday, and 8 AM to 11 PM on Saturday and Sunday). During that time, a faculty member is always available for consultation. During nighttime hours (11 PM to 7 AM Monday through Friday, and 11 PM to 8 AM Saturday and Sunday), trainees interpret studies more independently; however, they can use our paging system to contact a faculty member for consultation. The “examination end” time stamp was used to determine whether a study was performed during daytime or nighttime.

At our institution, we do not use report templates for neuroradiology examinations. This choice likely increases the variability among our reports and has an impact on the extent of revisions to the preliminary reports performed by our faculty.

In an automated fashion, the percentage character change between the preliminary report generated by the trainee and the final report revised and signed by faculty was determined. The character change was defined as the total number of single-character changes between the preliminary and final report. The percentage character change was defined as  $PCC = (100 \times \text{Total Number of Single Character Changes}) / (\text{Total Character Number in Original Report})$ . Because the total number of single-character changes can exceed the number of characters in the original report, this PCC value can be any non-negative percentage, even exceeding 100%.

### Distribution of neuroradiology reports by percentage character change

PCC	No. of Reports	Percentage of Total Reports	95% CI
0 (no change)	95	0.3%	0.2%–0.5%
0% < x ≤ 1%	10,892	31.4%	28.5%–34.5%
1% < x ≤ 5%	4888	14.1%	13.0%–15.2%
5% < x ≤ 10%	4232	12.2%	11.4%–13.0%
10% < x ≤ 25%	7351	21.2%	20.0%–22.5%
25% < x ≤ 50%	4918	14.2%	12.8%–15.7%
50% < x ≤ 100%	2007	5.8%	5.0%–6.8%
>100%	278	0.8%	0.6%–1.0%

### Statistical Analysis

Basic descriptive statistics were calculated to characterize the various key features of the preliminary and final reports. A multivariable linear regression model was used to evaluate the joint association between mean PCC and each of a variety of factors including the following: 1) the presence of a critical or missed finding, 2) whether the report was written during nighttime or daytime, 3) imaging technique (CT or MR imaging), 4) English language proficiency of both the trainee and the faculty, and 5) the seniority of both the trainee and the faculty. Point estimates and confidence intervals for model parameters were obtained using generalized estimating equations with a working independence correlation matrix and robust variance estimators to appropriately account for the possible correlation between reports involving the same trainee and faculty. Generalized estimating equations were also used to provide valid confidence intervals for the marginal PCC value distribution. Plots of model residuals by either attending or trainee were scrutinized to determine whether reports written or edited by any attending or trainee had a substantially greater mean PCC than predicted by the fitted model, adjusting for all factors listed above. This procedure allowed us to scrutinize whether results reported were driven primarily by one or several anomalous individuals. All hypothesis tests were 2-sided and conducted at a significance level of .05. All computations were performed by using the R statistical programming language.<sup>6</sup>

### RESULTS

In this study, 34,661 sets of preliminary/final reports were included. The mean PCC of all reports was 14.8%, with a minimum of 0%, a maximum of 701.2%, and a median of 6.6%. The distribution of reports by PCC is shown in the Table. Ninety-five reports had a PCC of 0%, indicating that there were no changes between the preliminary and the final reports.

Of all studies, 21,204 (61.2%) were CTs (with an average final character count of 1921.3) and 13,457 (38.8%) were MRIs (with average final character count of 2616.4). After we adjusted for the presence of a CF flag, missed finding, examination time, non-native-speaker status, and experience levels, the mean PCC for MR imaging reports was greater than that for CT reports by 3.6 percentage points (95% CI, +2.5 to +4.8%;  $P < .001$ ).

Of all examinations, 21,998 (63.5%) were interpreted by fellows; 2322 (6.7%), by first-year radiology residents; 4429 (12.8%), by second-year radiology residents; 3663 (10.6%), by third-year radiology residents (R3s); and 2249 (6.5%) by fourth-year radiology residents. When reports created by each category of trainee were compared with a baseline of the reports generated by

R1s, we found that after we adjusted for presence of a CF flag, missed finding, examination time, imaging technique, non-native-speaker status, and faculty experience level, reports created by R2s had a mean PCC lower by 5.4 percentage points (95% CI, –8.8% to –2.0%;  $P = .002$ ), reports created by R3s had a mean PCC lower by 5.9 percentage points (95% CI, –9.5% to –2.2%;  $P = .002$ ), reports created by R4s had a mean PCC lower by 8.2 percentage points (95% CI, –12.5% to –3.8%;  $P < .001$ ), and reports created by fellows had a mean PCC lower by 8.7 percentage points (95% CI, –12.2% to –5.2%;  $P < .001$ ).

The distribution of cases read by fellows and R1–4 are a product of our neuroradiology rotation and call schedules, with most neuroradiology cases being read by our fellows and R2s and R3s. Our R4s typically take electives related to their planned fellowship; therefore, the few R4s in our division end up staying for a neuroradiology fellowship.

Twelve of the 58 (20.6%) trainees were non-native English speakers, and they accounted for 8808 (25.4%) of all preliminary reports. After we adjusted for the presence of a CF flag, missed finding, examination time, imaging technique, faculty non-native-speaker status, and seniority, these reports had a mean PCC higher by 4.2 percentage points compared with those generated by the native-speaker trainees (95% CI, +0.7% to +7.6%;  $P = .018$ ).

Of all reports, 4091 (11.8%) were marked with a critical finding flag, and 282 of these (6.9% of reports with a critical finding, 0.8% of all reports) were marked with a missed finding flag. After we adjusted for examination time, imaging technique, non-native-speaker status, and experience levels, reports with a CF flag but no missed finding had a mean PCC higher by 1.8 percentage points compared with those without any CF flag (95% CI, +0.9% to +2.7%;  $P < .001$ ), while reports with flags for both a critical finding and missed finding had a mean PCC higher by 41.6 percentage points compared with those with only the CF flag (95% CI, +37.3 to +48.9%;  $P < .001$ ).

Of all reports, 20,123 (58.1%) were created during daytime shifts (under direct faculty supervision), and 14,538 (41.9%), during nighttime (no direct supervision; however, faculty were available for consultation via the paging system). No significant difference was detected between the mean PCC of daytime and nighttime reports (mean PCC higher during nighttime by 0.6 percentage points; 95% CI, –1.4% to +2.6%;  $P = .567$ ) after adjusting for the presence of a CF flag, imaging technique, non-native-speaker status, and experience levels. However, in our sample, the odds of finding a flag M in reports written at night were >2 times higher (OR estimate, 2.02; 95% CI, 1.48–2.77;  $P < .001$ ) than the odds of finding a flag M in reports written during the day.

Eighteen staff neuroradiologists reviewed preliminary reports generated by trainees. Among faculty, there were 4 junior attending neuroradiologists (3920 reports), 5 intermediate attending neuroradiologists (12,885 reports), and 9 senior attending neuroradiologists (17,856 reports). Compared with a baseline of reports finalized by junior neuroradiologists and adjusting for the presence of a CF flag, missed finding, examination time, imaging technique, non-native-speaker status, and trainee experience level, reports finalized by intermediate neuroradiologists showed no significant difference in mean PCC (lower for intermediate neuroradiologists by 0.7 percentage points; 95% CI, –4.2% to

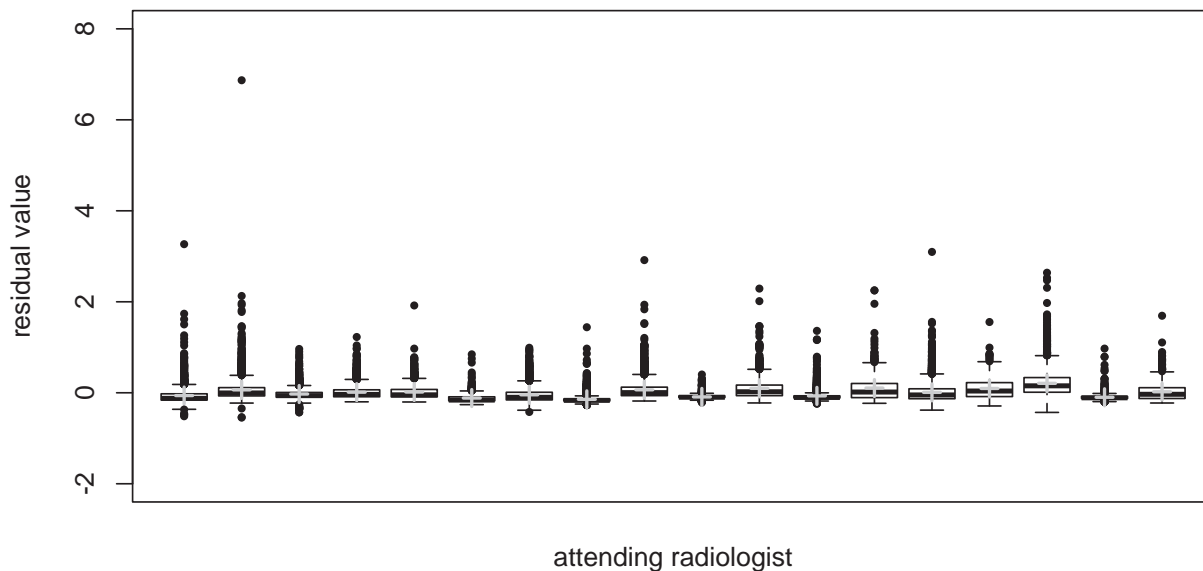


**FIG 1.** Plot of model residuals by attending radiologists. For each attending radiologist, a boxplot of residuals is shown in black and the average residual value is depicted in gray.

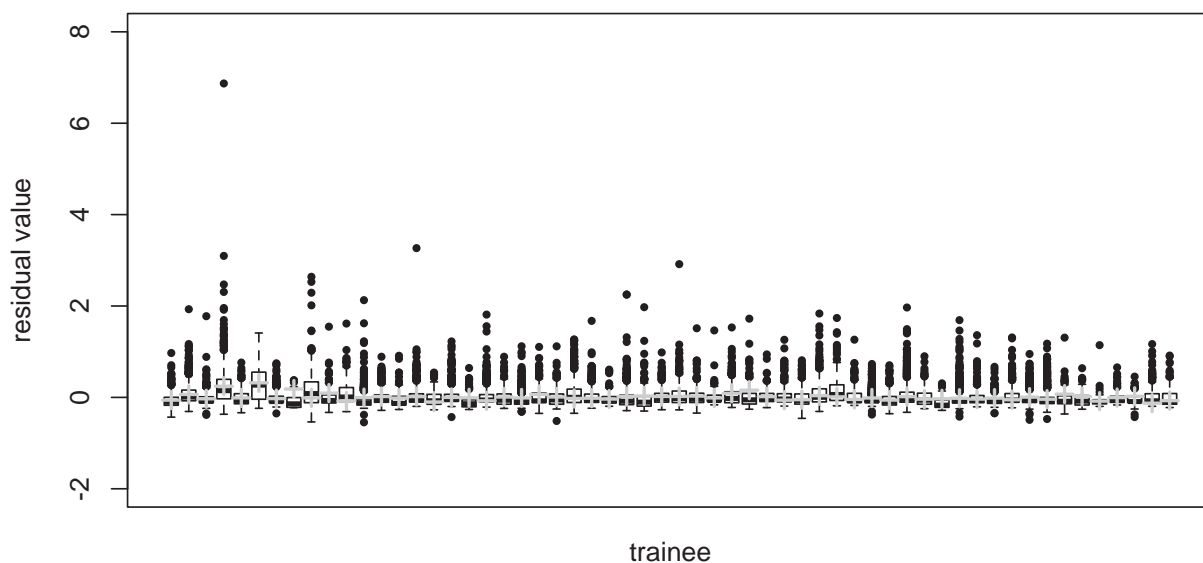


**FIG 2.** Plot of model residuals by trainees. For each trainee, a boxplot of residuals is shown in black and the average residual value is depicted in gray.

+2.9%;  $P = .720$ ), while reports finalized by senior neuroradiologists had a mean PCC lower by 6.8 percentage points (95% CI,  $-9.4$  to  $-4.2\%$ ;  $P < .001$ ).

Ten of 18 faculty (55.5%) were non-native English speakers, and they finalized 23,058 (66.5%) of all reports. After adjusting for the presence of a CF flag, missed finding, examination time, imaging technique, trainee non-native-speaker status, and experience levels, we detected no significant difference in the mean PCC for reports finalized by native and non-native-speaker faculty (mean PCC for non-native-speaker faculty higher by 1.1 percentage points; 95% CI,  $-0.8\%$  to  $+3.0\%$ ,  $P = .241$ ).

Plots of model residuals by attendings (Fig 1) did not identify any faculty who, on average, made a greater number of changes than predicted by the model. Plots of model residuals by trainees (Fig 2) also did not reveal any trainee who, on average, had a much

greater number of changes made to his or her reports than predicted by the model.

## DISCUSSION

Overall, in our sample, the mean PCC values were lower in trainees with greater seniority and experience. Reports created by R1s had the highest PCC, and reports created by fellows had the lowest PCC (lower by 8.9 percentage points compared with those generated by R1s). This finding supports our hypothesis that trainees learn to write higher quality reports during their training. The factor with the strongest association to mean PCC was the presence of a flag M or, in other words, a missed CF by a trainee, which, on average, increased the mean PCC by 41.6 percentage points. Even when not missed, the presence of a CF was associated with an increased mean PCC of 1.8 percentage points. Studies

with a CF typically contain more complex pathology; thus, their interpretations are more challenging. This difference increases the potential for error. Additionally, because the flagged studies, particularly ones with a flag M, may have greater implications for patient care, faculty may be more attentive to revising those reports, to ensure that all the findings are accurate and described with precise language. Reports for MR imaging examinations had a higher mean PCC by 3.7 percentage points compared with those for CT examinations. This is most likely caused by the increased complexity of MR imaging studies, which tend to have longer reports, contain more information, and can be more challenging to interpret, especially given the wide range of sequences and protocols. In addition, frequently, MR imaging is used in more complicated cases, increasing the probability that trainees may be exposed to unfamiliar imaging findings and disease processes.

We found a mean PCC higher by 4.0 percentage points in preliminary reports created by trainees who are non-native speakers. This may result from a range of stylistic and vocabulary differences among these trainees, as well as between the non-native-speaking trainees and native-speaking faculty, which could increase the extent of changes made to these reports. No statistically significant difference in the mean PCC was observed between reports finalized by native and non-native English-speaking faculty. This finding suggests that with extensive training and experience in neuroradiology, native and non-native English-speaking faculty adopt similar dictation styles. Few studies have looked at the native and non-native-speaker status of trainees in programs in the United States and its effect on the quality of radiology reports. One potential source of the difference in the mean PCC may be related to the accuracy of the voice-recognition system used by the trainees. Reports generated by non-native English speakers with accents using voice recognition have been shown to have higher error rates of approximately 11.6%, compared with 9.7% for native speakers.<sup>7</sup>

While no statistically significant difference in mean PCC was detected between reports finalized by junior and intermediate faculty, reports finalized by senior faculty exhibited a mean PCC lower by 6.9 percentage points. We hypothesize that junior faculty with limited supervisory experience may be less comfortable with alternate phrasing; thus, they make more changes when editing reports. After we adjusted for the presence of a CF flag, imaging technique, non-native-speaker status, and experience levels, we did not find a statistically significant difference in the mean PCC between studies read during the daytime (under direct supervision) and during the nighttime (without direct supervision, but with faculty available through the paging system). However, in our sample, the odds of finding a flag M in reports written without direct supervision were 2 times higher than the odds of finding a flag M in reports written under direct supervision. One potential explanation for the increased frequency of flag M's is that while supervised, trainees are more likely to consult with their attending neuroradiologist about challenging cases or findings of which they are unsure; thus, such preliminary reports have a lower potential for errors.

Previous studies have shown that the mean PCC values of subsequent sets of preliminary and final reports written by individual trainees exhibit a decreasing trend as trainees advance through radiology training. Sharpe et al<sup>8</sup> studied the average PCC of 6 trainees during their diagnostic radiology residency and

found similar trends among all of them, with the mean PCC falling from 15%–30% to below 15% after about 700 written reports. In our study, we have found a similar trend among all trainees in a large academic hospital because PCC values were lower in each consecutive year of residency and were lowest for fellows.

Our study found a mean PCC of 14.8% and a median PCC of 6.6%. Surrey et al<sup>5</sup> reported a mean value of 6.38%. A few likely factors caused this difference. Surrey et al reported no change between preliminary and final reports in 56.2% of report pairs. In our study, we observed no change in just 95 of the total 34,661 report pairs (~0.3%). This is most likely indicative of more conservative editing on the part of faculty in that study,<sup>5</sup> which would explain the lower mean PCC found. Our hospital does not use templates for radiologic reporting. Institutions using such templates would most likely report lower PCC values because the use of such templates increases conformity among reports and therefore may decrease the proportion of changes made by attending faculty. Although whether such templates were used in the study by Surrey et al is unknown, this is another factor potentially contributing to the differences in mean PCC between the 2 studies.

The influence of direct supervision of trainees by radiology faculty has been a subject of extensive scrutiny. Although trainees do not report any difference in educational value when working with and without direct supervision,<sup>9</sup> previous studies have found that interpretations done by unsupervised trainees had higher discrepancy rates, particularly among less experienced trainees (17% higher discrepancy rates for R2s compared with approximately 7.5% for R3s and R4s and 3.5% for fellows).<sup>2</sup> In a separate review of 18,185 studies interpreted by trainees without supervision, 28 cases of trainee discrepancy later caught by an attending radiologist were estimated to lead to increased morbidity in 11% of the cases and prolonged hospitalization in 25% of the cases, but no case exhibited implications for long-term patient health.<sup>10</sup> There is no consensus, however, with another study finding that just 0.3% of all discrepancies attributed to trainees having no direct supervision resulted in significant negative effects for patients.<sup>11</sup> We did not detect any significant difference in mean PCC between preliminary reports made under direct supervision (daytime) and indirect supervision (nighttime). This can be explained in a few ways: Either the paging system is a sufficient substitute for trainee-faculty consultation or trainees are more attentive while working without attending supervision and are able to largely offset the experience gap.

In this study, we found that the mean PCC was higher in MR imaging than in CT studies, and we hypothesize that this increase is due to a larger amount of discrepant readings and higher report complexity. Indeed, in a study of 416,413 studies read by trainees and reviewed by faculty, researchers found that the discrepancy rate was significantly higher for MR imaging (3.7%) than for CT (2.4%).<sup>12</sup> This same study also found that total discrepancy rates decreased as trainees gained experience, from 1.8% to 1.5%.

Previous applications of the PCC have largely focused on studying individual trainees, not inspecting wider trends in reporting. Researchers suggested using the PCC to identify trainees who may need increased individualized attention and to track the development of trainee reporting skills over the duration of their education. In our study, we assessed the influence of several factors on the PCC. To our knowledge, many of them, such as the

time of the study, native-speaking status, or critical finding flag, have not been examined in this manner. The primary goal of our study was to qualitatively assess which of these factors led to significant changes in the PCC (which had been shown to correlate inversely with report quality). A secondary goal was to achieve a relative quantitative estimate of the magnitude of the aforementioned effects. With our study, we were hoping to identify specific trends that could be targeted with educational effort to improve the quality of our preliminary reports.

The mean PCC itself as a measure of the clinical accuracy of a report has limitations because it weighs all changes equally. For example, reports with a few critical edits (eg, “no stroke” to “stroke”) could have low a PCC but large implications for patient care, and reports with extensive changes (eg, more detailed descriptions, secondary findings) could have a high PCC with little to no implications for patient care. In this study, we did not analyze the content of reports to determine to what extent the mean PCC measures stylistic changes versus meaning of a report. However, another study, performed at our institution by Huntley et al,<sup>13</sup> looking at all neuroradiology reports with a flag M during a 2-year period, did reveal that 73.8% of reports had addenda because of a missed CF, 21.7% had addenda because of a missed non-CF, and 4.6% had addenda because a report was changed from containing a CF to not containing a CF.

There are several limitations to this study. Most important, our study considered only reports generated during 12 consecutive months at 1 university hospital. This means that for example, the 2322 reports written by RIs were written by just 15 residents. With this low sample size, individual trends among trainees and faculty members can significantly influence the results of the entire group. In addition, our RIs come from various training paths, with some having greater experience and knowledge of radiology than others. Indeed, this sort of influence due to individual faculty members has been suggested in previous studies involving PCC.<sup>14</sup> Although in our sample, we did not identify any faculty or trainee outliers, repeating similar experiments at different hospitals and across time can help ensure the precision of our results. Also, while previous studies have shown that in large datasets, the PCC correlates with the clinical accuracy of the report,<sup>5</sup> to our knowledge, no studies have been performed to quantify the magnitude to which other factors, such as changes to formatting, grammar, or spelling, influence the PCC values in radiology. This subject is of particular importance when measuring the impact of variables such as non-native English-speaking status because in this study, we hypothesized that these variables affect the PCC significantly. At our institution, we do not use templates/structured reporting for neuroradiology studies. This feature likely increases the variability between reports and the extent of revisions to the preliminary reports.

## CONCLUSIONS











Our analysis showed that having a CF in the report, missing a finding, MR imaging technique, trainee and faculty experience levels, and non-native-speaker trainee status are associated with a higher degree of modification of a preliminary neuroradiology report. Understanding the factors that influence the extent of report revisions could improve the quality of report generation and trainee education.

Disclosures: Gorkem Sevinc—UNRELATED: Other: I have board memberships in Insight Medical Technologies and emocha Mobile Health. These companies are not relevant to this article. Insight Medical technologies provides expert medical consults to attorneys, and emocha Mobile Health is a mobile health platform company in the public health space. Jonathan S. Lewin—UNRELATED: Board Membership: American Roentgen Ray Society, Association of University Radiologists, Society of Chairs of Academic Radiology Departments, International Society for Strategic Studies in Radiology, Comments: no payment for any of the boards mentioned; Travel/Accommodations/Meeting Expenses Unrelated to Activities Listed: reimbursements from several of the societies noted above for board or committee meetings. David M. Yousem—UNRELATED: Consultancy: medicolegal consultations; Expert Testimony: medicolegal testimony; Payment for Lectures (including service on Speakers Bureaus): American College of Radiology Education Center\*; Royalties: 4 books published by Elsevier; Payment for Development of Educational Presentations: CMEInfo.com\*; Travel/Accommodations/Meeting Expenses Unrelated to Activities Listed: American Society for Neuroradiology international program. \*Money paid to the institution.

## REFERENCES

- Babiarz LS, Yousem DM. **Quality control in neuroradiology: discrepancies in image interpretation among academic neuroradiologists.** *AJNR Am J Neuroradiol* 2012;33:37–42 CrossRef Medline
- Viertel VG, Babiarz LS, Carone M, et al. **Quality control in neuroradiology: impact of trainees on discrepancy rates.** *AJNR Am J Neuroradiol* 2012;33:1032–36 CrossRef Medline
- ACGME Program Requirements for Graduate Medical Education in Diagnostic Radiology. [https://www.acgme.org/Portals/0/PFAssets/ProgramRequirements/420\\_diagnostic\\_radiology\\_2016.pdf](https://www.acgme.org/Portals/0/PFAssets/ProgramRequirements/420_diagnostic_radiology_2016.pdf). Effective July 1, 2016. Accessed July 14, 2016
- Sharpe RE Jr, Surrey D, Gorniak RJ, et al. **Radiology report comparator: a novel method to augment resident education.** *J Digit Imaging* 2012;25:330–36 CrossRef Medline
- Surrey D, Sharpe RE Jr, Gorniak RJ, et al. **QRSE: a novel metric for the evaluation of trainee radiologist reporting skills.** *J Digit Imaging* 2013;26:678–82 CrossRef Medline
- R. The R Project for Statistical Computing. <http://www.R-project.org/>. Accessed May 20, 2016
- Kanal K, Hangiandreou N, Sykes A, et al. **Initial evaluation of a continuous speech recognition program for radiology.** *J Digit Imaging* 2001;14:30–37 CrossRef Medline
- Sharpe RE, Pan K, Gorniak RJ, et al. **Tracking reporting metrics over the course of a resident/fellow training period: an automated methodology to evaluate progress in the reporting process.** In: *Proceedings of the Annual Meeting of the Society for Imaging Informatics*, Dallas, Texas. June 6–9, 2013
- McGrath JR, Mitra S, Nicola R. **The effect of overnight attending coverage on resident education at a large academic medical center.** In: *Proceedings of the Annual Meeting of the Association of University Radiologists*, Baltimore, Maryland. April 1–4, 2014
- Friedman SM, Merman E, Chopra A. **Clinical impact of diagnostic imaging discrepancy by radiology trainees in an urban teaching hospital emergency department.** *Int J Emerg Med* 2013;6:24 CrossRef Medline
- Ruchman RB, Jaeger J, Wiggins EF 3rd, et al. **Preliminary radiology resident interpretations versus final attending radiologist interpretations and the impact on patient care in a community hospital.** *AJR Am J Roentgenol* 2007;189:523–26 CrossRef Medline
- Weinberg BD, Richter MD, Champine JG, et al. **Radiology resident preliminary reporting in an independent call environment: multi-year assessment of volume, timeliness, and accuracy.** *J Am Coll Radiol* 2015;12:95–100 CrossRef Medline
- Huntley JH, Carone M, Yousem DM, et al. **Opportunities for targeted education: critical neuroradiologic findings missed or misinterpreted by residents and fellows.** *AJR Am J Roentgenol* 2015;205:1155–59 CrossRef Medline
- Surrey D, Sharpe RE, Gorniak RJ, et al. **Variability in the extent of edits made by attending radiologists to trainee radiology reports.** In: *Proceedings of the Annual Meeting of the Association of University Radiologists*, San Antonio, Texas. March 19–22, 2012

# Bidirectional Changes in Anisotropy Are Associated with Outcomes in Mild Traumatic Brain Injury

 S.B. Strauss,  N. Kim,  C.A. Branch,  M.E. Kahn,  M. Kim,  R.B. Lipton,  J.M. Provataris,  H.F. Scholl,  M.E. Zimmerman, and  M.L. Lipton



## ABSTRACT

**BACKGROUND AND PURPOSE:** Mild traumatic brain injury results in a heterogeneous constellation of deficits and symptoms that persist in a subset of patients. This prospective longitudinal study identifies early diffusion tensor imaging biomarkers of mild traumatic brain injury that significantly relate to outcomes at 1 year following injury.

**MATERIALS AND METHODS:** DTI was performed on 39 subjects with mild traumatic brain injury within 16 days of injury and 40 controls; 26 subjects with mild traumatic brain injury returned for follow-up at 1 year. We identified subject-specific regions of abnormally high and low fractional anisotropy and calculated mean fractional anisotropy, axial diffusivity, radial diffusivity, and mean diffusivity across all white matter voxels brain-wide and each of several white matter regions. Assessment of cognitive performance and symptom burden was performed at 1 year.

**RESULTS:** Significant associations of brain-wide DTI measures and outcomes included the following: mean radial diffusivity and mean diffusivity with memory; and mean fractional anisotropy, radial diffusivity, and mean diffusivity with health-related quality of life. Significant differences in outcomes were found between subjects with and without abnormally high fractional anisotropy for the following white matter regions and outcome measures: left frontal lobe and left temporal lobe with attention at 1 year, left and right cerebelli with somatic postconcussion symptoms at 1 year, and right thalamus with emotional postconcussion symptoms at 1 year.

**CONCLUSIONS:** Individualized assessment of DTI abnormalities significantly relates to long-term outcomes in mild traumatic brain injury. Abnormally high fractional anisotropy is significantly associated with better outcomes and might represent an imaging correlate of postinjury compensatory processes.

**ABBREVIATIONS:** AD = axial diffusivity; EZ-MAP = Enhanced Z Score Microstructural Assessment of Pathology; FA = fractional anisotropy; HRQoL = health-related quality of life; hFA = high fractional anisotropy; lFA = low fractional anisotropy; MD = mean diffusivity; mTBI = mild traumatic brain injury; PCS = postconcussion symptoms; RD = radial diffusivity; TBI = traumatic brain injury

Mild traumatic brain injury (mTBI) is associated with a heterogeneous constellation of deficits and symptoms that persist for the long term in 20% of patients who experience concussion.<sup>1</sup> The syndrome can entail cognitive impairment, most prominently in

memory, attention, and executive function, and postconcussion symptoms (PCS) and limitations in daily functioning.

Notwithstanding earlier constructs that frame PCS as largely factitious or psychogenic and without a biologic basis, it is now widely understood that even uncomplicated mTBI-related dysfunction results from structural pathology such as traumatic axonal injury.<sup>2,3</sup> The inability of imaging techniques such as CT and MR imaging to detect traumatic axonal injury has led to delayed understanding of the clinical mTBI syndrome, despite human (eg, Bigler, 2004<sup>2</sup>) and animal (eg, Mac Donald et al, 2007<sup>4</sup>) studies delineating trauma-related histopathology following even mild head trauma.


More recently, DTI has become an established means for the detection of human traumatic axonal injury pathology in vivo; the


Received August 4, 2015; accepted after revision April 25, 2016.

From the Department of Radiology (S.B.S., M.L.L.), Montefiore Medical Center, Bronx, New York; Departments of Radiology (N.K., M.L.L.), Physiology and Biophysics (C.A.B.), Epidemiology and Population Health (M.K., R.B.L.), and Psychiatry and Behavioral Sciences (M.L.L.), The Gruss Magnetic Resonance Research Center (N.K., C.A.B., M.E.K., H.F.S., M.L.L.), The Saul R. Korey Department of Neurology (R.B.L., M.E.Z.), and The Dominick P. Purpura Department of Neuroscience (M.L.L.), Albert Einstein College of Medicine, Bronx, New York; and Department of Emergency Medicine (J.M.P.), Jacobi Medical Center, Bronx, New York.

This work was supported by a National Institutes of Health grant NS082432-03 (M.L.L.).

Please address correspondence to Michael L. Lipton, MD, PhD, FACR, Albert Einstein College of Medicine, Jack and Pearl Resnick Campus, 1300 Morris Park Ave MRRC, Room 219C, Bronx, NY 10461; e-mail: michael.lipton@einstein.yu.edu

 Indicates open access to non-subscribers at [www.ajnr.org](http://www.ajnr.org)

 Indicates article with supplemental on-line photos.

<http://dx.doi.org/10.3174/ajnr.A4851>

**Table 1: Subject inclusion and exclusion criteria**

Inclusion Criteria	Exclusion Criteria
Age 18–70 years	Focal neurologic deficits
Availability for testing within 2 weeks of concussion	History of head injury (based on history and medical record)
Glasgow Coma Scale = 13–15	Chronic posttraumatic abnormal findings on CT/MRI
Loss of consciousness < 20 minutes	Hospitalization due to the current head injury
Posttraumatic amnesia < 24 hours	History of a neurodevelopmental or neurologic disorder
English or Spanish proficiency	Major psychiatric disorder
	Illicit drug use within 30 days

overwhelming consensus of >120 published studies indicates that despite methodologic heterogeneity, abnormally low fractional anisotropy (FA) derived from DTI is characteristic of patients with mTBI.<sup>5</sup> Cross-sectional associations of DTI abnormalities and functional outcomes support the clinical significance of these imaging findings.<sup>6–8</sup>

Despite strong evidence supporting the ability of DTI to detect clinically salient traumatic axonal injury pathology and its potential to identify patients at risk for poor long-term outcomes, to date DTI has not yet yielded a validated prognostic biomarker for several reasons: First, only a small number of longitudinal studies have assessed the relationship between early imaging and later outcomes.<sup>9,10</sup> Second, most studies define outcomes as performance on tests of cognitive function.<sup>7,8,11,12</sup> Only a few have examined the relationship between early imaging and subjective measures, which may more closely approximate real-world functioning, such as PCS<sup>10,11</sup> and health-related quality of life (HRQoL).<sup>13</sup> The morbidity of mTBI in real-world settings may reflect deficits not captured by standard formal cognitive testing, such as multimodal processing and divided attention.<sup>14</sup> Third, image-analysis approaches have largely (though not exclusively) used group-level delineation of DTI measures. However, delineation of ROIs at the group level, whether on an a priori basis or by using a voxelwise analysis, is insensitive to the unique spatial distribution of traumatic axonal injury, which is likely present in each patient. Finally, most studies report the association of low FA with poor mTBI outcomes<sup>7,8</sup> but do not report abnormally high FA. The few studies assessing the functional significance of abnormally high FA do so at a relatively short follow-up.<sup>9,15</sup> The objective of this study was to address current gaps in knowledge by characterizing the relationship between acute diffusion abnormalities in patients with uncomplicated mTBI and their 1-year functional outcomes, including cognition, PCS, and HRQoL. To address the importance of spatial heterogeneity of traumatic axonal injury across subjects, we used an individualized approach to identification of abnormality in each patient with mTBI, Enhanced Z Score Microstructural Assessment of Pathology (EZ-MAP),<sup>16,17</sup> and we considered both regional and brain-wide measures and their relationship outcome. If identified prospectively, those with worse prognosis could be targeted for studies of interventions designed to improve outcomes following mTBI.

## MATERIALS AND METHODS

### Subject Enrollment and Study Design

This study was approved by the Einstein Institutional Review Board and was conducted in accordance with the Health Insur-

ance Portability and Accountability Act. All subjects provided written, informed consent for participation in the study.

Thirty-nine subjects with mTBI were prospectively enrolled from 2 urban emergency departments.

Inclusion and exclusion criteria for subjects are detailed in Table 1. Subjects were evaluated in the emergency department within 48 hours of injury, and diagnosis of mTBI/concussion was made by an emergency department physician.

If CT was performed for clinical care of the current head injury, then an American Board of Radiology Certificate of Added Qualification–certified neuroradiologist reviewed the CT images. Subjects were excluded if skull fracture or any acute or chronic posttraumatic abnormality such as gliosis, localized encephalomalacia, or remote hemorrhage was identified.

Forty healthy volunteers were recruited from the community via printed advertisements. The inclusion criterion for controls was 18–70 years of age. Exclusion criteria were the same as those for subject enrollment. This study used a prospective, within-subjects design: The role of the group of 40 controls was to provide imaging for comparison, to allow identification of abnormal FA.

In this longitudinal study, imaging was performed within 16 days of injury (median, 7.5 days; range, 1–16 days), and cognitive function, PCS, and HRQoL were assessed at 1 year following injury.

### Data Acquisition

**Imaging.** Imaging was performed by using a 3T MR imaging scanner (Achieva TX; Philips Healthcare, Best, the Netherlands) with a 5-channel head coil (SENSE Head Coil; Philips Healthcare). T1-weighted whole-head structural imaging was performed by using sagittal 3D magnetization-prepared rapid acquisition of gradient echo imaging (TR/TE, 9/4.6 ms; FOV, 240 mm<sup>2</sup>; matrix, 240 × 240; section thickness, 1 mm). T2-weighted whole-head imaging was performed by using axial 2D turbo spin-echo imaging (TR/TE, 4000/100 ms; FOV, 240 mm<sup>2</sup>; matrix, 384 × 512; section thickness, 4.5 mm) and axial 2D fluid-attenuated inversion recovery turbo spin-echo (TR/TE, 1100/120 ms; TI, 2800 ms; FOV, 240 mm<sup>2</sup>; matrix, 384 × 512; section thickness, 4.5 mm; number of signals acquired, 1). DTI was performed by using single-shot spin-echo echo-planar imaging (TR/TE, 3800/88 ms; FOV, 240 mm<sup>2</sup>; matrix, 112 × 89; section thickness, 4.5 mm; independent diffusion-sensitizing directions, 32; *b*=800 s/mm<sup>2</sup> images).

### Outcome Measures

**Cognition.** Tests of cognitive function were administered to all subjects, by using IntegNeuro (Brain Resource Company, Sydney, Australia), a computerized battery of cognitive tasks.<sup>18</sup> A summary *z* score was computed for each of 3 cognitive domains (executive function, episodic memory, and attention), selected for study because of their known associations with the mTBI syndrome, by using an international database of >5000 age-, sex-, and education-matched healthy individuals, as detailed in Table 2.

**Table 2: Cognitive domains and component cognitive tasks**

Cognitive Domain	Constituent Cognitive Tasks
Executive Function	Digit Span Backward Switching of attention (digits/letters) Verbal interference Executive maze task
Episodic Memory	Verbal list learning task (immediate recall, delayed recall, and recognition)
Attention	Digit Span Forward Continuous Performance Task Switching of attention (digits) Visual memory

Premorbid intelligence was estimated by using the Spot-the-Word test, which is a measure of word recognition ability and lexical decision-making, with good reliability (0.88) and convergent validity (0.60–0.86).<sup>19</sup>

### Postconcussion Symptoms and Health-Related Quality of Life Outcome Measures

At 1 year postinjury, the Rivermead Post Concussion Symptoms Questionnaire<sup>20</sup> was administered to assess PCS, and the Sickness Impact Profile<sup>21</sup> was administered to assess HRQoL. Patients were classified as having postconcussion syndrome on the basis of outcomes at 1 year rather than 3 or 6 months; thus, those with postconcussion syndrome that lasted <1 year were not classified in this manner. This classification restricts the postconcussion syndrome patient group to those with more persistent and chronic symptoms.

The Rivermead Post Concussion Symptoms Questionnaire consists of a series of 16 symptoms; subjects are asked to rate the severity for each item, relative to preinjury experience, on a scale from 0 to 4. Symptoms are categorized into cognitive, somatic, or emotional factors; and each factor is used as an independent outcome measure.<sup>22</sup>

The Sickness Impact Profile includes 68 questions pertaining to daily functioning and is graded on a dichotomous scale (0 or 1) yielding 5 subscores. The physical dimension is assessed as “somatic autonomy” and “mobility control”; the psychological dimension, as “psychological autonomy and communication”; and the social dimension, as “mobility range” and “social behavior.”<sup>23</sup>

### Data Analysis

**Neuroradiology Assessment.** An American Board of Radiology Certificate of Added Qualification–certified neuroradiologist reviewed structural MR images for posttraumatic pathology, including hemorrhage, extra-axial collection, contusion, or traumatic axonal injury.

**Calculation of Diffusion Parameter Images.** The 32 diffusion-weighted image sets (32  $b=800$  s/mm<sup>2</sup> images) were corrected for head motion and eddy current effects by using an affine registration algorithm, with the  $b=0$  s/mm<sup>2</sup> image as the target, and tensor fitting was performed at each voxel by using the FMRIB Diffusion Toolbox (<http://fsl.fmrib.ox.ac.uk/fsl/fslwiki/FDT>).<sup>24</sup>

**Image Registration.** All analyses were performed after transformation of diffusion parameter images to match a high-resolution T1-weighted template (Montreal Neurological Institute).<sup>25</sup> The registration process includes correction for EPI distortions and linear

within-subject and nonlinear subject-to-template registration steps as previously reported.<sup>17</sup> This spatial normalization procedure has been shown to be robust across subjects.<sup>26</sup> Nonetheless, the results of each registration are critically assessed by viewing each stage of the registration output, with particular assessment of the alignment of brain surface; deep structures including the brain stem, corpus callosum, and fornix; and gray/white margins in both the deep gray matter structures and at the cortical margin. These landmarks must align within 2 voxel dimensions for the registration to be accepted, though alignment is typically nearly exact.

**White Matter Segmentation.** The FMRIB Automated Segmentation Tool (FAST; <http://fsl.fmrib.ox.ac.uk/fsl/fslwiki/FAST>)<sup>27</sup> was used to generate a white matter mask for the 3D T1-weighted template brain images. This mask was eroded by 3 voxels to eliminate locations most at risk of misregistration and was used to restrict subsequent statistical analysis of FA to white matter voxels.

**Subregion Segmentation of White Matter.** While the analysis was performed in the Montreal Neurological Institute template space, the Johns Hopkins University white matter atlas<sup>28</sup> was adapted and used for segmentation of white matter subregions. This segmentation procedure eliminates potential observer bias introduced by intra- and interrater variance inherent in manually delineated ROIs. With the FMRIB Linear Image Registration Tool (FLIRT; <http://www.fmrib.ox.ac.uk/>),<sup>27</sup> the T1-weighted template for the Johns Hopkins University white matter atlas was registered to the T1-weighted Montreal Neurological Institute template used for DTI analysis. The resulting transformation matrix was applied to the white matter segmentation volume of the Johns Hopkins University white matter atlas to bring it into registration with the Montreal Neurological Institute template. Individual Johns Hopkins University regions were combined to generate larger white matter regions used for analysis, as detailed below.

**Adjustment for Demographic Covariates.** Before lesion detection, multiple linear regression analysis was performed to adjust for the effects of age, sex, and education as detailed in Kim et al.<sup>17</sup> Regression coefficients were determined from control subjects only, to avoid potential interaction effects of mTBI on the aforementioned putative risk factors, and were applied to the voxels within each subject’s FA image, where covariate effects on individual voxels were significant at  $P < .05$  and >100 significant voxels formed a contiguous cluster.

**EZ-MAP Analysis for FA Lesion Detection.** The Enhanced Z Score Microstructural Assessment of Pathology<sup>17</sup> is a method for delineating abnormal regions in individual patients with mTBI. The EZ-MAP is based on a whole-brain voxelwise  $z$  score of a subject  $\left( Z \text{ Score} = \frac{y - \bar{x}}{sd(x)} \right)$ , calculated with the mean ( $\bar{x}$ ) and SD [ $sd(x)$ ] from healthy controls at each voxel, where we denote SD from healthy controls as  $sd(x)$ . We here omit the voxel index for notation convenience. The EZ-MAP is more robust than standard  $z$  score analysis because it incorporates estimated sampling variance of individual  $z$  scores by using a bootstrap procedure, which is finally calculated as  $EZ = \frac{Z \text{ Score}}{\hat{\sigma}^B(x)}$ .  $\hat{\sigma}^B(x) > 1$  due to sample-to-sample variation of  $z$  scores.<sup>17</sup> Ab-



normal clusters were further delineated by applying a cluster size threshold determined on the basis of the Gaussian random field theory. This technique has been optimized and validated previously for assessment of individual subjects, and the EZ-MAP showed greater robustness in varying control samples compared with the  $z$  score and the 1-versus-many  $t$  test, approaches that have been adopted in other single-subject analyses of FA imaging data in mTBI.<sup>16,17</sup> The EZ-MAP thus generated was thresholded with 2 criteria:  $|EZ| > 1.96$  for each voxel and cluster size  $P$  value 1% (corrected for multiple comparisons by the Gaussian random field theory).<sup>16,17</sup> A subject FA value from an abnormal FA lesion detected by EZ-MAP is in the range of magnitude:  $y < \bar{x} \pm 1.96 \times K(x)$ , where  $K(x) = sd(x) \times \hat{\sigma}^B(x)$ . Because  $\hat{\sigma}^B(x)$  is  $>1$  as aforementioned, the value of  $SD(K)$  from the control mean in the EZ-MAP is  $>1.96$ . Validation of the EZ-MAP method in Kim et al<sup>17</sup> serves as the premise for its application in the current study.

### Calculation of Imaging Variables

The procedure for calculating brain-wide and regional DTI measures for subsequent analysis is summarized in On-line Figs 1 and 2.

**Brain-Wide Imaging Measures.** Each subject-specific EZ-MAP of abnormal FA regions was segregated into 2 separate maps: 1) all voxels showing abnormally high FA, indicated below as *hFA*, and 2) all voxels showing abnormally low FA, referred to below as *lFA*. These maps were then used as masks and were applied to each subject's DTI parameter images: FA, axial diffusivity (AD), radial diffusivity (RD), and mean diffusivity (MD). Mean FA, AD, RD, and MD were thus calculated separately across all *hFA* voxels and across all *lFA* voxels, yielding 2 measures for each diffusion parameter in each subject. Additionally, the total volume (number of 1-mm<sup>3</sup> voxels) of *hFA* and *lFA* was also computed for each subject (On-line Fig 1).

**Regional Imaging Measures.** We selected 9 white matter regions known to be susceptible to mTBI and/or to serve functions associated with mTBI morbidity, as follows: the left frontal lobe, right frontal lobe,<sup>8</sup> left temporal lobe, right temporal lobe,<sup>10</sup> left thalamus, right thalamus,<sup>12</sup> left cerebellum and right cerebellum,<sup>29</sup> and corpus callosum (On-line Fig 2).<sup>7</sup>

Two new class variables were generated, representing the following: a) the presence (1) or absence (0) of *hFA* in each region, and b) the presence (1) or absence (0) of *lFA* for each region (On-line Fig 2). The 2 class variables were independently generated for each region. As a result, it is possible that *hFA* and *lFA* lesions will coexist within a single brain region. The 2 subgroups of subjects classified by using each class variable (a or b) were tested for significant differences in long-term outcomes.

### Statistical Analyses: Relationship between Early Imaging and Long-Term Outcomes

All statistical analyses were conducted in SPSS (Version 22.0, Released 2013; IBM, Armonk, New York). Both brain-wide and regional imaging measures (as defined above) were used in distinct analyses.

The Spearman rank correlation analysis is robust to outliers

**Table 3: Demographic and injury features of subjects and controls**

	Subjects	Controls
Mean age (yr) (range)	38.5 (24–64)	38.85 (20–60)
Sex	10 Men (38.5%) 16 Women (61.5%)	21 Men (52.5%) 19 Women (47.5%)
Mean years of education (range)	14.3 (8–24)	16.4 (2–26)
Mechanism of injury	Motor vehicle crash: 3 Sports accident: 2 Fall: 7 Assault: 7 Falling object: 7	NA
Posttraumatic amnesia	2/26	
Loss of consciousness	10/26	

**Note:**—NA indicates not applicable.

and was used to evaluate the monotonic association of brain-wide early imaging variables and long-term (1 year) outcomes.

In addition, a regional analysis of abnormal FA was performed to facilitate investigation of structure-function associations, despite the fact—which is an expected feature of traumatic brain injury (TBI) pathology—that not all subjects exhibited abnormalities in the same brain location. Student 2-sample  $t$  tests were used to compare long-term outcomes between groups of subjects who did-versus-did not exhibit *hFA* or *lFA* within a given anatomic region (listed above).

### False Discovery Rate Control for Statistical Analyses

The total number of hypotheses tested for association between imaging measures and long-term outcomes are as follows: In the brain-wide assessment of abnormal diffusion metrics across all areas of *hFA* and *lFA* in each subject, 5 imaging parameters (FA lesion volume, mean FA, mean AD, mean RD, and mean MD) were correlated with 12 outcomes for each total *hFA* and total *lFA*, totalling 120 ( $5 \times 2 \times 12$ ) tests. For regional analyses, we examined the difference between the 2 groups in 12 outcome measures for each of 9 brain regions, in which subjects were classified by the presence or absence of *hFA* and *lFA* within each brain region; 216 ( $2 \times 9 \times 12$ ) tests were required for these analyses. Thus, in total, 336 comparisons were performed across the entire study. We grouped the 336 comparisons into 10 subgroups by 5 outcome categories (memory, attention, executive, PCS, and HRQoL) and analysis approaches, brain-wide and regional. The significance of individual tests was determined by using the Benjamini Hochberg method at a false discovery rate = 0.15 for each subgroup.<sup>30,31</sup>

## RESULTS

### Study Subjects: Sample Size, Demographics, Mechanisms of Injury, and Baseline Functional Status

Thirty-nine subjects with mTBI and 40 control subjects met the inclusion criteria. Subjects with mTBI underwent DTI within 16 days of injury. Twenty-six subjects returned for 1-year follow-up and were included in the analysis. During the time elapsed between enrollment and follow-up, 6 of the 26 subjects moved to locations too far from the testing center to allow on-site, computerized cognitive assessment; they were, however, available to complete the Rivermead Post Concussion Symptoms Questionnaire and Sickness Impact Profile by phone interview.

Table 3 details demographic and injury characteristics of the 26 subjects and 40 controls used in the analysis. We found no

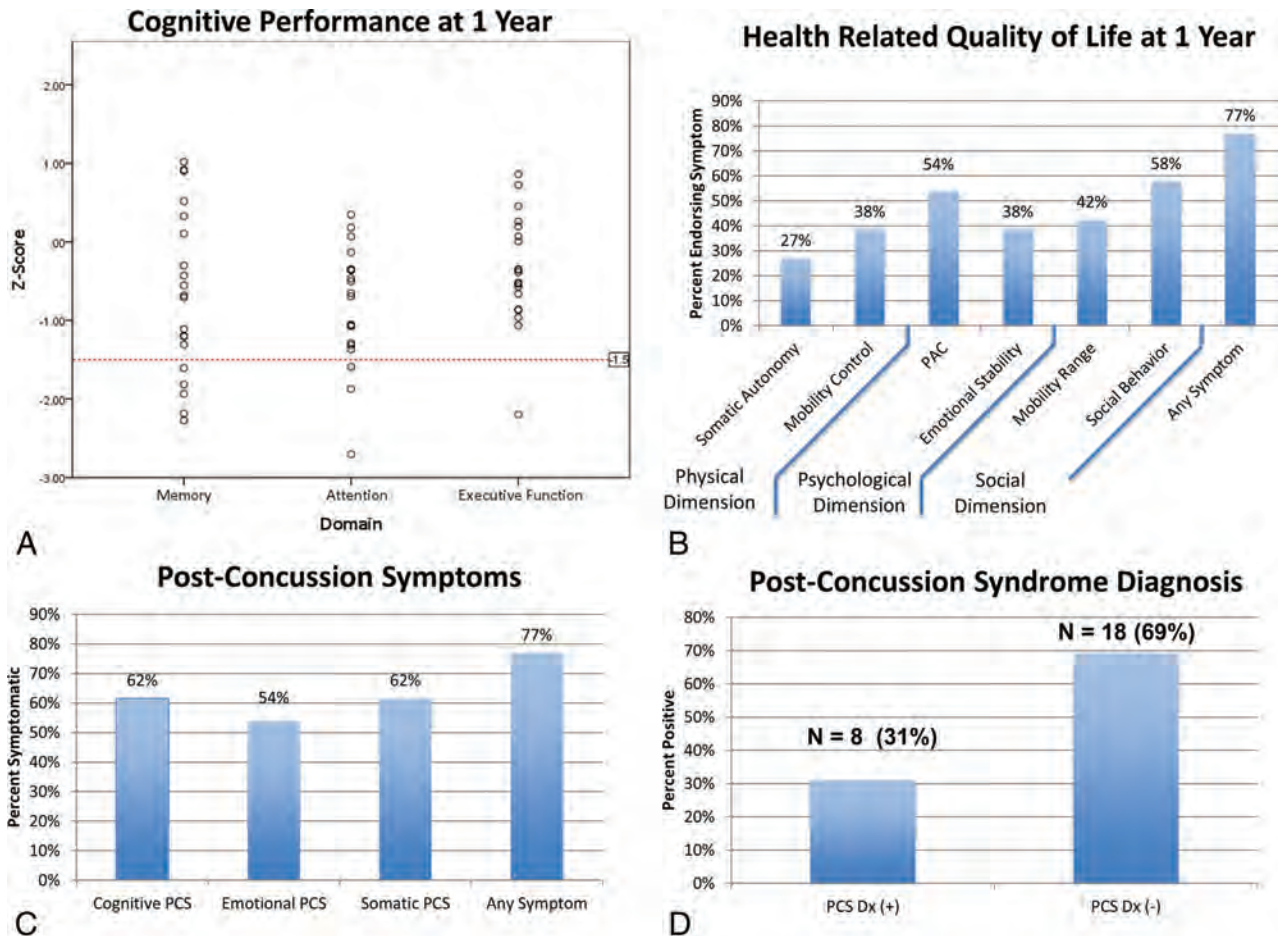


**FIG 1.** Outcomes in mTBI. *A*, Cognitive outcomes. The red dotted line indicates impairment in the given domain, defined as a z score less than  $-1.5$ . *B*, Health-related quality of life (Sickness Impact Profile), grouped according to dimension. *C*, Postconcussion symptoms (Rivermead Post Concussion Symptoms Questionnaire). *D*, Postconcussion syndrome diagnosis. PAC indicates psychological autonomy and communication.

significant difference in age ( $t = -0.134$ ,  $P = .894$ ), sex ( $\chi^2 = 1.247$ ,  $P = .264$ ), or years of education ( $t = -1.919$ ,  $P = .059$ ) between the 26 subjects and 40 controls. Nevertheless, potential effects of age, sex, and education were addressed by voxelwise regression adjustment, with application of regression coefficients to all FA voxels in which demographic covariate effects were significant at  $P < .05$  across  $>100$  contiguous voxels.<sup>16</sup> All subjects were diagnosed with mTBI in the emergency department, and no abnormalities were identified on conventional CT or MR imaging. In this relatively young sample, with a mean age of 38.5 years, changes of microvascular ischemia and stroke were not observed.

Preinjury cognitive ability was estimated through administration of the Spot-the-Word test, a measure of reading achievement, a “hold” ability that is resistant to the effects of brain injury.<sup>19</sup> We found no difference between the 26 subjects and a subset of 18 controls (those for whom data were available) on the Spot-the-Word test ( $t = -1.152$ ,  $P = .256$ ), indicating that the subjects’ preinjury intellectual functioning was not significantly different from that of controls. There were no differences in age ( $t = 1.353$ ,  $P = .184$ ), sex ( $\chi^2 = 0.834$ ,  $P = .361$ ), years of education ( $t = 1.227$ ,  $P = .228$ ), Spot-the-Word scores ( $t = -0.019$ ,  $P = .985$ ), and loss of consciousness at the time of injury ( $\chi^2 = 1.805$ ,  $P = .179$ ) between the 26 subjects included in the analysis

and the 13 subjects lost to follow-up (note that loss of consciousness data were available for only 12/13 lost to follow-up).

### Functional Outcomes at 1 Year: Cognitive Function, HRQoL, and PCS

Figure 1A depicts a range of z scores for each of the 3 cognitive domains, with impairment defined as z score values of  $>1.5$  SDs below the mean for the given domain. Figure 1B shows the prevalence of symptom endorsement related to HRQoL according to dimension (social, psychological, and physical). Figure 1C, -D demonstrate the prevalence of symptom endorsement related to PCS and the percentage of those meeting the criteria for the diagnosis of postconcussion syndrome based on the Rivermead Post Concussion Symptoms Questionnaire cutoff criterion.<sup>32</sup>

### Microstructural Abnormalities at the Time of mTBI

Using the procedures described above, we detected regions of hFA in 24/26 subjects (mean total volume = 9398  $\mu\text{L}$ ; maximum = 27,660  $\mu\text{L}$ ) and lFA in 25/26 subjects (mean total volume = 6923  $\mu\text{L}$ , maximum = 39,686  $\mu\text{L}$ ). All subjects showed at least 1 region of hFA or lFA, though not all showed both. The mean hFA averaged across all subjects (0.641) was significantly higher than the mean lFA (0.278,  $P < .001$ ). MD and RD were significantly higher

in *l*FA (0.625, 0.567) regions than in *h*FA regions (0.517, 0.357) ( $P < .001$ ,  $P < .001$ ). AD was not significantly different between *h*FA (0.805) and *l*FA (0.740) regions.

### Loss of Consciousness and Microstructural Abnormalities

Ten of 26 of subjects experienced loss of consciousness at the time of injury. Mean *h*FA and mean *l*FA values within 16 days of injury were not significantly different between those with and without loss of consciousness at the time of injury ( $t = -0.904$ ,  $P = .375$ ;  $t = 0.923$ ,  $P = .365$ , respectively).

### Relationship between Microstructural Abnormalities and Functional Outcomes

**Whole White Matter Assessment. Brain-Wide Imaging Measures and Cognitive Performance.** Imaging measures were associated with 1-year memory performance, but not with attention or executive function. The associations with memory were significant for higher RD from areas of *h*FA at baseline ( $\rho = -0.562$ ,  $P = .015$ ) and higher MD from areas of *h*FA at baseline ( $\rho = -0.488$ ,  $P = .040$ ) (On-line Fig 3).

**Brain-Wide Imaging Measures and PCS.** Neither *h*FA nor *l*FA were associated with PCS when averaged across the whole brain.

**Brain-Wide Imaging Measures and HRQoL.** Higher MD and higher RD from areas of *l*FA ( $\rho = 0.513$ ,  $P = .009$ ;  $\rho = 0.514$ ,  $P = .009$ ) were significantly associated with worse somatic autonomy. Lower mean FA from regions of *l*FA were significantly associated with worse psychologic autonomy and communication ( $\rho = -0.596$ ,  $P = .002$ ) and worse emotional stability ( $\rho = -0.581$ ,  $P = .002$ ) at 1 year postinjury (On-line Fig 4). FA, AD, RD, and MD from regions of *h*FA were not significantly associated with HRQoL.

**Regional White Matter Assessment. Regional Imaging Measures and Cognitive Performance.** Subjects with *h*FA in the left frontal and left temporal white matter performed better than those without *h*FA in these regions on tasks of attention at 1 year postinjury ( $t = 2.985$ ,  $P = .008$  and  $t = 3.322$ ,  $P = .004$ , respectively) (Fig 2).

**Regional Imaging Measures and PCS.** Subjects with *h*FA in the right thalamus white matter experienced fewer emotional postconcussion symptoms than did those without *h*FA in this region ( $t = -0.398$ ,  $P = .003$ ). Subjects with *h*FA in the left or right cerebellar hemisphere experienced fewer somatic postconcussion symptoms than did those without abnormality ( $t = -3.365$ ,  $P = .003$ ;  $t = -3.38$ ,  $P = .003$ , respectively) (Fig 3A, -C).

**Regional Imaging Measures and HRQoL.** There were no significant differences in HRQoL between individuals with and without *h*FA or *l*FA within individual regions.

## DISCUSSION

This prospective, longitudinal study leverages individualized assessment of DTI<sup>16,17</sup> to demonstrate associations between early imaging and 1-year mTBI outcomes.

Imaging studies of mTBI outcomes generally use either a priori ROI or group-level voxelwise comparisons of subjects and controls to extract imaging measures for study. Most important,

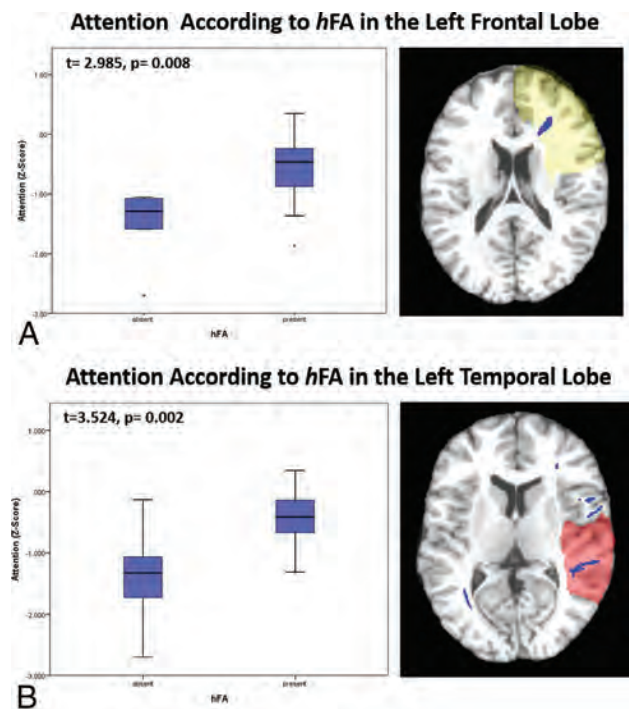


**FIG 2.** Associations between regional imaging measures and long-term cognitive outcomes. A, Subjects with high FA in the left frontal lobe perform significantly better on tasks of attention at 1 year postinjury than do those without it ( $t = 2.985$ ,  $P = .008$ ). B, Subjects with high FA in left temporal lobe perform significantly better on tasks of attention at 1 year postinjury than do those without it ( $t = 3.524$ ,  $P = .002$ ).

neither of these approaches acknowledges nor has the ability to characterize the widely recognized substantial spatial variation in injury location, which is a principal feature of mTBI.<sup>33</sup> As a result, these standard approaches will include areas with and without tissue injury in the imaging measures they study. We therefore used a technique that specifically identifies abnormalities in each individual patient (EZ-MAP), without dilution by values from normal tissue (inevitable with group-level delineation).

We have previously demonstrated the robustness<sup>17</sup> and application<sup>16</sup> of the EZ-MAP to the detection of microstructural abnormalities in patients with mTBI. In this study, we further demonstrate that the EZ-MAP method is highly effective in identifying brain pathology related to long-term outcomes. Similar to using the EZ-MAP, various other studies have used individual subject-level procedures<sup>33,34</sup> to detect pathology in DTI datasets from patients with mTBI. Our approach differs in that we used regression adjustment for covariates and EZ-MAP bootstrap resampling, to better characterize the population variance. Imaging measures summarized over brain subregions, such as the frontal lobe, surpassed whole-brain summary measures (eg, mean FA across all abnormal white matter voxels) in identifying relationships between DTI measures and functional outcomes. Although this result may be related to differences in the statistical approach between the whole-brain measures and subregion measures (correlation analysis versus dichotomous analysis, respectively), it potentially reveals an important phenomenon: Structure-function relationships are more effectively detected when measures are extracted from delimited brain regions relevant to a particular func-

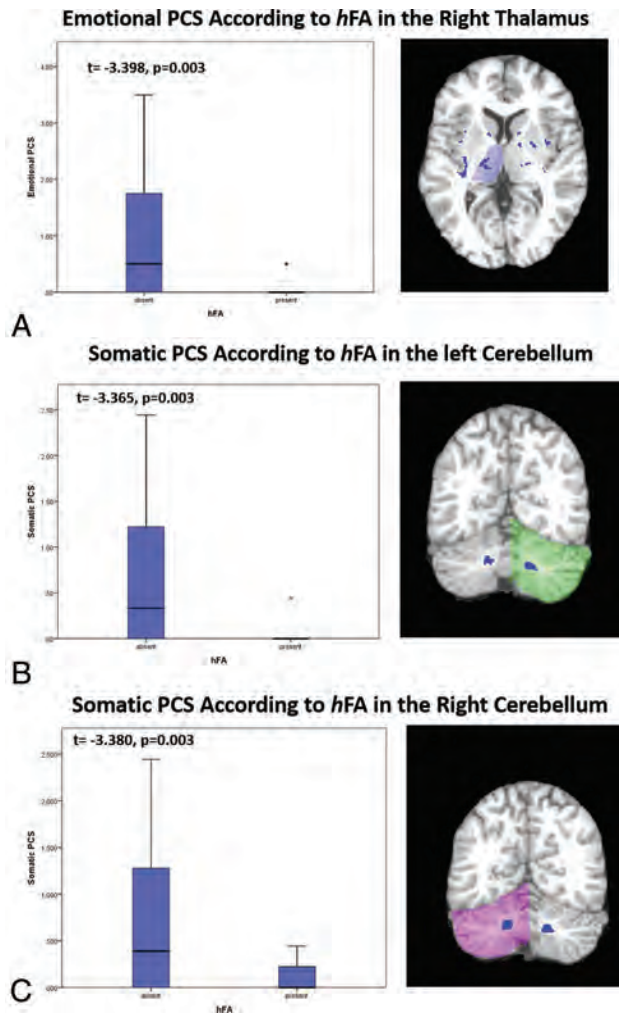


**FIG 3.** Associations between regional imaging measures and long-term functional outcomes. **A**, Subjects with *hFA* in the right thalamus have significantly fewer emotional postconcussion symptoms at 1 year than those without it ( $t = -3.398, P = .003$ ). Of those with *hFA* in the right thalamus, only 2 subjects reported emotional postconcussion symptoms. The *asterisk* indicates an outlier. **B**, Subjects with *hFA* in the left cerebellar white matter have significantly fewer somatic postconcussion symptoms at 1 year than those without *hFA* in the left cerebellum ( $t = -3.365, P = .003$ ). Of those with *hFA* in the left cerebellum, only 1 subject reported somatic postconcussion symptoms. The *asterisk* indicates an outlier. **C**, Subjects with *hFA* in the right cerebellar white matter have significantly fewer somatic postconcussion symptoms at 1 year than do those without high FA in the right cerebellum ( $t = -3.380, P = .003$ ). Of those with *hFA* in the left cerebellum, only 2 reported somatic postconcussion symptoms.

tion and not diluted by measures from regions not specifically supporting that function.

Using the EZ-MAP approach, we found regions of *hFA*, in addition to regions of *lFA*, in almost all subjects. A minority of prior studies, most of which used group-level techniques to identify abnormalities, also reported high FA and have attributed this finding to cytotoxic edema, altered myelin sheath water composition, or inflammation. Thus, *hFA* has been considered an additional biomarker for injury pathology due to mTBI.<sup>6,9,15</sup> In contrast, our use of individual-level delineation of abnormalities reveals associations of *hFA* with better long-term outcomes. These associations may reflect differences in the type of abnormality identified by using individual-level versus group-level ap-

proaches. Whereas *hFA* delineated at the group level might represent damage to common areas injured across subjects, regions of abnormally *hFA* identified at the individual level might reflect subject-specific compensatory mechanisms that enhance diffusion anisotropy through structural or functional changes, such as myelination or increased synaptogenesis at the level of the dendritic spine, which is mediated by actin polymerization.<sup>35</sup> Notably, studies have shown that short-term reversible increases in anisotropy develop with cognitive training, presumably through similar neuroplastic mechanisms.<sup>36</sup>

Relating structural changes to their functional consequences is important in understanding the import of imaging findings and characterizing injury effects in patients with TBI. Thus, the regional analyses we performed are most salient and reveal several interesting structure-function relationships. Notably, most literature on neuroanatomic structure-function relationships focuses on gray matter. However, white matter axons form the infrastructure of distributed neural networks, which underlie the domains of higher functioning so commonly impacted by the white matter injury that follows TBI.<sup>37,38</sup> We found significant regional associations of frontal and temporal *hFA* with performance on tasks of attention, tested by using the Digit Span Forward, Continuous Performance Task, and switching of attention (digits) tasks; the latter 2 depend on processing speed and therefore index neural network function. Moreover, the frontal<sup>39-41</sup> and temporal lobes<sup>42</sup> both directly play an important role in attention. The significant association of *hFA* in the thalamus with emotional PCS is not surprising, given the susceptibility of the thalamus to mTBI and its role as the major relay network of the brain, with extensive limbic and prefrontal connectivity.<sup>43,44</sup> We also identified associations of cerebellar abnormalities with somatic PCS, including dizziness, nausea/vomiting, double vision, and blurry vision, which reflect the role of the cerebellum in balance and spatial orientation.

In addition to FA, which characterizes overall coherence of diffusion direction, we explored the utility of AD, RD, and MD. Preclinical experimental studies posit low AD as a marker for intra-axonal injury and high RD as a marker for transaxonal/axolemmal injury and demyelination.<sup>4</sup> We found that high RD, but not low AD, significantly correlated with worse outcomes. We may not have identified abnormally low AD as a correlate of outcomes because the expected decrease in AD may be masked by increased AD related to gliosis and edema, which evolve in the late acute setting, the timeframe during which our subjects underwent DTI (mean, 7 days).<sup>45</sup> In a postmortem analysis of patients with multiple sclerosis, increased RD correlated with the severity of demyelination and decreased axonal attenuation, presumably because the 2 are interrelated.<sup>46</sup> We found that mean RD, but not mean AD, was significantly associated with memory and somatic autonomy in correlation analyses, consistent with this pattern. Because high RD may be a manifestation of transaxonal injury, as suggested by preclinical studies,<sup>47</sup> it may indicate more severe and irreparable axonal pathology and therefore might serve as a better early predictor of long-lasting dysfunction.

Several limitations of this study should be considered. Anisotropic voxels with 4.5-mm section thickness limit spatial resolution and may lead to spuriously low FA, particularly when multi-

ple crossing fibers are included within a single voxel.<sup>48</sup> Nonetheless, this limitation applies equally to mTBI and control subjects, who underwent identical imaging procedures; therefore, we do not expect a systematic bias to result. Despite the standardization of imaging, this limitation may partially account for the absence of significant associations between the presence of low FA and outcomes on the regional level. Moreover, the nature of the interdependence of the various DTI parameters should be noted because for instance, increased AD and RD might lead to high MD but not low FA, and an increase in AD alone would affect MD and FA. As such, primary identification of abnormality based on a summary measure such as FA may ultimately be of less value than a measure such as RD and may serve as the basis for future study. In our study, of the 39 subjects who underwent acute imaging, 26 completed PCS and HRQoL assessment (33% attrition) and 20 were available for cognitive testing (49% attrition). Attrition in mTBI cohorts is a particular challenge to research in head trauma because subjects are disinclined to follow-up either because they do not perceive themselves as injured or because of injury-related dysfunction and stress. The rate of attrition we encountered is well within the range reported in mTBI studies (35%–88%),<sup>49–51</sup> and we did not identify demographic or injury-severity differences between those who did or did not complete follow-up. Nonetheless, the possibility of bias due to selective attrition cannot be completely excluded. PCS and HRQoL are assessed by self-report, and studies have shown that symptoms related to postconcussion syndrome are common in other disease conditions, such as chronic pain,<sup>52</sup> and in healthy controls.<sup>53</sup> Thus, a further potential limitation is that symptom measures were not tested in the control sample. We addressed this issue by excluding subjects with preexisting conditions that might cause symptoms, including prior head injury, and by using tools that have been extensively validated and widely applied to TBI.<sup>20,21</sup> Ultimately, the shortcomings of subjective assessment tools underscore the importance of other, more objective indicators of impairment that might not otherwise be appreciated. This limitation is thus a major motivation for the current study. Finally, a future step might be to evaluate similar effects in a larger cohort of patients with mTBI and in a group of healthy controls.

## CONCLUSIONS

In this prospective, longitudinal study of urban subjects with mTBI, we confirm that both brain-wide and regional individualized quantification of microstructural changes shortly following mTBI are associated with important outcomes at 1 year after injury. We further identify abnormally high FA and support the hypothesis that it may be a marker of compensatory neural mechanisms and harbinger of favorable outcome, which may open new avenues toward TBI treatment.

Disclosures: Mimi Kim—RELATED: Grant: National Institutes of Health\*; UNRELATED: Consultancy: Lupus Foundation of America; Grants/Grants Pending: National Institutes of Health.\* Richard B. Lipton—RELATED: Grant: National Institutes of Health R01\*; UNRELATED: Consultancy: serves as consultant and advisory board member or has received honoraria from Alder, Allergan, American Headache Society, Autonomic Technologies, Avanir Pharmaceuticals, Boehringer Ingelheim, Boston Scientific, Bristol Myers Squibb, Colucid Pharmaceuticals, Dr Reddy's Laboratories, ElectroCore, Eli Lilly, eNeura Therapeutics, Informa, Merck & Co, Novartis, Pfizer, Teva, and Vedanta; Grants/Grants Pending: receives research support from the National

Institutes of Health\*: POIAG003949 (Program Director), POIAG027734 (Project Leader), ROIAG025119 (Investigator), ROIAG022374–06A2 (Investigator), ROIAG034119 (Investigator), ROIAG12101 (Investigator), 23NS05140901A1 (Mentor), and K23NS47256 (Mentor), and the National Headache Foundation\*; Payment for Lectures (including service on Speakers Bureaus): lecture honoraria for Continuing Medical Education–accredited lectures from the American Headache Society, the American Academy of Neurology, and the Headache Cooperative of New England; Payment for Development of Educational Presentations: American Headache Society, Comments: Chronic Migraine Education Program; Stock/Stock Options: eNeura Therapeutics. Michael L. Lipton—UNRELATED: Expert Testimony: Various (on behalf of defendants and plaintiffs); Grants/Grants Pending: Resurrecting Lives Foundation,\* Comments: grant for research on imaging in blast TBI; Patents (planned, pending or issued): image-processing methodology (patent pending)\*; Royalties: Springer (MRI physics book); Other: the Dana Foundation,\* Comments: grant for study of imaging in sports TBI. \*Money paid to the institution.

## REFERENCES

- Ruff R. Two decades of advances in understanding of mild traumatic brain injury. *J Head Trauma Rehabil* 2005;20:5–18 CrossRef Medline
- Bigler ED. Neuropsychological results and neuropathological findings at autopsy in a case of mild traumatic brain injury. *J Int Neuropsychol Soc* 2004;10:794–806 Medline
- Johnson VE, Stewart W, Smith DH. Axonal pathology in traumatic brain injury. *Exp Neurol* 2013;246:35–43 CrossRef Medline
- Mac Donald C, Dikranian K, Song S, et al. Detection of traumatic axonal injury with diffusion tensor imaging in a mouse model of traumatic brain injury. *Exp Neurol* 2007;205:116–31 CrossRef Medline
- Shenton M, Hamoda H, Schneiderman J, et al. A review of magnetic resonance imaging and diffusion tensor imaging findings in mild traumatic brain injury. *Brain Imaging Behav* 2012;6:137–92 CrossRef Medline
- Bazarian JJ, Zhong J, Blyth B, et al. Diffusion tensor imaging detects clinically important axonal damage after mild traumatic brain injury: a pilot study. *J Neurotrauma* 2007;24:1447–59 CrossRef Medline
- Niogi S, Mukherjee P, Ghajar J, et al. Extent of microstructural white matter injury in postconcussive syndrome correlates with impaired cognitive reaction time: a 3T diffusion tensor imaging study of mild traumatic brain injury. *AJNR Am J Neuroradiol* 2008;29:967–73 CrossRef Medline
- Lipton ML, Gulko E, Zimmerman ME, et al. Diffusion-tensor imaging implicates prefrontal axonal injury in executive function impairment following very mild traumatic brain injury. *Radiology* 2009;252:816–24 CrossRef Medline
- Mayer A, Ling J, Mannell M, et al. A prospective diffusion tensor imaging study in mild traumatic brain injury. *Neurology* 2010;74:643–50 CrossRef Medline
- Smits M, Houston GC, Dippel DW, et al. Microstructural brain injury in post-concussion syndrome after minor head injury. *Neuroradiology* 2011;53:553–63 CrossRef Medline
- Alhilali LM, Yaeger K, Collins M, et al. Detection of central white matter injury underlying vestibulopathy after mild traumatic brain injury. *Radiology* 2014;272:224–32 CrossRef Medline
- Grossman EJ, Ge Y, Jensen JH, et al. Thalamus and cognitive impairment in mild traumatic brain injury: a diffusional kurtosis imaging study. *J Neurotrauma* 2012;29:2318–27 CrossRef Medline
- Levin HS, Wilde E, Troyanskaya M, et al. Diffusion tensor imaging of mild to moderate blast-related traumatic brain injury and its sequelae. *J Neurotrauma* 2010;27:683–94 CrossRef Medline
- Sbordone RJ. The hazards of strict reliance on neuropsychological tests. *Appl Neuropsychol Adult* 2014;21:98–107 CrossRef Medline
- Wilde E, McCauley S, Hunter J, et al. Diffusion tensor imaging of acute mild traumatic brain injury in adolescents. *Neurology* 2008;70:948–55 CrossRef Medline
- Lipton ML, Kim N, Park YK, et al. Robust detection of traumatic axonal injury in individual mild traumatic brain injury patients: intersubject variation, change over time and bidirectional changes

- in anisotropy. *Brain Imaging Behav* 2012;6:329–42 CrossRef Medline
17. Kim N, Branch CA, Kim M, et al. **Whole brain approaches for identification of microstructural abnormalities in individual patients: comparison of techniques applied to mild traumatic brain injury.** *PLoS One* 2013;8:e59382 CrossRef Medline
  18. Williams LM, Simms E, Clark CR, et al. **The test-retest reliability of a standardized neurocognitive and neurophysiological test battery: “neuromarker.”** *Int J Neurosci* 2005;115:1605–30 CrossRef Medline
  19. Yuspeh RL, Vanderploeg RD. **Spot-the-Word: a measure for estimating premorbid intellectual functioning.** *Arch Clin Neuropsychol* 2000;15:319–26 CrossRef Medline
  20. King N, Crawford S, Wenden F, et al. **The Rivermead Post Concussion Symptoms Questionnaire: a measure of symptoms commonly experienced after head injury and its reliability.** *J Neurol* 1995;242:587–92 CrossRef Medline
  21. Bergner M, Bobbitt RA, Pollard WE, et al. **The Sickness Impact Profile: validation of a health status measure.** *Med Care* 1976;14:57–67 Medline
  22. Potter S, Leigh E, Wade D, et al. **The Rivermead Post Concussion Symptoms Questionnaire: a confirmatory factor analysis.** *J Neurol* 2006;253:1603–14 CrossRef Medline
  23. Bergner M, Bobbitt RA, Carter WB, et al. **The Sickness Impact Profile: development and final revision of a health status measure.** *Med Care* 1981;19:787–805 Medline
  24. Smith SM, Johansen-Berg H, Jenkinson M, et al. **Acquisition and voxelwise analysis of multi-subject diffusion data with tract-based spatial statistics.** *Nat Protoc* 2007;2:499–503 CrossRef Medline
  25. Holmes CJ, Hoge R, Collins L, et al. **Enhancement of MR images using registration for signal averaging.** *J Comput Assist Tomogr* 1998;22:324–33 CrossRef Medline
  26. Ardekani BA, Guckemus S, Bachman A, et al. **Quantitative comparison of algorithms for inter-subject registration of 3D volumetric brain MRI scans.** *J Neurosci Methods* 2005;142:67–76 CrossRef Medline
  27. Smith SM, Jenkinson M, Woolrich MW, et al. **Advances in functional and structural MR image analysis and implementation as FSL.** *Neuroimage* 2004;23:S208–19 CrossRef Medline
  28. Oishi K, Zilles K, Amunts K, et al. **Human brain white matter atlas: identification and assignment of common anatomical structures in superficial white matter.** *Neuroimage* 2008;43:447–57 CrossRef Medline
  29. Mac Donald CL, Johnson AM, Cooper D, et al. **Detection of blast-related traumatic brain injury in U.S. military personnel.** *N Engl J Med* 2011;364:2091–100 CrossRef Medline
  30. Benjamini Y, Hochberg Y. **Controlling the false discovery rate: a practical and powerful approach to multiple testing.** *Journal of the Royal Statistical Society: Series B (Statistical Methodology)* 1995:289–300
  31. Genovese CR, Lazar NA, Nichols T. **Thresholding of statistical maps in functional neuroimaging using the false discovery rate.** *Neuroimage* 2002;15:870–78 CrossRef Medline
  32. Sterr A, Herron KA, Hayward C, et al. **Are mild head injuries as mild as we think? Neurobehavioral concomitants of chronic post-concussion syndrome.** *BMC Neurol* 2006;6:7 CrossRef Medline
  33. Mayer AR, Bedrick EJ, Ling JM, et al. **Methods for identifying subject-specific abnormalities in neuroimaging data.** *Hum Brain Map* 2014;35:5457–70 CrossRef Medline
  34. Bouix S, Pasternak O, Rathi Y, et al. **Increased gray matter diffusion anisotropy in patients with persistent post-concussive symptoms following mild traumatic brain injury.** *PLoS One* 2013;8:e66205 CrossRef Medline
  35. Bonhoeffer T, Yuste R. **Spine motility: phenomenology, mechanisms, and function.** *Neuron* 2002;35:1019–27 CrossRef Medline
  36. Scholz J, Klein MC, Behrens TE, et al. **Training induces changes in white-matter architecture.** *Nat Neurosci* 2009;12:1370–71 CrossRef Medline
  37. Filley CM. **White matter: beyond focal disconnection.** *Neurol Clin* 2011;29:81–97, viii CrossRef Medline
  38. Filley CM. **White matter: organization and functional relevance.** *Neuropsychol Rev* 2010;20:158–73 CrossRef Medline
  39. Foster J, Eskes G, Stuss D. **The cognitive neuropsychology of attention: a frontal lobe perspective.** *Cognitive Neuropsychology* 1994;11:133–47 CrossRef
  40. Olton DS, Wenk GL, Church RM, et al. **Attention and the frontal cortex as examined by simultaneous temporal processing.** *Neuropsychologia* 1988;26:307–18 CrossRef Medline
  41. Nagahama Y, Okada T, Katsumi Y, et al. **Dissociable mechanisms of attentional control within the human prefrontal cortex.** *Cereb Cortex* 2001;11:85–92 CrossRef Medline
  42. Bocquillon P, Dujardin K, Betrouni N, et al. **Attention impairment in temporal lobe epilepsy: a neurophysiological approach via analysis of the P300 wave.** *Hum Brain Mapp* 2009;30:2267–77 CrossRef Medline
  43. Grossman EJ, Jensen JH, Babb JS, et al. **Cognitive impairment in mild traumatic brain injury: a longitudinal diffusional kurtosis and perfusion imaging study.** *AJNR Am J Neuroradiol* 2013;34:951–57, S1–3 CrossRef Medline
  44. Grossman EJ, Inglesse M. **The role of thalamic damage in mild traumatic brain injury.** *J Neurotrauma* 2016;33:163–67 CrossRef Medline
  45. Mac Donald CL, Dikranian K, Bayly P, et al. **Diffusion tensor imaging reliably detects experimental traumatic axonal injury and indicates approximate time of injury.** *J Neurosci* 2007;27:11869–76 CrossRef Medline
  46. Klawiter EC, Schmidt RE, Trinkaus K, et al. **Radial diffusivity predicts demyelination in ex vivo multiple sclerosis spinal cords.** *Neuroimage* 2011;55:1454–60 CrossRef Medline
  47. Song SK, Sun SW, Ju WK, et al. **Diffusion tensor imaging detects and differentiates axon and myelin degeneration in mouse optic nerve after retinal ischemia.** *Neuroimage* 2003;20:1714–22 CrossRef Medline
  48. Oouchi H, Yamada K, Sakai K, et al. **Diffusion anisotropy measurement of brain white matter is affected by voxel size: underestimation occurs in areas with crossing fibers.** *AJNR Am J Neuroradiol* 2007;28:1102–06 CrossRef Medline
  49. Paniak C, Toller-Lobe G, Reynolds S, et al. **A randomized trial of two treatments for mild traumatic brain injury: 1 year follow-up.** *Brain Injury* 2000;14:219–26 CrossRef Medline
  50. Emanuelson I, Andersson Holmkvist E, Björklund R, et al. **Quality of life and post-concussion symptoms in adults after mild traumatic brain injury: a population-based study in western Sweden.** *Acta Neurol Scand* 2003;108:332–38 CrossRef Medline
  51. Corrigan JD, Harrison-Felix C, Bogner J, et al. **Systematic bias in traumatic brain injury outcome studies because of loss to follow-up.** *Arch Phys Med Rehabil* 2003;84:153–60 CrossRef Medline
  52. Smith-Seemiller L, Fow NR, Kant R, et al. **Presence of post-concussion syndrome symptoms in patients with chronic pain vs mild traumatic brain injury.** *Brain Inj* 2003;17:199–206 CrossRef Medline
  53. Chan RC. **Base rate of post-concussion symptoms among normal people and its neuropsychological correlates.** *Clin Rehabil* 2001;15:266–73 CrossRef Medline

# Image Quality Required for the Diagnosis of Skull Fractures Using Head CT: A Comparison of Conventional and Improved Reconstruction Kernels

S. Takagi, M. Koyama, K. Hayashi, and T. Kawauchi

## ABSTRACT

**BACKGROUND AND PURPOSE:** Although skull fractures are generally assessed on bone images obtained by using head CT, the combined multikernel technique that enables evaluation of both brain and bone through a change in the window settings of an image set has been reported. The purpose of this retrospective study was to determine the image quality required for the accurate assessment of skull fractures by using head CT.

**MATERIALS AND METHODS:** A random sample of 50 patients (25 nonfracture and 25 simple nondisplaced skull fractures) was selected, and sets of conventional brain and bone images and improved combined multikernel images were reconstructed (4614 images). Three radiologists indicated their confidence levels regarding the presence of skull fractures by marking on a continuous scale for each image set. The mean area under the receiver operating characteristic curve was calculated for each kernel, and the statistical significance of differences was tested by using the Dorfman-Berbaum-Metz method.

**RESULTS:** Although a difference in the diagnostic performance of the 3 radiologists was suggested, the mean area under the curve value showed no significant differences among the 3 reconstruction kernels ( $P = .95$  [bone versus combined]),  $P = .91$  [bone versus brain]), and  $P = .88$  [brain versus combined]). However, the quality of brain images was distinctly poorer than the quality of the other 2 images.

**CONCLUSIONS:** There was no significant difference in the diagnostic performance of brain, bone, and combined multikernel images for skull fractures. Skull fracture diagnosis is made possible by brain image assessments. Combined multikernel images offer the advantage of high-quality brain and bone images.

**ABBREVIATIONS:** AUC = area under the receiver operating characteristic curve; ROC = receiver operating characteristic

The quality of CT images reconstructed with conventional filtered back-projection depends on the type of reconstruction kernel used. In head CT, low-pass filter kernels that decrease higher spatial frequencies and noise are generally used to reconstruct brain images, whereas high-pass filter kernels that preserve higher spatial frequencies and increase noise are generally used to reconstruct bone images.<sup>1,2</sup> In all cases, the reconstruction of brain images is required. In contrast, according to the policy of each institution, bone images are reconstructed either in all cases or only for patients with clinically suspected bone disease. Because

assessment of bone tissue is not required for all cases, worthless images increase if there is reconstruction for all cases. However, when bone images are reconstructed only in case of clinical suspicion, additional reconstruction is required if the need for bone images is determined after examination (in the situation of assessing brain images) or if the radiology technician forgets to reconstruct before sending the images (despite reconstruction of bone image being ordered in advance). Furthermore, bone image reconstruction is not possible once the raw data are deleted from the CT device. Although observers have to assess the bone tissue on brain images reconstructed by low-pass filter kernels in such cases, to our knowledge, the diagnostic performance for bone lesions has not been reported.

To resolve this issue, the usefulness of a combined multikernel technique that enables the evaluation of both brain and bone through a change in the window settings of an image set for the assessment of skull fractures has been reported.<sup>3,4</sup> The use of this technique not only decreases the number of stored images and

Received February 21, 2016; accepted after revision May 5.

From the Faculty of Health Sciences (S.T.), Hokkaido University, Hokkaido, Japan; and Radiological Center (M.K.), National Defense Medical College Hospital, Saitama, Japan; and Department of Radiology (K.H., T.K.), National Defense Medical College, Saitama, Japan.

Please address correspondence to Satoshi Takagi, PhD, Faculty of Health Sciences, Hokkaido University, Kita 12, Nishi 5, Kita-ku, Sapporo, Hokkaido 060-0812, Japan; e-mail: rt.stakagi@gmail.com

<http://dx.doi.org/10.3174/ajnr.A4861>

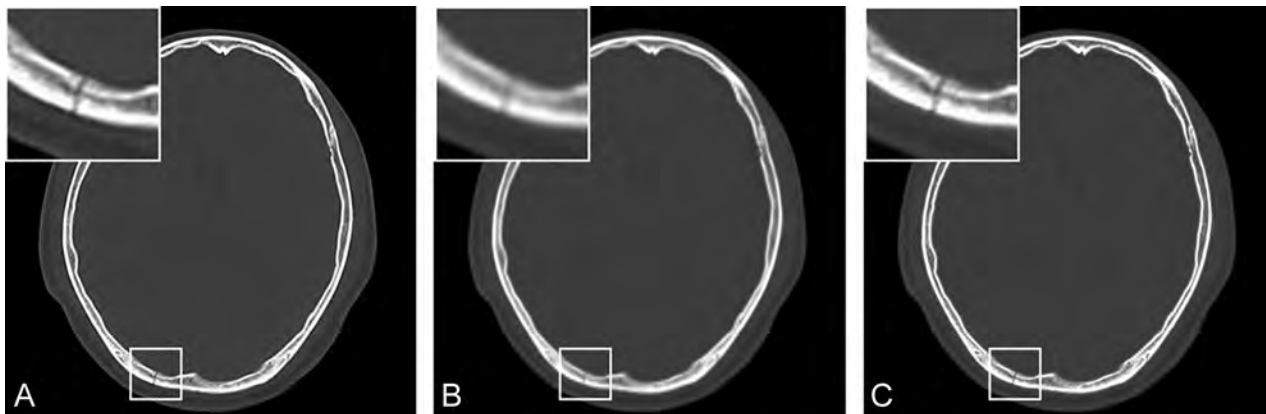


**FIG 1.** Images obtained by using bone window settings for a 44-year-old man with a nondisplaced occipital bone fracture. *A*, Bone image. *B*, Brain image. *C*, Combined multikernel image. Though the skull fracture is detectable on all images, the quality of the brain image is distinctly poorer than the quality of the other 2 images. The quality of the combined multikernel image is almost equal to that of the bone image.

**AUC values for the different CT reconstruction kernels used for the diagnosis of skull fractures**

Observer	Reconstruction Kernel		
	Bone	Brain	Combined
1	0.840	0.853	0.812
2	0.945	0.943	0.915
3	0.946	0.946	0.998
Mean	0.910	0.914	0.908

simplifies head CT examinations, but also enables the assessment of bone tissue in all cases. However, the diagnostic performance of this technique has not been sufficiently investigated.

The purpose of this study was to determine the CT image quality required for the assessment of skull fractures by using receiver operating characteristic (ROC) analysis of different reconstruction kernels and to evaluate the diagnostic performance of the combined multikernel technique for skull fractures.

**MATERIALS AND METHODS**

**Data Base**

A random sample of 50 patients (25 nonfracture and 25 simple nondisplaced skull fractures; age, 16–86 years) who visited National Defense Medical College Hospital between 2007 and 2014 was selected for this retrospective study, which was approved by our institutional review board. The requirement for informed consent was waived. All head CT examinations were performed by using a 64-row multidetector CT scanner (Aquilion 64; Toshiba Medical Systems, Tokyo, Japan). The technical protocol was as follows: peak tube voltage, 120 kV; tube current, 300 mA; gantry rotation period, 1.0 seconds; section collimation, 0.5 mm × 64; and pitch factor, 0.64. The image sets were reconstructed with separate reconstruction kernels (brain, FC21; bone, FC30) at the same thickness (5 mm gapless). The field of view for each image set was modified according to individual requirements. Combined multikernel head CT images were generated by combining the brain and bone images by using the threshold method with customized software developed by Microsoft Visual C# (Microsoft, Redmond, Washington).<sup>3</sup> A total of 4614 images (1538 images per kernel type, approximately 31 images per patient) were analyzed.

**Observer Study**

Three radiologists with 10, 15, and 27 years of experience, respectively, independently assessed all patients by using a 3-megapixel, 20.8-inch, monochrome, liquid crystal display monitor. Each type of reconstruction kernel was evaluated once at an interval of more than 4 weeks to prevent learning bias. Images with each type of reconstruction kernel were presented in a random order. The window settings were fixed for all images (window width, 2000 HU; window level, 400 HU). The radiologists indicated their confidence levels regarding the presence of skull fractures by marking on a continuous scale (0–100 on a 100-mm scale, where “0” represented normal and “100” represented definite existence of a skull fracture). No clinical information was provided to the observers.

**Statistical Analysis**

ROC analysis was used to evaluate the diagnostic performance of the 3 types of reconstruction kernels. Area under the receiver operating characteristic curve (AUC) values were calculated by using ROCKIT software (ROCKIT 0.9B Beta Version, University of Chicago, Chicago, Illinois).<sup>5</sup> The statistical significance of differences in mean AUC values among the 3 reconstruction kernels was tested by using the Dorfman-Berbaum-Metz method, which included both reader variation and case sample variation by an ANOVA approach by using the DBM MRMC software (DBM MRMC 2.1 Beta Version 2 [University of Chicago]).<sup>6,7</sup> A *P* value < .05 was considered statistically significant.

**RESULTS**

Conventional brain and bone images and a generated combined multikernel image are shown in Fig 1. The AUC values obtained for each observer and each reconstruction kernel are shown in the Table. The mean receiver operating characteristic curves for the 3 observers were generated by PlotROC software (University of Chicago) and are shown in Fig 2 for comparison of the different reconstruction kernels. The skull fracture is clearly seen on the bone and combined multikernel images. Thus, the mean AUC value showed no significant difference between them (*P* = .95). Conversely, although the skull fracture is detectable, the quality of the brain image is distinctly poorer than the quality of the other 2



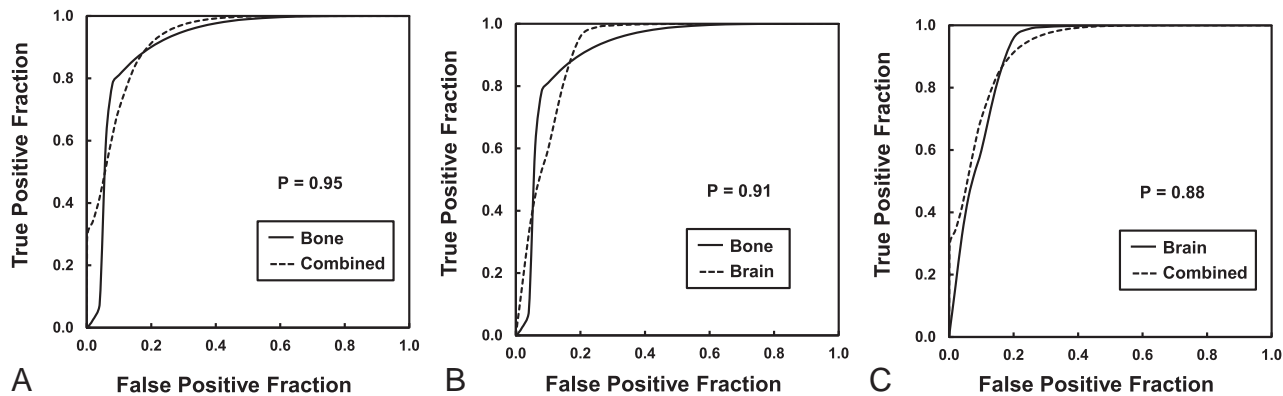


**FIG 2.** Comparison of mean ROC curves for the 3 observers for the detection of skull fractures by using 3 different CT reconstruction kernels. A, Bone versus combined. B, Bone versus brain. C, Brain versus combined. There is no significant difference in the mean AUC values among the 3 types of reconstruction kernels.

images. However, the mean AUC value showed no significant difference between the brain image and the bone ( $P = .91$ ) and combined multikernel images ( $P = .88$ ). Therefore, although a difference in AUC values was suggested among the 3 observers, the effect of the type of reconstruction kernel on the diagnostic performance was not statistically significant.

## DISCUSSION

We determined the CT image quality required for the assessment of skull fractures by using ROC analysis of different reconstruction kernels and evaluated the diagnostic performance of the combined multikernel technique for skull fractures. Skull fractures are strongly associated with epidural hematoma in patients with acute head injuries.<sup>1,8</sup> Furthermore, the relationship between skull fractures and the development of a delayed epidural hematoma after the evacuation of a contralateral hematoma has also been reported.<sup>9,10</sup> Therefore, misdiagnosis of skull fracture because of poor image quality caused by the use of inadequate reconstruction kernels should be avoided.

Generally, skull fractures must be diagnosed by using bone images.<sup>1,2</sup> However, we observed no significant differences in diagnostic performance among the 3 types of reconstruction kernels used for the assessment of skull fractures in this study. This was an interesting finding, suggesting that the diagnostic performance of head CT for skull fractures does not depend on the image quality, even if images are reconstructed by low-pass filter kernels that decrease higher spatial frequencies. In fact, the skull fracture also could be detected on brain images because of the lower CT value (Fig 1). However, the quality of brain images was distinctly poorer than the quality of bone and combined multikernel images.

Though the quality of combined multikernel images for the diagnosis of skull fractures has been reported to be poorer than the quality of bone images,<sup>3</sup> we observed no significant differences in the present study. The quality of combined multikernel images has also been reported to be clearly better than the quality of brain images when bone window settings are used and equal to the quality of brain images when brain window settings are used.<sup>3</sup> Conversely, the disadvantages of conventional 2D bone images and the efficacy of additional 3D CT image reconstruction have been reported.<sup>2,11</sup> Therefore, we recommend combined multi-

kernel image and 3D image reconstruction for improved diagnostic performance for skull fractures and simplification of head CT examinations.

Recently, the usefulness of full iterative reconstruction techniques with regard to a lower radiation dose and improved image quality has been reported.<sup>12-20</sup> The CT value for each tissue and the window settings in the full iterative reconstruction technique remain unchanged compared with those in the conventional filtered back-projection technique. Model-based iterative reconstruction has no reconstruction parameters.<sup>12,13</sup> Therefore, it enables the evaluation of each tissue through a change in the window settings of an image set and avoids the unnecessary reconstruction of several image sets at each level. However, model-based iterative reconstruction requires more than 30 minutes for the reconstruction process, which is not feasible for emergency cases.<sup>15-17</sup> Conversely, knowledge-based iterative model reconstruction allows rapid reconstruction in less than 5 minutes,<sup>18</sup> which is acceptable in clinical settings. However, because knowledge-based iterative reconstruction requires several reconstruction parameters (image definition and noise reduction),<sup>19,20</sup> there is a requirement of reconstruction of 2 image sets for optimum diagnosis of both the brain parenchyma and the skull. Therefore, we believe that the combined multikernel technique can be applied not only with the conventional filtered back-projection technique, but also with the more recent full iterative reconstruction technique.

This study has some limitations. First, although the types of reconstruction kernels differ among CT device manufacturers, we analyzed only a pair of reconstruction kernels in the present study. However, the diagnostic performance might differ for other pairs of reconstruction kernels in equipment provided by other manufacturers. Second, the evaluation time for each image set was not measured. Although the AUC values were similar, the quality of brain images was poorer than the quality of the other 2 images. Because the type of reconstruction kernel should not burden the observer, further studies should take observer stress caused by image quality into account.

## CONCLUSIONS

In this study, there was no significant difference in the diagnostic performance of brain, bone, and combined multikernel images for skull fractures. Therefore, it was revealed that the diagnosis of

skull fracture is made possible by the assessment of brain images. However, the quality of brain images is distinctly poor, and combined multikernel images offer the advantage of high-quality brain and bone images. The combined multikernel technique might be applicable to other reconstruction procedures, such as the more recent full iterative reconstruction technique. Thus, further studies that reveal the usefulness of the combined multikernel technique by comparing other pairs of reconstruction kernels are required for clinical application.

## ACKNOWLEDGMENTS

The authors thank Teppei Okamura for his cooperation in this study.

## REFERENCES

1. Lolli V, Pezzullo M, Delpierre I, et al. **MDCT imaging of traumatic brain injury.** *Br J Radiol* 2016;89:20150849 CrossRef Medline
2. Dundamadappa SK, Thangasamy S, Resteghini N, et al. **Skull fractures in pediatric patients on computerized tomogram: comparison between routing bone window images and 3D volume-rendered images.** *Emerg Radiol* 2015;22:367–72 CrossRef Medline
3. Takagi S, Nagase H, Hayashi T, et al. **Combined multi-kernel head computed tomography images optimized for depicting both brain parenchyma and bone.** *J Xray Sci Technol* 2014;22:369–76 CrossRef Medline
4. Weiss KL, Cornelius RS, Greeley AL, et al. **Hybrid convolution kernel: optimized CT of the head, neck, and spine.** *AJR Am J Roentgenol* 2011;196:403–06 CrossRef Medline
5. Metz CE, Herman BA, Shen JH. **Maximum likelihood estimation of receiver operating characteristic (ROC) curves from continuously-distributed data.** *Stat Med* 1998;17:1033–53 Medline
6. Dorfman DD, Berbaum KS, Metz CE. **Receiver operating characteristic rating analysis. Generalization to the population of readers and patients with the jackknife method.** *Invest Radiol* 1992;27:723–31 CrossRef Medline
7. Hillis SL, Berbaum KS, Metz CE. **Recent developments in the Dorfman-Berbaum-Metz procedure for multireader ROC study analysis.** *Acad Radiol* 2008;15:647–61 CrossRef Medline
8. Hayashi T, Kameyama M, Imaizumi S, et al. **Acute epidural hematoma of the posterior fossa—cases of acute clinical deterioration.** *Am J Emerg Med* 2007;25:989–95 CrossRef Medline
9. Su TM, Lee TH, Chen WF, et al. **Contralateral acute epidural hematoma after decompressive surgery of acute subdural hematoma: clinical features and outcome.** *J Trauma* 2008;65:1298–302 CrossRef Medline
10. Mohindra S, Mukherjee KK, Gupta R, et al. **Decompressive surgery for acute subdural haematoma leading to contralateral extradural haematoma: a report of two cases and review of literature.** *Br J Neurosurg* 2005;19:490–94 Medline
11. Orman G, Wagner MW, Seeburg D, et al. **Pediatric skull fracture diagnosis: should 3D CT reconstructions be added as routine imaging?** *J Neurosurg Pediatr* 2015;16:426–31 CrossRef Medline
12. Patino M, Fuentes JM, Hayano K, et al. **A quantitative comparison of noise reduction across five commercial (hybrid and model-based) iterative reconstruction techniques: an anthropomorphic phantom study.** *AJR Am J Roentgenol* 2015;204:W176–83 CrossRef Medline
13. Löve A, Olsson ML, Siemund R, et al. **Six iterative reconstruction algorithms in brain CT: a phantom study on image quality at different radiation dose levels.** *Br J Radiol* 2013;86:20130388 CrossRef Medline
14. den Harder AM, Willeminck MJ, Budde RP, et al. **Hybrid and model-based iterative reconstruction techniques for pediatric CT.** *AJR Am J Roentgenol* 2015;204:645–53 CrossRef Medline
15. Fontarensky M, Alfidja A, Perignon R, et al. **Reduced radiation dose with model-based iterative reconstruction versus standard dose with adaptive statistical iterative reconstruction in abdominal CT for diagnosis of acute renal colic.** *Radiology* 2015;276:156–66 CrossRef Medline
16. Scott Kriegshauser J, Naidu SG, Paden RG, et al. **Feasibility of ultra-low radiation dose reduction for renal stone CT using model-based iterative reconstruction: prospective pilot study.** *Clin Imaging* 2015;39:99–103 CrossRef Medline
17. Notohamiprodjo S, Deak Z, Meurer F, et al. **Image quality of iterative reconstruction in cranial CT imaging: comparison of model-based iterative reconstruction (MBIR) and adaptive statistical iterative reconstruction (ASiR).** *Eur Radiol* 2015;25:140–46 CrossRef Medline
18. Mehta D, Thompson R, Morton T, et al. **Iterative model reconstruction: simultaneously lowered computed tomography radiation dose and improved image quality.** *Med Phys Int* 2013;1:147–55
19. Nakaura T, Iyama Y, Kidoh M, et al. **Comparison of iterative model, hybrid iterative, and filtered back projection reconstruction techniques in low-dose brain CT: impact of thin-slice imaging.** *Neuro-radiology* 2016;58:245–51 CrossRef Medline
20. Suzuki S, Haruyama T, Morita H, et al. **Initial performance evaluation of iterative model reconstruction in abdominal computed tomography.** *J Comput Assist Tomogr* 2014;38:408–14 CrossRef Medline

# Optimized, Minimal Specific Absorption Rate MRI for High-Resolution Imaging in Patients with Implanted Deep Brain Stimulation Electrodes

A.M. Franceschi, G.C. Wiggins, A.Y. Mogilner, T. Shepherd, S. Chung, and Y.W. Lui

## ABSTRACT

**BACKGROUND AND PURPOSE:** Obtaining high-resolution brain MR imaging in patients with a previously implanted deep brain stimulator has been challenging and avoided by many centers due to safety concerns relating to implantable devices. We present our experience with a practical clinical protocol at 1.5T by using 2 magnet systems capable of achieving presurgical quality imaging in patients undergoing bilateral, staged deep brain stimulator insertion.

**MATERIALS AND METHODS:** Protocol optimization was performed to minimize the specific absorption rate while providing image quality necessary for adequate surgical planning of the second electrode placement. We reviewed MR imaging studies performed with a minimal specific absorption rate protocol in patients with a deep brain stimulator in place at our institution between February 1, 2012, and August 1, 2015. Images were reviewed by a neuroradiologist and a functional neurosurgeon. Image quality was qualitatively graded, and the presence of artifacts was noted.

**RESULTS:** Twenty-nine patients (22 with Parkinson disease, 6 with dystonia, 1 with essential tremor) were imaged with at least 1 neuro-modulation implant in situ. All patients were imaged under general anesthesia. There were 25 subthalamic and 4 globus pallidus implants. Nineteen patients were preoperative for the second stage of bilateral deep brain stimulator placement; 10 patients had bilateral electrodes in situ and were being imaged for other neurologic indications, including lead positioning. No adverse events occurred during or after imaging. Mild device-related local susceptibility artifacts were present in all studies, but they were not judged to affect overall image quality. Minimal aliasing artifacts were seen in 7, and moderate motion, in 4 cases on T1WI only. All preoperative studies were adequate for guidance of a second deep brain stimulator placement.

**CONCLUSIONS:** An optimized MR imaging protocol that minimizes the specific absorption rate can be used to safely obtain high-quality images in patients with previously implanted deep brain stimulators, and these images are adequate for surgical guidance.

**ABBREVIATIONS:** DBS = deep brain stimulator; RF = radiofrequency; SAR = specific absorption rate

Deep brain stimulation is an effective treatment for medically refractory movement disorders, including Parkinson disease, essential tremor, and dystonia. Imaging plays a critical role in stereotactic targeting and long-term assessment. Preoperative MR images routinely used for deep brain stimulator (DBS) placement guidance include a high-resolution T1-weighted sequence used to identify standard anatomic landmarks such as the anterior/posterior commissures and high-resolution T2-weighted MR imaging routinely used to target the subthalamic nucleus, the

most common structure targeted in deep brain stimulation for Parkinson disease. For patient safety and to judge treatment efficacy, placing bilateral leads in staged unilateral procedures can be advantageous. Due to the precision required for stereotaxis and the size of the anatomic structures (Fig 1), immediate preoperative imaging is the standard of care. When staged procedures are used, this necessitates imaging with 1 electrode in place for subsequent placement of the second electrode. Additionally, electrode-in imaging may be required to assess lead placement. Manufacturer's guidelines for performing MR imaging with DBSs in situ are extremely conservative; this feature makes acquiring diagnostic and therapeutic imaging in these patients challenging.

The recommended head specific absorption rate (SAR) limit for Medtronic DBS systems (Medtronic, Minneapolis, Minnesota) has been 0.1 W/kg (compared with the usual normal mode,

Received November 18, 2015; accepted after revision May 4, 2016.

From the Departments of Radiology (A.M.F., G.C.W., T.S., S.C., Y.W.L.) and Neurosurgery (A.Y.M.), New York University School of Medicine, New York, New York.

Please address correspondence to Yvonne W. Lui, MD, Department of Neuroradiology, 660 First Ave, 2nd Floor, New York, NY 10016-6481; e-mail: Yvonne.lui@nyumc.org

<http://dx.doi.org/10.3174/ajnr.A4865>

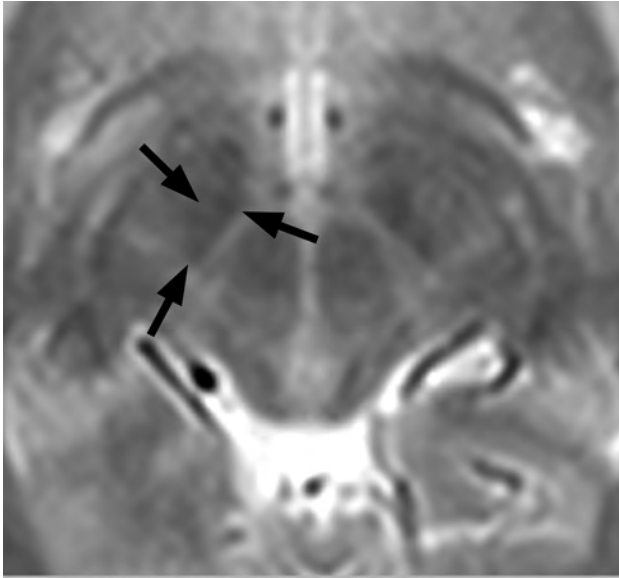


**FIG 1.** The smallest of the basal ganglia nuclei can be delineated on appropriate T2-weighted imaging through a region just cephalad to the midbrain. The subthalamic nucleus, a frequent target for deep brain stimulation, is outlined by arrows on the patient's right.

which calls for SAR < 3.2 W/kg). These devices are rated conditional at 1.5T. The main safety concern is heating the electrode due to energy deposition, and a few prior complications have been reported in the literature<sup>1,2</sup>; however, Larson et al<sup>3</sup> described 405 patients imaged with implanted DBS systems by using a variety of different scanning protocols, and their review suggests that a head SAR up to 3.0 W/kg may be applied without untoward incidents. Other potential interactions between MR imaging and implantable neuromodulators include magnetic field interactions, induced stimulation, effects on neurostimulator function, and artifacts from the device. In a single published article, Sarkar et al<sup>4</sup> reported being able to achieve diagnostic quality within the manufacturer's SAR limit with research 3D spin-echo sequences. The research sequences used in that study are not universally available, and the method they used most likely underestimated the loss of the signal-to-noise ratio. There is no clear consensus in the literature as to the optimal SAR and MR imaging parameters for safe imaging of patients with DBS electrodes.

The purpose of this study was to describe our experience with an MR imaging protocol by using product sequences, optimized for both therapeutic image quality in patients with implanted DBS electrodes and low SAR on 1.5T clinical scanners.

## MATERIALS AND METHODS

The study was approved by the institutional review board, and the imaging protocol was approved by the institutional MR imaging safety committee.

### Patients

Patients with neuromodulation devices, including Itrel II Model 7424, Soletra Model 7426, Kinetra Model 7428, Activa PC Model 37601, Activa RC Model 37612, Activa SC Model 37602, Activa SC Model 37603 (Medtronic), referred by the Center for Neuromodulation at the New York University Department of Neurosurgery for

MR imaging, were included in this protocol. Patients with bilateral DBS devices all had separate pacemakers, separated by 6 cm.

### Protocol Optimization

Axial T1-weighted magnetization prepared rapid acquisition of gradient echo is an intrinsically low-SAR sequence and requires little optimization. SAR-limited T2-weighted protocols were constructed by varying TRs, resolutions, flip angles, and radiofrequency (RF) pulse types. Use of the manufacturer-supplied low-SAR RF pulse reduced the SAR to 58% of the value with the default RF pulse. The target resolution to provide diagnostic information was 1 mm in-plane with a 2.5-mm section. The applied strategy was to keep TEs and flip angles constant and to reduce the SAR by lowering the number of RF pulses per unit of time in the sequence by increasing TRs and reducing the number of averages. It was not possible to meet the implant manufacturer's 0.1 W/kg SAR limit within reasonable scan times by this strategy. Therefore, the 0.1 W/kg SAR limit was only reached by additionally reducing the excitation flip angle and the phase resolution (to reduce encoding steps and thus reduce the number of RF pulses). Longer-than-normal scan times of up to 13 minutes were tolerated, given that patients were anesthetized. The SAR level associated with each sequence was determined by examining the scanner log files after running each sequence on a healthy volunteer and subsequently by monitoring the SAR levels recorded in the DICOM header for individual patient scans. Both sequences provided imaging through the ROI from the corpus callosum to the base of the pons.

Our initial tests showed that at SAR = 0.1 W/kg and 0.4 W/kg, the quality of the study was insufficient for stereotaxis. At an SAR of ~0.7 W/kg, we were able to achieve images adequate for intraoperative stereotaxis, and the images were reviewed by a neuro-modulation neurosurgeon (A.Y.M.) and a neuroradiologist (Y.W.L.) for adequacy (Fig 2). Therefore, the following protocol was set up: MPRAGE obtained in the axial plane with the following parameters: TR = 1870 ms, TE = 4 ms, flip angle = 15°, number of signal averages = 1, FOV = 260 × 260 mm, matrix size = 256 × 256, section thickness = 1.5 mm, 176 sections; a T2-weighted sequence obtained in the axial plane with the following parameters: TR = 2500 ms, TE = 80–83 ms, flip angle = 150°, number of signal averages = 4, FOV = 260 × 260 mm, matrix size = 256 × 256, section thickness = 2.5 mm, low SAR RF pulse. Using these parameters, we recorded ~1.0 W/kg SAR or lower for our test images obtained on an Avanto 1.5T horizontal bore magnet (Siemens, Erlangen, Germany), with a circularly polarized transmit-receive head coil.

Of note, fast spin-echo inversion recovery sequences are routinely used to identify the globus pallidus internus, the primary surgical target used to treat dystonia, but are targeted less frequently than the subthalamic nucleus in Parkinson disease. Preliminary calculations revealed that it would not be possible to modify the sequence to create usable images with acceptable SARs. Surgical targeting for the GPi was thus performed on the T2 images.

### Scanning and Patient Monitoring

Device impedance was checked by personnel from the Center for Neuromodulation before imaging preoperative patients. Patients

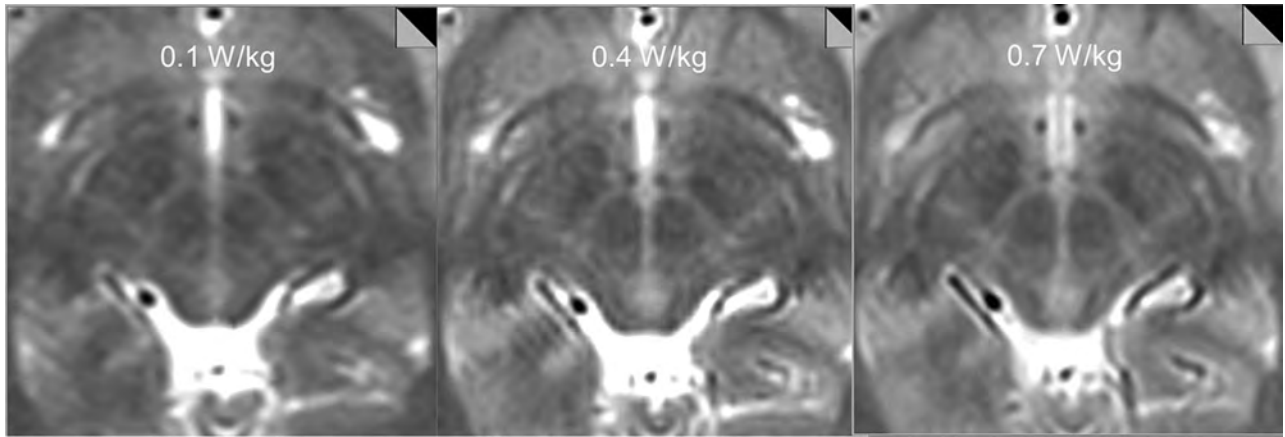


**FIG 2.** Tests on a volunteer subject show decreasing anatomic detail of the subthalamic region with decreasing SAR. T2-weighted images obtained with an SAR = 0.1 W/kg and 0.4 W/kg were deemed insufficient for stereotaxis by consensus view between the neuromodulation neurosurgeon and neuroradiologist, while images obtained with an SAR of 0.7 W/kg were adequate for intraoperative stereotaxis.

with abnormal impedance readings, broken leads, or electrodes not connected to the pacemaker were excluded because free wires are potentially more hazardous. DBS devices were deactivated before imaging by trained personnel. Imaging was performed by using either an Avanto or Aera 1.5T magnet (Siemens) with circularly polarized transmit-receive head coils, with the patient under general anesthesia to minimize motion in this patient cohort with primary movement disorders. Following imaging, devices were reprogrammed and inspected by trained neuromodulation staff. Patients were strictly monitored during and after MR imaging for complications.

### Surgical Technique

MR imaging scans were all obtained 1–4 weeks before DBS surgery. The day of the operation, a stereotactic headframe (Leksell G frame; Elekta Instruments, Stockholm, Sweden) was affixed to the head with the patient under local anesthesia, and a high-resolution CT scan was performed (120 kV, 325 mAs, detector configuration of 128 at 0.6-mm collimation). The CT data were then fused via standard stereotactic neurosurgical software (Brainlab, Munich, Germany) to the MR imaging scans for surgical targeting.

### Patients

We retrospectively reviewed the institutional data base of patients who underwent implantation of DBS electrodes between February 1, 2012, and August 1, 2015, by using the optimized low-SAR protocol. Patients who underwent clinical MR imaging performed at our institution with a DBS device in place during imaging were included. No specific exclusion criteria were applied. Chart review was performed to determine outcome, as measured by the rate of subsequent lead revision required relating directly to complications from MR imaging.

### Image Analysis

All MR images were reviewed by a board-certified neuroradiologist (Y.W.L.) and a neurosurgeon specializing in neuromodulation (A.Y.M.). Images were aligned parallel to the anterior/posterior commissure plane. The subthalamic nucleus was assessed on the T2 images on an axial section 4 mm below the anterior/posterior

commissure plane ( $z = -4$ ). The globus pallidus was assessed on the axial T2 section containing the anterior/posterior commissures ( $z = 0$ ). Overall image quality was graded as either acceptable or not acceptable for stereotactic surgical guidance on the basis of consensus review for the presurgical patients. The presence of device-related artifacts and any other artifacts was noted, and a comment was made about the impact on image quality. Data were extracted from the DICOM header for each patient scan regarding SAR deposition for each sequence. Comparison of SARs was made between magnets by using the Student  $t$  test with a significance level  $\alpha = .05$ .

### RESULTS

Twenty-nine patients (23 male/6 female) were included. The mean age was  $58 \pm 14$  years (range, 16–75 years). All subjects (22 with Parkinson disease, 6 with dystonia, 1 with essential tremor) had neuromodulation implants in situ (Activa PC Models No. 37601 and 37603; Medtronic). There were 25 subthalamic and 4 globus pallidus implants; 10 patients had bilateral electrodes. Of the 29 patients, 5 were scanned on the Aera system and 24, on the Avanto.

Average imaging time was 6 minutes 17 seconds for MPRAGE and 12 minutes 16 seconds for T2. The average SAR deposition for MPRAGE was  $0.114 \pm 0.021$  for the Avanto system,  $0.090 \pm 0.001$  for the Aera system, and  $0.109 \pm 0.021$  overall. The average SAR deposition for the T2-weighted sequence was  $1.037 \pm 0.214$  for the Avanto system,  $0.828 \pm 0.091$  for the Aera system, and  $0.987 \pm 0.210$  overall. SAR depositions for both MPRAGE and T2-weighted sequences were significantly lower on the Aera system ( $P = .012$  and  $P = .03$ , respectively) (Fig 3). Four patients underwent MPRAGE imaging only, for reasons not specified on retrospective review.

All patients tolerated imaging well, with successful completion of MR imaging. No clinical adverse events were reported during or immediately after imaging. All images were deemed by consensus review to be adequate for surgical stereotaxis and were used for subsequent surgical guidance. At an average follow-up time of 553 days  $\sim$  1.5 years (range, 2–1251 days; standard deviation, 374 days), there were no adverse patient outcomes and no cases re-

quiring lead replacement resulting directly from MR imaging complications.

Consensus review of imaging revealed mild device-related local susceptibility artifacts present in all studies that were judged not to affect overall image quality required for subsequent stereotaxis. Mild aliasing artifacts (seen only on T1-weighted images) were present in 6/29 (21%) cases, and apparent motion artifacts were seen in 4/29 (14%) cases, all seen on MPRAGE sequences (Fig 4). No such artifacts were present on T2-weighted images.

## DISCUSSION

Our results demonstrate the effective use of an optimized imaging protocol balancing image quality and low SAR to scan patients with DBS implants for surgical planning. The T2-weighted images used applied an average SAR of 0.987 seconds, which, though still higher than the original manufacturer's recommendations, is lower than that published in the literature by using standard sequences and less than one-third the usual SAR when scanning in normal mode. The MPRAGE sequences used in this study were in the range of 0.1 W/kg SAR. Low SAR imaging is accomplished with longer imaging times, the use of a low SAR RF pulse, and

adjustment of image resolution and was found to be well-tolerated by patients, without complications.

Imaging patients with implantable devices is challenging because of potential safety concerns and artifacts arising from the device, such as local susceptibility effects and spatial distortion. While it is possible to image patients with Medtronic DBS devices,<sup>5-7</sup> there is limited published information describing appropriate SARs for preoperative planning. Rezaei et al<sup>8</sup> summarized the major safety concerns of imaging patients with implanted devices, with one of the primary concerns being heating of electrodes due to energy deposition from the transmit RF field. Their in vitro tests showed changes in the temperature of an electrode tip of up to 25.3°C by using a transmit/receive body coil in contrast to a maximum change in temperature of 7.1°C by using a transmit-receive head coil. Irreversible lesions in brain tissue can occur at temperatures of 45°C and higher (ie, 8°C above normal body temperature). The degree of electrode heating depends on a number of factors, including routing of the leads, position and orientation of the device, type of coil used, whether leads are connected to the neurostimulator device, where the device is located relative to the isocenter of the MR imaging unit, and energy deposition during imaging or SAR. In the literature, there are 2 reported cases of complications from overheating of DBS electrodes.<sup>1,2</sup> In the first case, a body coil was used for excitation, and in the other, the patient had free, unconnected leads present. Additional transient adverse events such as dystonia have also been reported.<sup>9</sup>

Due to these potential adverse events, the device manufacturer (Medtronic) issued very conservative guidelines, most notably a head SAR limit of 0.1 W/kg (the usual limit is >30 times that at 3.2 W/kg). Despite a single report<sup>4</sup> of 6 subjects in whom quality MR images were obtained by using research sequences that were within the manufacturer's SAR limit, our tests concur with the more widespread experience that this power limitation is insufficient to produce therapeutic-quality T2-weighted images

for surgical planning (Fig 2) with FDA-approved sequences. In December 2015, Medtronic issued updated guidelines in which they suggested switching to the use of B1 + root mean square to calculate RF power with a maximum of 2.0 μT, though they continue to recommend that if B1 + root mean square is not available, the maximum SAR remains 0.1 W/kg.

Relatively low SAR imaging is accomplished with longer imaging times, use of a low SAR RF pulse, and adjustment of image resolution and is well-tolerated by patients, without complications. We found artifacts to be minimal and more prominent on MPRAGE. Susceptibility effects in the brain parenchyma from the lead itself were minor. Potential room for improvement in image quality may be obtained by shortening the TE (from 104 to below 90 TE) and reducing the

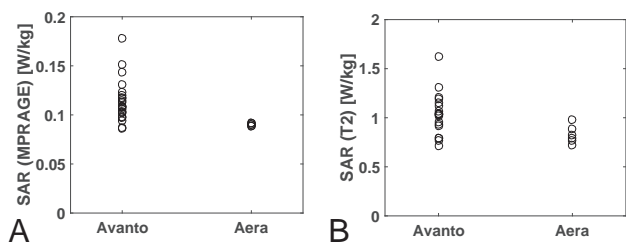


**FIG 3.** SAR deposition was significantly lower on the Aera system for both MPRAGE ( $P = .01$ ) (A) and T2-weighted images ( $P = .03$ ) (B). On the Aera system, all patients were imaged by using an SAR < 1 W/kg, and the SAR SD was small:  $\pm 0.02$  and  $\pm 0.09$  W/kg for MPRAGE and T2-weighted images, respectively.

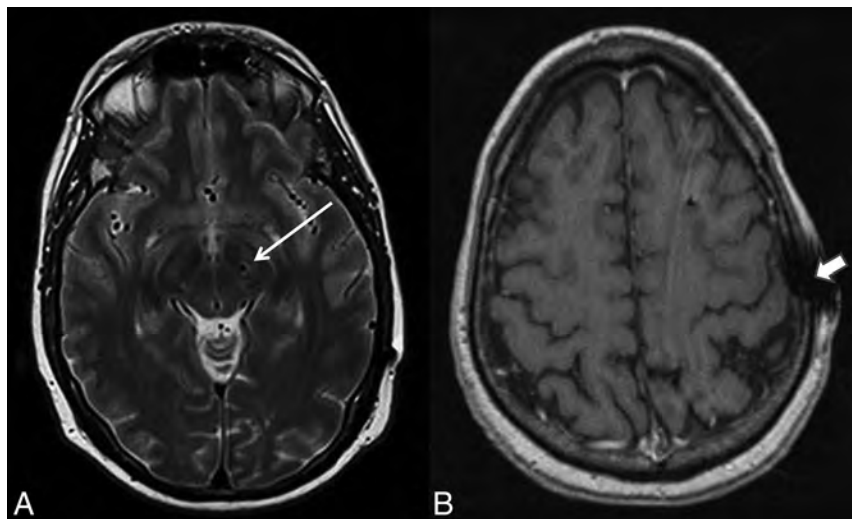


**FIG 4.** A, Susceptibility from the electrode was very minimal within the adjacent brain parenchyma on T2-weighted images (arrow). B, Device-related local susceptibility in the scalp at the site of electrode entry was seen in most cases on the MPRAGE sequence and was not thought to affect image quality. Additionally, a minority of cases showed artifacts likely attributable to stimulated echoes arising from peripheral fat on MPRAGE images only (arrowhead). Overall, all images were judged to be adequate for presurgical guidance.

bandwidth (from 195 to 160 Hz/pixel). Limiting section coverage to only the electrode target region would allow more averaging and higher resolution for the same SAR level.

Our results indicate significantly lower SAR for both pulse sequences on the Aera scanner compared with the Avanto scanner with a lower SD of SAR values, which could be due to a variety of factors including coil selection. The 2 magnet systems have a number of differences, including bore diameter, software version, and coil. In our clinical practice, specifications for the Aera and Avanto magnet systems are as follows: D13, 70 cm diameter bore, circularly polarized send/receive Aera head coil with integrated preamplifier: 315 × 475 × 360 mm (length × width × height) and B17, 60 cm diameter bore, circularly polarized Avanto head coil with 2 integrated preamplifiers: 480 × 330 × 270 mm (length × width × height), respectively. SAR levels reported by different scanners can also vary for the same actual delivered energy, and this has motivated the manufacturer's recent shift to using B1 + root mean square as the safety metric for DBS implants. Different magnets and magnet systems can affect SAR and individualized phantom scanning, and testing should be performed before clinical implementation.

The primary indication for our subjects was presurgical targeting and electrode placement/location confirmation. One limitation of this protocol is that it may not be suitable for other indications such as assessing new or additional pathology. In fact, the protocol does not include whole-brain coverage, which would result in higher SAR. Furthermore, all of our scans were obtained with the patient under general anesthesia, thereby allowing slightly longer scan time without motion. Scan time would certainly be a limitation for awake subjects.

## CONCLUSIONS

Here we introduce a practical, low-SAR MR imaging protocol that can effectively and safely obtain high-quality and high-resolution preoperative images for DBS surgical guidance in patients with a previously implanted electrode. In our multiyear experience with an average T2 head SAR of 0.987 W/kg, there are no recorded adverse events to date. Optimized coil design, such as the incorporation of a multi-element receive array in a geometry that still allows the use of the stereotactic frame, could improve image quality without increasing the SAR.

Disclosures: Graham C. Wiggins—UNRELATED: Grants/Grants Pending: National Institutes of Health/National Institute of Biomedical Imaging and Bioengineering grant No. P41EB017183, Comments: The Center for Advanced Imaging Innovation and Research (CAI<sup>2</sup>R, www.cai2r.net) at New York University School of Medicine is supported by National Institutes of Health/National Institute of Biomedical Imaging and

Bioengineering grant No. P41 EB017183. Alon Y. Mogilner—UNRELATED: Consultancy: Medtronic Neurological; Fees for Participation in Review Activities such as Data Monitoring Boards, Statistical Analysis, Endpoint Committees, and the Like: Medtronic Neurological. Timothy Shepherd—UNRELATED: Grants/Grants Pending: National Institutes of Health National Institute of Aging (NIH 1K23 AG048622-01). \*Comments: Alzheimer disease research. This work does not relate to the article in any way; Patents (planned, pending or issued): Velona Technologies. \*Comments: I have several recent provisional and full patents. 1) Three of these relate to medical devices for image-guided procedures. I am also in the process of cofounding a start-up company, Velona Technologies, with the goal of bringing these products to market. This work does not relate to the article in any way. 2) An additional patent is related to using multiparametric MRI for evaluating gamma knife radiosurgery treatment responses. This work does not relate to the article in any way; Other: Brainlab contract. \*Comments: Through the above patent related to using multiparametric MRI for evaluating gamma knife radiosurgery treatment responses, I am the Principal Investigator on a 2-year industry-funded project ("contract") from Brainlab to study the clinical uses of multiple MRI parameters for predicting and evaluating tumor response to gamma knife therapies. This work does not relate to the article in any way. Yvonne W. Lui—UNRELATED: Grants/Grants Pending: National Institutes of Health R01. \*Money paid to the institution.

## REFERENCES

1. Nutt JG, Anderson VC, Peacock JH, et al. **DBS and diathermy interaction induces severe CNS damage.** *Neurology* 2001;56:1384–86 CrossRef Medline
2. Henderson JM, Tkach J, Phillips M, et al. **Permanent neurological deficit related to magnetic resonance imaging in a patient with implanted deep brain stimulation electrodes for Parkinson's disease: case report.** *Neurosurgery* 2005;57:E1063; discussion E1063 CrossRef Medline
3. Larson PS, Richardson RM, Starr PA, et al. **Magnetic resonance imaging of implanted deep brain stimulators: experience in a large series.** *Stereotact Funct Neurosurg* 2008;86:92–100 Medline
4. Sarkar SN, Papavassiliou E, Hackney DB, et al. **Three-dimensional brain MRI for DBS patients within ultra-low radiofrequency power limits.** *Mov Disord* 2014;29:546–49 CrossRef Medline
5. Chhabra V, Sung E, Mewes K, et al. **Safety of magnetic resonance imaging of deep brain stimulator systems: a serial imaging and clinical retrospective study.** *J Neurosurg* 2010;112:497–502 CrossRef Medline
6. Fraix V, Chabardes S, Krainik A, et al. **Effects of magnetic resonance imaging in patients with implanted deep brain stimulation systems.** *J Neurosurg* 2010;113:1242–45 CrossRef Medline
7. Tagliati M, Jankovic J, Pagan F, et al; National Parkinson Foundation DBS Working Group. **Safety of MRI in patients with implanted deep brain stimulation devices.** *Neuroimage* 2009;47(suppl 2):T53–57 CrossRef Medline
8. Rezaei AR, Baker KB, Tkach JA, et al. **Is magnetic resonance imaging safe for patients with neurostimulation systems used for deep brain stimulation?** *Neurosurgery* 2005;57:1056–62; discussion 1056–62 CrossRef Medline
9. Spiegel J, Fuss G, Backens M, et al. **Transient dystonia following magnetic resonance imaging in a patient with deep brain stimulation electrodes for the treatment of Parkinson disease: case report.** *J Neurosurg* 2003;99:772–74 CrossRef Medline

## Regarding Off-Label Scanning of MR Conditional Devices

The article by Franceschi et al<sup>1</sup> highlights a safety issue of increasing concern for radiologists regarding the safe scanning of patients with implants, particularly active implantable medical devices such as deep brain stimulators (DBSs) or vagal nerve stimulators.

Implants are tested for suitability for MR imaging by the vendors, who may contract out the specific tests to independent experts. The results of the tests are then used by the vendors when they apply for device approval from the FDA. In addition, results from various modeling calculations may be presented. If the FDA is convinced by the results, they approve labeling of the device on the basis of the tests. I have often heard that this labeling is “guidance” from the FDA. However, the FDA does not provide guidance; it only approves “labeling.” This distinction is important. The FDA only approves labeling for actual conditions in tests (experimental and/or modeling) that have been presented to them.

DBS systems and their labeling are an excellent example of this process. The danger is that heating or induced currents in the electrodes could cause brain injury to the patient. As noted by Franceschi et al, DBS systems from Medtronic are labeled “MR Conditional,” with restrictive limits on the radiofrequency (rf) specific absorption rate (SAR) of 0.1 W/kg (head). This condition is so limiting that it often is not practical to image patients under this restriction and still produce images (especially T2-weighted) of sufficient quality. Thus, we have sites such as that of Franceschi et al attempting to optimize their protocols to provide an SAR as low as possible while still producing an image of acceptable diagnostic quality. Franceschi et al have found, as have other groups (eg, references 4-7 of the article), that these patients can be scanned without harm by using somewhat higher limits.

One might ask why vendors do not test under more realistic conditions. This is a good question and is illustrative of the somewhat opaque labeling-approval process. The vendor’s concern in these cases may be for the FDA to approve the MR Conditional labeling. From the resulting labeling, we in the community do not know whether the vendor conducted the testing under the gentlest of conditions possible because the vendor prefers not to re-

veal to the FDA tests that would possibly endanger the labeling approval. In other words, there is motivation to have the device labeled MR Conditional, even if the test conditions may not result in diagnostic-quality images. Once the labeling is approved, it is up to the sites to decide whether they will follow the labeling. Scanning by using parameters that exceed the labeling limits is considered off-label use.

The situation is similar to that of pharmaceutical drugs. Drugs have FDA-approved labeling indicating suitability for treating specific conditions/illnesses. Intrepid clinicians may intuit that the drug may be useful for treating other conditions and may prescribe the drug off-label and accept the possible liability. They may then publish articles or otherwise communicate to colleagues that this drug seems to be effective for other uses. Eventually, a literature trail may develop, and a consensus is built that the drug is indeed a suitable treatment for this off-label condition. The drug company may even think the drug useful for this other indication, but it only conducted tests for the initial indications to gain FDA approval to market the drug. After all, clinical drug trials are expensive. However, once it becomes a somewhat established practice to prescribe the drug off-label, the drug company benefits from the sales for the new indication without having had to go through the process of additional FDA approval and labeling. After several studies have appeared in the literature, the drug company may then apply for new labeling approval from the FDA, submitting the published studies as evidence of safety and efficacy, without having to fund (expensive) studies.

A similar situation applies to implants. What are the incentives for a company to do more testing when the clinical community will do it for them? If clinical researchers are willing to accept the risks of developing off-label conditions, publishing their results, and building a case for safe scanning under conditions exceeding the label, a vendor’s incentive to test for anything but the absolute mildest conditions diminishes.

This state of affairs impedes patient care. A risk-averse site may refuse to scan patients having these devices because they think they cannot produce sufficient-quality images without subjecting the patient to potentially unsafe scanning conditions, even



though there may be a clear need for the examination (eg, see reference 7 in Franceschi et al). However, there is no “guidance” for whether the limits were truly established or whether the vendor simply performed the minimum necessary to achieve the desired MR Conditional labeling.

What is the solution? First, I applaud the effort of Franceschi et al and others who are willing to undertake systematic optimization of parameters. However, perhaps the imaging community should urge more responsibility from the device vendors and the FDA. In fairness, as noted in Franceschi et al, the DBS vendor Medtronic has made recent advances in improving their DBS devices to be more robust in withstanding radiofrequency from a body coil, enabling full-body scanning. They have also revised the labeling for these new versions of the DBS to present the rf limits in terms of  $B_1 + \text{root mean square (rms)}$  values; this revision is becoming popular because it is not model-dependent, while SAR is. The new DBS labeling of  $B_1 + \text{rms}$  of  $\leq 2 \mu\text{T}$  allows a higher power rf than the previous 0.1 W/kg SAR limit, thus improving image quality. I applaud this advance.

Even without additional testing, the labels could still provide more information. For example, in the case of the DBS devices, instead of simply saying that “an applied SAR up to 0.1 W/kg (0.05 W/lb) may be used,” the labeling could say: “Tests using a sequence with an SAR of 0.1 W/kg resulted in a temperature rise of

xxx degrees Celsius in a water-polyacrylate phantom of 2 L [or whatever the test conditions/models actually were]. Higher SAR conditions have not been tested.” (To be fair, there are devices for which the labeling does provide this information.) This communication alone would give additional information for those making decisions about scanning (“guidance”!). In my opinion, MR Conditional labeling should not be approved unless the testing reflects conditions that would reliably produce diagnostic-quality images. (Note that I am not saying they have to be textbook-quality images.) Approval of labeling for unrealistically mild scanning conditions leads to uncertainty. However, the FDA and the vendors have no reason to change their practices without pressure from the clinical community, and I hope this commentary stimulates further discussion on this topic.

## REFERENCE


















1. Franceschi AM, Wiggins GC, Mogilner AY, et al. **Optimized, minimal specific absorption rate MRI for high-resolution imaging in patients with implanted deep brain stimulation electrodes.** *AJNR Am J Neuroradiol* 2016 Jul 14. [Epub ahead of print] CrossRef Medline

 **M.S. Brown**

Department of Radiology  
University of Colorado Anschutz Medical Center  
Aurora, Colorado

<http://dx.doi.org/10.3174/ajnr.A4932>

# Early Biomarkers from Conventional and Delayed-Contrast MRI to Predict the Response to Bevacizumab in Recurrent High-Grade Gliomas

 D. Daniels,  D. Guez,  D. Last,  C. Hoffmann,  D. Nass,  A. Talianski,  G. Tsarfaty,  S. Salomon,  A.A. Kanner,  D.T. Blumenthal,  F. Bokstein,  S. Harnof,  D. Yekutieli,  S. Zamir,  Z.R. Cohen,  L. Zach, and  Y. Mardor



## ABSTRACT

**BACKGROUND AND PURPOSE:** The interpretation of the radiologic response of bevacizumab-treated patients with recurrent high-grade gliomas represents a unique challenge. Delayed-contrast MR imaging was recently introduced for calculating treatment-response-assessment maps in patients with brain tumors, providing clear separation between active tumor and treatment effects. We studied the application of standard and delayed-contrast MR imaging for assessing and predicting the response to bevacizumab.

**MATERIALS AND METHODS:** Twenty-four patients with recurrent high-grade gliomas were scanned before and during bevacizumab treatment by standard and delayed-contrast MR imaging. The mean change in lesion volumes of responders (overall survival,  $\geq 1$  year) and nonresponders (overall survival,  $< 1$  year) was studied. The lesion volumes at baseline and the changes in lesion volumes 1 month after treatment initiation, calculated from standard and delayed-contrast MRIs, were studied as possible predictors of outcome. In scans acquired at progression, the average change in lesion volume from previous follow-up in standard and delayed-contrast MRIs was compared.

**RESULTS:** Response and progression patterns were identified from the mean change in lesion volumes, depicted from conventional T1WI, delayed contrast-enhanced MR imaging, and DSC MR imaging. Thresholds for early prediction of response were calculated by using these sequences. For each predictor, sensitivity, specificity, positive predictive values, and negative predictive values were calculated, reaching 85.7%, 87.5%, 75%, and 93.3% for conventional T1WI; 100%, 87.5%, 77.8%, and 100% for delayed-contrast MR imaging; and 75%, 78.6%, 50%, and 91.7% for DSC MR imaging. The benefit of delayed-contrast MR imaging in separating responders and nonresponders was further confirmed by using log-rank tests (conventional T1WI,  $P = .0022$ ; delayed-contrast MR imaging,  $P < .0001$ ; DSC MR imaging,  $P = .0232$ ) and receiver operating characteristic analyses. At progression, the increase in lesion volumes in delayed-contrast MR imaging was 37.5% higher than the increase in conventional T1WI ( $P < .01$ ); these findings suggest that progression may be depicted more effectively in treatment-response-assessment maps.

**CONCLUSIONS:** The benefit of contrast-enhanced MR imaging for assessing and predicting the response to bevacizumab was demonstrated. The increased sensitivity of the treatment-response-assessment maps reflects their potential contribution to the management of bevacizumab-treated patients with recurrent high-grade glioma.

**ABBREVIATIONS:** BlueV = blue volume calculated from the TRAMS; FLAIRV = FLAIR hyperintense volume calculated from precontrast FLAIR MRI; HGG = high-grade glioma; HPV = hyperperfusion volume calculated from DSC MRI; OS = overall survival; PFS = progression-free survival; RANO = Response Assessment in Neuro-Oncology; TIGdV = enhancing volume calculated from contrast-enhanced T1WI; TRAM = treatment-response-assessment map

**B**evacizumab is an antiangiogenic drug, FDA-approved for patients with recurrent glioblastoma multiforme. Bevacizumab

commonly results in prolonged progression-free survival (PFS) and faster reduction of corticosteroid treatment; however, the role of bevacizumab in overall survival (OS) remains controversial.<sup>1-4</sup> Radiologically, bevacizumab treatment is often accompa-

Received January 12, 2016; accepted after revision May 2.

From the Oncology Institute (L.Z., A.T.), Advanced Technology Center (D.G., D.L., D.D., S.S., Y.M.), Department of Neurosurgery (Z.R.C., S.H.), Radiology Institute (C.H., G.T.), and Pathology Institute (D.N.), Sheba Medical Center, Ramat-Gan, Israel; Sackler Faculty of Medicine (L.Z., D.D., C.H., G.T., Z.R.C., Y.M., S.H.) and School of Mathematical Sciences (D.Y., S.Z.), Tel-Aviv University, Tel-Aviv, Israel; and Neuro-Oncology Service (D.T.B., F.B.) and Stereotactic Radiosurgery Unit (A.A.K.), Tel-Aviv Sourasky Medical Center, Tel-Aviv, Israel.


This work was performed in partial fulfillment of the requirements for a PhD degree by Dianne Daniels at the Sackler Faculty of Medicine, Tel Aviv University, Israel.

This work was supported by a generous donation from Roche Pharmaceuticals, the Joseph Sagol PhD Scholarship for Dianne Daniels, and a research grant from Brainlab AG.

Paper previously presented, in part or whole, at: Annual Meeting of the European Association of Neuro-oncology, October 9–12, 2014; Turin, Italy; Annual Meeting of the American Society of Functional Neuroradiology, March 18–20, 2015; Tucson, Arizona; and Annual Meeting of the American Society for Radiation Oncology, October 18–21, 2015; San Antonio, Texas.

Please address correspondence to Dianne Daniels, PhD, The Advanced Technology Center, Sheba Medical Center, Tel-Hashomer, 52621; e-mail: dianne.daniels@sheba.health.gov.il

 Indicates article with supplemental on-line appendices and table.

 Indicates article with supplemental on-line photo.

<http://dx.doi.org/10.3174/ajnr.A4866>

nied by a dramatic decrease in contrast enhancement due to vascular normalization, causing unique challenges in interpreting the radiographic response.<sup>5-7</sup>

Several studies have demonstrated that treatment-response criteria and changes on contrast-enhanced T1WI may serve as predictors of PFS and OS in patients treated with bevacizumab,<sup>8-12</sup> while other studies have identified only weak relationships between imaging and OS. This difference may be explained by the difficulty in defining subtle enhancing tumor boundaries after the start of bevacizumab therapy.<sup>12</sup> In addition, several physiologic parameters such as relative CBV and hyperperfusion volume (HPV, the fraction of contrast-enhancing volume with relative CBV above a predetermined threshold), calculated from DSC MR imaging, and ADC histogram analysis and functional diffusion maps, calculated from DWI, were also shown to be associated with outcome.<sup>13-16</sup> The clinical utility of these physiologic imaging techniques has not yet been confirmed, and methodic concerns such as standardization of measurement parameters, artifact minimization, and improvement of spatial resolution remain unresolved.<sup>6,7</sup>

Treatment-response-assessment maps (TRAMs) were recently introduced, providing high-resolution differentiation between tumor and nontumor tissues (such as radionecrosis and pseudoprogression) in patients with high-grade gliomas (HGGs) and those with brain metastases undergoing standard treatment.<sup>17,18</sup> TRAMs are calculated by subtracting conventional T1WI (acquired a few minutes postcontrast) from delayed T1WI (acquired with a delay of >1 hour postcontrast). These maps depict the spatial distribution of contrast accumulation and clearance.

This model-independent technique is based on robust T1WI sequences, enabling separation between active tumor (contrast clearance at the delayed time point, blue in the TRAMs) and treatment effects (contrast accumulation, red). The TRAMs were validated histologically in 51 patients having undergone resection, resulting in 100% sensitivity and 92% positive predictive value to active tumor. One explanation for the difference between the 2 populations may be found in the vessel morphology typically present in these regions<sup>17,18</sup>: In blue tumor regions, vessel lumens were viable and undamaged, while vessels in the red regions presented different stages of vessel necrosis. Here, we studied the application of standard and delayed-contrast MR imaging for assessing and predicting the response to bevacizumab.

## MATERIALS AND METHODS

### Patients and Treatment

This prospective study was conducted after approval of the local ethics committee at Sheba Medical Center. Written informed consent was obtained from all patients.

Included were patients with recurrent HGG who failed the standard first-line therapy (maximal surgical resection, radiation therapy, and concomitant and adjuvant chemotherapy with temozolomide) and were candidates for bevacizumab, older than 18 years of age, and willing to sign the informed consent form. Exclusion criteria were World Health Organization performance status of  $\leq 3$ , contraindications to undergoing MR imaging, and contraindications to bevacizumab administration.

Twenty-four patients with HGG who underwent standard chemoradiation treatment and had progressed were recruited and

scanned before and periodically after the initiation of bevacizumab treatment (10 mg/kg every 14 days). Six were women, and the mean age at recruitment was  $54 \pm 13$  years, ranging from 25 to 73 years. At recruitment, 15 patients had undergone gross total resection; 2, subtotal resections; and 7, biopsies. HGG histology included the following: 17 with World Health Organization grade IV (16 with glioblastoma multiforme; 1 gliosarcoma) and 7 grade III (3 with anaplastic astrocytomas; 3 with anaplastic oligodendroglioma; 1 with anaplastic oligoastrocytoma).

### MR Imaging: Data Acquisition

Patients underwent MR imaging before treatment (following progression), 1 month posttreatment, and every 2–3 months thereafter or earlier according to their clinical condition. Patients were scanned between 2 and 8 times, up to 94 imaging sessions. All patients had a pretreatment scan, acquired  $15 \pm 9$  days before treatment, and a 1-month follow-up scan, acquired  $36 \pm 9$  days posttreatment.

The MRIs were acquired by using 1.5T and 3T MR imaging systems (Optima MR450w and Signa HD; GE Healthcare, Milwaukee, Wisconsin). The patients were scanned up to ~30 minutes after contrast injection by using the hospital standard brain tumor protocol, which included DSC MR imaging, FSE T2WI, pre- and postcontrast T2-FLAIR imaging, EPI-based DWI, SWI, and high-resolution spin-echo T1WI, which were acquired before and 2 minutes 54 seconds  $\pm$  1 minute 24 seconds, on average, after contrast injection (immediately after DSC MR imaging). The patients were then taken out of the MR imaging system and were asked to return for a short scan performed 75 minutes 12 seconds  $\pm$  6 minutes 6 seconds after contrast injection, which included the same high-resolution, spin-echo T1WI sequence. T1WIs were acquired with TE = 22 ms, TR = 240 ms, FOV =  $26 \times 19.5$  cm, section thickness of 5 mm with a 0.5-mm gap, and  $512 \times 512$  pixels. DSC MRIs were acquired with TE = 50 ms, TR = 2000 ms, flip angle =  $70^\circ$ , FOV =  $26 \times 19.5$  cm, 5/0.5-mm section thickness, and  $96 \times 128$  pixels. A standard single dose (0.1 mmol/kg) of Gd-DOTA (Dotarem, 0.5 mmol/mL; Guerbet, Aulnay-sous-Bois, France) was injected intravenously by using an automatic injection system 6 seconds after starting DSC MR imaging.

### MR Imaging: Data Analysis

All image analysis was performed by using Matlab (Version R2010a; MathWorks, Natick, Massachusetts).

The TRAMs were calculated as previously described,<sup>17,18</sup> and several parameters were calculated from conventional and delayed-contrast MR imaging, as defined below:

- Enhancing volume calculated from contrast-enhanced T1WI (T1GdV)
- FLAIR hyperintense volume calculated from precontrast FLAIR MRI (FLAIRV)
- Blue volume calculated from the TRAMs (BlueV), representing efficient clearance of contrast from the tissue
- Hyperperfused volume calculated from DSC-MRI (HPV)
- Mean ADC value calculated from DWI (mean ADC).

T1GdVs, FLAIRVs, and BlueVs were calculated by using a semiautomatic segmentation algorithm. A detailed description of this algorithm and the calculations of HPV and mean ADC are presented in On-line Appendix A.

### **Assessment of Progression**

For each follow-up scan, radiologic outcome was assessed from the change in T1GdVs and FLAIRVs from the previous scan, by using the same thresholds for 2D-T1WI prescribed by the Response Assessment in Neuro-Oncology (RANO) group guidelines.<sup>5</sup> In short, a decrease of  $\geq 50\%$  in T1GdV with stable or reduced FLAIRV was considered a response; an increase of  $\geq 25\%$  in T1GdV or an increase of  $> 25\%$  in FLAIRV, not attributed to other causes, or the appearance of any new lesion was considered progression. PFS was calculated as the time difference between initiation of bevacizumab treatment and the acquisition of the first MR imaging scan indicating progression.

### **Separating Responders and Nonresponders**

Patients with an OS of  $\geq 1$  year were considered responders, and those with an OS of  $\leq 1$  year, nonresponders.

### **Response Patterns**

In an attempt to identify reliable imaging parameters for early assessment of response and nonresponse to bevacizumab, the mean values of the changes in lesion volumes were plotted separately for responders and nonresponders as a function of time for the following parameters: T1GdVs, FLAIRVs, BlueVs, HPVs, and mean ADCs. The separation between responders and nonresponders was studied for the different parameters at the 1-month follow-up.

### **Early Assessment of Response to Bevacizumab Treatment**

To determine the threshold for each predictor, we plotted the logarithmic values of patients' PFS as a function of the logarithmic values of the change (ratio) in lesion volume after 1 month of treatment for T1GdVs, BlueVs, and HPVs. A linear function was fitted to each plot (log-log plots of PFS versus volume change) and thresholds for differentiating responders and nonresponders were determined for each of the 3 parameters by calculating the change (ratio) in lesion volume corresponding to a PFS of 6 months.

To establish the validity of these predictors for early (1-month) assessment of response to bevacizumab, we divided the patients into 2 groups defined by the thresholds of each of the 3 predictors determined above (T1GdV, BlueV, and HPV): Responders were below the threshold; nonresponders, above it. The median OS of the groups determined by these thresholds was calculated and compared by using log-rank analysis.

Receiver operating characteristic analysis was performed for comparing the ability of the 1-month change in T1GdV, BlueV, and HPV to aid early prediction of PFS and OS, by using the area under the curve as a measure of performance.

### **Statistical Analysis**

Statistical analysis was performed by using GraphPad InStat (Version 3.05; GraphPad Software, San Diego, California).

The median OS of the responders and nonresponders was cal-

culated and compared by using log-rank analysis. Comparison of the unpaired differences between responders and nonresponders and comparison of the baseline radiologic parameters of the responders with those of the nonresponders were performed by using an unpaired *t* test with a Welch correction. The correlation between patients' PFS and OS was studied by using linear regression.

In all follow-up scans for which progression was determined, the change (ratio) in T1GdVs since the previous follow-up was compared with that of BlueVs and HPVs by using Wilcoxon matched-pairs signed ranks. This method was also used to compare FLAIRVs and mean ADC values before and after treatment.

In all analyses,  $P < .05$  was considered a significant difference.

## **RESULTS**

### **Separating Responders and Nonresponders**

Seven of the 24 recruited patients (29.2%, of which 57.1% were grade IV; 42.9%, grade III; 28.6% underwent biopsy; 14.3%, subtotal resection; 57.1%, gross total resection) were responders, and 17 (70.8%, of which 76.5% were grade IV; 23.5%, grade III; 29.4% underwent biopsy; 11.8%, subtotal resection; 58.8%, gross total resection) were nonresponders.

The median PFS of all patients was 3.5 months (95% CI, 2.3–7.6 months). Eight of the 24 patients had a PFS of  $\geq 6$  months, and 16 had a PFS of  $< 6$  months. The median OS of all patients was 9.2 months (95% CI, 8.2–11.6 months). The median OS of the responders was significantly higher than that of the nonresponders: 24.1 months (95% CI, 14.8–34.4 months) versus 8.7 months (95% CI, 5.4–9.2 months) ( $P < .0001$ ). Significant correlation was found between patients' PFS and OS ( $r^2 = 0.94$ ,  $P < .0001$ ). Seven of the 8 patients with a PFS of  $\geq 6$  months reached an OS of  $\geq 1$  year (3 were alive at the time of analysis), and all patients with a PFS of  $< 6$  months did not.

At 1 month, the response was determined in 15 (62.5%) patients. However, 8 of them showed only short-term benefit (OS of  $< 1$  year, with a median OS of 6.9 months; 95% CI, 5.2–11.4 months), while only 7, as mentioned above (less than half of the initially responding patients), showed a long-term response.

### **Treatment Outcome is Independent of Pretreatment Radiologic Markers**

No statistically significant differences were found between any of the baseline parameters of the responding and nonresponding patients: T1GdV:  $32.9 \pm 13.4/29.4 \pm 4.6$  mL,  $P = .81$ ; BlueVs:  $17.3 \pm 7.7/15.1 \pm 2.2$  mL,  $P = .80$ ; FLAIRVs:  $156.5 \pm 34.3/127.7 \pm 15.0$  mL,  $P = .46$ ; HPV:  $14.2 \pm 5.1/12.6 \pm 2.2$  mL,  $P = .79$ ; mean ADCs:  $9.8 \pm 1.0/1.1 \pm 0.6 \times 10^{-3}$  mm<sup>2</sup>/s,  $P = .57$ .

Examples demonstrating that the response to bevacizumab is independent of pretreatment tumor volumes are given in Fig 1.

### **Response Patterns**

Responders showed a significant decrease in lesion volumes at the 1-month follow-up (T1GdVs: decrease to  $20.1\% \pm 3.8\%$  of baseline volume; BlueVs:  $13.7\% \pm 2.3\%$ ; HPVs:  $15.1\% \pm 5.5\%$ ), followed by decreased and stable lesion volumes on the next follow-ups. Nonresponders showed a smaller decrease at the 1-month follow-up (T1GdVs:  $64.7\% \pm 9.3\%$ ; BlueVs:  $63.3\% \pm 9.4\%$ ;

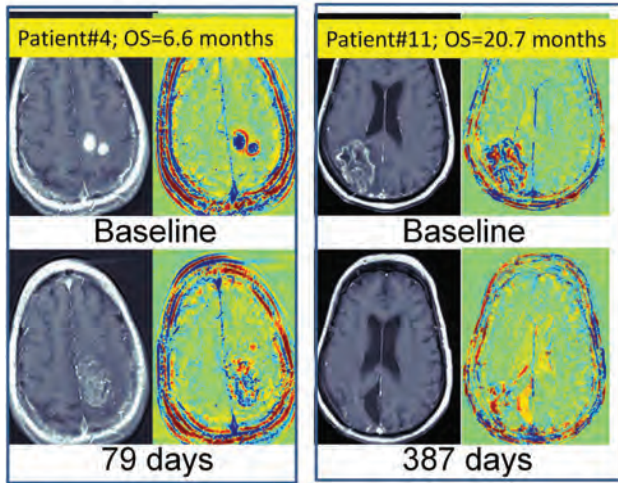


**FIG 1.** Examples demonstrating that the response to bevacizumab is independent of pretreatment tumor volumes: Shown are axial contrast-enhanced T1-weighted MRIs and TRAMs calculated 5 days before bevacizumab treatment and 79 days post-initiation of treatment of a nonresponding patient (left) with a relatively small pretreatment tumor. Also shown are contrast-enhanced T1-weighted MRIs and TRAMs calculated 7 days before bevacizumab treatment and 387 days post-initiation of treatment of a responding patient (right) with a relatively large pretreatment tumor. One month after the initiation of treatment, the nonresponding patient's tumor volumes increased (blue up to 131% of initial volume, and TI, up to 103%). Despite the large initial tumor volume, the responding patient showed significant reduction in tumor volume (blue down to 21% of initial volume, and TI, down to 25%), which remained low for >15 months posttherapy. Both patients showed decreased FLAIR volumes.

HPVs:  $53.4\% \pm 13.4\%$ ), followed by a significant increase in the next follow-ups (Fig 2).

The separation between responders and nonresponders was studied at the 1-month follow-up and was found significant for the following: T1GdVs:  $P = .0003$ ; BlueVs:  $P < .0001$ ; HPVs:  $P = .017$ .

When we compared FLAIRVs and mean ADCs before and after 1 month of treatment for all patients (responders and nonresponders), the decrease after the initiation of treatment was significant (FLAIRVs:  $P = .001$ ; mean ADCs:  $P = .0002$ ), but there was no significant difference between responders and nonresponders (FLAIRVs:  $P = .29$  and ADCs:  $P = .49$ ).

#### Early Assessment of Response to Bevacizumab Treatment

When plotted on a log-log scale, PFS showed significant linear correlation with the change in lesion volume for all 3 predictors: The correlation coefficient of BlueV ( $r^2 = 0.80$ ;  $P < .0001$ ) was found to be higher than that of T1GdV ( $r^2 = 0.58$ ;  $P = .0002$ ), and HPV ( $r^2 = 0.55$ ;  $P = .0015$ ).

The thresholds for differentiating responders and nonresponders calculated from this fit analysis were 0.32 for T1GdV, 0.29 for BlueV, and 0.19 for HPV. Accordingly, if the change in lesion volume 1 month after initiation of bevacizumab is lower than these thresholds (for example, if T1GdV decreases to below 29% of its pretreatment volume, ie,  $\frac{T1GdV_{1\text{ month}}}{T1GdV_{\text{baseline}}} < 0.29$ , the patient is predicted to be a responder; if the change is above these thresholds, the patient is predicted to be a nonresponder. The Table summarizes the median OS of the groups determined by

these thresholds and the  $P$  values resulting from log-rank analysis. Kaplan-Maier curves are presented in Fig 3.

Using the thresholds determined from PFS values, we calculated the sensitivity, specificity, positive predictive values, and negative predictive values to the response (OS of  $\geq 1$  year) for each of the 3 predictors reaching 100%, 87.5%, 77.8%, and 100% for TRAMs; 85.7%, 87.5%, 75%, and 93.3% for contrast-enhanced MR imaging; and 75%, 78.6%, 50%, and 91.7% for DSC MRI.

Receiver operating characteristic analysis applied to predefined clinical end points of PFS at  $\geq 6$  months and OS at  $\geq 1$  year demonstrated the added value of the TRAMs (Fig 3): For prediction of PFS, the areas under the curve were the following:  $0.831 \pm 0.099$ ,  $P = .03$  for T1GdV;  $0.938 \pm 0.062$ ,  $P = .005$  for BlueV; and  $0.815 \pm 0.106$ ,  $P = .04$  for HPV. For OS of  $\geq 1$  year, the areas under the curve were the following:  $0.893 \pm 0.079$ ,  $P = .02$  for T1GdV;  $0.946 \pm 0.056$ ,  $P = .008$  for BlueV; and  $0.821 \pm 0.119$ ,  $P = .06$  for HPV.

#### Sensitivity to Progression

Progression was determined in 13 of the 94 imaging sessions. When we compared the change in T1GdVs relative to the previous follow-up with that of the BlueVs, the increase in BlueVs was found to be 37.5% higher than the increase in T1GdVs (95% CI, 6%–81%,  $P = .013$ ), suggesting that progression may be depicted more effectively in the TRAMs. An example is shown in Fig 4.

When we compared the change in T1GdVs relative to the previous follow-up with that of the HPVs, the difference in the increase was not significant ( $P = .91$ ).

Comparison of the TRAMs with conventional MR imaging can be found in On-line Appendix B. The effects of re-irradiation during bevacizumab treatment can be found in On-line Appendix C.

#### DISCUSSION

The application of the TRAMs for differentiating tumor and non-tumor tissues in patients with brain tumor following conventional treatment was recently demonstrated and validated histologically.<sup>17,18</sup> Unlike other methods (such as PWI), the TRAMs present a model-independent approach with minimal sensitivity to susceptibility artifacts. We applied the TRAMs to monitor 24 patients before and during bevacizumab treatment. The primary end point was to assess whether the TRAMs provide additional information regarding a recurrent HGG response to bevacizumab treatment over conventional MR imaging. Response and progression patterns were identified from the mean change in lesion volumes with time, depicted from conventional T1WI, delayed contrast-enhanced MR imaging, and DSC MR imaging. Thresholds for early (1 month) prediction of response were calculated by using these sequences. The predictor calculated from the TRAMs demonstrated higher sensitivity, specificity, and positive and negative predictive values. The benefit of delayed-contrast MR imaging in separating responders and nonresponders was further confirmed by using log-rank and receiver operating characteristic analyses, showing improved performance as measured by the area under the curve for prediction of PFS at  $\geq 6$  months compared with T1GdV and HPV. For prediction of OS at  $\geq 1$  year, both

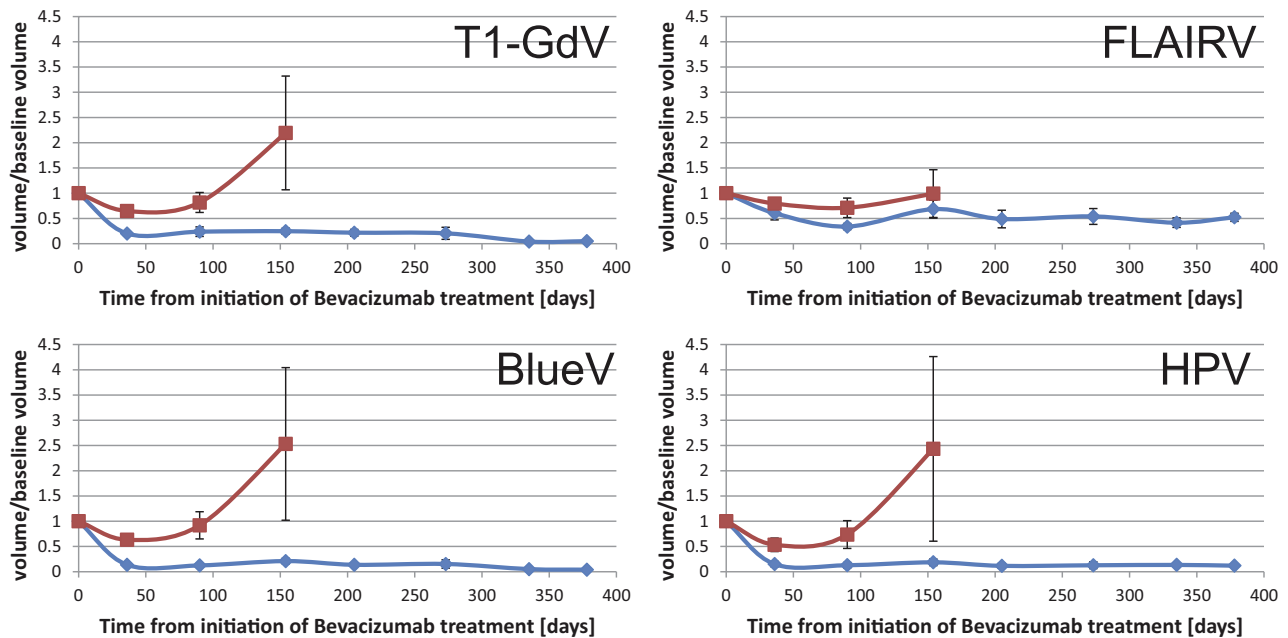


**FIG 2.** Response patterns. The mean values of the changes in lesion volumes relative to baseline were plotted separately for the responders (blue) and nonresponders (red) as a function of time (days) after initiation of bevacizumab treatment for the following parameters: enhancing volumes on contrast-enhanced T1-weighted MR imaging, FLAIR hyperintensity volumes on precontrast FLAIR, blue volumes on the TRAMs, and hyperperfused volumes on perfusion-weighted MR imaging–based maps.

#### Log-rank analysis of suggested predictors<sup>a</sup>

Method	Median PFS (95% CI) (mo) (Responders/Nonresponders)	P Value (Log-Rank Analysis)	Median OS (95% CI) (mo) (Responders/Nonresponders)	P Value (Log-Rank Analysis)
T1GdV	11.3 (5.6–19.6) / 2.8 (1.8–4.5)	.0112	14.8 (11.6–20.7) / 8.2 (5.4–9.2)	.0022
BlueV	15.4 (9.1–31.4) / 2.8 (1.3–3.5)	<.0001	20.7 (14.6–34.4) / 6.9 (5.2–9.2)	<.0001
HPV	5.6 (3.3–9.1) / 2.8 (1.8–4.5)	.0837	11.6 (9.0–14.8) / 6.6 (5.2–9.2)	.0232

<sup>a</sup> The patients were divided into responders and nonresponders using predictors from T1GdV, BlueV, and HPV. The median PFS and OS values of the responders and nonresponders as determined by these thresholds are presented and compared with log-rank analysis.

BlueV and T1GdV seem to be strong predictors. At progression, the increase in lesion volumes in delayed-contrast MR imaging was significantly higher than the increase in conventional T1WI; these findings suggest that progression may be better depicted in the TRAMs.

Despite 62.5% of the recruited patients showing a positive radiologic response to bevacizumab at the 1-month standard MR imaging, only 29.2% demonstrated a long-term response. These numbers suggest that a more reliable tool for early prediction of long-term response to bevacizumab is required. When studying the response pattern to bevacizumab, we noted that responders presented an initial sharp decrease in tumor volume, which persisted for a prolonged time. Although an initial decrease in tumor volume was also evident in the nonresponding group, it was significantly less and was followed by significant growth, occurring ~3 months after initiation of treatment, signifying tumor progression. This difference between responders and nonresponders depicted in Fig 2 for

T1GdVs, BlueVs, and HPVs suggested that these parameters may be strong predictors of long-term response.

It is claimed<sup>19</sup> that bevacizumab may reduce the enhancing volumes in patients with recurrent HGG by reducing treatment effects and not necessarily by antitumor effects. Here, the ability of the TRAMs to differentiate tumor and treatment effects pretreatment is applied to demonstrate the antitumor effects of bevacizumab. All 7 responders had significant BlueVs in the pretreatment TRAMs. This finding, together with significant correlations between the reduction in BlueVs and outcome, suggests that bevacizumab not only reduces the treatment effects, but induces antitumor effects. Most interesting, the response to bevacizumab showed no correlation with initial tumor volumes or any other baseline radiologic parameter.

The estimated median OS in our study (9.2 months) is in agreement with that in previous publications.<sup>2,8</sup> Specifically, the Bevacizumab and Irinotecan or Temozolomide in Treating Patients With Recurrent or Refractory Glioblastoma Multiforme or Gliosarcoma (ACRIN/RTOG) study presented a similar OS of 270 days for 123 patients with recurrent HGG treated with bevacizumab.<sup>8</sup> Similarly, the authors applied contrast-enhanced T1 as a predictor for OS. However, they used the RANO cutoff as a threshold to demonstrate the prognostic value of early radiologic progression in OS, while we derived a threshold by using PFS data, which are based on the extent of early response. The percentage of early progression at 1-month follow-ups in our data (12.5%) is also consistent with the early progression rate seen at 8 weeks in their study (12%). However, our predictors separated responders and nonresponders efficiently at 1 month, while in the ACRIN/RTOG results, the difference in median OS between initially responding patients and those with stable disease (by using the RANO cutoff at 50%) was not found to be statistically significant.

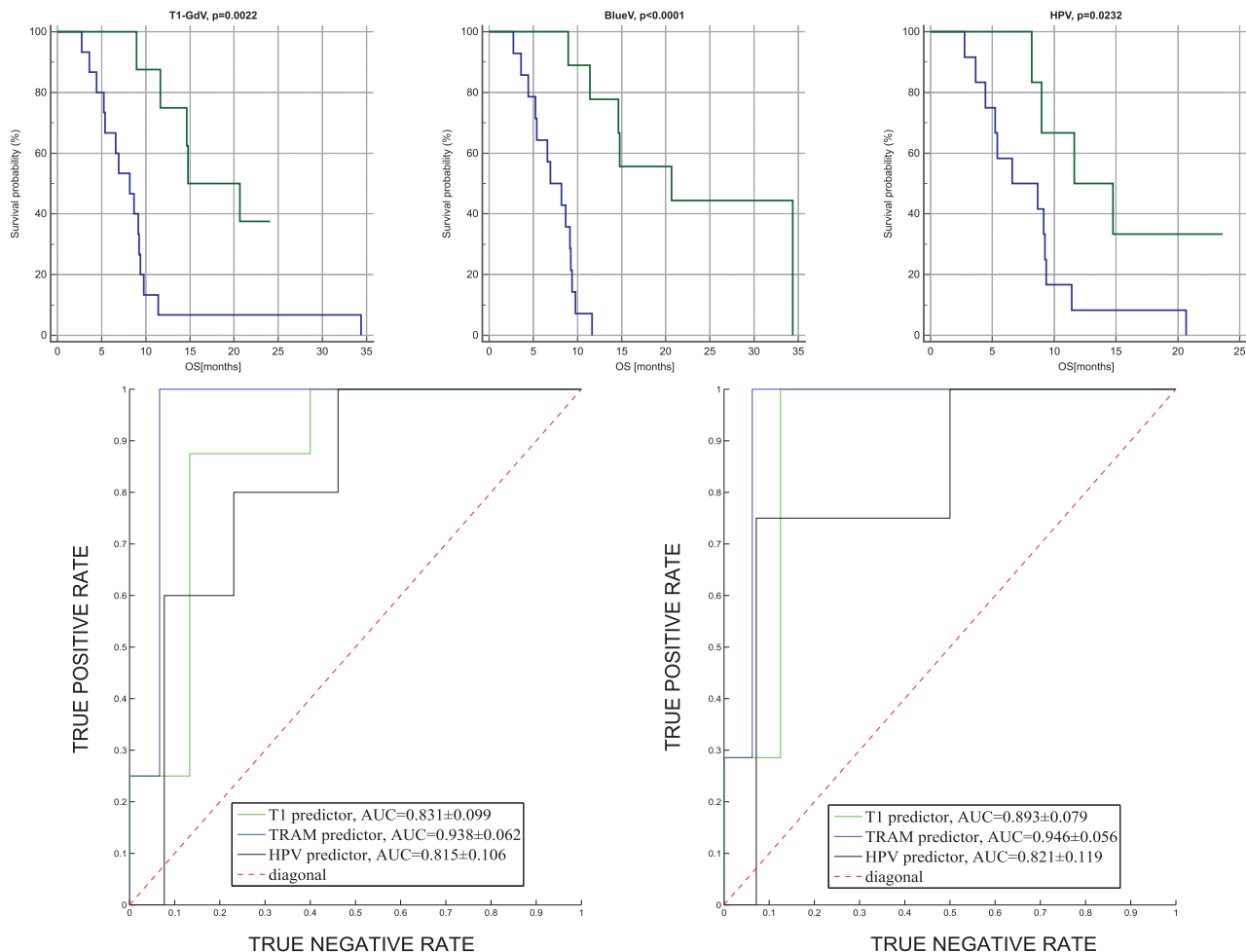


**FIG 3.** Kaplan-Meier curves demonstrating the application of 3 MR imaging–based predictors for separating responders to bevacizumab from nonresponders. Shown are Kaplan-Meier curves by using 1-month change (ratio) in T1GdV  $\leq 0.32$  (upper left), BlueV  $\leq 0.29$  (upper middle), and HPV  $\leq 0.19$  (upper right) as predictors for OS. Receiver operating characteristic curves of the 3 predictors applied for prediction of 6-month PFS (left) and 1-year OS (right) are presented below.

We noted that the mean ADC of all patients decreased slightly (but statistically significantly) posttreatment. This decrease may be explained by the reduction of extracellular fluids after vessel wall normalization. Still, our ADC data did not provide predictive information regarding response and nonresponse to bevacizumab.

A significant disadvantage of the TRAMs is their inability to depict nonenhancing tumor components. In our experience, images in most patients depicted a decrease in tumor enhancement during bevacizumab treatment, which may be due to blood vessel normalization; however, vessel normalization does not seem complete because most cases had some level of contrast leakage, enabling us to study its late clearance and accumulation by using the TRAMs. The low number of responding patients ( $n = 7$ ) requires additional studies to establish the results demonstrated here. We also assumed that similar to standard treatments, blue in the TRAMs represents active tumor, while red represents nontumor tissues, considering that nonenhancing regions may consist of additional tumor tissues. Histologic validation of these assumptions is yet to be performed.

Generally, PFS is considered a good surrogate for OS. How-

ever, in the case of recurrent HGG treated by bevacizumab, determination of radiologic progression is challenging and 6-month PFS values may not be reliable. In this study, response was determined by using OS, also a reliable measure of clinical outcome in the case of bevacizumab treatment, and predictors of response were confirmed to provide significant separation in OS by log-rank analysis. Moreover, the calculated PFS by using the method described here was significantly correlated with OS.

The studied cohort of patients was heterogeneous with respect to histology, previous resections, and re-irradiation treatment received after failure of bevacizumab, which can potentially give rise to confounding results. However, the median OS of patients with grades III and IV was not found to be statistically different, and the percentages of patients previously undergoing gross total resection and subtotal resection and biopsy in the responding and nonresponding groups were similar; this finding suggests no significant bias due to these considerations. The 7 patients who underwent re-irradiation were all from the nonresponding group, suggesting no significant bias toward the response due to this difference as well.

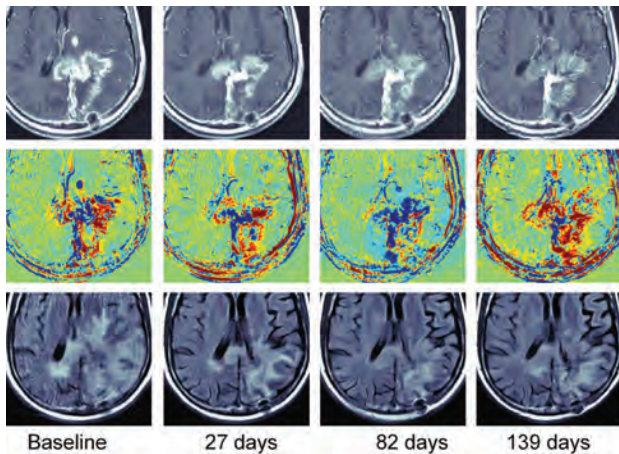


**FIG 4.** An example of a patient progressing under bevacizumab and responding to re-irradiation under bevacizumab: Shown are axial contrast-enhanced T1WI (upper row), TRAMs (middle row), and T2 FLAIR images (lower row), at baseline, 27 days, 82 days, and 139 days after initiation of bevacizumab treatment. Lesion volumes at baseline were the following: enhancing T1: 54.1 mL; blue: 21.2 mL; and FLAIR hyperintensity: 165.9 mL. At 1 month, a reduction was seen in all: T1 reached 59% of its baseline volume; blue, 79%; and FLAIR, 43%. At day 83, progression was determined, consistent with the patient's clinical deterioration. T1 reached 84% of its baseline volume (but an increase to 142% relative to the previous scan volume), and blue reached 140% of its baseline volume (an increase to 177% relative to the previous scan), reflecting the stronger sensitivity of TRAMs to progression. FLAIR hyperintensity continued to decrease (25%). At this point, it was decided that the patient should undergo re-irradiation and continue bevacizumab treatment. The next follow-up, at day 139, was acquired 1 month after the initiation of re-radiation. Compared with the previous examination, there was a dramatic increase in FLAIR (172%), as can be expected postirradiation; no change in T1 (99.7%); and a dramatic decrease in blue (61%). In addition, hyperperfused volume increased to 132%; and average apparent diffusion coefficient, to 108% (data not shown). The patient was clinically stable after re-irradiation and lived 5 more months.

## CONCLUSIONS

The benefit of standard and delayed-contrast MR imaging for assessing and predicting the response to bevacizumab was demonstrated. The increased sensitivity of delayed-contrast MR imaging reflects its potential contribution to the management of bevacizumab-treated patients with recurrent HGG.

Disclosures: Dianne Daniels—RELATED: Grant: Joseph Sagol PhD Scholarship\*; UNRELATED: Patents (planned, pending or issued): I am an inventor on pending patents, some licensed to Brainlab AG. Deborah T. Blumenthal—UNRELATED: Board Membership: Vascular Biogenics (Medical Advisory Board). Yael Mardor—RELATED: Grant: from Brainlab AG,\* donation from Roche Pharmaceuticals\*; Consulting Fee or Honorarium: Brainlab AG; Support for Travel to Meetings for the Study or Other Purposes: Brainlab AG; UNRELATED: Consultancy: Brainlab AG; Grants/Grants Pending: Israel Science Foundation and Israeli Office of Commerce; Patents (planned, pending or issued): I am an inventor on pending patents, some licensed to Brainlab AG; Travel/Accommodations/Meeting Expenses Unrelated to Activities Listed: Brainlab AG. David Guez—UNRELATED: Patents (planned, pending or issued): I am an inventor on pending patents, some licensed to Brainlab AG. David Last—UNRELATED: Patents (planned, pending or issued): I am an inventor on pending patents, some licensed to Brainlab AG. Leor Zach—UNRELATED: Patents (planned, pending or issued): I am an inventor on pending patents, some licensed to Brainlab AG. \*Money paid to the institution.

## REFERENCES

1. Friedman HS, Prados MD, Wen PY, et al. **Bevacizumab alone and in combination with irinotecan in recurrent glioblastoma.** *J Clin Oncol* 2009;27:4733–40 CrossRef Medline

2. Chamberlain MC. **Bevacizumab for the treatment of recurrent glioblastoma.** *Clin Med Insights Oncol* 2011;5:117–29 CrossRef Medline
3. Le Rhun E, Rhun EL, Taillibert S, et al. **The future of high-grade glioma: where we are and where we are going.** *Surg Neurol Int* 2015;6(suppl 1):S9–S44 CrossRef Medline
4. Khasraw M, Ameratunga MS, Grant R, et al. **Antiangiogenic therapy for high-grade glioma.** *Cochrane Database Syst Rev* 2014;9:CD008218 CrossRef Medline
5. Wen PY, Macdonald DR, Reardon DA, et al. **Updated response assessment criteria for high-grade gliomas: Response Assessment in Neuro-Oncology Working Group.** *J Clin Oncol* 2010;28:1963–72 CrossRef Medline
6. Pope WB, Young JR, Ellingson BM. **Advances in MRI assessment of gliomas and response to anti-VEGF therapy.** *Curr Neurol Neurosci Rep* 2011;11:336–44 CrossRef Medline
7. Hygino da Cruz LC Jr, Rodriguez I, Domingues RC, et al. **Pseudoprogression and pseudoreponse: imaging challenges in the assessment of posttreatment glioma.** *AJNR Am J Neuroradiol* 2011;32:1978–85 CrossRef Medline
8. Boxerman JL, Zhang Z, Safriel Y, et al. **Early post-bevacizumab progression on contrast-enhanced MRI as a prognostic marker for overall survival in recurrent glioblastoma: results from the ACRIN 6677/RTOG 0625 Central Reader Study.** *Neuro Oncol* 2013;15:945–54 CrossRef Medline
9. Prados M, Cloughesy T, Samant M, et al. **Response as a predictor of survival in patients with recurrent glioblastoma treated with bevacizumab.** *Neuro Oncol* 2011;13:143–51 CrossRef Medline
10. Ellingson BM, Cloughesy TF, Lai A, et al. **Quantitative volumetric analysis of conventional MRI response in recurrent glioblastoma treated with bevacizumab.** *Neuro Oncol* 2011;13:401–09 CrossRef Medline
11. Huang RY, Rahman R, Hamdan A, et al. **Recurrent glioblastoma: volumetric assessment and stratification of patient survival with early posttreatment magnetic resonance imaging in patients treated with bevacizumab.** *Cancer* 2013;119:3479–88 CrossRef Medline
12. Ellingson BM, Kim HJ, Woodworth DC, et al. **Recurrent glioblastoma treated with bevacizumab: contrast enhanced T1-weighted subtraction maps improve tumor delineation and aid prediction of survival in a multicenter clinical trial.** *Radiology* 2014;271:200–10 CrossRef Medline
13. Schmainda KM, Prah M, Connelly J, et al. **Dynamic-susceptibility contrast agent MRI measures of relative cerebral blood volume predict response to bevacizumab in recurrent high-grade glioma.** *Neuro Oncol* 2014;16:880–88 CrossRef Medline
14. Aquino D, Di Stefano AL, Scotti A, et al. **Parametric response maps of perfusion MRI may identify recurrent glioblastomas responsive to bevacizumab and irinotecan.** *PLoS One* 2014;9:e90535 CrossRef Medline
15. Sawlani RN, Raizer J, Horowitz SW, et al. **Glioblastoma: a method for predicting response to antiangiogenic chemotherapy by using MR perfusion imaging: pilot study.** *Radiology* 2010;255:622–28 CrossRef Medline
16. Ellingson BM, Sahebjam S, Kim HJ, et al. **Pretreatment ADC histogram analysis is a predictive imaging biomarker for bevacizumab treatment but not chemotherapy in recurrent glioblastoma.** *AJNR Am J Neuroradiol* 2014;35:673–79 CrossRef Medline
17. Zach L, Guez D, Last D, et al. **Delayed contrast extravasation MRI: a new paradigm in neuro-oncology.** *Neuro Oncol* 2015;17:457–65 CrossRef Medline
18. Zach L, Guez D, Last D, et al. **Delayed contrast extravasation MRI for depicting tumor and non-tumoral tissues in primary and metastatic brain tumors.** *PLoS One* 2012;7:e52008 CrossRef Medline
19. Taal W, Oosterkamp HM, Walenkamp AM, et al. **Single-agent bevacizumab or lomustine versus a combination of bevacizumab plus lomustine in patients with recurrent glioblastoma (BELOB trial): a randomised controlled phase 2 trial.** *Lancet Oncol* 2014;15:943–53 CrossRef Medline



# Diffusion-Weighted Imaging for Predicting and Monitoring Primary Central Nervous System Lymphoma Treatment Response

W.-Y. Huang, J.-B. Wen, G. Wu, B. Yin, J.-J. Li, and D.-Y. Geng



## ABSTRACT

**BACKGROUND AND PURPOSE:** Whether ADC value predicts the therapy response and outcomes of primary central system lymphoma remains controversial. This study assessed the minimum ADC correlated with treatment response in patients with primary central nervous system lymphoma undergoing methotrexate-based chemotherapy.

**MATERIALS AND METHODS:** Thirty-five patients with primary central nervous system lymphoma underwent conventional MR imaging and DWI before chemotherapy and after 1 and 5 cycles of chemotherapy. Treatment response was determined according to the International PCNSL Collaborative Group criteria and was classified as a complete response, partial response, or progressive disease. Pretreatment minimum ADC, minimum ADC after 1 cycle, minimum ADC after 5 cycles, and change in minimum ADC were compared among the different response groups. The Pearson correlation test was calculated between these ADC parameters and tumor response.

**RESULTS:** The pretreatment minimum ADC of the progressive disease group was lower than that of the complete response and partial response groups, but there was no significant difference among them. The minimum ADC after 1 cycle and minimum ADC after 5 cycles were statistically significantly higher than the pretreatment minimum ADC. A comparison among groups showed that minimum ADC after 1 cycle, minimum ADC after 5 cycles, minimum ADC change, and the percentage of minimum ADC change were all significantly different among the 3 groups. A significant positive correlation was observed between the percentage of minimum ADC after 1 cycle of chemotherapy and the size reduction percentage after 5 cycles of chemotherapy. The minimum ADC change and the percentage of minimum ADC change performed better in the differentiation of the final treatment response, specifically in complete response and partial response from progressive disease.

**CONCLUSIONS:** The minimum ADC after 1 cycle and minimum ADC changes were better correlated with the treatment response than the pretreatment minimum ADC. Minimum ADC after early therapy may potentially be used to predict and monitor the response of primary central nervous system lymphoma to chemotherapy.

**ABBREVIATIONS:** ADC<sub>min</sub> = minimum ADC; ADC<sub>min,early</sub> = ADC<sub>min</sub> after 1 cycle; ADC<sub>min,pre</sub> = pretreatment ADC<sub>min</sub>; CR = complete response; PCNSL = primary central nervous system lymphoma; PD = progressive disease; PR = partial response

Primary central nervous system lymphoma (PCNSL) is a rare subtype of non-Hodgkin lymphoma, which is confined to the brain, eyes, and/or leptomeninges. The overall incidence of PCNSL in the immunocompetent population has been increasing during the past several years, and it is one of the few malignant

primary brain tumors that is sensitive to both chemotherapy and radiation therapy.<sup>1,2</sup> Methotrexate-based chemotherapy is the cornerstone of therapy in PCNSL, while whole-brain irradiation is recommended for patients with recidivation. Patients who are at low risk of tumor recidivation may benefit from methotrexate-based chemotherapy alone. On the contrary, high-risk patients may require further chemotherapy and/or whole-brain irradiation for consolidation of the response.<sup>3,4</sup>

Until recently, no proved imaging biomarkers could indi-

Received February 2, 2016; accepted after revision May 11.

From the Departments of Radiology (W.-Y.H., J.-J.L.) and Radiotherapy (G.W.), Hainan General Hospital, Haikou, Hainan, China; and Department of Radiology (J.-B.W., B.Y., D.-Y.G.), Huashan Hospital, Fudan University, Shanghai, China.

Wei-Yuan Huang and Jian-Bo Wen contributed equally to this work and should be considered co-first authors.

This research was supported by funding from the National Key Discipline Project, the Hainan Provincial Key Foundation Project (ZDXM2015066), and the National Natural Science Foundation of China under grant No. 81471627.

Please address correspondence to Jian-Jun Li, MD, Department of Radiology, Hainan General Hospital, No. 19 Xiuhua Rd, Xiuying District, Haikou, Hainan, China;

e-mail: lijianjunhgh@163.com; Dao-Ying Geng, MD, Department of Radiology, Huashan Hospital, Fudan University, No. 12 Wulumuqi Rd, Jing'an District, Shanghai, China; e-mail: gengdaoying2245@163.com

Indicates open access to non-subscribers at [www.ajnr.org](http://www.ajnr.org)

<http://dx.doi.org/10.3174/ajnr.A4867>

**Table 1: Response criteria for primary central nervous system lymphoma**

Response	Brain Imaging	Corticosteroid Dose	Eye Examination Findings	CSF Cytology Findings
CR	No contrast enhancement	None	Normal	Negative
CRu	No contrast enhancement	Any	Normal	Negative
PR	Minimal abnormality	Any	Minor RPE abnormality	Negative
	50% Decrease in enhancing tumor No contrast enhancement	Irrelevant Irrelevant	Minor RPE abnormality or normal Decrease in vitreous cells or retinal infiltrate	Negative Persistent or suspicious
PD	25% Increase in lesion Any new site of disease: CNS or systemic	Irrelevant	Recurrent or new ocular disease	Recurrent or positive

**Note:**—CRu indicates unconfirmed complete response; RPE, retinal pigment epithelium.

cate tumor refractoriness to methotrexate-based chemotherapy and predict therapeutic outcomes in PCNSL treatment. Such biomarkers would provide clinicians with strong evidence for making clinical decisions, which might generate the early start of second-line salvage therapy in high-risk patients with PCNSL and likely contribute to personalized therapeutic strategies to detect tumor recurrence without delay and improve prognosis.<sup>5</sup>

Noninvasive MR diffusion-weighted imaging of the brain is based on the differential diffusion rates or the Brownian motion of water. It is an essential technique used to diagnose acute infarct in the brain, due to its ability to detect cytotoxic edema derived by altered water diffusion due to cellular damage. DWI has also been widely used in neuro-oncology to assess tumor pathology characteristics.<sup>6</sup> Specifically, the apparent diffusion coefficient values derived from DWI have been shown to correlate with tumor cellularity, glioma grade, and treatment response.<sup>6–9</sup> Some previous research has also suggested that pretherapeutic ADC values in tumor may be biomarkers noninvasively predictive of treatment response in patients with PCNSL.<sup>5</sup> However, a number of other studies have not shown tumor ADC metrics to be predictive of response.<sup>10</sup>

To our knowledge, no research has reported whether dynamic changes of ADC values are related to treatment responses in patients with PCNSL. Thus, we assessed pre- and posttherapeutic ADC values in responsive or prognostic subgroups of patients with PCNSL in an effort to identify which tumors may experience recurrence and disease progression at an early stage.

## MATERIALS AND METHODS

### Patient Population

Thirty-five patients with biopsy-proved PCNSL (26 men, 9 women; mean age,  $58 \pm 15$  years; all immunocompetent) treated at the Huashan Hospital of Fudan University between October 2007 and February 2010 were selected for this retrospective study.

Inclusion criteria were patients being 18 years of age or older; histologic confirmation of PCNSL by stereotactic needle biopsy; serology negative for human immunodeficiency virus; no evidence of systemic non-Hodgkin lymphoma as demonstrated by PET-CT or CT of the chest, abdomen, and pelvis and bone marrow aspirate and biopsy; and baseline laboratory values being leukocytes  $\geq 4000/L$ , platelets  $\geq 100,000/L$ , and creatinine  $\leq 1.5$  mg/dL or creatinine clearance  $\geq 50$  cm<sup>3</sup>/min/1.73 m<sup>2</sup> without any corticosteroids before treatment. All patients had a pathologic

diagnosis of diffuse large B-cell PCNSL as defined by the World Health Organization and received methotrexate-based induction chemotherapy. Of the 53 patients who met the inclusion criteria for this investigation, 48 were studied on the basis of having undergone pretherapeutic contrast-enhanced MR imaging of the brain with DWI. Furthermore, 35 of the 48 patients had pretherapeutic, interval, and posttreatment follow-up contrast-enhanced MR imaging of the brain with DWI. Exclusion criteria consisted of any other active primary malignancy, preexisting immunodeficiency, and prior treatment for PCNSL. Pretreatment evaluations included baseline ophthalmologic examination (including dilated fundus examination, slit lamp examination, and color photography of the posterior pole) to assess ocular involvement and lumbar puncture to assess leptomeningeal involvement.

### Treatment and Response Evaluation

Each methotrexate treatment cycle was administered in the hospital setting. Every patient received methotrexate-based chemotherapy, including methotrexate, 3–8 g/m<sup>2</sup>/day 1, + dexamethasone, 15 mg/days 1–3, + idarubicin, 15 mg/day 2 and every 21 days for 5 cycles. The response was assessed by using the International PCNSL Collaborative Group criteria, based on imaging, corticosteroid use, CSF cytology, and slit lamp examination in cases of CSF or ocular involvement (Table 1).<sup>11</sup> Patients who achieved a complete response (CR) were defined as having resolution of contrast-enhancing lesions on follow-up MR imaging and, if indicated, by CSF cytologic analysis (if the CSF cytology was positive for malignant cells at the time of diagnostic staging). Patients who achieved a partial response (PR) were defined as an interval decrease in contrast-enhancing lesion volume. Progressive disease (PD) were defined as an interval increase in contrast-enhancing lesion volume or the development of new enhancing lesions on follow-up contrast-enhanced MR imaging or involve the eye or CSF.<sup>5</sup> All follow-up imaging was performed no longer than 2 weeks after completion of all planned therapy to assess overall treatment response.<sup>12</sup>

### MR Imaging Protocol

Patients underwent MR imaging before receiving their first course of therapy (pretreatment); at an earlier stage of <48 hours after the end of the patient's first chemotherapy cycle, as indicated by the last chemotherapeutic injection (early treatment); and at the completion of all the standard treatments associated with the regular review of clinical time (posttreatment). None of the patients had begun corticosteroid treat-

**Table 2: Comparison of ADC<sub>min</sub> values among CR, PR, and PD groups<sup>a</sup>**

	No.	ADC <sub>min</sub> <sub>pre</sub>	ADC <sub>min</sub> <sub>early</sub>	ADC <sub>min</sub> <sub>post</sub>	ADC <sub>min</sub> Change <sup>b</sup>	Percentage ADC <sub>min</sub> Change <sup>c</sup>
CR	12	566.56 ± 120.84	849.09 ± 182.45	858.06 ± 185.89	282.54 ± 110.40	51.17 ± 21.44
PR	15	487.54 ± 78.00	669.73 ± 130.28	677.14 ± 131.47	182.19 ± 88.28	37.52 ± 20.02
PD	8	476.13 ± 93.36	456.65 ± 93.36	432.55 ± 88.85	-19.49 ± 13.46	-4.17 ± 2.60
Total	35	512.03 ± 103.15	682.52 ± 203.52	683.26 ± 213.34	170.50 ± 142.03	32.68 ± 27.67
<i>P</i> value		.072	.000	.000	.000	.000
CR-PR		.045	.003	.003	.006	.63
CR-PD		.051	.000	.000	.000	.000
PR-PD		.792	.002	.001	.000	.000

**Note:**—ADC<sub>min</sub><sub>post</sub> indicates ADC<sub>min</sub> after 5 cycles.

<sup>a</sup> All ADC values are reported as  $100 \times 10^{-6}$  mm<sup>2</sup>/s. Data are means.

<sup>b</sup> ADC<sub>min</sub> Change = ADC<sub>min</sub><sub>early</sub> - ADC<sub>min</sub><sub>pre</sub>.

<sup>c</sup> Percentage ADC<sub>min</sub> Change = (ADC<sub>min</sub><sub>early</sub> - ADC<sub>min</sub><sub>pre</sub>)/ADC<sub>min</sub><sub>pre</sub>.

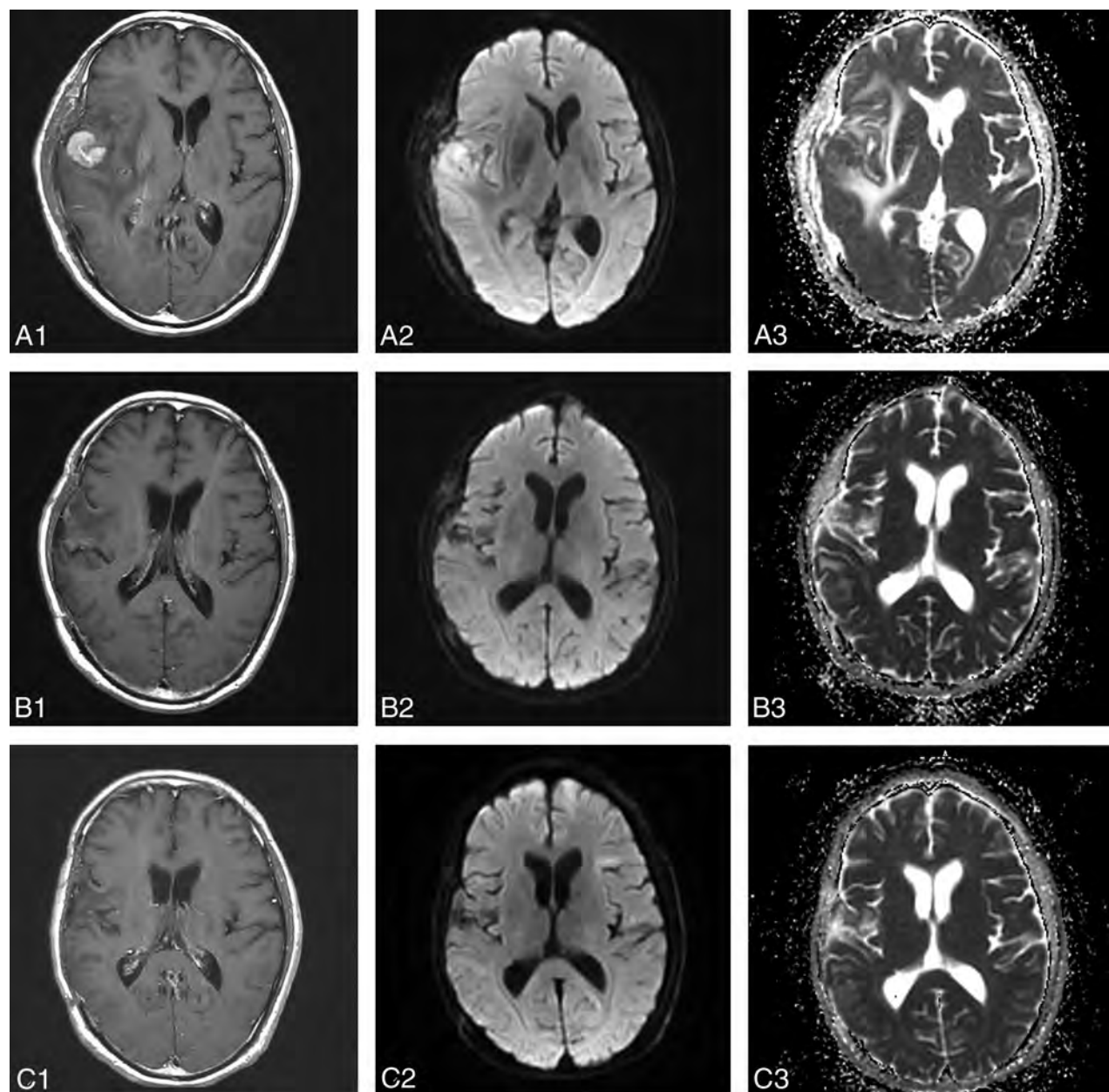


**FIG 1.** MR images in a 54-year-old man with diffuse large B-cell PCNSL, belonging to the CR group (A1, A2, A3, before therapy; B1, B2, B3, after 1 cycle of chemotherapy; C1, C2, C3, after 5 cycles of chemotherapy). Contrast-enhanced T1-weighted image shows an apparent enhanced tumor on the right temporal lobe (A1). The tumor shows hyperintense on the DWI (A2, B2). The pretherapeutic ADC<sub>min</sub> of the tumor was  $668 \times 10^{-6}$  mm<sup>2</sup>/s (A3). After 1 cycle of chemotherapy, the size of tumor has decreased significantly (B1, B2) and the ADC<sub>min</sub> of the tumor has increased to  $1014 \times 10^{-6}$  mm<sup>2</sup>/s (B3). After 5 cycles of chemotherapy, the tumor has almost disappeared (C1), and the ADC<sub>min</sub> has increased to  $1026 \times 10^{-6}$  mm<sup>2</sup>/s (C2, C3).

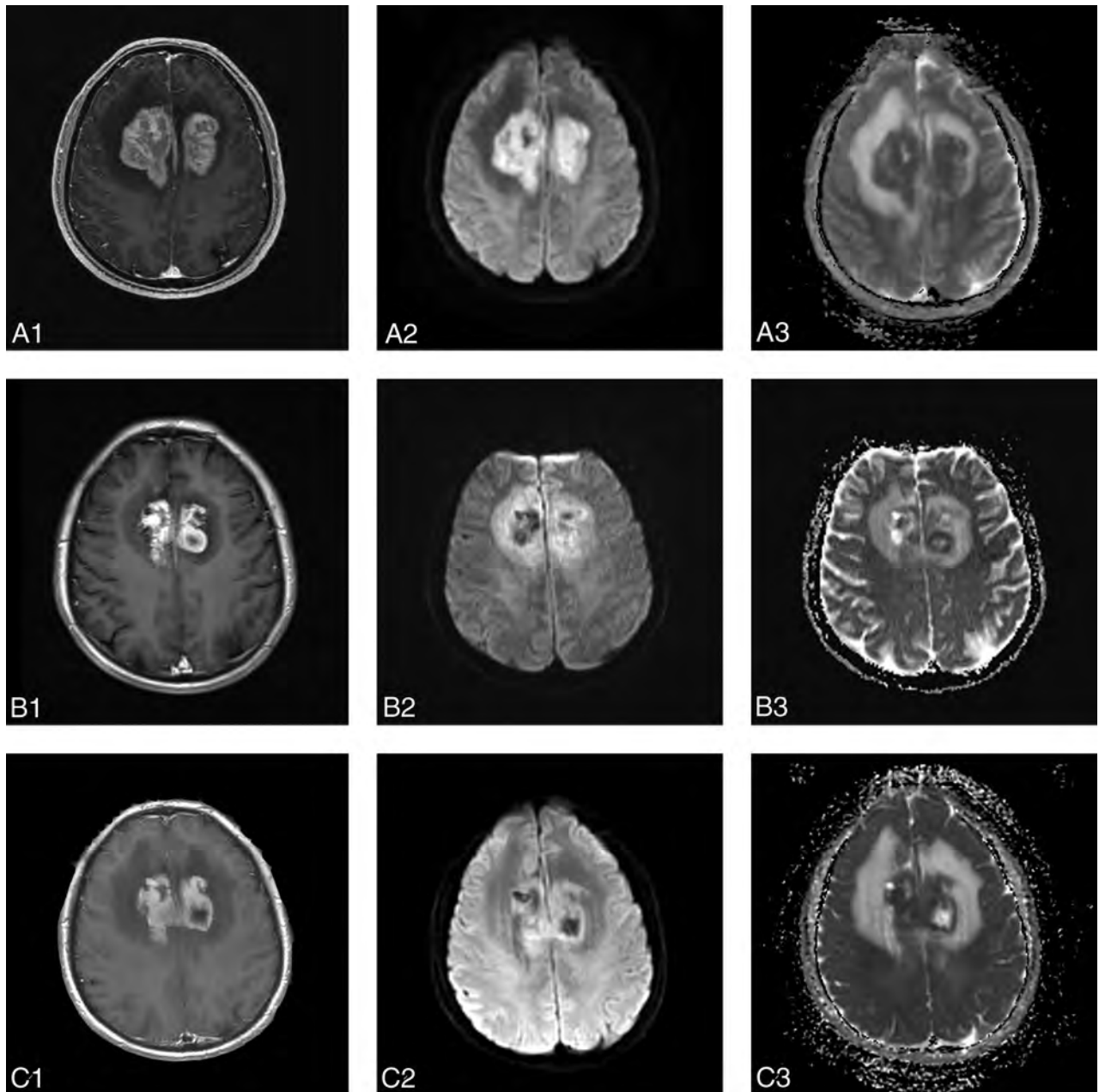


**FIG 2.** MR images in a 53-year-old man with diffuse large B-cell PCNSL belonging to the PR group (A1, A2, A3, before therapy; B1, B2, B3, after 1 cycle of chemotherapy; C1, C2, C3, after 5 cycles of chemotherapy). An apparent enhanced tumor on the bilateral frontal lobe and corpus callosum (A1). On the DWI, the tumor is apparently hyperintense in relation to adjacent structures (A2, B2, C2). The baseline ADCmin of the tumor was  $420 \times 10^{-6} \text{ mm}^2/\text{s}$  (A3). After 1 cycle of chemotherapy, the size of the tumor has decreased slightly (B1, B2) and the ADCmin has increased to  $764 \times 10^{-6} \text{ mm}^2/\text{s}$  (B3). After 5 cycles of chemotherapy, the size of the tumor has continued to decrease (C1), while the ADCmin has decreased to  $617 \times 10^{-6} \text{ mm}^2/\text{s}$  (C2, C3).

ment, radiation therapy, or chemotherapy or had a previous brain biopsy at the first MR imaging.

All patients were imaged by using a 3T clinical MR imaging scanner (Tim Trio; Siemens, Erlangen, Germany). MR imaging examinations included conventional contrast-enhanced T1-weighted imaging and DWI sequences obtained according to a standardized protocol: axial T1-weighted spin-echo (TR/TE, 2000/17 ms), axial T2-weighted fast spin-echo (TR/TE, 3000/98 ms), axial fluid-attenuated inversion recovery (TR/TE/TI, 8000/102/2200 ms), axial diffusion-weighted echo-planar imaging (TR/TE, 5000/82 ms; section thickness/intersection gap, 5/0 mm; matrix size,  $130 \times 130$ ; FOV,

$20 \times 23 \text{ cm}$ ; 3 directions; b-value, 0 and  $1000 \text{ s}/\text{mm}^2$ ) acquired in the transverse plane throughout the infratentorial and supratentorial brain, and contrast-enhanced T1-weighted imaging. Gd-DTPA (Magnevist; Bayer HealthCare Pharmaceuticals, Wayne, New Jersey) was the intravenous contrast agent for the MR imaging study at  $0.1 \text{ mmol}/\text{kg}$  of body weight.

#### MR Image Processing

All MR imaging and DWI was analyzed by 2 experienced radiologists (W.-Y.H. with 8 years of experience in clinical MR imaging and J.-B.W. with 5 years of experience in clinical MR imaging).

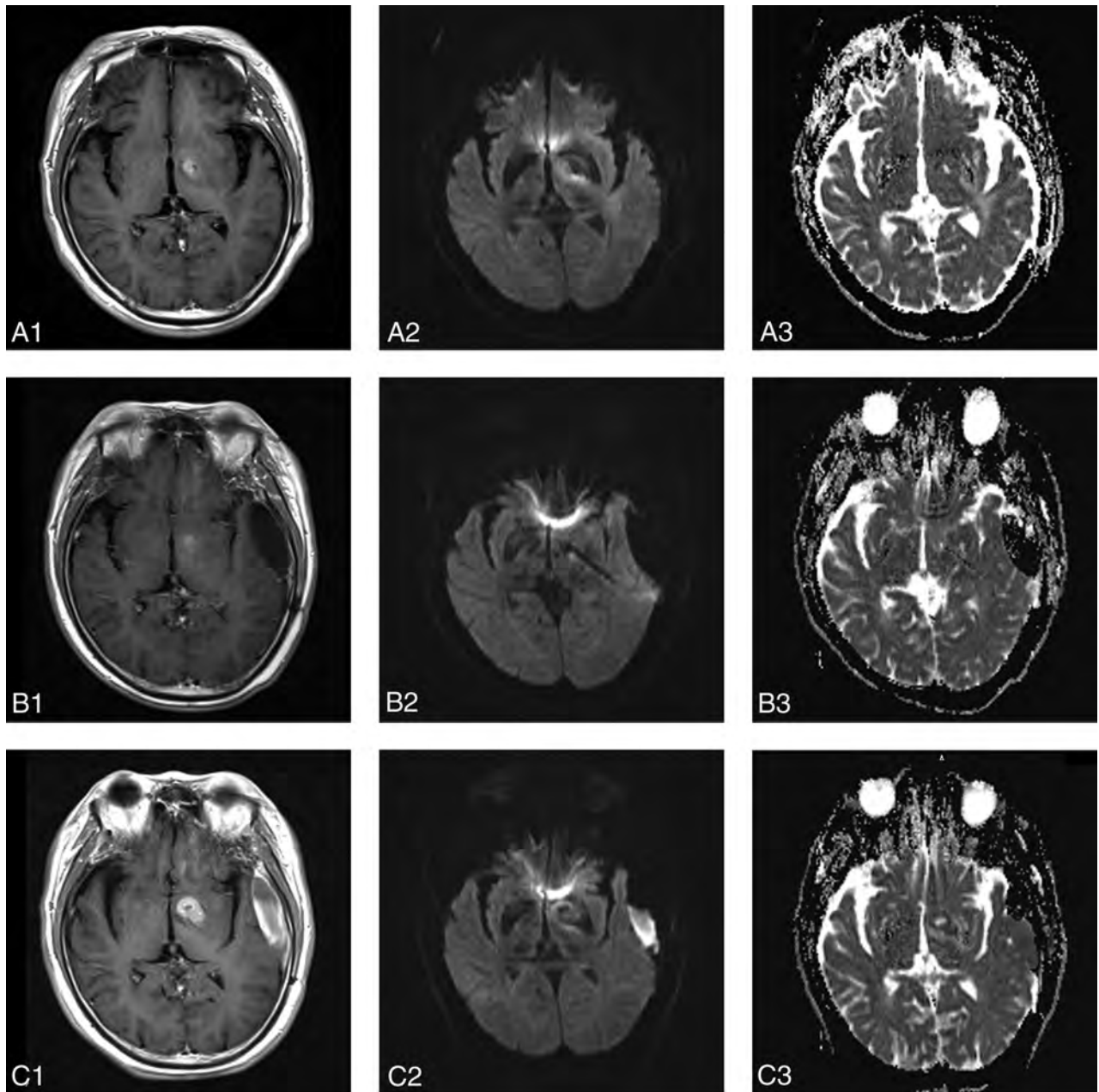


**FIG 3.** MR images in a 68-year-old man with diffuse large B-cell PCNSL, belonging to the PD group (A1, A2, A3, before therapy; B1, B2, B3, after 1 cycle of chemotherapy; C1, C2, C3, after 5 cycles of chemotherapy). An apparent enhanced tumor on the left basal ganglia region (A1). On the DWI, the tumor is apparent hyperintense (A2, B2, C2). The baseline ADCmin of the tumor was  $554 \times 10^{-6} \text{ mm}^2/\text{s}$  (A3). After 1 cycle of chemotherapy, the size of tumor has decreased slightly (B1, B2). However, the ADCmin of the tumor has not increased but decreased to  $536 \times 10^{-6} \text{ mm}^2/\text{s}$  (B3). After 5 cycles of chemotherapy, the size of tumor (C1) has increased compared with A1 and B1 and the ADCmin of the tumor continued to decrease to  $478 \times 10^{-6} \text{ mm}^2/\text{s}$  (C2, C3).

The ADC map was calculated from DWI, by using software provided by the manufacturer (syngo; Siemens). ROIs were manually placed within the solid components of the tumor. The ROIs were as large as possible and were placed to avoid areas of cystic, necrotic, or hemorrhagic components in the tumor. Each neuro-radiologist drew 3 ROIs to obtain the minimum ADC (ADCmin). The minimum ADC value among these values was chosen as the result. An average of the results of 2 neuro-radiologists was used as the patient's ADCmin. When multifocal lesions were observed, the ADCmin was measured for each lesion and the mean ADCmin was calculated for multifocal lesions (<5 lesions).

The volumetric response of tumors to treatment was evaluated according to the Response Evaluation Criteria In Solid Tumors criteria.<sup>15</sup> The longest tumor diameter before and after treatment was measured on axial contrast-enhanced T1-weighted images, and the change of tumor diameter was calculated according to the following equations: Change in Tumor Diameter =  $\text{Diameter}_{\text{pre}} - \text{Diameter}_{\text{post}}$ ; Percentage of Change in Tumor Diameter =  $(\text{Diameter}_{\text{pre}} - \text{Diameter}_{\text{post}}) / \text{Diameter}_{\text{pre}}$  with "pre" and "post" indicating before and after.

The ADCmin change in tumor was calculated on the basis of the following equations: Change in ADCmin = ADCmin after 1 cycle

$(ADC_{min_{early}}) - \text{pretreatment } ADC_{min} (ADC_{min_{pre}})$ ; Percentage of Change in  $ADC_{min} = (ADC_{min_{early}} - ADC_{min_{pre}}) / ADC_{min_{pre}}$ .

If the enhancing lesion was not detected after chemotherapy, then the ROIs were defined in the area where the tumor was initially present.

### Statistical Analysis

Statistical analyses were performed by using statistical software (SPSS, Version 13.0; IBM, Armonk, New York). The intraclass correlation coefficient of  $ADC_{min}$  measure between the 2 radiologist was calculated. One-way analysis of variance was used to compare pretreatment  $ADC_{min}$  values, changes in  $ADC_{min}$  values, tumor diameter, and changes in tumor diameter among the CR, PR, and PD groups, and the comparison among groups was performed by using the least significant difference method for the post hoc evaluation. Linear regression models were used to examine size change and  $ADC$  measures. The Pearson correlation was performed to determine whether the pretreatment mean  $ADC_{min}$  value and percentage  $ADC_{min}$  change of the tumor after 1 month of chemotherapy were significantly related to the percentage size reduction of the tumor after chemotherapy. The differences between pretreatment and posttreatment  $ADC$  values as well as pretreatment and posttreatment tumor diameters were calculated by using a paired-samples  $t$  test. A  $P$  value  $< .05$  was a statistically significant difference.

### RESULTS

Thirty-five patients with PCNSL were enrolled in this study. The mean pretreatment diameter of the tumors was  $5.07 \pm 2.02$  cm (range, 1.75–11.02 cm). Standard International PCNSL Collaborative Group criteria follow-up of the tumor response classified 12 patients as having CR, 15 patients as having PR, and 8 patients as having PD. The intraclass correlation coefficient of  $ADC$  measures between the 2 radiologists was 0.73.

#### Pretreatment Prediction of Therapeutic Response

The pretreatment tumor diameter of the PR ( $n = 15$ ) group was larger than that of the CR ( $n = 12$ ) and PD ( $n = 8$ ) groups, but there was no significant difference among them ( $F = 1.17, P = .33$ ). The pretreatment  $ADC_{min}$  of the PD group was lower than that in the CR and PR groups, but there was no significant difference among them ( $F = 2.87, P = .07$ ) (Table 2).

#### Monitoring and Early Assessment of Therapeutic Response

The mean  $ADC_{min}$  value for the CR and PR groups increased to different extents during chemotherapy (Table 2). For the CR group, the mean  $ADC_{min}$  value after 1 cycle of chemotherapy increased by 49.9%, and it was statistically significantly higher than the pretreatment  $ADC$  value ( $P < .001$ ). The  $ADC_{min}$  value after 1 cycle and after 5 cycles of chemotherapy was statistically significantly higher than the pretreatment values ( $P < .001, P < .001$ ), but there was no statistically significant difference between the  $ADC_{min}$  values after 1 and 5 cycles of chemotherapy ( $P = .17$ ) (Fig 1).

For the PR group, the  $ADC_{min}$  value after therapy increased

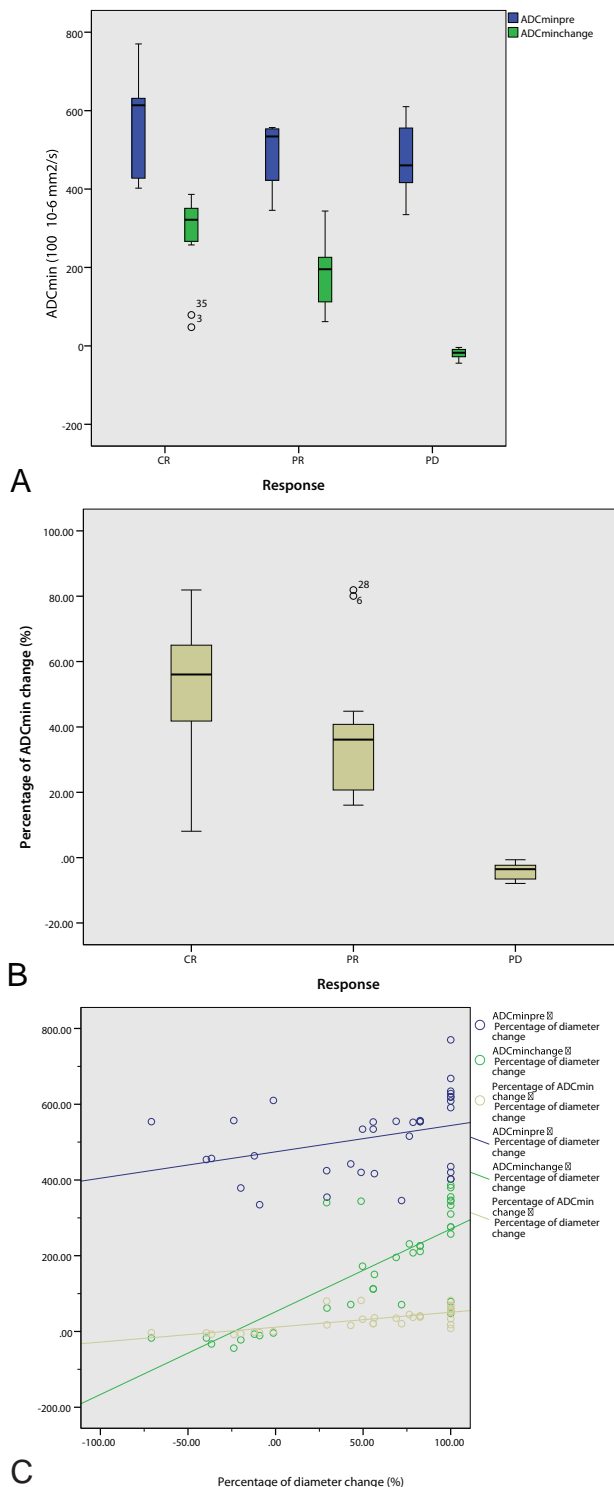


**FIG 4.** A boxplot of  $ADC_{min_{pre}}$  and  $ADC_{min}$  early change in the CR, PR, and PD groups (A). A boxplot of percentage  $ADC_{min}$  change in the CR, PR, and PD groups (B).  $ADC_{min}$  early change and percentage  $ADC_{min}$  change values can differentiate the 3 groups. The percentage  $ADC_{min}$  change performed better in differentiating the final treatment response, specifically differentiating the CR and PR groups from the PD group (A and B). C, Correlation between  $ADC_{min_{pre}}$  and percentage of the diameter ( $R^2 = 0.046$ , blue), correlation between  $ADC_{min}$  early change and percentage of the diameter ( $R^2 = 0.576$ , green), and the correlation between the percentage of  $ADC_{min}$  early change and percentage of the diameter ( $R^2 = 0.717$ , yellow).

**Table 3: Comparison of tumor diameter among CR, PR, and PD groups**

	No.	Diameter <sub>pre</sub> (cm)	Diameter <sub>early</sub> (cm)	Diameter <sub>post</sub> (cm)	Diameter Change (cm) <sup>a</sup>	Percentage Diameter Change <sup>b</sup>
CR	12	4.41 ± 1.46	2.45 ± 1.08	0.00 ± 0.00	4.41 ± 1.46	100
PR	15	5.60 ± 2.35	4.71 ± 2.39	2.03 ± 1.19	3.57 ± 2.07	60.75 ± 18.53
PD	8	5.06 ± 2.02	5.23 ± 2.42	6.21 ± 2.50	-1.16 ± 0.87	26.62 ± 22.16
Total	35	5.07 ± 2.02	4.03 ± 2.31	2.29 ± 2.71	2.78 ± 2.73	54.24 ± 50.38
<i>P</i> value		.325	.007	.000	.000	.000
CR-PR		.137	.008	.001	.201	.000
CR-PD		.486	.005	.000	.000	.000
PR-PD		.543	.570	.000	.000	.000

<sup>a</sup> Diameter Change = Diameter<sub>pre</sub> - Diameter<sub>post</sub>.

<sup>b</sup> Percentage Diameter Change = (Diameter<sub>pre</sub> - Diameter<sub>post</sub>)/Diameter<sub>pre</sub>.

gradually, though the increments were relatively small. The ADC<sub>min</sub> values after 1 cycle and after 5 cycles of chemotherapy were statistically significantly higher than the pretreatment values ( $P < .001$ ,  $P < .001$ ), but there was no statistically significant difference between ADC<sub>min</sub> values after 1 and 5 cycles of chemotherapy ( $P = .60$ ) (Fig 2).

The mean ADC<sub>min</sub> value for the PD group decreased slightly or showed no obvious change during chemotherapy. The post-treatment ADC<sub>min</sub> values for the patients with PD appeared to increase slightly compared with the pretreatment ADC<sub>min</sub> values. The ADC<sub>min</sub> values after 1 and 5 cycles of chemotherapy were statistically significantly higher than pretreatment values ( $P = .01$ ,  $P = .04$ ), but there was no statistically significant difference between the ADC<sub>min</sub> values after 1 and 5 cycles of chemotherapy ( $P = .28$ ) (Fig 3).

The comparison among groups showed that ADC<sub>min</sub><sub>early</sub>, ADC<sub>min</sub> after 5 cycles, ADC<sub>min</sub> change, and percentage of ADC<sub>min</sub> change were all significantly different among the 3 groups (CR, PR, and PD). Specifically, the mean percentage of ADC<sub>min</sub> changes of the tumors after 1 cycle of chemotherapy was 55.68% for CR, 37.52% for PR, and -3.78% for PD, and there was a significant difference among these values ( $F = 22.10$ ,  $P < .001$ ) (Table 2). Comparison of pretreatment ADC<sub>min</sub>, ADC<sub>min</sub> early change, and percentage ADC<sub>min</sub> change indicated that the ADC<sub>min</sub> change and percentage ADC<sub>min</sub> change performed better in differentiating the final treatment response, specifically differentiating the CR and PR groups from the PD group (Fig 4A, -B).

The mean percentage diameter of early changes of the tumors after 5 cycles of chemotherapy was 46.43% for CR, 20.83% for PR, and -1.46% for PD, and there was a significant difference among these values ( $F = 22.10$ ,  $P < .001$ ) (Table 3).

A positive correlation was observed between ADC<sub>min</sub><sub>pre</sub> and the size reduction percentage after 5 cycles of chemotherapy (Pearson coefficient, 0.34;  $P = .05$ ). In addition, a significant positive correlation was observed between the early ADC<sub>min</sub> changes, early percentage of ADC<sub>min</sub> changes after 1 cycle of chemotherapy, and size reduction percentage after 5 cycles of chemotherapy (Pearson coefficient, 0.58,  $P < .001$ ; 0.72,  $P < .001$ , respectively) (Fig 4C).

## DISCUSSION

Traditionally, an assessment of solid cancer therapy effectiveness relies on comparison of changes in tumor size by images obtained before and after the therapeutic intervention. However, tumor

size measurement by using images (CT or MR imaging) is insensitive to early treatment changes and cannot monitor changes in tissue structure at the cellular level.<sup>14</sup> DWI can detect relatively small changes in tissue structure at the cellular level because it is specifically sensitive to cellular status, density, and microstructural organization.<sup>15</sup> The combination of DWI with conventional MR imaging enables morphologic and physiologic changes to be assessed during the same examination. The extremely high DWI

signal intensity is characteristic of MR imaging findings in PCNSL due to the high cell density, and cell density has a great differential value for tumors of the brain.<sup>16,17</sup> Previous studies have shown a significant inverse correlation between cellularity and ADC values in PCNSL, suggesting ADC as a surrogate marker of tumor proliferation.<sup>17</sup> ADC has shown promise in the prognostication of response to therapy for non-Hodgkin lymphoma, even if not technically in the central nervous system.<sup>18</sup> DWI-derived ADC values provide an opportunity to quantitatively and serially follow treatment-induced changes in PCNSL, and specifically, ADC<sub>min</sub> values were more powerful than ADC mean or ADC 25% values.<sup>5</sup> Here, we aimed to confirm the validity of ADC<sub>min</sub> measurement as an imaging biomarker of therapy response in immunocompetent patients with PCNSL.

The validity of pretherapeutic ADC as a predictor of clinical outcomes in patients with PCNSL remains controversial. Several studies have proposed that the lower the pretherapy baseline tumor ADC values, the shorter the progression-free survival and overall survival in patients with lymphoma.<sup>6,5,19</sup> However, a new study showed no association between a higher baseline ADC and CR, and no differences were observed in progression-free survival or overall survival according to the baseline ADC among the CR, PR, and PD groups.<sup>10</sup>

In our study, the pretherapeutic ADC<sub>min</sub> of the PD ( $476.14 \pm 93.36 \times 10^{-6} \text{ mm}^2/\text{s}$ ) group was lower than that in the CR ( $566.56 \pm 120.84 \times 10^{-6} \text{ mm}^2/\text{s}$ ) and PR ( $487.54 \pm 78.00 \times 10^{-6} \text{ mm}^2/\text{s}$ ) groups; however, there was no significant difference among these values. The mean percentage of ADC<sub>min</sub> change of the tumor after 1 cycle of chemotherapy was 55.68% for CR, 37.52% for PR, and -3.78% for PD, and there was a significant difference observed among them. Our results indicate that the ADC<sub>min</sub> changes and percentage changes after early therapy could more precisely predict treatment response than the pretreatment ADC<sub>min</sub> value. Although tumors with higher pretherapeutic ADC values and lower signal intensity at DWI responded better to treatment, neither the pretherapeutic diameter nor pretherapeutic ADC<sub>min</sub> could completely predict the PCNSL outcome from methotrexate-based chemotherapy. A possible explanation is that pretherapeutic cellularity cannot precisely reflect the treatment response. However, cellularity reduction caused by chemotherapy drugs increases ADC<sub>min</sub>. Thus, posttherapeutic ADC<sub>min</sub> growth might indicate the later tumor regression or decelerated growth and enable early detection of tumor response. Change is a better assessment strategy based on pre-

therapeutic data. Another explanation is the lack of sufficient statistical power due to the relatively small sample size.

Previous studies have confirmed that effective anticancer treatment resulted in an increase in water diffusion. Studies with animal models found that chemotherapy increased the tumor ADC value within days through reducing cellularity as a result of apoptosis and/or cell death.<sup>20,21</sup> The ADC value also rose with greater histologic changes (such as a progressive increase in tumor extracellular space and an increase in pleomorphism, giant cells, and cells with the characteristic morphologic features of apoptosis) because water mobility was increased by the greater extracellular space and membrane permeability.<sup>22</sup>

In this study, the mean ADCmin values for patients with CR and PR all increased after treatment.<sup>13,23,24</sup> The posttreatment ADCmin values of the CR group increased rapidly compared with the pretreatment values. In the PR group, the ADCmin value changed moderately, while in PD, it changed slightly and even decreased slightly after therapy. The percentage ADCmin change of the tumor after 1 cycle of chemotherapy correlated positively with the percentage size reduction of the tumor after 5 cycles of chemotherapy; this finding suggests that significant changes in tumor ADCmin values that occurred after treatment might indicate a better response to therapy. However, a minute change in tumor ADCmin values might indicate a less satisfactory outcome or even a therapeutically unresponsive tumor.

One hypothesis is that successful treatment of a tumor will result in significant damage to tumor cells in the form of a loss of cell membrane integrity with a subsequent reduction in tumor cell density. We observed that necrosis appeared in the center of the lesion in some cases after therapy, suggesting increases in the movement of water molecule diffusion, resulting in changes in tumor ADC values. Moreover, intratumoral edema, necrosis, and/or cysts may appear or increase due to damage to tumor cells or dynamic reorganization of the heterogeneous tumor structure after treatment. In addition, through dynamic changes of the ADCmin and diameter pre- and postchemotherapy, it was found that the change in mean ADCmin value occurred in advance of changes in tumor diameter, indicating that DWI is not dependent on relatively slow changes in tumor volume. Thus, DWI may be capable of providing earlier indications of therapeutic outcome due to molecular and cellular changes that typically precede observable macroscopic changes in gross tumor size. These findings offer a window of opportunity to modify the initial treatment regimen to improve the clinical outcome and minimize the morbidity associated with prolonged and ineffective treatment.

These results demonstrate the feasibility of using the ADCmin of DWI for the prediction of treatment outcomes in patients with PCNSL undergoing chemotherapy. Early identification of patients likely to have a poor response facilitates a chemoradiation regimen that may enable an early change in the treatment plan, such as addition of radiation therapy.

This study has a number of limitations. First, the follow-up time was short; thus, the correlation among the parameters obtained from DWI, the progression-free survival, and overall survival in patients with PCNSL could not be analyzed. Thus, further studies are needed to confirm the predictive value of ADCmin for the final prognosis. Second, the study included only cases of dif-

fuse large B-cells of the PCNSL and did not contain other pathologic types, such as Burkitt or T-cell types. Third, the study size was relatively small for the comparison of the pretherapeutic ADCmin among groups.

## CONCLUSIONS

Correlation between the percentage of ADCmin changes of a tumor after 1 cycle of chemotherapy and treatment outcomes provides a potential basis that may ultimately lead to the use of DWI for predicting and monitoring treatment response.

## REFERENCES

1. Nakajima S, Okada T, Yamamoto A, et al. **Differentiation between primary central nervous system lymphoma and glioblastoma: a comparative study of parameters derived from dynamic susceptibility contrast-enhanced perfusion-weighted MRI.** *Clin Radiol* 2015;70:1393–99 CrossRef Medline
2. Bhagavathi S, Wilson JD. **Primary central nervous system lymphoma.** *Arch Pathol Lab Med* 2008;132:1830–34 Medline
3. Kansara R, Shenkier TN, Connors JM, et al. **Rituximab with high dose methotrexate in primary central nervous system lymphoma.** *Am J Hematol* 2015;90:1149–54 CrossRef Medline
4. PDQ Adult Treatment Editorial Board. **Primary CNS Lymphoma Treatment.** Bethesda, Maryland: National Cancer Institute. Updated September 21, 2015. <http://www.cancer.gov/types/lymphoma/patient/primary-cns-lymphoma-treatment-pdq>. Accessed June 9, 2016 Medline
5. Barajas RF Jr, Rubenstein JL, Chang JS, et al. **Diffusion-weighted MR imaging derived apparent diffusion coefficient is predictive of clinical outcome in primary central nervous system lymphoma.** *AJNR Am J Neuroradiol* 2010;31:60–66 CrossRef Medline
6. Wieduwilt MJ, Valles F, Issa S, et al. **Immunochemotherapy with intensive consolidation for primary CNS lymphoma: a pilot study and prognostic assessment by diffusion-weighted MRI.** *Clin Cancer Res* 2012;18:1146–55 CrossRef Medline
7. Lee EJ, Lee SK, Agid R, et al. **Preoperative grading of presumptive low-grade astrocytomas on MR imaging: diagnostic value of minimum apparent diffusion coefficient.** *AJNR Am J Neuroradiol* 2008;29:1872–77 CrossRef Medline
8. Guo AC, Cummings TJ, Dash RC, et al. **Lymphomas and high-grade astrocytomas: comparison of water diffusibility and histologic characteristics.** *Radiology* 2002;224:177–83 CrossRef Medline
9. Lee KC, Moffat BA, Schott AF, et al. **Prospective early response imaging biomarker for neoadjuvant breast cancer chemotherapy.** *Clin Cancer Res* 2007;13:443–50 CrossRef Medline
10. Morris PG, Correa DD, Yahalom J, et al. **Rituximab, methotrexate, procarbazine, and vincristine followed by consolidation reduced-dose whole-brain radiotherapy and cytarabine in newly diagnosed primary CNS lymphoma: final results and long-term outcome.** *J Clin Oncol* 2013;31:3971–79 CrossRef Medline
11. Abrey LE, Batchelor TT, Ferreri AJ, et al; International Primary CNS Lymphoma Collaborative Group. **Report of an international workshop to standardize baseline evaluation and response criteria for primary CNS lymphoma.** *J Clin Oncol* 2005;23:5034–43 CrossRef Medline
12. Iwadate Y1, Suganami A, Ikegami S, et al. **Non-deep-seated primary CNS lymphoma: therapeutic responses and a molecular signature.** *J Neurooncol* 2014;117:261–68 CrossRef Medline
13. Prasad SR, Jhaveri KS, Saini S, et al. **CT tumor measurement for therapeutic response assessment: comparison of unidimensional, bidimensional, and volumetric techniques initial observations.** *Radiology* 2002;225:416–19 CrossRef Medline
14. Liua Y, Baia R, Suna H, et al. **Diffusion-weighted imaging in predicting and monitoring the response of uterine cervical cancer to combined chemoradiation.** *Clin Radiol* 2009;64:1067–74 CrossRef Medline
15. Server A, Kulle B, Maehlen J, et al. **Quantitative apparent diffusion coefficients in the characterization of brain tumors and associated peritumoral edema.** *Acta Radiol* 2009;6:683–89 CrossRef Medline



16. Zacharia TT, Law M, Naidich TP, et al. **Central nervous system lymphoma characterization by diffusion-weighted imaging and MR spectroscopy.** *J Neuroimaging* 2008;18:411–17 CrossRef Medline
17. Africa E, Pauciulo A, Vadalà R, et al. **Primary central nervous system lymphoma: role of DWI in the differential diagnosis.** *Rays* 2005;30:221–26 Medline
18. Wu X, Kellokumpu-Lehtinen PL, Pertovaara H, et al. **Diffusion-weighted MRI in early chemotherapy response evaluation of patients with diffuse large B-cell lymphoma: a pilot study—comparison with 2-deoxy-2-fluoro-D-glucose-positron emission tomography/computed tomography.** *NMR Biomed* 2011;24:1181–90 CrossRef Medline
19. Valles FE, Perez-Valles CL, Regalado S, et al. **Combined diffusion and perfusion MR imaging as biomarkers of prognosis in immunocompetent patients with primary central nervous system lymphoma.** *AJNR Am J Neuroradiol* 2013;34:35–40 CrossRef Medline
20. Fujimoto H, Kazama T, Nagashima T, et al. **Diffusion-weighted imaging reflects pathological therapeutic response and relapse in breast cancer.** *Breast Cancer* 2014;21:724–31 CrossRef Medline
21. Chenevert TL, Stegman LD, Taylor JM, et al. **Diffusion magnetic resonance imaging: an early surrogate marker of therapeutic efficacy in brain tumors.** *J Natl Cancer Inst* 2000;92:2029–36 CrossRef Medline
22. Chenevert TL, McKeever PE, Ross BD. **Monitoring early response of experimental brain tumors to therapy using diffusion magnetic resonance imaging.** *Clin Cancer Res* 1997;3:1457–66 Medline
23. Moffat BA, Chenevert TL, Lawrence TS, et al. **Functional diffusion map: a noninvasive MRI biomarker for early stratification of clinical brain tumor response.** *Proc Natl Acad Sci USA* 2005;102:5524–29 CrossRef Medline
24. Moffat BA, Hall DE, Stojanovska J, et al. **Diffusion imaging for evaluation of tumor therapies in preclinical animal models.** *MAGMA* 2004;17:249–59 CrossRef Medline

# A Simple Automated Method for Detecting Recurrence in High-Grade Glioma

T.K. Yanagihara, J. Grinband, J. Rowley, K.A. Cauley, A. Lee, M. Garrett, M. Afghan, A. Chu, and T.J.C. Wang



## ABSTRACT

**SUMMARY:** Our aim was to develop an automated multiparametric MR imaging analysis of routinely acquired imaging sequences to identify areas of focally recurrent high-grade glioma. Data from 141 patients treated with radiation therapy with a diagnosis of high-grade glioma were reviewed. Strict inclusion/exclusion criteria identified a homogeneous cohort of 12 patients with a nodular recurrence of high-grade glioma that was amenable to focal re-irradiation (cohort 1). T1WI, FLAIR, and DWI data were used to create subtraction maps across time points. Linear regression was performed to identify the pattern of change in these 3 imaging sequences that best correlated with recurrence. The ability of these parameters to guide treatment decisions in individual patients was assessed in a separate cohort of 4 patients who were treated with radiosurgery for recurrent high-grade glioma (cohort 2). A leave-one-out analysis of cohort 1 revealed that automated subtraction maps consistently predicted the radiologist-identified area of recurrence (median area under the receiver operating characteristic curve = 0.91). The regression model was tested in preradiosurgery MRI in cohort 2 and identified 8 recurrent lesions. Six lesions were treated with radiosurgery and were controlled on follow-up imaging, but the remaining 2 lesions were not treated and progressed, consistent with the predictions of the model. Multiparametric subtraction maps can predict areas of nodular progression in patients with previously treated high-grade gliomas. This automated method based on routine imaging sequences is a valuable tool to be prospectively validated in subsequent studies of treatment planning and posttreatment surveillance.

**ABBREVIATIONS:** FSL = fMRI of the Brain Software Library; GBM = glioblastoma; GKRS = gamma knife radiosurgery; HGG = high-grade glioma; ROC = receiver operating characteristic

High-grade glioma (HGG) consists of World Health Organization grade III and IV gliomas, with glioblastoma (GBM) being the most common primary intracranial malignancy.<sup>1</sup> Prognosis is particularly poor in GBM, with 5-year survival <10% and median time to recurrence of approximately 6–7 months.<sup>2,3</sup> Most recurrences are within or adjacent to the primary tumor site,<sup>4</sup> and multicentric disease is a very uncommon entity.<sup>5,6</sup>

Because posttreatment changes occur within areas at highest risk of tumor recurrence, discerning expected radiographic changes from evolving tumor presents a major challenge in neuroradiology.

There is often debate regarding the proper assessment of MR imaging in the routine surveillance of patients with HGG.<sup>7–10</sup> Imaging assessment may be limited by tumor heterogeneity, radiation therapy–related changes, and the effects of systemic agents.<sup>11</sup> Attempts to standardize imaging assessment have previously been by implementation of the criteria of Macdonald et al<sup>12</sup> and now the Response Assessment in Neuro-Oncology criteria.<sup>13</sup> However, there remains inherent subjectivity to tumor measurements, and the Response Assessment in Neuro-Oncology does not provide information regarding the spatial distribution of brain tumor progression. Approaches to improve prognostic imaging assessment include perfusion-weighted imaging,<sup>14,15</sup> spectroscopy,<sup>16</sup> highly diffusion-weighted imaging,<sup>17</sup> and PET.<sup>18</sup>

The purpose of our study was to develop a method of quantifying changes in standard MR imaging parameters that is automated and does not rely on subjective user input. We applied digital subtraction maps by comparing images obtained across time (temporal subtraction maps) from multiple imaging se-

Received February 26, 2016; accepted after revision May 16.

From the Departments of Radiation Oncology (T.K.Y., J.R., A.L., M.G., M.A., A.C., T.J.C.W.) and Radiology (J.G., K.A.C.) and Herbert Irving Comprehensive Cancer Center (T.J.C.W.), Columbia University Medical Center, New York, New York; Division of Neuroradiology (K.A.C.), Geisinger Medical Center, Danville, Pennsylvania; and Department of Radiation Oncology (M.A.), Albany Medical Center, Albany, New York.

This publication was supported by the National Center for Advancing Translational Sciences, National Institutes of Health, through grant No. ULI TR000040.

The content is solely the responsibility of the authors and does not necessarily represent the official views of the National Institutes of Health.

Please address correspondence to Ted K. Yanagihara, MD, PhD, Department of Radiation Oncology, Columbia University Medical Center, 622 West 168th St, CHONY Basement North Room B11; e-mail: tky2102@columbia.edu

Indicates open access to non-subscribers at [www.ajnr.org](http://www.ajnr.org)

Indicates article with supplemental on-line appendix.

Indicates article with supplemental on-line photos.

<http://dx.doi.org/10.3174/ajnr.A4873>

quences. A primary goal was to rely only on standard imaging acquisitions and to use accessible image analysis techniques to reduce barriers to general use. We hypothesized that standardized thresholds to define changes in gadolinium-enhanced T1WI, FLAIR hyperintensity, and diffusion restriction could provide an automated method to identify areas of nodular HGG recurrence.

We searched a large, single-institution data base for a highly selected group of patients with HGG with a well-defined area of recurrence in the setting of prior standard-of-care treatment for malignant glioma and other clinical signs of disease progression. These patients served as a training set to generate the pattern of change in MR imaging signal across gadolinium-enhanced T1WI, FLAIR, and apparent diffusion coefficient values that best correlated with tumor progression. This pattern was then validated in a separate group of patients treated with radiosurgery for recurrent HGG. Radiosurgery is very rarely used in the treatment of HGG, but this select group offers the ideal scenario to validate our measure.

Because radiosurgery delivers a highly conformal dose of radiation, the predictions of the model can be tested inside and outside the treatment field by reviewing posttreatment MR imaging.

## MATERIALS AND METHODS

### Patients

All patients included in this study either had their informed consent waived on the basis of the retrospective nature of the analysis (before March 2015) or signed informed consent for participation (beginning in March 2015). Data acquisition was performed in compliance with all applicable Health Insurance Portability and Accountability Act regulations and was approved by the institutional review board of Columbia University. The study spanned March 2013 to November 2015, and MR imaging data were collected at a single institution on one of a variety of scanners. We chose March 2013 as the start date for the analysis, when the institution began routinely considering patients for focal re-irradiation for recurrent glioblastoma on the basis of the opening of a multicenter study investigating the role of re-irradiation in recurrent GBM. All MR imaging data consisted of standard clinical scan acquisitions and were not obtained for research purposes.

We searched our intradepartmental data base for all patients with a pathologic diagnosis of HGG who also met all of the following criteria: 1) underwent gross total or subtotal resection followed by concurrent temozolomide and radiation therapy; 2) were treated with either hypofractionated radiation of 4005 cGy in 15 fractions or standard fractionation of 5940–6000 cGy in 30–33 fractions; 3) had at least 2 postradiation MR imaging scans with no findings suspicious for progression; 4) developed disease progression that was deemed unequivocal by a board-certified neuroradiologist; 5) had all MR imaging available for review, including gadolinium-enhanced T1WI, FLAIR, and ADC measures; and 6) was the subject of an interdisciplinary discussion (ie, tumor board) resulting in agreement that the patient had experienced a clinically meaningful focal recurrence amenable to re-irradiation.

From an initial group of 141 consecutive patients referred for radiation therapy for HGG (On-line Fig 1), these criteria yielded 22 patients with recurrent HGG who met the inclusion criteria above. Of these, 12 patients were included in the initial analysis (cohort 1), and a separate cohort of 4 patients was identified with

gamma knife radiosurgery (GKRS) delivered to focal nodular recurrence (cohort 2). Disease recurrence was proved by pathology in 7 patients, all in cohort 1 (58.3%).

### Image Processing and Statistical Analysis

Additional methods, including all image-processing routines, are provided in the On-line Appendix. All diffusion-weighted scans were acquired at 2 b-values of 0 and 1000 s/mm<sup>2</sup>. Image processing was performed with the fMRI of the Brain Software Library<sup>19</sup> (FSL; <http://www.fmrib.ox.ac.uk/fsl>) and Matlab (MathWorks, Natick, Massachusetts). Brain extraction was performed for each imaging sequence, which was coregistered with a linear algorithm by using the most recently obtained T1WI gadolinium-enhanced scan.

All sites of disease recurrence were delineated by hand by using FSL software on the T1WI gadolinium-enhanced scans, and inverted linear registration matrices based on a mutual information cost function were applied to the ROIs to perform the analyses in their native space. Areas of disease recurrence were identified on the basis of radiology reports. Only the report for the scan being contoured was available for review, and we were blinded to the ultimate outcome. Signal from the tumor ROI was normalized to signal from voxels outside the tumor volume plus a margin to allow for microscopic disease, to account for signal variability between scans and MR imaging scanners. Specifically, manually drawn tumor volumes were expanded by at least 1.5–2 cm outside any surgical cavity, contrast-enhancing area, and FLAIR hyperintensity (ie, similar to the standard approach to defining the radiation clinical target volume). Voxels outside this margin were considered free of infiltrating tumor and were considered the “normal” brain. The brain was then normalized, by division, to the mean signal obtained from the nontumor brain volume for further analysis.

A subtraction image was created on the basis of scans from 2 dates: 1) the MR imaging scan that demonstrated the radiologist-defined area of tumor recurrence, and 2) the scan before the recurrence that was last read as stable, with no evidence of disease recurrence.

Temporal changes in signal between these 2 scan dates were analyzed by converting the difference image into z scores, which we term the “temporal subtraction map” (Fig 1). To identify the optimal combination of z scores, we used a hypothesis-driven approach as opposed to an evaluation of all possible combinations of z scores. We reasoned that the latter approach may identify a mathematically better fit to the data but could generate a clinically meaningless pattern of change. Specifically, we hypothesized that tumor recurrence would follow a pattern of increased T1WI contrast enhancement along with a concurrent increase in FLAIR signal intensity with a corresponding decrease in ADC values. In cohort 1, a linear regression with these restricted ranges of z scores was performed to generate a least-squares fit to the criterion standard radiologists’ definition of the recurrent area. This identified the optimal relative weighting for each imaging sequence at the individual patient level. The least-squares intercept and parameter estimates from this model were then averaged to the group level to provide the common pattern across the test group of patients. The model was tested by using a leave-one-out approach

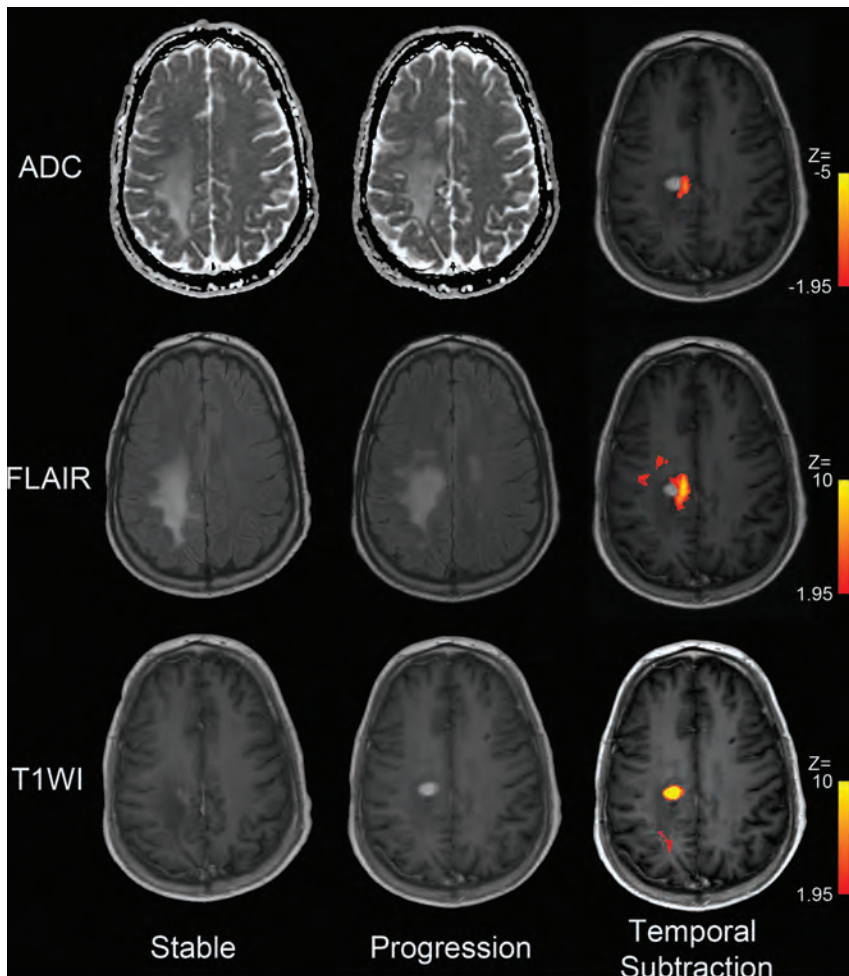


**FIG 1.** Temporal subtraction maps calculated for a representative patient from cohort 1. Column 1 is the MR imaging that was last read as “stable” by the interpreting radiologist. Column 2 is the next follow-up MR imaging demonstrating a nodular recurrence. A focal recurrence is visible in the right posterior frontal lobe with an area of contrast enhancement, increased FLAIR antero-medially, and a small focus of diffusion restriction medially. Automated digital subtraction maps displayed in column 3 demonstrate areas of significant change across the 2 time points for each imaging sequence.

within cohort 1, and receiver operating characteristic (ROC) curves were generated with the area under the curve computed. The mean parameter estimates for each imaging sequence were multiplied by the respective imaging sequence (ie, T1WI postcontrast, FLAIR, and ADC) for each patient in the GKRS cohort, and the mean least-squares intercept was added. This process resulted in a composite map based on the multiparametric data generated in cohort 1 to be validated in cohort 2.

Cohort 2 comprised all patients with a focal recurrence of malignant glioma that was treated with GKRS. Four patients met these criteria: Two patients had multifocal disease, and all potential lesions were evaluated. Radiosurgery is not typically a consideration in patients with recurrent HGG, but 4 exceptional patients experienced a local recurrence, in whom surgical intervention was not deemed appropriate. Across the 4 patients, 8 lesions were considered to potentially represent disease progression. Temporal subtraction maps were generated by registering the patient’s MR imaging scan that last showed stable findings to the first MR imaging scan with detectable disease progression. The recurrence

seen in this latter scan was the clinical motivation to treat the patient with GKRS in all 4 patients. The regression model generated in cohort 1 was then applied to the contrast-enhanced T1WI, FLAIR, and ADC temporal subtraction maps from each patient in cohort 2. This resulted in a single z statistic image for each patient in the validation cohort that represented the prediction of areas of the model representing active disease recurrence. A stringent statistical threshold was applied to each z statistic image so that voxels whose correlation to the model was  $<5$  SDs above the mean were filtered.

An additional cluster filter was applied so that only clusters in the top 1% by size were retained. The cluster filter removed numerous individual and small clusters of voxels particularly seen at anatomic boundaries where image coregistration may create artifacts. These thresholds were chosen to eliminate false-positives of the subtraction method, such as small clusters at anatomic boundaries or where differences in timing of gadolinium injection caused differences in vessel filling (On-line Appendix). The full range of unthresholded images is also provided in the On-line Appendix. The product z statistic image was then overlaid with the patient’s actual GKRS treatment plan and post-GKRS MR imaging scans to evaluate the accuracy of the predictions of the model.

Accurate image registration is critical in the generation of temporal subtraction maps. We demonstrate the accuracy of our image registration for all 48 coregistrations (ie, 3 images for each of 16 patients) by using the methods described by Klein et al,<sup>20</sup> with details provided in the On-line Appendix and On-line Fig 2.

## RESULTS

Patient characteristics from both patient groups are outlined in the Table. Cohort 1 consisted of 8 female and 4 male patients with a median age of 61.5 years. Nine patients had a primary diagnosis of GBM (World Health Organization grade IV), and 3 had anaplastic astrocytoma (World Health Organization grade III). Of the latter, 2 had a pathology-proved recurrence with GBM and the remaining patient was retreated on the basis of radiographic progression alone.

The initial course of radiation therapy was delivered at a dose of 6000 cGy in 8 patients, 5940 cGy in 2 patients, and 4005 cGy in 2 patients. The number of days between the end of radiation therapy and the MR imaging showing clear disease progression was a

## Patient characteristics

	Age		Initial Histology	Initial Radiation (cGy/fractions)	Recurrence Interval (days)	Subtraction Interval (days)	Tumor Recurrence Volume (mL)
	(yr)	Sex					
<b>Cohort 1 (model cohort)</b>							
1	42	M	AA	5940/33	3150	28	0.41
2	61	F	GBM	4005/15	298	49	2.70
3	44	F	GBM	5940/33	N/A	91	0.62
4	63	M	GBM	6000/30	137	73	8.67
5	62	F	GBM	6000/30	79	63	0.75
6	75	M	GBM	4005/15	418	56	2.33
7	62	F	GBM	6000/30	719	43	16.41
8	78	F	AA	6000/30	2518	98	1.62
9	55	M	GBM	6000/30	280	63	2.42
10	63	F	GBM	6000/30	159	88	3.27
11	34	F	AA	6000/30	253	37	0.86
12	32	F	GBM	6000/30	522	98	0.39
Median	62	—	—	6000/30	298	63	1.97
<b>Cohort 2 (radiosurgery cohort)</b>							
A	35	M	AA	5940/33	2961	98	0.22
B	53	M	GBM	6000/30	347	87	1.02
C	60	M	GBM	6000/30	663	50	8.88
D	84	M	GBM	4005/15	233	92	3.45
Median	57	—	—	6000/30	505	90	2.23

**Note:**—AA indicates anaplastic astrocytoma.

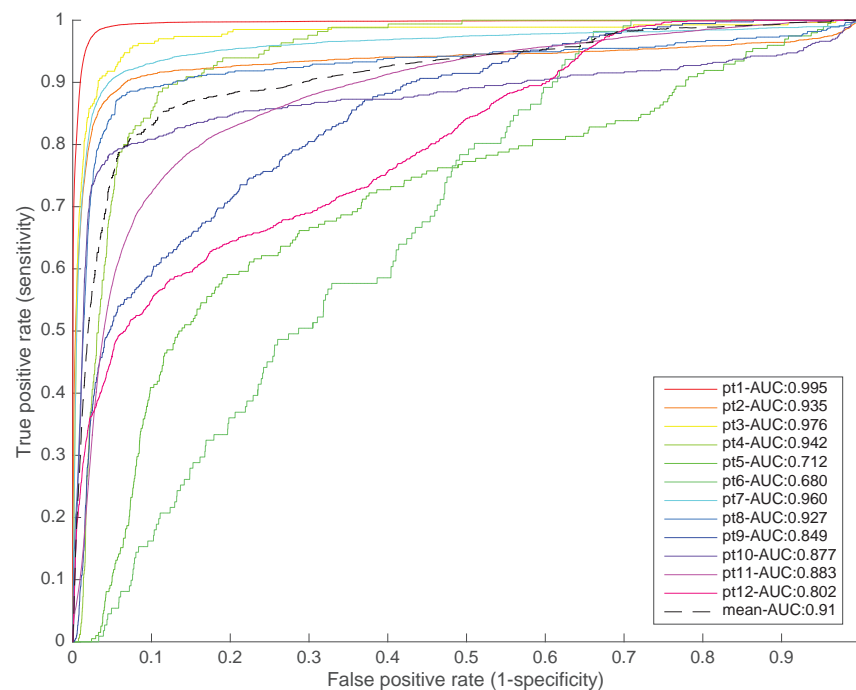


**FIG 2.** ROC curves from the leave-one-out cross-validation. Each curve and its area were computed by generating a model based on 11 patients and applying it to an individual patient.

median of 298 days (range, 79–3150 days) measured from the end of radiation therapy. When measured from the last MR imaging scan with “normal” findings (ie, the temporal subtraction interval), the interval was a median of 63 days (range, 28–98 days). The median volume of recurrent tumor was 1.97 mL (range, 0.39–16.41 mL). In the second cohort (patients A–D in the Table), all 4

patients were men with a median age of 57 years (range, 35–84 years). Three patients were diagnosed with GBM at recurrence, and 1 patient had a primary diagnosis of anaplastic astrocytoma with an aggressive multicentric recurrence that was not amenable to biopsy.

Two patients received 6000 cGy in their initial radiation course, 1 received 5940 cGy, and 1 received 4005 cGy. The recurrence interval was a median of 505 days (range, 233–2961 days), and the temporal subtraction interval was a median of 90 days (range, 50–98 days). The median volume of tumor recurrence was 2.23 mL (range, 0.22–8.88 mL).

ROC curves were generated on the basis of the entire brain, as opposed to a ROI analysis, for each of the 12 patients in cohort 1 and are depicted along with the area under the curve in Fig 2. The mean area under the curve for the leave-one-out analysis was 0.88 with an SD of 0.1. The regression model was sensitive and specific, with an area under the curve of  $\geq 0.8$  in all except 2 patients.

The regression model was applied to temporal subtraction maps for each of the 4 patients in cohort 2. Results from individual patients are presented to demonstrate the spatial resolution of the model predictions and without depiction of ADC images for brevity.

In patient A, 2 foci of recurrent disease (sum volume of 8.88 mL) were identified. A right inferior temporal lesion was identified as likely recurrent tumor (Fig 3A, -B), and voxels within the lesion were highly correlated with the model (Fig 3C). The lesion was treated with GKRS (Fig 3D) and became increasingly necrotic but was stable in size at 35-day (Fig 3E, -F) and 66-day (Fig 3G, -H) follow-up. Similarly, a left inferior temporal lesion was observed (On-line Fig 3A, -B), and the model confirmed this as an area of likely recurrent tumor (On-line Fig 3C). GKRS to this area was performed (On-line Fig 3D), and follow-up imaging demonstrated that the lesion remained stable in size at 35 days (On-line Fig 3E, -F) and 66 days

(On-line Fig 3G, -H) posttreatment. However, the primary lesion in the right posterior frontal lobe was imaged (Fig 4A, -B) and predicted by the model to have active tumor within a circumferential area of the enhancing rim (Fig 4C). This lesion was not treated by GKRS (Fig 4D) and progressed at 35 days (Fig 4E, -F). By 66 days (Fig 4G, -H), there was a dramatic increase in size with

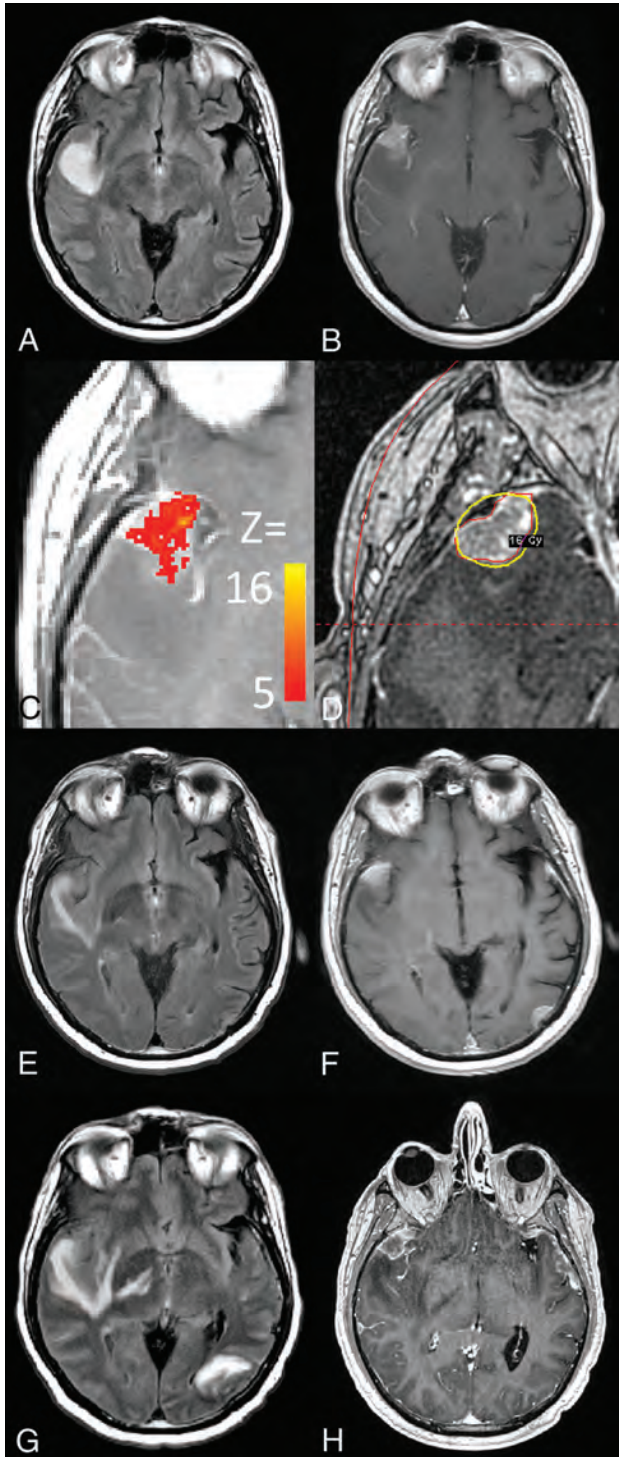


**FIG 3.** Patient A from the Table was found to have an area of focal recurrence in the right temporal lobe seen on follow-up imaging (A and B) and the multiparametric subtraction map (C). The area was also treated with radiosurgery (D) and remained stable at 35 (E and F) and 66 days (G and H).

the tumor crossing to the contralateral hemisphere and causing mass effect with a midline shift. Unthresholded axial images are also provided for patient A in On-line Fig 4.

Further demonstrations of the application of the method in 3 patients are provided in the On-line Appendix and On-line Figs 3–17.

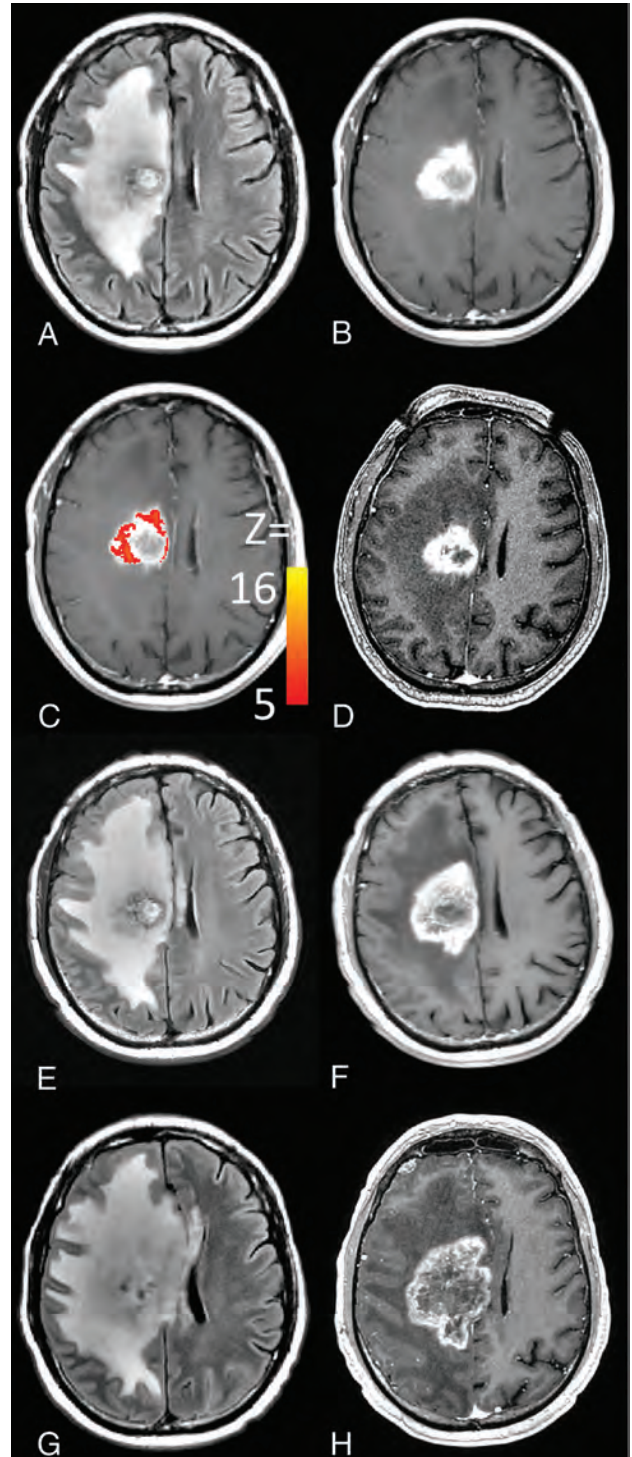


**FIG 4.** Evaluation of the primary lesion from patient A (A and B) demonstrates an area at risk of recurrence as determined by the multiparametric subtraction map (C). This region was not included in the radiosurgery treatment plan (D) and did progress at 35 days (E and F). Progression was more pronounced at 66 days (G and H).

## DISCUSSION

Nearly all patients with a diagnosis of HGG experience local recurrence of their disease despite aggressive tri-modality therapy. Surveillance MR imaging for patients with HGG typically involves a qualitative review of relevant images with careful attention paid to abnormal enhancement, changes in T2 or fluid-attenuated in-

version recovery patterns, and areas of restricted diffusion. A limitation of this qualitative approach is the subjectivity in the relative value (ie, weighting) of each imaging sequence reviewed and the interreader variability that may result. To improve on this qualitative approach, Ellingson et al<sup>21</sup> have applied digital subtraction of pre- from postadolinium T1WI to more accurately isolate areas of enhancing tumor. The investigators demonstrate both the qualitative value of the technique in visualizing tumor and the quantitative relationship between subtraction maps and survival. Subtraction maps were first developed 2 decades ago,<sup>22,23</sup> but their application in HGG has not been adopted. More recent advances, such as PWI, have improved surveillance and continue to be investigated, with multiparametric approaches showing particular promise.<sup>24,25</sup> PWI was not acquired routinely in patients included in this study, but future analyses would benefit from the addition of this technique.

In this study, we sought to develop an analytic approach that is quantitative, requires minimal subjective user input, makes spatial predictions to guide decisions regarding local therapies, and is based on readily available imaging tools. To this end, we identified a homogeneous group of patients with a well-defined spatial recurrence and a comprehensive clinical assessment leading to the recommendation for retreatment with radiation therapy.

Analysis of these data revealed a consistent pattern of change in T1WI, FLAIR, and ADC signal intensities. When the regression model was applied to a separate cohort of patients who were treated with conformal radiosurgery, spatially discernable areas at risk of tumor progression were identified with high specificity. A leave-one-out validation was performed in the 12 patients used to develop the regression model, which confirmed its high sensitivity and specificity. We then performed a hypothetical test of the model in a cohort of 4 patients treated with GKRS. Results were not sent to the PACS because of the investigational nature of the study, but results can be stored in a format that would permit using PACS in the future.

GKRS is an atypical method to treat HGG because this disease tends to recur diffusely but can occasionally recur focally. This unique group of patients is an ideal cohort in which to test the application of temporal subtraction maps because disease progression within and outside the highly conformal GKRS dose distribution can be monitored with time.

Across the 4 patients in cohort 2, the model predicted that 5 lesions were at high risk of recurrence and these were treated with GKRS. Follow-up imaging demonstrated the stability of all 5 lesions for at least 64 days (ie, 66 days in patient A, 248 days in patient B, 95 days in patient C, and 64 days in patient D). The model also predicted active tumor in the enhancing rim or adjacent to the primary lesion in 2 patients. These areas were not treated with GKRS and were found to have progressed at the next available imaging follow-up (35 days in patient A and 53 days in patient C).

Limitations of this study are its retrospective nature, small patient size due to strict inclusion criteria, and the analytic methods needing to be validated prospectively before being applied to clinical practice more generally. A further limitation is the reliance on image registration to develop temporal subtraction maps. Poor coregistration leads to artifacts in the *z* statistic map, partic-

ularly at anatomic boundaries such as the brain outline. We addressed this limitation by creating 2 stringent statistical filters, including a *z* score threshold of 5 SDs above the mean and a spatial cluster threshold leaving only the top 1 percentile. While this feature serves to confirm the robust performance of the regression model on temporal subtraction maps within the brain parenchyma, there may be increased type II errors, particularly if the suspected recurrence is small or at the brain surface. Our assessment of registration accuracy demonstrates that even with the generally high agreement with linear registration in FSL, there were 3 outliers (of 48 registrations) in which the registration was poor. While this automated analytic tool may help reduce subjective bias, the potential for false-negative results and reliance on accurate image registration highlight its role as a supplement to clinical judgment rather than a fully automated method of treatment planning.

An additional limitation is the reliance on the radiologist's opinion as the "ground truth" in our analysis. Although more than half of the recurrences in cohort 1 were proved by pathology, a pathologic diagnosis was not obtained in the 4 patients in cohort 2, and this omission may increase susceptibility to false-positive results. While this caveat is important to consider, our inclusion criteria required that patients be selected for re-irradiation on the basis of a comprehensive clinical assessment. This decision was made as part of institutional policy and was not related to the present study, which should mitigate the presence of false-positive results.

## CONCLUSIONS

We applied a data-driven model to temporal subtraction maps of gadolinium-enhanced T1WI, FLAIR, and ADC images in patients with recurrent HGG. This automated method could be used to discern tumor regions that may benefit from additional local therapy, such as conformal radiosurgery. Future work will validate this approach prospectively to facilitate broader clinical application.

Disclosures: Jack Grinband—UNRELATED: Grants/Grants Pending: American Society of Neuroradiology 2016 Research Scientist Award.\* Tony J.C. Wang—UNRELATED: Board Membership: American Cancer Society North Jersey Leadership Advisory Board; Travel/Accommodations/Meeting Expenses Unrelated to Activities Listed: Abbvie \*Money paid to the institution.

## REFERENCES

1. Brandes AA. **State-of-the-art treatment of high-grade brain tumors.** *Semin Oncol* 2003;30:4–9 CrossRef Medline
2. Hegi ME, Diserens A, Gorlia T, et al. **MGMT gene silencing and benefit from temozolomide in glioblastoma.** *N Engl J Med* 2005;352:997–1003 CrossRef Medline
3. Stupp R, Hegt ME, Manson WP, et al; European Organisation for Research and Treatment of Cancer Brain Tumour and Radiation Oncology Groups, National Cancer Institute of Canada Clinical Trials Group. **Effects of radiotherapy with concomitant and adjuvant temozolomide versus radiotherapy alone on survival in glioblastoma in a randomised phase III study: 5-year analysis of the EORTC-NCIC trial.** *Lancet Oncol* 2009;10:459–66 CrossRef Medline
4. Chan JL, Lee SW, Fraass BA, et al. **Survival and failure patterns of high-grade gliomas after three-dimensional conformal radiotherapy.** *J Clin Oncol* 2002;20:1635–42 CrossRef Medline
5. Barnard RO, Geddes JF. **The incidence of multifocal cerebral**

- gliomas: a histologic study of large hemisphere sections. *Cancer* 1987;60:1519–31 CrossRef Medline
6. Djalilian HR, Shah MV, Hall WA. Radiographic incidence of multicentric malignant gliomas. *Surg Neurol* 1999;51:554–57; discussion 557–58 CrossRef Medline
  7. Jain R, Scarpace LM, Ellika S, et al. Imaging response criteria for recurrent gliomas treated with bevacizumab: role of diffusion weighted imaging as an imaging biomarker. *J Neurooncol* 2010;96:423–31 CrossRef Medline
  8. Schaff L, Donovan L, Lassman AB, et al. Imct-18pd-1 inhibitors for recurrent high grade glioma (Hgg). *Neuro-Oncology* 2015;17:v111.113–v111 CrossRef
  9. Telles BA, D'Amore F, Lerner A, et al. Imaging of the posttherapeutic brain. *Top Magn Reson Imaging* 2015;24:147–54 CrossRef Medline
  10. Boxerman JL, Ellingson BM. Response assessment and magnetic resonance imaging issues for clinical trials involving high-grade gliomas. *Top Magn Reson Imaging* 2015;24:127–36 CrossRef Medline
  11. Brandsma D, van den Bent MJ. Pseudoprogression and pseudoreponse in the treatment of gliomas. *Curr Opin Neurol* 2009;22:633–38 CrossRef Medline
  12. Macdonald DR, Cascino TL, Schold SC Jr, et al. Response criteria for phase II studies of supratentorial malignant glioma. *J Clin Oncol* 1990;8:1277–80 Medline
  13. Wen PY, Macdonald DR, Reardon DA, et al. Updated response assessment criteria for high-grade gliomas: Response Assessment in Neuro-Oncology Working Group. *J Clin Oncol* 2010;28:1963–72 CrossRef Medline
  14. Law M, Young RJ, Babb JS, et al. Gliomas: predicting time to progression or survival with cerebral blood volume measurements at dynamic susceptibility-weighted contrast-enhanced perfusion MR imaging. *Radiology* 2008;247:490–98 CrossRef Medline
  15. Lee J, Jain R, Khalil K, et al. Texture feature ratios from relative CBV maps of perfusion MRI are associated with patient survival in glioblastoma. *AJNR Am J Neuroradiol* 2016;37:37–43 CrossRef Medline
  16. Li Y, Lupo JM, Parvataneni R, et al. Survival analysis in patients with newly diagnosed glioblastoma using pre-and postradiotherapy MR spectroscopic imaging. *Neuro Oncol* 2013;15:607–17 CrossRef Medline
  17. Mardor Y, Pfeffer R, Spiegelmann R, et al. Early detection of response to radiation therapy in patients with brain malignancies using conventional and high b-value diffusion-weighted magnetic resonance imaging. *J Clin Oncol* 2003;21:1094–100 CrossRef Medline
  18. Pyka T, Gempt J, Ringel F, et al. Prediction of glioma recurrence using dynamic 18F-fluoroethyltyrosine PET. *AJNR Am J Neuroradiol* 2014;35:1924–29 CrossRef Medline
  19. Jenkinson M, Beckmann CF, Behrens TE, et al. FSL. *Neuroimage* 2012;62:782–90 CrossRef Medline
  20. Klein A, Andersson J, Ardekani BA, et al. Evaluation of 14 nonlinear deformation algorithms applied to human brain MRI registration. *Neuroimage* 2009;46:786–802 CrossRef Medline
  21. Ellingson BM, Kim HJ, Woodworth DC, et al. Recurrent glioblastoma treated with bevacizumab: contrast-enhanced T1-weighted subtraction maps improve tumor delineation and aid prediction of survival in a multicenter clinical trial. *Radiology* 2014;271:200–10 CrossRef Medline
  22. Lee VS, Flyer MA, Weinreb JC, et al. Image subtraction in gadolinium-enhanced MR imaging. *AJNR Am J Neuroradiol* 1996;167:1427–32 Medline
  23. Melhem ER, Mehta NR. Dynamic T1-weighted spin-echo MR imaging: the role of digital subtraction in the demonstration of enhancing brain lesions. *J Magn Reson Imaging* 1999;9:503–08 CrossRef Medline
  24. Prager AJ, Martinez N, Beal K, et al. Diffusion and perfusion MRI to differentiate treatment-related changes including pseudoprogression from recurrent tumors in high-grade gliomas with histopathologic evidence. *AJNR Am J Neuroradiol* 2015;36:877–85 CrossRef Medline
  25. Cha J, Kim ST, Kim HJ, et al. Analysis of the layering pattern of the apparent diffusion coefficient (ADC) for differentiation of radiation necrosis from tumour progression. *Eur Radiol* 2013;23:879–86 CrossRef Medline



# Diagnostic Performance of Routine Brain MRI Sequences for Dural Venous Sinus Thrombosis

 D. Patel,  M. Machnowska,  S. Symons,  R. Yeung,  A.J. Fox,  R.I. Aviv, and  P. Jabeahdar Maralani

## ABSTRACT

**BACKGROUND AND PURPOSE:** Signs suggestive of unexpected dural venous sinus thrombosis are detectable on routine MR imaging studies without MRV. We assessed performance characteristics and interrater reliability of routine MR imaging for the diagnosis of dural venous sinus thrombosis, focusing on the superior sagittal, transverse, and sigmoid sinuses.

**MATERIALS AND METHODS:** This case series included 350 patients with MRIs performed with contrast-enhanced MRV and 79 patients with routine MRIs performed within 48 hours of a CTV from 2008 to 2014 (total,  $n = 429$ ). Routine MR images were separated from the contrast-enhanced MRVs and CTVs. Three neuroradiologists, blinded to clinical data, independently reviewed the MRIs for signs of dural venous sinus thrombosis, including high signal on sagittal T1, loss of flow void on axial T2, high signal on FLAIR, high signal on DWI, increased susceptibility effects on T2\*-weighted gradient recalled-echo imaging, and filling defects on axial contrast-enhanced spin-echo T1WI and/or volumetric gradient-echo T1WI. Two neuroradiologists independently reviewed contrast-enhanced MRVs and CTVs to determine the consensus gold standard. Interrater reliability was calculated by using the  $\kappa$  coefficient.

**RESULTS:** Contrast-enhanced MRV and CTV confirmed that dural venous sinus thrombosis was present in 72 of 429 cases (16.8%). The combination of routine MR sequences had an overall sensitivity of 79.2%, specificity of 89.9%, and moderate interrater reliability ( $\kappa = 0.50$ ). The 3 readers did not have similar performance characteristics. 69.4% of positive cases had clinical suspicion of dural venous sinus thrombosis indicated on imaging requisition.

**CONCLUSIONS:** Routine MR images can suggest dural venous sinus thrombosis with high specificity in high-risk patients, even in cases without clinical suspicion.

**ABBREVIATIONS:** CE-3D-T1WI = volumetric contrast-enhanced GRE T1-weighted imaging; CEMRV = contrast-enhanced MRV; CE-SE-T1WI = contrast-enhanced spin-echo T1-weighted imaging; DVST = dural venous sinus thrombosis; GRE = T2\*-weighted gradient recalled-echo imaging

Dural venous sinus thrombosis (DVST) is a condition that ranges from being undiagnosed to leading to serious morbidity and mortality, including venous infarction and intracranial hemorrhage.<sup>1</sup> DVST has a highly variable clinical presentation, from asymptomatic to acute or subacute headaches, signs or symptoms of increased intracranial pressure, focal neurologic deficits, or seizures.<sup>2,3</sup> The diagnosis is important to consider even in younger patients, with risk factors such as genetic and acquired

prothrombotic states, trauma, and infections or inflammatory conditions.<sup>1,2</sup>

Although early and accurate diagnosis is important for initiation of treatment and prevention of serious complications, the median diagnostic delay from symptom onset is 7 days.<sup>1-4</sup> When DVST is suspected, the current criterion standard for diagnosis is either contrast-enhanced MRV (CEMRV) or CTV.<sup>5</sup> However, the imaging signs of unexpected DVST are seen during interpretation of routine MR imaging studies performed without dedicated CEMRV, concurrent CTV, or relevant clinical history. Typical findings might include visualization of intraluminal thrombus or a filling defect and lack of flow, or flow voids.<sup>2</sup> Signs suggestive of DVST on standard brain MR imaging are reported in the literature with highly variable diagnostic accuracy and can be difficult to interpret in daily practice.<sup>2,6-8</sup> Understanding the diagnostic performance of routine MR imaging for the evaluation of DVST is especially important when DVST is not clinically suspected or CT or MR venography has not been ordered. A false-positive inter-

Received February 1, 2016; accepted after revision April 25.

From the Department of Medical Imaging, University of Toronto, Sunnybrook Health Sciences Centre, Toronto, Ontario, Canada.

Paper previously presented at: Annual Meeting of the American Society of Neuroradiology and the Foundation of the ASNR Symposium, April 25–30, 2016; Chicago, Illinois.

Please address correspondence to Pejman Jabeahdar Maralani, MD, FRCPC, Department of Medical Imaging, University of Toronto, Sunnybrook Health Sciences Centre, AG 270C, 2075 Bayview Ave, Toronto, ON, M4N 3M5; e-mail: Pejman.Maralani@sunnybrook.ca

<http://dx.doi.org/10.3174/ajnr.A4843>

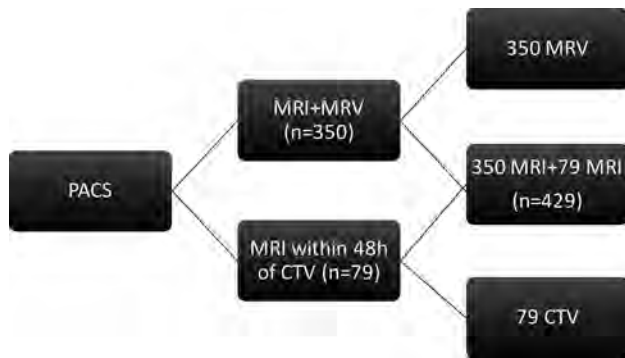


**FIG 1.** Patient selection and image separation.

pretation of DVST based on routine MR imaging will lead to unnecessary patient anxiety, require further imaging and associated health care costs, and increase patient risk from exposure to contrast media or radiation from CTV. False-negative interpretations can lead to devastating complications such as intracranial venous hypertension, hemorrhage, and venous infarction. The aim of this study was to assess the performance characteristics and interrater reliability of signs of DVST, not including cortical or deep vein thrombosis, on routine brain MR imaging, including T1, T2, T2\*-weighted gradient recalled-echo imaging (GRE), FLAIR, DWI, and postcontrast T1 sequences in comparison with CEMRV and CTV as the reference standard.

## MATERIALS AND METHODS

### Patient Selection

This case series study was approved by the institutional review board with a waiver of informed consent. The PACS was searched for patients who had both MR imaging and CEMRV or MR imaging and CTV from April 2008 to June 2014. The study included 350 MRIs performed with CEMRV and 79 MRI studies performed within 48 hours of a CTV for a total of 429 patients (Fig 1). Patients with prior surgical intervention that altered the anatomy of the dural venous sinuses were excluded because the dural sinuses cannot be assessed without a dedicated venogram study. No patients received anticoagulation between MR imaging and CTV. The patients were numbered in the order of their imaging study retrieval. Demographics and clinical information, including underlying conditions and indications for imaging, were recorded in a separate data base.

### Imaging Protocol

MR imaging was performed by using 1.5T TwinSpeed Excite (GE Healthcare, Milwaukee, Wisconsin) and 3T Achieva TX (Philips Healthcare, Best, the Netherlands) scanners using a standard 8-channel head coil.

The MR imaging sequences of interest and parameters (TR/TE/flip angle) for 1.5T were the following: sagittal T1 (2163 ms/25.5 ms/90°), axial T2 (1067 ms/35 ms/20°), axial T2 FLAIR (8600 ms/114.3 ms/90°), axial GRE (1200 ms/35 ms/20°), axial DWI (7000 ms/71.4 ms/90°), axial contrast-enhanced spin-echo T1 (CE-SE-T1WI) (350 ms/20 ms/0°), and volumetric contrast-enhanced GRE T1 (CE-3D-T1WI) (8.6 ms/4.2 ms/20°). The MR imaging sequences of interest and parameters (TR/TE/flip angle) for 3T were the following: T1 (9.5 ms/2.3 ms/8°), T2 (3793 ms/120

ms/90°), FLAIR (9000 ms/125 ms/90°), GRE (812 ms/16 ms/18°), DWI (3339 ms/45.8 ms/90°), SWI (15.9 ms/22.5 ms/15°), CE-SE-T1WI (553.7 ms/13 ms/90°), and CE-3D-T1WI (9.5 ms/2.3 ms/8°). CEMRV was performed with the following parameters (TR/TE/flip angle) for 1.5T and 3T: 4.2 ms/1.4 ms/25° and 3.9 ms/1.5 ms/30°. The patients were injected with 0.1 mmol/kg of gadobutrol (Gadovist; Bayer Schering Pharma, Berlin, Germany), maximum of 10 mL, by using a bolus-tracking technique and a power injector (Spectris MR injector; MedRad, Indianola, Pennsylvania) at a rate of 1.5 mL/s.

CTV was performed by using a LightSpeed 64-section scanner (GE Healthcare) as a dedicated protocol from C3 to the vertex, 0.625-mm helical. Iodixanol (Visipaque 320; GE Healthcare, Piscataway, New Jersey) was administered intravenously at an injection rate of 3–4 mL/s by using a bolus-tracking technique. Both CTV and CEMRV images had coronal, sagittal, and axial maximum-intensity-projection reformats. CT angiograms with good opacification of the dural venous sinuses were not included in the study because we wanted to use only dedicated CTV or CEMRV as our gold standard.

### Image Analysis

Images were anonymized and downloaded to an off-line workstation and were separated into 3 datasets: first, MR images with sequences of interest including T1, T2, GRE, FLAIR, DWI, SWI, CE-SE-T1WI, and CE-3D-T1WI without any vascular imaging; second, CTV source images with MIPs; and third, CEMRV source images with MIPs (Fig 1).

Of the 429 cases, the routine MR imaging dataset contained 418 cases with T1, 71 with T2, 420 with GRE, 417 with FLAIR, 421 with DWI, 139 with SWI, 241 with CE-SE-T1WI, and 199 with CE-3D-T1WI. Of the 72 cases positive for DVST by CEMRV or CTV, there were 71 cases with T1, 8 with T2, 70 with GRE, 69 with FLAIR, 71 with DWI, 15 with SWI, 44 with CE-SE-T1WI, and 23 with CE-3D-T1WI. The smaller sample sizes of T2, CE-SE-T1WI, and CE-3D-T1WI occurred because axial T2 was eliminated from the routine brain MRI and MRV at our institution in mid-2008 and CE-SE-T1WI was replaced by CE-3D-T1WI in 2010.

Signs of DVST investigated included high signal on sagittal T1, loss of flow void on axial T2, loss of flow void or hyperintense signal on FLAIR, increased susceptibility effects on axial GRE and SWI, high signal on axial DWI, and the presence of filling defects on axial CE-SE-T1WI and/or on CE-3D-T1WI. In each case, evaluation of all sequences of interest was performed at the same time to reflect usual clinical practice.

Three neuroradiologists, blinded to patient information and reports, independently reviewed the MR imaging sequence of interest for signs of DVST. In each case, the readers indicated the presence or absence of DVST as their overall impression. They also stated which individual sequences demonstrated findings of DVST. Readers had access to each of the MR imaging sequences of interest at the same time. Readers evaluated the superior sagittal sinus, right and left transverse sinuses, and right and left sigmoid sinuses.

Two neuroradiologists, blinded to patient information, reports, and the results from the sequence-of-interest analysis, independently reviewed CEMRV and CTV datasets to determine

the consensus reference standard. These neuroradiologists did not review the standard MR images from the CEMRV as in clinical practice. Disagreement was resolved by consensus after review by a third neuroradiologist. The cases were reviewed in multiple 1-hour sessions to reduce the influence of reader fatigue.

### Data Analysis

Individual reader results were compared against the reference standard and used to determine reader sensitivity, specificity, and accuracy for the combination of routine MR imaging signs. The performance characteristics of individual readers were compared with the McNemar test and SPSS software, Version 20.0 (IBM, Armonk, New York). Although in clinical practice MR imaging studies are read by individual radiologists, for this study, the performance of routine MR imaging was calculated on the basis of the most votes of the 3 readers when the sequences of interest were combined. The cases were also analyzed by comparing results from the 1.5T-versus-3T MR imaging scanners. Positive predictive and negative predictive values and accuracies of the consensus read were not reported because of the selective sample of this study and lack of prevalence data. Interrater reliability was calculated for each MR imaging sequence individually and combined by using  $\kappa$  coefficients with SAS 9.4 (SAS Institute, Cary, North Carolina). The agreement was considered slight if  $\kappa$  values were 0–0.20; fair if, 0.21–0.40; moderate if, 0.41–0.60; substantial if, 0.61–0.80; and almost perfect if, 0.81–1.<sup>9</sup> Results were expressed as mean  $\pm$  SD.  $P < .05$  was considered significant.

**Table 1: Patient characteristics**

	DVST (n = 72)	Non-DVST (n = 357)	Total (n = 429)
Age (yr) (mean)	51.4 $\pm$ 16.8	45.8 $\pm$ 17.0	46.7 $\pm$ 17.1
Female (No.) (%)	45 (62.5)	239 (66.9)	284 (66.2)
3T MRI (No.) (%)	16 (22.2)	130 (36.4)	146 (34.0)

## RESULTS

### Clinical Findings

There were 145 men and 284 women with a mean age of 46.7  $\pm$  17.1 years (Table 1). Women composed more than one-half of the sample volume (62.5%) and cases positive for DVST (66.2%). Two-thirds of the cases were performed on a 1.5T scanner (Table 1).

CEMRV and CTV confirmed that DVST was present in 72/429 cases (16.8%). The mean age of patients with DVST was 51.4  $\pm$  16.8 years.

The most common underlying predisposition for DVST was primary brain neoplasm or brain metastasis (19.4%), followed by traumatic brain injury (13.9%) and intracranial hemorrhage (subdural, subarachnoid, or intraparenchymal hemorrhage) (12.5%) (Fig 2). Only 1 patient demonstrated an underlying coagulation disorder (antiphospholipid antibody syndrome). Infectious or inflammatory factors included systemic lupus erythematosus, herpes simplex encephalitis, vasculitis, and abscess/osteomyelitis at the skull base (6.94%). Two patients in the intensive care unit were positive for DVST without a clear etiology (Fig 2).

The most commonly stated clinical indication for imaging was suspicion of DVST (Fig 3). For the cases positive for DVST, 69.4% had suspicion of DVST indicated, so 30.6% of positive cases were clinically unexpected DVST. Of the total 207 cases imaged with the explicit indication of “rule out DVST,” 50 (24.2%) were positive for it.

### Performance Characteristics

When we compared the performance characteristics of the 3 readers, reader 1 had significantly higher sensitivity than reader 2, and reader 2 had significantly higher specificity and accuracy than both readers 1 and 3 (Table 2). The most accurate reader (87.7%) had higher specificity (91.4%) at the expense of lower sensitivity (70.8%).

Routine MR imaging had an overall sensitivity of 79.2% and specificity of 89.9% based on the most votes of the 3 readers when

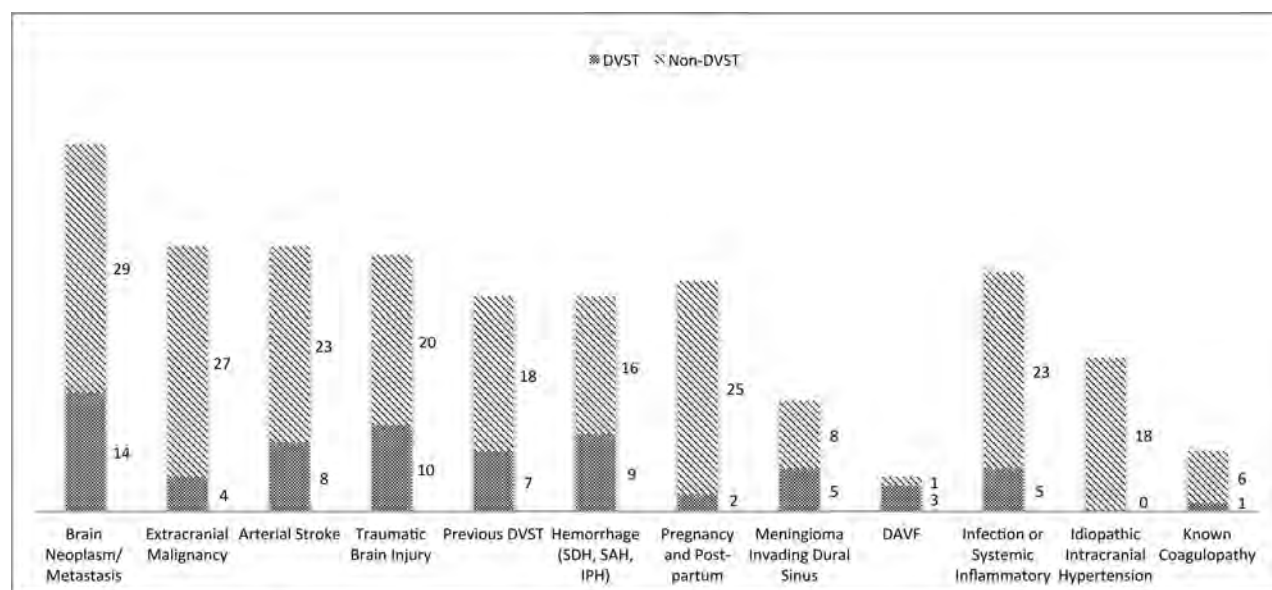


**FIG 2.** Etiology or underlying condition based on electronic medical records. SDH indicates subdural hemorrhage; IPH, intraparenchymal hemorrhage; DAVF, dural arteriovenous fistula.

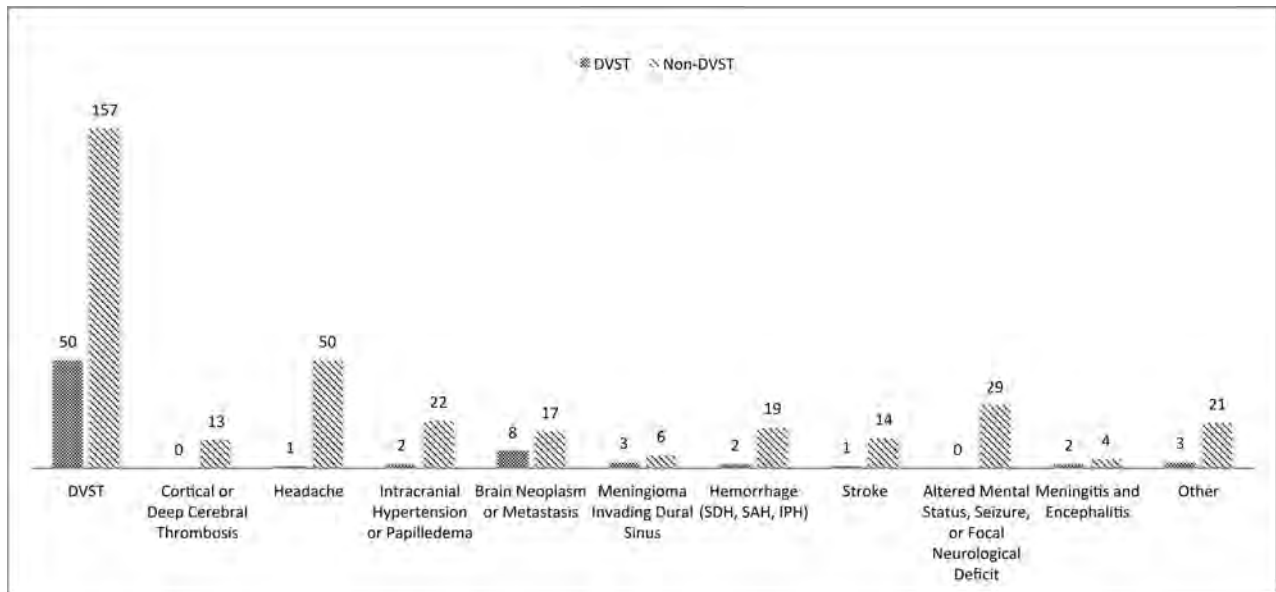


**FIG 3.** Indications for imaging based on the imaging requisition form. SDH indicates subdural hemorrhage; IPH, intraparenchymal hemorrhage.

**Table 2: Performance of routine MRI sequences compared with CEMRV or CTV for each reader**

	Sensitivity (%)	Specificity (%)	Accuracy (%)
Reader 1	84.7 <sup>a</sup>	82.1	82.5
Reader 2	70.8	91.4 <sup>b</sup>	87.7 <sup>b</sup>
Reader 3	72.2	84.3	82.3

<sup>a</sup> Statistically significant compared with reader 2 ( $P < .05$ ).

<sup>b</sup> Statistically significant compared with readers 1 and 3 ( $P < .05$ ).

**Table 3: Performance of MRI for the detection of DVST compared with CEMRV or CTV based on the most votes**

	Sensitivity (%)	Specificity (%)
MRI total ( $n = 429$ )	79.2	89.9
MRI total for 1.5T ( $n = 283$ )	85.7 <sup>a</sup>	87.2
MRI total for 3T ( $n = 146$ )	56.3 <sup>b</sup>	94.6 <sup>c</sup>

<sup>a</sup> Statistically significant compared with MRI Total ( $P < .05$ ).

<sup>b</sup> Statistically significant compared with MRI Total and 1.5T ( $P < .05$ ).

<sup>c</sup> Statistically significant compared with 1.5T ( $P < .05$ ).

the sequences of interest were combined (Table 3). The 3T scanner had significantly lower sensitivity compared with both 1.5T and total MR imaging and significantly higher specificity than 1.5T (Table 3). MR imaging signs of DVST are shown in Fig 4. SWI was not included in the analysis because it was not diagnostic due to susceptibility artifacts from the contents of the dural venous sinuses and the adjacent skull, and no interpretation could be made. There were no cases positive for DVST based on SWI. All cases with high signal on DWI ( $n = 14$ ) were associated with abnormal signal changes on T1 and/or FLAIR. Of the 31 cases true-positive for DVST on GRE, 12 were false-negative on T1; 2 cases, on T2; 20 cases, on DWI; 5 cases, on FLAIR; 8 cases, on CE-SE-T1WI; and no cases, on CE-3D-T1WI. GRE had true-positive findings in 6 cases that had false-negative findings on all the other sequences other than CE-3D-T1WI.

The interrater reliability with  $\kappa$  statistics demonstrated fair agreement for the non-contrast-enhanced sequences and moderate agreement for the contrast-enhanced sequences (Table 4).

## DISCUSSION

DVST is a relatively rare condition, and previous studies of DVST have had small sample sizes. This is a large study of 429 cases investigating the diagnostic accuracy of routine MR imaging for DVST. Each case was reviewed by 3 neuroradiologists. Due to the nonspecific nature of the clinical presentations, which may be asymptomatic, the radiologist reviewing standard brain MR imaging may be the first to consider the diagnosis of DVST. This study demonstrates that abnormal dural venous sinus signal on 7 common routine MR sequences can suggest the diagnosis of DVST with high specificity.

While data from Coutinho et al<sup>10</sup> and the International Study on Cerebral Vein and Dural Sinus Thrombosis demonstrated a female/male ratio of 3:1, with a median age of 34 years compared with 42 years, respectively, in our study, the female/male ratio for cases positive for DVST was less than expected (1.7:1) and patients diagnosed with DVST were older than expected ( $51.4 \pm 16.8$  years). Furthermore, whereas pregnancy, postpartum status, and oral contraceptives are among the most common underlying conditions in cases of DVST,<sup>3,11</sup> this was not true in our study. Neoplasia was a much more common etiologic factor compared with previous studies such as that of Lafitte et al,<sup>11</sup> in which neoplasia was identified in only 2 of 20 patients with positive findings. These results are most likely due to the selective group of patients presenting to our institution and the selection bias of our study. The patient population was from a large tertiary trauma, stroke, and cancer center, which helps explain the different demographics compared with previous studies.

Although DVST is not a common condition, there were 72 cases positive for it among 429 studied venograms (16.8%) at our tertiary care academic health center. These did not include any CTV studies that were not associated with MR imaging evaluation or any other patients who went undiagnosed. The prevalence of cerebral venous thrombosis has been estimated to be 5/1,000,000 in the general population, and a postmortem series of 182 subjects found an incidence of 9.3%.<sup>12,13</sup> In this study, cases were selected

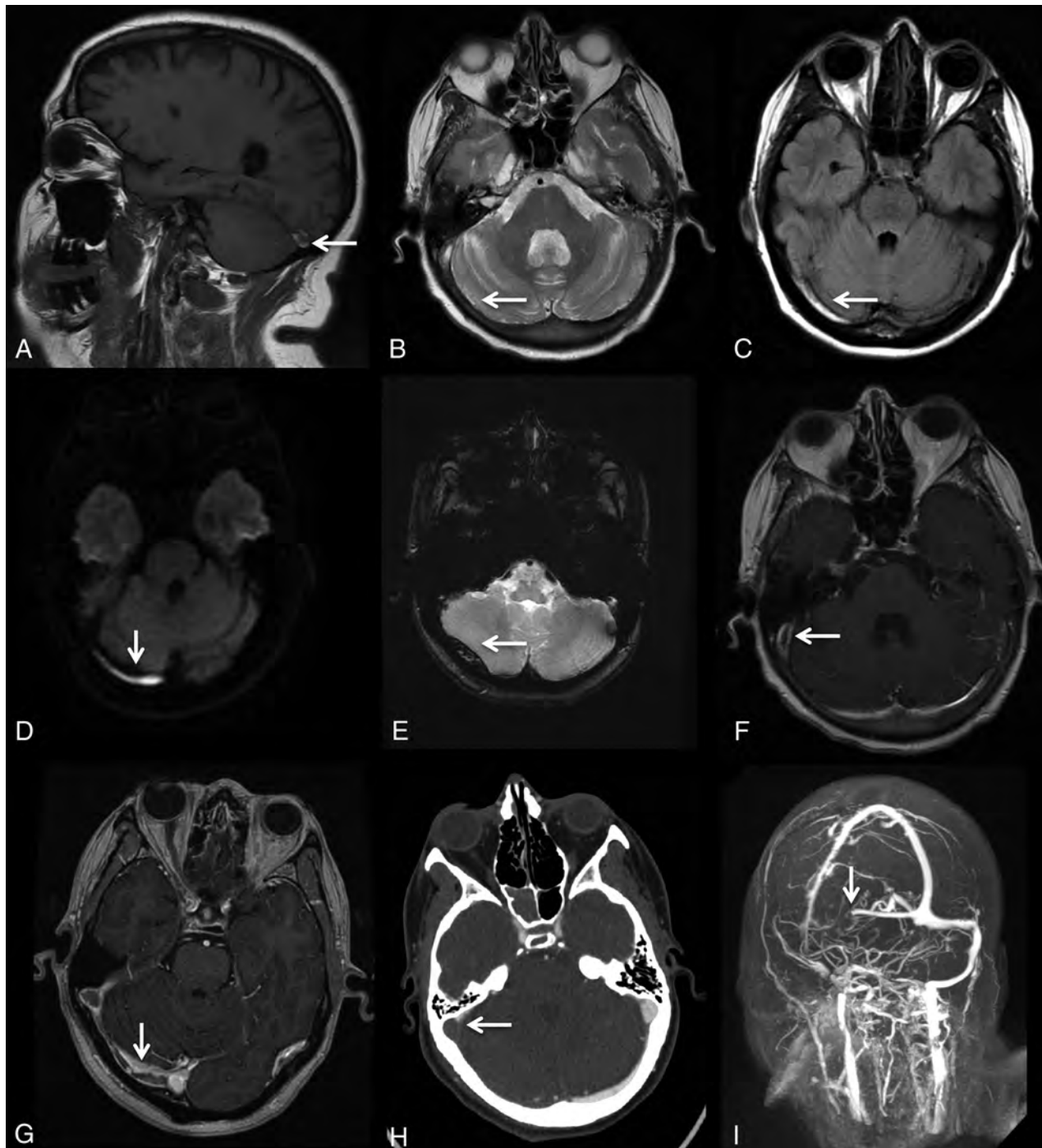


**FIG 4.** MR imaging signs of dural venous sinus thrombosis from multiple cases. *A*, Hyperintense signal in the right transverse sinus on sagittal T1. *B*, Loss of flow void in the right transverse sinus on axial T2. *C*, Hyperintense signal in the right transverse sinus on FLAIR. *D*, Hyperintense signal in the right transverse sinus on DWI. *E*, Blooming artifacts in the right transverse sinus on GRE. *F*, Filling defect in the right transverse/sigmoid sinus on CE-3D-T1WI. *G*, Filling defect in the right transverse/sigmoid sinus on CE-SE-T1WI. *H*, Filling defect in the right transverse/sigmoid sinus on CTV. *I*, Filling defect in the right transverse/sigmoid sinus on MIP-CEMRV.

from patients who had CTV or CEMRV, which puts them at a substantially higher pretest probability of having DVST than the general population, and this does not represent the prevalence of the disease. Therefore, positive predictive value, negative predictive value, and accuracy were not reported. While this omission limits the external validity of the study, the performance characteristics are relevant to those in similar populations in tertiary care centers.

Tang et al<sup>14</sup> found that DVST was indicated on the imaging requisitions in only 33% of MR imaging studies positive for thrombosis,<sup>6</sup> compared with our study in which 69.4% of cases positive for DVST had “suspected DVST” on their imaging requisitions. Some other indications for venography such as headache, intracranial hypertension, and meningioma invading the dural venous sinuses may be the cause or the effect of DVST. Thus, 30.6% of cases positive for DVST were found in patients

**Table 4: Interrater reliability for each MRI sequence individually and combined using the  $\kappa$  coefficient**

	$\kappa$	Agreement <sup>a</sup>
Sagittal T1 (n = 418)	0.28	Fair
Axial T2 (n = 71)	0.34	Fair
Axial GRE (n = 420)	0.40	Fair
Axial FLAIR (n = 417)	0.34	Fair
Axial DWI (n = 421)	0.33	Fair
Axial CE-SE-T1WI (n = 241)	0.42	Moderate
Axial CE-3D-T1WI (n = 199)	0.41	Moderate
MRI total (n = 429)	0.50	Moderate

<sup>a</sup> Agreement was considered slight if  $\kappa$  values were 0–0.20; fair if, 0.21–0.40; moderate if, 0.41–0.60; substantial if, 0.61–0.80; and almost perfect if, 0.81–1.

without clinical suspicion of it, highlighting the importance of routine MR imaging signs of DVST in unexpected situations.

The overall sensitivity of MR imaging (79.2%) was slightly lower than that in previously reported studies. Lafitte et al<sup>11</sup> reported that in 20 patients with clinically suspected DVST confirmed by digital subtraction angiography, MR imaging that included spin-echo T1- and T2-weighted imaging was 90% sensitive in diagnosing DVST, and >80% sensitivity was found in most studies. This finding can be explained, in part, by the high sample volume in our study, which is likely closer to the real performance of the sequence of interest in the diagnosis of DVST in samples from a tertiary care center.

The performance characteristics in this study are in keeping with the findings of Saindane et al,<sup>7</sup> who demonstrated that filling defects on CE-3D-T1WI had a sensitivity of 67% and a specificity of 100% for DVST compared with MRV. Sari et al<sup>8</sup> demonstrated that immediate CE-3D-T1WI had a sensitivity of 92.5%, specificity of 100%, and accuracy of 98.3% compared with their reference standard. They proposed that delayed acquisition of CE-3D-T1WI after contrast injection can lead to contrast enhancement of the thrombus, which lowers the sensitivity of the sequence.<sup>8</sup>

The reported sensitivity for hyperintense signal on DWI for intraluminal thrombus has been highly variable in the literature, ranging from 4% to 40%.<sup>2</sup> Our results corroborate the study by Favrole et al,<sup>15</sup> which noted that a high DWI signal is always found with concomitant signal changes on T1 and/or FLAIR sequences; thus, it may not provide much diagnostic value.

GRE identified cases that were false-negative for DVST on all of the other sequences other than CE-3D-T1WI, providing additional diagnostic value as part of a standard brain MR imaging. These results are consistent with the findings of Ihn et al,<sup>16</sup> who demonstrated that GRE was the only sequence that was positive for DVST in all 11 DVST cases in a study that included T1, T2, FLAIR, and CE-SE-T1WI. Altinkaya et al<sup>17</sup> have shown that GRE has high diagnostic performance for acute and subacute superior sagittal sinus and deep and cortical vein thrombosis, but not for transverse and sigmoid sinus thrombosis due to susceptibility artifacts from the skull base.

Multiple reasons have been proposed for the low sensitivity of MR imaging sequences for DVST. Hinman and Provenzale<sup>18</sup> reported that though in most cases, the diagnosis of DVST can be made on routine MR imaging on the basis of the loss of a normal flow void with abnormal signal intensity within the dural venous sinus, during the first 5 days after formation, an acute thrombus

can mimic a normal flow void on spin-echo T2-weighted imaging and may be isointense with gray matter on spin-echo T1-weighted imaging.<sup>16,19</sup> In this case, the hypointense signal on T2 can be mistaken for patency. In the subacute stage, the thrombus becomes progressively hyperintense on both spin-echo T1- and T2-weighted imaging.<sup>11</sup> Enhancement of a chronic thrombus can resemble normal flow.<sup>7,20,21</sup> In the chronic stage, contrast-enhanced T1-weighted images of DVST can enhance to resemble a patent sinus due to capillary channels or partial recanalization.<sup>6,7</sup> Routine MR images need to be evaluated with caution to avoid false-negative interpretations.

In our study, the specificity for DVST was high; this finding indicates a low number of false-positive interpretations. False-positives can occur if there is slow blood flow due to sinus hypoplasia, which can create a high signal that resembles a thrombus. This pitfall can be avoided by using multiple sequences and planes of section.<sup>22</sup> Filling defects caused by arachnoid granulations or other anatomic material in the sinuses may also resemble thrombus, but signal isointense to CSF and morphology can help differentiate them.<sup>6,23</sup>

In terms of interrater reliability, Ferro et al<sup>24</sup> showed that with a sample size of 40 cases, interrater reliability for DVST varies from moderate to excellent,  $\kappa$  range of 0.59–1, when comparing pairs of raters. In this study, for the individual MR images, there was considerable variability because  $\kappa$  statistics ranged from 0.28 to 0.42. The interrater reliability for overall thrombosis diagnosis was only moderate at 0.50, which reflects the difficulty in interpreting the signs suggestive of DVST. Individual radiologists each have their own propensity to make the diagnosis, which may explain why the performance characteristics of the 3 readers had significant differences.

### Limitations

Although readers were blinded to clinical history and whether venography was completed, readers were focused on searching for DVST, and the sample was chosen on the basis of patients who had undergone CEMRV or CTV in a tertiary care center. These features substantially increased the pretest probability of DVST compared with a random sample and promoted selection bias. This high prevalence would falsely increase the accuracy of MR imaging for DVST among the 3 readers. The accuracy of the readers was only reported to demonstrate individual differences, but it is not generalizable to daily practice for the reasons described above. Readers had access to some or all of the MR images (T1, T2 and/or FLAIR, GRE, DWI, SWI, CE-SE-T1WI, and/or CE-3D-T1WI), which would confound individual sequence test parameters. The neuroradiologists may have used secondary clues to the diagnosis other than those of interest such as hemorrhage, edema, or infarction to help them. The study included 18 patients with idiopathic intracranial hypertension, which is known to have abnormal transverse sinus morphology and flow; however, none of these patients were positive for DVST. In addition, the age of the thrombosis was not taken into account. The signal characteristics are dependent on the age of the thrombosis, and Idbaih et al<sup>25</sup> have shown that the sensitivity of routine MR images changes as the thrombus evolves.

## CONCLUSIONS

Abnormal dural venous sinus signal on routine MR images can suggest DVST with high specificity and moderate interrater reliability in high-risk patients. In patients with primary or metastatic brain cancer, these signs need to be taken very seriously, and this is particularly important in patients in whom there is no clinical suspicion of DVST.

Disclosures: Richard I. Aviv—UNRELATED: Grants/Grants Pending: Canadian Institutes of Health Research\*; Other: Biogen Foundation fellowship.\* Pejman Jabehdar Maralani—UNRELATED: Grants/Grants Pending: Radiological Society of North America,\* Brain Tumor Foundation of Canada.\* Comments: Both grants are related to a brain tumor project and not related to the submitted work. \*Money paid to the institution.

## REFERENCES

1. Stam J. Thrombosis of the cerebral veins and sinuses. *N Engl J Med* 2005; 352:1791–98 CrossRef Medline
2. Linn J, Brückmann H. Cerebral venous and dural sinus thrombosis: state-of-the-art imaging. *Clin Neuroradiol* 2010;20:25–37 CrossRef Medline
3. Ferro JM, Canhão P, Stam J, et al; ISCVT Investigators. Prognosis of cerebral vein and dural sinus thrombosis: results of the International Study on Cerebral Vein and Dural Sinus Thrombosis (ISCVT). *Stroke* 2004;35:664–70 Medline
4. Ferro JM, Canhão P, Stam J, et al; ISCVT Investigators. Delay in the diagnosis of cerebral vein and dural sinus thrombosis: influence on outcome. *Stroke* 2009;40:3133–38 CrossRef Medline
5. Khandelwal NI, Agarwal A, Kochhar R, et al. Comparison of CT venography with MR venography in cerebral sinovenous thrombosis. *AJR Am J Roentgenol* 2006;187:637–43 Medline
6. Provenzale JM, Kranz PG. Dural sinus thrombosis: sources of error in image interpretation. *AJR Am J Roentgenol* 2011;196:23–31 CrossRef Medline
7. Saindane AM, Mitchell BC, Kang J, et al. Performance of spin-echo and gradient-echo T1-weighted sequences for evaluation of dural venous sinus thrombosis and stenosis. *AJR Am J Roentgenol* 2013; 201:162–69 CrossRef Medline
8. Sari S, Verim S, Hamcan S, et al. MRI diagnosis of dural sinus-cortical venous thrombosis: immediate post-contrast 3D GRE T1-weighted imaging versus unenhanced MR venography and conventional MR sequences. *Clin Neurol Neurosurg* 2015;134: 44–54 CrossRef Medline
9. Altman DG. *Practical Statistics for Medical Research*. London: Chapman and Hall; 1991
10. Coutinho JM, Ferro JM, Canhão P, et al. Cerebral venous and sinus thrombosis in women. *Stroke* 2009;40:2356–61 CrossRef Medline
11. Lafitte F, Boukobza M, Guichard JP, et al. MRI and MRA for diagnosis and follow-up of cerebral venous thrombosis (CVT). *Clin Radiol* 1997;52:672–79 CrossRef Medline
12. Towbin A. The syndrome of latent cerebral venous thrombosis: its frequency and relation to age and congestive heart failure. *Stroke* 1973;4:419–30 CrossRef Medline
13. Saposnik G, Barinagarrementeria F, Brown RD Jr, et al; American Heart Association Stroke Council and the Council on Epidemiology and Prevention. Diagnosis and management of cerebral venous thrombosis: a statement for healthcare professionals from the American Heart Association/American Stroke Association. *Stroke* 2011;42:1158–92 CrossRef Medline
14. Tang PH, Chai J, Chan YH, et al. Superior sagittal sinus thrombosis: subtle signs on neuroimaging. *Ann Acad Med Singapore* 2008;37: 397–401 Medline
15. Favrole P, Guichard JP, Crassard I, et al. Diffusion-weighted imaging of intravascular clots in cerebral venous thrombosis. *Stroke* 2004; 35:99–103 Medline
16. Ihn YK, Jung WS, Hwang SS. The value of T2\*-weighted gradient-echo MRI for the diagnosis of cerebral venous sinus thrombosis. *Clin Imaging* 2013;37:446–450 CrossRef Medline
17. Altinkaya N, Demir S, Alkan O, et al. Diagnostic value of T2\*-weighted gradient-echo MRI for segmental evaluation in cerebral venous sinus thrombosis. *Clin Imaging* 2015;39:15–19 CrossRef Medline
18. Hinman JM, Provenzale JM. Hypointense thrombus on T2-weighted MR imaging: a potential pitfall in the diagnosis of dural sinus thrombosis. *Eur J Radiol* 2002;41:147–52 CrossRef Medline
19. Dormont D, Anxionnat R, Evrard, et al. MRI in cerebral venous thrombosis. *J Neuroradiol* 1994;21:81–99 Medline
20. Dormont D, Sag K, Biondi A, et al. Gadolinium-enhanced MR of chronic dural sinus thrombosis. *AJNR Am J Neuroradiol* 1995;16: 1347–52 Medline
21. Leach JL, Wolujewicz M, Strub WM. Partially recanalized chronic dural sinus thrombosis: findings on MR imaging, time-of-flight MR venography, and contrast-enhanced MR venography. *AJNR Am J Neuroradiol* 2007;28:782–89 Medline
22. Mas JL, Meder JF, Meary E, et al. Magnetic resonance imaging in lateral sinus hypoplasia and thrombosis. *Stroke* 1990;21:1350–56 Medline
23. Leach JL, Jones BV, Tomsick TA, et al. Normal appearance of arachnoid granulations on contrast-enhanced CT and MR of the brain: differentiation from dural sinus disease. *AJNR Am J Neuroradiol* 1996;17:1523–32 Medline
24. Ferro JM, Morgado C, Sousa R, et al. Interobserver agreement in the magnetic resonance location of cerebral vein and dural sinus thrombosis. *Eur J Neurol* 2007;14:353–56 CrossRef Medline
25. Idbaih A, Boukobza M, Crassard I, et al. MRI of clot in cerebral venous thrombosis: high diagnostic value of susceptibility-weighted images. *Stroke* 2006;37:991–95 CrossRef Medline

# Three-Territory DWI Acute Infarcts: Diagnostic Value in Cancer-Associated Hypercoagulation Stroke (Trousseau Syndrome)

P.F. Finelli and A. Nouh

## ABSTRACT

**BACKGROUND AND PURPOSE:** DWI infarcts involving the bilateral anterior and posterior circulation suggest an embolic etiology. In the absence of an identifiable embolic source, we analyzed DWI lesions involving these 3 cerebral territories to determine the diagnostic value for ischemic infarction caused by cancer-associated hypercoagulation.

**MATERIALS AND METHODS:** A retrospective analysis of all brain MR imaging studies at our institution from July 2014 to June 2015 was conducted, yielding 4075 studies. Of those, 17% ( $n = 709$ ) contained the terms “restricted-diffusion” plus either “numerous,” “innumerable,” “multiple,” or “bilateral.” Of these 709 reports, 6% ( $n = 41$ ) of DWI lesions involving 3 or more vascular territories of the bilateral anterior and posterior circulation were analyzed.

**RESULTS:** Of the 41 patients, 19 separate etiologies were identified, the most frequent being malignancy-related infarctions (22% [ $n = 9$ ]) and hypoxic-ischemic injury (12% [ $n = 5$ ]). Only 2 patients had an indeterminate etiology. The most frequent etiology of infarctions not suspected clinically or radiographically was malignancy ( $P < .001$ ). Infarctions of malignancy had a characteristic appearance, being nonenhancing, nonring-appearing clusters or single areas of restricted diffusion of 0.5–2 cm with a peripheral location or larger vascular territories, uncommonly in a watershed distribution, and with absence of diffuse cortical ribbon or deep gray nuclei involvement.

**CONCLUSIONS:** Approximately 1 in 5 ischemic infarcts in patients with DWI lesions involving 3 vessel territories are malignancy related. In the absence of an identifiable embolic source, ischemic infarction with cancer-associated hypercoagulation accounts for 75% of cases. Cancer-associated hypercoagulation infarction should be considered, particularly when no other cause is apparent.

**ABBREVIATION:** TS = Trousseau syndrome

Up to 15% of patients with malignancy may experience a thromboembolic cerebrovascular event during their clinical course.<sup>1</sup> In addition, malignancy is frequently overlooked as a cause of stroke and is commonly undiagnosed until a second event occurs.<sup>2</sup> Though the paraneoplastic hypercoagulable state is complex and not fully understood, it is an established mechanism of thrombosis in malignancy. The importance of diagnosing cancer-associated hypercoagulation is appreciated because it may be the heralding manifestation of occult malignancy. Treatment with heparin has been demonstrated effective in preventing thrombotic events, including stroke.<sup>3,4</sup>

Trousseau syndrome (TS) is a hypercoagulable state, associ-

ated with cancer, that includes various disorders probably involving multiple overlapping mechanisms. It has been suggested the term “Trousseau syndrome” be restricted to unexplained thrombotic events that either precede the diagnosis of an occult visceral malignancy or appear concomitantly with the tumor.<sup>5</sup> Cerebral infarction, mostly caused by in situ thrombosis in medium and small vessels, is thought to be related to the prothrombic state of TS. Verrucous endocarditis associated with cerebral emboli, infection, or therapy-related strokes are alternative causes of ischemic infarction.<sup>2,6</sup> Given the familiar usage of TS by some authors to refer to cancer-associated hypercoagulation,<sup>5</sup> we use TS in that context in this discussion.

DWI primarily defines ischemic infarcts in malignancy as small and involving multiple vessel territories,<sup>6–9</sup> with the number of territories involved correlating with the likelihood of this syndrome.<sup>4,10–12</sup> However, studies specifically evaluating MR imaging in cerebral infarction with TS and its diagnostic value in establishing causality are lacking. Distinct from prior reports where patient selection was based on the presence of stroke with malig-

Received March 23, 2016; accepted after revision April 28.

From the Department of Neurology, Hartford Hospital and University of Connecticut School of Medicine, Hartford, Connecticut.

Please address correspondence to Pasquale F. Finelli, MD, Department of Neurology, Hartford Hospital and University of Connecticut School of Medicine, 80 Seymour St, Hartford, CT 06102-5037; e-mail: pasquale.finelli@hhchealth.org

<http://dx.doi.org/10.3174/ajnr.A4846>



### Etiologies of 3 territory diffusion-weighted lesions

No.	Clinical/MR Imaging, DWI, Enhancement Features
Suspected etiology ( <i>n</i> = 29)	
Trauma	1 History of trauma, imaging-associated sequelae of trauma, subarachnoid hemorrhage, shear pattern
Demyelinating	1 Age, history of multiple sclerosis, periventricular/corpus callosum predilection
Hypoxic-ischemic	5 Hypotension, deep nuclei and cortical ribbon involvement
Metastasis	3 History of malignancy and/or ring or enhancing lesion
Seizure	1 Seizures, deep nuclei and/or cortical ribbon enhancement
HIV-related ( <i>n</i> = 2)	
Toxoplasmosis	1 HIV, periventricular, ring, enhancing, target sign, rarely shows restricted diffusion
Fungal abscess	1 HIV, ring, enhancing, numerous restricted-diffusion lesions
Cerebral emboli ( <i>n</i> = 10)	
Endocarditis	4 Fever, leukocytosis, murmur, ring, enhancing
Air	1 Followed esophagogastroduodenoscopy
Fat	1 Followed long bone fracture
Atrial fibrillation	2 No source other than atrial fibrillation found
Aortic atheroma	1 Significant arch atheroma noted
Aortic dissection	1 Patient had concomitant aortic dissection
Postoperative ( <i>n</i> = 6)	
Aneurysm coiling	1 Symptoms developed postoperatively
Cardiac surgery	4 Symptoms developed postoperatively
Aortic aneurysm repair	1 Symptoms developed postoperatively
Not suspected ( <i>n</i> = 10)	
Malignancy-related	
	9 Lung ( <i>n</i> = 4), colon ( <i>n</i> = 2), renal ( <i>n</i> = 1), pancreas ( <i>n</i> = 1), bladder ( <i>n</i> = 1)
Intravascular lymphoma	1 Proven by brain biopsy
Indeterminate ( <i>n</i> = 2)	
Incomplete history	1 Lost to follow-up
Multiple etiologies	1 Possible fat emboli vs Trousseau syndrome

nancy or vice versa, our patient selection was based on the presence of numerous, innumerable, multiple, or bilateral lesions on MR imaging. At our institution, we have experienced many cases of 3-cerebral territory infarctions associated with malignancy. However, the association of 3-territory DWI infarcts and malignancy has not been studied.

We speculate that selecting patients by using MR criteria allows for a more accurate assessment of diagnosing TS-related infarction compared with selection criteria using history of stroke and cancer because the potential for error exists when cancer history is overlooked or undiagnosed. In this study, we assessed the etiology of DWI-defined 3-territory infarcts, with attention to their diagnostic value in TS-related stroke.

### MATERIALS AND METHODS

We sought to analyze the MR imaging characteristics of patients with DWI lesions involving 3 vascular territories (namely, the bilateral anterior and the posterior circulation) and correlate them with individual etiologies. A retrospective chart review at our institution was conducted after approval from the institutional review board for conducting research. All data on brain MR imaging conducted from July 1, 2014 to June 30, 2015 were included, encompassing 4075 studies with radiology reports. A search tool for the terms “restricted-diffusion” plus either “numerous,” “innumerable,” “multiple,” or “bilateral” yielded 709 studies. Of these studies, only reports with multiple DWI lesions that involved 3 vascular territories that included bilateral anterior and posterior circulation were analyzed. After exclusion, only 41 studies met criteria for analysis. Studies were reviewed and eval-

uated for radiographic appearance of DWI lesions. Lesions with MR characteristics of ischemic infarction (hyperintense on DWI and restricting on ADC) were deemed as infarction. The underlying etiology was determined from a chart review process. Lesion etiology was dichotomized into a “suspected” cohort (clinically suspected and documented or suggested by MR imaging report) and a “not suspected” cohort (clinically not suspected or documented and/or not suggested by radiology report) during hospitalization. The “not suspected” cohort represents the patients in whom etiology was not suspected by the treating physician or suggested by the radiologist because of the clinical history given and reported radiology reading.

### RESULTS

Of 41 patients reviewed, a suspected etiology for 3-territory DWI lesions was identified in approximately 71% (*n* = 29), not suspected in approximately 24% (*n* = 10), and indeterminate in approximately 5% (*n* = 2). A total of 19 separate etiologies were identified, in-

cluding only 2 patients with indeterminate etiology. An embolic source, namely cardiac or large vessel, was the most common etiology in the “suspected” cohort. Of these 16 patients, only 1 had concomitant systemic malignancy. In the “not suspected” cohort of 10 patients, 9 had a concomitant systemic malignancy and 1 had intravascular lymphoma. In the absence of an identifiable embolic source, the presence of concomitant systemic malignancy was significantly associated with 3-territory DWI infarctions (*P* < .001). The Table lists etiologies of all patients with 3-territory DWI lesions with supporting clinical and radiographic features.

Moreover, patients with underlying malignancy represented approximately 29% (*n* = 12) of all patients. In 9 patients, malignancy as cause of stroke etiology was diagnosed in a retrospective fashion after excluding all other potential causes and the concomitant presence of active malignancy. The mean age was  $61 \pm 27$  years and 66% were men. The malignancies in our cohort included lung cancer (*n* = 4), colon cancer (*n* = 2), and 1 case each for renal, bladder, and pancreatic cancer. In only 2 patients, cause was indeterminate because of incomplete history or multiple possible etiologies. Although 1 patient with 3-territory infarctions during hospitalization was diagnosed with biopsy-proved intravascular lymphoma, it was not suspected by the treating physician or suggested by radiology report as the etiology.

In the “suspected” cohort, 3 patients had known metastatic cancer with 3-territory DWI involvement. However, lesions were ring-enhancing and suggestive of metastatic tumor spread to

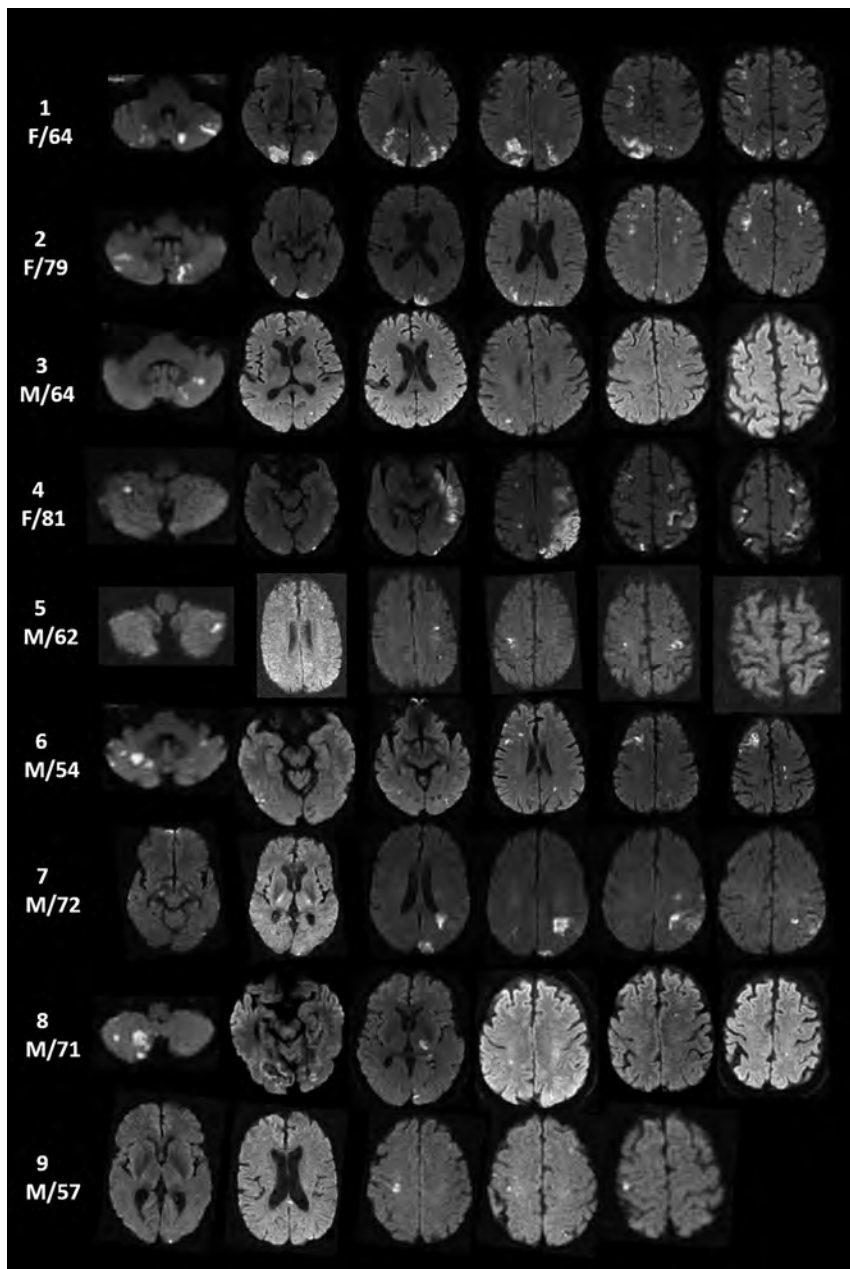


**FIGURE.** DWI infarcts involving bilateral anterior and posterior circulation (3 territory) with TS in 9 study group patients.

the brain. Other causes of 3-territory DWI lesions not defined as ischemic infarctions included infection, demyelination, seizure, and trauma. In the suspected cohort, an established embolic source was found in 10 patients and occurred postoperatively in 6 patients. Though the 3-territory pattern is the most compelling MR imaging feature of malignancy-related ischemic infarctions, characteristic radiographic DWI findings for malignancy-related infarction are often noted. These include nonenhancing, nonring clusters or single areas of restricted diffusion of 0.5–2 cm with a peripheral preference or large vascular territories, uncommonly in a watershed distribution, with absence of diffuse cortical ribbon or deep gray involvement (Figure).

if echocardiogram shows no valvular pathology or intracardiac clot, TS should be a leading consideration. A transesophageal echocardiogram is necessary to exclude a cardioembolic source.

In our study, we sought to evaluate the role of MR imaging in aiding with the diagnostic approach to multiple territory infarctions. Therefore, our approach was notably based on MR imaging as the identifying feature. We acknowledge that because of the retrospective nature of the study, linking the etiology of the 3-territory infarctions to malignancy is speculative based on excluding other causes as documented by the work-up completed by the treating physician. Moreover, it is possible that patients with true malignancy-related infarctions or TS involving only 1 or 2 territories were not accounted for in this study. Longitudinal data,

## DISCUSSION

DWI infarction in multiple territories has been reported,<sup>4,10-12</sup> including 3-territory lesions,<sup>4,10</sup> yet a clear expression of the diagnostic significance of this MR imaging pattern with TS-related infarction has not been articulated. In our study, among the 12 patients without a suspected etiology, malignancy-related ischemic events were the source in 9 (75%). Though not unique, the diffusion-weighted MR imaging features in our patients with malignancy-related infarction were highly suggestive.

In a prospective study evaluating embolic signals detected by transcranial Doppler in 74 patients with malignancy-related infarction, embolic signals were more commonly seen in patients lacking conventional stroke risk factors ( $P = .034$ ) and were correlated strongly with D-dimer levels and the number of embolic signals detected ( $P = < .001$ ).<sup>13</sup> The excess of embolic signal in patients with malignancy may explain the 3-territory DWI pattern observed or support this hypothesis, though this cannot exclude the possibility of intrinsic medium- and small-vessel thrombosis.

DWI lesions in our patient cohort also manifested diffuse changes that involve deep gray nuclei and/or cortical ribbon as seen with hypoxia-ischemia and seizure, whereas ring lesions, with or without enhancement, were associated with infection, metastasis, and endocarditis. Only endocarditis was associated with a peripheral predilection. TS-related infarction in the context of 3-territory DWI infarcts without an identifiable cause was not considered by the clinician or radiologist in our patients. Furthermore, in the presence of both malignancy and atrial fibrillation,

such as prolonged cardiac monitoring to evaluate the possibility of atrial fibrillation in patients where etiology was not diagnosed during hospitalization, were not available. However, a substantial work-up was completed during hospitalization as 19 separate etiologies were identified.

Elevated D-dimer level, a direct measure of activated coagulation, is associated with malignancy and has been used as a measure of hypercoagulability in studies investigating stroke and malignancy.<sup>6,7</sup> However, this biomarker is not specific to the hypercoagulable status of malignancy and can be elevated in several other conditions, such as infection, venous thromboembolism, and stroke.<sup>14</sup> D-dimer levels were not reported in our study because of the few patients who had these levels tested during hospitalization. However, the aim of this study was to highlight the diagnostic value of the 3-territory DWI pattern as an additional diagnostic tool in the stroke work-up. In addition, because of the few patients in this study and the lack of patients with active malignancy and stroke of undetermined etiology involving 1 or 2 territories, the positive or negative predictive value of 3-territory DWI infarcts could not be calculated.

## CONCLUSIONS

DWI infarcts involving 3 specific vascular territories, in the absence of an identifiable embolic source or other disease associated with such lesions, are highly suggestive of cancer-associated hypercoagulation stroke. Because TS-related stroke may be the heralding manifestation of an occult malignancy, work-up should include D-dimer and fibrinogen levels; tumor biomarkers; screening for deep vein thrombosis; CT of chest, abdomen, and pelvis; and PET scan when other tests are negative. Given the efficacy of heparin in preventing thrombotic events in cancer-associated hypercoagulation, timely diagnosis is paramount. As described here, the 3-territory DWI infarct pattern can provide an important diagnostic clue to an otherwise underrecognized cause of stroke. Future prospective studies evaluating patients with malignancy-related infarction with TS are needed to quantify the

proportion of patients with 3-territory infarctions versus other MR patterns.

## REFERENCES

1. Graus F, Rogers LR, Posner JB. **Cerebrovascular complications in patients with cancer.** *Medicine* 1985;64:16–35 CrossRef Medline
2. Taccone FS, Jeanette SM, Bleic SA. **First-ever stroke as initial presentation of systemic cancer.** *J Stroke Cerebrovasc Dis* 2008;17:169–74 CrossRef Medline
3. Murinello A, Guedes P, Rocha G, et al. **Trousseau's syndrome due to asymptomatic pancreatic adenocarcinoma.** *GE Port J Gastroenterol* 2013;20:172–76 CrossRef
4. Kwon HM, Kang BS, Yoon BW. **Stroke as the first manifestation of concealed cancer.** *J Neurol Sci* 2007;258:80–83 CrossRef Medline
5. Varki A. **Trousseau's syndrome: multiple definitions and multiple mechanisms.** *Blood* 2007;110:1723–29 CrossRef Medline
6. Grisold W, Oberndorfer S, Struhal W. **Stroke and cancer: a review.** *Acta Neurol Scand* 2009;119:1–16 CrossRef Medline
7. Kim SG, Hong JM, Kim HY, et al. **Ischemic stroke in cancer patients with and without conventional mechanisms: a multicenter study in Korea.** *Stroke* 2010;41:798–801 CrossRef Medline
8. Schwarzbach CJ, Schaefer A, Ebert A, et al. **Stroke and cancer: the importance of cancer-associated hypercoagulation as a possible stroke etiology.** *Stroke* 2012;43:3029–34 CrossRef Medline
9. Chen Y, Zeng J, Xie X, et al. **Clinical features of systemic cancer patients with acute cerebral infarction and its underlying pathogenesis.** *Int J Clin Exp Med* 2015;8:4455–63 Medline
10. Kim SJ, Park JH, Lee MJ, et al. **Clues to occult cancer in patients with ischemic stroke.** *PLoS One* 2012;7:e44959 CrossRef Medline
11. Bang OY, Seok JM, Kim SG, et al. **Ischemic stroke and cancer: stroke severely impacts cancer patients, while cancer increases the number of strokes.** *J Clin Neurol* 2011;7:53–59 CrossRef Medline
12. Hong CT, Tsai LK, Jeng JS. **Patterns of acute cerebral infarcts in patients with active malignancy using diffusion-weighted imaging.** *Cerebrovasc Dis* 2009;28:411–16 CrossRef Medline
13. Seok JM, Kim SG, Kim JW, et al. **Coagulopathy and embolic signal in cancer patients with ischemic stroke.** *Ann Neurol* 2010;68:213–19 CrossRef Medline
14. Lippi G, Bonfanti L, Saccenti C, et al. **Causes of elevated D-dimer in patients admitted to a large urban emergency department.** *Eur J Intern Med* 2014;25:45–48 CrossRef Medline

# Comparison of CTA- and DSA-Based Collateral Flow Assessment in Patients with Anterior Circulation Stroke

I.G.H. Jansen, O.A. Berkhemer, A.J. Yoo, J.A. Vos, G.J. Lycklama à Nijeholt, M.E.S. Sprengers, W.H. van Zwam, W.J. Schonewille, J. Boiten, M.A.A. van Walderveen, R.J. van Oostenbrugge, A. van der Lugt, H.A. Marquering, and C.B.L.M. Majoie; on behalf of the MR CLEAN investigators (www.mrclean-trial.org)



## ABSTRACT

**BACKGROUND AND PURPOSE:** Collateral flow is associated with clinical outcome after acute ischemic stroke and may serve as a parameter for patient selection for intra-arterial therapy. In clinical trials, DSA and CTA are 2 imaging modalities commonly used to assess collateral flow. We aimed to determine the agreement between collateral flow assessment on CTA and DSA and their respective associations with clinical outcome.

**MATERIALS AND METHODS:** Patients randomized in MR CLEAN with middle cerebral artery occlusion and both baseline CTA images and complete DSA runs were included. Collateral flow on CTA and DSA was graded 0 (absent) to 3 (good). Quadratic weighted  $\kappa$  statistics determined agreement between both methods. The association of both modalities with mRS at 90 days was assessed. Also, association between the dichotomized collateral score and mRS 0–2 (functional independence) was ascertained.

**RESULTS:** Of 45 patients with evaluable imaging data, collateral flow was graded on CTA as 0, 1, 2, 3 for 3, 10, 20, and 12 patients, respectively, and on DSA for 12, 17, 10, and 6 patients, respectively. The  $\kappa$ -value was 0.24 (95% CI, 0.16–0.32). The overall proportion of agreement was 24% (95% CI, 0.12–0.38). The adjusted odds ratio for favorable outcome on mRS was 2.27 and 1.29 for CTA and DSA, respectively. The relationship between the dichotomized collateral score and mRS 0–2 was significant for CTA ( $P = .01$ ), but not for DSA ( $P = .77$ ).

**CONCLUSIONS:** Commonly applied collateral flow assessment on CTA and DSA showed large differences, indicating that these techniques are not interchangeable. CTA was significantly associated with mRS at 90 days, whereas DSA was not.

**ABBREVIATIONS:** CS = collateral score; IAT = intra-arterial therapy; MR CLEAN = Multicenter Randomized Clinical Trial of Endovascular Treatment of Acute Ischemic Stroke in the Netherlands

Recently, the effectiveness of intra-arterial therapy (IAT) in patients with acute ischemic stroke of the anterior circulation treated within 6 hours after symptom onset was established by

multiple randomized controlled trials.<sup>1–5</sup> In the Multicenter Randomized Clinical Trial of Endovascular Treatment of Acute Ischemic Stroke in the Netherlands (MR CLEAN), the largest of these trials, a substantial number of patients did not reach functional independence, despite high recanalization rates after IAT. Other trials showed higher recanalization rates, with better overall patient outcome. Contrary to MR CLEAN, these latter trials used neuroimaging for patient selection. In the Endovascular Treatment for Small Core and Anterior Circulation Proximal Occlusion with Emphasis on Minimizing CT to Recanalization Times (ESCAPE) trial, a CTA collateral score (CS) was used for this purpose.<sup>3</sup>

Collaterals are defined as a network of vascular channels that variably restore blood flow when the main supplying artery is blocked.<sup>6</sup> A good collateral circulation is believed to be of major importance for sustaining the penumbra in patients with acute ischemic stroke, is considered predictive of final infarct volume, and is associated with improved clinical outcome after both intravenous thrombolysis and IAT.<sup>7–16</sup>

The criterion standard for the assessment of collateral flow is multivessel DSA.<sup>17</sup> This generates images with high spatial and

Received March 14, 2016; accepted after revision May 11.

From the Departments of Radiology (I.G.H.J., O.A.B., M.E.S.S., C.B.L.M.M.) and Biomedical Engineering and Physics (H.A.M.), Academic Medical Center, Amsterdam, the Netherlands; Departments of Neurology (O.A.B.) and Radiology (A.v.d.L.), Erasmus MC University Medical Center, Rotterdam, the Netherlands; Texas Stroke Institute (A.J.Y.), Plano, Texas; Departments of Radiology (J.A.V.) and Neurology (W.J.S.), St. Antonius Hospital, Nieuwegein, the Netherlands; Departments of Radiology (G.J.L.N.) and Neurology (J.B.), Haaglanden Medical Center, The Haag, the Netherlands; Departments of Radiology (W.H.v.Z.), and Neurology (R.J.v.O.), Cardiovascular Research Institute, Maastricht, the Netherlands; and Department of Radiology (M.A.A.v.W.), Leiden University Medical Center, Leiden, the Netherlands.

H.A. Maquering and C.B.L.M. Majoie shared senior authorship of this article.

Paper previously presented at: Annual Meeting of the European Stroke Organization, April 17–19, 2015; Glasgow, Scotland, in the form of an oral presentation by Ivo G.H. Jansen.

Please address correspondence to Ivo G.H. Jansen, MD, Department of Radiology, GI–230, Academic Medical Center, University of Amsterdam, PO Box 22660, 1100 DD Amsterdam, the Netherlands; e-mail: i.g.jansen@amc.nl

Indicates article with supplemental on-line table.

<http://dx.doi.org/10.3174/ajnr.A4878>

temporal resolution, which allows the evaluation of contrast flow into the ischemic region via collaterals.<sup>18,19</sup> However, in practice, multivessel DSA is considered impractical as a primary diagnostic procedure for acute ischemic stroke triage because speed of treatment is an important factor in these cases. In addition, the expected benefit is low relative to the resources needed. Single-vessel DSA is the pragmatic choice but has several drawbacks, including incomplete assessment of the MCA or anterior cerebral artery territory. Alternatively, CTA is currently used for assessment of collateral flow because of its 24/7 availability and short acquisition time.<sup>8–10</sup> Also, good interrater agreement for this technique has been reported.<sup>10,20</sup> Additionally, CTA has the advantage of allowing visualization of collateral flow from all vessels at once, both intra- and extracranial.<sup>9</sup> A drawback of CTA, however, is the lack of temporal information. Multiphase CTA could solve this problem, but it is not yet widely available.

The purpose of this substudy of MR CLEAN was to assess the agreement between CTA and DSA for grading of collateral flow in patients with acute ischemic stroke due to proximal anterior circulation occlusion, analogous to current practice. In addition, we investigated the association of CTA and DSA collateral grades with clinical outcome as measured on the mRS.

## MATERIALS AND METHODS

### Patient Inclusion and Study Design

The design of MR CLEAN has been published previously.<sup>1</sup> In short, MR CLEAN was a randomized clinical trial of IAT in addition to the usual care versus usual care alone in patients with a proximal intracranial occlusion in the anterior circulation demonstrated on vessel imaging, treatable within 6 hours after symptom onset. The inclusion criteria for the current substudy were the availability of baseline CTA combined with a complete DSA run of the ipsilateral ICA territory showing a middle cerebral artery occlusion (M1 or M2), including a lateral projection. Exclusion criteria were occlusion of the ipsilateral cervical ICA or ICA terminus, the presence of multiple ipsilateral occlusions, an ipsilateral hypoplastic A1 segment, and occurrence of contralateral flash filling (resulting in dilution of contrast by blood from the contralateral circulation). Approval from the local institutional review board was obtained, and all patients or their legal representatives gave written informed consent to participate. The MR CLEAN study protocol was approved by a central medical ethics committee and the research board of each participating center.

### Imaging Assessment

All imaging data were collected before this substudy, as part of the overall evaluation in MR CLEAN. The relevant scan protocols of CTA and DSA used in this study are shown in the On-line Table. The data were anonymized before assessment. The CS on CTA source imaging was determined in separate sessions by pairs of experienced neuroradiologists, with at least 5 years of experience. Discrepancies between the initial readers were solved by a third reader. CS on DSA was determined by 1 experienced neuroradiologist (A.J.Y., with >10 years of experience). All readers were blinded to clinical findings, and the initial readers were blinded to each other's scores. On both CTA and DSA, CS was graded on a 4-point scale, with zero representing absent collateral flow of the

**Table 1: Patient characteristics<sup>a</sup>**

Baseline Characteristic	Value
Patients	45
Median age (range) (yr)	63 (44–85)
Sex ratio (M/F)	22/23
Stroke side (L/R)	22/23
DSA occlusion site	M1 (n = 35), M2 (n = 10)
Clot migration (CTA to DSA)	ICA-T to M1 (n = 1) M1 to M2 (n = 6) M2 to M1 (n = 1)
IVT (yes/no)	36/9
Median NIHSS at baseline (range)	16 (6–30)
Median time onset to CTA (range) (min)	204 (21–496)
Median time onset to DSA (range) (min)	260 (108–390)

**Note:**—ICA-T indicates ICA terminus; IVT, intravenous thrombolysis. R, right; L, left.  
<sup>a</sup> Range is displayed in parentheses. IVT displays if patients received IVT prior to IAT. Time to CTA and time to DSA represent the median time in minutes from symptom onset to the acquisition of CTA and DSA scans, respectively.

occluded territory, 1 representing poor collateral flow (<50% flow of the occluded territory), 2 representing intermediate collateral flow (between 50% and 100% flow of the occluded territory), and 3 representing good collateral flow (100% flow of the occluded territory).<sup>15,21</sup>

### Clinical Outcome Assessment

The mRS is a 7-point scale on which functional independence of the patient is measured, ranging from 0 (no symptoms) to 6 (dead). In MR CLEAN, the mRS was constructed from a follow-up interview at 90 days, which was conducted by an experienced trial investigator (blinded to the treatment-group allocation) by telephone with the patient, proxy, or health care provider.

### Statistical Analysis

Analysis was performed by using SPSS software (Version 22.0 for Windows; IBM, Armonk, New York). We assessed interobserver reliability for collateral flow on CTA by estimating the agreement beyond chance with quadratic weighted  $\kappa$  statistics. Interobserver reliability was considered poor at a  $\kappa$ -value of 0, slight between 0.01 and 0.20, fair between 0.21 and 0.40, moderate between 0.41 and 0.60, substantial between 0.61 and 0.80, almost perfect between 0.81 and 0.99, and perfect at 1.0.<sup>22</sup> Quadratic weighted  $\kappa$  statistics were also used to determine consistency between both modalities. Ninety-five percent confidence intervals were set to quantify uncertainty. The overall observed proportion of agreement of CS scoring between both methods was determined. Multivariable ordinal logistic regression analysis was performed to determine the adjusted odds ratio of a shift toward better clinical outcome on the mRS, adjusted for early successful recanalization, which was defined as a modified Thrombolysis in Cerebral Infarction score of 2B or higher. Additionally, for secondary analyses, CS was dichotomized into poor (absent and poor collateral flow) and good (moderate and good collateral flow), and mRS was dichotomized into a score of 0–2 (functional independence) versus 3–6.  $\chi^2$  tests were performed to determine the association between dichotomized CS and mRS 0–2 for both modalities in the entire population and for patients with early recanalization separately.

## RESULTS

Of the 500 patients in MR CLEAN, 84 met the inclusion criteria on quality of CTA and DSA imaging. Of these, 39 patients were excluded due to the presence of either ICA or ICA terminus occlusion ( $n = 25$ ), presence of multiple occlusions ( $n = 7$ ), occurrence of contralateral flash filling ( $n = 4$ ), a hypoplastic A1-segment ( $n = 2$ ), or motion artifacts ( $n = 1$ ). This exclusion left 45 patients available for comparison. Table 1 provides an overview of the relevant baseline characteristics of the included patients. Thirty-five patients had an M1, and 10, an M2 occlusion on DSA. In 8

of these patients, CTA clot location was different on DSA (in 6 patients from M1 on CTA to M2 on DSA, in 1 patient from the ICA terminus on CTA to M1 on DSA, and in 1 patient from M2 on CTA to M1 on DSA). Table 2 shows the distribution of CSs for CTA and DSA in all patients.

Interobserver agreement for collateral flow assessment on CTA had a quadratic weighted  $\kappa$ -value of 0.68 (95% CI, 0.40–0.96), indicating substantial agreement. Figure 1 gives examples of both methods. The quadratic weighted  $\kappa$ -value for the agreement between CTA and DSA was 0.24 (95% CI, 0.16–0.32). When patients in whom clot location differed between CTA and DSA were excluded from analysis, the quadratic weighted  $\kappa$ -value was 0.25 (95% CI, 0.13–0.38). The overall observed proportion of agreement was 24% (95% CI, 0.12–0.38).

There was a significant shift in mRS distribution toward better clinical outcome for CTA based on CS (adjusted OR, 2.27; 95% CI, 1.18–4.40;  $P = .015$ ) (Fig 2). For the DSA-based CS, there was no significant association (adjusted OR, 1.29; 95% CI, 0.76–2.21;  $P = .35$ ).

Of the 16 cases in which the dichotomized CS was graded as good on DSA (grades 2–3), in 13 (81%), it agreed with the CTA assessment. In contrast, of 29 cases in which dichotomized CS was graded as poor on DSA (grades 0–1), in only 10 (35%) did it agree with the CTA assessment. There was a significant relationship between dichotomized CS on CTA and mRS 0–2 in the entire population ( $\chi^2 = 6.7$ ,  $P = .010$ ) and for patients with early recanalization ( $\chi^2 = 5.2$ ,  $P = .023$ ). This was not the case for dichotomized CS on DSA in the total population ( $\chi^2 = 0.1$ ,  $P = .77$ ) or for patients with early recanalization ( $\chi^2 = 1.1$ ,  $P = .31$ ).

**Table 2: Distribution of collateral score for CTA and DSA in all patients<sup>a</sup>**

CTA CS	DSA CS				Total
	Absent (0)	Poor (1)	Moderate (2)	Good (3)	
Absent (0)	2	1	0	0	3
Poor (1)	4	3	2	1	10
Moderate (2)	5	8	4	3	20
Good (3)	1	5	4	2	12
Total	12	17	10	6	45

<sup>a</sup>The score corresponding with the relevant category is given in brackets.

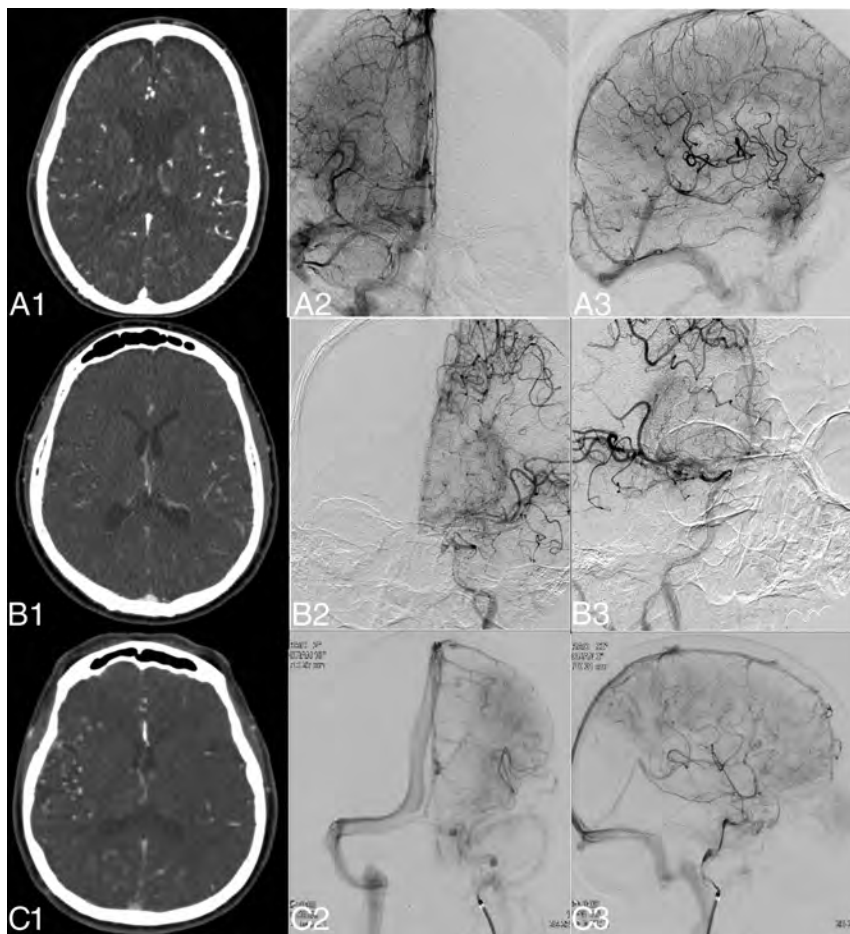


**FIG 1.** Examples of DSA- and CTA-based collateral scores in 3 different patients. Images were selected by a maximum amount of contrast in the middle cerebral artery for CTA and adequate opacity in the venous phase for DSA. In the left column, the CTA image is shown (A1–C1); in the middle column, the anteroposterior DSA (A2–C2); and in the right column, the lateral DSA (A3–C3). A1–A3, Patient A with a right-sided M1 occlusion, which DSA assessed as grade 3, and CTA, as grade 3. B1–B3, Patient B with a left-sided M1 occlusion, which DSA assessed as grade 1, and CTA, as grade 3. C1–C3, Patient C with a left-sided M1 occlusion, which DSA assessed as grade 3 collateral flow, and CTA, as grade 1.

## DISCUSSION

With a straightforward grading scale, collateral flow on CTA and DSA has poor agreement, revealing that these approaches are not interchangeable. Irrespective of early recanalization, CTA-based collateral flow is significantly associated with clinical outcome, whereas DSA-based collateral flow is not.

In a recent study, Frolich et al<sup>23</sup> found that early triggering of CTA image acquisition could result in diminished visibility and underestimation of collateral flow. In contrast, the same group found that delaying CTA triggering relative to contrast injection could result in overestimation of collateral flow, due to washout of contrast within normal reference arteries, resulting in a relatively weaker opacification of the unaffected

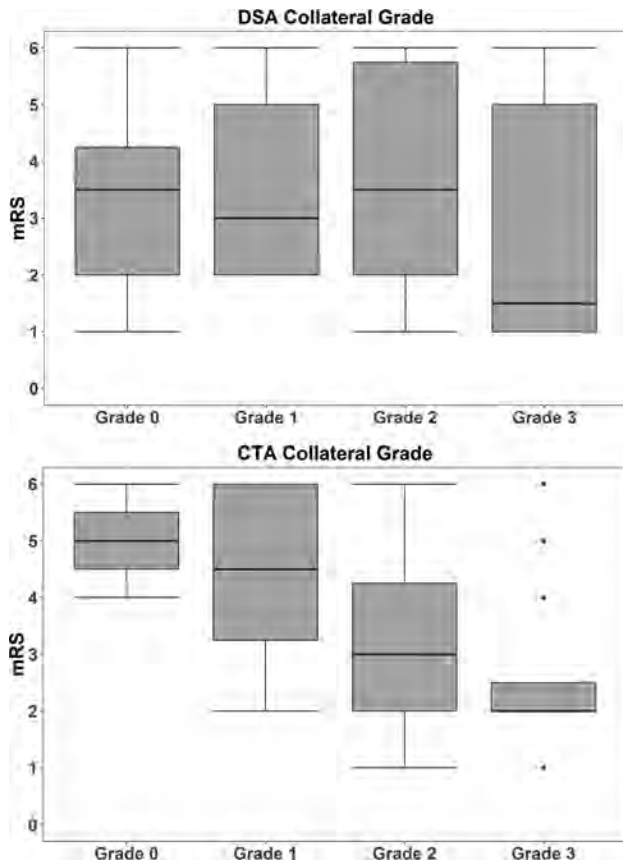


**FIG 2.** Distribution of CTA- and DSA-based collateral grades on the modified Rankin Scale. For CTA-based collateral grades, a clear change in distribution can be seen toward better clinical outcome for higher collateral grades. For DSA-based collateral grades, there is no change in distribution on mRS for higher collateral grades.

hemisphere. Nambiar et al<sup>13</sup> also recently reported this washout effect. Both this over- and underestimation could account for the poor agreement found in our study because CTA only provides a snapshot at a set time point, whereas DSA gives information about collateral flow with time.

In the case of DSA, a complete collateral flow assessment requires imaging of both left and right carotid and 1 or both vertebral arteries.<sup>16</sup> The delay required for diagnostic DSA and the need for a fast response in acute ischemic stroke management are seen as reasons for not performing DSA collateral imaging routinely in clinical practice, though alternative methods of IAT patient selection on DSA are currently being studied.<sup>24</sup> Given the potential of collateral flow assessment as a patient-selection tool for IAT, CTA is seen as the imaging technique of choice because it is already obtained for documenting vessel occlusion status, given its availability and low cost.<sup>20</sup> Another promising alternative is multiphase CTA, as was used for the inclusion of patients with moderate-to-good collaterals in ESCAPE. This also provides fast information on the degree of collateral flow but in a time-resolved manner, without the need for complicated postprocessing. Menon et al<sup>25</sup> reported high interrater reliability for this method. Time-invariant CTA based on CTP has also been mentioned and has so far shown good interrater agreement and agreement with DSA.<sup>26</sup> Kim et al<sup>27</sup> compared collateral flow on time-invariant CTA images with DSA and showed a high level of agreement be-

tween the 2 modalities, considerably higher than that in the current study. Time-invariant CTA, like DSA and multiphase CTA, has the advantage of giving information of blood flow across time.

There are some limitations to this study. The most important is that validation of DSA as a criterion standard for collateral flow assessment should be based on multivessel imaging. In our study, all patients underwent single-vessel DSA as part of IAT, due to the importance of rapid treatment. Therefore, collateral flow originating from the posterior circulation or the contralateral side could not be assessed, and this omission could have resulted in incomplete information on the degree of collateral flow.<sup>13</sup> However, because 4-vessel diagnostic DSA is currently not being used routinely, our study is focused on a more pragmatic approach to collateral flow assessment, analogous to current clinical practice. Additionally, our study was designed to minimize this limitation, ensuring, for example, that patients with ICA terminus occlusions or hypoplastic A1 segments were excluded; this exclusion allowed assessment of collateral flow from the ipsilateral anterior and middle cerebral arteries. In addition, in about 20% of patients, differences in clot location were observed between CTA and DSA, most likely due to clot migration. However when these patients were excluded from the analysis, no difference in the level of agreement between modalities compared with the full analysis was observed. Finally, CTA was performed by using different scanner protocols, due to the large number of centers participating in MR CLEAN. These protocol differences could influence the degree of collateral flow observed. However, we believe that this heterogeneity and the incorporation of cases showing clot migration in our study population add to the generalizability of our study.

Collateral flow could be considered an important target for selection of patients for IAT because it is becoming increasingly clear that patients with poor collateral flow have marginal benefit of treatment.<sup>28</sup> It can be argued that due to the lack of interchangeability between CTA and DSA, the lack of association between DSA and clinical outcome, and the low application of multivessel DSA in current clinical practice, CTA could be sufficient for this purpose. For future studies excluding patients with poor collateral flow as in ESCAPE, the use of single-vessel DSA for collateral flow assessment could prove precarious. To uphold the role of DSA-based collateral assessment in future patient selection for IAT, further research is warranted to confirm the ability of accurately assessing poor or absent collateral flow on CTA, ideally compared with the criterion standard multivessel DSA. The findings of this study show that the direct comparison of collateral scores acquired by different modalities must be approached with caution. In the near future, it is possible that collateral flow will aid in patient selection for IAT. It is therefore important to consider the properties of the technique with which collateral assessment is performed and how these will affect collateral grading itself, as well as clinical outcome prediction.

## CONCLUSIONS

Commonly applied collateral flow assessment on CTA and DSA showed large differences, indicating that these techniques are not interchangeable. CTA was significantly associated with mRS at 90 days, whereas DSA was not.

## ACKNOWLEDGMENTS

MR CLEAN investigators: Olvert A. Berkhemer, MD, 1, 2; Puck S.S. Fransen, MD, 2, 3; Debbie Beumer, MD, 2, 4; Lucie A. van den Berg, MD, 5; Hester F. Lingsma, MD, PhD, 7; Albert J. Yoo, MD, 8; Wouter J. Schonewille, MD, 9; Jan Albert Vos, MD, PhD, 10; Paul J. Nederkoorn, MD, PhD, 5; Marieke J.H. Wermer, MD, PhD, 11; Marianne A.A. van Walderveen, MD, PhD, 12; Julie Staals, MD, PhD, 4; Jeannette Hofmeijer, MD, PhD, 13; Jacques A. van Oostayen, MD, PhD, 14; Geert J. Lycklama à Nijeholt, MD, PhD, 15; Jelis Boiten, MD, PhD, 16; Patrick A. Brouwer, MD, 3; Bart J. Emmer, MD, PhD, 3; Sebastiaan F. de Bruijn, MD, PhD, 17; Lukas C. van Dijk, MD, 18; L. Jaap Kappelle, MD, PhD, 19; Rob H. Lo, MD, 20; Ewoud J. van Dijk, MD, PhD, 21; Joost de Vries, MD, PhD, 22; Paul L.M. de Kort, MD, PhD, 23; Jan S.P. van den Berg, MD, PhD, 24; Boudewijn A.A.M. van Hasselt, MD, 25; Leo A.M. Aerden, MD, PhD, 26; René J. Dallinga, MD, 27; Marieke C. Visser, MD, PhD, 28; Joseph C.J. Bot, MD, PhD, 29; Patrick C. Vroomen, MD, PhD, 30; Omid Eshghi, MD, 31; Tobien H.C.M.L. Schreuder, MD, 32; Roel J.J. Heijboer, MD, 33; Koos Keizer, MD, PhD, 34; Alexander V. Tielbeek, MD, PhD, 35; Heleen M. den Hertog, MD, PhD, 36; Dick G. Gerrits, MD, 37; Renske M. van den Berg-Vos, MD, PhD, 38; Giorgos B. Karas, MD, 39; Ewout W. Steyerberg, MD, PhD, 7; H. Zwenneke Flach, MD, 26; Henk A. Marquering, PhD, 40, 1; Marieke E.S. Sprengers, MD, PhD, 1; Sjoerd F.M. Jenniskens, MD, PhD, 41; Ludo F.M. Beenen, MD, 1; René van den Berg, MD, PhD, 1; Peter J. Koudstaal, MD, PhD, 2; Wim H. van Zwam, MD, PhD, 6; Yvo B.W.E.M. Roos, MD, PhD, 5; Aad van der Lugt, MD, PhD, 3; Robert J. van Oostenbrugge, MD, PhD, 4; Charles B.L.M. Majoie, MD, PhD, 1; and Diederik W.J. Dippel, MD, PhD, 2.

Affiliations: 1) Department of Radiology, Academic Medical Center, Amsterdam, the Netherlands; 2) Department of Neurology, Erasmus MC University Medical Center, Rotterdam, the Netherlands; 3) Department of Radiology, Erasmus MC University Medical Center, Rotterdam, the Netherlands; 4) Department of Neurology, Maastricht University Medical Center and Cardiovascular Research Institute, Maastricht, the Netherlands; 5) Department of Neurology, Academic Medical Center, Amsterdam, the Netherlands; 6) Department of Radiology, Maastricht University Medical Center, Maastricht, the Netherlands; 7) Department of Public Health, Erasmus MC University Medical Center, Rotterdam, the Netherlands; 8) Department of Radiology, Texas Stroke Institute, Plano, Texas; 9) Department of Neurology, Sint Antonius Hospital, Nieuwegein, the Netherlands; 10) Department of Radiology, Sint Antonius Hospital, Nieuwegein, the Netherlands; 11) Department of Neurology, Leiden University Medical Center, Leiden, the Netherlands; 12) Department of Radiology, Leiden University Medical Center, Leiden, the Netherlands; 13) Department of Neurology, Rijnstate Hospital, Arnhem, the Netherlands; 14) Department of Radiology, Rijnstate Hospital, Arnhem, the Netherlands; 15) Department of Radiology, MC Haaglanden, The Hague, the Netherlands; 16) Department of Neurology, MC Haaglanden, The Hague, the Netherlands; 17) Department of Neurology, HAGA Hospital, The Hague, the Netherlands; 18) Department of Radiology, HAGA Hospital, The Hague, the Netherlands; 19) Department of Neurology, University Medical Center, Utrecht, the Netherlands; 20) Department of

Radiology, University Medical Center, Utrecht, the Netherlands; 21) Department of Neurology, Radboud University Medical Center, Nijmegen, the Netherlands; 22) Department of Neurosurgery, Radboud University Medical Center, Nijmegen, the Netherlands; 23) Department of Neurology, Sint Elisabeth Hospital, Tilburg, the Netherlands; 24) Department of Neurology, Isala Klinieken, Zwolle, the Netherlands; 25) Department of Radiology, Isala Klinieken, Zwolle, the Netherlands; 26) Department of Neurology, Reinier de Graaf Gasthuis, Delft, the Netherlands; 27) Department of Radiology, Reinier de Graaf Gasthuis, Delft, the Netherlands; 28) Department of Neurology, VU Medical Center, Amsterdam, the Netherlands; 29) Department of Radiology, VU Medical Center, Amsterdam, the Netherlands; 30) Department of Neurology, University Medical Center, Groningen, the Netherlands; 31) Department of Radiology, University Medical Center, Groningen, the Netherlands; 32) Department of Neurology, Atrium Medical Center, Heerlen, the Netherlands; 33) Department of Radiology, Atrium Medical Center, Heerlen, the Netherlands; 34) Department of Neurology, Catharina Hospital, Eindhoven, the Netherlands; 35) Department of Radiology, Catharina Hospital, Eindhoven, the Netherlands; 36) Department of Neurology, Medical Spectrum Twente, Enschede, the Netherlands; 37) Department of Radiology, Medical Spectrum Twente, Enschede, the Netherlands; 38) Department of Neurology, Sint Lucas Andreas Hospital, Amsterdam, the Netherlands; 39) Department of Radiology, Sint Lucas Andreas Hospital, Amsterdam, the Netherlands; 40) Department of Biomedical Engineering and Physics, Academic Medical Center, Amsterdam, the Netherlands; and 41) Department of Radiology, Radboud University Medical Center, Nijmegen, the Netherlands.

Data-Monitoring and Safety Board: Chair: Martin M. Brown, National Hospital for Neurology and Neurosurgery, London, United Kingdom. Member: Thomas Liebig, Medizinische Fakultät, University Köln, Germany. Independent Statistician: Theo Stijnen, Leiden University Medical Center, Leiden, the Netherlands.

Advisory Board: Tommy Andersson, neurointerventionist, Karolinska University Hospital, Stockholm, Sweden; Heinrich Mattle, neurologist, University Hospital, Bern, Switzerland; Nils Wahlgren, neurologist, Karolinska Hospital, Stockholm, Sweden.

Research nurses/local trial coordinators: Esther van der Heijden, Naziha Ghannouti, Erasmus MC University Medical Center, Rotterdam, the Netherlands; Nadine Fleitour, Imke Hooijenga, Academic Medical Center, Amsterdam, the Netherlands; Corina Puppels, Wilma Pelikaan, Sint Antonius Hospital, Nieuwegein, the Netherlands; Annet Geerling, Radboud University Nijmegen Medical Center, Nijmegen, the Netherlands; Annemieke Lindl-Velema, Maastricht University Medical Center, Maastricht, the Netherlands; Gina van Vemde, Isala Klinieken, Zwolle, the Netherlands; Ans de Ridder, Paut Greebe, University Medical Center, Utrecht, the Netherlands; José de Bont-Stikkelbroeck, Sint Elisabeth Hospital, Tilburg, the Netherlands; Joke de Meris, MC Haaglanden, The Hague, the Netherlands; Kirsten Janssen, Leiden University Medical Center, Leiden, the Netherlands; Willy Struijk, HAGA Hospital, The Hague, the Netherlands; Tiny Simons, Atrium MC, Heerlen, the Netherlands; Gert Messchendorp, Friedus van der Minne, University Medical Cen-



ter, Groningen, the Netherlands; and Hester Bongenaar, Catharina Hospital, Eindhoven, the Netherlands.


PhD/Medical Students: Silvan Licher, Nikki Boodt, Adriaan Ros, Esmee Venema, Ilse Slokkers, Raymie-Jayce Ganpat, Maxim Mulder, Nawid Saiedie, Alis Heshmatollah, Stefanie Schipperen, Stefan Vinken, Tiemen van Boxtel, Jeroen Koets, Erasmus MC University Medical Center, Rotterdam, the Netherlands; Merel Boers, Emilie Santos, Jordi Borst, Ivo Jansen, Manon Kappelhof, Marit Lucas, Ralph Geuskens, Renan Sales Barros, Roeland Dobbe, Marloes Csizmadia, Academic Medical Center, Amsterdam, the Netherlands.

DISCLOSURES: Albert J. Yoo—UNRELATED: Grants/Grants Pending: Penumbra,\* Neuravi,\* Comments: Core Imaging Lab activities. Jan Albert Vos—UNRELATED: Grants/Grants Pending: Cordis/Cardinal Health,\* Boston Scientific,\* Comments: unrestricted departmental educational grants, not related to patients with acute stroke; Payment for Lectures (including service on Speakers Bureaus): Cordis/Cardinal Health, Comments: lectures not related to the subject of patients with acute stroke. Wim H. van Zwam—RELATED: Consulting Fee or Honorarium: Stryker,\* Comments: speaker's honorarium (Stryker supports MR CLEAN via funding to the institution). Aad van der Lugt—RELATED: Grant: The MR CLEAN trial was partly funded by the Dutch Heart Foundation and by nominal, unrestricted grants from Angiocare BV, Medtronic/Covidien/ev3, Medac GmbH/LAMEPRO, Penumbra, Stryker, and Top Medical/Concentric.\* Henk A. Marquering—OTHER RELATIONSHIPS: confounder of Nico-lab. Charles B.L.M. Majoie—RELATED: Grant: TWIN Foundation,\* Dutch Heart Foundation\*; UNRELATED: Payment for Lectures (including service on Speakers Bureaus): Stryker.\* \*Money paid to the institution.

## REFERENCES

1. Berkhemer OA, Fransen PS, Beumer D, et al. **A randomized trial of intraarterial treatment for acute ischemic stroke.** *N Engl J Med* 2015; 372:11–20 CrossRef Medline
2. Campbell BC, Mitchell PJ, Kleinig TJ, et al; EXTEND-IA Investigators. **Endovascular therapy for ischemic stroke with perfusion-imaging selection.** *N Engl J Med* 2015;372:1009–18 CrossRef Medline
3. Goyal M, Demchuk AM, Menon BK, et al; ESCAPE Trial Investigators. **Randomized assessment of rapid endovascular treatment of ischemic stroke.** *N Engl J Med* 2015;372:1019–30 CrossRef Medline
4. Saver JL, Goyal M, Bonafe A, et al; SWIFT PRIME Investigators. **Stent-retriever thrombectomy after intravenous t-PA vs. t-PA alone in stroke.** *N Engl J Med* 2015;372:2285–95 CrossRef Medline
5. Jovin TG, Chamorro A, Cobo E, et al; REVASCAT Trial Investigators. **Thrombectomy within 8 hours after symptom onset in ischemic stroke.** *N Engl J Med* 2015;372:2296–306 CrossRef Medline
6. Faber JE, Chilian WM, Deindl E, et al. **A brief etymology of the collateral circulation.** *Arterioscler Thromb Vasc Biol* 2014;34:1854–59 CrossRef Medline
7. Bang OY, Saver JL, Kim SJ, et al. **Collateral flow predicts response to endovascular therapy for acute ischemic stroke.** *Stroke* 2011;42: 693–99 CrossRef Medline
8. Menon BK, O'Brien B, Bivard A, et al. **Assessment of leptomeningeal collaterals using dynamic CT angiography in patients with acute ischemic stroke.** *J Cereb Blood Flow Metab* 2013;33:365–71 CrossRef Medline
9. Lima FO, Furie KL, Silva GS, et al. **The pattern of leptomeningeal collaterals on CT angiography is a strong predictor of long-term clinical outcome in stroke patients with large vessel intracranial occlusion.** *Stroke* 2010;41:2316–22 CrossRef Medline
10. Menon BK, Smith EE, Modi J, et al. **Regional leptomeningeal score on CT angiography predicts clinical and imaging outcomes in patients with acute anterior circulation occlusions.** *AJNR Am J Neuroradiol* 2011;32:1640–45 CrossRef Medline
11. Liebeskind DS, Jahan R, Nogueira RG, et al. **Impact of collaterals on successful revascularization in Solitaire FR with the intention for thrombectomy.** *Stroke* 2014;45:2036–40 CrossRef Medline
12. Maas MB, Lev MH, Ay H, et al. **Collateral vessels on CT angiography predict outcome in acute ischemic stroke.** *Stroke* 2009;40:3001–05 CrossRef Medline
13. Nambiar V, Sohn SI, Almekhlafi MA, et al. **CTA collateral status and response to recanalization in patients with acute ischemic stroke.** *AJNR Am J Neuroradiol* 2014;35:884–90 CrossRef Medline
14. Ramaiah SS, Mitchell P, Dowling R, et al. **Assessment of arterial collateralization and its relevance to intra-arterial therapy for acute ischemic stroke.** *J Stroke Cerebrovasc Dis* 2014;23:399–407 CrossRef Medline
15. Tan IY, Demchuk AM, Hopyan J, et al. **CT angiography clot burden score and collateral score: correlation with clinical and radiologic outcomes in acute middle cerebral artery infarct.** *AJNR Am J Neuroradiol* 2009;30:525–31 CrossRef Medline
16. Liebeskind DS. **Collateral circulation.** *Stroke* 2003;34:2279–84 Medline
17. Liebeskind DS, Tomsick TA, Foster LD, et al; IMS III Investigators. **Collaterals at angiography and outcomes in the Interventional Management of Stroke (IMS) III trial.** *Stroke* 2014;45:759–64 CrossRef Medline
18. Higashida RT, Furlan AJ, Roberts H, et al; Technology Assessment Committee of the American Society of Interventional and Therapeutic Neuroradiology, Technology Assessment Committee of the Society of Interventional Radiology. **Trial design and reporting standards for intra-arterial cerebral thrombolysis for acute ischemic stroke.** *Stroke* 2003;34:e109–37 CrossRef Medline
19. Chng SM, Petersen ET, Zimine I, et al. **Territorial arterial spin labeling in the assessment of collateral circulation: comparison with digital subtraction angiography.** *Stroke* 2008;39:3248–54 CrossRef Medline
20. McVerry F, Liebeskind DS, Muir KW. **Systematic review of methods for assessing leptomeningeal collateral flow.** *AJNR Am J Neuroradiol* 2012;33:576–82 CrossRef Medline
21. Tan JC, Dillon WP, Liu S, et al. **Systematic comparison of perfusion-CT and CT-angiography in acute stroke patients.** *Ann Neurol* 2007;61:533–43 CrossRef Medline
22. Viera AJ, Garret JM. **Understanding interobserver agreement: the kappa statistic.** *Fam Med* 2005;37:360–63 Medline
23. Frölich AM, Wolff SL, Psychogios MN, et al. **Time-resolved assessment of collateral flow using 4D CT angiography in large-vessel occlusion stroke.** *Eur Radiol* 2014;24:390–96 CrossRef Medline
24. Al-Ali F, Elias JJ, Tomsick TA, et al. **Relative influence of capillary index score, revascularization, and time on stroke outcomes from the Interventional Management of Stroke III Trial.** *Stroke* 2015;46: 1590–94 CrossRef Medline
25. Menon BK, d'Este CD, Qazi EM, et al. **Multiphase CT angiography: a new tool for the imaging triage of patients with acute ischemic stroke.** *Radiology* 2015;275:510–20 CrossRef Medline
26. Smit EJ, Vonken EJ, van Seeters T, et al. **Timing-invariant imaging of collateral vessels in acute ischemic stroke.** *Stroke* 2013;44:2194–99 CrossRef Medline
27. Kim SJ, Noh HJ, Yoon CW, et al. **Multiphase perfusion computed tomography as a predictor of collateral flow in acute ischemic stroke: comparison with digital subtraction angiography.** *Eur Neurol* 2012;67:252–55 CrossRef Medline
28. Menon BK, Qazi E, Nambiar V, et al; Interventional Management of Stroke III Investigators. **Differential effect of baseline computed tomographic angiography collaterals on clinical outcome in patients enrolled in the Interventional Management of Stroke III Trial.** *Stroke* 2015;46:1239–44 CrossRef Medline

# A Semiautomatic Method for Multiple Sclerosis Lesion Segmentation on Dual-Echo MR Imaging: Application in a Multicenter Context

 L. Storelli,  E. Pagani,  M.A. Rocca,  M.A. Horsfield,  A. Gallo,  A. Biseco,  M. Battaglini,  N. De Stefano,  H. Vrenken,  D.L. Thomas,  L. Mancini,  S. Ropele,  C. Enzinger,  P. Preziosa, and  M. Filippi



## ABSTRACT

**BACKGROUND AND PURPOSE:** The automatic segmentation of MS lesions could reduce time required for image processing together with inter- and intraoperator variability for research and clinical trials. A multicenter validation of a proposed semiautomatic method for hyperintense MS lesion segmentation on dual-echo MR imaging is presented.

**MATERIALS AND METHODS:** The classification technique used is based on a region-growing approach starting from manual lesion identification by an expert observer with a final segmentation-refinement step. The method was validated in a cohort of 52 patients with relapsing-remitting MS, with dual-echo images acquired in 6 different European centers.

**RESULTS:** We found a mathematic expression that made the optimization of the method independent of the need for a training dataset. The automatic segmentation was in good agreement with the manual segmentation (dice similarity coefficient = 0.62 and root mean square error = 2 mL). Assessment of the segmentation errors showed no significant differences in algorithm performance between the different MR scanner manufacturers ( $P > .05$ ).

**CONCLUSIONS:** The method proved to be robust, and no center-specific training of the algorithm was required, offering the possibility for application in a clinical setting. Adoption of the method should lead to improved reliability and less operator time required for image analysis in research and clinical trials in MS.

**ABBREVIATIONS:** DE = dual-echo; PD = proton density

Assessment of the disease burden using MR images from patients with MS, for research and clinical trials, requires quantification of the volume of hyperintense lesions on T2-weighted images.<sup>1</sup> However, lesion segmentation remains challenging, and the required accuracy and reproducibility are difficult to achieve. Ideally, segmentation should be automated or require minimum operator input to minimize the operator time re-

quired and reduce bias<sup>2-4</sup>; however, manual segmentation is still the “gold standard.”

Though several methods for fully automated MS lesion segmentation have been published, their performances are difficult to compare. This is because they are usually validated without a common framework,<sup>5</sup> and even if validated within the same framework (such as the MS lesion segmentation challenge presented at the International Conference on Medical Image Computing and Computer Assisted Intervention [MICCAI] 2008<sup>6</sup>), the validation is done by using a small dataset of cases and does not include a dual-echo (DE) proton-density (PD)/T2-weighted image dataset. In addition, most methods are optimized and tested on FLAIR MR images that benefit from CSF signal suppression and better contrast between focal lesions and the surrounding tissue<sup>7-9</sup> compared with the more established techniques that use DE sequences. Large datasets of DE MR images from past

Received March 16, 2016; accepted after revision May 11.

From the Neuroimaging Research Unit (L.S., E.P., M.A.R., P.P., M.F.), and Institute of Experimental Neurology, Division of Neuroscience, Department of Neurology (M.A.R., P.P., M.F.), San Raffaele Scientific Institute, Vita-Salute San Raffaele University, Milan, Italy; Xinapse Systems (M.A.H.), Colchester, United Kingdom; MRI Center “SUN-FISM” and Institute of Diagnosis and Care “Hermitage-Capodimonte” (A.G., A.B.), and I Division of Neurology, Department of Medical, Surgical, Neurological, Metabolic and Aging Sciences (A.G., A.B.), Second University of Naples, Naples, Italy; Department of Neurological and Behavioral Sciences (M.B., N.D.S.), University of Siena, Italy; Department of Radiology and Nuclear Medicine, MS Centre Amsterdam (H.V.), VU Medical Centre, Amsterdam, the Netherlands; Neuroradiological Academic Unit (D.L.T., L.M.), UCL Institute of Neurology, London, United Kingdom; and Department of Neurology (S.R., C.E.) and Clinical Division of Neuroradiology, Vascular and Interventional Radiology, Department of Radiology (C.E.), Medical University of Graz, Austria.

This study was partially supported by Fondazione Italiana Sclerosi Multiple (FISM2013/S/1). D.L.T. is supported by the UCL Leonard Wolfson Experimental Neurology Centre (grant PR/ylr/18575).

Please address correspondence to Massimo Filippi, MD, Neuroimaging Research Unit, Institute of Experimental Neurology, Division of Neuroscience, San Raffaele Scientific Institute, Vita-Salute San Raffaele University, Via Olgettina, 60, 20132 Milan, Italy; e-mail: filippi.massimo@hsr.it

 Indicates article with supplemental on-line appendix and tables.

<http://dx.doi.org/10.3174/ajnr.A4874>

studies are available, and their acquisition is still common for both research and clinical trials, so there is still the need to develop methods for lesion segmentation on these data.<sup>10</sup>

We have previously proposed a semiautomated method based on a region-growing approach for MS lesion segmentation on DE MR images that results in a considerable reduction in the time required for lesion segmentation compared with manual segmentation and shows good agreement with the ground truth.<sup>11</sup>

Most large MR imaging studies of MS involve multiple scanning centers with different scanner manufacturers.<sup>12</sup> Though all centers would use a common scanning protocol with pulse sequence parameters restricted within certain ranges, there are inevitable differences in image contrast because of hardware and software differences. The aim of the current study was to analyze the training procedure required by the algorithm and to validate the lesion-segmentation method proposed in a multicenter context. The method was validated by comparing the lesion segmentations (obtained using the proposed method) with manual segmentations across different MR scanner manufacturers.

## **MATERIALS AND METHODS**

### **Background**

The method was presented at the BrainLes MICCAI workshop 2015<sup>11</sup> and validated for a single acquisition center on 20 patients. The On-line Appendix provides the methodologic framework of the lesion-segmentation technique.

### **MR Imaging Acquisition**

The dataset consisted of 52 patients with MS, part of a project on imaging correlates of cognitive impairment in MS, acquired in 6 European centers that are part of the MAGNIMS consortium (Amsterdam, Graz, London, Milan, Naples, and Siena) by using 3T MR imaging scanners from a range of manufacturers (2 scanners from Philips Healthcare [Best, the Netherlands], 2 from GE Healthcare [Milwaukee, Wisconsin], and 2 from Siemens [Erlangen, Germany]). To be included, patients had to be aged between 20 and 65 years and have a diagnosis of relapsing-remitting MS,<sup>13</sup> no relapse or corticosteroid treatment within the month before scanning, and no history of psychiatric conditions (On-line Table 1). Only MR imaging sequences without visually relevant artifacts were selected for the current analysis.

The research protocol was approved by the local ethics review boards of participating centers, and all patients gave written informed consent.

A similar MR imaging acquisition protocol was used for all patients: DE TSE; TR = 4000–5380 ms; TE<sub>1</sub> = 10–23 ms; TE<sub>2</sub> = 90–102 ms; echo-train length = 5–11; 44 contiguous, 3-mm-thick axial sections, parallel to the anterior/posterior commissure plane; matrix size = 256 × 256; rectangular field of view = 75%; and field of view = 250 × 250 mm<sup>2</sup>.

The characteristics of MR hardware and number of patients acquired at each center are summarized in On-line Table 2.

### **Analysis of the Training Procedure**

The use of different scanners could cause hardware-dependent differences in image quality. In this study, we assumed that patients scanned with the same radiofrequency coils and MR imag-

ing protocol on different scanners from the same manufacturer would have comparable image quality and, therefore, could be grouped together for the analysis.

Manual identification of lesions was used to initialize the algorithm, and manual segmentation was used for the training and validation of the proposed method. Both tasks were performed with software for medical image analysis (Jim Version 6.0; Xinapse Systems, Colchester, United Kingdom). Manual identification and segmentation of lesions was performed by an experienced rater with 7 years' experience in MS lesion segmentation. In the case of doubt in lesion identification, a senior rater was consulted.

For image standardization (step 1), a group of 12 patients (2 from each center) with a low lesion load was selected. A high lesion load was avoided because a high number of hyperintense lesions could relevantly alter the shape of the image intensity histograms and affect the estimation of the standard parameters. For computation of the standard parameters, scans from healthy patients would be preferable, but these are not always available in a clinical environment.

Because the method required a training step, the selection of a reliable set representative of the entire dataset, in terms of lesion load and sample size for each MR manufacturer, was investigated. Patients were grouped by scanner manufacturer. A threshold function (step 3) was calculated for each group and steadily decreased the number of patients included in the training set. First, all patients were included, and then at each step, 3 patients were removed from each group. The choice of which patients to remove was made by attempting to maintain a balanced lesion load (ie, a variation within ±10%) across the 3 different MR manufacturers. This analysis was performed to assess the relationship between the sample size and the threshold function for each MR scanner manufacturer to lead to a proper selection of the training set for this method. A straight line was fitted to the seed intensity values plotted against the optimal threshold values, obtaining the threshold function for the initial region growing. The linear relationship between the normalized seed intensity and the optimal threshold values was empirically obtained.

To evaluate the sensitivity of the segmentation results to the slope of the threshold function, 17 simulated threshold functions were generated to initialize the region growing. These functions consisted of a straight line passing from a common point (described in detail in the Results) with a slope varying from 0.1 to 0.9 in steps of 0.05 (a wider range of values than that found in the training). Lesion segmentation was performed without the refinement step to evaluate only the effect of a different slope on the results.

The optimal threshold function was selected from the simulated ones by maximizing the dice similarity coefficient between the manually and automatically outlined lesions (as described below).

Moreover, we investigated whether the 2 parameters identifying the optimal training straight line could be estimated directly from the image to be segmented, thus avoiding the need of a training procedure implying the acquisition of an extra group of patients and the manual lesion segmentation.

Because we found that training based on manual segmentation

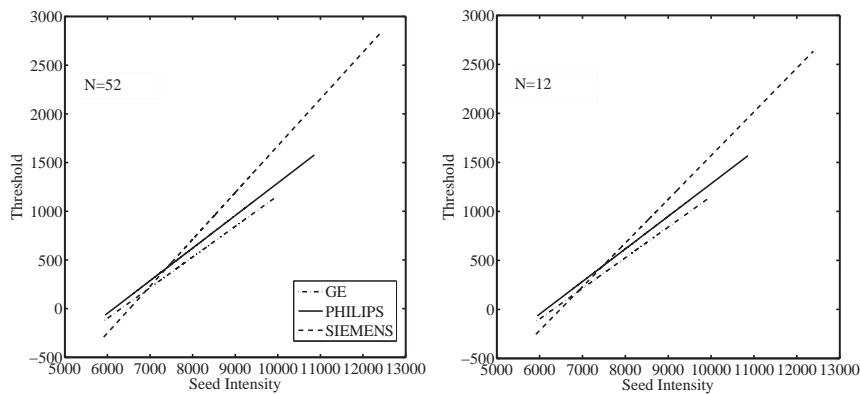


**FIG 1.** Threshold functions obtained after the training step for each different scanner manufacturer at the decreasing of the training set sample sizes (ie, number of patients included) as indicated. It is possible to observe that with decreasing sample size, the linear regression functions did not modify their trends.

could be avoided (see Results), the entire dataset could be used as a test dataset, and the optimized procedure was applied to the whole group of patients.

### Statistical Analysis

The root mean square error in lesion volume for the proposed method relative to the manual segmentation was computed. The root mean square error values, grouped by scanner manufacturer, were compared to evaluate any performance differences between MR manufacturers. It was assumed that the observations from the 3 manufacturer groups were independent of each other. The Wilcoxon-Mann-Whitney test was used to test for differences in errors between the groups. This is a nonparametric test of the null hypothesis (that 2 independent samples come from the same population) against an alternative hypothesis. The test was performed pair-wise between the 3 groups: test 1 was performed between the lesion-segmentation errors on the images acquired on Siemens scanners compared with Philips scanners; test 2 was between Siemens scanners and GE scanners; test 3 was between GE scanners and Philips scanners. The segmentations produced by the proposed method were compared with manual segmentations performed by an expert physician by using the dice similarity coefficient. Dice similarity coefficient values range from 0 to 1, where 0 corresponds to no overlap between the 2 segmentations and 1 corresponds to perfect overlap. The false-positive fraction, false-negative fraction, and true-positive fraction were computed for each lesion to indicate the percentage of voxels correctly or incorrectly classified as lesion by the method. The “ground truth” for assessing the true- and false-positive rates was the binary lesion mask obtained after manual segmentation, comparing individual lesions pixel-by-pixel between the manual and automatic mask.

### RESULTS

The threshold functions (plots of threshold value against seed intensity) showed a similar trend with decreasing of the number of patients included in the training set: as the sample size decreased, the fitted lines maintained a similar slope and passed through an approximately similar point (Fig 1). The seed intensity at this “common point” was found to be the intensity of the GM peak on the standardized histogram. This is because the image

standardization process fixed the GM peak for the PD-weighted images to the same intensity value. Thus, this value as seed point would produce similar thresholds during the training and after the fitting operation on the training set these points were interpolated, producing a single “common point” between the functions. Furthermore, on the y-axis, this point represents the intensity variation on the GM standard intensity distribution that discriminates the lesion intensity values, which mostly overlap with GM intensity values, from the surrounding tissue (WM).

The effect of a different slope of the threshold functions on the segmentation results was evaluated. The slope of the threshold function was varied between 0.1 and 0.9, and higher dice similarity coefficient scores were found (dice similarity coefficient >0.6) at higher values of slope (>0.7), though this improvement was not significant.

From those findings, the thresholds used in initial seed growing were expressed as:

$$T = m \times (I_{seed_i} - I_{GM}) + \sigma_{GM}$$

where  $T$  is the threshold for the region growing,  $m$  stands for slope (fixed to 0.9),  $I_{seed_i}$  is the seed intensity value for lesion  $i$ ; and  $I_{GM}$  and  $\sigma_{GM}$  were the intensity of the GM peak and the standard deviation of the GM distribution on the standard histogram, respectively. The equation was used to compute the threshold function, and then the method was performed without training on manual segmentation.

Comparison of data between the different scanners showed that there was no evidence that lesion-segmentation errors came from different distributions. The mean values of segmentation errors for each MR manufacturer were 1.99 mL for GE, 1.59 mL for Philips, and 1.86 mL for Siemens. The statistical test performed between the groups revealed no differences of segmentation performance between manufacturers (Test 1,  $P = .65$ ; Test 2,  $P = .44$ ; and Test 3,  $P = .30$ ).

The validation metrics were extracted for the lesion load of each patient, considering each lesion as a connected region in 3D space for the computation of its total volume. Fig 2 graphically reports the metrics evaluated for each patient over all lesions. The following were obtained after averaging the metrics over all patients: dice similarity coefficient = 0.62; root mean square error = 2 mL; true-positive fraction = 0.76; false-positive fraction = 0.36; and false-negative fraction = 0.22.

An example lesion-segmentation result is shown in Fig 3.

### DISCUSSION

Because manual segmentation is time-consuming and subject to inter- and intraobserver variability, automatic segmentation of MS lesions is an active research field with many proposals presented in recent years.<sup>5</sup> The method validated in this study has several advantages. First, it works on DE MR images. Most pro-

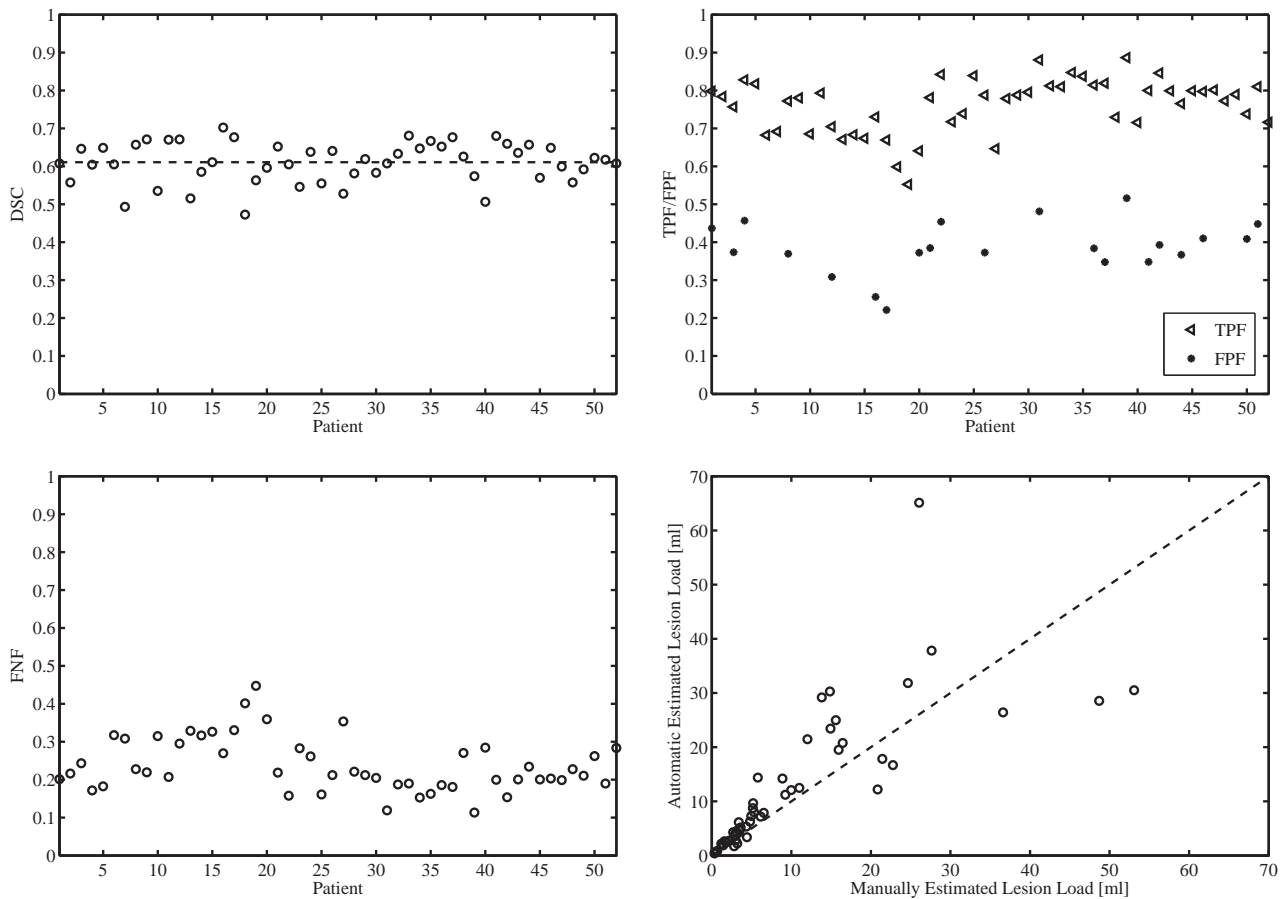


**FIG 2.** Dice similarity coefficient values (*top left*), mean true-positive fraction/false-positive fraction values (*top right*), and mean false-negative fraction values (*bottom left*) are shown for each patient. In the *bottom right*, a scatterplot to compare manual lesion load with automatic lesion load is shown. The *dashed line* is the line of identity.

posed methods segment lesions on FLAIR sequences that benefit from suppression of the CSF signal and better contrast between focal lesions and the surrounding background.<sup>7-9,14-16</sup> However, much data have been and are currently being acquired for research and clinical trials by using DE PD/T2-weighted images. Thus, with use of the proposed method, it should be possible to rapidly analyze these large sets of images. Second, despite the limitation of the manual identification of lesions by an expert physician, this initialization ensures the correct identification of all lesions and avoids the problem of the identification of entire false-positive lesions (because only possible misclassification of lesion pixels can occur). This is a common challenge for fully automatic lesion-segmentation methods, which tend to be affected by the image quality.<sup>4</sup> In the method proposed, we avoid this issue by maintaining manual identification of lesions and automating the segmentation task that is the most time-consuming operation. Some automatic lesion-segmentation tools with available code (LST, SLS, and Lesion-TOADS) expect FLAIR images as input. As a consequence, a comparison with our method would be unfair. Moreover, most proposed methods have been validated on a restricted number of cases and within single centers or simulated MR imaging acquisitions.<sup>5,17,18</sup> In addition, a validation of the method based on data provided by the MICCAI Grand Challenge workshop 2008 would be unfeasible because of the absence of a DE sequence in the dataset.<sup>6,19</sup> In this study, a validation of the

method against manual segmentation in a multicenter context was presented, proving that the method was robust to scanner differences and that its performance was not dependent on MR software and hardware.

During an initial assessment of the size of the training set needed, it was found that the threshold functions extracted for the initial region-growing algorithm were not noticeably affected by including fewer patients, and there were no significant differences between the threshold functions computed from each scanner manufacturer group. Moreover, using the simulated threshold functions demonstrated that once their intersection point was found, changes to the slope introduced only a small nonsignificant improvement at higher values; thus, the most important feature of the threshold function was the crossing point of the lines, which was a result of the standardization process.

These results allowed us to find an expression for the threshold function used in the initial region-growing part of the algorithm, thus avoiding the training step by using manual segmentation. Because the segmentation results improved when using a higher slope of the threshold function, 0.9 was selected to allow the use of higher thresholds and a less restricted region-growing segmentation. This is because of the stop condition on the threshold value (see equation in the On-line Appendix): a higher threshold implies a higher difference between the seed point and the  $i$ -th pixel intensity value that stops the region growing, so a larger range of

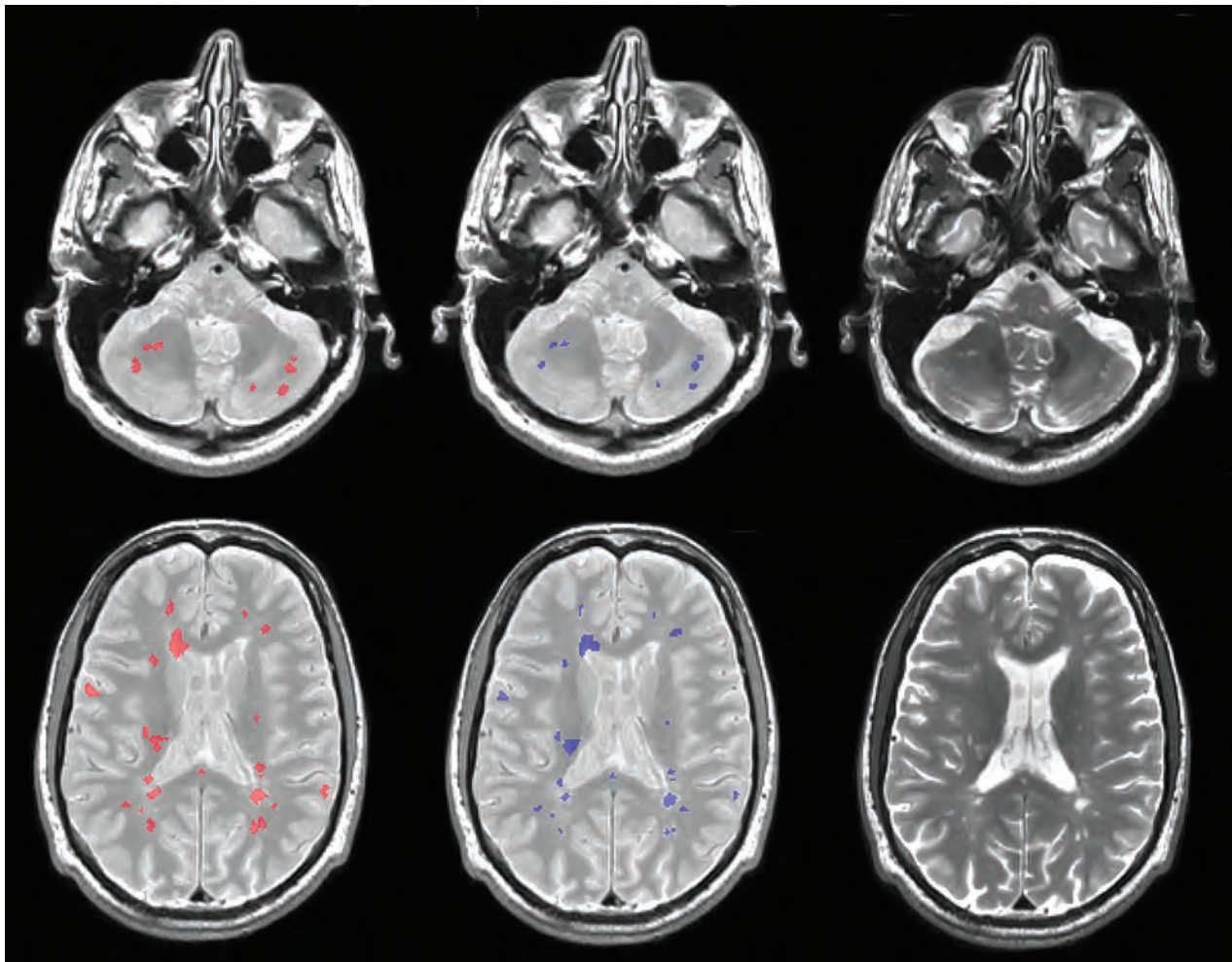


**FIG 3.** Example lesion segmentations for 2 patients (rows) from 2 different scanners by the proposed method (*red*) compared with the expert operator segmentation (*blue*). The corresponding T2-weighted images are shown in the right column.

intensities are classifiable as lesion (less restricted segmentation). This was made possible because we included an edge detection step in the segmentation that acts as a barrier to stop the region growing even if a too-high threshold is used. Because of noise or artifacts on the images, the 2 stop conditions were used in combination for a good result. However, using a high slope for the threshold function might generate a bias between lesions with higher and lower intensity values relative to the crossing point of the straight line; that is, with a high slope, lower-intensity lesions would have lower threshold values, causing a more restricted region growing, whereas the opposite would be observed for higher-intensity lesions. This bias was avoided by applying a threshold refinement step, in which a more robust threshold is computed to restart the region growing, thus correcting too-restricted segmentation caused by lower threshold values. Hence, using our equation to find the threshold function, we avoided the training step by using manual segmentation, making the applicability of the proposed technique easier in clinical settings. Regarding the possible bias between different lesion loads, it seemed that the difference between automatic and manual lesion load becomes larger with increasing lesion load (Fig 2). This could be explained by the fact that a high lesion load could be caused by many small lesions or a few but very large lesions. In the first case, a difference of a few

pixels between the automatic and manual-segmented lesion (that is visually undetectable), summed up for all lesions, could result in a relevant difference in the quantification of lesion load between the 2 methods. In the second case, a difference of more pixels (for example at lesion border [again, visually undetectable]) could result in a relevant difference in lesion-load quantification between manual and automatic segmentation.

The stability and robustness of the method was assessed when working on data from different scanner manufacturers. The initial step in image analysis standardizes the intensity values between the PD-weighted MR imaging scans, allowing the use of fixed intensity parameters. The method was not significantly affected by possible hardware or software-dependent differences between MR imaging scanners.

Lesion segmentation performed with the new method showed good agreement with the ground truth (dice similarity coefficient = 0.62 and true-positive fraction = 0.76). The difference between the lesion load estimated using the proposed method and with manual segmentation gave a mean error of 19% (root mean square error = 2 mL), with low misclassification of lesion voxels (false-negative fraction = 0.22 and false-positive fraction = 0.36).

The evidence of the benefit for operator time required to segment lesions was demonstrated in our previous work.<sup>11</sup> In the

current study, the important reduction in time for the segmentation task was confirmed. For the lesion loads we considered, the average time for manual lesion segmentation of a single MR imaging scan was approximately 50 minutes for the segmentation task only, whereas for the new method, the average time for the same task was approximately 55 seconds, a reduction in time of approximately 98.2%.

In cases where lesions have intensity similar to that of CSF, the method gives segmentations that extend beyond the real boundary of the lesions. This happened in very few cases in this study and was mainly for periventricular lesions. It may be possible to improve this in the future by introducing further information about lesions, perhaps by using other MR tissue contrasts such as coregistered T1-weighted images. This improvement also could be useful for a more certain lesion boundary delineation in case of diffuse lesions in patients with high lesion load. Notably, the method did not encounter difficulties in segmenting subcortical/cortical lesions. This is because of the edge-detection step using the high-pass filter; the borders of subcortical/cortical lesions were well defined with respect to the surrounding tissue, different from what happened to periventricular lesions that had intensity values similar to the CSF on DE scans.

The method implemented is based on a 2D region-growing approach because it started from initial seed points positioned in 2D. 2D implementation was chosen because images were not acquired by using 3D MR images; therefore, resolution along the z-axis (section thickness) is lower than the axial one. The adaptation of the method to a 3D approach could be a future extension when 3D MR images are available to reduce the interaction time of the expert. Similarly, the applicability of the method on different images (eg, pre- and postcontrast T1-weighted sequences) would require some modifications and retraining of the method for the new contrasts.

The algorithm relies on manual identification of lesions, which must be performed by an expert operator, and the most time-consuming task (ie, outlining each lesion) is fully automated. However, it would be preferable to avoid all manual intervention to remove any operator dependence. In the future, it might be possible to fully automate T2-hyperintense lesion segmentation by using other MR imaging contrasts such as FLAIR or double inversion recovery sequences.<sup>20</sup> Finally, the reproducibility of the method should be evaluated in longitudinal studies.

## CONCLUSIONS

In this study, we evaluated the performance and stability of a semiautomatic method for MS lesion segmentation by using DE data acquired from different centers with different scanners compared with manual segmentation by an expert physician. The method proved to be robust and stable when working on data from different scanner manufacturers. It emerged also that no center-specific training of the algorithm was required, making the method suitable for direct use on a wide range of images. Adoption of the method should lead to improved reliability and less operator time required for image analysis in research and clinical trials in MS.

Disclosures: Maria Assunta Rocca—RELATED: Grant: Fondazione Italiana Sclerosi Multipla (FISM2013/s/1)\*; UNRELATED: Grants/Grants Pending: Italian Ministry of Health and Fondazione Italiana Sclerosi Multipla\*; Payment for Lectures (including service on speakers bureaus): Biogen Idec, Novartis, Genzyme, Teva Pharmaceutical Industries. Mark A. Horsfield—UNRELATED: Employment: Xinapse Systems, Comments: full-time employer; Stock/Stock Options: Xinapse Systems. Nicola De Stefano—UNRELATED: Board Membership: Biogen Idec, Merck Serono SA, Novartis; Consultancy: Schering, Biogen Idec, Teva Pharmaceutical Industries, Novartis, Genzyme, Merck; Grants/Grants Pending: Italian Association of Multiple Sclerosis,\* Novartis\*; Payment for Lectures (including service on speakers bureaus): Schering,\* Biogen Idec,\* Teva Pharmaceutical Industries,\* Novartis,\* Genzyme,\* Merck Serono SA,\* Hugo Vrenken—UNRELATED: Grants/Grants Pending: Pfizer,\* Novartis,\* Merck-Serono,\* Teva,\* Dutch MS Research Foundation\*; Payment for Lectures (including service on speakers bureaus): Novartis,\* Massimo Filippi—RELATED: Grant: Fondazione Italiana Sclerosi Multipla (FISM2013/s/1)\*; UNRELATED: Board Membership: Teva Pharmaceutical Industries; Consultancy: Biogen Idec, Novartis, and Teva Pharmaceutical Industries; Grants/Grants Pending: Biogen Idec,\* Teva Pharmaceutical Industries,\* Novartis,\* Italian Ministry of Health,\* Fondazione Italiana Sclerosi Multipla,\* Cure PSP,\* Alzheimer's Drug Discovery Foundation (ADDF),\* the Jacques and Gloria Gossweiler Foundation (Switzerland),\* and ARiSLA (Fondazione Italiana di Ricerca per la SLA)\*; Payment for Lectures (including service on speakers bureaus): Biogen Idec, Excemed, Novartis, and Teva Pharmaceutical Industries; Other: Springer, Comments: editor-in-chief of the *Journal of Neurology*. \*Money paid to the institution.

## REFERENCES

- Filippi M, Rocca MA, De Stefano N, et al. **Magnetic resonance techniques in multiple sclerosis: the present and the future.** *Arch Neurol* 2011;68:1514–20 CrossRef Medline
- Johnston B, Atkins MS, Mackiewicz B, et al. **Segmentation of multiple sclerosis lesions in intensity corrected multispectral MRI.** *IEEE Trans Med Imaging* 1996;15:154–69 CrossRef Medline
- Sajja BR, Datta S, He R, et al. **Unified approach for multiple sclerosis lesion segmentation on brain MRI.** *Ann Biomed Eng* 2006;34:142–51 CrossRef Medline
- Van Leemput K, Maes F, Vandermeulen D, et al. **Automated segmentation of multiple sclerosis lesions by model outlier detection.** *IEEE Trans Med Imaging* 2001;20:677–88 CrossRef Medline
- García-Lorenzo D, Francis S, Narayanan S, et al. **Review of automatic segmentation methods of multiple sclerosis white matter lesions on conventional magnetic resonance imaging.** *Med Image Anal* 2013;17:1–18 CrossRef Medline
- Styner M, Lee J, Chin B, et al. **3D segmentation in the clinic: a grand challenge II: MS lesion segmentation.** *MIDAS Journal* 2008. <http://hdl.handle.net/10380/1509>
- García-Lorenzo D, Prima S, Arnold DL, et al. **Trimmed-likelihood estimation for focal lesions and tissue segmentation in multi-sequence MRI for multiple sclerosis.** *IEEE Trans Med Imaging* 2011;30:1455–67 CrossRef Medline
- Khayati R, Vafadust M, Towhidkhal F, et al. **Fully automatic segmentation of multiple sclerosis lesions in brain MR FLAIR images using adaptive mixtures method and Markov random field model.** *Comput Biol Med* 2008;38:379–90 CrossRef Medline
- Souplet J, Lebrun C, Ayache N, et al. **An automatic segmentation of T2-FLAIR multiple sclerosis lesions.** *MIDAS Journal* 2008. <http://hdl.handle.net/10380/1451>
- Erbayat Altay E, Fisher E, Jones SE, et al. **Reliability of classifying multiple sclerosis disease activity using magnetic resonance imaging in a multiple sclerosis clinic.** *JAMA Neurol* 2013;70:338–44 CrossRef Medline
- Storelli L, Pagani E, Rocca MA, et al. **A semi-automatic method for segmentation of multiple sclerosis lesions on dual-echo magnetic resonance images.** *Lect Notes Comput Sci* 2016;9556:80–90 CrossRef
- Schnack HG, van Haren NE, Hulshoff Pol HE, et al. **Reliability of brain volumes from multicenter MRI acquisition: a calibration study.** *Hum Brain Mapp* 2004;22:312–20 CrossRef Medline
- Polman CH, Reingold SC, Banwell B, et al. **Diagnostic criteria for multiple sclerosis: 2010 revisions to the McDonald criteria.** *Ann Neurol* 2011;69:292–302 CrossRef Medline

14. Subbanna N, Precup D, Arnold D, et al. **IMaGe: iterative multilevel probabilistic graphical model for detection and segmentation of multiple sclerosis lesions in brain MRI.** *Inf Process Med Imaging* 2015;24:514–26 Medline
15. Jain S, Sima DM, Ribbens A, et al. **Automatic segmentation and volumetry of multiple sclerosis brain lesions from MR images.** *Neuroimage Clin* 2015;8:367–75 CrossRef Medline
16. Mechrez R, Goldberger J, Greenspan H. **Patch-based segmentation with spatial consistency: application to MS lesions in brain MRI.** *Int J Biomed Imaging* 2016;2016:7952541 CrossRef Medline
17. Freifeld O, Greenspan H, Goldberg J. **Multiple sclerosis lesion detection using constrained GMM and curve evolution.** *Int J Biomed Imaging* 2009;2009:715124 CrossRef Medline
18. Galimzianova A, Pernuš F, Likar B, et al. **Stratified mixture modeling for segmentation of white-matter lesions in brain MR images.** *Neuroimage* 2016;124:1031–43 CrossRef Medline
19. Strumia M, Schmidt FR, Anastasopoulos C, et al. **White matter MS-lesion segmentation using a geometric brain model.** *IEEE Trans Med Imaging* 2016;35:1636–46 CrossRef Medline
20. Veronese E, Calabrese M, Favaretto A, et al. **Automatic segmentation of gray matter multiple sclerosis lesions on DIR images.** *IFMBE Proc* 2014;41:241–44 CrossRef



# Ataxia Severity Correlates with White Matter Degeneration in Spinocerebellar Ataxia Type 7

C.R. Hernandez-Castillo, I. Vaca-Palomares, F. Barrios, L. Martinez, M.-C. Boll, and J. Fernandez-Ruiz



## ABSTRACT

**BACKGROUND AND PURPOSE:** There is a scarcity of information on the effect of white matter degeneration in patients with spinocerebellar ataxia type 7. Therefore, we investigated the WM integrity in a large group of patients with spinocerebellar ataxia type 7 by using Tract-Based Spatial Statistics.

**MATERIALS AND METHODS:** Thirty-three patients with a molecular diagnosis of spinocerebellar ataxia type 7 and their age- and sex-matched healthy controls participated in this study. The patients' ataxia severity was evaluated with the Scale for the Assessment and Rating of Ataxia. Voxelwise analyses of diffusion metrics, including fractional anisotropy and mean diffusivity, were performed with Tract-Based Spatial Statistics. The correlation between WM abnormalities and ataxia severity was then calculated.

**RESULTS:** Tract-Based Spatial Statistics analysis revealed WM abnormalities in the cerebellum and the cerebellar peduncles, as well as in other major cortical and subcortical pathways. Further analysis between the Scale for the Assessment and Rating of Ataxia score and WM mean diffusivity showed significant associations only in key areas related to motor control and visuospatial processing, including the cerebellar WM, the middle occipital WM, the superior cerebellar peduncle, and bilateral anterior thalamic radiation. No significant associations between fractional anisotropy and the Scale for the Assessment and Rating of Ataxia were found.

**CONCLUSIONS:** These results suggest a significant contribution of local cerebellar and cerebellar-midbrain connections to ataxic impairment in spinocerebellar ataxia type 7. The results also suggest an involvement of cortical WM abnormalities including tracts within the occipital and frontal cortices. These findings contribute to a more comprehensive view of the clinical impact of the white matter degeneration in spinocerebellar ataxia type 7.

**ABBREVIATIONS:** FA = fractional anisotropy; MD = mean diffusivity; SARA = Scale for the Assessment and Rating of Ataxia; SCA = spinocerebellar ataxia; SCA7 = spinocerebellar ataxia type 7; TBSS = Tract-Based Spatial Statistics

Spinocerebellar ataxia type 7 (SCA7) is an autosomal dominant cerebellar ataxia caused by a mutation consisting in the expansion of the cytosine-adenine-guanine trinucleotide in the codon region of the chromosome 3p21, encoding the protein ataxin 7.<sup>1</sup>

SCA7 is considered one of the rarest forms of genetic autosomal dominant cerebellar ataxia.<sup>2</sup> Clinically, SCA7 is characterized by a combination of cerebellar ataxia and macular degeneration and is the only spinocerebellar ataxia that manifests in permanent blindness.<sup>3,4</sup> Furthermore, patients may eventually develop other neurologic deficits, including loss of manual dexterity, speech dysarthria, dysphagia, and eye movement abnormalities.<sup>2</sup> A number of neuropathologic studies have documented the anatomic consequences of the neurodegenerative process. These include severe degeneration of the cerebellar cortex and other cortical regions.<sup>5,6</sup>

MR imaging techniques such as diffusion tensor imaging can produce high-resolution structural images of white matter tracts. On the basis of the measurement of water diffusion properties, DTI allows quantifying the tissue microstructure and inferring its integrity.<sup>7</sup> This MR imaging technique also enables mapping of white matter tract changes across the life span and alterations in neurologic disorders, becoming an important tool in the study of neurodegenerative diseases.<sup>8,9</sup> Diffusion properties include mean

Received March 28, 2016; accepted after revision May 26.

From the Consejo Nacional de Ciencia y Tecnología-Instituto de Neuroetología (C.R.H.-C.), Universidad Veracruzana, Veracruz, Mexico; Departamento de Fisiología (I.V.-P., J.F.-R.), Facultad de Medicina, and Instituto de Neurobiología (F.B.), Universidad Nacional Autónoma de México, Mexico City, Mexico; and Departamento de Neurogenética y Biología Molecular (L.M.) and Laboratorio de Investigación Clínica (M.-C.B.), Instituto Nacional de Neurología y Neurocirugía, "Manuel Velasco Suárez," Mexico City, México.

This work was supported by Consejo Nacional de Ciencia y Tecnología grant 220871 and Universidad Nacional Autónoma de México grant PAPIIT IN214716 to J.F.-R.

Please address correspondence to Juan Fernandez-Ruiz, PhD, Departamento de Fisiología, Facultad de Medicina, Universidad Nacional Autónoma de México, UNAM, Av. Universidad 3000, Coyoacán, Distrito Federal, México, 04510; e-mail: jfr@unam.mx

Indicates open access to non-subscribers at [www.ajnr.org](http://www.ajnr.org)

<http://dx.doi.org/10.3174/ajnr.A4903>

diffusivity (MD) (also referred to as apparent diffusion coefficient) and fractional anisotropy (FA). In neurodegenerative diseases including spinocerebellar ataxias (SCAs), both MD and FA have gained widespread acceptance as sensitive indicators for quantifying microstructural damage to white matter, showing the

associations between the white matter integrity and behavioral impairment in some cases.<sup>6,10-13</sup> Among several studies using diffusion measurements, only a preliminary study has explored the white matter integrity in a small group of patients with SCA7,<sup>6</sup> reporting significant FA decreases that correlate with the number of years passed from the onset of symptoms. However, the contribution of the degeneration of projection fibers to the patients' impairments was not explored, possibly due to the small number of subjects. To test this hypothesis, we explored the relationship between ataxia severity and WM metrics that result from the statistical analysis of diffusion tensor imaging in a larger cohort of patients with SCA7.

**Table 1: Demographic information of the SCA7 group**

ID	Sex	Age (yr)	Years from Onset	MMSE	MoCA	SARA
P01	F	21	1	26	NC	4
P02	M	20	1	29	NC	4
P03	F	68	1	24	NC	6
P04	F	18	4	27	NC	7
P05	F	35	6	26	NC	8.5
P06	F	44	6	26	16	9
P07	F	64	13	28	12	9.5
P08	M	44	4	24	18	11
P09	F	22	2	26	NC	11
P10	M	52	7	26	16	12
P11	F	45	7	26	21	12
P12	M	23	3	24	27	12.5
P13	M	47	6	26	14	13
P14	M	25	4	26	13	14
P15	M	64	10	26	15	14.5
P16	M	38	13	27	18	14.5
P17	F	43	21	26	NC	15
P18	M	35	14	26	9	16
P19	M	60	6	26	13	16
P20	M	30	6	25	12	16
P21	M	34	10	28	NC	17
P22	M	30	5	26	NC	17
P23	F	32	6	27	NC	19
P24	M	18	8	26	16	19.5
P25	F	40	13	25	NC	23
P26	M	54	6	25	NC	24
P27	M	61	7	22	NC	25
P28	M	29	7	21	17	25
P29	F	40	21	22	18	27
P30	F	39	23	25	18	27
P31	F	42	17	23	15	29.5
P32	M	19	7	22	10	29.5
P33	F	51	8	26	18	30

**Note:**—MMSE indicates Mini-Mental State Examination; MoCA, Montreal Cognitive Assessment; NC, not completed; ID, identification.

## MATERIALS AND METHODS

### Subjects

Thirty-three patients with a molecular diagnosis of SCA7 were invited to participate in this study (15 right-handed women; mean age,  $39.0 \pm 14.6$  years). The Scale for the Assessment and Rating of Ataxia (SARA)<sup>14</sup> was used as a semiquantitative valuation of movement impairment, comprising 8 items related to gait, stance, sitting, speech, finger-chase test, nose-finger test, fast alternating movements, and the heel-shin test.<sup>15</sup> Extended information about the SCA7 group can be found in Table 1. Thirty-three age- and sex-matched controls (15 right-handed women; mean age,  $41.7 \pm 13.8$  years) participated in the study. The control group declared that they did not have any history of neurologic or psychiatric disorders. All procedures were in accordance with the ethical standards of the Declaration of Helsinki of 1975 and the applicable revisions at the time of the investigation. Therefore, the committees on human experimentation of the Universidad Nacional Autónoma de México specifically approved this study. All participants gave their written informed consent before entering the study.

### Image Acquisition

Images were acquired by using a 3T Achieva MR imaging scanner (Philips Healthcare, Best, the Netherlands). The study included the acquisition of a structural high-resolution volume and diffu-

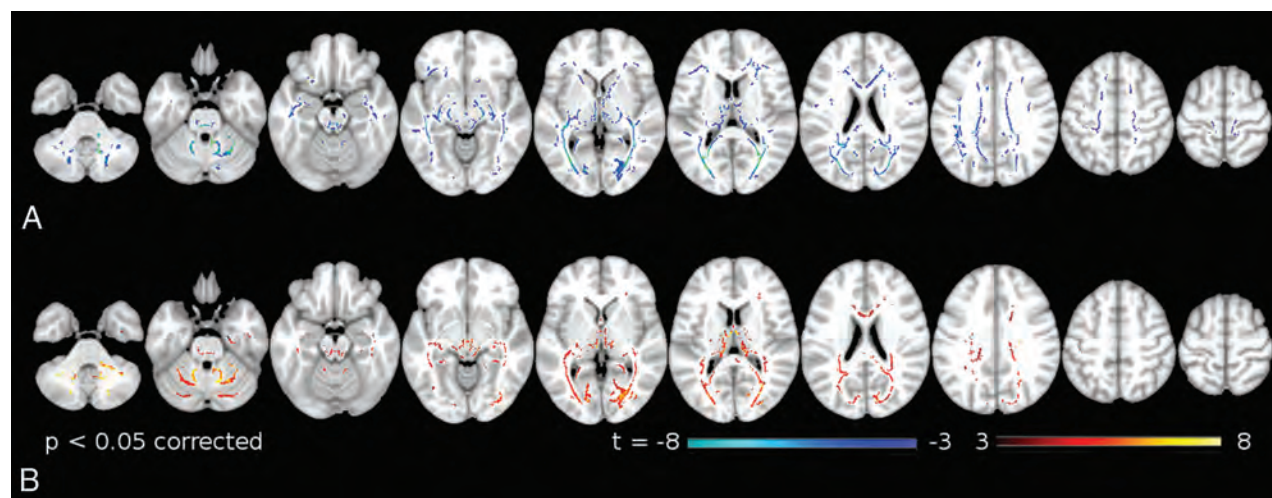


**FIG 1.** TBSS significant differences in diffusion measurements between patients with SCA7 and healthy controls. A, Fractional anisotropy. B, Mean diffusivity. Warm and cold colors indicate an increase and decrease in these measures in patients with SCA7, respectively.

**Table 2: Significant group differences in fractional anisotropy between patients with SCA7 and healthy controls<sup>a</sup>**

Anatomic Region	Voxels	T-Value	X	Y	Z
Right superior cerebellar peduncle	1797	18.9	7	-47	-28
Left corticospinal tract	1009	11	-13	-56	-28
Left anterior corona radiata	733	6.86	-26	31	11
Body of corpus callosum	327	4.04	-6	13	22
Right corticospinal tract	262	11	13	-50	-43
Left uncinate fasciculus	253	6.27	-21	18	-12
Left superior longitudinal fasciculus	180	5.08	-10	27	49
Left inferior longitudinal fasciculus	177	5.75	-40	-47	-13
Right superior longitudinal fasciculus	162	4.53	36	-13	34
Left anterior limb of the internal capsule	134	5.07	-20	17	5
Left cingulate WM	131	6.36	-6	3	34
Left inferior fronto-occipital fasciculus	121	4.89	-16	35	33
Left superior longitudinal fasciculus	114	4.75	-44	-41	13
Right superior longitudinal fasciculus	112	4.22	51	-7	23

<sup>a</sup> Coordinates are in millimeters in Montreal Neurological Institute space. Labels are from the Johns Hopkins University white matter atlas.

**Table 3: Significant group differences in mean diffusivity between patients with SCA7 and healthy controls<sup>a</sup>**

Anatomic Region	Voxels	T-Value	X	Y	Z
Right middle cerebellar peduncle	2712	11.1	26	-51	-37
Left middle cerebellar peduncle	2047	12.6	-26	-48	-38
Left anterior thalamic radiation	911	5.12	-3	-11	11
Right inferior fronto-occipital fasciculus	855	5.19	19	-83	16
Left inferior longitudinal fasciculus	628	4.21	-14	-81	2
Left posterior thalamic radiation	350	3.23	-35	-44	8
Right inferior longitudinal fasciculus	182	4.39	37	-74	2
Right cingulate WM	141	3.59	27	-45	-2
Right posterior corona radiata	112	5.22	29	-34	19
Right anterior thalamic radiation	108	4.16	1	-20	-10
Splenium of corpus callosum	104	4.91	19	-50	22
Left cingulate WM	101	3.58	-28	-50	-1
Left inferior longitudinal fasciculus	100	3.38	-17	-77	15

<sup>a</sup> Coordinates are in millimeters in Montreal Neurological Institute space. Labels are from the Johns Hopkins University white matter atlas.

sion tensor imaging. For detailed acquisition parameters, please see Hernandez-Castillo et al.<sup>11</sup>

### Diffusion Tensor Preprocessing

The FSL software (<http://www.fmrib.ox.ac.uk/fsl>) was used to process and analyze the raw DTI data.<sup>16</sup> First, we corrected the eddy current effects; second, the eddy-corrected diffusion-weighted images were spatially normalized by using a rigid-body transformation. Last, the diffusion tensor model was adjusted to generate the fractional anisotropy maps for each participant.

### Tract-Based Spatial Statistics

The statistical analysis was performed in a voxelwise manner by using the standard Tract-Based Spatial Statistics (TBSS; <http://fsl.fmrib.ox.ac.uk/fsl/fslwiki/TBSS>) methodology reported elsewhere.<sup>17</sup> The TBSS procedure had the following steps: All subjects' FA data were aligned into a 1-mm isotropic FA target image in standard space (FMRIB58\_FA standard space image; [http://fsl.fmrib.ox.ac.uk/fsl/fslwiki/FMRIB58\\_FA](http://fsl.fmrib.ox.ac.uk/fsl/fslwiki/FMRIB58_FA)) by using the FMRIB Nonlinear Registration Tool (FNIRT; <http://fsl.fmrib.ox.ac.uk/fsl/fslwiki/FNIRT>).<sup>18</sup> Next, the mean FA image was calculated and thinned to create a mean FA skeleton, which represented the centers of all tracts common to the group. This process had 2 steps: 1) averaging the warped FA images, and then 2) thresholding at FA > 0.2. Each subject's aligned FA data were then projected onto

this skeleton. Using the same nonlinear registration derived from the FA analysis, we projected MD data onto the skeleton before voxelwise statistical analysis across subjects.<sup>17</sup>

Differences in DTI (FA, MD) parameters between patients with SCA7 and healthy controls were assessed by using a permutation-based nonparametric independent 2-sample *t* test (FSL Randomize tool; <http://fsl.fmrib.ox.ac.uk/fsl/fslwiki/Randomise/>).<sup>19</sup> Age was included in the design matrix as a covariate of no interest. Correction for multiple comparisons was assessed by using threshold-free cluster enhancement.<sup>20</sup> We generated 5000 permutations of the data, producing uncorrected and family-wise error-corrected statistical maps. Only those voxels surviving this correction at a *P* value < .05 showed a significant group difference. In a second analysis, we explored the correlation between the ataxia severity and WM measurements (FA and MD). We performed a 1-sample *t* test of the SCA7 group for FA and MD independently, which included the SARA score in the design matrix.

## RESULTS

TBSS group comparison revealed significant FA decreases in patients with SCA7 (Fig 1A and Table 2) in the white matter

tracts, including the inferior/middle/superior cerebellar peduncles, the bilateral internal/external capsule, the bilateral corona radiata, the bilateral optical radiation, and the occipital/temporal/frontal white matter.

TBSS group comparison revealed significant MD increases in patients with SCA7 (Fig 1B and Table 3) in the cerebellar WM, including the medial lemniscus, the middle cerebellar peduncle, the optical radiations, the bilateral corona radiata, the posterior limbs of internal capsule, and the corticospinal tract.

We found associations between the patients' SARA scores and mean diffusivity in several abnormal WM tracts. Specifically, we found SARA associations with MD in the right middle occipital WM, stria terminalis, superior cerebellar peduncle, anterior cerebellar WM, superior longitudinal fasciculus, and the anterior thalamic radiation (Fig 2 and Table 4). No significant association was found between the SARA scores and FA.

## DISCUSSION

In this study, we used Tract-Based Spatial Statistics to assess the white matter abnormalities in a group of patients with SCA7 compared with matched healthy controls and the relationship between the white matter integrity and the ataxia severity in the patient group. Our results showed significant differences in FA

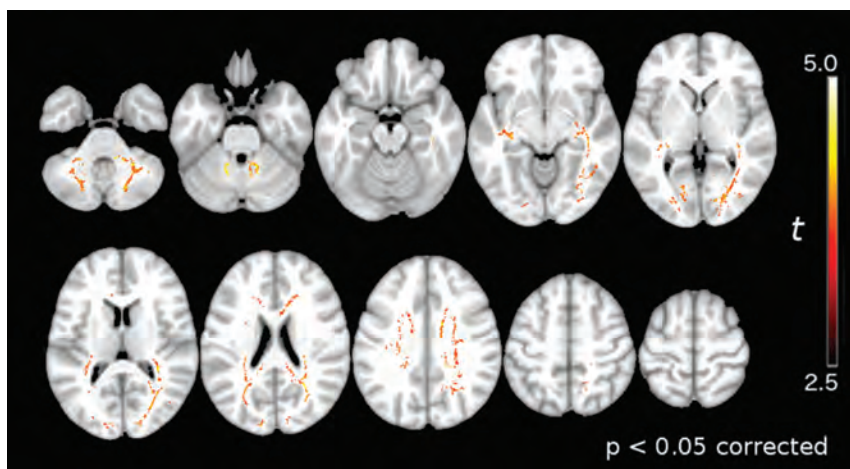


**FIG 2.** White matter regions where MD correlates with the SARA score in the SCA7 group. Warm colors indicate significant correlations between MD values and SARA scores.

**Table 4: White matter regions showing significant correlation between MD and the SARA score in the SCA7 group<sup>a</sup>**

Anatomic Region	Voxels	T-Value	X	Y	Z
Right inferior longitudinal fasciculus	6428	6.74	40	-74	6
Right superior cerebellar peduncle	1420	9.16	7	-43	-23
Left cerebellum anterior lobule	1014	7.03	-14	-53	-28
Left inferior fronto-occipital fasciculus	684	7.89	-19	-86	-9
Right anterior thalamic radiation	239	5.92	14	-60	49
Right superior longitudinal fasciculus	158	5.54	44	-34	34
Left anterior thalamic radiation	148	10.1	-3	-9	12

<sup>a</sup> Coordinates are in millimeters in Montreal Neurological Institute space. Labels are from the Johns Hopkins University white matter atlas.

and MD when comparing patients with SCA7 with healthy controls and a correlation between the ataxia severity and MD changes in the patient group.

Previous neuropathologic reports have shown loss of myelinated fibers in the cerebellar white matter, corpus callosum, red nucleus capsule, oculomotor nerve, lateral lemniscus, mesencephalic trigeminal tract, abducens nerve, trapezoid body, pontocerebellar fibers, pyramidal tract, internal arcuate and olivocerebellar fibers, cuneate, and gracile fascicles, as well as the spinocerebellar tracts.<sup>5,6</sup> Our results support those findings but also extend them by showing abnormalities in the occipital WM, the stria terminalis, and the thalamic radiations not previously reported. As expected, the cerebellar WM and the cerebellar peduncles showed a decrease in FA and an increase of MD, implying SCA7-related microstructural changes in the afferent and efferent projections of the cerebellum. The combination of white matter degeneration and gray matter loss in the cerebellum results in a variety of clinical motor impairments, including ataxia and extrapyramidal signs.<sup>21</sup> In the same way, the degeneration of the thalamic radiations affects the information flow between the cerebellum and the motor and frontal cortices, which might result in the loss of coordination and dexterity in this set of patients.

The most relevant finding of this study is the association of the white matter mean diffusivity and the ataxia severity in this group of patients. The higher correlation between MD and SARA was found in the white matter of the middle occipital gyrus, which is

involved in visual and spatial processing.<sup>22,23</sup> Similarly, the superior longitudinal fasciculus showed significant correlation, which suggests a malfunction in the projections between the occipital-to-frontal cortices, including the premotor areas. A failure of these pathways could affect the planning and action of visuospatial tasks, especially in this disease because it has been reported to show decreases in the functional connectivity between the occipital and motor cortices.<sup>24,25</sup> Future studies, including neuropsychological evaluation focused on visuospatial performance combined with ophthalmologic data, should be helpful in corroborating this hypothesis.

Other white matter regions showing significant correlation between the MD and SARA score were the superior cerebellar peduncles and the white matter in the anterior cerebellum. On the basis of the distribution of the neuropathologic changes in SCA7, this result was expected.<sup>5,6</sup> Several reports have shown that lesions in these regions can lead to motor incoordination and loss of movement dexterity.<sup>26</sup> Both the cerebellar peduncles and the anterior cerebellum

have been reported as degenerated in previous MR imaging studies in SCA2.<sup>6,24</sup> However, in previous studies, no significant correlations were found between the changes in the water diffusion properties and SARA scores, probably due to the small number of participants recruited.<sup>6</sup>

No significant correlations between FA and SARA were found. FA and MD are not equivalent measurements<sup>27,28</sup>; and as expected in our group comparison, FA and MD maps led to different results (Fig 1). In addition to MD and FA, other water diffusion properties such as axial diffusivity and radial diffusivity have been reported in previous studies, including SCA1, SCA2, and Friedreich ataxia.<sup>10,29</sup> In this work, we focused on the analyses of FA and MD because the other measurements are subcomponents of the apparent diffusion coefficient. Furthermore, several studies of patients with neurodegenerative diseases have suggested that MD is more useful and sensitive to neurodegeneration than the other measurements.<sup>8,9,30</sup>












## CONCLUSIONS

Our results show that specific changes in the diffusion properties of white matter resulting from the SCA7 mutation are associated with the severity of the ataxia. The distribution of the mean diffusivity abnormalities and its association with SARA scores suggest a disruption of information flow between motor-, visual-, and sensory-integration areas. Overall, these findings contribute to a better understanding of the neural basis of the symptomatology of patients with SCA7.

## REFERENCES

1. Garden GA, La Spada AR. **Molecular pathogenesis and cellular pathology of spinocerebellar ataxia type 7 neurodegeneration.** *Cerebellum* 2008;7:138–49 CrossRef Medline
2. Hugosson T, Gränse L, Ponjavic V, et al. **Macular dysfunction and morphology in spinocerebellar ataxia type 7 (SCA 7).** *Ophthalmic Genet* 2009;30:1–6 CrossRef Medline
3. Miller RC, Tewari A, Miller JA, et al. **Neuro-ophthalmologic features of spinocerebellar ataxia type 7.** *J Neuroophthalmol* 2009;29:180–86 CrossRef Medline
4. Michalik A, Martin JJ, Van Broeckhoven C. **Spinocerebellar ataxia type 7 associated with pigmentary retinal dystrophy.** *Eur J Hum Genet* 2004;12:2–15 CrossRef Medline
5. Masciullo M, Modoni A, Pomponi MG, et al. **Evidence of white matter involvement in SCA 7.** *J Neurol* 2007;254:536–38 CrossRef Medline
6. Alcauter S, Barrios FA, Diaz R, et al. **Gray and white matter alterations in spinocerebellar ataxia type 7: an in vivo DTI and VBM study.** *Neuroimage* 2011;55:1–7 CrossRef Medline
7. Mori S, Zhang J. **Principles of diffusion tensor imaging and its applications to basic neuroscience research.** *Neuron* 2006;51:527–39 CrossRef Medline
8. Acosta-Cabrero J, Williams GB, Pengas G, et al. **Absolute diffusivities define the landscape of white matter degeneration in Alzheimer's disease.** *Brain* 2010;133:529–39 CrossRef Medline
9. Della Nave R, Ginestroni A, Tessa C, et al. **Regional distribution and clinical correlates of white matter structural damage in Huntington disease: a tract-based spatial statistics study.** *AJNR Am J Neuroradiol* 2010;31:1675–81 CrossRef Medline
10. Della Nave R, Ginestroni A, Tessa C, et al. **Brain white matter damage in SCA1 and SCA2: an in vivo study using voxel-based morphometry, histogram analysis of mean diffusivity and tract-based spatial statistics.** *Neuroimage* 2008;43:10–19 CrossRef Medline
11. Hernandez-Castillo CR, Galvez V, Mercadillo R, et al. **Extensive white matter alterations and its correlations with ataxia severity in SCA 2 patients.** *PLoS One* 2015;10:e0135449 CrossRef Medline
12. Hernandez-Castillo CR, Vaca-Palomares I, Galvez V, et al. **Cognitive deficits correlate with white matter deterioration in spinocerebellar ataxia type 2.** *J Int Neuropsychol Soc* 2016;22:486–91 CrossRef Medline
13. Li H, Ma J, Zhang X. **Diffusion tensor imaging of spinocerebellar ataxia type 12.** *Med Sci Monit* 2014;20:1783–91 CrossRef Medline
14. Schmitz-Hübsch T, du Montcel ST, Baliko L, et al. **Scale for the assessment and rating of ataxia: development of a new clinical scale.** *Neurology* 2006;66:1717–20 CrossRef Medline
15. Weyer A, Abele M, Schmitz-Hübsch T, et al. **Reliability and validity of the scale for the assessment and rating of ataxia: a study in 64 ataxia patients.** *Mov Disord* 2007;22:1633–37 CrossRef Medline
16. Smith SM, Jenkinson M, Woolrich MW, et al. **Advances in functional and structural MR image analysis and implementation as FSL.** *Neuroimage* 2004;23:S208–19 CrossRef Medline
17. Smith SM, Jenkinson M, Johansen-Berg H, et al. **Tract-based spatial statistics: voxelwise analysis of multi-subject diffusion data.** *Neuroimage* 2006;31:1487–505 CrossRef Medline
18. Jenkinson M, Bannister P, Brady M, et al. **Improved optimization for the robust and accurate linear registration and motion correction of brain images.** *Neuroimage* 2002;17:825–41 CrossRef Medline
19. Nichols TE, Holmes AP. **Nonparametric permutation tests for functional neuroimaging: a primer with examples.** *Hum Brain Mapp* 2002;15:1–25 CrossRef Medline
20. Winkler AM, Ridgway GR, Webster MA, et al. **Permutation inference for the general linear model.** *Neuroimage* 2014;92:381–97 CrossRef Medline
21. Hernandez-Castillo CR, Galvez V, Diaz R, et al. **Specific cerebellar and cortical degeneration correlates with ataxia severity in spinocerebellar ataxia type 7.** *Brain Imaging Behav* 2016;10:252–57 CrossRef Medline
22. Renier LA, Anurova I, De Volder AG, et al. **Preserved functional specialization for spatial processing in the middle occipital gyrus of the early blind.** *Neuron* 2010;68:138–48 CrossRef Medline
23. Martínez A, Anllo-Vento L, Sereno MI, et al. **Involvement of striate and extrastriate visual cortical areas in spatial attention.** *Nat Neurosci* 1999;2:364–69 CrossRef Medline
24. Hernandez-Castillo CR, Alcauter S, Galvez V, et al. **Disruption of visual and motor connectivity in spinocerebellar ataxia type 7.** *Mov Disord* 2013;28:1708–16 CrossRef Medline
25. Hernandez-Castillo CR, Galvez V, Morgado-Valle C, et al. **Whole-brain connectivity analysis and classification of spinocerebellar ataxia type 7 by functional MRI.** *Cerebellum Ataxias* 2014;1:2 CrossRef Medline
26. Schmahmann JD. **Disorders of the cerebellum: ataxia, dysmetria of thought, and the cerebellar cognitive affective syndrome.** *J Neuropsychiatry Clin Neurosci* 2004;16:367–78 CrossRef Medline
27. Cosottini M, Giannelli M, Siciliano G, et al. **Diffusion-tensor MR imaging of corticospinal tract in amyotrophic lateral sclerosis and progressive muscular atrophy.** *Radiology* 2005;237:258–64 CrossRef Medline
28. Pierpaoli C, Barnett A, Pajevic S, et al. **Water diffusion changes in Wallerian degeneration and their dependence on white matter architecture.** *Neuroimage* 2001;13(6 pt 1):1174–85 CrossRef Medline
29. Mandelli ML, De Simone T, Minati L, et al. **Diffusion tensor imaging of spinocerebellar ataxias types 1 and 2.** *AJNR Am J Neuroradiol* 2007;28:1996–2000 CrossRef Medline
30. Vos SB, Jones DK, Jeurissen B, et al. **The influence of complex white matter architecture on the mean diffusivity in diffusion tensor MRI of the human brain.** *Neuroimage* 2012;59:2208–16 CrossRef Medline

# Geographic Differences in Endovascular Treatment and Retreatment of Cerebral Aneurysms

 A.S. Turk,  S.C. Johnston,  S. Hetts,  J. Mocco,  J. English,  Y. Murayama,  C.J. Prestigiacomo,  D. Lopes,  Y.P. Gobin,  K. Carroll, and  C. McDougall

## ABSTRACT

**BACKGROUND AND PURPOSE:** Comparing outcomes between endovascular aneurysm coiling trials can be difficult because of heterogeneity in patients and end points. We sought to understand the impact of geography on aneurysm retreatment in patients enrolled in the Matrix and Platinum Science Trial.

**MATERIALS AND METHODS:** Post hoc analysis was performed on data from the Matrix and Platinum Science trial. Patients were stratified as either North American or international. Baseline patient demographics, comorbidities, aneurysm characteristics, procedural complications, and clinical and angiographic outcomes were compared.

**RESULTS:** We evaluated 407 patients from 28 North American sites and 219 patients from 15 international sites. Patient demographics differed significantly between North American and international sites. Aneurysms were well occluded postprocedure more often at international than North American sites ( $P < .001$ ). Stents were used significantly more often at North American sites (32.7% [133 of 407]) compared with international sites (10.0% [22 of 219];  $P < .001$ ). At 455 days, there was no difference in the proportion of patients alive and free of disability ( $P = .56$ ) or with residual aneurysm filling ( $P = .10$ ). Ruptured aneurysms were significantly more likely to have been retreated at North American sites within the first year ( $P < .001$ ) and at 2 years ( $P < .001$ ). Among all patients for whom the treating physician believed there to be Raymond 3 aneurysm filling at follow-up, absolute rates of retreatment at international and North American sites were similar by 2-year follow-up.

**CONCLUSIONS:** Data from the Matrix and Platinum Science Trial demonstrate that aneurysm retreatment occurs with different frequency and at different times in different regions of the world. This trend has critical value when interpreting trials reporting short-term outcomes, especially when judgment-based metrics such as retreatment are primary end points that may or may not take place within the defined study follow-up period. Though these variations can be controlled for and balanced within a given randomized trial, such differences in practice patterns must be accounted for in any attempt to compare outcomes between different trials. Despite these differences, endovascular-treated intracranial aneurysms around the world have similar clinical outcomes.

The International Subarachnoid Aneurysm Trial<sup>1,2</sup> was the landmark prospective randomized trial demonstrating the safety and effectiveness of endovascular treatment of ruptured aneurysms compared with surgical clipping. More recently, results from the Barrow Ruptured Aneurysm Trial<sup>3</sup> further support

coiling as a treatment technique associated with good patient outcomes comparable with clipping in the setting of SAH. Moreover, the results of several recently published multinational randomized controlled trials<sup>4-6</sup> demonstrated ruptured and unruptured aneurysms can be safely and effectively treated by using various coil types. Many comparisons generalizing results of these various trials have been made. However, comparing outcomes between trials can be difficult and misleading because of different trial

Received February 2, 2016; accepted after revision May 5.

From the Departments of Radiology (A.S.T.) and Neurosurgery (A.S.T.), Medical University of South Carolina, Charleston, South Carolina; Clinical and Translational Science Institute (S.C.J.), University of California, San Francisco, San Francisco, California; Dell Medical School at The University of Texas at Austin (S.C.J.), Austin, Texas; Department of Radiology and Biomedical Imaging (S.H.), University of California, San Francisco School of Medicine, San Francisco, California; Department of Neurosurgery (J.M.), Icahn School of Medicine at Mount Sinai, New York, New York; California Pacific Medical Center (J.E.), San Francisco, California; Department of Neurosurgery (Y.M.), Jikei University Hospital, Tokyo, Japan; Department of Neurological Surgery (C.J.P.), University of Medicine and Dentistry of New Jersey, Newark, New Jersey; Department of Neurosurgery (D.L.), Rush University Medical Center, Chicago, Illinois; Department of Neurosurgery (Y.P.G.), Weill Cornell Medical College,

New York, New York; Stryker Corporation (K.C.), Fremont, California; and Department of Neurosurgery (C.M.), Barrow Neurological Institute, St. Joseph's Hospital and Medical Center, Phoenix, Arizona.

Please address correspondence to Aquilla S. Turk, III, DO, Departments of Radiology and Neurosurgery, Medical University of South Carolina, Charleston, SC 29425; e-mail: turk@musc.edu

<http://dx.doi.org/10.3174/ajnr.A4857>

**Table 1: Patient demographics**

Variable	Location, (n [%])		P Value
	North America	International	
Total patients	407	219	
No. of sites	28	15	
Female sex	309 (75.9%)	131 (59.8%)	<.001
Age > 55 yr	218 (53.6%)	88 (40.2%)	<.001
White	350 (86.0%)	158 (72.1%)	<.001
Current/previous smoker	261 (64.1%)	130 (59.4%)	.24
>1 cardiovascular risk factor	124 (30.5%)	33 (15.1%)	<.001
Hypertension	217 (53.3%)	83 (37.9%)	<.001
Hyperlipidemia/hypercholesterolemia	122 (30.0%)	34 (15.5%)	<.001
Diabetes	43 (10.6%)	11 (5.0%)	.02
Coronary disease	63 (15.5%)	10 (4.6%)	<.001
Prior cerebrovascular accident	54 (13.3%)	15 (6.8%)	.02
Hunt and Hess grade 3 or 4 in ruptured patients	38/115 (33.0%)	24/113 (21.2%)	.045

designs and patient populations.<sup>7</sup> Analyses of subgroups from different trials cannot overcome these problems.

The very low bleeding or rebleeding rates of treated aneurysms has led most trial investigators to use angiographic outcomes to compare device performance. However, there are no agreed-upon standards for acceptable angiographic outcomes. Recently, the value of target aneurysm recurrence was explored as a new clinically relevant composite end point in a large-scale multicenter randomized trial comparing outcomes of patients with intracranial saccular aneurysms treated with 2 different embolic coil types.<sup>4,8,9</sup> In this study, target aneurysm recurrence was defined as clinically relevant aneurysm recurrence resulting in target aneurysm re-intervention, rupture/rupture, and/or death from an unknown cause. The advantage of this end point is that it is definitive that the event has happened and that these events are of clear relevance to the patient. The disadvantage of these end points is the variability of the decision to retreat because physician judgment often varies with the training, economic incentives, and regulatory structure of the local health system.

Both angiographic assessments and the decision to retreat aneurysms are subjective, leaving tremendous opportunity for individual or regional factors to influence trial results. We sought to understand the impact of geography on aneurysm retreatment in patients randomized in the Matrix and Platinum Science Trial.

## MATERIALS AND METHODS

The Matrix and Platinum Science Trial was a randomized controlled trial of 626 intent-to-treat patients. The methodology and primary outcomes of this trial have been previously published.<sup>4</sup> Anticipating variability in retreatment rates across enrolling sites, the trial stratified randomization by both aneurysm rupture status and enrolling site. For this analysis, the Matrix and Platinum Science Trial data base was interrogated and all aneurysms divided into groups based on geographic location of the medical center where they were treated. All baseline patient demographics, including cardiovascular risk factors, were documented. Aneurysm location, rupture status, and characteristics were also evaluated. Angiographic and clinical outcomes were compared. An independent core radiology laboratory performed all angiographic analyses.

All patients in the Matrix and Platinum Science Trial were used for this analysis. For data dependent upon core laboratory

angiographic analysis, patients with unreadable images were excluded. Patients were categorized into 2 groups: North American and international sites (including sites in Europe, Australia, and China). Few patients were enrolled in Asia and Australia; therefore, they were combined with Europe to create the complete international cohort. Patients were further explored based on their baseline rupture status, comorbidities, and angiographic core laboratory evaluations. Retreatment rates within each subgroup were calculated and compared.

We used logistic regression modeling to answer our research questions: 1)

“What are the predictive characteristics of retreatment in ruptured and unruptured aneurysms?” and 2) “Are there differences in retreatment rates between geographies?” All baseline aneurysm characteristics and immediate postprocedure angiography readings by the core laboratory were first tested in univariate models to determine the association with the retreatment outcome. All potential covariates with a *P* value ≤ .10 in a univariate model were included in the covariate pool drawn upon during the stepwise multivariate model selection process. In the final model, only those covariates with a *P* value < .05 were retained. Finally, to control for potential site effect, we used a generalized linear mixed-effect model within the 2 subsets of baseline ruptured or unruptured cohorts. In this model, we specified “site” as the random effect so that retreatment rates were not assumed to be equal among sites and, therefore, we could estimate common odds ratios across sites. Geography and stent usage (for unruptured aneurysms) were forced as fixed effects.

Kaplan-Meier survival curves were constructed to evaluate the difference in days to first retreatment between North American and international patient subgroups. Separate curves were constructed for baseline ruptured and baseline unruptured patients. The log-rank test was used for the *P* value calculations of the difference between the 2 curves from 2 regions.

## RESULTS

Between March 2007 and October 2009, 626 patients were randomized into the Matrix and Platinum Science Trial at 43 sites in 11 countries. Among 407 North American patients enrolled at 28 sites, 115 had ruptured aneurysms and 292 had unruptured aneurysms. The 15 international sites treated 219 patients, of whom 113 had ruptured aneurysms and 106 had unruptured aneurysms. (Table 1). Approximately 95% of patients in both the North American and international subgroups had follow-up data available after 1 year (>275 days); follow-up data were available after 2 years (>640 days) for 81.0% and 84.5% of North American and international patients, respectively.

### Baseline Demographics

Patient demographics differed between North American and international groups, with the most significant differences being the

proportions of female patients with ruptured aneurysms, white patients, and patients with more than 1 cardiovascular risk factor (Table 1 and Table 2).

### Angiographic and Clinical Outcomes

Core laboratory occlusion assessment was performed by using the modified 3-point Raymond scale.<sup>10</sup> Immediately postprocedure, a higher proportion of patients treated at North American sites

had a Raymond score of 3 (residual aneurysm) compared with patients at international sites (43.5% [140 of 322] versus 26.5% [44 of 166];  $P < .001$ ). This higher proportion of postprocedure residual aneurysms among North American patients was observed in both ruptured (29.8% [28 of 94] versus 16.7% [13 of 78]) and unruptured (49.1% [112 of 228] versus 35.2% [31 of 88]) subgroups. However, the proportion of patients with a packing attenuation  $> 25\%$  was similar in North American (42.5% [173 of 407]) and international (38.4% [84 of 219]) groups. Stents were used more frequently in unruptured aneurysms treated in North American than international sites (44% versus 19%, respectively;  $P < .001$ ).

At 30 days, patients with ruptured aneurysms were more likely to have been discharged from North American sites than patients treated at international sites (85.2% [98 of 115] versus 66.4% [75 of 113];  $P < .001$ ).

At 455 days, there was no difference in the proportion of patients alive and free of disability among those with ruptured aneurysms (North American: 90.4% [94 of 104] versus international: 94.0% [94 of 100]) and unruptured aneurysms (North American: 95.4% [250 of 262] versus international: 97.0% [97 of 100]) and no significant difference in the proportion of patients with core laboratory adjudicated residual aneurysms (36.4% versus 28.7%;  $P = .10$ ). Ruptured aneurysms were more likely to have been retreated at North American sites compared with international sites (21.7% versus 4.4%;  $P < .001$ ), whereas there were no significant regional differences in retreatment rates among patients with unruptured aneurysms. Kaplan-Meier curves demonstrate no difference in freedom from retreatment in patients in the unruptured group and a sustained difference in patients in the ruptured group (Figure).

Multivariate analysis of ruptured aneurysms at 455 days demonstrated that geography (adjusted common odds ratio 6.2; 95% CI, 2.0–18.8;  $P < .001$ ), neck size  $\geq 4$  mm (adjusted common odds ratio 4.3; 95% CI, 1.6–11.5;  $P = .004$ ), and residual aneurysm on postprocedure angiogram (adjusted common odds ratio 7.2; 95% CI, 2.6–19.7;  $P < .001$ ) were the most significant predictors of retreatment (Table 3). For unruptured aneurysms at 455 days, dome size  $\geq 10$  mm (adjusted common odds ratio 4.1; 95% CI, 1.2–14.2;  $P = .025$ ) and residual aneurysm on postprocedure angiogram (adjusted common odds ratio 3.6; 95% CI, 1.1–12.4;  $P = .040$ ) were significant predictors of retreatment. Geography was not an independent predictor of retreatment in unruptured aneurysms.

Multivariate analysis of ruptured aneurysms at 820 days demonstrated that predictors of retreatment did not change from 455 days (Table 4). In the unruptured cohort, the only significant predictor of retreatment at 820 days was dome size  $\geq 10$  mm (adjusted common odds ratio 5.3; 95% CI, 1.6–17.7;  $P = .007$ ). Postprocedure angiographic results were no longer significant at 820 days.

### DISCUSSION

One of the most striking findings in this study is the significantly higher retreatment rate of aneurysms in North Amer-

**Table 2: Aneurysm characteristics**

Variable	Location, (n [%])		P Value
	North America	International	
Total patients	407	219	
Aneurysm size $> 10$ mm	85 (20.9%)	45 (20.5%)	.92
Posterior circulation aneurysm	65 (16.0%)	18 (8.2%)	$< .001$
Aneurysm neck width $\geq 4$ mm	159 (39.1%)	67 (30.6%)	.04
Ruptured aneurysm	115 (28.3%)	113 (51.6%)	$< .001$
Dome-to-neck ratio $< 1.5$	118 (29.0%)	53 (24.2%)	.20

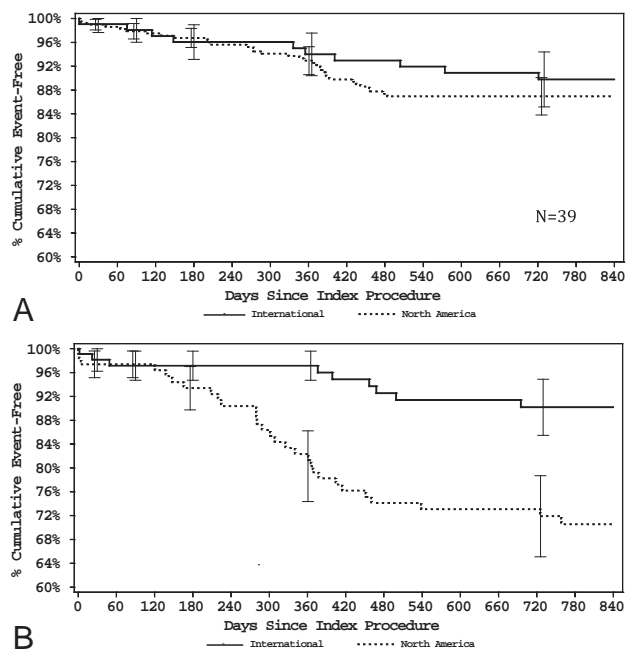


**FIGURE.** A, Unruptured aneurysms—freedom from retreatment. B, Ruptured aneurysms—freedom from retreatment.

**Table 3: Multivariate analysis: predictors of retreatment for 398 unruptured aneurysms**

Parameter	Follow-Up			
	455 Days		820 Days	
	OR (95% CI)	P Value	OR (95% CI)	P Value
Dome size ( $\geq 10$ mm vs $< 10$ mm)	4.12 (1.19–14.2)	.0253	5.28 (1.58–17.7)	.0071
Neuroform <sup>a</sup> used at index 1 vs 0	0.54 (0.20–1.44)	.2142	0.49 (0.19–1.23)	.1269
Neck size ( $\geq 4$ mm vs $< 4$ mm)	1.39 (0.47–4.13)	.5470	1.85 (0.71–4.83)	.2068
North America 1 vs 0	2.22 (0.69–7.14)	.1788	1.53 (0.57–4.08)	.3973
Core laboratory postprocedure Raymond scale 2 vs 1	1.13 (0.24–5.39)	.8759	0.79 (0.21–2.97)	.7313
Core laboratory postprocedure Raymond scale 3 vs 1	3.62 (1.06–12.4)	.0405	2.31 (0.84–6.38)	.1056
Aneurysm size ( $< 10$ mm vs $\geq 10$ mm)	0.40 (0.11–1.42)	.1576	0.62 (0.19–1.99)	.4212

**Note:**—OR indicates odds ratio.

<sup>a</sup> Stryker Neurovascular, Kalamazoo, Michigan.



**Table 4: Multivariate analysis: predictors of retreatment for 228 ruptured aneurysms**

Parameter	Follow-Up			
	455 Days		820 Days	
	OR (95% CI)	P Value	OR (95% CI)	P Value
Dome size ( $\geq 10$ mm vs $< 10$ mm)	7.45 (0.82–67.4)	.0737	2.63 (0.30–23.2)	.3831
Neuroform <sup>a</sup> used at index 1 vs 0	7.99 (1.40–45.5)	.0195	3.03 (0.42–22.1)	.2717
Neck size ( $\geq 4$ mm vs $< 4$ mm)	4.30 (1.60–11.5)	.0041	3.11 (1.14–8.52)	.0273
North America 1 vs 0	6.19 (2.04–18.8)	.0014	3.42 (1.28–9.15)	.0145
Core laboratory postprocedure Raymond scale 2 vs 1	1.27 (0.39–4.13)	.6930	1.02 (0.30–3.50)	.9694
Core laboratory postprocedure Raymond scale 3 vs 1	7.17 (2.61–19.7)	.0002	6.24 (2.29–17.0)	.0004
Aneurysm size ( $< 10$ mm vs $\geq 10$ mm)	7.96 (1.45–43.7)	.0174	1.08 (0.29–4.06)	.9050

**Note:**—OR indicates odds ratio.

<sup>a</sup> Stryker Neurovascular, Kalamazoo, Michigan.

ica, especially among ruptured aneurysms and in the first 455 days postprocedure. Though the difference in retreatment rates between North America and international sites was persistent out to 820 days (Figure), there appears to be eventual consistency in global retreatment rates among patients judged to have residual aneurysms at follow-up. At 820 days, 55.7% of North American residual aneurysms had been retreated compared with 47.6% in international sites. Earlier in follow-up, at 455 days, 49.2% of North American residual aneurysms had already been retreated compared with just 19.0% of international residual aneurysms.

The geographic differences in frequency of retreatment were only significant in the ruptured aneurysm cohort. This could indicate a North American preference to treat the rupture minimally, with a willingness to do a follow-up retreatment if necessary. It also may be tied to an increased use of stents in patients with unruptured aneurysms in North America, though multivariate analysis did not show the impact of stents on retreatment rates to be significant at 455 or 820 days (Table 3).

Differences between geographies were present, beginning with patient baseline characteristics and extending through aneurysm treatment and subsequent follow-up. North American operators treated significantly more patients who were older in age with multiple cardiovascular risk factors and more likely to have a higher Hunt and Hess grade. When North American operators identified residual aneurysm filling at follow-up, they were more likely to immediately retreat these remnants than operators in other regions of the world.

A significantly higher proportion of aneurysms treated at North American sites had residual filling immediately postprocedure than aneurysms treated at international sites (43.5% versus 26.5%, respectively). These initial occlusion rates indicate a more aggressive treatment approach at international sites. However, similar packing densities across regions imply that physicians are implanting similar volumes of coils. This discrepancy could be attributed to complex aneurysm morphologies and the imperfect nature of packing attenuation calculations that assume an elliptical aneurysm shape.

Stent-assisted coiling was used significantly more frequently in North America and was associated with better angiographic outcomes at 455 days than aneurysms treated by coiling alone. Though there were more ischemic events associated with stented

aneurysms, multivariate analysis demonstrated that this was because of the width of the aneurysm neck and a history of stroke.<sup>11</sup>

Despite these differences, there was no significant difference in mRS between North American and international cohorts at 455 days.

Though these data of 626 patients are strengthened through the prospective randomized trial design, retrospective identification of subgroups for analysis remains a limitation. The utilization of an angiographic core laboratory also further strengthens the data, though

21.1% of North American patients and 25.1% of international patients had no core laboratory reading at 455 days because of image quality issues or other protocol violations. Although we have used statistical models to create common odds ratios for estimation of predictive characteristics of retreatment, the management of intracranial aneurysms may potentially be different from site to site and country to country. Therefore, inferences of predictive characteristics of various treatment modalities remain a limitation of our analysis and require future powered randomized controlled studies.

## CONCLUSIONS

Data from the Matrix and Platinum Science Trial demonstrate that aneurysm retreatment occurs with different frequency and at different times in different regions of the world. This trend has critical value when interpreting trials reporting short-term outcomes, especially when judgment-based metrics such as retreatment are primary end points that may or may not take place within the defined study follow-up period. Though these variations can be controlled for and balanced within a given randomized trial, such differences in practice patterns must be accounted for in any attempt to compare outcomes among different trials. Despite these differences, endovascular-treated intracranial aneurysms around the world have similar clinical outcomes.

Disclosures: Aquilla S. Turk—*RELATED: Grant:* Stryker Medical,\* *Comments:* fellowship grant; *Consulting Fee or Honorarium:* Stryker Medical, *Comments:* speaking engagements (no payment); *Support for Travel to Meetings for the Study or Other Purposes:* Stryker Medical, *Comments:* airfare and hotel booking for conferences and speaking engagements; *UNRELATED: Consultancy:* Penumbra,\* Microvention,\* Medina Medical\*; *Grants/Grants Pending:* Microvention,\* Penumbra\*; *Payment for Lectures (including service on speakers bureaus):* Penumbra,\* Covidien,\* Microvention,\* Medina Medical,\* Siemens.\* Steven Hettis—*RELATED: Grant:* Stryker Neurovascular,\* *Comments:* University of California, San Francisco was the core angiographic imaging laboratory for the Matrix and Platinum Science Trial; *UNRELATED: Consultancy:* Stryker Neurovascular, *Comments:* occasional educational presentations to company employees on diagnosis and treatment of stroke; *Grants/Grants Pending:* Stryker Neurovascular,\* Microvention,\* Terumo,\* Siemens,\* *Comments:* University of California, San Francisco is the core imaging laboratory for the Adjuvant Tamoxifen: Longer Against Shorter (ATLAS), Surpass Flow Diverter for Intracranial Aneurysms (SURMOUNT), and Microvention Flow Redirection Intraluminal Device (FRED) trials. University of California, San Francisco has research contracts for evaluation of Siemens angiography equipment; *Royalties:* Penumbra, *Comments:* potential royalties from a preclinical device in oncology; *Stock/Stock Options:* Medina Medical. *Comments:* stock options earned for participation on scientific advisory board before company acquisition. J. Mocco—*UNRELATED: Consultancy:* Lazurus Effect, Reverse Medical, Pulsar, Edge Therapeutics, Medina. Joey English—

UNRELATED: *Consultancy*: Stryker Neurovascular, Medtronic, Silk Road Medical, *Comments*: unrelated to the Transform Balloon or any work described in the manuscript; *Expert Testimony*: expert witness regarding neurointerventional procedures (unrelated to the use of the Transform Balloon Microcatheter); *Payment for Development of Educational Presentations*: Stryker Neurovascular, *Comments*: assisted in the creation of educational materials regarding neurointerventional procedures for fellows, nurses, and radiology technicians. Yuichi Murayama—RELATED: *Grant*: Stryker\*; *Consulting Fee or Honorarium*: Stryker, *Comments*: an inventor of Matrix coil; receives royalties from Stryker; UNRELATED: *Grants/Grants Pending*: Siemens.\* Charlie J. Prestigiacomo—UNRELATED: *Board Membership*: International Brain Research Foundation, *Comments*: board member volunteer; *Consultancy*: Stryker, *Comments*: lecturer to fellowship course once per year and participant on Scientific Advisory Board, paid as honorarium and cost of travel; *Stock/Stock Options*: Ther-mopeutix, *Comments*: earned from participation on Scientific Advisory Board; *Travel/Accommodations/Meeting Expenses Unrelated to Activities Listed*: Cod-man, *Comments*: for participation on Data Safety Monitoring Board. Demetrius Lopes—UNRELATED: *Consultancy*: Stryker; *Grants/Grants Pending*: Stryker; *Payment for Lectures (including service on speakers bureaus)*: Stryker; *Payment for Development of Educational Presentations*: Stryker. Kirsten Carroll—RELATED: *Other*: Stryker, *Comments*: conducted the work on this submission as part of employment duties; UNRELATED: *Stock/Stock Options*: Stryker. Cameron G. McDougall—UNRELATED: *Consultancy*: Microvention, ev3. \*Money paid to the institution.

## REFERENCES

- Molyneux A, Kerr R, Stratton I, et al. **International Subarachnoid Aneurysm Trial (ISAT) of neurosurgical clipping versus endovascular coiling in 2143 patients with ruptured intracranial aneurysms: a randomised trial.** *Lancet* 2002;360:1267–74 [CrossRef Medline](#)
- Molyneux AJ, Kerr RS, Birks J, et al. **Risk of recurrent subarachnoid haemorrhage, death, or dependence and standardised mortality ratios after clipping or coiling of an intracranial aneurysm in the International Subarachnoid Aneurysm Trial (ISAT): long-term follow-up.** *Lancet Neurol* 2009;8:427–33 [CrossRef Medline](#)
- McDougall CG, Spetzler RF, Zabramski JM, et al. **The Barrow Ruptured Aneurysm Trial.** *J Neurosurg* 2012;116:135–44 [CrossRef Medline](#)
- McDougall CG, Claiborne Johnston S, Gholkar A, et al. **Bioactive versus bare platinum coils in the treatment of intracranial aneurysms: the MAPS (Matrix and Platinum Science) trial.** *AJNR Am J Neuroradiol* 2014;35:935–42 [CrossRef Medline](#)
- Molyneux AJ, Clarke A, Sneade M, et al. **Cerecyte coil trial: angiographic outcomes of a prospective randomized trial comparing endovascular coiling of cerebral aneurysms with either Cerecyte or bare platinum coils.** *Stroke* 2012;43:2544–50 [CrossRef Medline](#)
- White PM, Lewis SC, Gholkar A, et al. **Hydrogel-coated coils versus bare platinum coils for the endovascular treatment of intracranial aneurysms (HELPS): a randomised controlled trial.** *Lancet* 2011; 377:1655–62 [CrossRef Medline](#)
- Naggara ON, Lecler A, Oppenheim C, et al. **Endovascular treatment of intracranial unruptured aneurysms: a systematic review of the literature on safety with emphasis on subgroup analyses.** *Radiology* 2012;263:828–35 [CrossRef Medline](#)
- McDougall CG, Johnston SC, Gholkar A, et al. **Counterpoint-target aneurysm recurrence: measuring what matters.** *AJNR Am J Neuroradiol* 2015;36:4–6 [CrossRef Medline](#)
- Pierot L, Fiehler J, White P. **Point-TAR: a useful index to follow-up coiled intracranial aneurysms?** *AJNR Am J Neuroradiol* 2015;36:2–4 [CrossRef Medline](#)
- Raymond J, Guilbert F, Weill A, et al. **Long-term angiographic recurrences after selective endovascular treatment of aneurysms with detachable coils.** *Stroke* 2003;34:1398–403 [CrossRef Medline](#)
- Hetts SW, Turk A, English JD, et al. **Stent-assisted coiling versus coiling alone in unruptured intracranial aneurysms in the Matrix and Platinum Science trial: safety, efficacy, and mid-term outcomes.** *AJNR Am J Neuroradiol* 2014;35:698–705 [CrossRef Medline](#)

# Prophylactic Antiplatelet Medication in Endovascular Treatment of Intracranial Aneurysms: Low-Dose Prasugrel versus Clopidogrel

E.J. Ha, W.S. Cho, J.E. Kim, Y.D. Cho, H.H. Choi, T. Kim, J.S. Bang, G. Hwang, O.K. Kwon, C.W. Oh, M.H. Han, and H.S. Kang

## ABSTRACT

**BACKGROUND AND PURPOSE:** Prophylactic antiplatelet medication is beneficial in decreasing thromboembolic complications during endovascular treatment of unruptured intracranial aneurysms. The efficacy may be limited by variability of individual response to antiplatelet medication, especially clopidogrel. We compared the efficacy of 2 antiplatelet medications, low-dose prasugrel and clopidogrel, in patients undergoing endovascular treatment of unruptured aneurysms.

**MATERIALS AND METHODS:** From November 2014 to July 2015, 194 patients with a total of 222 unruptured aneurysms underwent endovascular treatment at a single institution. Laboratory and clinical data from the prospectively maintained registry were used in this study. Antiplatelet medication was given the day before endovascular treatment (prasugrel 20 mg or 30 mg or clopidogrel 300 mg). Response to the antiplatelet medication was measured by the VerifyNow system. Periprocedural adverse event rates between the 2 groups were compared.

**RESULTS:** There were no significant differences in the baseline characteristics of patients and aneurysms between the 2 groups. The P2Y12 reaction unit values were lower (clopidogrel group versus prasugrel group,  $242.7 \pm 69.8$  vs  $125.7 \pm 79.4$ ;  $P < .0001$ ) and percentage inhibition values were higher ( $22.1\% \pm 19.7\%$  vs  $60.2 \pm 24.7\%$ ;  $P < .0001$ ) in the prasugrel group. There were no thromboembolic events, but there was 1 procedural bleed in each group, without any clinical consequences.

**CONCLUSIONS:** The prasugrel group showed more effective and consistent platelet inhibition. We may omit the antiplatelet response assay with the low-dose prasugrel premedication before the endovascular treatment of patients with unruptured aneurysms. Further study is required to determine whether there is benefit of this strategy regarding clinical outcome.

**ABBREVIATIONS:** CPG = clopidogrel; PRU = P2Y12 reaction unit; PSG = prasugrel

Coil embolization is accepted as a safe and effective treatment in patients with intracranial aneurysms.<sup>1</sup> However, it is not without risk, and thromboembolism during the procedure is a serious and common complication of coil embolization.<sup>2</sup> Increasing evidence has demonstrated the efficacy of prophylactic antiplatelet therapy in patients undergoing endovascular treatment of unruptured intracranial aneurysms with or without stent assistance.<sup>3-7</sup> One of the representative antiplatelet agents is clopidogrel (CPG), which inhibits the P2Y12

adenosine diphosphate receptor on the platelet cell membrane. CPG has become a standard medication for patients with risk of cerebral infarction and myocardial infarction.<sup>8,9</sup> To minimize the thromboembolic complications during the procedure, an antiplatelet protocol centered upon CPG has been adopted.<sup>5,6,10</sup>

However, the efficacy of prophylactic CPG therapy is variable among patients. Some patients show resistance to CPG, and procedure-related thromboembolic events occur more frequently among them.<sup>10-13</sup> Some reports have demonstrated higher numbers of acute ischemic lesions in patients with CPG resistance.<sup>14,15</sup>

Recently, a new generation of P2Y12 adenosine diphosphate-receptor antagonists has been developed. One such drug is prasugrel (PSG).<sup>16</sup> The purpose of this study was to identify the role of low-dose PSG premedication in preventing thromboembolic events and to compare its effectiveness with CPG. We performed a comparative study between a low-dose PSG group and a CPG group in terms of platelet-response variability and periprocedural adverse event rates.

Received September 15, 2015; accepted after revision May 9, 2016.

From the Departments of Neurosurgery (E.J.H., W.S.C., J.E.K., H.S.K.) and Radiology (Y.D.C., M.H.H.), Seoul National University College of Medicine, Seoul National University Hospital, Seoul, Korea; Department of Neurosurgery (H.H.C.), Dongguk University Ilsan Hospital, Gyeonggi, Korea; and Department of Neurosurgery (T.K., J.S.B., G.H., O.K.K., C.W.O.), Seoul National University Bundang Hospital, Gyeonggi, Korea.

Please address correspondence to Hyun-Seung Kang, MD, PhD, Department of Neurosurgery, Seoul National University College of Medicine, Seoul National University Hospital, 101 Daehak-ro, Jongno-gu, Seoul 03080, Korea; e-mail: hsk4428@yahoo.com

<http://dx.doi.org/10.3174/ajnr.A4864>

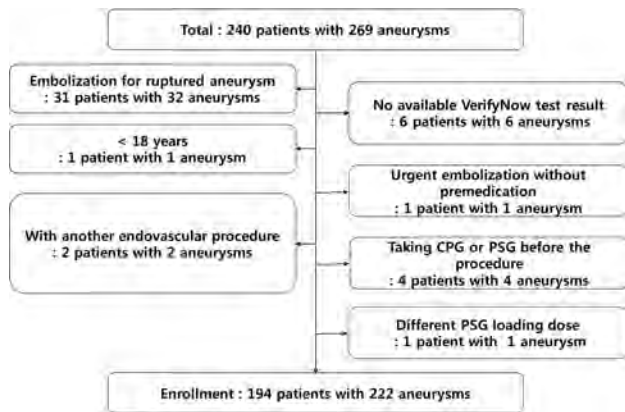


FIG 1. Patient selection flowchart.

## MATERIALS AND METHODS

### Study Design and Patient Population

After approval by the Seoul National University Hospital Institutional Review Board (No. 1503–090-657), we retrospectively identified 240 consecutive patients (with 269 aneurysms) who underwent endovascular treatment between November 2014 and July 2015 according to a prospectively maintained data base. The study included patients who were older than 18 years and were treated for unruptured intracranial aneurysms. Excluded were those who had ruptured, infectious, or traumatic aneurysms; who had a previous history of intracranial hemorrhage; who underwent parent arterial occlusion; who underwent urgent treatment without antiplatelet premedication; who had no platelet function test results available; who took a different PSG loading dose (15 mg); and who had already been taking CPG or PSG for other reasons before the aneurysmal treatment. As a result, 194 patients with a total of 222 aneurysms were enrolled (Fig 1).

The patients were divided into the CPG group and the low-dose PSG group; the choice of antiplatelet agents was determined by the referring physicians. The CPG group included 96 patients (with 106 aneurysms) who received CPG as a premedication, and the low-dose PSG group included 98 patients (with 116 aneurysms).

### Periprocedural Antiplatelet Medication

In the CPG group, a 300-mg loading dose of CPG was given the day before the procedure, and an additional 75 mg of CPG was given on the morning of the procedure. If the patient showed a high P2Y12 reaction unit (PRU) value, we gave an additional antiplatelet agent (aspirin). If a stent-assisted procedure was anticipated, we routinely gave additional aspirin to the patient without considering the PRU values, and if the patient was a poor responder to CPG (ie, PRU > 285), we added cilostazol (200 mg per day).<sup>10</sup> Conversely, in the PSG group, the patients received typically a 20-mg loading dose of PSG the day before the procedure and an additional 5 mg of PSG was administered on the morning of the procedure.

After the embolization procedures, antiplatelet medication was continued if necessary, depending on the presence of underlying atherosclerotic steno-occlusive diseases, stent implantation, or coil loop protrusion during the procedure. Patients in the CPG group undergoing stent implantation were recommended dual-

or triple-antiplatelet (for CPG poor responders) agents for 3 months. Patients in the PSG group undergoing stent implantation received 5 mg of PSG for 3 months; then, life-long aspirin medication was recommended.

### Blood Sample Acquisition and Platelet Activity Measurement

Whole blood was obtained 6 hours after antiplatelet agent loading in both groups. Residual platelet reactivity was measured by using the VerifyNow assay (Accumetrics, San Diego, California). We obtained 3 values: platelet reactivity to isothrombin receptor–activating peptide, or BASE; PRU; and percentage inhibition. BASE is a platelet reaction unit and serves as an estimate of baseline platelet reactivity. PRU reflects residual P2Y12 receptor activity. Percentage inhibition is a calculated value from a formula:

$$\text{Percentage Inhibition} = \frac{(\text{BASE} - \text{PRU})}{\text{BASE}} \times 100$$

Therefore, high PRU and low percentage inhibition indicate a lower effectiveness of adenosine-diphosphate receptor–antagonist therapy.

### Coil Embolization Procedure and Procedure-Related Complications

Endovascular coil embolization was performed by using a standardized protocol in a neuroangiography suite. Most procedures were performed on patients under general anesthesia. Systemic anticoagulation with heparin was done from the start of the procedure. Heparin was usually administered as a bolus of 3000 IU intravenously after insertion of the introducer sheath and infused additionally at a rate of 1000 IU per hour with monitoring of the activated clotting time. The target activated clotting time was 250–300 seconds.

A simple coiling procedure (single microcatheter placement and coil deployment), multiple microcatheter technique, balloon-assisted technique, stent-assisted coil embolization, combination of the former techniques, and flow diversion were used at the discretion of the treating physician.

The procedure-related thromboembolism was defined as thrombus formation and/or distal embolism observed during the procedure or clinically recognized ischemic deficits (including transient ischemic attack) that occurred within 60 days of the procedure. Procedural thromboembolism included procedural clot or any ischemic events found after treatment, and periprocedural thromboembolism included the vascular territory–specific events related to the treated lesions within 60 days of the procedure. In the latter, alternative etiologies were ruled out after evaluation by stroke neurologists. Events of procedure-related bleeding also were recorded.

### Statistical Analysis

Categorical data were presented as frequencies and group percentages, and continuous data were presented as mean  $\pm$  SD. The Fisher exact test or  $\chi$ -square test was used for comparison of discrete data. An independent *t* test was conducted to compare the unpaired continuous data. All tests were 2-tailed, and statistical significance was considered at *P* < .05. Analyses were performed by using Statistical Package for the Social Sciences for Windows version 20.0 (IBM, Armonk, New York). Bleeding events and ad-

**Table 1: Baseline characteristics of patients<sup>a</sup>**

Characteristic	CPG	PSG	P Value
No. of patients	96	98	
No. of aneurysms	106	116	
Sex (F/M)	63/33	68/30	.646
Age (yr)	56.4 ± 11.4	57.7 ± 10.5	.418
Body weight (kg)	62.3 ± 9.7	61.8 ± 10.8	.765
Body mass index	24.5 ± 3.1	24.2 ± 4.0	.573
Hypertension	38.5%	43.9%	.469
Diabetes	6.3%	8.2%	.783
Hyperlipidemia	53.1%	50.0%	.670
Smoking	31.3%	26.5%	.631
Triglycerides (mg/dL)	106.9 ± 52.1	117.3 ± 67.5	.234
HDL cholesterol (mg/dL)	51.1 ± 13.7	56.0 ± 33.9	.190
LDL cholesterol (mg/dL)	99.1 ± 29.6	107.5 ± 29.3	.052

**Note:**—HDL indicates high-density lipoprotein; LDL, low-density lipoprotein.

<sup>a</sup> All the continuous variables are presented as mean ± SD.

**Table 2: Baseline characteristics of aneurysms**

Characteristic	CPG	PSG	P Value
Aneurysm volume (mm <sup>3</sup> )	0.121 ± 0.402	0.141 ± 0.674	.807
Location (no. [%])			.867
Internal carotid artery	54 (50.9)	56 (48.3)	
Anterior cerebral artery	29 (27.4)	30 (25.9)	
Middle cerebral artery	13 (12.3)	19 (16.4)	
Posterior circulation	10 (9.4)	11 (9.5)	
Previously ruptured	3	5	.555
Shape			.686
Saccular	103	112	
Fusiform	1	0	
Dissecting	1	1	
Post-clip remnant	1	2	
Partially thrombosed	0	1	

**Table 3: Procedural characteristics in each group**

Characteristic	CPG	PSG	P Value
Treatment times			.270
First treatment	98	101	
Repeated treatment	8	15	
Treatment modality			.116
Simple coiling	40	46	
Stent-assisted	23	19	
Multiple microcatheter	23	31	
Balloon-assisted	8	16	
Combined <sup>a</sup>	10	4	
Flow diversion	2	0	

<sup>a</sup> Combined procedures are stent-assisted and balloon-assisted, multiple microcatheter and balloon-assisted, or multiple microcatheter and stent-assisted.

verse thromboembolic events were reported in a descriptive manner.

### Approval

This study was conducted according to the principles outlined in the Declaration of Helsinki. The protocol was approved by Seoul National University Hospital's Institutional Review Board (No. 1503-090-657).

### RESULTS

The baseline characteristics of patients, treated aneurysms, and procedural characteristics are summarized in Table 1, Table 2, and Table 3, respectively. No significant differences were found in the baseline characteristics between the PSG and CPG groups. In the PSG group, 90 patients received 20-mg loading doses and 8

**Table 4: Comparison of procedure-related complications**

Complication	CPG	PSG	P Value
Thromboembolism	0	0	NS
Aneurysm perforation	1 (0.9%)	1 (0.9%)	NS

**Note:**—NS indicates not significant.

**Table 5: Comparison of platelet function test results using VerifyNow P2Y12 assay**

Test	CPG	PSG	P Value
BASE	311.8 ± 41.1	313.7 ± 41.6	.753
PRU	242.7 ± 69.8	125.7 ± 79.4	<.001
Percentage inhibition (%)	22.1 ± 19.7	60.2 ± 24.7	<.001

**Note:**—BASE indicates platelet reactivity to isothrombin receptor-activating peptide.

patients received 30-mg loading doses. There were 32 stent-assisted procedures performed in the CPG group and 23 performed in the PSG group.

There were no procedure-related thromboembolic events (Table 4). There was 1 procedural bleeding event in each group; in the CPG group, it was an aneurysmal rupture during the procedure. Diffuse SAH was identified on immediate postoperative CT scan. In the PSG group, there was also 1 hemorrhagic complication case. A small amount of SAH developed because of microguidewire perforation of the aneurysmal sac during the procedure. However, they were not clinically significant. There was no procedure-related permanent morbidity or mortality in either group.

The platelet function test results are summarized in Table 5. There were no significant differences in the BASE values (CPG group vs PSG group, 311.8 ± 41.1 vs 313.7 ± 41.6, respectively;  $P = .753$ ), but PRU values were significantly lower (242.7 ± 69.8 vs 125.7 ± 79.4, respectively;  $P < .0001$ ) and percentage inhibition values were higher (22.1% ± 19.7% vs 60.2% ± 24.7%, respectively;  $P < .0001$ ) in the PSG group. The histogram of the PRU values of the CPG group showed a bell-shaped distribution (Fig 2). The PSG group showed a distribution of PRU values shifted to the left side compared with the CPG group. When we set a PRU cutoff value of 285 to determine the resistance to adenosine-diphosphate antagonists,<sup>10</sup> 30.2% (29 of 96) and 1.0% (1 of 98) of the patients in the CPG group and the PSG group, respectively, showed resistance ( $P = .001$ ).

In the CPG group, 54 patients (56%) were given dual-antiplatelet agents, and 11 patients (12%) were given triple-antiplatelet agents. The remaining 31 patients (32%) were given CPG only. In the PSG group, 89 of 98 patients (91%) were given PSG only; only 9 patients had dual-antiplatelet agents. The rate of using multiple antiplatelet agents was significantly higher in the CPG group ( $P < .001$ ).

When we analyzed the antiplatelet effect of PSG according to the loading doses (30 mg versus 20 mg), there were meaningful differences in PRU values between the 2 groups. The PRU value was significantly lower in the 30-mg group (30 mg versus 20 mg, 68.7 ± 72.3 vs 132.2 ± 80.7;  $P = .0046$ ). We also analyzed the relationship between clinical and laboratory characteristics and PRU in the PSG group (Table 6). PRU values were significantly lower in those with lower body weight (< 60 kg;  $P < .001$ ), statin users ( $P = .02$ ), smokers ( $P < .001$ ), and those with higher low density-lipoprotein levels ( $P < .001$ ).

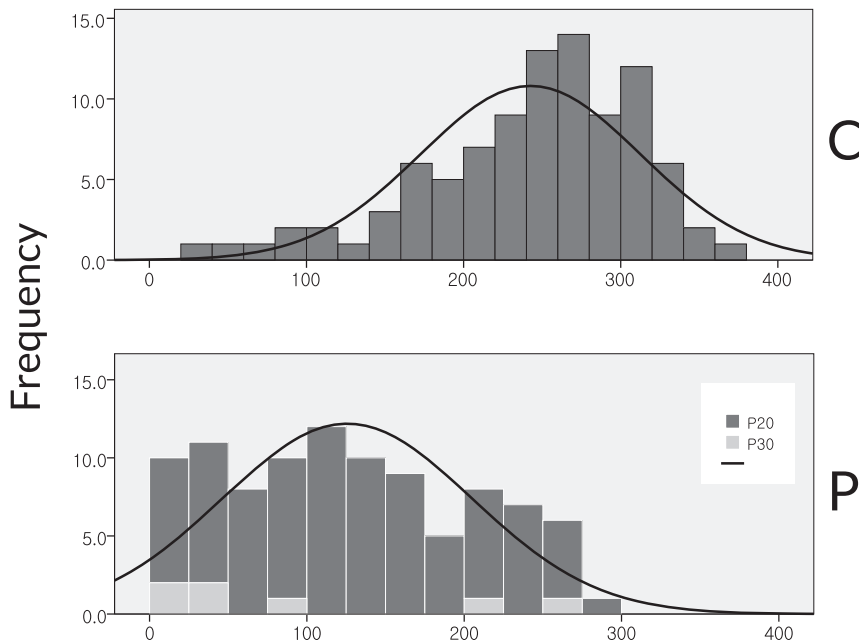


**FIG 2.** PRU value distribution in CPG and PSG groups. C indicates CPG group; P, PSG group; P20, PSG 20-mg loading dose; P30, PSG 30-mg loading dose.

**Table 6: Relations between patient characteristics and PRU in the PSG group**

Clinical and Laboratory Variables <sup>a</sup>	P Value	PRU
Sex (M)	.18	129.6 ± 49.0 vs 130.3 ± 68.0
Age (<65 yr)	.17	122.6 ± 59.4 vs 148.0 ± 65.4
Body weight (<60 kg)	<.001	102.3 ± 54.5 vs 156.7 ± 55.2
Hypertension (no)	.20	120.6 ± 62.2 vs 142.0 ± 60.1
Diabetes mellitus (yes)	.31	127.5 ± 63.8 vs 157.0 ± 37.6
Statin use (yes)	.02	109.5 ± 42.8 vs 148.2 ± 72.3
Smoking status (current or past smoker)	<.001	77.4 ± 26.1 vs 148.2 ± 61.5
Alcohol intake (yes)	.24	110.6 ± 106.5 vs 135.0 ± 50.6
Hematocrit level (<38%)	.84	128.5 ± 69.4 vs 131.8 ± 55.0
Platelet count (<227 × 10 <sup>3</sup> )	.58	125.6 ± 61.5 vs 135.0 ± 63.0
HDL cholesterol level (<40 mg/dL)	.89	125.6 ± 50.1 vs 129.2 ± 64.2
LDL cholesterol level (≥130 mg/dL)	<.001	69.5 ± 21.1 vs 145.9 ± 59.1

**Note:**—HDL indicates high-density lipoprotein; LDL, low-density lipoprotein.

<sup>a</sup> A group of patients denoted within the parentheses showed decreased residual platelet activity.

## DISCUSSION

### Antiplatelet Resistance and Coil Embolization of Unruptured Aneurysms

In previous studies, CPG premedication contributed to reduction in procedure-related thromboembolism without increasing the risk of procedural bleed.<sup>4-6</sup> In a study by Kang et al,<sup>6</sup> the rates of absolute and relative risk reduction were 5.2% (from 12.6% to 7.4%) and 41%, respectively. Furthermore, the logistic regression analysis proved CPG premedication as an independent factor related to thromboembolic events. Thus, the classic protocol for antiplatelet prophylaxis in the neurointerventional field has mainly been composed of CPG.

However, there was a problem of variable responsiveness to CPG. Though there are controversies on the utility of platelet-inhibition testing, variable responsiveness to CPG has led practitioners to perform laboratory tests to evaluate platelet reactivity after CPG administration, especially before interventional procedures. Several studies in the field of cardiology demonstrated that high PRU values were associated with increased periprocedural

myocardial infarction as well as mortality after percutaneous coronary intervention.<sup>17-19</sup> In the neurointerventional field, a series of studies since the first publication in this field in 2010 have demonstrated the association between antiplatelet drug resistance and periprocedural ischemic events in reference to endovascular treatment of intracranial aneurysms.<sup>10,13-15,19-21</sup> Kang et al<sup>10</sup> showed that procedure-related thromboembolic events occurred more frequently in patients with higher PRU, especially in the fourth quartile. Furthermore, in a randomized clinical trial, modification of antiplatelet treatment based on the functional assay provided benefit in terms of thromboembolic event rate.<sup>22</sup> Additional doses or other kinds of antiplatelet agents would bring complexities of the premedication protocols and increased costs, which prompted us to search for an effective antiplatelet regimen with less variability.

### Antiplatelet Premedication with Low-Dose PSG

PSG, a third-generation thienopyridine, has shown significant reduction in rates of ischemic events in patients undergoing coronary intervention.<sup>23-25</sup> It also has been shown to increase the bleeding risk in patients with acute coronary syndrome.<sup>25</sup> Both CPG and PSG are prodrugs that require biotransformation to active metabolites by cytochrome P450 enzymes.<sup>16</sup> Though the active metabolites of both drugs have a similar affinity for the P2Y<sub>12</sub> receptor in vitro, the

in vivo difference in response appears to be mediated by differences in the metabolic pathways leading to the formation of the active metabolites. Hepatic esterases shunt most (approximately 85%) of CPG to a dead-end inactive pathway, with the remaining prodrug requiring 2 separate cytochrome P450-dependent oxidative steps.<sup>26</sup> In contrast, esterases are part of the activation pathway with PSG, and PSG is oxidized to its active metabolite in a single cytochrome P450-dependent step without an apparent dead-end inactive pathway.<sup>27</sup> The genes that encode the cytochrome P450 enzymes are polymorphic, with certain alleles demonstrated to confer reduced enzymatic function, thereby interfering with the production of the drug metabolites. The action of CPG is more dependent on the genetic polymorphism of the cytochrome P450 enzyme, and it varies among people.

The occasional poor response to CPG gives us concern for the increased risk of procedural complications, and the complicated individual tailoring sometimes confuses medical personnel in our daily practice. PSG has demonstrated a superior antiplatelet effect

compared with CPG, especially in cardiology. However, usage of PSG in the field of cerebrovascular diseases is quite limited for fear of the risk of intracranial hemorrhage.<sup>25</sup>

In the current study, we focused on the role of low-dose PSG premedication in patients undergoing coil embolization for unruptured intracranial aneurysms. This study is the largest among the clinical studies on the usage of prophylactic PSG in the neurointerventional field<sup>28,29</sup> and shows the efficacy and safety of the reduced-dose PSG regimen, composed of a 20-mg loading dose and a 5-mg maintenance dose. (In the TRITON-TIMI 38 trial, the medication protocol was a 60-mg loading dose and a 10-mg daily maintenance dose.<sup>25</sup>) In our series, we used 30 mg as the loading dose during the early phase. After a few cases, we found that PRU values were sometimes too low. All 7 patients taking the 30-mg loading dose showed a “hyper-response” (PRU value < 240)<sup>10</sup> and 4 showed PRU values < 60 (a criterion for “hyper-response” in another publication).<sup>12</sup> PRU values were below 10 in 2 patients and between 10 and 60 in another 2. Therefore, we reduced the loading dose of PSG to 20 mg. The mean PRU values were  $68.7 \pm 72.3$  and  $132.2 \pm 80.7$  in the 30-mg and 20-mg loading groups, respectively ( $P = .0046$ ). We could infer that the optimal loading dose of PSG for sufficient suppression of platelet function without increased bleeding risk in our cohort would be less than 30 mg.

In the current study, patients in the PSG group consistently showed significantly lower PRU values. The overall distribution of PRU values was shifted to the left, as shown in Fig 2. On the basis of VerifyNow test results, only 1 patient showed high PRU over the cutoff value of 285 (the patient’s PRU was 295 and percentage inhibition was 15%).

Most patients in the CPG group (68%) were given additional (1 or 2) antiplatelet agents. Conversely, only 9 patients in the PSG group (9%) took dual-antiplatelet agents, and 7 of them had already taken aspirin for other medical reasons. The single-agent therapy with low-dose PSG showed at least comparable protective antithromboembolic effects compared with CPG-based combination antiplatelet therapy. In terms of side effects of PSG, especially procedural-related bleeding, there was only 1 event, which did not lead to any clinical impairment of the patient.

CPG-based combination antiplatelet therapy is a widely used prophylactic regimen for stent-assisted coil embolization procedures. In our series, 14 patients underwent stent-supported coil embolization under low-dose PSG premedication only. They did not show any thromboembolic complications during the procedure and the following 2 months. Single-antiplatelet premedication with PSG seems to be sufficient even in cases requiring stent-supported coil embolization. Though PSG is more expensive than CPG, the total medication cost would be similar considering the combination antiplatelet therapy in the CPG group. The antiplatelet medication protocol will become simpler with use of the “low-dose PSG protocol.” In addition, we also might reduce cost by omitting the platelet function assay because consistent platelet inhibition was verified with PSG.

The limitations of the current study include its retrospective nature and relatively small number of patients. Further study is anticipated to see whether the low-dose PSG protocol can bring benefits regarding the clinical outcome, especially in the setting of a larger, prospective, randomized, multicenter trial.

## CONCLUSIONS

In our study, the PSG group showed more effective and consistent platelet inhibition than the CPG group. With this antiplatelet regimen, we may omit the antiplatelet response assay and additional antiplatelet medication. Further study is anticipated to see whether this strategy can bring benefits regarding the clinical outcome.

Disclosures: Moon Hee Han—UNRELATED: Consultancy: Microvention.\* \*Money paid to the institution.

## REFERENCES

1. Molyneux A, Kerr R, Stratton I, et al. **International Subarachnoid Aneurysm Trial (ISAT) of neurosurgical clipping versus endovascular coiling in 2143 patients with ruptured intracranial aneurysms: a randomised trial.** *Lancet* 2002;360:1267–74 CrossRef Medline
2. Derdeyn CP, Cross DT 3rd, Moran CJ, et al. **Postprocedure ischemic events after treatment of intracranial aneurysms with Guglielmi detachable coils.** *J Neurosurg* 2002;96:837–43 CrossRef Medline
3. Ries T, Buhk JH, Kucinski T, et al. **Intravenous administration of acetylsalicylic acid during endovascular treatment of cerebral aneurysms reduces the rate of thromboembolic events.** *Stroke* 2006;37:1816–21 CrossRef Medline
4. Yamada NK, Cross DT 3rd, Pilgram TK, et al. **Effect of antiplatelet therapy on thromboembolic complications of elective coil embolization of cerebral aneurysms.** *AJNR Am J Neuroradiol* 2007;28:1778–82 CrossRef Medline
5. Hwang G, Jung C, Park SQ, et al. **Thromboembolic complications of elective coil embolization of unruptured aneurysms: the effect of oral antiplatelet preparation on periprocedural thromboembolic complication.** *Neurosurgery* 2010;67:743–48 CrossRef Medline
6. Kang HS, Han MH, Kwon BJ, et al. **Is clopidogrel premedication useful to reduce thromboembolic events during coil embolization for unruptured intracranial aneurysms?** *Neurosurgery* 2010;67:1371–76; discussion 1376 CrossRef Medline
7. Rahme RJ, Zammer SG, El Ahmadieh TY, et al. **The role of antiplatelet therapy in aneurysm coiling.** *Neurol Res* 2014;36:383–88 CrossRef Medline
8. CAPRIE Steering Committee. **A randomised, blinded, trial of clopidogrel versus aspirin in patients at risk of ischaemic events (CAPRIE).** *Lancet* 1996;348:1329–39 CrossRef Medline
9. Yusuf S, Zhao F, Mehta SR, et al. **Effects of clopidogrel in addition to aspirin in patients with acute coronary syndromes without ST-segment elevation.** *N Engl J Med* 2001;345:494–502 CrossRef Medline
10. Kang HS, Kwon BJ, Kim JE, et al. **Preinterventional clopidogrel response variability for coil embolization of intracranial aneurysms: clinical implications.** *AJNR Am J Neuroradiol* 2010;31:1206–10 CrossRef Medline
11. Serebruany VL, Steinhubl SR, Berger PB, et al. **Variability in platelet responsiveness to clopidogrel among 544 individuals.** *J Am Coll Cardiol* 2005;45:246–51 CrossRef Medline
12. Delgado Almandoz JE, Kadkhodayan Y, Crandall BM, et al. **Variability in initial response to standard clopidogrel therapy, delayed conversion to clopidogrel hyper-response, and associated thromboembolic and hemorrhagic complications in patients undergoing endovascular treatment of unruptured cerebral aneurysms.** *J Neurointerv Surg* 2014;6:767–73 CrossRef Medline
13. Kim MS, Jo KI, Yeon JY, et al. **Association between postprocedural infarction and antiplatelet drug resistance after coiling for unruptured intracranial aneurysms.** *AJNR Am J Neuroradiol* 2016;37:1099–105 CrossRef Medline
14. Kim B, Kim K, Jeon P, et al. **Thromboembolic complications in patients with clopidogrel resistance after coil embolization for unruptured intracranial aneurysms.** *AJNR Am J Neuroradiol* 2014;35:1786–92 CrossRef Medline

15. Asai T, Miyachi S, Izumi T, et al. **Relationship between low response to clopidogrel and periprocedural ischemic events with coil embolization for intracranial aneurysms.** *J Neurointerv Surg* 2016;8:752–55 CrossRef Medline
16. Mega JL, Close SL, Wiviott SD, et al. **Cytochrome P450 genetic polymorphisms and the response to prasugrel: relationship to pharmacokinetic, pharmacodynamic, and clinical outcomes.** *Circulation* 2009;119:2553–60 CrossRef Medline
17. Gurbel PA, Bliden KP, Samara W, et al. **Clopidogrel effect on platelet reactivity in patients with stent thrombosis: results of the CREST Study.** *J Am Coll Cardiol* 2005;46:1827–32 CrossRef Medline
18. Matetzky S, Shenkman B, Guetta V, et al. **Clopidogrel resistance is associated with increased risk of recurrent atherothrombotic events in patients with acute myocardial infarction.** *Circulation* 2004;109:3171–75 CrossRef Medline
19. Hochholzer W, Trenk D, Bestehorn HP, et al. **Impact of the degree of peri-interventional platelet inhibition after loading with clopidogrel on early clinical outcome of elective coronary stent placement.** *J Am Coll Cardiol* 2006;48:1742–50 CrossRef Medline
20. Yang H, Li Y, Jiang Y, et al. **Thromboelastography for monitoring platelet function in unruptured intracranial aneurysm patients undergoing stent placement.** *Interv Neuroradiol* 2015;21:61–68 CrossRef Medline
21. Yang H, Li Y, Jiang Y. **Insufficient platelet inhibition and thromboembolic complications in patients with intracranial aneurysms after stent placement.** *J Neurosurg* 2015 Nov 20. [Epub ahead of print] Medline
22. Hwang G, Huh W, Lee JS, et al. **Standard vs modified antiplatelet preparation for preventing thromboembolic events in patients with high on-treatment platelet reactivity undergoing coil embolization for an unruptured intracranial aneurysm: a randomized clinical trial.** *JAMA Neurol* 2015;72:764–72 CrossRef Medline
23. Wiviott SD, Antman EM, Braunwald E. **Prasugrel.** *Circulation* 2010;122:394–403 CrossRef Medline
24. Wiviott SD, Braunwald E, McCabe CH, et al. **Intensive oral antiplatelet therapy for reduction of ischaemic events including stent thrombosis in patients with acute coronary syndromes treated with percutaneous coronary intervention and stenting in the TRITON-TIMI 38 trial: a subanalysis of a randomised trial.** *Lancet* 2008;371:1353–63 CrossRef Medline
25. Wiviott SD, Braunwald E, McCabe CH, et al. **Prasugrel versus clopidogrel in patients with acute coronary syndromes.** *N Engl J Med* 2007;357:2001–15 CrossRef Medline
26. Sangkuhl K, Klein TE, Altman RB. **Clopidogrel pathway.** *Pharmacogenet Genomics* 2010;20:463–65 CrossRef Medline
27. Cattaneo M. **Fast, potent, and reliable inhibition of platelet aggregation.** *Eur Heart J Suppl* 2009;11:G9–13 CrossRef
28. Stetler WR, Chaudhary N, Thompson BG, et al. **Prasugrel is effective and safe for neurointerventional procedures.** *J Neurointerv Surg* 2013;5:332–36 CrossRef Medline
29. Akbari SH, Reynolds MR, Kadkhodayan Y, et al. **Hemorrhagic complications after prasugrel (Effient) therapy for vascular neurointerventional procedures.** *J Neurointerv Surg* 2013;5:337–43 CrossRef Medline



# Mechanical Thrombectomy in Patients with Acute Ischemic Stroke and Lower NIHSS Scores: Recanalization Rates, Periprocedural Complications, and Clinical Outcome

J. Pfaff, C. Herweh, M. Pham, S. Schönenberger, S. Nagel, P.A. Ringleb, M. Bendszus, and M. Möhlenbruch



## ABSTRACT

**BACKGROUND AND PURPOSE:** Mechanical thrombectomy, in addition to intravenous thrombolysis, has become standard in acute ischemic stroke treatment in patients with large-vessel occlusion in the anterior circulation. However, previous randomized controlled stroke trials were not focused on patients with mild-to-moderate symptoms. Thus, there are limited data for patient selection, prediction of clinical outcome, and occurrence of complications in this patient population. The purpose of this analysis was to assess clinical and interventional data in patients treated with mechanical thrombectomy in case of ischemic stroke with mild-to-moderate symptoms.

**MATERIALS AND METHODS:** We performed a retrospective analysis of a prospectively collected stroke data base. Inclusion criteria were anterior circulation ischemic stroke treated with mechanical thrombectomy at our institution between September 2010 and October 2015 with an NIHSS score of  $\leq 8$ .

**RESULTS:** Of 484 patients, we identified 33 (6.8%) with the following characteristics: median NIHSS = 5 (interquartile range, 4–7), median onset-to-groin puncture time = 320 minutes (interquartile range, 237–528 minutes). Recanalization (TICI = 2b–3) was achieved in 26 (78.7%) patients. Two cases of symptomatic intracranial hemorrhage were observed. Favorable (mRS 0–2) and moderate (mRS 0–3) clinical outcome at 90 days was achieved in 21 (63.6%) and 30 (90.9%) patients, respectively.

**CONCLUSIONS:** The clinical outcome of patients undergoing mechanical thrombectomy for acute ischemic stroke with mild stroke due to large-vessel occlusion appears to be predominately favorable, even in a prolonged time window. However, although infrequent, angiographic complications could impair clinical outcome. Future randomized controlled trials should assess the benefit compared with the best medical treatment.

**ABBREVIATION:** IQR = interquartile range

In several randomized multicenter stroke trials, mechanical thrombectomy has proved to be an effective treatment for large intracranial vessel occlusion in patients with acute ischemic stroke in the anterior circulation.<sup>1–5</sup> With the exception of the Multicenter Randomized Clinical Trial of Endovascular Treatment for Acute Ischemic Stroke in the Netherlands (MR CLEAN) trial<sup>4</sup> and Extending the Time for Thrombolysis in Emergency

Neurological Deficits–Intra-Arterial (EXTEND-IA),<sup>1</sup> all of those stroke trials did not include patients with minor-to-moderate stroke symptoms but focused on patients with a moderate or severe stroke with a score of at least 6–8 or higher on the National Institutes of Health Stroke Scale. Consequently, the median NIHSS score for patients who underwent mechanical thrombectomy was about 15–17 in all trials; including the MR CLEAN and EXTEND-IA trials.

Large intracranial vessel occlusions are not necessarily associated with a high baseline NIHSS score and could be missed in patients with low NIHSS scores.<sup>6</sup> In a large single-center cohort, 72% of the patients presenting with mild stroke symptoms did not undergo advanced stroke imaging (eg, CT angiography or CT perfusion) before intravenous thrombolysis. However, visualization of a possible proximal occlusion is essential for further treatment decisions. If thrombus length exceeds 8 mm, intravenous thrombolysis has almost no potential to recanalize the occluded vessel.<sup>7,8</sup> The chance for a good clinical outcome

Received March 4, 2016; accepted after revision May 5.

From the Departments of Neuroradiology (J.P., C.H., M.P., M.B., M.M.) and Neurology (S.S., S.N., P.A.R.), University of Heidelberg, Heidelberg, Germany.

Christian Herweh, Mirko Pham, Silvia Schönenberger, Simon Nagel, and Peter Arthur Ringleb contributed to data collection and reporting of this study.

The authors declare that there is no conflict of interest. This research received no specific grant from any funding agency in the public, commercial, or not-for-profit sectors.

Please address correspondence to Markus Möhlenbruch, MD, Universität Heidelberg, Abteilung für Neuroradiologie, Im Neuenheimer Feld 400, 69120 Heidelberg, Germany; e-mail: markus.moehlenbruch@med.uni-heidelberg.de

<http://dx.doi.org/10.3174/ajnr.A4862>

(mRS 0–2) is only 7.7% in such cases.<sup>7</sup> Furthermore, despite intravenous thrombolysis, mortality is 1.3%, and 30.3% of the patients who presented with mild initial stroke symptoms could not ambulate independently at discharge.<sup>9</sup>

Even though the complication rate in mechanical thrombectomy is low, the clinical benefit for the patient has to outperform the cost and potential risks. Here, we assessed the outcome of patients with acute ischemic minor-to-moderate stroke who underwent mechanical thrombectomy at our institution. We present data on the location of occlusions, thrombus length, collateral status, recanalization rates, periprocedural complications, and clinical outcome.

## **MATERIALS AND METHODS**

### **Patient Selection**

This analysis was approved by our local ethics committee. Due to its retrospective character, the requirement for subsequent written informed consent was waived.

From a prospectively collected acute ischemic stroke data base, we selected patients who presented with a minor or moderate stroke (NIHSS  $\leq 8$ ) and underwent mechanical thrombectomy at our institution between September 2010 and October 2015. The NIHSS cutoff of  $\leq 8$  was used because of the lack of a consistent definition for minor or mild stroke symptoms in the literature.<sup>10</sup> Furthermore, this specific NIHSS inclusion criterion was used to fill the gap between (almost) nonexistent symptoms and the NIHSS inclusion criteria covered by most of the large randomized stroke trials. Each patient was examined by a neurologist, including a detailed assessment of the NIHSS score, in the emergency department on admission. Patients with suspected acute ischemic stroke underwent a standardized stroke imaging protocol: either CT (including a non-contrast-enhanced CT, CT perfusion, and CT angiography) or MR imaging (including axial DWI, TOF-MRA, axial SWI, axial FLAIR, contrast-enhanced MRA of the aortic arch and cervical arteries, and axial PWI) for assessment of eligibility for intravenous thrombolysis and mechanical thrombectomy. The decision between MR imaging and CT was made individually, depending on MR imaging eligibility and the availability of MR imaging and CT scanners, the patient's condition, and known or unknown time of symptom onset.

### **Stroke Therapy**

Administration and dosing of intravenous thrombolysis followed national and international guidelines and was limited to patients treated within 4.5 hours after symptom onset.

Patients were considered eligible for mechanical thrombectomy by the treating neurologist and neurointerventionalist if an occlusion of a major artery was detected by CTA or MRA and initial imaging excluded hemorrhage. In case of unknown symptom onset, patients were considered eligible for mechanical thrombectomy according to imaging criteria. There was no lower limit to stroke severity, and identical stroke severity thresholds were used for mechanical thrombectomy and intravenous thrombolysis. No age limit was defined, but eligibility for mechanical thrombectomy was made individually on the basis of the patient's

comorbidities, prestroke condition, and the assumed will of the patient.

Intraprocedural use of mechanical and/or pharmacologic treatment remained at the discretion of the treating physicians. General anesthesia was routinely administered during mechanical thrombectomy between September 2010 and July 2013. Since August 2013, procedures were also performed with the patient under conscious sedation.<sup>11</sup> Peri-interventional management and monitoring of physiologic target values, according to our in-house standard operating procedure adapted to the patient and situation, were performed by the neurointensivist.

### **Postinterventional Management**

All patients were admitted to either our neurologic intensive care unit or stroke unit after mechanical thrombectomy and treated according to in-house standard operating procedures. Follow-up imaging (either CT or MR imaging) was routinely performed at 20–36 hours after treatment or earlier if neurologic deterioration occurred. Postinterventional NIHSS and modified Rankin Scale scores were assessed by detailed physical examinations performed by the treating physicians in our wards. Follow-up assessment (including the modified Rankin Scale score) after 3 months was obtained by an inpatient visit or a structured telephone interview by a neurologist not blinded to the type of treatment.

### **Data Collection**

Data collection included baseline demographics (age and sex) and medical history (eg, atrial fibrillation, hypertension, congestive heart failure, coronary artery disease, hypercholesterolemia, diabetes mellitus, history of smoking, and previous stroke) and symptom-onset time and stroke severity as measured by the NIHSS. The time of stroke imaging and the start of angiography were captured automatically by the CT scanners and angiography system. The location of the occlusion and thrombus length were assessed on angiographic images, and the degree of collateral supply was scored according to Tan et al<sup>12</sup>: 0 = absence of collateral vessels in the MCA territory; 1 = collateral supply filling of  $>0\%$  but  $\leq 50\%$  of the occluded MCA territory; 2 = collateral supply filling  $>50\%$  but  $<100\%$  of the occluded MCA territory; 3 = 100% collateral supply filling the occluded MCA territory. Devices and medication used during the intervention procedures, number of thrombectomy maneuvers, and intraprocedural complications were evaluated according to the treatment protocols. Angiographic outcome by the modified Thrombolysis in Cerebral Infarction scale<sup>13</sup> and complications (eg, vessel perforation, dissection) were assessed by a senior neurointerventionalist (M.M.). Cerebral infarction and posttreatment intracranial hemorrhage (by the criteria from the Heidelberg Bleeding Classification<sup>14</sup>) were assessed by using routine follow-up imaging performed 20–36 hours after intervention or earlier in case of clinical deterioration.

### **Statistical Analysis**

All statistical analyses were performed by using SPSS Statistics 21.0.0.0 (IBM, Armonk, New York).

**Table 1: Baseline characteristics of patients with minor to mild stroke who received mechanical thrombectomy**

	Patients (n = 33)
Age (yr) (mean) (SD)	68 (16)
Male (%)	14 (42.4)
Hypertension (%)	21 (63.6)
Diabetes mellitus (%)	4 (12.1)
Atrial fibrillation (%)	13 (39.4)
Coronary artery disease (%)	7 (21.2)
Congestive heart failure (%)	3 (9.1)
Hypercholesterolemia (%)	8 (24.2)
Previous stroke (%)	0
History of smoking (%)	8 (24.2)
Prestroke mRS	
0 (%)	28 (84.8)
1 (%)	2 (6.1)
2 (%)	1 (3)
3 (%)	2 (6.1)
Initial NIHSS score (median) (IQR)	5 (4–7)
CT	n = 18
MR imaging	n = 15
ASPECTS <sup>a</sup> (median) (IQR)	
CT	10 (9–10)
MR imaging	8 (7–9) <sup>b</sup>
Time from stroke onset to imaging (min) (median) (IQR)	175 (72–279)
Intravenous tPA (%)	22 (66.7)
Time from stroke onset to intravenous tPA <sup>c</sup> (min) (median) (IQR)	156 (94–238)
Time from stroke onset to groin puncture (min) (median) (IQR)	320 (237–528)
Occlusion site	
ICA (excluding carotid T) (%)	4 (12.1)
Tandem occlusion (cervical ICA and carotid T/M1)	3 (9.1)
Carotid T (%)	2 (6.1)
M1 (%)	17 (51.5)
M2 (%)	7 (21.2)
Collateral status	
0 (%)	0
1 (%)	2 (6.1)
2 (%)	7 (21.2)
3 (%)	24 (72.7)
Thrombus length (mm)	12 (10–16)

<sup>a</sup> According to modality.

<sup>b</sup> MR-ASPECTS assessed on axial diffusion-weighted images.

<sup>c</sup> For patients eligible for intravenous thrombolysis.

## RESULTS

Between September 2010 and October 2015, 484 patients underwent mechanical thrombectomy due to acute ischemic stroke in the anterior circulation at our institution. Thirty-three of these (6.8%) patients were identified with a pretherapeutic NIHSS score of  $\leq 8$  (for patient baseline characteristics, see Table 1). Most often, mechanical thrombectomy was performed with a stent retriever with distal aspiration with an intermediate catheter ( $n = 29$ ; 87.9%). Four patients (12.1%) were treated with primary aspiration thrombectomy. Ten of 33 (30.3%) patients underwent additional carotid artery stent placement due to cervical carotid artery occlusion ( $n = 4$ ), stenosis ( $n = 3$ ), or dissection ( $n = 3$ ). For the type and manufacturer of the devices used and number of recanalization maneuvers performed, see Table 2.

## Angiographic Outcome

With a median of 2 recanalization maneuvers (interquartile range [IQR], 1–3), TICI 2b–3 was achieved in 26/33 (78.8%) patients (TICI 2b:  $n = 11$ , 33.3%; TICI 2c:  $n = 2$ , 6.1%; TICI 3:  $n = 13$ , 39.4%). In 7/33 (21.2%) patients, TICI 2a was achieved.

## Periprocedural Complications and Frequency of Infarction and Hemorrhage in the MCA Territory

We observed 1 case of vessel perforation causing a fatal subarachnoid hemorrhage. Additionally, 5/33 (15.1%) patients had angiographically occult, minor ipsilateral SAH detected in the routine follow-up CT 20–36 hours after mechanical thrombectomy without the need of further treatment (Heidelberg Bleeding Classification: class 3c). There were no patients with an embolism in a new vascular territory. Furthermore, no cases of air emboli, vasospasm, or device detachment were observed.

On the basis of previously unknown peripheral artery disease, 1 patient had a subtotal occlusion of the femoral artery with subcritical limb ischemia after deployment of a vascular closure device (Angio-Seal VIP; St. Jude Medical, Minnetonka, Minnesota), requiring surgical removal and endarterectomy.

Follow-up CT imaging revealed partial infarction in the MCA territory in 23/30 (69.7%) patients with a median posttreatment ASPECTS of 8 (IQR, 7–10). In 2/30 (6.7%) patients, hemorrhagic transformation/confluent petechiae without space-occupying effect within the infarcted area in the MCA territory occurred (Heidelberg Bleeding Classification: class 1b/HI2). In addition to the above-mentioned fatal SAH, a second patient sustained a fatal symptomatic intracranial hemorrhage within the infarcted area (Heidelberg Bleeding Classification: class 2/PH2).

## Clinical Outcome

At 90 days, clinical outcome according to the modified Rankin Scale was the following—0:  $n = 4$  (12.1%); 1:  $n = 10$  (30.3%); 2:  $n = 7$  (21.2%); 3:  $n = 9$  (27.3%); 4:  $n = 0$ ; 5:  $n = 0$ ; 6:  $n = 3$  (9.1%).

## DISCUSSION

### Treatment Rationale

In general, proximal occlusions in acute ischemic stroke are associated with a poor clinical outcome.<sup>15</sup> However, as mentioned earlier, proximal occlusions are not necessarily associated with an initial high NIHSS and could be missed in patients with low NIHSS scores.<sup>6</sup> In a large single-center cohort, 488/1398 (35%) patients treated with intravenous thrombolysis for acute ischemic stroke presented with mild symptoms.<sup>16</sup> Most of these patients had a favorable outcome after 3 months (mRS 0–2, 82%). However, only 136/488 (28%) patients underwent advanced stroke imaging (CT angiography or CT perfusion) before treatment. For most patients, there was no information on the site of vascular occlusion.<sup>16</sup> Visualization of the proximal occlusion is a key factor for further treatment decisions because intravenous thrombolysis has a very limited potential to recanalize occluded vessels if thrombus length exceeds 8 mm.<sup>7,8</sup> In our analysis, the median thrombus length was 12 mm.

Previously published data from the Get With The Guidelines—Stroke program by the American Heart Association/American Stroke Association show that 29,200/93,517 (31.2%) patients with

**Table 2: List of types, manufacturers, and number of maneuvers for mechanical thrombectomy**

Device	Manufacturer	Size	No. of Patients Treated <sup>a</sup>	Total No. of Maneuvers
Capture	MindFrame <sup>b</sup>	4.0 × 20 mm	2	2
Catch Mini	Balt <sup>c</sup>	3 × 15 mm	1	2
ERIC	MicroVention <sup>d</sup>	4 × 24 mm	3	4
Revive	Codman Neurovascular <sup>e</sup>	4.5 × 22 mm	6	17
Solitaire 2	Covidien <sup>b</sup>	4 × 20 mm	15	31
Solitaire 2	Covidien	6 × 30 mm	4	4
Trevo ProVue	Stryker <sup>f</sup>	4 × 20 mm	1	2
Trevo ProVue	Stryker	3 × 20 mm	1	1
SofiaPlus	MicroVention	6F	4 <sup>g</sup>	4
Adapt Stent <sup>h</sup>	Boston Scientific <sup>i</sup>	9 × 32 mm	1	
Carotid Wallstent <sup>h</sup>	Boston Scientific	9 × 40 mm	5	
Carotid Wallstent <sup>h</sup>	Boston Scientific	7 × 30 mm	3	
Enterprise Stent <sup>h</sup>	Codman & Shurtleff <sup>e</sup>	4 × 37 mm	1	
Solitaire 2 <sup>h</sup>	Covidien	6 × 30 mm	1	

<sup>a</sup> Some patients were treated with different stent retrievers.

<sup>b</sup> Irvine, California.

<sup>c</sup> Montmorency, France.

<sup>d</sup> Tustin, California.

<sup>e</sup> Raynham, Massachusetts.

<sup>f</sup> Kalamazoo, Michigan.

<sup>g</sup> Primary aspiration thrombectomy.

<sup>h</sup> Implanted devices.

<sup>i</sup> Natick, Massachusetts.

acute ischemic stroke did not receive intravenous thrombolysis because of mild or improving symptoms.<sup>17</sup> Most important, patients with mild strokes who did not receive acute recanalization therapy experienced a poor clinical outcome at 90 days (mRS 3–5 in about 27%–32%; mRS 6, 2%–5%).<sup>17,18</sup> Hence, according to other authors,<sup>18,19</sup> it is of major importance to also screen patients with acute ischemic stroke with mild-to-moderate symptoms for large-vessel occlusion. Considering the occlusion site, thrombus length, collateral status, and extent of early signs of ischemia on pretreatment imaging, mechanical thrombectomy should not be withheld.

### Major Findings

The main finding of our retrospective analysis is that clinical outcome in patients with acute ischemic stroke due to large-vessel occlusion and a lower NIHSS score is predominately favorable after mechanical thrombectomy. We report favorable clinical outcome (mRS 0–2 at 90 days) in 21/33 (63.6%) and moderate clinical outcome (mRS 0–3 at 90 days) in 30/33 (90.9%) patients. In comparison with data from Strbian et al,<sup>16</sup> clinical outcome of our patients does not seem to differ considerably from that in patients treated with intravenous thrombolysis alone. However, there are some relevant differences in the patient populations of both studies: First, 72% of the patients in the cohort of Strbian et al did not have advanced stroke imaging. Therefore, the presence of a proximal occlusion, occlusion site, thrombus length, collateral status, and perfusion deficit remain uncertain. Second, in our patient cohort, median onset-to-intravenous thrombolysis time was 156 minutes, which means that intravenous thrombolysis was, on average, administered later than in the previously mentioned study. Third, in our patients, mechanical thrombectomy was often initiated after a prolonged time window exceeding the eligibility period for intravenous thrombolysis. Nonetheless, 90 days after mechanical thrombectomy, 30/33 (90.9%) patients had

mRS 0–3, which is comparable with the scores of patients who received only intravenous thrombolysis for mild acute ischemic stroke (460/488; 94%) but were treated within a shorter time window. Our findings might indicate a possible treatment effect in patients with a prolonged window who would otherwise be ineligible for acute stroke treatment.

Twelve of 33 (36.4%) of our patients had an mRS of 3–6 at 90 days after stroke and therefore would be categorized as having poor clinical outcome in most interventional stroke trials. However, none of our patients were assessed as mRS 4 or 5 after 3 months. Most patients with poor outcome (27.3%) had a moderate disability and were able to walk unassisted. These data are in accordance with previous studies showing that patients with lower NIHSS scores/minor or mild stroke symptoms could have moderate-to-poor clinical outcomes.<sup>17–19</sup>

Unfortunately, the mortality rate was 9.1% (3/33). Because intravenous thrombolysis did not improve the clinical condition, mechanical thrombectomy was initiated in a prolonged time window in 1 patient with a very poor outcome (mRS 6). Two patients sustained fatal symptomatic intracranial hemorrhage after intravenous thrombolysis and mechanical thrombectomy. From other studies, it is known that patients have a certain risk of symptomatic intracranial hemorrhage after intravenous and/or endovascular stroke therapy of up to 8.1%.<sup>1–5,16,20</sup> In summary, with the exception of 3 cases, most patients who underwent mechanical thrombectomy for acute ischemic stroke with low NIHSS scores had a favorable or at least moderate clinical outcome after 3 months.

Angiographic outcome based on the recanalization rate (TICI = 2b–3; 78.8%) was similar or even higher than that in previous large interventional stroke trials.<sup>1–5</sup> There were no unexpected interventional complications such as air emboli, device detachment, or emboli into a new vascular territory. Angiographically occult, minor ipsilateral subarachnoid hemorrhages were detected in 5/33 (15.1%) patients but had no impact on clinical outcome, which is consistent with previously published data.<sup>21</sup>

There were 2 procedure-related complications: a subtotal occlusion of the femoral artery requiring an operation and an intracranial vessel perforation causing a fatal subarachnoid hemorrhage. Groin complications following catheterization are not uncommon (0.4%–9%).<sup>22–24</sup> The risk of groin complications is higher in an emergency setting, increases with a medical history of peripheral artery disease and the use of larger catheters (≥7F), and varies depending on the vascular closure device deployed.<sup>23–25</sup> Asymptomatic subarachnoid hemorrhage and angiographically occult vessel perforations can be detected quite frequently in follow-up imaging after mechanical thrombectomy in

up to 16.1% of patients.<sup>21,26</sup> Angiographically apparent vessel perforations and symptomatic subarachnoid hemorrhage occur in 0.6%–2.9% of patients after mechanical thrombectomy,<sup>1,4,5,27,28</sup> and reports addressing the immediate treatment of vessel perforation after mechanical thrombectomy have been published.<sup>29</sup> In our case, despite stent deployment without any problems and after a previous retrieval maneuver that had already recanalized the middle cerebral artery main branch, symptomatic subarachnoid hemorrhage occurred following a second retrieval maneuver, causing an MCA perforation (distal M2 segment).

### Limitations

This study has several limitations. There is a potential selection bias in this analysis because all patients underwent advanced stroke imaging (including CT or MR angiography and CT or MR perfusion) before treatment. Patients who did not undergo advanced stroke imaging during the observation period might have been missed for treatment evaluation. Furthermore, we did not have a control group of patients with low NIHSS scores and confirmed proximal occlusion who did not receive mechanical thrombectomy. Due to its focus on acute ischemic stroke in the anterior circulation, this analysis has only a limited value for acute ischemic stroke in the posterior circulation.

There are several uncertainties in patient selection for stroke treatment, and the small sample size of this analysis does not allow a clear NIHSS value as a cutoff for the recommendation for interventional stroke treatment. However, very low NIHSS scores were identified as a potential equipoise point with the least consensus on treatment decision.<sup>30</sup> Therefore, our results with an overall favorable clinical outcome after acute ischemic stroke with low NIHSS scores due to large-vessel occlusion underscore the need for a randomized controlled trial in these patients.

### CONCLUSIONS

The clinical outcome of patients undergoing mechanical thrombectomy for acute ischemic mild stroke due to large-vessel occlusion appears to be predominately favorable, even in a prolonged time window. However, although infrequent, angiographic complications could impair clinical outcome. Future randomized controlled trials should assess the benefit compared with the best medical treatment.

Disclosures: Johannes Pfaff—UNRELATED: Grants/Grants Pending: Siemens\*; Payment for Lectures (including service on Speakers Bureaus): Siemens, Comments: payment for lectures during Deutscher Röntgenkongress 2015 (German X-Ray Congress); Travel/Accommodations/Meeting Expenses Unrelated to Activities Listed: Stryker Neurovascular, Comments: travel/accommodations/meeting expenses for Jahrestagung der Deutschen Gesellschaft für Neuroradiologie 2015 (annual meeting of the German Society for Neuroradiology). Mirko Pham—UNRELATED: Grants/Grants Pending: project grant from Guerbet,\* memorial stipend from Else Kröner-Fresenius-Foundation\*; Travel/Accommodations/Meeting Expenses Unrelated to Activities Listed: travel reimbursement or speaker honorarium from Penumbra, Covidien, and Bayer HealthCare. Simon Nagel—UNRELATED: Consultancy: Brainomix; Grants/Grants Pending: Brainomix\*; Payment for Lectures (including service on Speakers Bureaus): Bayer HealthCare\*; Travel/Accommodations/Meeting Expenses Unrelated to Activities Listed: Böhlinger Ingelheim.\* Peter A. Ringleb—UNRELATED: Payment for Lectures (including service on Speakers Bureaus): Böhlinger Ingelheim, Bayer HealthCare, Pfizer, Bristol-Myers Squibb, Comments: lecture fees. Martin Bendszus—UNRELATED: Board Membership: Data Safety Monitoring Board Vascular Dynamics; Consultancy: Codman Neuro, F. Hoffmann-La Roche, Guerbet; Grants/Grants Pending: Novartis,\* Hopp Foundation,\* Deutsche Forschungsgemeinschaft (German Research Foundation),\* Siemens\*; Payment for Lectures (in-








cluding service on Speakers Bureaus): Novartis, Codman Neuro, F. Hoffmann-La Roche, Guerbet, Teva, Bayer HealthCare. Markus Möhlenbruch—UNRELATED: Board Membership: Codman Neuro; Consultancy: MicroVention, phenox; Payment for Lectures (including service on Speakers Bureaus): Codman Neuro, MicroVention.\* Money paid to the institution.

### REFERENCES

- Campbell BC, Mitchell PJ, Kleinig TJ, et al; EXTEND-IA Investigators. Endovascular therapy for ischemic stroke with perfusion-imaging selection. *N Engl J Med* 2015;372:1009–18 CrossRef Medline
- Jovin TG, Chamorro A, Cobo E, et al; REVASCAT Trial Investigators. Thrombectomy within 8 hours after symptom onset in ischemic stroke. *N Engl J Med* 2015;372:2296–306 CrossRef Medline
- Saver JL, Goyal M, Bonafe A, et al; SWIFT PRIME Investigators. Stent-retriever thrombectomy after intravenous t-PA vs. t-PA alone in stroke. *N Engl J Med* 2015;372:2285–95 CrossRef Medline
- Berkhemer OA, Fransen PS, Beumer D, et al; MR CLEAN Investigators. A randomized trial of intraarterial treatment for acute ischemic stroke. *N Engl J Med* 2015;372:11–20 CrossRef Medline
- Goyal M, Demchuk AM, Menon BK, et al; ESCAPE Trial Investigators. Randomized assessment of rapid endovascular treatment of ischemic stroke. *N Engl J Med* 2015;372:1019–30 CrossRef Medline
- Maas MB, Furie KL, Lev MH, et al. National Institutes of Health Stroke Scale Score is poorly predictive of proximal occlusion in acute cerebral ischemia. *Stroke* 2009;40:2988–93 CrossRef Medline
- Riedel CH, Zimmermann P, Jensen-Kondering U, et al. The importance of size: successful recanalization by intravenous thrombolysis in acute anterior stroke depends on thrombus length. *Stroke* 2011;42:1775–77 CrossRef Medline
- Behrens L, Möhlenbruch M, Stampfl S, et al. Effect of thrombus size on recanalization by bridging intravenous thrombolysis. *Eur J Neurol* 2014;21:1406–10 CrossRef Medline
- Romano JG, Smith EE, Liang L, et al. Outcomes in mild acute ischemic stroke treated with intravenous thrombolysis: a retrospective analysis of the Get With the Guidelines-Stroke registry. *JAMA Neurol* 2015;72:423–31 CrossRef Medline
- Fischer U, Baumgartner A, Arnold M, et al. What is a minor stroke? *Stroke* 2010;41:661–66 CrossRef Medline
- Schönenberger S, Möhlenbruch M, Pfaff J, et al. Sedation vs. Intubation for Endovascular Stroke Treatment (SIESTA): a randomized monocentric trial. *Int J Stroke* 2015;10:969–78 CrossRef Medline
- Tan IY, Demchuk AM, Hopyan J, et al. CT angiography clot burden score and collateral score: correlation with clinical and radiologic outcomes in acute middle cerebral artery infarct. *AJNR Am J Neuroradiol* 2009;30:525–31 CrossRef Medline
- Goyal M, Fargen KM, Turk AS, et al. 2C or not 2C: defining an improved revascularization grading scale and the need for standardization of angiography outcomes in stroke trials. *J Neurointerv Surg* 2014;6:83–86 CrossRef Medline
- von Kummer R, Broderick JP, Campbell BCV, et al. The Heidelberg Bleeding Classification: classification of bleeding events after ischemic stroke and reperfusion therapy. *Stroke* 2015;46:2981–86 CrossRef Medline
- Smith W, Tsao J, Billings M, et al. Prognostic significance of angiographically confirmed large vessel intracranial occlusion in patients presenting with acute brain ischemia. *Neurocrit Care* 2006;4:14–17 CrossRef Medline
- Strbian D, Piironen K, Meretoja A, et al; Helsinki Stroke Thrombolysis Registry Group. Intravenous thrombolysis for acute ischemic stroke patients presenting with mild symptoms. *Int J Stroke* 2013;8:293–99 CrossRef Medline
- Smith EE, Fonarow GC, Reeves MJ, et al. Outcomes in mild or rapidly improving stroke not treated with intravenous recombinant tissue-type plasminogen activator: findings from Get With The Guidelines-Stroke. *Stroke* 2011;42:3110–15 CrossRef Medline
- Mokin M, Masud MW, Dumont TM, et al. Outcomes in patients with acute ischemic stroke from proximal intracranial vessel occlu-

- sion and NIHSS score below 8. *J Neurointerv Surg* 2014;6:413–17 CrossRef Medline
19. Kim JT, Park MS, Chang J, et al. **Proximal arterial occlusion in acute ischemic stroke with low NIHSS scores should not be considered as mild stroke.** *PLoS One* 2013;8:e70996 CrossRef Medline
  20. Hacke W, Kaste M, Bluhmki E, et al; ECASS Investigators. **Thrombolysis with alteplase 3 to 4.5 hours after acute ischemic stroke.** *N Engl J Med* 2008;359:1317–29 CrossRef Medline
  21. Yoon W, Jung MY, Jung SH, et al. **Subarachnoid hemorrhage in a multimodal approach heavily weighted toward mechanical thrombectomy with Solitaire stent in acute stroke.** *Stroke* 2013;44:414–19 CrossRef Medline
  22. Shah VA, Martin CO, Hawkins AM, et al. **Groin complications in endovascular mechanical thrombectomy for acute ischemic stroke: a 10-year single center experience.** *J Neurointerv Surg* 2016;8:568–70 CrossRef Medline
  23. Stegemann E, Hoffmann R, Marso S, et al. **The frequency of vascular complications associated with the use of vascular closure devices varies by indication for cardiac catheterization.** *Clin Res Cardiol* 2011;100:789–95 CrossRef Medline
  24. Nasser TK, Mohler ER 3rd, Wilensky RL, et al. **Peripheral vascular complications following coronary interventional procedures.** *Clin Cardiol* 1995;18:609–14 CrossRef Medline
  25. Carey D, Martin JR, Moore CA, et al. **Complications of femoral artery closure devices.** *Catheter Cardiovasc Interv* 2001;52:3–7; discussion 8 Medline
  26. Pfaff J, Herweh C, Pham M, et al. **Mechanical thrombectomy of distal occlusions in the anterior cerebral artery: recanalization rates, periprocedural complications, and clinical outcome.** *AJNR Am J Neuroradiol* 2016;37:673–78 CrossRef Medline
  27. Dorn F, Stehle S, Lockau H, et al. **Endovascular treatment of acute intracerebral artery occlusions with the Solitaire stent: single-center experience with 108 recanalization procedures.** *Cerebrovasc Dis* 2012;34:70–77 CrossRef Medline
  28. Behme D, Gondecki L, Fiethen S, et al. **Complications of mechanical thrombectomy for acute ischemic stroke: a retrospective single-center study of 176 consecutive cases.** *Neuroradiology* 2014;56:467–76 CrossRef Medline
  29. Leishangthem L, Satti SR. **Vessel perforation during withdrawal of Trevo ProVue stent retriever during mechanical thrombectomy for acute ischemic stroke.** *J Neurosurg* 2014;121:995–98 CrossRef Medline
  30. Balucani C, Bianchi R, Feldmann E, et al. **To treat or not to treat? Pilot survey for minor and rapidly improving stroke.** *Stroke* 2015;46:874–76 CrossRef Medline

# Effect of Intracranial Atherosclerotic Disease on Endovascular Treatment for Patients with Acute Vertebrobasilar Occlusion

 Y.W. Kim,  J.M. Hong,  D.G. Park,  J.W. Choi,  D.-H. Kang,  Y.S. Kim,  O.O. Zaidat,  A.M. Demchuk,  Y.H. Hwang, and  J.S. Lee



## ABSTRACT

**BACKGROUND AND PURPOSE:** Although intracranial atherosclerotic disease is often encountered during endovascular treatment for acute vertebrobasilar occlusions, its clinical implication is not well-known. We aimed to evaluate whether intracranial atherosclerotic disease influences the clinical outcomes following endovascular treatment of acute vertebrobasilar occlusive stroke.

**MATERIALS AND METHODS:** Fifty-one patients with acute vertebrobasilar occlusive stroke were included. The onset-to-groin puncture time was  $\leq 12$  hours, and aspiration- or stent-based thrombectomy was used as the primary treatment method. Following primary endovascular treatment, intracranial atherosclerotic disease (IAD group) was angiographically diagnosed when a fixed focal stenosis was observed at the occlusion site, whereas embolism (embolic group) was diagnosed if no stenosis was observed. Clinical and treatment variables were compared in both groups, and IAD was evaluated as a prognostic factor for clinical outcomes.

**RESULTS:** The baseline NIHSS score tended to be lower (14 versus 22,  $P = .097$ ) in the IAD group ( $n = 19$ ) than in the embolic group ( $n = 32$ ). The procedural time was longer in the IAD group (96 versus 61 minutes,  $P = .002$ ), despite similar rates of TIC1 2b–3 (89.5% versus 87.5%,  $P = 1.000$ ). The NIHSS score at 7 days was higher (21 versus 8,  $P = .060$ ) and poor outcomes (mRS 4–6 at 3 months) were more frequent in the IAD group (73.7% versus 43.8%,  $P = .038$ ). IAD (odds ratio, 5.469; 95% CI, 1.09–27.58;  $P = .040$ ) was independently associated with poor outcomes.

**CONCLUSIONS:** An arterial occlusion related to IAD was associated with a longer procedural time and poorer clinical outcome. Further studies are warranted to elucidate the appropriate endovascular strategy.

**ABBREVIATIONS:** FAST = forced arterial suction thrombectomy; IAD = intracranial atherosclerotic disease

Acute vertebrobasilar occlusive stroke is a condition with high morbidity and mortality.<sup>1</sup> With the advancement of endovascular treatment, the prognosis of acute ischemic stroke due to

intracranial large-artery occlusion has improved.<sup>2–8</sup> Recently, successful clinical trials of endovascular treatment have been conducted, but these studies have mostly targeted anterior circulation occlusions.<sup>4–8</sup> Evidence of endovascular treatment for posterior circulation occlusions is still lacking, though a few recent studies have shown better clinical outcomes compared with previous results.<sup>9,10</sup>


Underlying stenosis due to intracranial atherosclerotic disease (IAD) is often encountered during endovascular treatment for acute intracranial large-artery occlusion. Regarding the pathomechanism of stroke, in situ thrombotic occlusions may occur in addition to hemodynamic compromise due to stenosis.<sup>11–13</sup> This IAD-related occlusion causes acute ischemic stroke and was reported to be more frequent in the posterior circulation than in the anterior circulation.<sup>14</sup> According to previous literature, the prognosis of acute vertebrobasilar occlusions has been associated with various factors, including the initial severity of neurologic deficits, time to treatment, location of the occlusion, degree of collaterals, treatment modalities, and timely reperfusion.<sup>1,10,11,15–18</sup> Nevertheless, to our knowledge, IAD

Received November 7, 2015; accepted after revision April 24, 2016.

From the Departments of Neurology (Y.W.K., Y.H.H.), Radiology (Y.W.K., D.-H.K., Y.S.K.), and Neurosurgery (D.-H.K.), Kyungpook National University School of Medicine and Hospital, Daegu, Republic of Korea; Departments of Neurology (J.M.H., D.G.P., J.S.L.) and Radiology (J.W.C.), Ajou University School of Medicine and Hospital, Suwon, Republic of Korea; Department of Neurology (O.O.Z.), Froedtert Hospital and Medical College of Wisconsin, Milwaukee, Wisconsin; and Departments of Clinical Neurosciences and Radiology (A.M.D.), Hotchkiss Brain Institute, University of Calgary, Calgary, Alberta, Canada.

This research was partly supported by the Basic Science Research Program through the National Research Foundation of Korea funded by the Ministry of Education (NRF-2014RIA1A1008249, J.S.L.).

Please address correspondence to Jin Soo Lee, MD, PhD, Department of Neurology, Ajou University School of Medicine and Hospital, San 5, Woncheon-dong, Yeongtong-gu, Suwon, Kyungki-do, 443–721, Republic of Korea; e-mail: jinsoo22@gmail.com; Yang-Ha Hwang, MD, PhD, Department of Neurology, Kyungpook National University School of Medicine and Hospital, 130, Dongduk-ro, Jung-gu, Daegu, 41944, Daegu, Republic of Korea, e-mail: yangha.hwang@gmail.com

 Indicates open access to non-subscribers at [www.ajnr.org](http://www.ajnr.org)

<http://dx.doi.org/10.3174/ajnr.A4844>

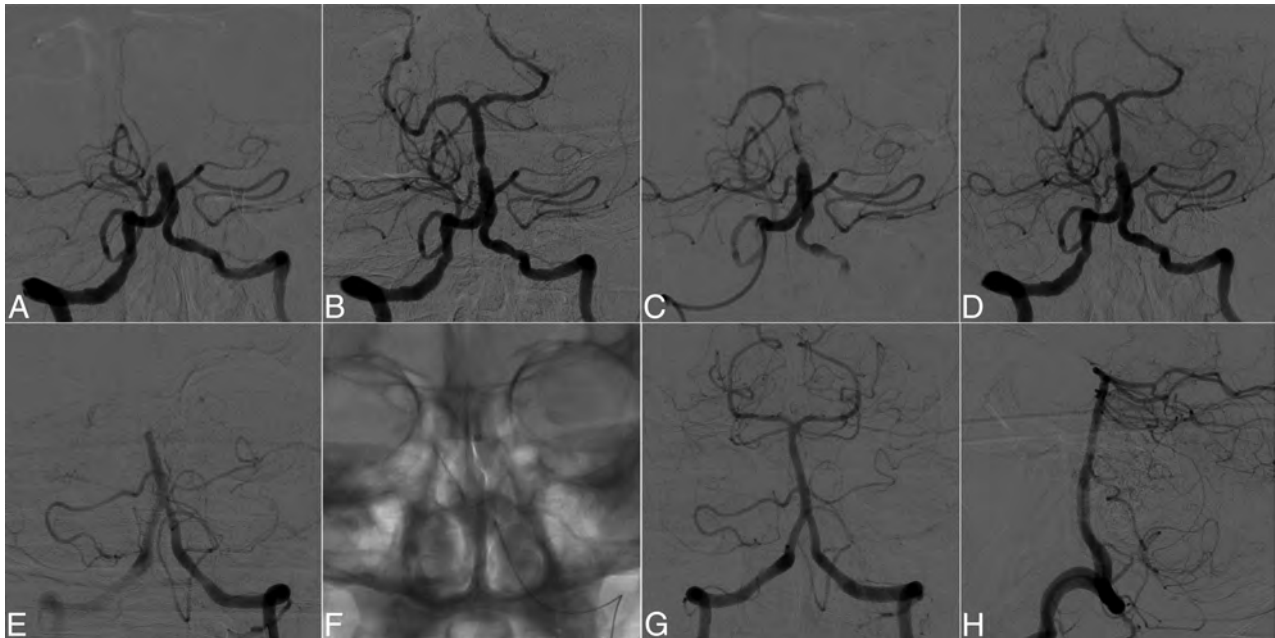


**FIG 1.** Sequential angiographic images of a patient with an atherosclerotic basilar occlusion (A–D) and a patient with an embolic basilar occlusion (E–H). An occlusion in the basilar artery in a 70-year-old woman (A). Note significant focal stenosis at the occlusion site after the first pass of thrombectomy (B). Follow-up angiography after 10 minutes demonstrates that the vessel is occluding again (C). Significant fixed focal stenosis in the final angiogram after repeat thrombectomy (D). An occlusion in the basilar artery of a 63-year-old man (E). A single forced arterial suction thrombectomy (F), and complete reperfusion of the basilar artery without residual stenosis as shown on the Towne and lateral views, respectively (G and H).

has not been evaluated as a prognostic factor, especially in posterior circulation occlusions.

In the present study, we evaluated whether IAD influences the clinical outcome following endovascular treatment of acute ischemic stroke caused by vertebrobasilar occlusion. We compared the interventional factors and clinical outcome between IAD-related and embolic occlusions.

## MATERIALS AND METHODS

### Patients

From consecutive patients with acute ischemic stroke admitted to 2 Korean university hospitals between March 2009 and March 2014, we retrospectively reviewed and enrolled those who met the following criteria: 1) patients who showed acute neurologic symptoms attributable to intracranial vertebral and/or basilar artery occlusion identified by CTA or MRA, 2) time from onset of symptoms to groin puncture of  $\leq 12$  hours, and 3) endovascular treatment by using the forced arterial suction thrombectomy (FAST) method with a Penumbra reperfusion catheter (Penumbra, Alameda, California) or stent-based thrombectomy as the primary treatment. Patients were excluded if reperfusion was never observed, because both angiographic etiologies cannot be differentiated; or another etiology of stroke, including vasculitis, arterial dissection, or Moyamoya disease, was diagnosed by transfemoral cerebral angiography. The institutional review board of both hospitals approved this study, and informed consent was obtained from patients and/or their caregivers.

Using transfemoral cerebral angiography, we diagnosed IAD when a significant fixed focal stenosis was observed at the occlusion site during endovascular treatment or final angiography (Fig 1A–D). Significant stenosis was defined according to the follow-

ing criteria: 1) degree of fixed stenosis of  $>70\%$ ,<sup>19</sup> or 2) moderate stenosis with either flow and perfusion impairment on angiography or an evident tendency toward reocclusion,<sup>13</sup> even after sufficient primary endovascular treatment was performed. Underlying IAD can be observed from partial recanalization spontaneously or after intravenous thrombolytic treatment, but these cases were excluded in this study because primary thrombectomy devices for intracranial occlusions were allowed. An embolism was diagnosed if no stenosis was observed with sufficient blood flow and without a reocclusion tendency (Fig 1E–H). The steps used to diagnose IAD in an occlusion during endovascular treatment are summarized in Fig 2. Patients were classified into the IAD or embolic group, and the clinical and treatment variables were compared.

### Acute Stroke Management Protocol and Endovascular Procedure

The initial neurologic examination, which included the NIHSS, was performed in the emergency department. Nonenhanced brain CT was performed to evaluate brain parenchyma and to exclude intracerebral hemorrhage, while CTA or MRA was used to assess arterial occlusions. In terms of intravenous thrombolysis, recombinant tissue plasminogen activator was administered to patients within a 3-hour (until December 2012) or 4.5-hour window (from January 2013) according to the stroke guidelines.<sup>20</sup> Additionally, endovascular treatment was used in the following cases: 1) a baseline NIHSS score of  $\geq 4$ , 2) baseline modified Rankin Scale score of  $\leq 2$ , 3) the presence of vertebrobasilar occlusion on CTA or MRA, 4) no intracerebral hemorrhage on brain CT, and 5) groin puncture time of  $\leq 12$  hours from the onset of symptoms.



- 1 Confirm the intracranial large artery occlusion and exclude uncommon cerebral arterial diseases such as dissection, Moyamoya disease, and vasculitis by initial transfemoral cerebral angiography.
- 2 Exclude pure embolism when the occluded vessel is completely recanalized after primary thrombectomy.\*
- 3 Determine whether a remnant focal stenosis is significant following primary thrombectomy, or spontaneous or intravenous thrombolysis-induced partial recanalization.
  - \* It is significant if the stenotic degree is over 70%. [or]
  - It is significant if the reocclusion tendency or flow impairment seen through the stenotic degree is moderate.
- 4 To angiographically exclude periprocedural complications such as vessel injury or vasospasm, repeat angiography is performed 10–20 minutes after final recanalization.

**FIG 2.** Steps to angiographically diagnosing intracranial atherosclerotic disease in an occlusion.

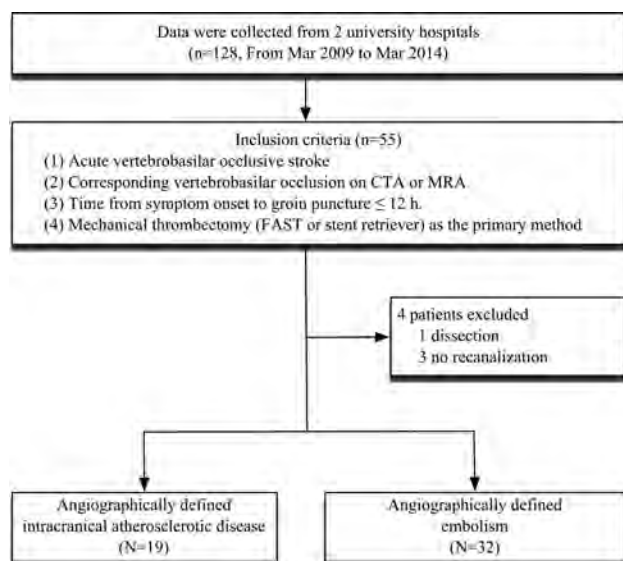


**FIG 3.** Flowchart of the present study.

First, a guide catheter was positioned from the femoral artery to the distal V2 segment of the dominant vertebral artery. In most cases, we used a conventional access device such as the Shuttle-SL guide sheath (Cook, Bloomington, Indiana) or Envoy (Codman & Shurtleff, Raynham, Massachusetts), and not a balloon catheter, for posterior circulation treatment. Then, the neurointerventionalists decided to perform a mechanical thrombectomy by using a Penumbra reperfusion catheter (041/4MAX/3MAX; Penumbra) or a stent retriever (Solitaire AB/FR; Covidien, Irvine, California) as the primary strategy. For the FAST method, the Penumbra reperfusion catheter was placed at the proximal end of the clot. After wedging the clot into the catheter tip for several minutes, we withdrew the catheter gently while maintaining a negative pressure by using a 50-mL syringe.<sup>21</sup> In case of stent retrieval, a microcatheter was advanced through the occluded segment, and selective angiography was performed distal to the clot to confirm the landing zone of the stent retriever. The microcatheter was placed about 1 cm beyond the distal margin of the clot, and the stent retriever was deployed for several minutes. The stent retriever and microcatheter were drawn back into the guide catheter under remote aspiration through the guide catheter by suction by using a 50-mL syringe.

These procedures were repeated until successful reperfusion. If reperfusion was not achieved or the occlusion was sustained, we applied rescue treatments, including the switching strategy,<sup>22</sup>

angioplasty,<sup>23</sup> stent placement,<sup>24</sup> and intra-arterial tirofiban infusion,<sup>13</sup> with consensus from the neurointerventionalist and neurologist. Follow-up angiography was performed 10–20 minutes after recanalization. If there were no changes or improvement of flow between the angiographic runs, the endovascular procedure was completed. However, if flow impairment or reocclusion occurred, we performed additional procedures, including repetitive mechanical thrombectomy or rescue treatments.

### Clinical and Radiographic Evaluation

Data regarding the patient demographics, laboratory findings, imaging findings, and time intervals (ie, the symptom onset-to-door time, door-to-groin puncture, and groin puncture to reperfusion) were collected. The procedural time was defined from the groin puncture to reperfusion. The NIHSS scale was assessed at baseline, on day 7, or at discharge if the patient was discharged earlier than day 7. The clinical outcome was assessed by using the mRS at 3 months, which was classified as favorable (mRS score, 0–3) or poor (mRS score, 4–6). Neurologists and neuroradiologists from each hospital independently reviewed the radiologic data of their own hospital while blinded to the clinical information.

Locations of the occlusions were defined as follows: 1) the intracranial vertebral artery (limited to a single vertebral artery), from the V4 segment of the vertebral artery to below the vertebrobasilar junction; 2) the proximal basilar artery, from the vertebrobasilar junction to the anterior inferior cerebellar artery level; 3) the middle basilar artery, from the anterior inferior cerebellar artery to the superior cerebellar artery level; and 4) the distal basilar artery, from the superior cerebellar artery to the basilar artery top level.<sup>15</sup> The presence of any posterior communicating artery was also recorded to assess the collateral flow.

The status of reperfusion was measured by using a TIC1 score.<sup>25</sup> Successful reperfusion was defined as a TIC1 score of 2b or 3. All patients underwent a follow-up nonenhanced brain CT scan 1 day after endovascular treatment. An intracerebral hemorrhage was classified according to the second European-Australasian Acute Stroke Study classification,<sup>26</sup> and symptomatic intracerebral hemorrhage was defined as any hemorrhage associated with an NIHSS score increase of  $\geq 4$  within 24 hours.<sup>2</sup>

### Statistical Analysis

Statistical analyses were performed by using SPSS for Windows (Version 20.0; IBM, Armonk, New York). The  $\chi^2$  test or Fisher exact test was used for frequency comparisons, and the independent *t* test and Mann-Whitney *U* test were used for continuous and nonparametric variables, respectively. Binary logistic regression analysis was performed to confirm whether IAD was an independent predictor of poor outcome at 3 months. For this analysis, age, the baseline NIHSS score, the absence of intravenous rtPA, onset-to-reperfusion time, failed revascularization, and the

**Table 1: Baseline demographics and characteristics**

	IAD	Embolism	P Value
No.	19	32	
Age (yr) (mean)	66.89 ± 10.90	67.84 ± 10.79	.763
Female sex (No.) (%)	6 (31.6)	11 (34.4)	.838
Hypertension	17 (89.5%)	21 (65.6%)	.096 <sup>a</sup>
Diabetes	8 (42.1%)	6 (18.8%)	.071
Hyperlipidemia	11 (57.9%)	12 (37.5%)	.157
Atrial fibrillation	2 (10.5%)	13 (40.6%)	.023
Baseline NIHSS (median) (IQR)	14 (6–23)	22 (14.5–26.5)	.097 <sup>b</sup>
Intravenous rtPA	4 (21.1%)	20 (62.5%)	.004
Calcification on brain CT			.018
None	3 (16.7%)	18 (58.1%)	
Calcification in situ	5 (27.8%)	4 (12.9%)	
Calcification proximal to the occlusion	10 (55.6%)	9 (29.0%)	
Occlusion location on CTA			<.001
Distal BA	2 (15.4%)	21 (87.5%)	
Middle BA	5 (38.5%)	2 (8.3%)	
Proximal BA	4 (30.8%)	0 (0%)	
Intracranial VA	2 (15.4%)	0 (0%)	
Other and mixed	0 (0%)	1 (4.2%)	
Presence of PcomA	16 (84.2%)	27 (84.4%)	1.000

**Note:**—IQR indicates interquartile range; BA, basilar artery; VA, vertebral artery; PcomA, posterior communicating artery.

<sup>a</sup> Fisher exact *t* test.

<sup>b</sup> Mann-Whitney *U* test.

**Table 2: Angiographic and clinical outcomes**

	IAD	Embolism	P Value
Primary endovascular treatment methods			.711 <sup>a</sup>
FAST (No.) (%)	15 (78.9%)	27 (84.4%)	
Stent retriever	4 (21.1%)	5 (15.6%)	
Frequency of rescue treatment	13 (68.4%)	6 (18.8%)	<.001
Switching strategy	3 (16.7%)	2 (6.2%)	.348 <sup>a</sup>
Intra-arterial tirofiban	6 (31.6%)	0 (0%)	.002 <sup>a</sup>
Stenting	6 (31.6%)	4 (12.5%) <sup>b</sup>	.146 <sup>a</sup>
Angioplasty	6 (31.6%)	4 (12.5%) <sup>b</sup>	.146 <sup>a</sup>
Reocclusion during the procedure	11 (57.9%)	5 (15.6%)	.002
Onset-to-groin puncture time (mean) (min)	310.47 ± 136.57	263.13 ± 146.28	.258
Door-to-groin puncture time (mean) (min)	131.78 ± 46.94	137.13 ± 44.36	.694
Procedure time (mean) (min)	96.42 ± 46.03	61.16 ± 31.84	.002
Onset-to-recanalization time (mean) (min)	415.74 ± 128.51	330.66 ± 154.33	.049
Successful recanalization	17 (89.5%)	28 (87.5%)	1.000 <sup>a</sup>
Intracerebral hemorrhage			.867
Hemorrhagic infarction type 1	1 (5.3%)	3 (9.4%)	
Hemorrhagic infarction type 2	2 (10.5%)	3 (9.4%)	
Parenchymal hematoma type 1	—	—	
Parenchymal hematoma type 2	—	—	
Subarachnoid hemorrhage	0	3 (9.4%)	.285 <sup>a</sup>
NIHSS at 7 days (median) (IQR)	21 (9–26)	8 (5–21.5)	.060 <sup>c</sup>
mRS 0–2 at 3 mo	2 (10.5%)	12 (37.5%)	.037
mRS 0–3 at 3 mo	5 (26.3%)	18 (56.2%)	.038
Mortality at 3 mo	4 (21.1%)	7 (21.9%)	1.000 <sup>a</sup>

**Note:**—IQR indicates interquartile range.

<sup>a</sup> Fisher exact *t* test.

<sup>b</sup> The rescue treatment was not for the intracranial occlusion site but for extracranial proximal vertebral artery stenosis. Those cases were related to extracranial-to-intracranial tandem occlusions.

<sup>c</sup> Mann-Whitney *U* test.

absence of a collateral posterior communicating artery were adjusted. A *P* value <.05 was considered statistically significant.

## RESULTS

Of 55 enrolled patients, 4 were excluded for the following reasons: Three had an undetermined etiology related to no angiographic reperfusion, and one had vertebral artery dissection (Fig 3). Finally, 51 patients were included. IAD accounted for 37.3% (*n* =

19) of patients, whereas an embolism accounted for 62.7% (*n* = 32). The baseline demographics were similar between the 2 groups (Table 1). A trend toward lower baseline NIHSS scores was observed in the IAD group compared with the embolic group (median, 14 versus 22; *P* = .097). Among the stroke risk factors, atrial fibrillation was more prevalent in the embolic group (10.5% versus 40.6%, *P* = .023). The location of the occlusion on CTA was different between the 2 groups. Occlusions in the middle basilar artery were more frequent in the IAD group (38.5% versus 8.3%), whereas occlusions in the distal basilar artery (15.4% versus 87.5%) were more frequent in the embolic group (overall, *P* < .001). The incidence of intravenous rtPA administration was higher in the embolic group than in the IAD group (21.1% versus 62.5%, *P* = .004). The onset-to-groin puncture time did not differ between the IAD and embolic groups (310 ± 137 minutes versus 263 ± 146 minutes, *P* = .258).

The rate of successful reperfusion did not differ between groups (89.5% versus 87.5%, *P* = 1.000). The frequency of primary endovascular treatment methods also did not differ; the FAST method with a Penumbra reperfusion catheter was most commonly used (78.9% versus 84.4%, *P* = .711). The procedural time was significantly longer in the IAD group than in the embolic group (mean, 96.42 ± 46.03 minutes versus 61.16 ± 31.84 minutes; *P* = .002). During the endovascular procedure, reocclusion after reperfusion of the target vessel occurred more frequently in the IAD group (57.9% versus 15.6%, *P* = .002), and this group required rescue treatment more frequently (68.4% versus 18.8%, *P* < .001). Between the IAD and embolic groups, we used the following rescue treatments: conversion to another mechanical thrombectomy device (16.7% versus 6.2%, respectively; *P* = .348), angioplasty (31.6% versus 12.5%, respectively; *P* = .146), stent placement (31.6%

versus 12.5%, respectively; *P* = .146), and the administration of intra-arterial tirofiban (31.6% versus 0%, respectively; *P* = .002). Four patients in the embolic group had extracranial-to-intracranial tandem occlusions, so angioplasty and stent placement were performed for extracranial proximal vertebral artery stenosis. Detailed information on the angiographic and clinical outcomes is presented in Table 2.

The NIHSS score at 7 days tended to be higher (median, 21 versus 8;  $P = .060$ ), and a favorable outcome at 3 months was less frequent in the IAD group compared with the embolic group (26.3% versus 56.2%,  $P = .038$ ; Fig 4). In the IAD group, 50% of patients had an mRS score of 5 compared with 13% in the embolic group; however, the mortality rate did not differ between groups (21.1% versus 21.9%, respectively;  $P = 1.000$ ). Hemorrhagic complications also did not differ. By multiple logistic regression analysis, IAD (odds ratio, 5.469; 95% confidence interval, 1.085–25.580;  $P = .040$ ) was an independent predictor of a poor outcome (Table 3).

## DISCUSSION

In the current study, we achieved an overall successful reperfusion rate of 83.3%. In addition, 45.1% of the clinical outcomes were favorable, and the mortality rate was 21.6% after endovascular treatment of acute vertebrobasilar occlusions. These outcomes were comparable with those in previous studies.<sup>17,27</sup> However, the outcomes were distinctive when occlusions were divided according to angiographically defined classifications (ie, IAD-related and embolic occlusions). In our analysis, IAD was an independent risk factor for poor outcomes.

IAD-related occlusions were frequent in our population. In the current study, IAD accounted for about 40% of the acute vertebrobasilar occlusions. This incidence is much higher than that in the Western population, in which intracranial stenosis was observed in only 5.5% of patients with stent-retriever thrombectomy.<sup>28</sup> On the contrary, intracranial stenosis was observed in 22.9% of patients with multimodal endovascular treatment in a Korean study.<sup>29</sup> IAD may be more frequent in the posterior cir-

ulation than in the anterior circulation. In another study from a Korean hospital, IAD accounted for 37% and 9% of posterior and anterior circulations, respectively.<sup>14</sup> Along with a high incidence of IAD in the posterior circulation due to acute ischemic stroke, poor prognosis was a clinical implication in the current study.

Differentiating and defining IAD is of clinical importance because secondary or rescue endovascular treatment would be needed and the proper treatment method is essential. Our definition system was solely based on angiographic findings to determine the endovascular treatment strategy, and it was different from that of the Trial of ORG 10172 in Acute Stroke Treatment classification, which requires a full cardioembolism work-up and a secondary prevention plan.<sup>30</sup> As mentioned already, hidden IAD is frequently observed in occlusions, and rescue treatment is often needed and should be urgently determined in the angiography suite.

To differentiate and define IAD, we used several steps based on an intracranial large-artery occlusion, as described in Fig 2. The first step was to exclude other uncommon etiologies such as dissection, Moyamoya disease, and vasculitis.<sup>14</sup> Transfemoral cerebral angiography before endovascular treatment can show these uncommon etiologies because it is the criterion standard. The second step is to rule out pure embolism, which can be confirmed by primary thrombectomy endovascular treatment. If full recanalization without remnant stenosis is achieved at the occlusion site, the occlusion is thought to be due to a distant embolism. Because we do not need to consider additional therapy in the angiography suite, whether the embolic mechanism was unclear is irrelevant. If a focal fixed stenosis is sustained, interventionalists should consider whether IAD may be hidden in the occlusion.

The third step is to confirm whether the stenosis is significant. If severe stenosis is still observed after a repeat primary thrombectomy, IAD must be present. Usually, a stenotic degree of >70% is considered a significant risk factor for the recurrence of ischemic stroke.<sup>19</sup> A stenotic degree of <70% but with a stenotic lesion that has been repeatedly occluded or a flow that is not fluent is also considered a significant stenosis.<sup>13</sup> The fourth step is to wait 10–20 minutes after recanalization. We can assess reocclusion and differentiate the iatrogenic vessel injury or vasospasm. By following these steps, we can define the underlying

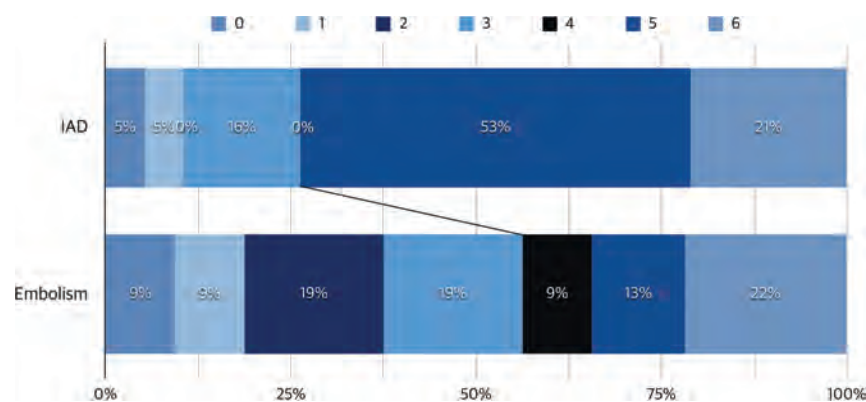


**FIG 4.** Modified Rankin Scale score at 3 months for each group. A favorable outcome is significantly less frequent in the intracranial atherosclerotic disease group compared with the embolism group, despite a similar mortality (mRS, 0–3: 26.3% versus 56.2%;  $P = .038$ ).

**Table 3: Multiple logistic regression analyses for IAD as a poor prognostic factor at 3 months**

Variables	For Predicting mRS 4–6		For Predicting mRS 3–6	
	OR (95% CI)	P Value	OR (95% CI)	P Value
Age	1.036 (0.972–1.105)	.275	1.023 (0.947–1.105)	.568
Baseline NIHSS	1.060 (0.976–1.151)	.164	1.049 (0.956–1.151)	.316
Intravenous rtPA, not infused	1.818 (0.456–7.247)	.397	6.065 (0.998–36.860)	.050
IAD	5.469 (1.085–27.580)	.040	8.738 (0.960–79.570)	.054
Onset-to-reperfusion time	0.999 (0.994–1.003)	.593	0.995 (0.988–1.002)	.179
Failed revascularization (TICI 0–2a)	8.531 (0.724–100.580)	.089	5.711 (0.300–108.677)	.246
Absence of the collateral PcomA	1.330 (0.210–8.444)	.762	2.316E+9 (0.000 to -1.797E+308)	.999

**Note:**—PcomA indicates posterior communicating artery.

IAD, which should exclude uncommon etiologies and procedural complications. During endovascular treatment, transfemoral cerebral angiography can be performed in real-time to determine whether there is an underlying IAD.

Various factors in IAD-related occlusions seemed to have affected the outcome. First, the location possibly affected it. Baseline CTA findings highlighted differences in the location of the occlusions. In accordance with prior studies,<sup>11,15,16</sup> the most common location of occlusions was the proximal and middle basilar artery in the IAD group and the distal basilar artery in the embolic group. Additionally, the location of the occlusion is associated with the prognosis.<sup>11,31</sup> For instance, an occlusion of the proximal and middle basilar artery, which serves most of the pons, can be related to extensive ischemia of the pons, leading to a fatal condition such as locked-in syndrome.<sup>32</sup> In the Stenting vs Aggressive Medical Management for Preventing Recurrent Stroke in Intracranial Stenosis study, the basilar artery trunk was associated with poor outcomes because those procedures may disturb the blood flow of basilar perforators.<sup>33</sup> In the IAD group of our study, >50% of patients had an mRS score of 5, and the locked-in syndrome can be associated with such disabilities.

Second, depending on the angiographic classification, the endovascular procedure differed. The IAD group required a longer procedural time than the embolic group, despite a similar final reperfusion rate. Frequent arterial reocclusions that required repetitive thrombectomy procedures and additional rescue treatments were attributed to the longer procedural duration. Theoretically, endovascular treatment by using mechanical thrombectomy with FAST and a stent retriever can remove a thrombus in the IAD lesion.<sup>34</sup> In addition, the IAD lesion must have factors such as plaque disruption, endothelial damage or irritation, or a local platelet activation-prone situation,<sup>35</sup> which causes frequent acute arterial reocclusion during endovascular treatment.<sup>13</sup> In the current study, 68.4% of the IAD group required rescue treatment for reocclusion.

This study has several potential limitations. First, it was retrospective in nature, though the data were prospectively registered at each hospital. This study was intended for patients who were undergoing endovascular treatment; because the enrolled patients were not randomized and were limited to achieving recanalization, some selection bias may exist. Nonetheless, only 3 patients were excluded due to reperfusion failure, so its effect on the analyses was probably minor. Second, there may be confounding factors, including the choice of rescue treatment and management strategies after endovascular treatment, because the data were collected from 2 different university hospitals. Third, the radiologic definition system differentiating IAD-related and embolic occlusions should be further validated. Although we have focused on the usage of this system for hyperacute treatment and have done our best to gather expert opinions, there are still weaknesses. We do not know what happened in patients whose occluded arteries were never recanalized. In addition, about 10% of patients with atrial fibrillation were still present in the IAD group. Finally, this study did not provide a good strategy for endovascular treatment of IAD-related occlusions in the posterior circula-

tion. Therefore, further studies are warranted to determine a better strategy.

## CONCLUSIONS

In patients with acute vertebrobasilar stroke who underwent endovascular treatment, IAD-related arterial occlusion was associated with a complicated endovascular procedure and poor clinical outcomes despite successful reperfusion.

Disclosures: Osama O. Zaidat—UNRELATED: Consultancy: Stryker, Medtronic; Expert Testimony: payment to both me and my institution; Patents (planned, pending or issued): patent pending. Andrew M. Demchuk—UNRELATED: Grants/Grants Pending: Medtronic.\* Comments: unrestricted grant for the Endovascular Treatment for Small Core and Proximal Occlusion Ischemic Stroke trial; Consultancy: Medtronic, Comments: honorarium for Continuing Medical Education events. \*Money paid to the institution.

## REFERENCES

1. Smith WS. **Intra-arterial thrombolytic therapy for acute basilar occlusion: pro.** *Stroke* 2007;38:701–03 CrossRef Medline
2. Saver JL, Jahan R, Levy EI, et al; SWIFT Trialists. **Solitaire flow restoration device versus the Merci retriever in patients with acute ischaemic stroke (SWIFT): a randomised, parallel-group, non-inferiority trial.** *Lancet* 2012;380:1241–49 CrossRef Medline
3. Nogueira RG, Lutsep HL, Gupta R, et al; TREVO 2 Trialists. **Trevo versus Merci retrievers for thrombectomy revascularisation of large vessel occlusions in acute ischaemic stroke (TREVO 2): a randomised trial.** *Lancet* 2012;380:1231–40 CrossRef Medline
4. Berkhemer OA, Fransen PSS, Beumer D, et al. **A randomized trial of intraarterial treatment for acute ischemic stroke.** *N Engl J Med* 2015; 372:11–20 CrossRef Medline
5. Campbell BC, Mitchell PJ, Kleinig TJ, et al; EXTEND-IA Investigators. **Endovascular therapy for ischemic stroke with perfusion-imaging selection.** *N Engl J Med* 2015;372:1009–18 CrossRef Medline
6. Goyal M, Demchuk AM, Menon BK, et al; ESCAPE Trial Investigators. **Randomized assessment of rapid endovascular treatment of ischemic stroke.** *N Engl J Med* 2015;372:1019–30 CrossRef Medline
7. Jovin TG, Chamorro A, Cobo E, et al; REVASCAT Trial Investigators. **Thrombectomy within 8 hours after symptom onset in ischemic stroke.** *N Engl J Med* 2015;372:2296–306 CrossRef Medline
8. Saver JL, Goyal M, Bonafé A, et al; SWIFT PRIME Investigators. **Stent-retriever thrombectomy after intravenous t-PA vs. t-PA alone in stroke.** *N Engl J Med* 2015;372:2285–95 CrossRef Medline
9. Eom YI, Hwang YH, Hong JM, et al. **Forced arterial suction thrombectomy with the Penumbra reperfusion catheter in acute basilar artery occlusion: a retrospective comparison study in 2 Korean university hospitals.** *AJNR Am J Neuroradiol* 2014;35:2354–59 CrossRef Medline
10. Singer OC, Berkefeld J, Nolte CH, et al; ENDOSTROKE Study Group. **Mechanical recanalization in basilar artery occlusion: the ENDOSTROKE study.** *Ann Neurol* 2015;77:415–24 CrossRef Medline
11. Eckert B, Kucinski T, Pfeiffer G, et al. **Endovascular therapy of acute vertebrobasilar occlusion: early treatment onset as the most important factor.** *Cerebrovasc Dis* 2002;14:42–50 CrossRef Medline
12. Schulte-Altedorneburg G, Hamann GF, Mull M, et al. **Outcome of acute vertebrobasilar occlusions treated with intra-arterial fibrinolysis in 180 patients.** *AJNR Am J Neuroradiol* 2006;27:2042–47 Medline
13. Kang DH, Kim YW, Hwang YH, et al. **Instant reocclusion following mechanical thrombectomy of in situ thromboocclusion and the role of low-dose intra-arterial tirofiban.** *Cerebrovasc Dis* 2014;37: 350–55 CrossRef Medline
14. Lee JS, Hong JM, Lee KS, et al. **Endovascular therapy of cerebral arterial occlusions: intracranial atherosclerosis versus embolism.** *J Stroke Cerebrovasc Dis* 2015;24:2074–80 CrossRef Medline
15. Cross DT 3rd, Moran CJ, Akins PT, et al. **Relationship between clot**

- location and outcome after basilar artery thrombolysis. *AJNR Am J Neuroradiol* 1997;18:1221–28 Medline**
16. Voetsch B, DeWitt LD, Pessin MS, et al. **Basilar artery occlusive disease in the New England Medical Center Posterior Circulation Registry.** *Arch Neurol* 2004;61:496–504 CrossRef Medline
  17. Miteff F, Faulder KC, Goh AC, et al. **Mechanical thrombectomy with a self-expanding retrievable intracranial stent (Solitaire AB): experience in 26 patients with acute cerebral artery occlusion.** *AJNR Am J Neuroradiol* 2011;32:1078–81 CrossRef Medline
  18. Pfefferkorn T, Holtmannspötter M, Schmidt C, et al. **Drip, ship, and retrieve: cooperative recanalization therapy in acute basilar artery occlusion.** *Stroke* 2010;41:722–26 CrossRef Medline
  19. Kasner SE, Chimowitz MI, Lynn MJ, et al; Warfarin Aspirin Symptomatic Intracranial Disease Trial Investigators. **Predictors of ischemic stroke in the territory of a symptomatic intracranial arterial stenosis.** *Circulation* 2006;113:555–63 CrossRef Medline
  20. Jauch EC, Saver JL, Adams HP, et al; American Heart Association Stroke Council, Council on Cardiovascular Nursing, Council on Peripheral Vascular Disease, Council on Clinical Cardiology. **Guidelines for the early management of patients with acute ischemic stroke: a guideline for healthcare professionals from the American Heart Association/American Stroke Association.** *Stroke* 2013;44:870–947 CrossRef Medline
  21. Kang DH, Hwang YH, Kim YS, et al. **Direct thrombus retrieval using the reperfusion catheter of the Penumbra system: forced-suction thrombectomy in acute ischemic stroke.** *AJNR Am J Neuroradiol* 2011;32:283–87 CrossRef Medline
  22. Kang DH, Kim YW, Hwang YH, et al. **Switching strategy for mechanical thrombectomy of acute large vessel occlusion in the anterior circulation.** *Stroke* 2013;44:3577–79 CrossRef Medline
  23. Kashiwagi J, Kiyosue H, Hori Y, et al. **Endovascular recanalization of acute intracranial vertebrobasilar artery occlusion using local fibrinolysis and additional balloon angioplasty.** *Neuroradiology* 2010;52:361–70 CrossRef Medline
  24. Eckert B, Koch C, Thomalla G, et al. **Aggressive therapy with intravenous abciximab and intra-arterial rtPA and additional PTA/stenting improves clinical outcome in acute vertebrobasilar occlusion: combined local fibrinolysis and intravenous abciximab in acute vertebrobasilar stroke treatment (FAST)—results of a multicenter study.** *Stroke* 2005;36:1160–65 CrossRef Medline
  25. Higashida RT, Furlan AJ, Roberts H, et al; Technology Assessment Committee of the Society of Interventional Radiology. **Trial design and reporting standards for intra-arterial cerebral thrombolysis for acute ischemic stroke.** *Stroke* 2003;34:e109–37 CrossRef Medline
  26. Hacke W, Kaste M, Fieschi C, et al. **Randomised double-blind placebo-controlled trial of thrombolytic therapy with intravenous alteplase in acute ischaemic stroke (ECASS II): Second European-Australasian Acute Stroke Study Investigators.** *Lancet* 1998;352:1245–51 CrossRef Medline
  27. Lutsep HL, Rymer MM, Nesbit GM. **Vertebrobasilar revascularization rates and outcomes in the MERCI and multi-MERCI trials.** *J Stroke Cerebrovasc Dis* 2008;17:55–57 CrossRef Medline
  28. Gascou G, Lobotesis K, Machi P, et al. **Stent retrievers in acute ischemic stroke: complications and failures during the perioperative period.** *AJNR Am J Neuroradiol* 2014;35:734–40 CrossRef Medline
  29. Yoon W, Kim SK, Park MS, et al. **Endovascular treatment and the outcomes of atherosclerotic intracranial stenosis in patients with hyperacute stroke.** *Neurosurgery* 2015;76:680–86; discussion 686 CrossRef Medline
  30. Adams HP Jr, Bendixen BH, Kappelle LJ, et al. **Classification of subtype of acute ischemic stroke: definitions for use in a multicenter clinical trial—TOAST. Trial of Org 10172 in Acute Stroke Treatment.** *Stroke* 1993;24:35–41 CrossRef Medline
  31. Brandt T, von Kummer R, Müller-Küppers M, et al. **Thrombolytic therapy of acute basilar artery occlusion: variables affecting recanalization and outcome.** *Stroke* 1996;27:875–81 CrossRef Medline
  32. Nordgren RE, Markesbery WR, Fukuda K, et al. **Seven cases of cerebromedullospinal disconnection: the “locked-in” syndrome.** *Neurology* 1971;21:1140–48 CrossRef Medline
  33. Fiorella D, Derdeyn CP, Lynn MJ, et al; SAMMPRIS Trial Investigators. **Detailed analysis of periprocedural strokes in patients undergoing intracranial stenting in Stenting and Aggressive Medical Management for Preventing Recurrent Stroke in Intracranial Stenosis (SAMMPRIS).** *Stroke* 2012;43:2682–88 CrossRef Medline
  34. Lee JS, Hong JM, Lee KS, et al. **Primary stent retrieval for acute intracranial large artery occlusion due to atherosclerotic disease.** *J Stroke* 2016;18:96–101 CrossRef Medline
  35. Bang OY. **Intracranial atherosclerosis: current understanding and perspectives.** *J Stroke* 2014;16:27–35 CrossRef Medline

# Virtual-versus-Real Implantation of Flow Diverters: Clinical Potential and Influence of Vascular Geometry

 P. Bouillot,  O. Brina,  H. Yilmaz,  M. Farhat,  G. Erceg,  K.-O. Lovblad,  M.I. Vargas,  Z. Kulcsar, and  V.M. Pereira



## ABSTRACT

**BACKGROUND AND PURPOSE:** Intracranial stents have become extremely important in the endovascular management of complex intracranial aneurysms. Sizing and landing zone predictions are still very challenging steps in the procedure. Virtual stent deployment may help therapeutic planning, device choice, and hemodynamic simulations. We aimed to assess the predictability of our recently developed virtual deployment model by comparing in vivo and virtual stents implanted in a consecutive series of patients presenting with intracranial aneurysms.

**MATERIALS AND METHODS:** Virtual stents were implanted in patient-specific geometries of intracranial aneurysms treated with the Pipeline Embolization Device. The length and cross-section of virtual and real stents measured with conebeam CT were compared. The influence of vessel geometry modifications occurring during the intervention was analyzed.

**RESULTS:** The virtual deployment based on pre- and poststent implantation 3D rotational angiography overestimated (underestimated) the device length by  $13\% \pm 11\%$  ( $-9\% \pm 5\%$ ). These differences were highly correlated ( $R^2 = 0.67$ ) with the virtual-versus-real stent radius differences of  $-6\% \pm 7\%$  ( $5\% \pm 4\%$ ) for predictions based on pre- and poststent implantation 3D rotational angiography. These mismatches were due principally to implantation concerns and vessel-shape modifications.

**CONCLUSIONS:** The recently proposed geometric model was shown to predict accurately the deployment of Pipeline Embolization Devices when the stent radius was well-assessed. However, unpredictable delivery manipulations and variations of vessel geometry occurring during the intervention might impact the stent implantation.

**ABBREVIATIONS:** 3DRA = 3D rotational angiography; FDS = flow-diverter stent; PED = Pipeline Embolization Device

Conventional treatment of intracranial aneurysms consists of the external or internal obliteration of the sac by surgical or endovascular approaches, respectively. The rupture risk of the treated aneurysm is therefore stopped by preventing the blood from circulating inside the aneurysm cavity.<sup>1</sup> The recent advent of flow-diverter stents (FDSs) has modified the treatment strategy for uncoilable aneurysms of the internal carotid artery.<sup>2-4</sup> Indeed,

the low-porosity layer of FDS wires covering the neck induces intra-aneurysmal flow changes that promote progressive thrombosis and a complete exclusion of the aneurysm from the circulation.<sup>5,6</sup> In addition, FDSs are responsible for the remodeling of the artery wall covered by the stent, preventing aneurysm regrowth as encountered in conventional treatment.<sup>3,7</sup> It has been also shown that the thrombosed aneurysms have the capacity to fully resorb and consequently improve the symptomatology of aneurysms with mass effect.<sup>8,9</sup> However, the mechanism of action of FDSs is still not totally understood and about 15%–25% of aneurysms remain with circulation, even after multiple-layer implantations.<sup>2,9</sup>


Various implantation concerns, including device sizing and positioning, can impact the device wall apposition negatively, the porosity at the neck level, and, consequently, the treatment outcome. For instance, insufficient stent appositions are known to be associated with vessel stenosis.<sup>10</sup> The alteration of the porosity at the neck due to the device deformation might cause an impairment of the endothelialization of the device scaffold.<sup>11,12</sup> The device sizing impacting the stent porosity was shown to influence the intra-aneurysmal flow modification.<sup>13</sup>

Received December 23, 2015; accepted after revision April 24, 2016.

From the Division of Neuroradiology (P.B., O.B., H.Y., G.E., K.-O.L., M.I.V., Z.K.), University Hospitals of Geneva, Geneva, Switzerland; Laboratory for Hydraulic Machines (P.B., M.F.), École Polytechnique Fédérale de Lausanne, Lausanne, Switzerland; and Division of Neuroradiology (V.M.P.), Department of Medical Imaging, and Division of Neurosurgery (V.M.P.), Department of Surgery, Toronto Western Hospital, University Health Network, Toronto, Ontario, Canada.

This study was supported by Swiss National Science Foundation grants (SNF 32003B\_160222 and SNF 320030\_156813) and the Academic Health Science Center - Alternate Funding Plan (AHSC AFP) Innovation Fund.

Please address correspondence to Vitor Mendes Pereira, MD, MSc, Toronto Western Hospital, 3MCL-436, 399 Bathurst St, Toronto, ON, M5T 2S8 Canada; e-mail: vitormpbr@hotmail.com

 Indicates open access to non-subscribers at [www.ajnr.org](http://www.ajnr.org)

<http://dx.doi.org/10.3174/ajnr.A4845>

Currently, there is no clinical tool to predict these stent properties accurately and provide clinical insight to the practitioner. Furthermore, hemodynamic simulations have shown high potential in predicting intracranial aneurysm thrombosis.<sup>14-16</sup> These hemodynamic simulations require reliable and fast virtual stent-deployment methodologies.

Therefore, we have recently proposed<sup>17</sup> a virtual stent-deployment method able to predict the local properties of braided stents (wire location, angles, porosities) and implantation parameters (stent length, landing zone) with minimal computational cost. Contrary to other methods that involve either cumbersome finite element analysis<sup>18-21</sup> or complex phenomenologic constraints<sup>13,20,22-26</sup> to simulate the stent dynamics, the proposed model is based on a minimal number of geometric assumptions (ie, a constant interwire distance and tubular stent envelope), which were validated in vitro and in vivo for the Pipeline Embolization Device (PED; Covidien, Irvine, California).

In the present study, we aimed to extend the promising results of Bouillot et al<sup>17</sup> to a larger cohort of patients. Therefore, we compared qualitatively and quantitatively real PED deployments with their virtual counterpart in a broad panel of aneurysm configurations.

## MATERIALS AND METHODS

### Patient Selection and Data Imaging

The imaging data acquired during FDS implantation procedures served to measure the actual device position and the vessel geometry for further virtual stent implantation.

**Patient Selection.** Patients scheduled to be treated with PED were included consecutively in this study (ethics committee authorization: 12-179, IRB-HUG, Geneva, Switzerland). Every case had an incidentally discovered or symptomatic saccular aneurysm of the anterior circulation without any sign of rupture. All patients received double antiplatelet therapy with clopidogrel and aspirin before the procedure and 6 months thereafter. Intra-arterial nimodipine was used when necessary to counter local vasospasms during the intervention.

**Prestent 3DRA.** The pre-FDS implantation vessel geometry was provided by 3D rotational angiography (3DRA) performed before implantation for each case. The contrast agent was injected through the distal access catheter (Navien 5F; Covidien).

**Conebeam CT of the Actual Stent.** Directly after PED implantation, a contrast-enhanced conebeam CT (VasoCT; Philips Healthcare, Best, the Netherlands) was performed to visualize the FDS apposition to the vessel wall. An intra-arterial solution of 20% contrast media and 80% saline was used to opacify the vessel lumen without hampering stent depiction. The combination of high spatial resolution (135- $\mu$ m matrix voxels,  $n = 256$ ) and the good contrast sensitivity of conebeam CT is particularly adapted to imaging small structures such as PED radiopaque wires.<sup>27</sup>

**Poststent 3DRA.** After a pilot phase, we identified vessel geometry modifications and introduced postimplantation 3DRA to get the consistency of the vascular geometry before and after stent placement. Indeed, we have recently shown<sup>17</sup> that tenuous variations of the vessel diameter have an important impact on the

virtual stent prediction, reinforcing the importance of relying on vessel reconstruction.

### Image Analysis and Virtual Stent Deployment

The arteries were segmented with an interactive watershed analysis<sup>28,29</sup> performed on the gradient of the reconstructed 3DRA volume (146- $\mu$ m matrix voxels,  $n = 256$ ). This segmentation method ensured a reliable and reproducible reconstruction of the vessel geometry. In particular, the critical vessel diameter was user-independent. Subsequently, the parent vessel centerline and radius (defined as the minimal distance of the vessel boundaries from the centerline) were calculated by using VMTK<sup>30</sup> ([www.vmtk.org](http://www.vmtk.org)) and regularized to remove the short spatial scale fluctuations and minimize the effect of the intracranial aneurysm neck.<sup>17</sup> This information was used to build the tubular envelope with a circular cross-section on which the stent wires were woven, assuming a constant interwire distance. To mimic the real implantations, we selected the distal end of each stent manually on the vessel centerline according to the actual stent position based on the conebeam CT images, and it served as input to the virtual deployment algorithm described in Bouillot et al.<sup>17</sup>

The virtual stent was computed with the weaving parameters of the actual device (nominal length/diameter of the stent with its number/width of wires) given for PED in Bouillot et al.<sup>17</sup> In parallel, a manual threshold segmentation of the conebeam CT by using OsiriX Imaging Software (<http://www.osirix-viewer.com>) provided the location of the radiopaque wires of the actual stent. Finally, all these 3D data (pre-/postimplantation vessel boundaries, filaments of the virtual stents, and radiopaque wires of the real stents) were manually registered by using ParaView software (Kitware; <http://paraview.org>) for further comparison analysis.

### Quantitative Analysis

The cross-section of the real stent envelope was measured on conebeam CT data in orthogonal planes along the centerline of the virtual stent. We analyzed its shape, assuming an elliptic cross-section as described in Bouillot et al.<sup>17</sup> The 2 measured minor and major radii of the real stent were subsequently compared with the radius of the tubular virtual stent. Also, the length differences between real and virtual stents were estimated with the help of the ParaView software.

The variations of vessel geometries pre-/poststent implantation were quantified on the basis of the virtual stent envelopes. Their radii are representative of the minor radius of the vessel in which the influence of the intracranial aneurysm is removed. Once averaged along the virtual stent centerline, the resulting radius value provides a valuable quantification of the vessel size along the stent.

## RESULTS

### Patients

Twenty patients were treated with a single-layer PED without major perioperative or delayed complications. All aneurysms were located at the internal carotid artery either in the cavernous ( $n = 2$ ) or paraclinoid portion ( $n = 18$ ). Eight patients underwent 3DRA post-FDS implantation for the evaluation of vessel geom-

etry modifications occurring during the intervention and their impact on the stent deployment.

### **Virtual-versus-Real Stent Implantation**

Qualitative comparisons between virtual and real stent implantations are given in Figs 1 and 2, in which the real (based on segmented conebeam CT) and virtual (based on segmented pre- and postimplantation 3DRAs) stents are superimposed on the corresponding vessel shape (pre- and poststent implantation, respectively). These figures show the good overall agreement between virtual and real stents. In general, the shape of the stent envelope was well-predicted by the virtual deployment despite the large variety of implanted vessel geometries. In particular, the regularization at the intracranial aneurysm neck guaranteed a good apposition of the stent at both sides of the neck while avoiding penetration and stent radius overestimation at the level of the aneurysm.

These observations were confirmed quantitatively in Figs 1–3. On the one hand, a very small difference of  $3\% \pm 1\%$  between the minor and major radii of the real stent cross-section (ie, eccentricity of  $0.25 \pm 0.04$ ) was measured, confirming the assumed circular cross-section of the virtual stent. On the other hand, the assessed virtual stent radius followed the main features of the real stent along the implanted vessel. However, the short-scale radius fluctuations were underestimated due to the stent envelope regularization process.<sup>14</sup> Slight radial underestimations (overestimations) of  $-6\% \pm 7\%$  ( $P < .05$ ) ( $5\% \pm 4\%$ ,  $P < .05$ ) were also observed in the virtual deployments based on 3DRA pre-(post-)FDS implantation. As a consequence, the predictions based on pre-(post-)3DRA acquisitions overestimated (underestimated) the FDS length by  $13\% \pm 11\%$  ( $P < .05$ ) ( $-9\% \pm 5\%$ ,  $P < .05$ ). Figure 3A shows the relation between the length differences (virtual-real) and the radial mismatches, highlighting the strong correlation between these 2 values ( $R^2 = 0.67$ ). The not significant intercept of  $0.027 \pm 0.016$  ( $P = .11$ ) indicated that the proposed stent deployment methodology provides an accurate prediction of the stent length when the radius of its envelope is correctly assessed. This is confirmed by correcting the virtual stent envelope radius (based on pre-FDS implantation 3DRA) by an increase of 6%, corresponding to the average radial mismatch between the virtual and real stents measured on conebeam CT data. These corrected deployments had no significant length differences,  $1\% \pm 12\%$  ( $P = .73$ ), removing the original length shift of 13% but increasing slightly the variation range.

For comparison, the length of simplified cylindrical deployments (ie, assuming a cylindrical stent envelope) such as those generally provided by the stent manufacturers was also computed. Their constant stent radius was set by using the vessel radius computed from 3DRA pre-stent implantation averaged around the aneurysm neck (ie, the average radius of the virtual stent envelope). This cylindrical model overestimated by  $29\% \pm 13\%$  ( $P < .05$ ) the length of the stent (ie, 2.2 times more than the proposed virtual deployment [Fig 3C.1] with a much larger variation range). These cylindrical-versus-real stent length differences were plotted against the radial mismatches in Fig 3B. Despite the good correlation ( $R^2 = 0.71$ ), the cylindrical model is not able to predict the correct FDS length when its radius is well-assessed. This feature is dem-

onstrated by the significant intercept of  $0.20 \pm 0.02$  ( $P < .05$ ), which indicates a recurring  $\sim 20\%$  stent length overestimation of the cylindrical model.

### **Procedural Factors Impacting Deployment**

Both the shape and the size of the vessels were modified during the procedure. On the one hand, the vessel curvature tended to decrease due to its interaction with the stent bending, as encountered, for instance, in cases 1, 5, and 20, in which this straightening led to distal or proximal registration mismatch of vessel geometries. On the other hand, the artery systematically and uniformly dilated during the implantation procedure except for case 20 (Fig 2). Quantitatively, the vessel size increased by  $11\% \pm 7\%$  ( $P < .05$ ) between 3DRA pre- and post-FDS implantation. These dilations were not strictly located around the FDS location but affected fully the parent vessel, therefore excluding any radiopaque stent wire artifacts.

Regarding the deployment itself, images in 8 patients (labeled in red in Figs 1 and 2) showed intended manipulations of the device just after release to improve the stent apposition. These manipulations directly influenced the final state (eg, length, radius) of the device as shown in Fig 4 for case 17. These 8 cases included all the outliers of the boxplots in Fig 3C, -D and the most distant points from the linear trends in Fig 3A, -B. Therefore, the virtual-real mismatch of the stent length decreased to  $8\% \pm 8\%$  with a lower variation range when considering only the 12 deployments performed without additional manipulation. Furthermore, an improvement of the correlation between radius-versus-length mismatch (virtual-real) was also observed as indicated by the increase of coefficient of determination,  $R^2 = 0.75$ , computed from these 12 cases.

## **DISCUSSION**

During the past decade, the rising use of intracranial stents and flow-diverter devices for the treatment of intracranial aneurysms has strongly stimulated biomechanical research in the simulation of stent deployment and its impact on the vasculature and hemodynamics. In particular, the device and implantation modeling is constantly refined (including the design and material properties of the device,<sup>21</sup> its interaction with the vessel,<sup>21</sup> the deployment procedure,<sup>19</sup> the computational scheme<sup>20</sup>), increasing the precision of the model at the expense of the computational cost and manual intervention. However, the relevance of each model component is still debated because comparisons with in vivo stent implantations are poorly reported. In the present work, we aimed to fill this gap by comparing virtual and real FDS deployments in a cohort of patients. On the one hand, this work allowed testing the accuracy of the recently proposed deployment model for braided stents.<sup>17</sup> On the other hand, the vessel geometry modifications occurring during the endovascular procedure and their impact on the stent implantation were also investigated.

The virtual deployment was based on some assumptions (ie, constant interwire distance and circular cross-section), which were validated in vitro and in vivo on braided stents.<sup>17</sup> Under these assumptions and knowing PED parameters (interwire distance, wire number, and length and width assessed from manufacturer data or measured experimentally<sup>17,31</sup>), the proposed



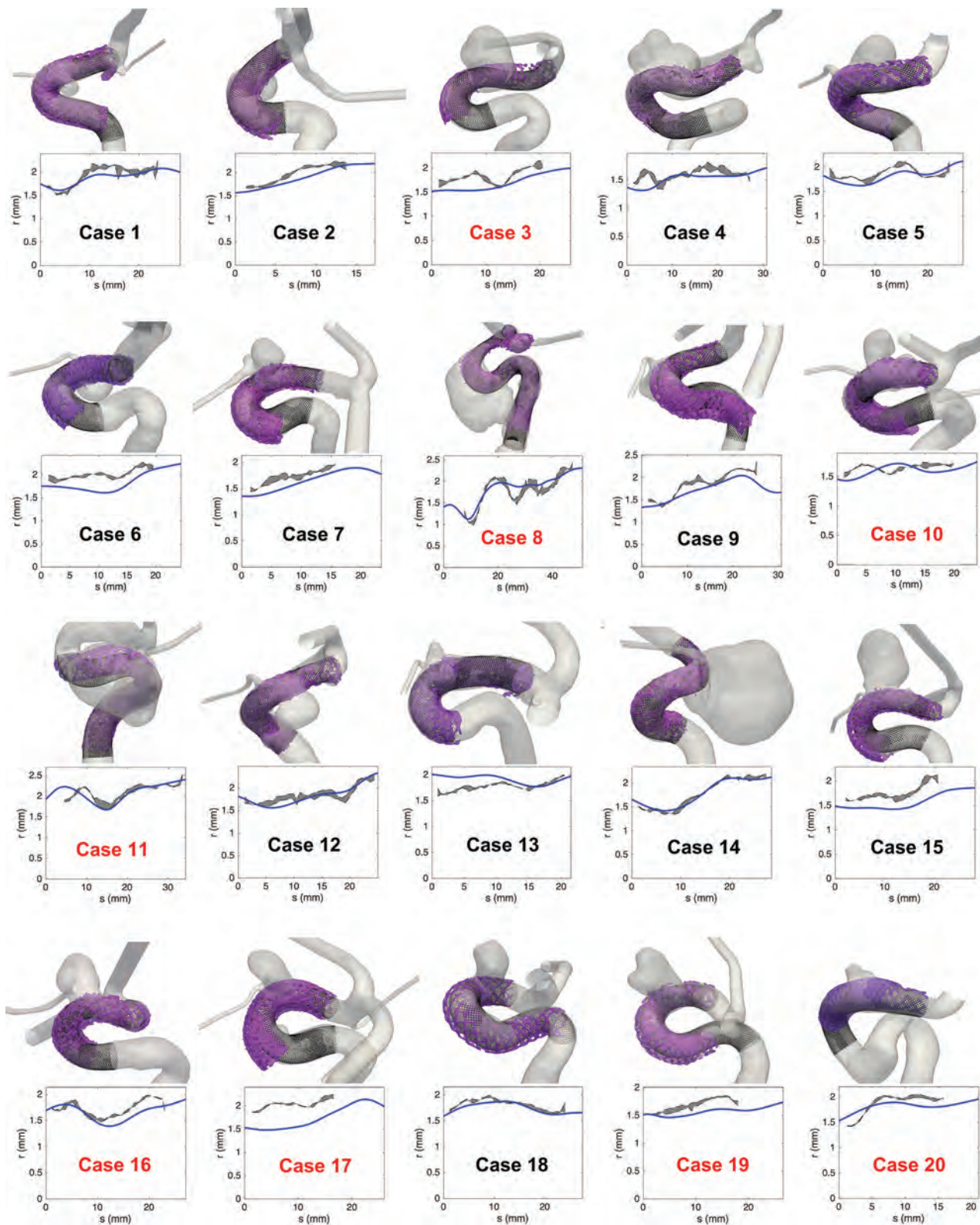


**FIG 1.** Visual (*upper row*) and quantitative (*lower row*) comparison between real and virtual FDS implantations in 20 patients. *Upper row.* The black lines are the wires of the virtual stents deployed in the 3DRA prestant geometry (gray transparent surface). The semitransparent purple surface represents the radiopaque wires of the real stents segmented from conebeam CT. *Lower row.* Radius ( $r$ ) of the stents versus the position ( $s$ ) along the centerline of the stents (the origin is taken at the distal end). The blue line represents the radius of the virtual stent based on the 3DRA prestant acquisition, while the gray area shows the minor-major radius range of the real stent cross-section based on the conebeam CT poststent acquisition. The implantations labeled in red required additional manipulation to improve the stent apposition.

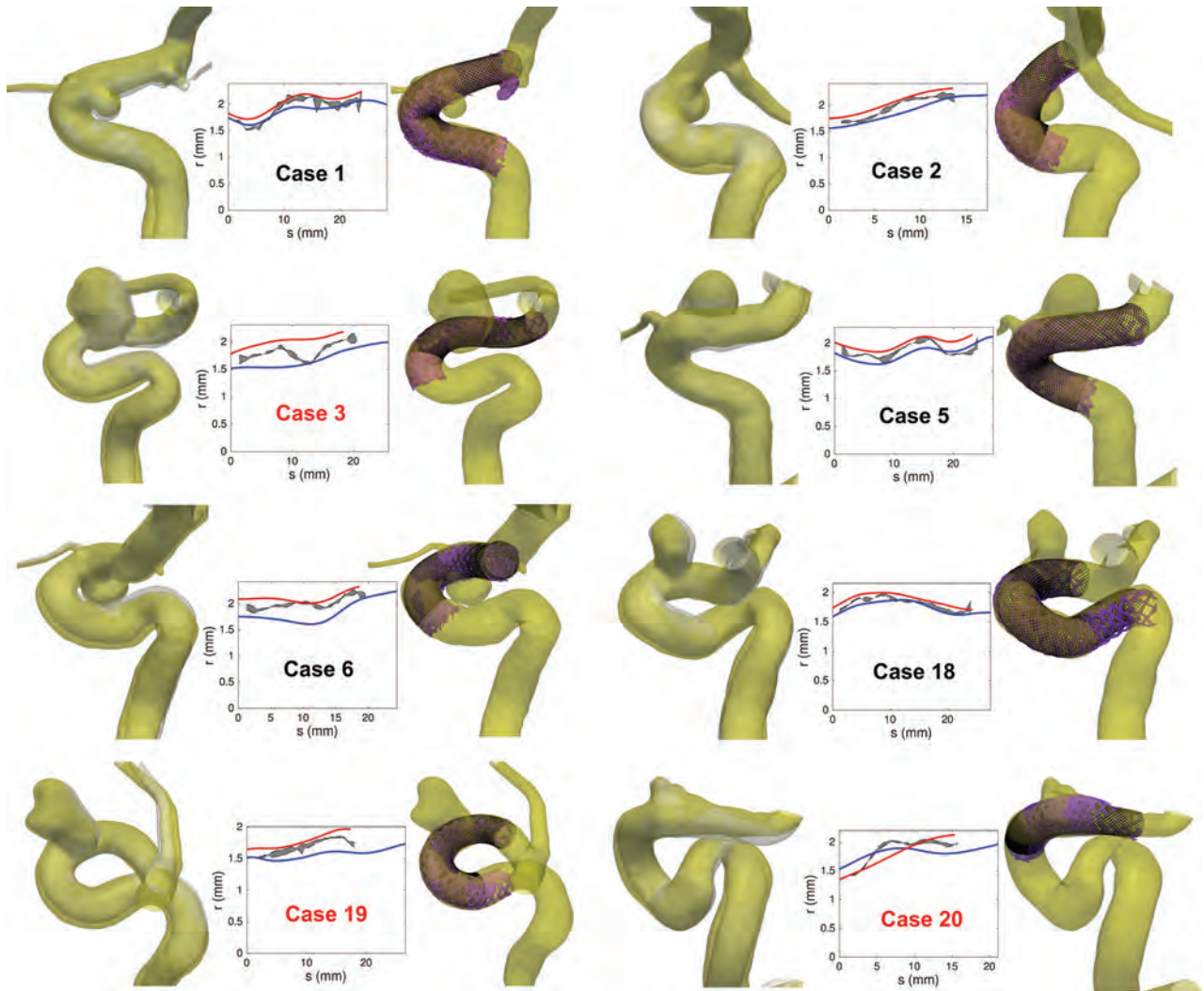


**FIG 2.** *Left columns*, Visual comparison between the 3DRA geometries post-FDS implantations (yellow surface) and pre-FDS implantations (gray surface) for 8 patients. The post- and pre-FDS implantation vessel boundaries were manually registered by using ParaView software. *Middle columns*, Radius ( $r$ ) of the stents versus the position ( $s$ ) along the centerline of the stents (the origin is taken at the distal end). The blue (red) line represents the radius of the virtual stent based on 3DRA pre- and (post)-stent acquisitions, while the gray area shows the minor-major radius range (measured on conebeam CT) of the real stent cross-section based on conebeam CT poststent acquisition. *Right columns*, Visual comparison between real and virtual FDS implantations. The black lines are the wires of the virtual stents deployed in the 3DRA poststent geometry. The semitransparent purple surface represents the radiopaque wires of the real stents segmented from conebeam CT. The implantations labeled in red required additional manipulation to improve the stent apposition.

model could predict the main features of real FDSs (length, shape, filament location, porosity, and landing zone) without any free parameters. The measured low stent cross-section eccentricity confirmed the assumed tubular envelope of the virtual stent even if noisy in vivo conebeam CT prevented the characterization of the radiopaque wires of the PED as seen with in vitro measurements.<sup>17</sup>

The assessment of the virtual stent radius was shown to play an important role in the prediction accuracy. When based on pre-FDS implantation imaging, this radius was generally underestimated. On the contrary, the radii extracted from post-FDS 3DRAs were all slightly overestimated. These radial differences impacted directly the virtual stent deployment as confirmed with the high correlation between the real/virtual stent radius and length differences. This strong relation showed that the deployment model guarantees an accurate stent prediction when the radius of the stent envelope is correctly assessed as already suggested in Bouillot et al.<sup>17</sup>

The differences between real and virtual stents were partly due to the vessel geometry variations of shape and size occurring during the intervention, along with the procedure itself. In addition to the vessel straightening reported by King et al,<sup>32</sup> a recurring vasodilation was observed after FDS implantation. These vessel modifications varied strongly from patient to patient and were not confined to the FDS surroundings. This finding indicates that the radial force of the FDS is one among other factors impacting the vessel geometry such as the mechanical impact of the catheter and vasodilator drug (nimodipine) administration. These unpredictable effects were broadly ignored in most of the previous work on virtual deployment and would require additional investigation. Furthermore, various per- and postdelivery mechanical actions performed by the operator can impact the final state of the device. For instance, the improvement of the wall apposition or proximal behavior of the stent requires additional manipulation

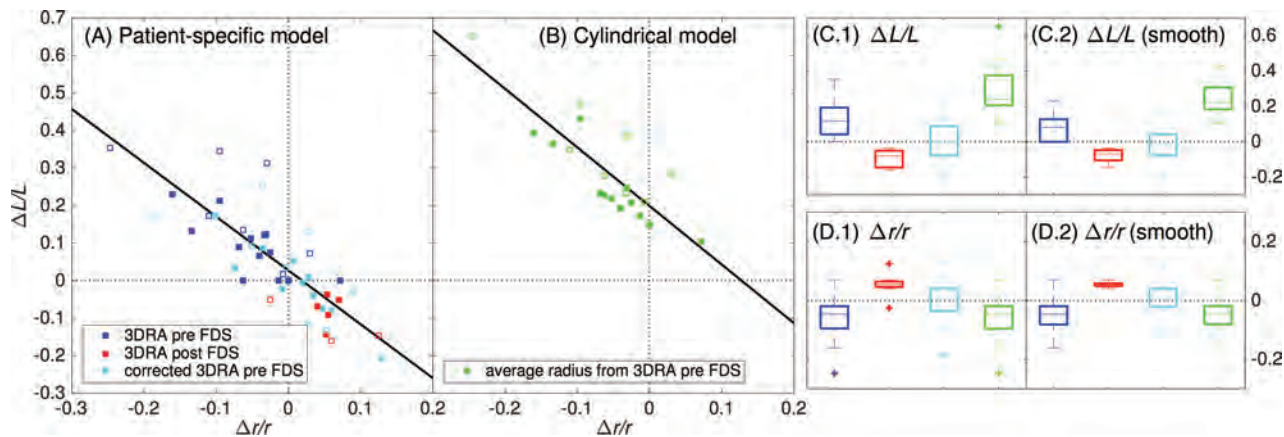


**FIG 3.** Virtual-versus-measured mismatch of the FDS radius [ $\Delta r/r = 2(r_{\text{vir}} - r_{\text{mes}})/(r_{\text{vir}} + r_{\text{mes}})$ ] and length [ $\Delta L/L = 2(L_{\text{vir}} - L_{\text{mes}})/(L_{\text{vir}} + L_{\text{mes}})$ ]. **A**,  $\Delta L/L$  versus  $\Delta r/r$  for the virtual deployment based on the geometric (patient-specific) model. The virtual deployments represented by the blue (red) squares are based on the vessel radius computed from segmented 3DRA pre- (post-)FDS implantation. The former were corrected by 6% (cyan boxes) to take into account the average radial difference with the measured stent radius in the virtual deployments. The straight black line represents the linear trend ( $R^2 = 0.67$ ) with  $0.027 \pm 0.016$  ( $\Delta L/L$  intercept) and  $-1.43 \pm 0.20$  (slope). **B**,  $\Delta L/L$  versus  $\Delta r/r$  for a cylindrical deployment based on the average radius of the 3DRA pre-FDS (green boxes). The straight black line represents the linear trend ( $R^2 = 0.71$ ) with  $0.20 \pm 0.02$  ( $\Delta L/L$  intercept) and  $-1.56 \pm 0.23$  (slope). The filled (empty) boxes correspond to the implantations without (with) additional delivery manipulation (eg, case 17 in Fig 4). C1–2 and D1–2, The virtual-versus-measured FDS radius and length mismatches, respectively. The analysis in C1 and D1 takes into account all the cases while the analysis in C2 and D2 is restricted to the 12 implantations without additional delivery manipulation. The color code is the same as that in the subsets A and B.

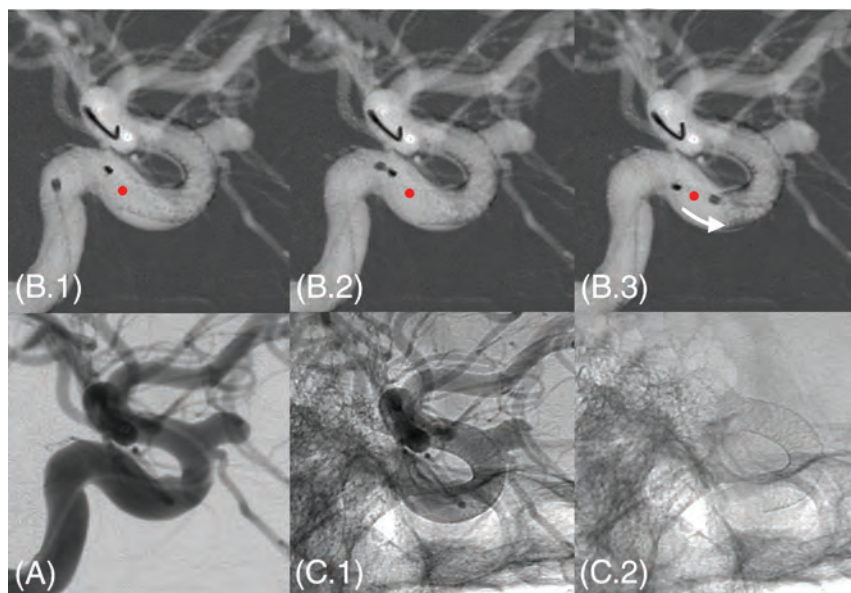


**FIG 4.** Additional manipulation intended to improve the stent apposition in case 17. Image (A) represents the DSA preimplantation. On 3 consecutive roadmap captures (B1–3), the proximal end of the stent was pushed forward by using the tip of the microcatheter to improve the expansion of the stent within the landing zone. This manipulation induced a visible shortening of the device highlighted by the red dot (initial position of the proximal end of the stent just after release) and the white arrow in B3. C1 and C2, Unsubtracted captures just after implantation, respectively, with and without contrast agent injection.

for expanding the device as shown in Fig 4. These pre- and postdelivery manipulations generally result in a compaction and therefore a shortening of the device, which are obviously not taken into account in our model.

Despite the vessel geometry variations and deployment concerns, the virtual deployment based on 3DRA pre-FDS implantation predicted the FDS length with an accuracy of about 10%. Moreover, the virtual FDS length was not biased, contrary to simplified cylindrical deployments, thus ensuring accurate predictions

when the stent radius is correctly assessed (ie, the vessel geometry does not vary substantially during the intervention). Most interesting, the performance of our virtual deployment was improved when the 8 cases with additional manipulation were removed from the analysis.

The minimal computational cost (only about 1 second on a laptop) and manual intervention (selection of the neck location and stent distal position) of the proposed virtual deployment are appropriate for a potential clinical application to anticipate the device positioning. Furthermore, because the underlying mathematic model is applicable to any braided stent, the virtual deployment can be extended to other types of devices. However, the circular cross-section and constant interwire distance assumptions, which have been experimentally confirmed on PEDs, should be tested with any other devices.

Conceptually, the FDS serves 2 functions in the treatment of aneurysms:

It redirects blood flow and it can act as a scaffold for neointimal colonization. The reported issues associated with flow diversion concern nearly exclusively the treatment efficacy and its delayed complications (aneurysm rupture after treatment, side branch occlusion), which are basically related to hemodynamic changes, biologic factors, and medication strategies.<sup>33,34</sup> However very few reports are dedicated to procedural complications and, in particular, the implantation and the deployment concerns of such complex devices. Due to its woven structure and its high wire

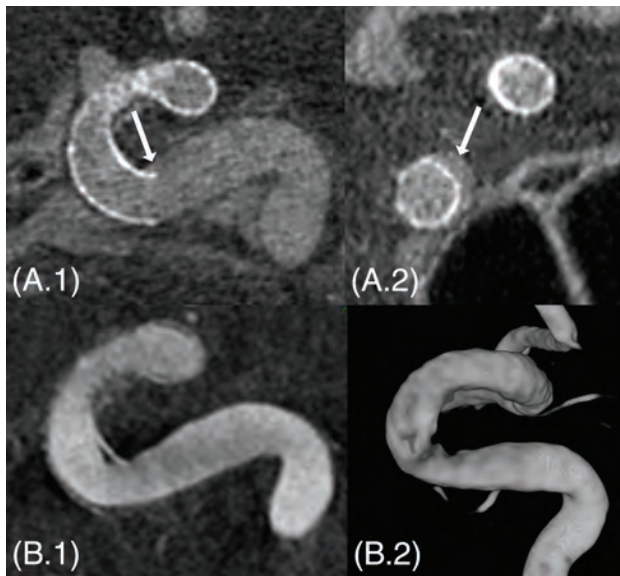


**FIG 5.** A patient (case 16) with proximal insufficient stent apposition visible on conebeam CT in sagittal (A.1) and coronal (A.2) sections (white arrows). At the 6-month follow-up 3DRA, a slight narrowing is visible in the inner curvature of the internal carotid artery siphon (B.1 and B.2). This narrowing might be a bit overestimated on the 3D rendering (B.2).

density, the deployment of the FDS is not a straightforward manipulation. Zanaty et al<sup>35</sup> concluded in a recent review that a careful manipulation of the device and a proper deployment reduced the procedure-related complications. Case 16 in Fig 5 illustrates these deployment concerns and their related delayed influence on the parent vessel. An insufficient stent apposition is visible in the inner curvature of the proximal carotid siphon immediately after implantation. Although this insufficient stent apposition is not considered an issue in this kind of procedure, one can see a vessel narrowing in the insufficient stent apposition area on the 6-month follow-up 3D angiogram. Even if the patient remained asymptomatic, the physician would have preferred to avoid such stent proximal behavior during the procedure.

Deployment issues related to the landing zone of the proximal end of the stent have already been reported by different in vivo and in vitro experiments conducted by Reymond et al.<sup>36</sup> Particularly, they described the accordion effect, which is a protrusion of the stent inside the aneurysm associated with a too-short landing zone. In addition, they observed a transition zone of variable porosity at the neck level associated with an inhomogeneous endothelial tissue colonization of the device scaffold, which could be associated with a treatment failure. Besides, Estrade et al<sup>37</sup> reported a case with very bad delayed outcomes related to implantation issues: A too-short landing zone and an oversized device induced a proximal conically deformed stent and a stenosis followed by immediate thromboembolic complications.

On the basis of these observations, we strongly believe that the proposed virtual deployment tool could assist the clinician in avoiding the complications described above. In practice, the deployment prediction together with its possible variability can be assessed preoperatively (ie, as soon as the 3DRA is acquired), providing additional information for optimizing the choice of the device (type, length, and diameter). Furthermore, the prediction

of the proximal end of the device is essential for selecting the implantation location, ensuring an adequate landing zone. To improve the prediction accuracy and guide the practitioner perioperatively, this deployment method could be also associated with a live imaging tool. Indeed, 2D-3D registration and live imaging tracking methods could be used to locate the actual device position during the deployment to refine continuously the virtual stent prediction and the associated landing zone. Therefore, the operator could be updated on the final state of the stent while manipulating the device. Finally, our method also provides crucial information such as the filament location and neck porosity for further hemodynamic evaluation with computational fluid dynamics simulations.<sup>13-16</sup>

## CONCLUSIONS

By comparing the predictions of the geometric model for braided stents with their in vivo counterparts in a consecutive series of patients, we emphasized the importance of the vessel radius and delivery manipulations in the model-prediction accuracy. However, the vessel geometry was shown to vary greatly during the intervention, impacting the virtual stent behavior. Independent of these implantation concerns, the proposed virtual deployment predicted the length of the PEDs with a precision of about 10%. Because the proposed stent modeling tool presents minimal computational cost and manual intervention, it has a direct clinical relevance to assist the clinician preoperatively in selecting the optimal device and anticipating its proximal position.

Disclosures: Pierre Bouillot—RELATED: Grant: Swiss National Science Foundation.\* Zsolt Kulcsar—UNRELATED: Consultancy: Stryker Neurovascular, Medtronic, Codman; Payment for Lectures (including service on Speakers Bureaus): Penumbra.\*Money paid to the institution.

## REFERENCES

1. Brinjikji W, Kallmes DF, Kadirvel R. Mechanisms of healing in coiled intracranial aneurysms: a review of the literature. *AJNR Am J Neuroradiol* 2015;36:1216–22 CrossRef Medline
2. Becske T, Kallmes DF, Saatci I, et al. Pipeline for uncoilable or failed aneurysms: results from a multicenter clinical trial. *Radiology* 2013; 267:858–68 CrossRef Medline
3. Turjman F, Levrier O, Combaz X, et al. EVIDENCE trial: design of a phase 2, randomized, controlled, multicenter study comparing flow diversion and traditional endovascular strategy in unruptured saccular wide-necked intracranial aneurysms. *Neuroradiology* 2015; 57:49–54 CrossRef Medline
4. Pereira VM, Kelly M, Vega P, et al. New Pipeline Flex device: initial experience and technical nuances. *J Neurointerv Surg* 2015;7:920–25 CrossRef Medline
5. Pereira VM, Bonnefous O, Ouared R, et al. A DSA-based method using contrast-motion estimation for the assessment of the intra-aneurysmal flow changes induced by flow-diverter stents. *AJNR Am J Neuroradiol* 2013;34:808–15 CrossRef Medline
6. Pereira VM, Brina O, Delattre BM, et al. Assessment of intra-aneurysmal flow modification after flow diverter stent placement with four-dimensional flow MRI: a feasibility study. *J Neurointerv Surg* 2015;7:913–19 CrossRef Medline
7. Ferns SP, Sprengers ME, van Rooij WJ, et al. Coiling of intracranial aneurysms a systematic review on initial occlusion and reopening and retreatment rates. *Stroke* 2009;40:E523–29 CrossRef Medline
8. Zhou Y, Yang PF, Fang YB, et al. A novel flow-diverting device (Tubridge) for the treatment of 28 large or giant intracranial aneurysms: a single-center experience. *AJNR Am J Neuroradiol* 2014;35:2326–33 CrossRef Medline

9. Brinjikji W, Murad MH, Lanzino G, et al. **Endovascular treatment of intracranial aneurysms with flow diverters: a meta-analysis.** *Stroke* 2013;44:442–47 CrossRef Medline
10. Heller RS, Malek AM. **Parent vessel size and curvature strongly influence risk of incomplete stent apposition in Enterprise intracranial aneurysm stent coiling.** *AJNR Am J Neuroradiol* 2011;32:1714–20 CrossRef Medline
11. Bing F, Darsaut TE, Salazkin I, et al. **Stents and flow diverters in the treatment of aneurysms: device deformation in vivo may alter porosity and impact efficacy.** *Neuroradiology* 2013;55:85–92 CrossRef Medline
12. Makoyeva A, Bing F, Darsaut TE, et al. **The varying porosity of braided self-expanding stents and flow diverters: an experimental study.** *AJNR Am J Neuroradiol* 2013;34:596–602 CrossRef Medline
13. Mut F, Cebral JR. **Effects of flow-diverting device oversizing on hemodynamics alteration in cerebral aneurysms.** *AJNR Am J Neuroradiol* 2012;33:2010–16 CrossRef Medline
14. Ouared R, Larrabide I, Brina O, et al. **Computational fluid dynamics analysis of flow reduction induced by flow-diverting stents in intracranial aneurysms: a patient-unspecific hemodynamics change perspective.** *J Neurointerv Surg* 2016 Feb 15. [Epub ahead of print] CrossRef Medline
15. Kulcsár Z, Augsburger L, Reymond P, et al. **Flow diversion treatment: intra-aneurysmal blood flow velocity and WSS reduction are parameters to predict aneurysm thrombosis.** *Acta Neurochir* 2012;154:1827–34 CrossRef Medline
16. Mut F, Raschi M, Scivano E, et al. **Association between hemodynamic conditions and occlusion times after flow diversion in cerebral aneurysms.** *J Neurointerv Surg* 2015;7:286–90 CrossRef Medline
17. Bouillot P, Brina O, Ouared R, et al. **Geometrical deployment for braided stent.** *Med Imag Anal* 2016;30:85–94 CrossRef Medline
18. Kim JH, Kang TJ, Yu WR. **Mechanical modeling of self-expandable stent fabricated using braiding technology.** *J Biomech* 2008;41:3202–12 CrossRef Medline
19. Ma D, Dumont TM, Kosukegawa H, et al. **High fidelity virtual stenting (HiFiVS) for intracranial aneurysm flow diversion: in vitro and in silico.** *Ann Biomed Eng* 2013;41:2143–56 CrossRef Medline
20. Bernardini A, Larrabide I, Petrini L, al. **Deployment of self-expandable stents in aneurysmal cerebral vessels: comparison of different computational approaches for interventional planning.** *Comput Methods Biomech Biomed Engin* 2012;15:303–11 CrossRef Medline
21. De Bock S, Iannaccone F, De Santis G, et al. **Our capricious vessels: the influence of stent design and vessel geometry on the mechanics of intracranial aneurysm stent deployment.** *J Biomech* 2012;45:1353–59 CrossRef Medline
22. Janiga G, Rössl C, Skalej M, et al. **Realistic virtual intracranial stenting and computational fluid dynamics for treatment analysis.** *J Biomech* 2013;46:7–12 CrossRef Medline
23. Appanaboyina S, Mut F, Löhner R, et al. **Simulation of intracranial aneurysm stenting: techniques and challenges.** *Comput Method Appl M* 2009;198:3567–82 CrossRef
24. Larrabide I, Kim M, Augsburger L, et al. **Fast virtual deployment of self-expandable stents: method and in vitro evaluation for intracranial aneurysmal stenting.** *Med Imag Anal* 2012;16:721–30 CrossRef Medline
25. Spranger K, Ventikos Y. **Which spring is the best? Comparison of methods for virtual stenting.** *IEEE Trans Biomed Eng* 2014;61:1998–2010 CrossRef Medline
26. Flórez-Valencia L, Orkisz M, Montagnat J. **3D graphical models for vascular-stent pose simulation.** *Machine Graphics & Vision* 2004;13:235–48
27. Kizilkilic O, Kocer N, Metaxas GE, et al. **Utility of VasoCT in the treatment of intracranial aneurysm with flow-diverter stents.** *J Neurosurg* 2012;117:45–49 CrossRef Medline
28. Higgins WE, Ojard EJ. **Interactive morphological watershed analysis for 3D medical images.** *Comput Med Imaging Graph* 1993;17:387–95 CrossRef Medline
29. Meyer F. **Topographic distance and watershed lines.** *Signal Process* 1994;38:113–25 CrossRef
30. Antiga L, Piccinelli M, Botti L, et al. **An image-based modeling framework for patient-specific computational hemodynamics.** *Med Biol Eng Comput* 2008;46:1097–112 CrossRef Medline
31. Bouillot P, Brina O, Ouared R, et al. **Particle imaging velocimetry evaluation of intracranial stents in sidewall aneurysm: hemodynamic transition related to the stent design.** *PLoS One* 2014;9:e113762 CrossRef Medline
32. King RM, Chueh JY, van der Bom IM, et al. **The effect of intracranial stent implantation on the curvature of the cerebrovasculature.** *AJNR Am J Neuroradiol* 2012;33:1657–62 CrossRef Medline
33. Gascou G, Lobotesis K, Brunel H, et al. **Extra-aneurysmal flow modification following Pipeline embolization device implantation: focus on regional branches, perforators, and the parent vessel.** *AJNR Am J Neuroradiol* 2015;36:725–31 CrossRef Medline
34. Kulcsár Z, Houdart E, Bonafé A, et al. **Intra-aneurysmal thrombosis as a possible cause of delayed aneurysm rupture after flow-diversion treatment.** *AJNR Am J Neuroradiol* 2011;32:20–25 CrossRef Medline
35. Zanaty M, Chalouhi N, Tjoumakaris SI, et al. **Flow-diversion panacea or poison?** *Front Neurol* 2014;5:21 CrossRef Medline
36. Reymond P, Bohraus Y, Perren F, et al. **Validation of a patient-specific one-dimensional model of the systemic arterial tree.** *Am J Physiol Heart Circ Physiol* 2011;301:H1173–82 CrossRef Medline
37. Estrade L, Makoyeva A, Darsaut TE, et al. **In vitro reproduction of device deformation leading to thrombotic complications and failure of flow diversion.** *Interv Neuroradiol* 2013;19:432–37 Medline

# Wall Apposition Is a Key Factor for Aneurysm Occlusion after Flow Diversion: A Histologic Evaluation in 41 Rabbits

A. Rouchaud, C. Ramana, W. Brinjikji, Y.-H. Ding, D. Dai, T. Gunderson, J. Cebral, D.F. Kallmes, and R. Kadirvel



## ABSTRACT

**BACKGROUND AND PURPOSE:** Robust wall apposition for flow-diverter stents may be important for endothelialization. Using a large series of experimental aneurysms treated with the Pipeline Embolization Device, the objectives of this study were to 1) assess interobserver agreement for the evaluation of wall apposition on posttreatment DSA and evaluate its association with aneurysm occlusion, and 2) measure the relationship between wall apposition assessed with histology and aneurysm occlusion rate after treatment.

**MATERIALS AND METHODS:** Saccular aneurysms were created in 41 rabbits and treated with the Pipeline Embolization Device. DSA was performed just after the deployment of the device and at follow-up. Three investigators independently graded wall apposition on posttreatment DSA as good or poor. A histopathologist blinded to the angiographic results graded the wall apposition on histologic samples. We examined the correlation between angiographic occlusion and wall apposition with histology and angiography.

**RESULTS:** Wall apposition evaluated on histology was strongly associated with saccular aneurysm occlusion. Sensitivity and specificity of wall apposition to predict complete occlusion at follow-up were 76.9% and 84.0%, respectively, with an overall accuracy of 81.6%. In this experimental study, DSA was suboptimal to assess flow-diverter apposition, with moderate interobserver agreement and low accuracy.

**CONCLUSIONS:** Good wall apposition is strongly associated with complete occlusion after flow-diverter therapy. In this study, DSA was suboptimal for assessing wall apposition of flow-diverter stents. These findings suggest that improved tools for assessing flow diverter–stent wall apposition are highly relevant.

**ABBREVIATIONS:** FDS = flow-diverter stent; PED = Pipeline Embolization Device

Flow-diverter stents (FDSs) are now largely accepted as the standard of care in the treatment of select aneurysms because of their high rates of angiographic occlusion and good clinical outcomes.<sup>1–3</sup> Because the mechanism of aneurysm occlusion after FDS treatment is likely related to stent endothelialization derived

exclusively from cells in the adjacent parent artery,<sup>4</sup> it appears important to have good wall apposition to promote endothelialization.<sup>5</sup> However, to our knowledge, correlation between aneurysm occlusion and wall apposition has not previously been evaluated in FDSs. Despite no evidence of this correlation, several tools are currently being evaluated to assess wall apposition of flow-diverter stents.<sup>6–8</sup>

Using a large series of elastase-induced aneurysms in rabbits treated with the Pipeline Embolization Device (PED; Covidien, Irvine, California), the objective of this study was to assess interobserver agreement for the evaluation of wall apposition on posttreatment DSA, evaluate its association with aneurysm occlusion, and measure the relationship between wall apposition assessed with histology and aneurysm occlusion rates after implantation.

## MATERIALS AND METHODS

### *In Vivo Experiments*

The Mayo Clinic Animal Care and Use Committee approved the animal procedures. Some rabbits used in this study were originally used in other investigations.<sup>9,10</sup> Elastase-induced aneurysms were created in 41 New Zealand white rabbits. Aneurysm creation

Received October 6, 2015; accepted after revision April 27, 2016.

From the Applied Neuroradiology Laboratory (A.R., C.R., W.B., Y.-H.D., D.D., D.F.K., R.K.) and Departments of Radiology (W.B., D.F.K.) and Health Sciences Research, Division of Biomedical Statistics and Informatics (T.G.), Mayo Clinic, Rochester, Minnesota; Interventional Neuroradiology NEURI Center (A.R.), Hôpital Bicêtre, Le Kremlin-Bicêtre, France; and Department of Bioengineering (J.C.), George Mason University, Fairfax, Virginia.

This work was supported by research grant NS0767491 from the National Institutes of Health and Medtronic. Aymeric Rouchaud was supported by research grants from the French Society of Radiology and Therese Planiol Foundation.

Please address correspondence to Aymeric Rouchaud, MD, Applied Neuroradiology Laboratory, Mayo Clinic, 200 First St SW, Rochester, MN 55905; e-mail: aymeric.rouchaud@gmail.com

Indicates open access to non-subscribers at [www.ajnr.org](http://www.ajnr.org)

Indicates article with supplemental on-line table.

Indicates article with supplemental on-line photos.

<http://dx.doi.org/10.3174/ajnr.A4848>

procedures were performed as previously described by our study group.<sup>11</sup> Aneurysms were treated at least 3 weeks after creation.<sup>12</sup> Subjects were premedicated with aspirin (10 mg/kg orally) and clopidogrel (10 mg/kg orally) 2 days before the treatment procedure; this medication regimen was continued for 1 month after embolization. The detailed procedure was previously published.<sup>9,10</sup> All endovascular procedures were performed with the Advantx DLX (GE Healthcare, Milwaukee, Wisconsin) Angio Suite equipped with an image amplifier. Imaging field of view was 11 cm with a frame rate of 2 frames per second, and the x-ray dose per frame was 500  $\mu$ R. The spatial resolution was 1.5 lines pairs per millimeter.

A 5F guide catheter (Envoy; Codman & Shurtleff, Raynham, Massachusetts) was briefly placed into the aortic arch, and DSA was performed. Heparin (500 U intravenously) was administered, and then a microcatheter (Marksman; Covidien) was placed over a microguidewire (Transend; Stryker, Kalamazoo, Michigan) into the subclavian artery distal to the aneurysm cavity. The wire was removed and the PED was advanced into the distal aspect of the microcatheter. The device was deployed across the neck of the aneurysm from the subclavian artery to the brachiocephalic trunk, with no protrusion of the proximal landing zone in the aortic arch. The microcatheter was removed, and DSA was performed through the guide catheter 5 minutes after deployment. No additional angioplasty to improve wall apposition or 3D acquisition were performed.

The implanted PED was selected according to the diameter of the artery. Details regarding proximal and distal diameters of the parent artery as well as the size of the implanted PEDs are available in the On-line Table.

Rabbits were humanely killed at day 30 ( $n = 18$ ), day 90 ( $n = 11$ ), and day 180 ( $n = 12$ ) after the procedure. At the time of death, the animals were deeply anesthetized. DSA of the aortic arch was performed to evaluate aneurysm occlusion. The animals then were euthanized with a lethal injection of pentobarbital. Aneurysm and parent artery tissue were immediately fixed in 10% neutral buffered formalin.

### Data Analysis

**Angiographic Evaluation.** A single experienced reader, blinded to wall-apposition status (DSA and histologic evaluations), assessed angiographic aneurysm occlusion at follow-up according to a 2-point classification: complete (100%) or incomplete occlusion.

Selected postprocess (pixel shift) images of the posttreatment DSA were independently examined by 3 investigators, blinded to histologic wall-apposition evaluation, to grade wall-apposition status on posttreatment DSA. Wall-apposition status on DSA was evaluated according to a dichotomous outcome, noted as either good or poor apposition depending on the presence or absence of visible contrast media between the stent and the parent artery. (Illustrative images for good and poor wall apposition are presented in On-line Figs 1 and 2).

**Histopathologic Processing and Wall-Apposition Evaluation.** A histopathologist blinded to the angiographic results did the processing and analysis for wall apposition as previously described.<sup>9</sup> After routine tissue processing, the fixed samples were embedded

in paraffin. Aneurysm samples were processed at 1000- $\mu$ m intervals in a sagittal orientation with use of an IsoMet Low Speed Saw (Buehler, Lake Bluff, Illinois). The metal stents were carefully removed under a dissecting microscope. The samples then were re-embedded in paraffin, sectioned at 5–6  $\mu$ m, and stained with hematoxylin-eosin.

Wall apposition was evaluated according to a dichotomous outcome, with either good or poor wall apposition of the stent. The evaluation was performed at the level of the aneurysm neck. A good histologic wall apposition meant that the stent was well apposed on the entire surface parent artery adjacent to the aneurysm ostium.

### Statistical Analysis

All statistical analyses were performed in R statistical and computing software version 3.1.1 (<http://www.r-project.org/>).  $\kappa$  and intraclass correlation coefficient statistics were calculated by using the irr package (version 0.84). Agreement among 3 readers for DSA assessment of posttreatment wall apposition was assessed by using the intraclass correlation coefficient method.<sup>13</sup> Cohen  $\kappa$  was also displayed for pair-wise comparisons of raters.  $\kappa$  also was used to assess agreement between the reference method of histology and DSA by using a consensus score agreed to by 2 radiologists for each method.

We calculated sensitivity, specificity, and accuracy of posttreatment DSA and histologic wall-apposition evaluations in predicting the occurrence of aneurysm occlusion at follow-up. The Wilson Score 95% CI is reported for each statistic. The Fisher exact test was performed to test for association between wall apposition assessed by histology at follow-up and occlusion outcome at follow-up.

## RESULTS

### Population and Angiographic Follow-Up Outcome

This study included 41 consecutively treated rabbits. All aneurysms were saccular. The mean aneurysm size was 9.41 mm (95% CI, 8.41–10.41) in the complete-occlusion group and 9.47 mm (95% CI, 8.03–10.91) in the incomplete-occlusion group. There was no significant difference in aneurysm sizes across groups ( $t$  test  $P$  value = .94). The length of follow-up varied from 30 days to 180 days, with a mean length of 90 days. Rabbits were euthanized at day 30 ( $n = 18$ ), day 90 ( $n = 11$ ), and day 180 ( $n = 12$ ).

Follow-up DSA was available for 40 rabbits, of which 67.5% ( $n = 27$ ) had complete occlusion and 32.5% ( $n = 13$ ) had incomplete occlusion. Angiographic complete-occlusion rates at 30, 90, and 180 days were not statistically different at 52.9% ( $n = 9$ ), 72.7% ( $n = 8$ ), and 83.3% ( $n = 10$ ), respectively ( $\chi^2$   $P$  value = .25).

### Wall-Apposition Evaluation on Posttreatment DSA

Immediate posttreatment DSA was available for 41 rabbits. Wall-apposition status evaluated on posttreatment DSA by the 3 independent readers demonstrated a good wall-apposition rate of 61.0% ( $n = 75$  of 123 readings) and a poor wall-apposition rate of 39.0% ( $n = 48$ ). The consensus DSA evaluation yielded 63.4% ( $n = 26$ ) good wall apposition and 36.6% ( $n = 15$ ) poor wall apposition. All 3 readers rated similar proportions of wall appo-

**Table 1: Contingency table for wall-apposition assessment on posttreatment DSA**

Wall Apposition	Follow-up DSA Outcome		Total
	Complete Occlusion	Incomplete Occlusion	
Good	15	10	25
Poor	12	3	15
Total	27	13	40

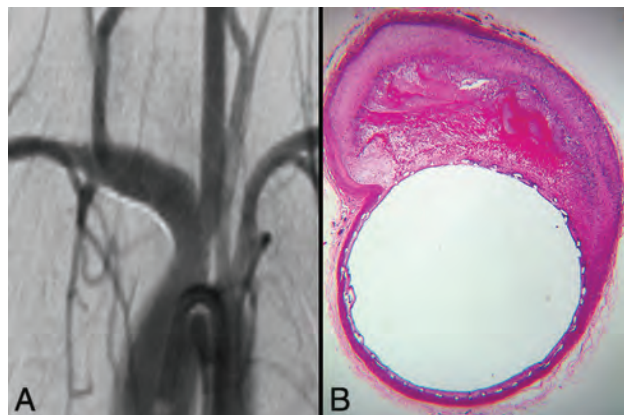


**FIG 1.** Histology and DSA illustrative correlation of good wall apposition associated with complete aneurysm occlusion. A, Follow-up DSA objectively shows complete occlusion of the aneurysm sac. B, Photomicrograph (hematoxylin-eosin staining, original magnification  $\times 100$ ) at the level of the aneurysm neck shows perfect wall apposition with complete aneurysm pouch occlusion filled with conjunctive tissue when using the PED.

sition as poor ( $n = 16$ ; 39%). Pair-wise  $\kappa$  between the 3 readers for DSA was  $\kappa = 0.487, 0.590,$  and  $0.385$ . Intraclass correlation among readers was  $0.488$  (95% CI,  $0.30-0.66$ ), indicating moderate interobserver agreement.

#### **Correlation between Consensus DSA Wall Apposition and Follow-Up Occlusion**

A contingency table is presented in Table 1. Sensitivity and specificity of good wall apposition evaluated on posttreatment DSA for the prediction of complete versus incomplete occlusion on follow-up DSA were 23.1% (95% CI,  $8.2-50.3$ ) and 55.5% (95% CI,  $37.3-72.4$ ), respectively. The overall accuracy of the wall apposition evaluated on posttreatment DSA for the prediction of complete versus incomplete occlusion at follow-up was 45.0% (95% CI,  $30.7-60.2$ ).

#### **Wall-Apposition Evaluation on Histology**

Histologic evaluation at time of follow-up DSA was available for 38 rabbits, of which 63.2% ( $n = 24$ ) had good wall apposition and 36.8% ( $n = 14$ ) had poor wall apposition.

#### **Correlation between Histologic Wall-Apposition Evaluation and Follow-Up Occlusion**

Illustrative histology images for good and poor wall apposition are presented in Fig 1 and Fig 2, respectively. A contingency table is presented in Table 2. Angiographic complete occlusion rates in good wall-apposition aneurysms of 77.8% (7 of 9) at 30 days, 100.0% (6 of 6) at 90 days, and 88.9% (8 of 9) at 180 days were not statistically different ( $\chi^2 P$  value = .44). Angiographic complete

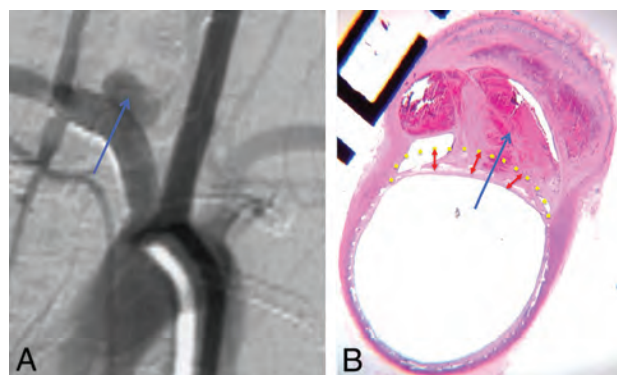


**FIG 2.** Histology and DSA illustrative correlation of poor wall apposition associated with incomplete aneurysm occlusion. Follow-up DSA objectively shows incomplete occlusion of the aneurysm sac (blue arrow) (A). Photomicrograph at the level of the aneurysm neck (hematoxylin-eosin staining, original magnification  $\times 100$ ) shows poor wall apposition (yellow dotted line) and filling of the aneurysm pouch with a partial thrombosis in the aneurysm sac (B).

**Table 2: Contingency table for wall-apposition assessment on histology**

Wall Apposition	Follow-up DSA Outcome		Total
	Complete Occlusion	Incomplete Occlusion	
Good	21	3	24
Poor	4	10	14
Total	25	13	38

occlusion rates in poor wall-apposition aneurysms of 25.0% (2 of 8) at 30 days, 25.0% (1 of 4) at 90 days, and 50.0% (1 of 2) at 180 days were not statistically different ( $\chi^2 P$  value = .77).

Sensitivity and specificity of wall apposition evaluated on histology for the prediction of complete versus incomplete occlusion on follow-up DSA were 76.9% (95% CI,  $49.7-91.8$ ) and 84.0% (95% CI,  $65.3-93.6$ ), respectively. The overall accuracy of the wall apposition evaluated on posttreatment DSA for the prediction of complete versus incomplete occlusion at follow-up was 81.6% (95% CI,  $66.6-90.8$ ). Histologically assessed wall apposition was significantly associated with occlusion at follow-up DSA (Fisher exact test  $P$  value  $< .001$ ; odds ratio, 15.7; 95% CI,  $2.63-133.2$ ).

## **DISCUSSION**

Our study of a large series of experimental aneurysms demonstrated that wall apposition is a crucial determinant for saccular aneurysm occlusion after FDS treatment. Wall apposition on histology was strongly correlated with aneurysm occlusion after treatment of intracranial aneurysms with flow diverters, suggesting that if good wall apposition is not present, adjunctive measures such as balloon inflation should be considered in some clinical settings to improve apposition and, thus, aneurysm occlusion rates.

In addition, our study demonstrated that assessment of wall apposition on posttreatment DSA suffers from low interobserver agreement and is poorly predictive of final aneurysm occlusion status. We acknowledge that the DSA system used for this experimental study in rabbits is not optimal and that the results cannot be extrapolated with DSA used in the clinical angiography suite. Indeed, these findings strongly suggest that operators should con-



sider alternative methodologies for assessing wall apposition with high-resolution contrast-enhanced conebeam CT such as VasoCT (Philips Healthcare, Best, the Netherlands),<sup>14</sup> DynaCT (Siemens, Erlangen, Germany),<sup>15</sup> and Innova CT (GE Healthcare) or with intravascular optical coherence tomography.<sup>8</sup>

This study correlates flow-diverter wall apposition with saccular aneurysm occlusion by using histologic evaluation. This is of high importance because wall apposition can be considered a key factor for the occurrence of saccular aneurysm nonocclusion. A potential biologic mechanism that could explain lower occlusion rates in cases of poor wall apposition is the fact that aneurysm occlusion after flow-diverter stent treatment is not exclusively related to intra-aneurysmal thrombosis, but is also driven by endothelialization of the device.<sup>4</sup> This endothelialization is relatively delayed and, we believe, derived exclusively from cells in the adjacent parent artery.<sup>4</sup> Based on this proposed mechanism, the malapposed portion of the device will fail to endothelialize because of the lack of direct contact with the parent artery in cases of poor wall apposition. This mechanism has also been discussed in the coronary intervention literature, and coronary stents that lack wall apposition fail to endothelialize.<sup>5,16</sup> Though our study proves that wall apposition is highly correlated with angiographic outcome, we also found that DSA was a suboptimal tool in assessing wall apposition.

Our current results are in accordance with the clinical study published by Saake et al,<sup>6</sup> who, in a study with 14 patients and evaluations made in consensus by 2 experienced neuroradiologists, reported that wall apposition was difficult to assess on intrarterial DSA. In their study, they did not find any significant difference between DSA and intravenous angiographic CT related to the deployment of the FDS, wall apposition of the stent in the nonaneurysmal parent vessel segments, and the aneurysmal neck coverage by the stent, but the reviewers preferred intravenous angiographic CT for evaluation of wall apposition. Beyond the fact that the angiography suite used in this experimental study is not optimal and differs from clinical ones, there are some explanations for why 2D DSA might be suboptimal in assessing wall apposition. 2D DSA cannot provide cross-sectional images; thus, there are limited views examining the relationship between the FDS and the vessel wall. In addition, DSA imaging acquisition is based on mask subtraction, making assessment of any contrast opacification between the subtracted device itself and the arterial wall quite difficult. Furthermore, there was motion artifact in our study because the experimental aneurysms are not located in the brain, but in the thorax, and are subject to ventilation movements.

Newer tools are currently being evaluated in the setting of FDS treatment of intracranial aneurysms to assess wall apposition. Flat panel CT with intra-arterial or intravenous opacification has a very high spatial resolution and can be done directly on the DSA table without any additional invasive procedure and with low radiation.<sup>6,7,17-22</sup> More recently, optical coherence tomography has been evaluated for intracranial procedures.<sup>8,23-27</sup> In addition, other endovascular techniques that are primarily used in cardiology but not yet used in neuroradiology, such as intravascular sonography<sup>24</sup> or endoluminal optical imaging (angioscopy),<sup>28</sup> seem promising in the assessment of wall apposition. Our study

suggests that these tools could someday be preferred over DSA for the assessment of wall apposition.

In cases of poor wall apposition demonstrated on postdeployment imaging, it could be useful to improve apposition with balloon expansion. Another option is the development of flow-diverter stents with higher radial force and conformability, which are key factors, for better wall apposition.<sup>29</sup> However, radial force is usually low in braided devices. We surmise that new flow-diverter devices with a laser-cut scaffold and a high mesh attenuation construct on the outer diameter could give higher radial force and better wall apposition.<sup>30</sup>

### Limitations

Our study is limited by its retrospective nature and the use of only selected images for the DSA readers' assessment. In addition, it is possible that a newer-generation angiography suite could provide better DSA images; 3D runs with multiplanar reconstructions might be better than 2D DSA to assess wall apposition, but we did not perform these acquisitions. Another limitation to our study is the motion artifact associated with the respiratory and cardiac motion in these rabbit aneurysms. However, it is important to point out that all images underwent postprocessing, including pixel shifting by an experienced radiologist before assessment by the blinded readers. Another limitation of this study is that only 1 experienced reader evaluated the histologic samples. However, this reader was blinded to the DSA outcomes. Regarding the choice of the appropriate device, sizing was sometimes difficult because of discrepancies in the artery diameter between the proximal and distal parts, but the braided stents have the ability to expand beyond their labeled diameter.

We did not use a previously published classification for wall-apposition assessment because we mainly focused at the level of the aneurysm neck, whereas the available classifications discussed the device deployment in the parent artery and not specifically at the neck.<sup>6</sup> Another limitation of this study is that rabbits were killed at different time points, which can modify the outcomes after implantation of the PED depending on the length of follow-up. However, we did not observe any statistically significant impact of time on complete occlusion rates. Also, this study focused on wall apposition as a key factor influencing aneurysm occlusion after flow diversion, but some other criteria that have not been analyzed in this specific study are also of high importance, such as hemodynamic effects, intra-aneurysmal thrombosis, and mesh attenuation.

### CONCLUSIONS

This study highlights that good wall apposition is key in obtaining complete occlusion of saccular aneurysms after FDS treatment. In this study, 2D DSA was found suboptimal for assessing wall apposition of FDSs, with only moderate interobserver agreement and low accuracy. Our inability to perform high-frame rate DSAs and C-arm CT acquisitions to evaluate wall apposition must be considered when assessing the significance of these results. Our study suggests that development of new tools for the assessment of wall apposition for flow-diverter stents is needed to improve angiographic outcomes in patients treated with FDSs.

Disclosures: Juan Cebra—RELATED: Grant: National Institutes of Health, Comments: research grant\*; UNRELATED: Grants/Grants Pending: National Institutes of Health,\* Philips,\* Comments: research grants. David F. Kallmes—UNRELATED: Board Membership: GE Healthcare,\* Comments: cost-effectiveness board; Consultancy: ev3/Covidien/Medtronic,\* Comments: planning and implementing clinical trials, clinical events committee, and steering committee; Grants/Grants Pending: Microvention,\* Sequent,\* Neurosigma,\* Surmodics,\* Codman,\* ev3/Covidien/Medtronic,\* Comments: preclinical research, clinical trials, and supply of devices; Travel/Accommodations/Meeting Expenses Unrelated to Activities Listed: ev3/Covidien/Medtronic,\* Comments: presentation at FDA panel meeting. Ramanathan Kadirvel—RELATED: Grant: National Institutes of Health. \*Money paid to the institution.

## REFERENCES

- Arrese I, Sarabia R, Pintado R, et al. **Flow-diverter devices for intracranial aneurysms: systematic review and meta-analysis.** *Neurosurgery* 2013;73:193–99; discussion 199–200 CrossRef Medline
- Brinjikji W, Murad MH, Lanzino G, et al. **Endovascular treatment of intracranial aneurysms with flow diverters: a meta-analysis.** *Stroke* 2013;44:442–47 CrossRef Medline
- Wakhloo AK, Gounis MJ. **Revolution in aneurysm treatment: flow diversion to cure aneurysms: a paradigm shift.** *Neurosurgery* 2014;61 Suppl 1:111–20 CrossRef Medline
- Kadirvel R, Ding YH, Dai D, et al. **Cellular mechanisms of aneurysm occlusion after treatment with a flow diverter.** *Radiology* 2014;270:394–99 CrossRef Medline
- Foin N, Gutiérrez-Chico JL, Nakatani S, et al. **Incomplete stent apposition causes high shear flow disturbances and delay in neointimal coverage as a function of strut to wall detachment distance: implications for the management of incomplete stent apposition.** *Circ Cardiovasc Interv* 2014;7:180–89 CrossRef Medline
- Saake M, Struffert T, Goelitz P, et al. **Angiographic CT with intravenous contrast agent application for monitoring of intracranial flow diverting stents.** *Neuroradiology* 2012;54:727–35 CrossRef Medline
- Ding D, Starke RM, Durst CR, et al. **DynaCT imaging for intraprocedural evaluation of flow-diverting stent apposition during endovascular treatment of intracranial aneurysms.** *J Clin Neurosci* 2014;21:1981–83 CrossRef Medline
- van der Marel K, Gounis MJ, Weaver JP, et al. **Grading of Regional Apposition after Flow-Diverter Treatment (GRAFT): a comparative evaluation of VasoCT and intravascular OCT.** *J Neurointerv Surg* 2015 Jul 28. [Epub ahead of print] CrossRef Medline
- Kallmes DF, Ding YH, Dai D, et al. **A new endoluminal, flow-disrupting device for treatment of saccular aneurysms.** *Stroke* 2007;38:2346–52 CrossRef Medline
- Kallmes DF, Ding YH, Dai D, et al. **A second-generation, endoluminal, flow-disrupting device for treatment of saccular aneurysms.** *AJNR Am J Neuroradiol* 2009;30:1153–58 CrossRef Medline
- Altes TA, Cloft HJ, Short JG, et al. **1999 ARRS Executive Council Award. Creation of saccular aneurysms in the rabbit: a model suitable for testing endovascular devices.** *American Roentgen Ray Society. AJR Am J Roentgenol* 2000;174:349–54 CrossRef Medline
- Fujiwara NH, Cloft HJ, Marx WF, et al. **Serial angiography in an elastase-induced aneurysm model in rabbits: evidence for progressive aneurysm enlargement after creation.** *AJNR Am J Neuroradiol* 2001;22:698–703 Medline
- Shrout PE, Fleiss JL. **Intraclass correlations: uses in assessing rater reliability.** *Psychol Bull* 1979;86:420–28 CrossRef Medline
- Kizilkilic O, Kocer N, Metaxas GE, et al. **Utility of VasoCT in the treatment of intracranial aneurysm with flow-diverter stents.** *J Neurosurg* 2012;117:45–49 CrossRef Medline
- Faragò G, Caldiera V, Tempira G, et al. **Advanced digital subtraction angiography and MR fusion imaging protocol applied to accurate placement of flow diverter device.** *J Neurointerv Surg* 2016;8:e5 CrossRef Medline
- Attizzani GF, Capodanno D, Ohno Y, et al. **Mechanisms, pathophysiology, and clinical aspects of incomplete stent apposition.** *J Am Coll Cardiol* 2014;63:1355–67 CrossRef Medline
- Aurboonyawat T, Schmidt PJ, Piotin M, et al. **A study of the first-generation Pipeline embolization device morphology using intraoperative angiographic computed tomography (ACT).** *Neuroradiology* 2011;53:23–30 CrossRef Medline
- Clarencon F, Piotin M, Pistocchi S, et al. **Evaluation of stent visibility by flat panel detector CT in patients treated for intracranial aneurysms.** *Neuroradiology* 2012;54:1121–25 CrossRef Medline
- Patel NV, Gounis MJ, Wakhloo AK, et al. **Contrast-enhanced angiographic cone-beam CT of cerebrovascular stents: experimental optimization and clinical application.** *AJNR Am J Neuroradiol* 2011;32:137–44 CrossRef Medline
- Jou LD, Mitchell BD, Shaltoni HM, et al. **Effect of structural remodeling (retraction and recoil) of the Pipeline embolization device on aneurysm occlusion rate.** *AJNR Am J Neuroradiol* 2014;35:1772–78 CrossRef Medline
- Caroff J, Mihalea C, Neki H, et al. **Role of C-arm VasoCT in the use of endovascular WEB flow disruption in intracranial aneurysm treatment.** *AJNR Am J Neuroradiol* 2014;35:1353–57 CrossRef Medline
- Poncyłjusz W, Biliński P, Safranow K, et al. **The LVIS/LVIS Jr. stents in the treatment of wide-neck intracranial aneurysms: multicentre registry.** *J Neurointerv Surg* 2015;7:524–29 CrossRef Medline
- Hayat U, Thondapu V, Asrar UI Haq M, et al. **Optical coherence tomography to evaluate coronary stent implantation and complications.** *Coron Artery Dis* 2015;26 Suppl 1:e55–68 CrossRef Medline
- Amoroso G, van Geuns RJ, Spaulding C, et al. **Assessment of the safety and performance of the STENTYS self-expanding coronary stent in acute myocardial infarction: results from the APPOSITION I study.** *EuroIntervention* 2011;7:428–36 CrossRef Medline
- Radu M, Jorgensen E, Kelbaek H, et al. **Strut apposition after coronary stent implantation visualised with optical coherence tomography.** *EuroIntervention* 2010;6:86–93 CrossRef Medline
- Ozaki Y, Okumura M, Ismail TF, et al. **The fate of incomplete stent apposition with drug-eluting stents: an optical coherence tomography-based natural history study.** *Eur Heart J* 2010;31:1470–76 CrossRef Medline
- Sawada T, Shite J, Negi N, et al. **Factors that influence measurements and accurate evaluation of stent apposition by optical coherence tomography. Assessment using a phantom model.** *Circ J* 2009;73:1841–47 CrossRef Medline
- McVeigh PZ, Sacho R, Weersink RA, et al. **High-resolution angioscopic imaging during endovascular neurosurgery.** *Neurosurgery* 2014;75:171–80; discussion 179–80 CrossRef Medline
- Kalmár G, Hübner F, Voelker W, et al. **Radial force and wall apposition of balloon-expandable vascular stents in eccentric stenoses: an in vitro evaluation in a curved vessel model.** *J Vasc Interv Radiol* 2002;13:499–508 CrossRef Medline
- Möhlenbruch MA, Herweh C, Jestaedt L, et al. **The FRED flow-diverter stent for intracranial aneurysms: clinical study to assess safety and efficacy.** *AJNR Am J Neuroradiol* 2015;36:1155–61 CrossRef Medline

# Vitamin D and Vulnerable Carotid Plaque

J.S. McNally, T.M. Burton, B.W. Aldred, S.-E. Kim, M.S. McLaughlin, L.B. Eisenmenger, G.J. Stoddard, J.J. Majersik, D.V. Miller, G.S. Treiman, and D.L. Parker



## ABSTRACT

**BACKGROUND AND PURPOSE:** MR imaging–detected carotid intraplaque hemorrhage indicates vulnerable plaque with high stroke risk. Angiotensin II stimulates intraplaque hemorrhage in animal models, and the angiotensin system is highly regulated by vitamin D. Our purpose was to determine whether low vitamin D levels predict carotid intraplaque hemorrhage in humans.

**MATERIALS AND METHODS:** In this cross-sectional study, 65 patients with carotid disease underwent carotid MR imaging and blood draw. Systemic clinical confounders and local lumen imaging markers were recorded. To determine the association of low vitamin D levels with MR imaging detected intraplaque hemorrhage, we performed multivariable Poisson regression by using generalized estimating equations to account for up to 2 carotid arteries per patient and backward elimination of confounders. MR imaging detected intraplaque hemorrhage volume was also correlated with vitamin D levels and maximum plaque thickness. Thirty-five patients underwent carotid endarterectomy, and histology-detected intraplaque hemorrhage was correlated with vitamin D levels and total plaque area.

**RESULTS:** Low vitamin D levels ( $<30$  ng/mL, prevalence ratio = 2.05,  $P = .03$ ) were a significant predictor of MR imaging detected intraplaque hemorrhage, along with plaque thickness (prevalence ratio = 1.40,  $P < .001$ ). MR imaging detected intraplaque hemorrhage volume linearly correlated with plaque thickness (partial  $r = 0.45$ ,  $P < .001$ ) and low vitamin D levels (partial  $r = 0.26$ ,  $P = .003$ ). Additionally, histology-detected intraplaque hemorrhage area linearly correlated with plaque area (partial  $r = 0.46$ ,  $P < .001$ ) and low vitamin D levels (partial  $r = 0.22$ ,  $P = .03$ ). The association of intraplaque hemorrhage volume with low vitamin D levels was also higher with ischemic stroke.

**CONCLUSIONS:** Low vitamin D levels and plaque thickness predict carotid intraplaque hemorrhage and outperform lumen markers of vulnerable plaque. This research demonstrates a significant link between low vitamin D levels and carotid intraplaque hemorrhage.

**ABBREVIATIONS:** AT1R = angiotensin II type 1 receptor; IPH = intraplaque hemorrhage; NADPH = nicotinamide adenine dinucleotide phosphate; PR = prevalence ratio

Large-artery atherosclerosis, including carotid disease, is a significant cause of ischemic stroke and an important therapeutic target.<sup>1</sup> Reports estimate that carotid disease accounts for 10%–15% of ischemic strokes.<sup>2,3</sup> Additionally, recurrent stroke is more highly associated with carotid atherosclerosis than other causes.<sup>4,5</sup>

While only 10%–15% of patients with stroke have large-artery atherosclerosis, approximately one-third of early recurrence occurs in this group.<sup>6,7</sup>

These past estimates are based on whether moderate or severe stenosis is present, defined for the carotid arteries as NASCET stenosis of  $>50\%$ .<sup>8</sup> More recent studies have questioned stenosis, finding that other markers predict unstable plaque better, including intraplaque hemorrhage (IPH). Carotid IPH is a better estimate of recurrent stroke risk, with a  $\sim 5$ -fold higher risk of recurrent stroke in all stenosis categories in multiple recent studies and meta-analyses.<sup>9–11</sup> Carotid IPH can be accurately detected with heavily T1-weighted sequences, including MPRAGE. Both

Received November 6, 2015; accepted after revision April 26, 2016.

From the Department of Radiology and Imaging Sciences, Utah Center for Advanced Imaging Research (J.S.M., B.W.A., S.-E.K., M.S.M., L.B.E., D.L.P.); Department of Neurology (T.M.B., J.J.M.); Department of Orthopedics, Study Design and Biostatistics Center (G.J.S.); Department of Pathology (D.V.M.); and Department of Surgery at the University of Utah and VA Salt Lake City Health Care System, Salt Lake City, Utah (G.S.T.).

This work was supported by a Radiological Society of North America Research Scholar Grant; a University of Utah Intramural Seed Grant; and a grant for the Study Design and Biostatistics Center, with funding, in part, from the National Center for Research Resources and the National Center for Advancing Translational Sciences, National Institutes of Health, grant 8UL1R000105 (formerly UL1R025764).

Paper previously presented at: Annual Meeting of the American Society of Neuroradiology and the Foundation of the ASNR Symposium, April 25–30, 2015; Chicago, Illinois.

Please address correspondence to J. Scott McNally, MD, PhD, University of Utah, Department of Radiology and Imaging Sciences, 30 North 1900 East #1A071, Salt Lake City, UT 84132-2140; e-mail: scott.mcnally@hsc.utah.edu

Indicates open access to non-subscribers at [www.ajnr.org](http://www.ajnr.org)

Indicates article with supplemental on-line table.

<http://dx.doi.org/10.3174/ajnr.A4849>

MPRAGE and TOF have low false-negative rates (3% versus 4%), but the MPRAGE sequence has a lower false-positive rate (20%) compared with TOF (44%).<sup>12</sup>

Despite MR imaging detection of IPH, no treatment has been shown to reverse these lesions. A potential treatment target is the angiotensin system, a major determinant of carotid plaque instability and stroke risk.<sup>13</sup> Angiotensin II stimulates adventitial neovascularity and is implicated in animal models of IPH.<sup>14</sup> Angiotensin II increases plaque microvessel angiogenesis through the endothelial angiotensin II type 1 receptor (AT1R).<sup>15</sup> AT1R activation leads to reactive oxygen species formation through the nicotinamide adenine dinucleotide phosphate (NADPH) oxidase and plaque inflammation.<sup>15</sup> Extrapolating from this, inhibition of the angiotensin system may prevent or decrease IPH.

The angiotensin system is highly regulated by an endogenous inhibitory axis, including vitamin D and the vitamin D receptor.<sup>16</sup> The vitamin D receptor is downregulated in atherosclerotic plaque in animal models.<sup>17</sup> Vitamin D deficiency has been associated with increased intima-media and plaque thickness in subclinical carotid atherosclerosis.<sup>18</sup> Serum vitamin D levels are negatively correlated with carotid intima-media thickness ( $r = -0.51$ ).<sup>19</sup> Prior studies have demonstrated a high prevalence of vitamin D insufficiency ( $<30$  ng/mL, 63.6%) and increased stroke risk in the Mountain West population of the United States.<sup>20</sup> This mirrors the prevalence of vitamin D deficiency ( $<20$  ng/mL) in the United States as a whole (41.6%).<sup>21</sup>

Our purpose was to determine whether low vitamin D levels predict carotid IPH in patients with carotid disease. Our hypothesis was that low vitamin D levels are associated with carotid IPH when controlling for systemic and local plaque confounders. If confirmed, this pathway may represent an important treatment target in patients with carotid IPH.

## MATERIALS AND METHODS

### Clinical Study Design

This was a cross-sectional study of patients with carotid disease, defined as  $\geq 2$ -mm-thick carotid plaque. Patients were consecutively recruited from neurovascular outpatient and inpatient services. Exclusions included patients younger than 18 years of age, prisoners, pregnancy, or those with contraindications to MR imaging (eg, pacemakers). There were no exclusion/inclusion criteria for carotid stenosis other than complete occlusion. Sixty-five patients were recruited and completed carotid MR imaging and blood draw.

**Ethics.** Institutional review board approval was obtained along with informed consent from all subjects. In subjects with impaired decisional capacity, legal authorized representative consent and patient assent was obtained.

### Serologic Analysis of Vitamin D and Angiotensin II

All patients underwent blood draw following IV placement for MR imaging. Samples were taken directly to the Associated Regional and University Pathologists for serum vitamin D analysis by quantitative high-performance liquid chromatography tandem mass spectrometry (25-hydroxyvitamin D<sub>2</sub> and D<sub>3</sub>; <http://ltd.aruplab.com/Tests/Pub/2002348>) and plasma angiotensin II analysis by quantitative immunoassay ([\[Tests/Pub/0098771\]\(http://ltd.aruplab.com/Tests/Pub/0098771\)\). Vitamin D levels were considered low/insufficient at  \$<30\$  ng/mL. Angiotensin II levels were considered high at  \$>18\$  ng/L.](http://ltd.aruplab.com/</a></p></div><div data-bbox=)

### Research MR Imaging Protocol

Images were obtained on 3T MR imaging scanners (Trio, Verio, Skyra and Prisma scanners; Siemens, Erlangen, Germany) with custom-made carotid coils.<sup>22</sup> Each MR imaging included brain DWI and carotid MPRAGE sequences acquired with custom neck coils described below.

### Subject-Specific Radiofrequency Coils

A modular system of subject-specific radiofrequency coil arrays was used to maximize signal to noise.<sup>23</sup> The head coil provides head immobilization, essential to carotid imaging.<sup>24</sup> Either 7-channel or 9-channel coils were used, connected to preamplifiers through low-resistance connectors, allowing them to be interchanged to fit necks of different shapes and sizes. These coils can image simultaneously with clinical head coils without extra positioning hardware.

### Carotid MPRAGE and IPH Determination

MPRAGE parameters were the following: 3D, TR/TE/TI = 6.39/2.37/370 ms, flip angle = 15°, FOV = 130 × 130 × 48 mm<sup>3</sup>, matrix = 256 × 256 × 48, voxel = 0.5 × 0.5 × 1.0 mm<sup>3</sup>, fat saturation, acquisition time =  $\sim 5$  minutes as described previously.<sup>25</sup> Images were obtained from 20 mm below to 20 mm above the carotid bifurcation at a 1.0-mm section thickness. Carotid IPH was defined by MPRAGE-positive plaque with  $\geq 2$ -fold signal compared with the sternocleidomastoid muscle (Fig 1).<sup>26</sup> We have previously shown that MPRAGE-positive plaque corresponds to carotid IPH on histology.<sup>26</sup> IPH volume was determined quantitatively with volumes traced from the PACS.

### Carotid Lumen Measurements

All non-IPH carotid lumen measurements were determined by consensus of 2 reviewers, blinded to brain MR imaging and clinical covariates. The entire carotid plaque was considered 1 unit, from 20 mm above to 20 mm below the bifurcation. Maximum plaque thickness was measured in the transverse plane on MPRAGE images, perpendicular to the center axis of the lumen (Fig 1). Lumen markers (stenosis, ulceration, and intraluminal thrombus) were determined from noncontrast TOF with parameters as follows: 3D, TR/TE = 25/4.02 ms, flip angle = 20°, FOV = 160 × 160 × 90 mm, matrix = 256 × 256, section thickness = 0.64 mm, 144 sections, acquisition time =  $\sim 3.5$  minutes. In all cases, duplex sonography was performed before study entry and was used as a complementary measure of stenosis. In cases of  $>70\%$  stenosis by either TOF or sonography or when stenosis measurements disagreed, lumen stenosis was confirmed by using contrast CTA or MRA. The percent diameter stenosis was determined with NASCET criteria, with a submillimeter measurement tool and  $[(a - b)/a] \times 100\%$ , where  $b$  is the diameter of maximal stenosis and  $a$  is the diameter of the ICA distal to the stenosis (Fig 1).<sup>27-29</sup> Multivariable regression was performed by using both NASCET and millimeter stenosis ( $b$ ), first described on CTA.<sup>30</sup> No near-occlusions were found in this dataset, as de-

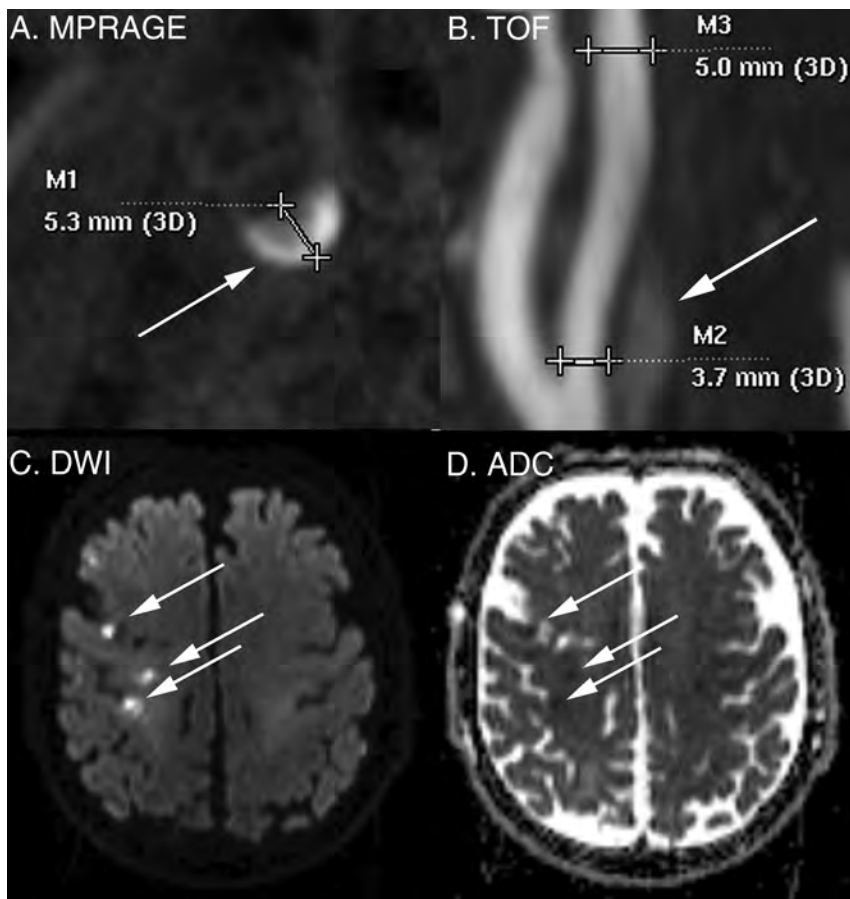


**FIG 1.** Carotid and brain MR imaging. Carotid IPH and maximum plaque thickness were detected by using the MPRAGE sequence as shown in this representative image with right-sided carotid IPH (A). 3D TOF MRA was used alongside duplex sonography in all patients to determine lumen findings, as in this subject with 26% stenosis by NASCET criteria (B). Stroke was determined by using the American Heart Association criteria supplemented with DWI, as in this example with recent right MCA distribution infarcts (C and D).

defined by visible bulb stenosis, a distal ICA diameter of  $\leq 3$  mm, and a distal ICA/distal external carotid artery ratio of  $\leq 1.25$ .<sup>29,30</sup> Ulceration was determined by using a size threshold of 2 mm.<sup>31</sup> Intraluminal thrombus was determined by a filling defect and confirmed in all cases with contrast CTA or MRA.<sup>32</sup>

### Ischemic Stroke Determination

Ischemic stroke was determined by using the American Heart Association definition of CNS infarction: brain or retinal cell death attributable to ischemia based on the following: 1) imaging evidence of cerebral or retinal ischemia in the carotid distribution, or 2) clinical symptoms persisting for  $\geq 24$  hours, with other etiologies excluded.<sup>33</sup> We reviewed neurovascular clinic or inpatient charts to determine the presence of recent stroke occurring at the time of recruitment. Asymptomatic (“silent”) recent infarcts were included as strokes and determined on brain DWI performed in all patients to supplement clinical determination of infarct by showing acuity and distribution (Fig 1). DWI-positive carotid territory infarcts were detected using DTI trace images, which are superior to conventional DWI in detecting recent infarcts.<sup>34,35</sup> The DTI parameters were 2D,  $128 \times 128$  matrix, 3-mm section thickness,  $b=2000$ , 20 directions. Brain DWI was interpreted by a Certificate of Added qualification–certified neuroradiologist.

### Clinical Characteristics

Clinical characteristics were determined by chart review, including cerebrovascular risk factors of age, male sex, diabetes, hypertension, hyperlipidemia, renal insufficiency, body mass index, and smoking status. We recorded the following cerebrovascular medications: antiplatelets, anticoagulants, statins, and antihypertensives, including antiangiotensin medications: angiotensin-converting enzyme inhibitors and angiotensin receptor blockers.

### Histologic Processing

In 35 patients who underwent carotid endarterectomy, each specimen was fixed in 10% neutral buffered formalin for histology. The ratio of the fixative to the specimen was at least 10:1. Specimens were decalcified in 1% Enhanced Decalcification Formulation (SL85–32; Statlab, Lewisville, Texas). Tissue cassettes were processed on an automated Vacuum Infiltrating Processor (Sakura, Alphen aan den Rijn, the Netherlands), embedded in paraffin wax, sectioned at 3- to 4-mm intervals, and stained with hematoxylin-eosin.

### Histology Interpretation of IPH

A pathologist outlined recent IPH by using hematoxylin-eosin, blinded to MPRAGE results. “Recent” IPH was defined by intact red blood cells or degenerated red blood cells on hematoxylin-eosin. Each carotid area positive for IPH was then compared with vitamin D levels.

### Statistical Analysis

Statistical modeling was performed by using generalized estimating equations to account for data clustering, with up to 2 carotid arteries per patient. Carotid arteries were treated as separate units grouped within subjects because IPH may be associated with local carotid plaque markers (eg, plaque thickness) and systemic clinical factors (eg, age). Because  $>1$  marker for IPH was being studied, potential confounding was investigated on the outcome variable, IPH. Therefore only 1 data table was required with  $P$  values from univariable generalized estimating equation Poisson regression models. Poisson regression directly estimates the prevalence ratio (PR), which is more intuitive to interpret than an odds ratio from a logistic regression approach (Zou and Donner<sup>36</sup>). Next, all potential confounders with  $P < .20$  from a univariable model were placed in an initial multivariable generalized estimating equation Poisson regression model for IPH, then eliminated in a backward fashion until all remaining variables met the threshold  $P < .10$ . A liberal significance criterion,  $P < .10$ , was used to protect against residual confounding (Maldonado and Greenland<sup>37</sup>).

**Table 1: Final MRI-IPH prediction model<sup>a</sup>**

Carotid IPH Predictor	PR	P Value	95% CI
Maximum plaque thickness, per 1-mm increase	1.40	<.001	1.18–1.67
Low vitamin D level of <30 ng/mL, low versus high	2.05	.03	1.06–3.96

<sup>a</sup>The final prediction model for the presence of MRI-detected carotid IPH depended on 2 factors: maximum plaque thickness and low vitamin D levels.

**Table 2: IPH prediction model with angiotensin system confounders<sup>a</sup>**

Carotid IPH Predictor	PR	P Value	95% CI
Maximum plaque thickness, per 1-mm increase	1.40	<.001	1.18–1.67
Low vitamin D level, <30 ng/mL, low versus high	2.07	.04	1.05–4.09
Angiotensin II level (ng/L), per 1-U increase	1.00	.80	0.99–1.01
ACE inhibitor use	1.05	.87	0.56–1.99
ARB use	0.93	.90	0.31–2.77

**Note:**—ARB indicates angiotensin receptor blockers.

<sup>a</sup>To illustrate the lack of confounding, we included markers of systemic angiotensin activity, including angiotensin II, ACE inhibitor use, and ARB use in addition to our final model of maximum plaque thickness and low vitamin D levels.

For hypothesis testing of markers predictive of IPH, we used the traditional  $P < .05$ . In binary outcome models, 5 outcome events for every predictor variable are sufficient to avoid overfitting.<sup>38</sup> With 48 carotid plaques positive for IPH and 80 negative for IPH, 48/5 or 9.6 or up to 9 predictor variables could be included in the model without overfitting, exceeding the number of variables in our final model. Additionally, we identified the following potential confounders with a scientific basis for confounding the association between vitamin D and IPH: angiotensin, angiotensin-converting enzyme inhibitor use, and angiotensin receptor blocker use. Because of the high potential for these to confound the vitamin D and IPH association, we used a combination of the 10% change in estimate and backward elimination and kept these potential confounders in a secondary analysis even though they were eliminated in the primary analysis. We also calculated IPH volume as a continuous variable and used a linear mixed-effects regression model to correlate carotid IPH with maximum plaque thickness and vitamin D levels, again accounting for up to 2 carotid arteries per patient. For the histology-outlined IPH area correlation with vitamin D levels, a random intercept linear regression model was used with an autoregressive correlation structure repeated-measures analysis of the 35 subjects that had undergone carotid endarterectomy. In this analysis, the “time” repetition variable was each histology slide, and the “group” variable was each carotid plaque. All statistical analyses were performed with STATA 13.1 (StataCorp, College Station, Texas).

## RESULTS

### Clinical Characteristics

Sixty-five patients were recruited, with a mean age  $72.3 \pm 8.3$  years, 90.8% men and 3.1% minorities. Patients had multiple cerebrovascular risk factors (69.2% current or prior smokers, 87.7% hypertensive, 84.6% hyperlipidemic, 44.6% diabetic) and were aggressively managed before enrollment (84.6% on antihypertensives, 89.2% on statins, 81.5% on antiplatelets) (On-line Table). These characteristics reflect the high prevalence of carotid disease in our population.

### Imaging and Clinical Characteristics by Vessel

Imaging and clinical characteristics were also listed by vessel and broken down by IPH status (positive versus negative) in the On-

line Table. Each patient contributed 2 carotid plaques, with the exception of 2 carotid occlusions that were excluded, leaving 128 carotid arteries for the final sample. Stenosis was worse in carotid arteries with IPH-positive versus negative plaque (NASCET stenosis of 53.9% versus 35.7% and millimeter stenosis of 2.25 versus 3.17 mm,  $P = .003$ ). Maximum plaque thickness was also higher (5.53 versus 4.08 mm,  $P < .001$ ), and there was a higher prevalence of ulceration (64.6% versus 37.5%,  $P = .02$ ) and intraluminal thrombus, though rare (6.3% versus 0.0%,  $P = .05$ ). Some factors were potential confounders be-

tween IPH-positive and negative status ( $P < .20$ ), requiring multivariable regression to determine essential IPH predictors.

### Multivariable Generalized Estimating Equation Poisson Regression Analysis for Carotid IPH Prediction

Multivariable generalized estimating equation Poisson regression analysis was performed to determine predictors of carotid IPH from the On-line Table. The initial model included 9 predictors with  $P < .20$ : NASCET stenosis, millimeter stenosis, maximum plaque thickness, ulceration, intraluminal thrombus, high angiotensin II ( $>18$  ng/L), vitamin D level ng/mL (continuous variable), low vitamin D level ( $<30$  ng/mL), and male sex. Table 1 shows the final model after sequential backward elimination of confounders with  $P > .10$ . The final model included maximum plaque thickness (PR = 1.40; 95% CI, 1.18–1.67;  $P < .001$ ) and low vitamin D levels (PR = 2.05; 95% CI, 1.06–3.96;  $P = .03$ ) as significant predictors of carotid IPH. Table 2 illustrates the lack of confounding by angiotensin II, angiotensin-converting enzyme inhibitor, and angiotensin receptor blockers use.

### Linear Mixed-Effects Regression Model of IPH Volume with Maximum Plaque Thickness and Low Vitamin D Levels

Carotid IPH volume significantly correlated with maximum plaque thickness ( $r = 0.45$ ,  $P < .001$ ) and low vitamin D levels ( $r = 0.26$ ,  $P = .003$ ) as depicted in the linear regression plot (Fig 2).

### Carotid IPH Histology and Vitamin D Levels

Histology-defined IPH area (Fig 3A) negatively correlated with vitamin D levels (Fig 3B). In addition, IPH area correlated with plaque area (partial  $r = 0.46$ ,  $P < .001$ ) and low-versus-normal vitamin D levels (partial  $r = 0.22$ ,  $P = .03$ ) (Fig 3C).

### Carotid IPH, Vitamin D Levels, and Stroke

IPH volume more negatively correlated with vitamin D levels with ischemic stroke (hollow squares, thick dashed line, partial  $r = -0.21$ ,  $P = .27$ ) compared to without it (solid circles, thick solid line, partial  $r = -0.06$ ,  $P = .53$ ) (Fig 4A). Vitamin D levels were also lower in patients with versus without stroke in the setting of IPH-negative plaque (mean,  $33.5 \pm 13.2$  ng/mL in 73 carotids versus  $26.2 \pm 17.4$  ng/mL in 7 carotids,  $P = .17$ ) and less so with IPH-positive plaque ( $27.8 \pm 12.6$  ng/mL in 25 carotids versus  $25.6 \pm 11.1$  ng/mL in 23 carotids,  $P = .51$ ) (Fig 4B).

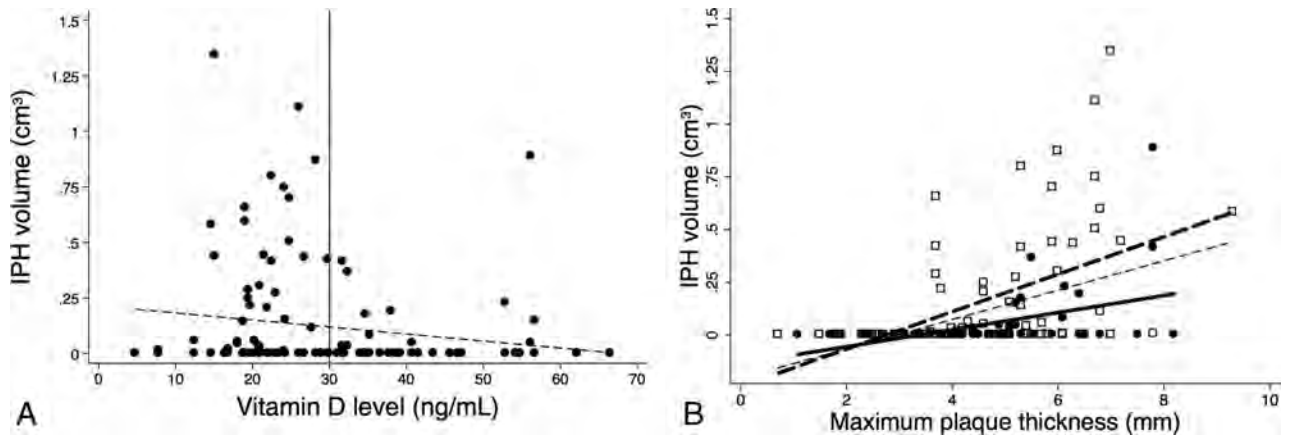


**FIG 2.** Linear regression of MR imaging–detected IPH volume, plaque thickness, and vitamin D status. Pooled data demonstrate the IPH volume negative correlation with vitamin D level (A) and correlation with maximal plaque thickness (partial  $r = 0.45$ ,  $P < .001$ , thin dashed line) and low-versus-normal vitamin D levels (partial  $r = 0.26$ ,  $P = .003$ ; low vitamin D level: empty squares and thick dashed line; normal vitamin D levels: solid circles and thick solid line, B).

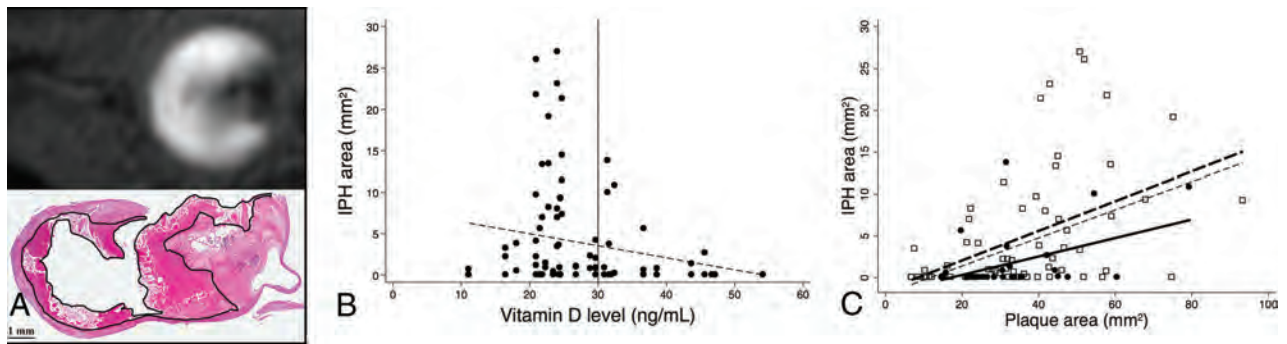


**FIG 3.** Linear regression of IPH area on histology, plaque area, and vitamin D status. Representative MPRAGE-positive plaque (upper image) and IPH area outlined on the corresponding hematoxylin-eosin stain (lower image) (A). Pooled data demonstrate the IPH area negatively correlating with vitamin D levels (B) and positively correlating with plaque area (partial  $r = 0.46$ ,  $P < .001$ , thin dashed line) and low-versus-normal vitamin D levels (partial  $r = 0.22$ ,  $P = .03$ , low vitamin D level: empty squares and thick dashed line; normal vitamin D level: solid circles and thick solid line) (C).

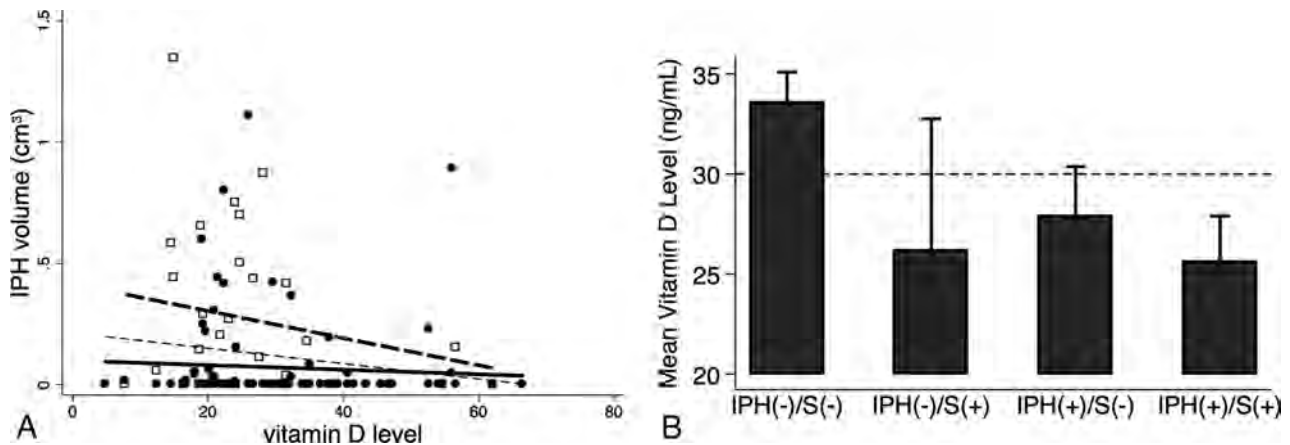


**FIG 4.** Association of IPH volume, vitamin D levels, and ischemic stroke. IPH volume was negatively correlated with vitamin D levels as in Fig 2A (thin dashed line). When stratified by ischemic stroke status, IPH volume was more negatively correlated with vitamin D levels (hollow squares, thick dashed line, partial  $r = -0.21$ ,  $P = .27$ ) in ischemic stroke compared to without it (solid circles, thick solid line, partial  $r = -0.06$ ,  $P = .53$ ) (A). Vitamin D levels were also lower in groups positive-versus-negative for stroke in the setting of IPH-negative plaque (mean,  $33.5 \pm 13.2$  ng/mL in 73 carotids versus  $26.2 \pm 17.4$  ng/mL in 7 carotids,  $P = .17$ ) and less so in the setting of IPH-positive plaque ( $27.8 \pm 12.6$  ng/mL in 25 carotid arteries versus  $25.6 \pm 11.1$  ng/mL in 23 carotid arteries,  $P = .51$ ) (B). S indicates carotid territory ischemic stroke status (positive or negative).

### Carotid IPH Volume Follow-Up

Two patients were re-evaluated after 1 year (Fig 5). Both were treated with medical therapy (statins, antiplatelets, and anti-

hypertensives) and both patients' primary care physicians were alerted to low vitamin D levels ( $<30$  ng/mL). Patient 1 was supplemented, vitamin D increased (baseline/1 year:  $18.1/26.8$

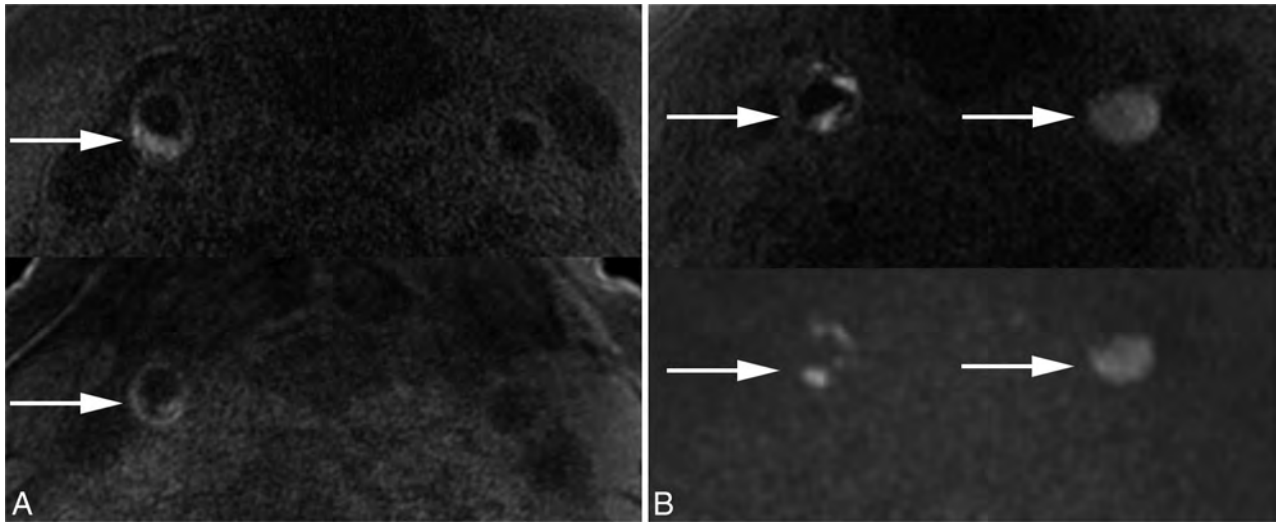


**FIG 5.** Vitamin D supplementation and follow-up. *A*, Patient 1: Baseline (*upper arrow*) versus 1-year follow-up (*lower arrow*) with vitamin D supplementation and medical therapy, including statins and antiplatelet and antihypertensive medications, demonstrates decreased IPH volume in a patient with no interval stroke (vitamin D baseline/1 year: 18.1/26.8 ng/mL; carotid IPH baseline/1 year: 0.151/0.115 cm<sup>3</sup>, or 24.1% decreased IPH volume). The patient remained asymptomatic in the year between the 2 scans. *B*, Patient 2: Baseline (*upper arrow*) versus 1-year follow-up (*lower arrow*) without vitamin D supplementation but with medical therapy, including statins and antiplatelet and antihypertensive medications, demonstrates minimally changed IPH volume (vitamin D baseline/1 year: 20.9/10.7 ng/mL; carotid IPH baseline/1 year: 1.041/0.996 cm<sup>3</sup>, or 4.3% decreased IPH volume). In addition, this patient had bilateral strokes in the year between the 2 scans.

ng/mL), carotid IPH volume decreased by 24.1% (baseline/1 year: 0.151/0.115 cm<sup>3</sup>), and he remained asymptomatic. Patient 2 was not supplemented, vitamin D levels decreased (baseline/1 year: 20.9/10.7 ng/mL), carotid IPH volume minimally decreased by 4.3% (baseline/1 year: 1.041/0.996 cm<sup>3</sup>), and he had sequential bilateral strokes.

## DISCUSSION

This work shows that both the presence and volume of carotid IPH are strongly associated with plaque thickness and low vitamin D levels, and not necessarily with percentage stenosis or other measures of carotid architecture. This finding supports the idea that low vitamin D levels may play a role in atherosclerosis and stroke risk. Considering its multiple health benefits, vitamin D testing may be worthwhile in patients with vulnerable carotid plaque.

Low vitamin D levels have been linked to cardiovascular disease in many prior studies.<sup>39</sup> Two cohort studies evaluating participants in the Framingham Heart Study (Offspring Cohort) and the Copenhagen City Heart Study found increased risk of ischemic stroke with lower vitamin D levels,<sup>40,41</sup> and a low vitamin D level is an independent predictor of ischemic stroke volume.<sup>42</sup> Most important, vitamin D supplementation decreases muscle atrophy, falls, hip fractures, and cognitive impairment and leads to functional improvement in patients with stroke.<sup>43,44</sup> Vitamin D also has many direct beneficial effects on the vasculature. Within 1 minute of treatment, vitamin D increases endothelial cell nitric oxide production.<sup>45</sup> Active vitamin D also improves endothelial function by decreasing AT1R and NADPH oxidase expression and increasing superoxide dismutase expression.<sup>46</sup>

An intriguing possibility is that low vitamin D levels may allow disinhibition of the local angiotensin system, leading to microvessel leakage of blood products. Alternatively, vitamin

D may have an effect on the lipid-rich necrotic core where microhemorrhages occur. Most interesting, while statins have been shown to decrease the carotid lipid-rich necrotic core<sup>47</sup> and decrease plaque inflammation,<sup>48</sup> statins do not ensure plaque stabilization. In trials in patients with IPH, including those with symptomatic low-grade (<50%) carotid stenosis, there is an extremely high stroke recurrence rate (46.0% per patient-year), despite aggressive therapy with statins, aspirin, and antihypertensives.<sup>49</sup> Most interesting, supplementing with vitamin D allows most statin-intolerant patients to tolerate statins and reach current low-density lipoprotein targets.<sup>50</sup> This finding suggests an interaction between statins and vitamin D, and optimizing both may be important in treating patients with carotid IPH.

One limitation of our study is its cross-sectional nature, making it difficult to determine causation between low vitamin D levels and carotid IPH. Another limitation is that unknown confounders may exist that we did not have data to control for in the regression analysis. These would include variables related to both predictor (vitamin D) and outcome (IPH). While we evaluated multiple factors that may influence both vitamin D levels and carotid IPH, including age, sex, body mass index, angiotensin system markers, and carotid markers including plaque thickness, we did not find a significant association between IPH and any of the factors listed except for plaque thickness. Still, it is possible that low vitamin D levels are linked to some other undiscovered confounder or sedentary lifestyle, which even surveys may fail to appropriately quantify.<sup>51</sup> Finally, our study recruited patients from the neurovascular clinic and inpatient settings who were predominantly overweight (average body mass index = 28.6), white (97%), and men (91%) and should be applied primarily to that population. Still, low vitamin D levels are highly prevalent in African American and Hispanic populations, and given the higher



rates of stroke and heart attack in these groups, further study in such minorities would be worthwhile.

Despite these limitations, in patients with carotid IPH, vitamin D screening and supplementation may be warranted. A trial of vitamin D supplementation in patients with carotid disease with low vitamin D levels could clarify whether vitamin D reduces or prevents IPH. Randomized controlled clinical trials may be warranted to determine the effect of vitamin D on preventing or reversing carotid IPH and its influence on future stroke risk. The relationship between vitamin D levels and IPH could be further investigated in animal models, including the *apolipoprotein E* knockout mouse model of atherogenesis coupled with vitamin D deficiency or vitamin D receptor knockout models.

## CONCLUSIONS

Vitamin D insufficiency was associated with both the presence and volume of carotid IPH in patients with carotid atherosclerosis. These results link low vitamin D levels with plaque vulnerability. Future clinical trials are needed to determine whether vitamin D supplementation can decrease IPH and subsequent stroke risk. Animal studies may also allow further insight into the role of vitamin D and receptor status in pathways leading to IPH.

Disclosures: Statistical analysis for this study was supported by the Study Design and Biostatistics Center grant\* with funding in part from the National Center for Research Resources and the National Center for Advancing Translational Sciences, National Institutes of Health, grant 8UL1TR000105. J. Scott McNally—RELATED: Grants: Radiological Society of North America Research Scholar Grant\* and University of Utah Intramural Seed Grant. Tina M. Burton—OTHER RELATIONSHIPS: Vascular Neurology Fellow at the National Institutes of Health/National Institute of Neurological Disorders and Stroke, from July 1, 2015, to present. Work related to this submission was performed prior to July 1, 2015. Jennifer J. Majersik—UNRELATED: Grants/Grants Pending: National Institutes of Health/National Institute of Neurological Disorders and Stroke. Dylan V. Miller—UNRELATED: Royalties: Elsevier Publishing; Travel/Accommodations/Meeting Expenses Unrelated to Activities Listed: College of American Pathologists, United States and Canadian Academy of Pathology. \*Money paid to the institution.

## REFERENCES

1. Go AS, Mozaffarian D, Roger VL, et al; American Heart Association Statistics Committee and Stroke Statistics Subcommittee. **Heart Disease and Stroke Statistics—2013 Update: a report from the American Heart Association.** *Circulation* 2013;127:e6–e245 CrossRef Medline
2. Petty GW, Brown RD Jr, Whisnant JP, et al. **Ischemic stroke subtypes: a population-based study of incidence and risk factors.** *Stroke* 1999;30:2513–16 CrossRef Medline
3. Flaherty ML, Kissela B, Khoury JC, et al. **Carotid artery stenosis as a cause of stroke.** *Neuroepidemiology* 2013;40:36–41 CrossRef Medline
4. Lee BI, Nam HS, Heo JH, et al; Yonsei Stroke Team. **Yonsei Stroke Registry: analysis of 1,000 patients with acute cerebral infarctions.** *Cerebrovasc Dis* 2001;12:145–51 CrossRef Medline
5. Tsantilas P, Kühnl A, Kallmayer M, et al. **Stroke risk in the early period after carotid related symptoms: a systematic review.** *J Cardiovasc Surg (Torino)* 2015;56:845–52 Medline
6. Lovett JK, Coull AJ, Rothwell PM. **Early risk of recurrence by subtype of ischemic stroke in population-based incidence studies.** *Neurology* 2004;62:569–73 CrossRef Medline
7. Redfors P, Jood K, Holmegaard L, et al. **Stroke subtype predicts outcome in young and middle-aged stroke sufferers.** *Acta Neurol Scand* 2012;126:329–35 CrossRef Medline
8. Adams HP Jr, Bendixen BH, Kappelle LJ, et al. **Classification of subtype of acute ischemic stroke: definitions for use in a multicenter clinical trial—TOAST. Trial of Org 10172 in Acute Stroke Treatment.** *Stroke* 1993;24:35–41 CrossRef Medline
9. Hosseini AA, Kandiyil N, Macsweeney ST, et al. **Carotid plaque hemorrhage on magnetic resonance imaging strongly predicts recurrent ischemia and stroke.** *Ann Neurol* 2013;73:774–84 CrossRef Medline
10. Gupta A, Baradaran H, Schweitzer AD, et al. **Carotid plaque MRI and stroke risk: a systematic review and meta-analysis.** *Stroke* 2013;44:3071–77 CrossRef Medline
11. Saam T, Hetterich H, Hoffmann V, et al. **Meta-analysis and systematic review of the predictive value of carotid plaque hemorrhage on cerebrovascular events by magnetic resonance imaging.** *J Am Coll Cardiol* 2013;62:1081–91 CrossRef Medline
12. Ota H, Yarnykh VL, Ferguson MS, et al. **Carotid intraplaque hemorrhage imaging at 3.0-T MR imaging: comparison of the diagnostic performance of three T1-weighted sequences.** *Radiology* 2010;254:551–63 CrossRef Medline
13. Regoli D, Plante GE, Gobeil F, Jr. **Impact of kinins in the treatment of cardiovascular diseases.** *Pharmacol Ther* 2012;135:94–111 CrossRef Medline
14. da Cunha V, Martin-McNulty B, Vincelette J, et al. **Angiotensin II induces histomorphologic features of unstable plaque in a murine model of accelerated atherosclerosis.** *J Vasc Surg* 2006;44:364–71 CrossRef Medline
15. Skultetyova D, Filipova S, Riecansek I, et al. **The role of angiotensin type 1 receptor in inflammation and endothelial dysfunction.** *Recent Pat Cardiovasc Drug Discov* 2007;2:23–27 Medline
16. Forman JP, Williams JS, Fisher ND. **Plasma 25-hydroxyvitamin D and regulation of the renin-angiotensin system in humans.** *Hypertension* 2010;55:1283–88 CrossRef Medline
17. Gupta GK, Agrawal T, Del Core MG, et al. **Decreased expression of vitamin D receptors in neointimal lesions following coronary artery angioplasty in atherosclerotic swine.** *PLoS One* 2012;7:e42789 CrossRef Medline
18. Carrelli AL, Walker MD, Lowe H, et al. **Vitamin D deficiency is associated with subclinical carotid atherosclerosis: the Northern Manhattan study.** *Stroke* 2011;42:2240–45 CrossRef Medline
19. Liu JX, Xiang J, Bu RF, et al. **Serum 25-hydroxyvitamin D concentration is negatively related to carotid artery intima-media thickness in type 2 diabetic patients**[In Chinese]. *Zhonghua Xin Xue Guan Bing Za Zhi* 2012;40:115–19 Medline
20. Anderson JL, May HT, Horne BD, et al; Intermountain Heart Collaborative (IHC) Study Group. **Relation of vitamin D deficiency to cardiovascular risk factors, disease status, and incident events in a general healthcare population.** *Am J Cardiol* 2010;106:963–68 CrossRef Medline
21. Forrest KY, Stuhldreher WL. **Prevalence and correlates of vitamin D deficiency in US adults.** *Nutr Res* 2011;31:48–54 CrossRef Medline
22. Hadley JR, Roberts JA, Goodrich KC, et al. **Relative RF coil performance in carotid imaging.** *Magn Reson Imaging* 2005;23:629–39 CrossRef Medline
23. Tate Q, Kim SE, Treiman G, et al. **Increased vessel depiction of the carotid bifurcation with a specialized 16-channel phased array coil at 3T.** *Magn Reson Med* 2013;69:1486–93 CrossRef Medline
24. Chapman BE, Minalga ES, Brown C, et al. **Reducing morphological variability of the cervical carotid artery in serial magnetic resonance imaging using a head and neck immobilization device.** *J Magn Reson Imaging* 2008;28:258–62 CrossRef Medline
25. Zhu DC, Ferguson MS, DeMarco JK. **An optimized 3D inversion recovery prepared fast spoiled gradient recalled sequence for carotid plaque hemorrhage imaging at 3.0 T.** *Magn Reson Imaging* 2008;26:1360–66 CrossRef Medline
26. McNally JS, Yoon HC, Kim SE, et al. **Carotid MRI detection of intraplaque hemorrhage at 3T and 1.5T.** *J Neuroimaging* 2015;25:390–96 CrossRef Medline
27. **North American Symptomatic Carotid Endarterectomy Trial: methods, patient characteristics, and progress.** *Stroke* 1991;22:711–20 CrossRef Medline

28. Fox AJ. **How to measure carotid stenosis.** *Radiology* 1993;186: 316–18 CrossRef Medline
29. Fox AJ, Eliasziw M, Rothwell PM, et al. **Identification, prognosis, and management of patients with carotid artery near occlusion.** *AJNR Am J Neuroradiol* 2005;26:2086–94 Medline
30. Bartlett ES, Walters TD, Symons SP, et al. **Quantification of carotid stenosis on CT angiography.** *AJNR Am J Neuroradiol* 2006;27:13–19 Medline
31. U-King-Im JM, Fox AJ, Aviv RI, et al. **Characterization of carotid plaque hemorrhage: a CT angiography and MR intraplaque hemorrhage study.** *Stroke* 2010;41:1623–29 CrossRef Medline
32. Menon BK, Singh J, Al-Khataami A, et al; Calgary CTA Study Group. **The donut sign on CT angiography: an indicator of reversible intraluminal carotid thrombus?** *Neuroradiology* 2010;52:1055–56 CrossRef Medline
33. Sacco RL, Kasner SE, Broderick JP, et al; American Heart Association Stroke Council, Council on Cardiovascular Surgery and Anesthesia, Council on Cardiovascular Radiology and Intervention, Council on Cardiovascular and Stroke Nursing, Council on Epidemiology and Prevention, Council on Peripheral Vascular Disease, Council on Nutrition, Physical Activity and Metabolism. **An updated definition of stroke for the 21st century: a statement for healthcare professionals from the American Heart Association/American Stroke Association.** *Stroke* 2013;44:2064–89 CrossRef Medline
34. McNally JS, Kim SE, Yoon HC, et al. **Carotid magnetization-prepared rapid acquisition with gradient-echo signal is associated with acute territorial cerebral ischemic events detected by diffusion-weighted MRI.** *Circ Cardiovasc Imaging* 2012;5:376–82 CrossRef Medline
35. Chou MC, Tzeng WS, Chung HW, et al. **T2-enhanced tensor diffusion trace-weighted image in the detection of hyper-acute cerebral infarction: comparison with isotropic diffusion-weighted image.** *Eur J Radiol* 2010;74:e89–94 CrossRef Medline
36. Zou GY, Donner A. **Extension of the modified Poisson regression model to prospective studies with correlated binary data.** *Stat Methods Med Res* 2013;22:661–70 CrossRef Medline
37. Maldonado G, Greenland S. **Simulation study of confounder-selection strategies.** *Am J Epidemiol* 1993;138:923–36 Medline
38. Vittinghoff E, McCulloch CE. **Relaxing the rule of ten events per variable in logistic and Cox regression.** *Am J Epidemiol* 2007;165: 710–18 CrossRef Medline
39. Norman PE, Powell JT. **Vitamin D and cardiovascular disease.** *Circ Res* 2014;114:379–93 CrossRef Medline
40. Wang TJ, Pencina MJ, Booth SL, et al. **Vitamin D deficiency and risk of cardiovascular disease.** *Circulation* 2008;117:503–11 CrossRef Medline
41. Brondum-Jacobsen P, Nordestgaard BG, Schnohr P, et al. **25-hydroxyvitamin D and symptomatic ischemic stroke: an original study and meta-analysis.** *Ann Neurol* 2013;73:38–47 CrossRef Medline
42. Turetsky A, Goddeau RP Jr, Henninger N. **Low serum vitamin D is independently associated with larger lesion volumes after ischemic stroke.** *J Stroke Cerebrovasc Dis* 2015;24:1555–63 CrossRef Medline
43. Sato Y, Iwamoto J, Kanoko T, et al. **Low-dose vitamin D prevents muscular atrophy and reduces falls and hip fractures in women after stroke: a randomized controlled trial.** *Cerebrovasc Dis* 2005;20: 187–92 CrossRef Medline
44. Yalbuздag SA, Sarifakioglu B, Afsar SI, et al. **Is 25(OH)D associated with cognitive impairment and functional improvement in stroke? A retrospective clinical study.** *J Stroke Cerebrovasc Dis* 2015;24: 1479–86 CrossRef Medline
45. Molinari C, Uberti F, Grossini E, et al. **1 $\alpha$ ,25-dihydroxycholecalciferol induces nitric oxide production in cultured endothelial cells.** *Cell Physiol Biochem* 2011;27:661–68 CrossRef Medline
46. Dong J, Wong SL, Lau CW, et al. **Calcitriol protects renovascular function in hypertension by down-regulating angiotensin II type 1 receptors and reducing oxidative stress.** *Eur Heart J* 2012;33: 2980–90 CrossRef Medline
47. Zhao XQ, Dong L, Hatsukami T, et al. **MR imaging of carotid plaque composition during lipid-lowering therapy a prospective assessment of effect and time course.** *JACC Cardiovasc Imaging* 2011;4: 977–86 CrossRef Medline
48. Dong L, Kerwin WS, Chen H, et al. **Carotid artery atherosclerosis: effect of intensive lipid therapy on the vasa vasorum—evaluation by using dynamic contrast-enhanced MR imaging.** *Radiology* 2011;260: 224–31 CrossRef Medline
49. Yoshida K, Sadamasa N, Narumi O, et al. **Symptomatic low-grade carotid stenosis with intraplaque hemorrhage and expansive arterial remodeling is associated with a high relapse rate refractory to medical treatment.** *Neurosurgery* 2012;70:1143–50; discussion 1150–51 CrossRef Medline
50. Khayznikov M, Kumar A, Wang P, et al. **Statin intolerance and vitamin D supplementation.** *N Am J Med Sci* 2015;7:339–40 Medline
51. Atkin AJ, Gorely T, Clemes SA, et al. **Methods of measurement in epidemiology: sedentary behaviour.** *Int J Epidemiol* 2012;41: 1460–71 CrossRef Medline

# Validation of a Hemodynamic Model for the Study of the Cerebral Venous Outflow System Using MR Imaging and Echo-Color Doppler Data

G. Gadda, A. Taibi, F. Sisini, M. Gambaccini, S.K. Sethi, D.T. Utriainen, E.M. Haacke, P. Zamboni, and M. Ursino



## ABSTRACT

**BACKGROUND AND PURPOSE:** A comprehensive parameter model was developed to investigate correlations between cerebral hemodynamics and alterations in the extracranial venous circulation due to posture changes and/or extracranial venous obstruction (stenosis). The purpose of this work was to validate the simulation results by using MR imaging and echo-color Doppler experimental blood flow data in humans.

**MATERIALS AND METHODS:** To validate the model outcomes, we used supine average arterial and venous extracerebral blood flow, obtained by using phase-contrast MR imaging from 49 individuals with stenosis in the acquisition plane at the level of the disc between the second and third vertebrae of the left internal jugular vein, 20 with stenosis in the acquisition plane at the level of the disc between the fifth and sixth vertebrae of the right internal jugular vein, and 38 healthy controls without stenosis. Average data from a second group of 10 healthy volunteers screened with an echo-color Doppler technique were used to evaluate flow variations due to posture change.

**RESULTS:** There was excellent agreement between experimental and simulated supine flows. Every simulated CBF fell inside the standard error from the corresponding average experimental value, as well as most of the simulated extracerebral arterial flow (extracranial blood flow from the head and face, measured at the level of the disc between second and third vertebrae) and venous flows. Simulations of average jugular and vertebral blood flow variations due to a change of posture from supine to upright also matched the experimental data.

**CONCLUSIONS:** The good agreement between simulated and experimental results means that the model can correctly reproduce the main factors affecting the extracranial circulation and could be used to study other types of stenotic conditions not represented by the experimental data.

**ABBREVIATIONS:** C2/C3 = acquisition plane at the level of the disc between second and third vertebrae; C5/C6 = acquisition plane at the level of the disc between fifth and sixth vertebrae; ECD = echo-color Doppler; IJV = internal jugular vein; LL-R ST = stenosis at the lower level of the right internal jugular vein; NST = nonstenotic; Pvs = venous sinuses pressure; Q = cerebral blood flow; Qex = extracranial blood flow from the head and face, measured at the level of the disc between second and third vertebrae; UL-L ST = stenosis at the upper level of the left internal jugular vein; VV = vertebral system

Cerebral hemodynamics plays a key role in brain physiology.<sup>1</sup> The interest in understanding the hemodynamics of the brain arises from human brain function being critically dependent on the proper values of cerebral blood inflow and outflow.<sup>2</sup> Unfortunately, experimental access to cerebral circulation dynamics is limited.

Within the complex problem of cerebral hemodynamics, the

cerebral venous system plays an important role. Indeed, cranial and extracranial veins form an intricate network of vessels, stressed by complex phenomena involving postural changes and the gravity field, which affect the dynamics of circulating blood.<sup>2</sup> In particular, the internal jugular vein (IJV), which is the dominant outflow vein from the brain,<sup>3</sup> is a collapsible vessel characterized by marked changes in its cross-sectional area, depending on transmural pressure on the vessel wall.<sup>4,5</sup> Section changes, in turn, affect its conductance. The overall phenomenon is influenced by the hydrostatic pressure gradient during the transition from the supine to sitting position.<sup>6,7</sup>

Received February 12, 2016; accepted after revision May 9.

From the Department of Physics and Earth Sciences (G.G., A.T., F.S., M.G.), and Vascular Diseases Center (P.Z.), University of Ferrara, Ferrara, Italy; MRI Institute for Biomedical Research (S.K.S., D.T.U., E.M.H.), Detroit, Michigan; and Department of Electrical, Electronic and Information Engineering (M.U.), University of Bologna, Bologna, Italy.

This study was partially supported by the Italian Ministry of Education, University and Research (MIUR Programme PRIN 2010–2011), grant No. 2010XE5L2R.

The rationale for this work was previously presented at: Annual International Conference of the IEEE Engineering in Medicine and Biology Society, August 25–29, 2015; Milan, Italy.

Please address correspondence to Giacomo Gadda, MSc, Department of Physics and Earth Sciences, Via Saragat 1, 44122 Ferrara, Italy; e-mail: giacomo.gadda@unife.it

Indicates open access to non-subscribers at [www.ajnr.org](http://www.ajnr.org)

<http://dx.doi.org/10.3174/ajnr.A4860>

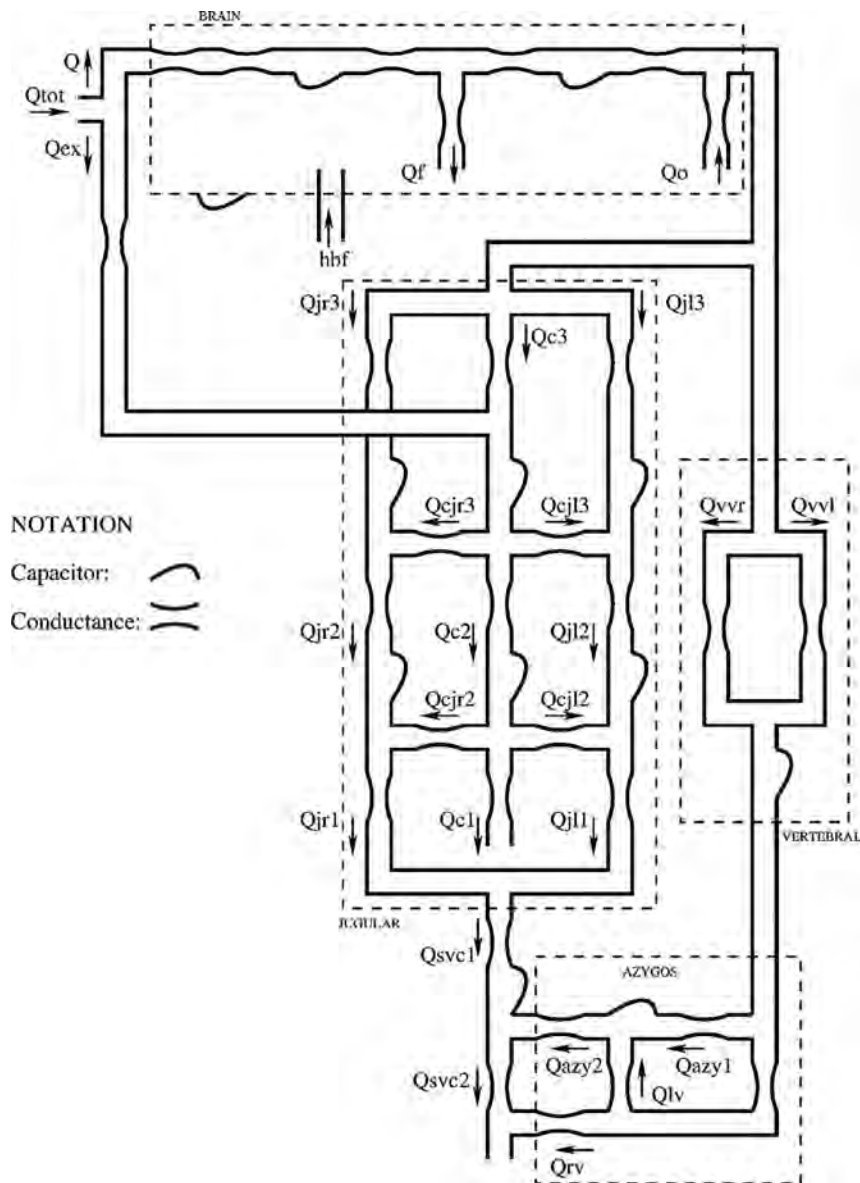


**FIG 1.** Scheme of the hemodynamic parameter model for the study of cerebral venous outflow.<sup>8</sup>

Due to the plethora of biophysical factors affecting brain circulation, it is difficult to gain an accurate quantitative understanding of its behavior and of the clinical implications of its alteration.

Recently, we developed a comprehensive lumped parameter model that links intracranial hemodynamics and the cerebral venous outflow system.<sup>8</sup> Its aim is to simulate the cranial and extracranial vessel pathway behavior and the mechanisms involved in the drainage process and to link them with the intracranial circulation and the action of cerebrovascular regulation mechanisms. The model represents a new tool for improving our understanding of this complex system.

The aim of this work was to provide a validation of the model, by using *in vivo* measurements performed in both healthy subjects and individuals with venous obstruction. We illustrate how the model parameters can be tuned to reproduce MR imaging and echo-color Doppler (ECD) data of average blood flow. With this model, we can simulate some important phenomena affecting the

extracranial venous system, such as the posture change or the presence of jugular obstructions (stenosis).<sup>9,10</sup> We took advantage of the availability of both MR imaging and ECD experimental data of blood flow to exploit the different advantages they provide. MR imaging includes phase-contrast imaging for flow quantification, along with 2D (TOF) MRV for anatomic assessment.<sup>11–13</sup> MR imaging-based techniques allow the inclusion of information about minor vessels besides the common carotid, internal carotid, and vertebral arteries; IJVs; and vertebral veins. The ECD technique,<sup>14</sup> even if not useful for detecting minor routes, is a cheaper and faster methodology, suitable for measurement of blood flow in both the supine and upright conditions. We used ECD to obtain information about the percentage variation of average flows due to a change of posture.

## MATERIALS AND METHODS

### Model Description

The mathematic model has been presented in a previous article.<sup>8</sup> Briefly, it is composed of 2 submodels built by using a compartmental method, a technique that simplifies distributed physical systems into a topology of discrete entities (ie, lumped parameters).<sup>15</sup> This approximation entails an important advantage because it allows complex systems to be represented with a relatively small number of parameters, each able to account for an entire physiologic or clinical characteristic in a concise way. The hemodynamic model for the study of cerebral

venous outflow is represented in Fig 1, in which every segment is a vessel or part of it.

The intracranial part of the model, developed by Ursino and Lodi,<sup>16</sup> is enclosed in the brain box. The extracranial part, developed starting from the work of Zamboni et al<sup>17</sup> and Gadda et al,<sup>8</sup> is outside it. Every segment  $x$  of Fig 1 consists of a hydraulic capacity (capacity of the generic segment  $x$  of the circulatory system) and a conductance (conductance of the generic segment  $x$  of the circulatory system); capacities simulate the property to accommodate volume,<sup>18</sup> while conductances simulate the property to drain blood.<sup>15</sup> All these parameters are included in the differential equations that compose the model.<sup>8</sup> Differential equations link together simulated blood flows, pressures, and time, accounting for mass preservation, energy losses, and effects due to posture changes.<sup>4–7</sup> The system of equations is managed by the software package Berkeley Madonna (<http://www.berkeleymadonna.com>).<sup>19,20</sup>

The mathematic submodel of the cerebral circulation simulates the hemodynamics of the arteriovenous cerebrovascular bed and the related mechanisms (regulation activity of cerebral arterioles, CSF production and reabsorption processes, the Starling resistor mechanism for the cerebral veins<sup>2</sup>).

The extracranial outflow submodel is composed of left and right IJVs, the vertebral system (VV), and the lumboazygos system. The biomechanical properties of the IJVs change along their lengths, because in the upright position, they act like collapsible tubes interacting with the hydrostatic pressure gradient.<sup>4-7</sup> Thus, the IJVs are modeled by dividing them into 3 segments (J3, J2, and J1, starting from the upper segment)<sup>21</sup> with different capacitive values and conductances switching from low to high values following a nonlinear relation of the transmural pressure.<sup>8</sup>

The segmentation of IJVs also makes the model a good tool to easily simulate how different stenotic patterns affect blood redistribution on the left and right sides of the jugular system.<sup>9</sup> We know that blood flow is not the same in the right and left IJVs and that both of these flows increase from J3 to J1 in normal conditions (physiologic pressure, absence of stenosis), because a quota of the head inflow is conveyed into the IJVs more caudally with respect to the brain vascular junctions.<sup>17,22</sup> To account for this behavior, we developed the model so that the IJVs are linked by a network of segments, each with constant capacitance and conductance, which simulates the presence of anastomotic connections between the IJVs, and by a connection segment with extracranial venous pathways (ie, with that part of the blood coming from the external arteries to serve the tissues outside the brain).

### **MR Imaging Data for Flow Quantification**

One hundred seven subjects were imaged with 3T MR imaging scanners at 4 imaging sites by using a 3T Signa HDxt scanner (GE Healthcare, Milwaukee, Wisconsin) with a 12-channel head/neck coil arrangement (site 1 [Newport Diagnostic Center, Newport Beach, California]), a 3T Trio scanner (Siemens, Erlangen, Germany) (sites 2 [Applied fMRI Institute, San Diego, California] and 3 [Synergy Health Concepts, Newport Beach, California]), and a 3T Verio scanner (Siemens) (site 4 [Wayne State University, Detroit Michigan]) with a 16-channel head/neck coil arrangement, after institutional review board approval. 2D (TOF) MRV was used to recognize vessels and stenosis, while phase-contrast imaging was used to quantify blood flow.<sup>11-13</sup> The whole population was divided into 3 different subgroups: 38 subjects classified as nonstenotic (NST), 20 subjects with stenosis at the lower level of the right IJV (LL-R ST), and 49 subjects with stenosis at the upper level of the left IJV (UL-L ST). We identified a vessel as stenotic when its cross-sectional area was  $<25 \text{ mm}^2$  at or caudal to the C3 level and  $<12.5 \text{ mm}^2$  cranial to the C3 level.<sup>13</sup> Venous vessel flows were measured through acquisition of phase-contrast images perpendicular to the IJVs at 2 levels: the upper level (C2/C3, at the disc between second and third vertebrae), and the lower level (C5/C6, at the disc between the fifth and sixth vertebrae). A maximum velocity encoding of 50 cm/s was used, and phase unwrapping was performed when the flow velocity exceeded this value. Vessel boundaries were delineated automatically by using a

full width at half maximum region-growing threshold method<sup>23,24</sup> with manual modification applied when appropriate. Signal Processing In NMR software (SPIN; MR Imaging Institute for Biomedical Research, Detroit, Michigan)<sup>25</sup> was used to quantify blood flows and to evaluate the presence and dimensions of IJV stenosis. Data were processed by analysts trained in MR signal processing with several years' experience each.

For all the subjects, we calculated the cerebral blood flow (Q) (the total blood volume entering the cranial cavity per unit time, defined as the sum of flows in the internal carotid and vertebral arteries at the C2/C3 level). The amount of flow drained by the right and left IJV is measured at both the C2/C3 and C5/C6 levels (here referred to as blood flow drained by the upper segment of the right internal jugular vein [Qjr3], blood flow drained by the upper segment of the left internal jugular vein [Qjl3], blood flow drained by the middle segment of the right internal jugular vein [Qjr2], and blood flow drained by the middle segment of the left internal jugular vein [Qjl2], respectively). The fraction of cerebral blood flow exiting the skull from the vertebral system measured at the level of the disc between the second and third vertebrae (Qvv) is the fraction of Q exiting the skull from the vertebral system, measured at the C2/C3 level. Finally, we took into account the flow in the external carotid arteries (Qex, the amount of extracranial blood to the head and face, measured at the C2/C3 level). We chose to calibrate the model so that it reproduced these experimental flows.

### **ECD Data for Supine and Upright Flow Comparison**

ECD data of 10 healthy volunteers from a recent work<sup>17</sup> were used as a reference for the average blood flow variation from the supine condition to the upright one. We used those experimental data to assess the average percentage flow variation in the upright jugular and vertebral ducts with respect to the supine condition. Unlike other datasets available in the literature, these data allowed us to assess the supine/sitting variation for all 3 different segments for both left and right IJVs (J3, J2, and J1, respectively), recently established by a recent scientific consensus.<sup>21</sup> We chose to calibrate the model so that it reproduced upright-to-supine percentage variation of total jugular (blood flow drained by the upper segment of the internal jugular veins [Qj3] = Qjr3 + Qjl3, blood flow drained by the middle segment of the internal jugular veins [Qj2] = Qjr2 + Qjl2, blood flow drained by the lower segment of the internal jugular veins [Qj1] = blood flow drained by the lower segment of the right internal jugular vein [Qjr1] + blood flow drained by the lower segment of the left internal jugular vein [Qjl1]) and vertebral (Qvv) flow.

### **Assignment of Model Parameters**

All parameters of the intracranial circulation have been taken from previous articles, where an accurate description can be found.<sup>8,16</sup> Parameters of the extracranial venous circulation were calculated to reproduce the average blood flow values measured with MR imaging only in the supine position. In particular, as described in Gadda et al,<sup>8</sup> the tuning was made by assuming a progressive pressure reduction from the venous sinuses (6 mm Hg) to the right atrium (5 mm Hg). Then, we properly tuned the model conductances (Table 1) to reproduce the supine average

flows in each portion of the model (Table 2). Finally, the supine/upright percentage variations detected with the ECD technique (Table 3) were used to assign conductance to the anastomoses not directly involved in supine conditions.

**Table 1: List of the conductance values to reproduce the average flow data reported in Table 2 and the flow percentage variation reported in Table 3**

G (mL/s × mm Hg)	NST	LL-R ST	UL-L ST
A)			
Gv1	0.60	3.9	7.7
kj13	6.00	6.00	0.86
kjr2	16.00	2.30	16.00
B)			
Gc2	11.00		
Gc3	21.43		
Gcj12	6.67		
Gcj13	16.00		
Gazy1	1.33		
Gazy2	1.78		
Gc1	1.18		
Gcjr2	6.67		
Gcjr3	21.00		
Gex	0.03		
Glv	0.89		
Grv	0.41		
Gsvc1	78.50		
Gsvc2	81.17		
Gvv2	0.83		
kj11	7.27		
Kj12	8.00		
kjr1	7.27		
Kjr3	13.00		

**Note:**—G indicates conductance; Gv1, conductance of the vertebral system (upper part); kj13, parameter for the basal conductance of the upper segment of the left jugular vein; Gazy1, conductance of the distal azygos vein; Gazy2, conductance of the proximal azygos vein; Gc1, conductance of the lower segment of the collateral network; Gc2, conductance of the middle segment of the collateral network; Gc3, conductance of the upper segment of the collateral network; Gcj12, conductance of the lower anastomotic connection (left side); Gcj13, conductance of the upper anastomotic connection (left side); Gcjr2, conductance of the lower anastomotic connection (right side); Gcjr3, conductance of the upper anastomotic connection (right side); Gex, conductance of the external carotid arteries; Glv, conductance of the lumbar vein; Grv, conductance of the renal vein; Gsvc1, conductance of the upper segment of the superior vena cava (jugular confluence); Gsvc2, conductance of the lower segment of the superior vena cava; Gvv2, conductance of the vertebral system (lower part); kj11, parameter for the basal conductance of the lower segment of the left jugular vein; kj12, parameter for the basal conductance of the middle segment of the left jugular vein; kjr1, parameter for the basal conductance of the lower segment of the right jugular vein; kjr3, parameter for the basal conductance of the upper segment of the right jugular vein; kjr2, middle segment of the right jugular vein.

**Table 2: MRI average data of flows related to cerebral, external, jugular, and vertebral circuits in the supine condition<sup>a</sup>**

MRI	n	Q	Qex	Qjr3	Qj13	Qjr2	Qj12	Qvv
NST	38	10.6 ± 1.6	2.8 ± 1.2	5.6 ± 2.1	3.1 ± 1.8	7.1 ± 2.4	4.4 ± 1.9	0.5 ± 0.6
LL-R ST	20	10.7 ± 1.8	3.0 ± 1.1	3.5 ± 2.5	4.0 ± 2.1	3.6 ± 2.7	4.7 ± 2.6	1.8 ± 1.6
UL-L ST	49	10.6 ± 1.8	3.2 ± 1.2	6.1 ± 2.5	0.8 ± 0.9	7.5 ± 2.1	2.1 ± 1.7	2.0 ± 1.6

<sup>a</sup> Flow values are reported in milliliters/second with SDs.

**Table 3: ECD average data of flow related to cerebral, jugular, and vertebral circuits in the supine NST condition<sup>a</sup>**

ECD	Q	Qj3	Qj2	Qj1	Qvv
Supine	10.6 ± 1.9	6.0 ± 2.6	8.9 ± 3.4	22.0 ± 10.3	1.1 ± 0.7
Upright	10.6 ± 1.9	4.1 ± 2.0	5.2 ± 3.3	20.4 ± 12.5	2.3 ± 1.2
Variation (%)	0	-32	-42	-7	+109

<sup>a</sup> Flow values are reported in milliliters/second with SDs.

To simulate patients with stenosis at the lower level of the right internal jugular vein (LL-R ST) and stenosis at the upper level of the left internal jugular vein (UL-L ST), some parameters must be changed from the basal value assigned before. We decided to maintain these parameters to a minimum, to reduce the number of ad hoc assumptions. Hence, patients with LL-R ST were characterized by a reduction in conductance of the right J2 tract (obtained through a reduction in the parameter for the basal conductance of the middle segment of the right jugular vein [kjr2]), while patients with UL-L ST were characterized by a reduction in conductance of the left J3 tract (obtained through a reduction in parameter for the basal conductance of the upper segment of the left jugular vein [kj13]). Both parameters were diminished by the same percentage variation, to fit the patient data. Finally, we assumed that the venous vascular bed compensates the chronic stenotic phenomena via an increase in the conductance of the vertebral path (parameter Gvv). This step-by-step optimization procedure (assumption of progressive pressure reduction, choice of proper conductances of large vessels to simulate supine NST flows, choice of proper conductances of anastomoses to simulate upright NST flows, variation of NST conductances to simulate vessel blockages and flows of stenotic cases) ensures that model solutions fit both healthy and stenotic flow outcomes with a unique set of parameters.

Finally, we are aware that the model has many parameters, so the solution may not be unique. However, we introduce some strong constraints to our model, such as physiologic values for pressure or change of conductances only in the vertebral segment and in the jugular segments affected by stenosis, to reduce the *df* in the parameter choice.

## RESULTS

### Model Parameters

Table 1 reports the conductances that have been calculated to reproduce experimental flow data. Conductances that must be changed to reproduce differences among normal and stenotic subjects are listed in Table 1 part A, while unchanged conductances are listed in Table 1, part B.

To properly simulate LL-R ST average flow data, we needed to decrease the conductance of the right J2 segment with respect to the NST case (-86%). The same percentage variation is needed in the left J3 segment to reach good simulations of the UL-L ST cases. In both situations, we also needed to considerably increase the conductance of the upper part of the vertebral system (Gvv1).

### Comparison between Supine MR Imaging Data and Model Outcomes

Table 2 summarizes the calculated average blood flows Q, Qex, Qjr3, Qj13, Qjr2, Qj12, and Qvv for every subgroup.

Figure 2 shows how the model simulates these flows at the equilibrium for the NST group.

Every jugular segment carries more flow than VV. In addition, average blood flow in the right IJV is greater than in the left one, for both C2/C3 and C5/C6 lev-

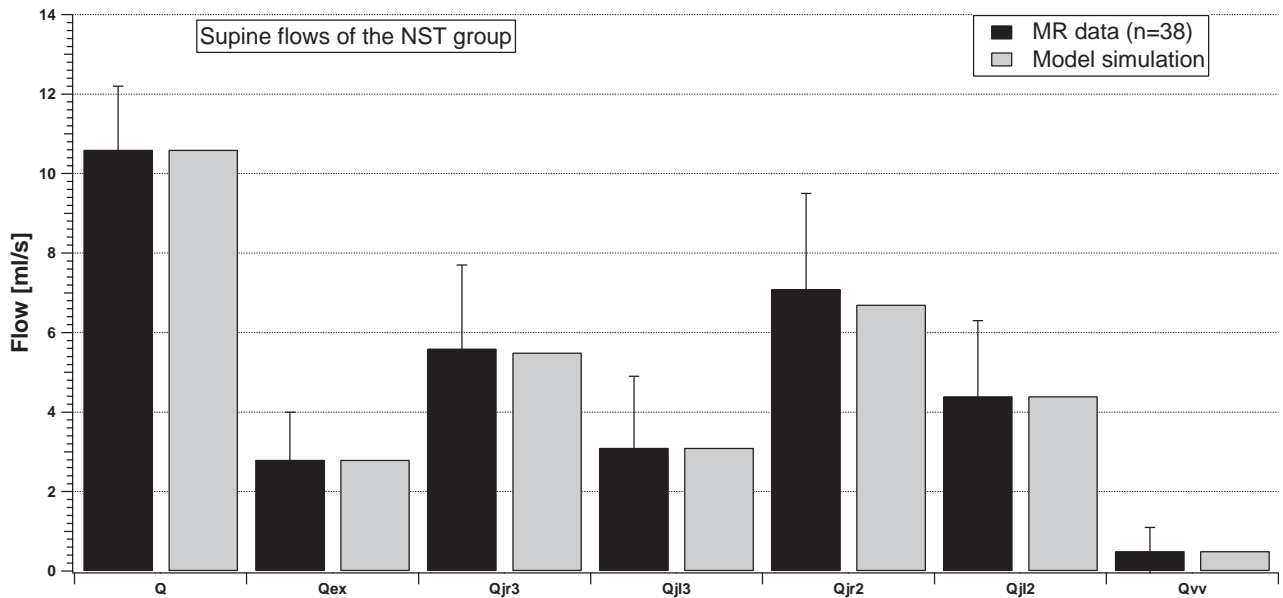


FIG 2. Comparison between supine MR imaging data (dark columns) and model simulation (light columns) of the NST group.

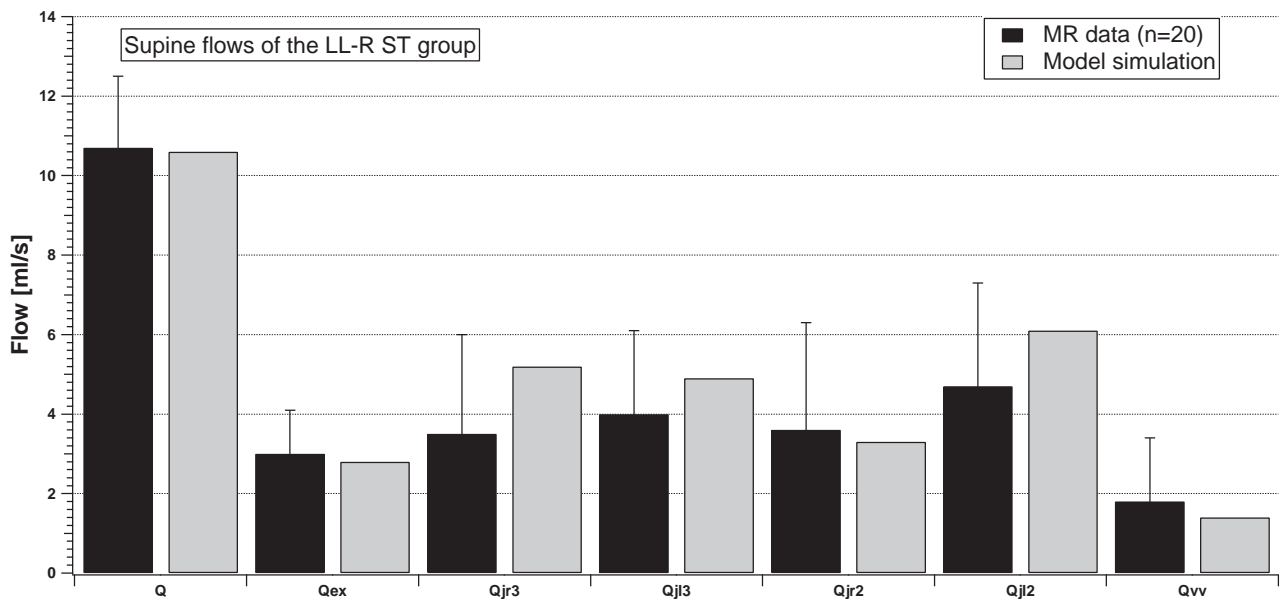


FIG 3. Comparison between supine MR imaging data (dark columns) and model simulation (light columns) of the LL-R ST group.

els ( $Q_{jr3} > Q_{jl3}$  and  $Q_{jr2} > Q_{jl2}$ ). Finally, average jugular flow increases from the upper to lower levels ( $Q_{jr2} > Q_{jr3}$  and  $Q_{jl2} > Q_{jl3}$ ). The model (light columns) properly reproduces the behavior of experimental flow. Indeed, all the simulations match the average values of the dataset.

Figures 3 and 4 compare the same flow for the LL-R ST and UL-L ST groups.

Average inflows of the 2 stenotic groups (Q and Qex) are similar to the NST inflows. Conversely, the average outflow behavior described in Fig 2 is now modified due to the presence of stenosis. Qvv is increased with respect to the NST case, being also sometimes greater or comparable with the flow in the IJV segments. The right-left IJV dominance is impaired, being the difference between average flows lost for the LL-R ST group ( $Q_{jr3} \approx Q_{jl3}$  and  $Q_{jr2} < Q_{jl2}$ ) or markedly increased for the UL-L ST group

( $Q_{jr3} \gg Q_{jl3}$  and  $Q_{jr2} \gg Q_{jl2}$ ). The light columns in Figs 3 and 4 show that the model outcomes can also reproduce these situations.

#### Comparison between ECD Data and Model Outcomes

Average blood flows Q, Qj3, Qj2, Qj1, and Qvv of 10 NST volunteers, measured by using the ECD technique, are reported in Table 3 with corresponding SDs. Table 3 also shows the percentage variations between the upright and supine flows. The absolute values reported in Table 3 may be affected by a proportional error, typical of the ECD technique, when moving from one tract to the next. Hence, we focused attention only on the percentage variations within each column.

Figure 5 compares jugular (sum of left and right) and vertebral flows for the simulation of an NST subject, to point out the vari-

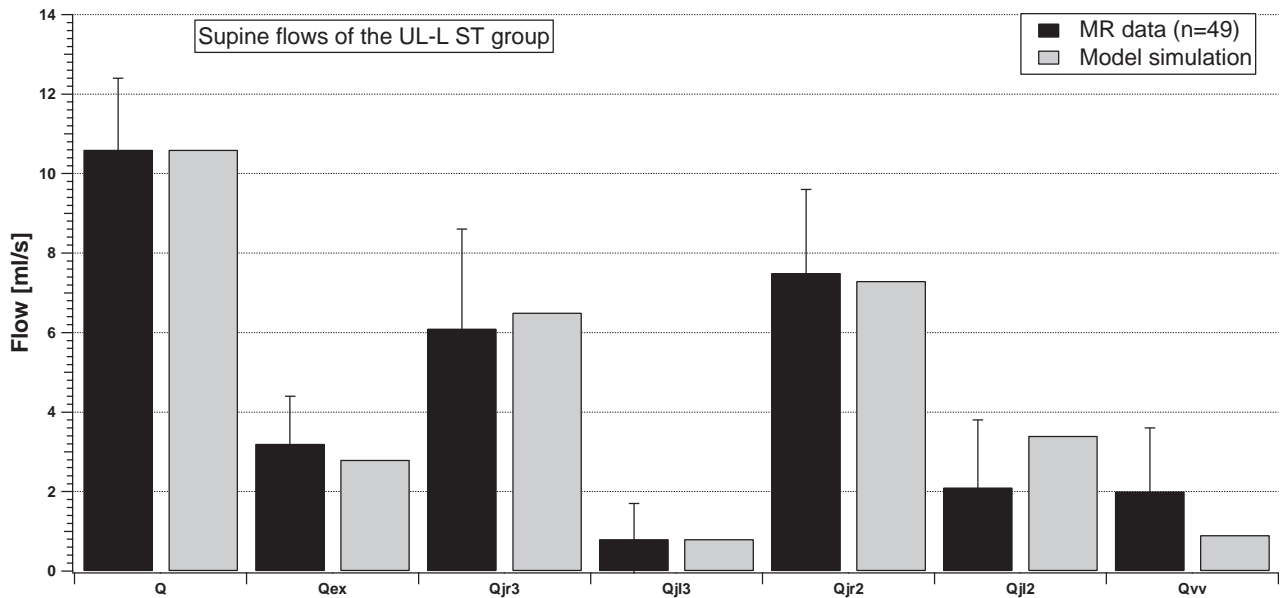


**FIG 4.** Comparison between supine MR imaging data (dark columns) and model simulation (light columns) of the UL-L ST group.

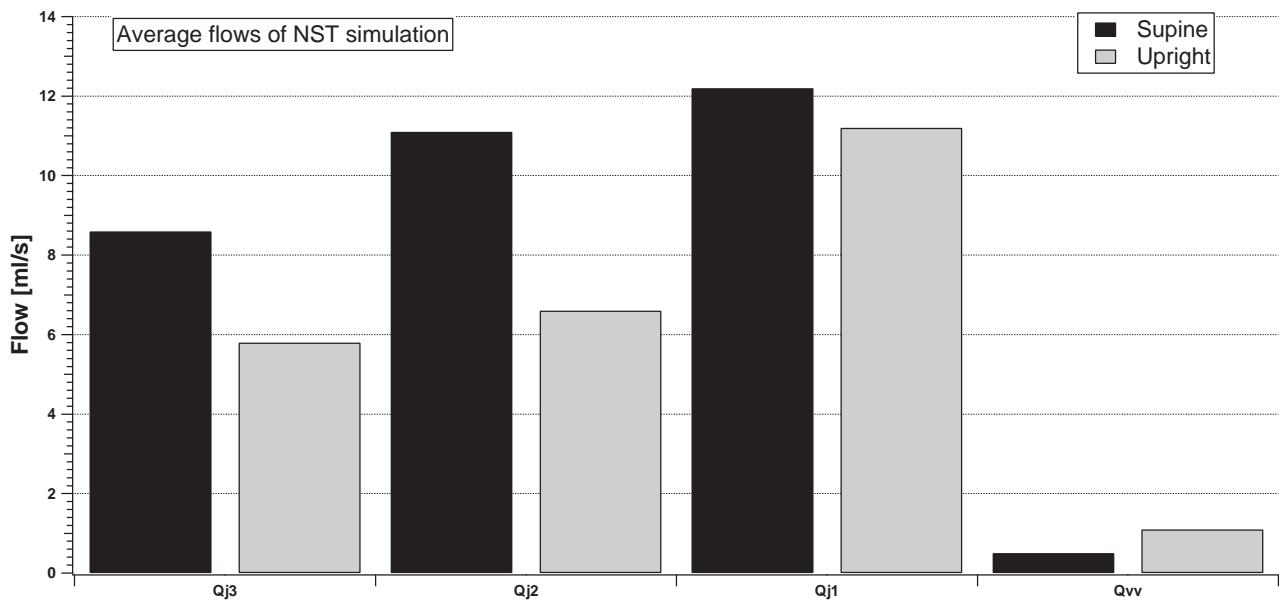


**FIG 5.** Comparison between supine and upright simulated total jugular (sum of left and right) and vertebral average flows of the NST group. The percentage changes are  $-32.6\%$ ,  $-40.5\%$ ,  $-8.1\%$ , and  $+120\%$ , which fit those in Table 3 very well.

ation between supine and upright posture in the 2 brain drainage routes.

IJVs are the dominant drainage pathway of the brain, and jugular flow increases from J3 to J1, independent of the posture. When passing to upright, the model simulates a flow decrease in every tract of the IJVs, with increase of the vertebral flow. These results match the experimental evidence of percentage flow variation due to posture change summarized in Table 2.

#### **Comparison between Supine and Upright Model Outcomes**

Figure 6 shows the model outcomes of the cerebral, external, jugular (left and right), and vertebral average flow in the supine and upright conditions for the NST group.

All jugular flows are reduced when the simulated NST subject is sitting, while the vertebral flow increases. Because this was a simulation of an NST condition, our aim was to reproduce the left-right dominance of the IJVs ( $Q_{jr3} > Q_{jl3}$ ,  $Q_{jr2} > Q_{jl2}$ , and  $Q_{jr1} > Q_{jl1}$ ), the prevalence of the IJV pathways with respect to the VV, and the increase of jugular flow from J3 to J1 ( $Q_{jr1} > Q_{jr2} > Q_{jr3}$  and  $Q_{jl1} > Q_{jl2} > Q_{jl3}$ ). Figure 6 shows that simulation results satisfy all these requirements.

Figures 7 and 8 compare the same simulated average flows for the LL-R ST and UL-L ST cases.

Q and Qex are not affected by the presence of stenosis. Thus, the cerebral autoregulatory mechanisms properly overcome the nonphysiologic conditions occurring downstream from the brain. Conversely, both LL-R ST and UL-L ST affect the outflow



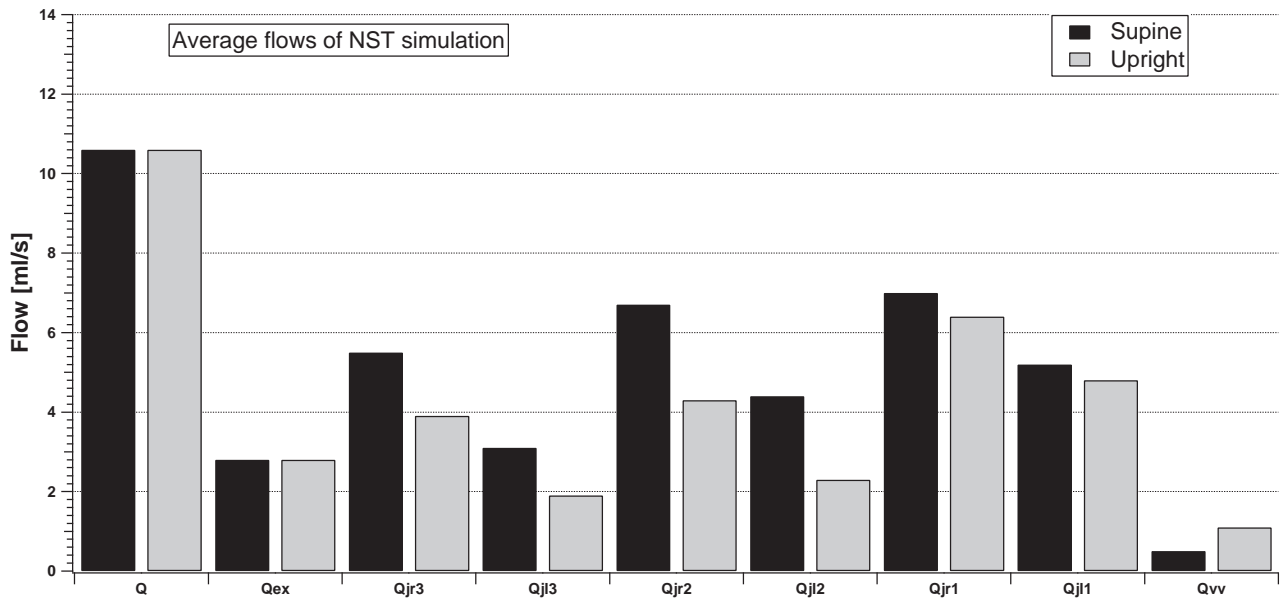


**FIG 6.** Model simulation of the cerebral, external, jugular (left and right), and vertebral average flows in supine and upright conditions for the NST group.

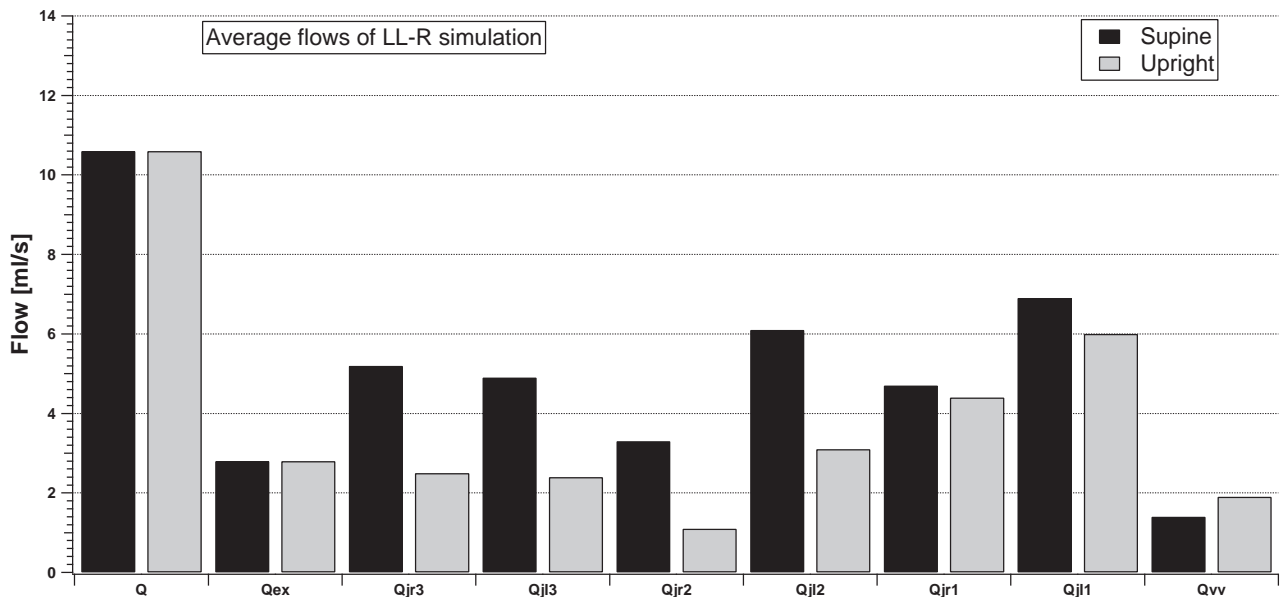


**FIG 7.** Model simulation of the cerebral, external, jugular (left and right), and vertebral average flows in the supine and upright condition for the LL-R ST group.

pathways. The VV carries more blood than in the NST simulation, also being comparable with some jugular segments. The left-right dominance is highlighted during simulation of the UL-L ST condition, while it is lost during simulation of the LL-R ST condition. The increase in the IJV average blood flow from J3 to J1 is now lost in the right IJV for a LL-R ST condition, with Qjr2 lower than Qjr1 and Qjr3, both for supine and upright simulations.

#### **Preliminary Results of Pressure Simulations**

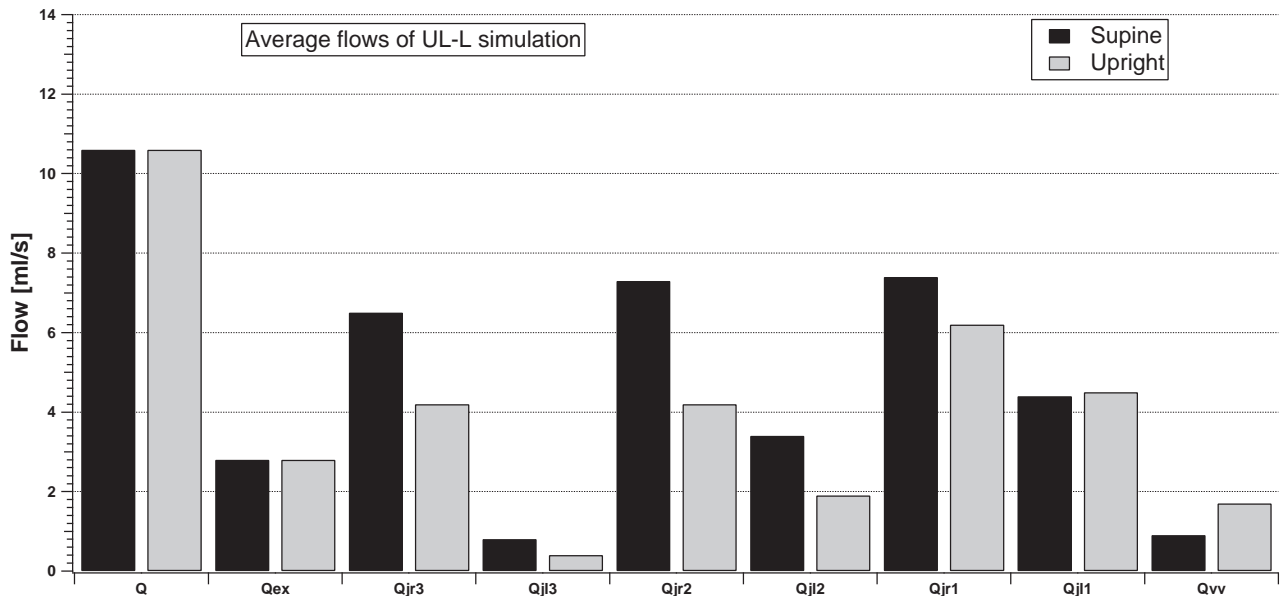
The model can simulate the variation of pressure as a function of time in every node of the hemodynamic circuit. One of the main consequences of a stenotic pattern on the intracranial equilibrium is a variation of pressure at the venous sinuses (Pvs),<sup>1</sup> the link between the extracranial and intracranial circulation. Changes in

this quantity can affect other intracranial parameters and thus the overall brain physiology.

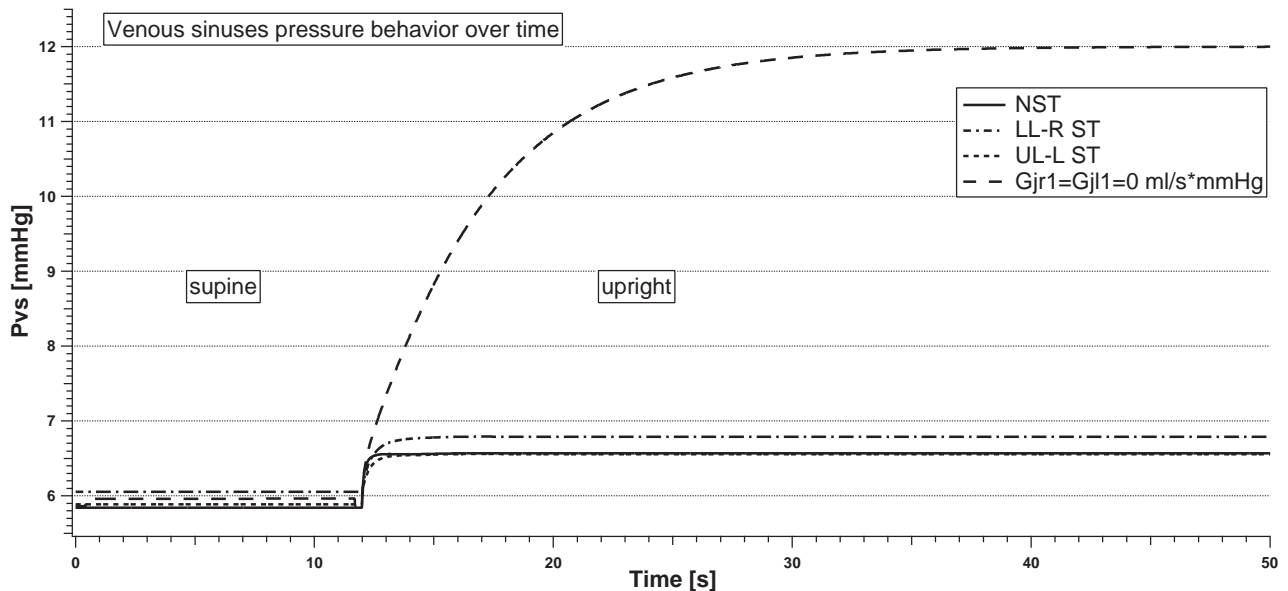
Clinical evidence supports the results of increased pressure due to the occurrence of extracranial stenosis.<sup>26</sup>

Figure 9 shows the temporal variation of Pvs due to the change of postural condition in different situations (NST, LL-R ST, UL-L ST, and total occlusion of IJVs at the J1 level, respectively).

There is no particular difference in Pvs values when a supine simulation is performed (range from 5.8 to 6.1 mm Hg). When they pass to upright, there is a slight increase of Pvs for the simulated NST, LL-R ST, and UL-L ST subjects (+0.7 mm Hg). Conversely, Pvs markedly increases (from 5.9 to 12.0 mm Hg) when a bilateral total obstruction occurs. The settling time for Pvs to



**FIG 8.** Model simulation of the cerebral, external, jugular (left and right), and vertebral average flows in the supine and upright condition for the UL-L ST group.



**FIG 9.** Venous sinuses pressure behavior with time in the supine and upright simulations for different stenotic patterns.

reach a new equilibrium can be quite different depending on the type of stenosis. In particular, it is shorter for the NST simulation (0.5 seconds), while it is delayed in case of stenosis (1.5 seconds for UL-L ST, 2 seconds for LL-R ST, and 30 seconds for the bilateral total occlusion case simulated).

## DISCUSSION

It is difficult to have a complete and detailed overview of the blood flows circulating to and from the braincase. Several researchers have studied the cerebral hemodynamics and its relationship with extracranial anatomic and posture changes.<sup>27,28</sup> First, average absolute values of blood flow could be considerably different among subjects because of physiologic variability. Second, due to the complex network of vessels and their variable interconnections, it is difficult to have a map of the circulation able to describe any

specific case in detail. Third, there is insufficient knowledge of the relationships between flow alterations and the degree of occurrence of events such as postural changes or stenosis. Finally, even in a situation that does not have variability factors, the assessment of blood flow values can be difficult for several reasons.

The model presented here is tuned by using large datasets of subjects, to be more confident about the average hemodynamic condition of a given type of stenotic pattern.

We benefited from the use of MR imaging techniques to have a detailed map of the vessels and of the blood circulating in them. The drawback of MR imaging for this work is that only supine data are available, whereas ECD allows both supine and upright assessment. However, ECD does not allow the evaluation of mi-

nor vessels, and it has a bias related to the operator dependence that can lead to incorrect evaluations.

This model is an attempt to summarize a complex system in a simple picture, taking into account all the available data for obtaining information not directly achievable with experimental noninvasive measurements, such as Pvs or intracranial pressure, very important for checking the status of the intracranial environment and, hopefully, for preventing neurologic diseases.

The model is built by using lumped elements, to summarize the different segments of the vascular system and reproduce experimental flows with a finite and easily tunable number of parameters. Such flows are the average of experimental measurements on several subjects (Tables 2 and 3), so we are confident that the model parameters reproduce a statistically significant circulatory behavior, including different clinical conditions (NST or a given stenotic pattern). The convergence of the model presented in this work has been investigated with all the experimental flows reported in Tables 2 and 3—that is, we checked that average flows reported in such tables are the mean value of Gaussian-like datasets. Therefore, we are confident that the model simulates the average condition of normal distributions of flow.

A fundamental model assumption is the existence of anastomotic connections between the left and right IJVs. These vessels are not measured, but they are necessary to explain the increase of flow along every nonstenotic IJV (Tables 2 and 3).

The model outcomes, after parameter tuning, are in excellent agreement with experimental supine average flow of the NST group (Fig 2). Indeed, all the main arterial and venous flows supplying the brain that we modeled fall inside the standard error from the corresponding experimental value. Moreover, model results satisfactorily match the supine/upright percentage variation in jugular and extrajugular pathways observed in a second group of 10 healthy controls (Fig 5). Therefore, we achieved the objective of tuning the model to reproduce an average healthy subject, from the point of view of the circulation.

Starting from the NST-tuned model, it is easy to reproduce pathologic conditions like the situations reported in Table 1. Such new simulations are obtained by changing some of the conductances to reproduce the MR imaging experimental flow data (Table 2). Results show that conductances are greatly reduced in the jugular stenotic area and increased in the vertebral pathway. This aspect could be an index of how the whole venous pattern is affected by the presence of a jugular stenosis. Indeed, the increase in the vertebral conductance may represent a chronic compensatory change performed to maintain adequate brain drainage to prevent cranial hypertension. This aspect is highlighted in Fig 9, where the temporal behavior of simulated Pvs with time is reported for different stenotic conditions. Intracranial autoregulatory mechanisms maintain cerebral blood flow at a physiologic value, both in supine and upright conditions (Figs 6–8). Pvs achieves a new equilibrium in a few seconds after the posture change. The situation is very different when IJVs are totally occluded, for example, at the lower part.

This model takes into account intracerebral mechanisms such as CSF circulation and the onset of IJV obstacles. Furthermore, a peculiar aspect of the model is the description of intracranial

blood flow autoregulatory mechanisms that play a pivotal role in maintaining an adequate cerebral perfusion in the different simulated conditions. The study of venous blood flow changes in patients with partial or total impairment in cerebral autoregulation may be the subject of future model applications.

The model allows simulating the change of posture from supine to upright, and, as in the work of Gisolf et al,<sup>28</sup> IJVs are divided into different segments to properly simulate the differences measured along the jugular length. In particular, we chose to divide IJVs into the 3 segments recently established in an international scientific consensus,<sup>21</sup> to make the model easily comparable with the most recent and validated experimental results.

We modeled intra- and extracranial circulation, so that the whole system can predict whether and how the occurrence of extracerebral stenotic patterns affect the pressure equilibrium in the braincase during most of the human lifetime (sitting or standing), potentially leading to long-term diseases due to pressure imbalance.

A limitation of the model is related to the assessment of venous compliances. We need experimental measurements to properly assess vessel compliances and give more effectiveness to the time-dependence results of pressures (Fig 9).

In addition, a future development will be the analysis of other types of stenotic patterns, such as lower-level left and upper-level right IJV obstructions.

## CONCLUSIONS

We have tuned a mathematic model for the brain-drainage simulation to predict the average cerebral drainage properties of a healthy (NST) human and of subjects affected by 2 different types of vascular diseases. The structure of the equations makes it possible to simulate the effects of changes in posture from the supine to upright position. Model outcomes can help relate blood flow redistributions to the type and degree of stenosis and evaluate quantitative assessment of the renewed intracranial pressure equilibrium.

Disclosures: Sean Sethi—UNRELATED: Employment: Magnetic Resonance Innovations, Comments: MRI-related data processing, software testing and research. David T. Utriainen—UNRELATED: Consultancy: AbbVie\*; Employment: Magnetic Resonance Innovations. \*Money paid to the institution.

## REFERENCES

1. Beggs CB. **Venous hemodynamics in neurological disorders: an analytical review with hydrodynamic analysis.** *BMC Med* 2013;11:142 CrossRef Medline
2. Schaller B. **Physiology of cerebral venous blood flow: from experimental data in animals to normal function in humans.** *Brain Res Brain Res Rev* 2004;46:243–60 Medline
3. Werner JD, Siskin GP, Mandato K, et al. **Review of venous anatomy for venographic interpretation in chronic cerebrospinal venous insufficiency.** *J Vasc Interv Radiol* 2011;22:1681–90; quiz 1691 CrossRef Medline
4. Fung YC. *Biomechanics: Circulation.* New York: Springer-Verlag; 1997:206–43
5. Kozlovsky P, Zaretsky U, Jaffa AJ, et al. **General tube law for collapsible thin and thick-wall tubes.** *J Biomech* 2014;47:2378–84 CrossRef Medline
6. Cirovic S, Walsh C, Fraser WD, et al. **The effect of posture and pos-**

- itive pressure breathing on the hemodynamics of the internal jugular vein. *Aviat Space Environ Med* 2003;74:125–31 Medline
7. Alperin N, Lee SH, Sivaramakrishnan A, et al. **Quantifying the effect of posture on intracranial physiology in humans by MRI flow studies.** *J Magn Reson Imaging* 2005;22:591–96 Medline
  8. Gadda G, Taibi A, Sisini F, et al. **A new hemodynamic model for the study of cerebral venous outflow.** *Am J Physiol Heart Circ Physiol* 2015;308:H217–31 CrossRef Medline
  9. Zamboni P, Galeotti R, Menegatti E, et al. **Chronic cerebrospinal venous insufficiency in patients with multiple sclerosis.** *J Neurol Neurosurg Psychiatry* 2009;80:392–99 Medline
  10. Zaniewski M, Simka M. **Biophysics of venous return from the brain from the perspective of the pathophysiology of chronic cerebrospinal venous insufficiency.** *Rev Recent Clin Trials* 2012;7:88–92 Medline
  11. Anderson CM, Edelman RR, Turski PA. *Clinical Magnetic Resonance Angiography.* New York: Raven Press; 1993
  12. Potchen EJ, Haacke EM, Siebert JE, et al. *Magnetic Resonance Angiography: Concepts & Applications.* St. Louis: Mosby-Year Book; 1993
  13. Haacke EM, Sethi SK, Jiang J, et al. **The role of magnetic resonance imaging in assessing venous vascular abnormalities in the head and neck: a demonstration of cerebrospinal venous insufficiency in a subset of multiple sclerosis patients.** *Veins Lymphatics* 2015;4:5012–20
  14. Novario R, Goddi A, Tanzi F, et al. **Physics and technology of medical diagnostic ultrasound.** *La Rivista del Nuovo Cimento* 2003;26:1–64
  15. Sorek S, Bear J, Karni Z. **Resistances and compliances of a compartmental model of the cerebrovascular system.** *Ann Biomed Eng* 1989; 17:1–12 Medline
  16. Ursino M, Lodi CA. **A simple mathematical model of the interaction between intracranial pressure and cerebral hemodynamics.** *J Appl Physiol* 1997;82:1256–69 Medline
  17. Zamboni P, Sisini F, Menegatti E, et al. **An ultrasound model to calculate the brain blood outflow through collateral vessels: a pilot study.** *BMC Neurol* 2013;13:81–90 CrossRef Medline
  18. Kresch E. **Compliance of flexible tubes.** *J Biomech* 1979;12:825–39 Medline
  19. Press WH, Teukolsky SA, Vetterling WT, et al. *Numerical Recipes in C.* New York: Cambridge University Press; 1992
  20. Berkeley Madonna: Modeling and Analysis of Dynamic Systems. <http://www.berkeleymadonna.com>. Accessed August 3, 2013
  21. Zamboni P, Morovic S, Menegatti E, et al. **Screening for chronic cerebrospinal venous insufficiency (CCSVI) using ultrasound: recommendations for a protocol.** *Int Angiol* 2011;30:571–97 Medline
  22. Chambers B, Chambers J, Churilov L, et al. **Internal jugular and vertebral vein volume flow in patients with clinically isolated syndrome or mild multiple sclerosis and healthy controls: results from a prospective sonographer blinded study.** *Phlebology* 2014;29: 528–35 CrossRef Medline
  23. Jiang J, Kokeny P, Ying W, et al. **Quantifying errors in flow measurement using phase contrast magnetic resonance imaging: comparison of several boundary detection methods.** *Magn Reson Imaging* 2015;33:185–93 CrossRef Medline
  24. Kokeny P, Jiang J, Haacke EM. **Assessing the effects of vessel segmentation boundary size on flow quantification error and comparing multiple automatic segmentation algorithms.** In: *Proceedings of the International Society for Magnetic Resonance in Medicine*, Salt Lake City, Utah. April 20–26, 2013
  25. The Magnetic Resonance Institute for Biomedical Research. <http://www.mrimaging.com/category.103.html>. Accessed January 11, 2016
  26. Zamboni P, Galeotti R. **The chronic cerebrospinal venous insufficiency syndrome.** *Phlebology* 2010;25:269–79 CrossRef Medline
  27. Marcotti S, Marchetti L, Cecconi P, et al. **An anatomy-based lumped parameter model of cerebrospinal venous circulation: can an extracranial anatomical change impact intracranial hemodynamics?** *BMC Neurol* 2015;15:95 CrossRef Medline
  28. Gisolf J, van Lieshout JJ, van Heusden K, et al. **Human cerebral venous outflow pathway depends on posture and central venous pressure.** *J Physiol* 2004;560(pt 1):317–27 CrossRef Medline

# DTI Analysis of Presbycusis Using Voxel-Based Analysis

W. Ma, M. Li, F. Gao, X. Zhang, L. Shi, L. Yu, B. Zhao, W. Chen, G. Wang, and X. Wang



## ABSTRACT

**BACKGROUND AND PURPOSE:** Presbycusis is the most common sensory deficit in the aging population. A recent study reported using a DTI-based tractography technique to identify a lack of integrity in a portion of the auditory pathway in patients with presbycusis. The aim of our study was to investigate the white matter pathology of patients with presbycusis by using a voxel-based analysis that is highly sensitive to local intensity changes in DTI data.

**MATERIALS AND METHODS:** Fifteen patients with presbycusis and 14 age- and sex-matched healthy controls were scanned on a 3T scanner. Fractional anisotropy, mean diffusivity, axial diffusivity, and radial diffusivity were obtained from the DTI data. Intergroup statistics were implemented on these measurements, which were transformed to Montreal Neurological Institute coordinates by using a nonrigid image registration method called large deformation diffeomorphic metric mapping.

**RESULTS:** Increased axial diffusivity, radial diffusivity, and mean diffusivity and decreased fractional anisotropy were found near the right-side hearing-related areas in patients with presbycusis. Increased radial diffusivity and mean diffusivity were also found near a language-related area (Broca area) in patients with presbycusis.

**CONCLUSIONS:** Our findings could be important for exploring reliable imaging evidence of presbycusis and could complement an ROI-based approach.

**ABBREVIATIONS:** DA = axial diffusivity; dB HL = decibel hearing level; DR = radial diffusivity; FA = fractional anisotropy; MD = mean diffusivity; PTA = pure-tone average

Age-related hearing loss, also known as presbycusis, is the most common sensory deficit in the aging population. Presbycusis is usually characterized by progressive hearing loss at high frequencies, which are particularly important for speech recogni-

tion. Hypofunction of the inner ear is the main reason for the peripheral component of presbycusis.<sup>1</sup> However, poor speech discrimination and deteriorated temporal sound processing reflect a possible central component of presbycusis.<sup>2,3</sup> Moreover, many animal studies have showed the existence of a central component of presbycusis.<sup>4,5</sup>

Recent studies of multiple MR imaging modalities have demonstrated their capabilities of offering reliable imaging markers for recognizing presbycusis. In a structural MR imaging study, the volume and surface area were decreased in the auditory cortex areas of patients with presbycusis compared with young healthy controls.<sup>6</sup> In a functional MR imaging study, patients with presbycusis showed higher blood oxygen level–dependent activation in response to acoustic stimuli in the temporal lobes compared with young healthy controls.<sup>7</sup>

The aforementioned imaging markers were mainly explored in gray matter, whereas white matter integrity, as one of the most sensitive indicators of axon damage or demyelination, requires further study. A widely used technique, DTI, has been considered as the most effective method for characterizing white matter organization. Multiple scalar measurements, including fractional

Received January 28, 2016; accepted after revision May 9.

From the Department of Otolaryngology (W.M., L.S.), the Second Hospital of Shandong University, The Central Hospital of Jinan City (W.M., L.Y.), and Shandong Medical Imaging Research Institute (F.G., X.Z., B.Z., G.W.), Shandong University, Jinan, China; College of Electronics and Information Engineering (M.L.), Sichuan University, Chengdu, China; Philips Healthcare (W.C.), Shanghai, China; and the Department of Radiation Oncology (X.W.), University of Nebraska Medical Center, Omaha, Nebraska.

W. Ma and M. Li contributed equally to this work.

This project was supported by the National Natural Science Foundation of China (grants 81171380/H1807 and 81371534), Shandong Provincial Natural Science Foundation of China (grant BS2015YY003), and Shandong Provincial Medical and Healthy Technology Development Program of China (grant 2015WS0176).

Please address correspondence to Guangbin Wang, MD, Shandong Medical Imaging Research Institute, Jing-wu Rd No. 324, Jinan 250021, People's Republic of China; e-mail: wgb7932596@hotmail.com

Indicates open access to non-subscribers at [www.ajnr.org](http://www.ajnr.org)

Indicates article with supplemental on-line table.

<http://dx.doi.org/10.3174/ajnr.A4870>

## Demographic and auditory function of the presbycusis and control groups

Demographics	Presbycusis	Control	P Value
No. of patients	15	14	
Age (yr) <sup>a</sup>	63.2 ± 2.6	62.4 ± 2.0	.38 <sup>b</sup>
Female, no. (%)	10 (66.7)	8 (57.1)	.60 <sup>c</sup>
Education levels (yr) <sup>a</sup>	10.7 ± 3.5	10.1 ± 2.6	.61 <sup>b</sup>
PTA (dB HL) <sup>a,d</sup>	30.7 ± 4.7	15.9 ± 1.4	<.001 <sup>b</sup>

<sup>a</sup>Data are given as mean ± standard deviation.

<sup>b</sup>The between-group differences were assessed with the 2-tailed Student *t* test.

<sup>c</sup>The between-group differences were assessed with the 2-tailed Pearson  $\chi^2$  test.

<sup>d</sup>The PTAs from both ears were averaged.

anisotropy (FA), mean diffusivity (MD), axial diffusivity (DA), and radial diffusivity (DR), can be calculated from DTI data through tensor calculation. These measurements are useful indicators for characterizing various types of pathology in the human brain.

Many DTI studies have reported changes in the auditory pathway and auditory cortex in patients with sensorineural hearing loss.<sup>8,9</sup> To our knowledge, only 1 study has reported a lack of white matter integrity in patients with mild presbycusis by applying an intergroup statistic on the ROI-based features, which was in the form of reconstructed auditory tracts.<sup>6</sup> Besides that, the study showed no obvious differences in any measured DTI parameters between mild presbycusis and expressed presbycusis. Although promising, a more reliable imaging marker of presbycusis could be established by designing more sophisticated experiments. First, the reconstructed auditory pathway was partly obscured by the optic radiation. This so-called “fiber-crossing issue” could be mitigated by using probabilistic tractography; however, the “gold standard” for validating the tractography, especially in the fiber-crossing area, has not been established. In addition, though using the average characteristic with an ROI is an effective manner of dimensional reduction and noise filtering,<sup>10</sup> a limitation is its reduced sensitivity to localized anatomic alterations that only affect parts of a predefined structure.<sup>11</sup> Therefore, we used a voxel-based analysis, which might be considered as an alternative way to explore the imaging makers of presbycusis in the white matter.

## MATERIALS AND METHODS

### Patients

This study was approved by the Shandong University institutional review board, and each participant provided informed consent. Fifteen patients with mild presbycusis (presbycusis group, 5 men and 10 women; mean age, 63.2 ± 2.6 years) who visited the department of otolaryngology of the central hospital of Jinan city were recruited in this study (Table). Hearing loss was defined as a speech-frequency pure-tone average (PTA) of thresholds at 0.5, 1, 2, and 4 kHz (air conduction) in the better-hearing ear, per the definition of hearing loss adjudicated by the World Health Organization. The PTA value of 25 decibel hearing level (dB HL) was accepted as the normal hearing threshold limit.<sup>12</sup> Inclusion criteria were mild hearing loss (defined as 25 dB HL < PTA ≤ 40 dB HL in the better-hearing ear) and age ≥ 60 years. Exclusion criteria were ear diseases that affect hearing thresholds and sensorineural hearing losses other than presbycusis; history of otologic surgery, ototoxic drug therapy, noise exposure, or hearing aid use;

asymmetric hearing loss with a difference in air conduction thresholds exceeding 20 dB in at least 2 frequencies between 0.5, 1, 2, and 4 KHz; conductive hearing loss (the mean air-bone differences at 0.5, 1, 2, and 4 KHz) >10 dB in 1 or both ears; and tinnitus, head trauma, lesions of the facial nerve, disorders of the cervical spine, or neurologic or psychiatric disease. The complete list of exclusion criteria was previously described.<sup>13</sup>

Fourteen age- and sex-matched healthy controls (control group, 6 men and 8 women; mean age, 62.4 ± 2.0 years; PTA ≤ 25 dB HL in the better-hearing ear) were recruited for this study. All controls were in good health and had no history of neurologic or psychiatric disease. Healthy controls were matched for education levels (Table).

None of the subjects were music professionals. All subjects were right-handed according to Li's Handedness Inventory, which was designed for Chinese populations.<sup>14,15</sup>

### Assessment of Auditory Function

An otoscopic examination was performed in all patients to remove cerumen and confirm the presence of an intact tympanic membrane. The hearing abilities of all patients were evaluated by using pure-tone audiometry and tympanometry. The pure-tone audiometry was performed with a Madsen Electronics Midimate 622 Clinical/Diagnostic Audiometer (GN Otometrics, Taastrup, Denmark) coupled with Telephonics TDH-39P headphones (Telephonics, Farmingdale, New York). Bone conduction was measured at 0.25, 0.5, 1, 2, and 4 KHz, and air conduction was measured at 0.125, 0.25, 0.5, 1, 2, 4, and 8 KHz. Hearing thresholds were detected with a resolution of 5 decibel steps. The PTA values of all patients' ears were calculated. The tympanometry was performed with a Madsen Electronics Zodiac 901 Middle Ear Analyzer (GN Otometrics) to confirm optimal middle-ear conditions.

### DTI and Data Processing

All patients were scanned on a 3T scanner (Achieva TX; Philips Healthcare, Best, the Netherlands) using an 8-channel phased-array head coil as a receiver. The DTI dataset was acquired with a multisection, single-shot, EPI, spin-echo sequence (TR/TE = 6281/67 ms; sensitivity encoding factor = 2.5). Sixty-five transverse sections were acquired parallel to the line connecting the anterior commissure to the posterior commissure with no section gap and 2.2-mm nominal isotropic resolution. Diffusion weighting was applied along 32 directions with a *b*-value of 700 seconds/mm<sup>2</sup>. Five minimally weighted images (5 B0 with *b* = 33 seconds/mm<sup>2</sup>) were acquired and averaged on the scanner as part of each DTI dataset.

The raw diffusion-weighted images were first coregistered to the B0 images and corrected for eddy current and patient motion with affine transformation by using Automated Image Registration (<http://bishopw.loni.ucla.edu/air5/>).<sup>16</sup> The 6 elements of the diffusion tensor were calculated for each pixel with multivariate linear fitting by using DTIStudio (Johns Hopkins University, Baltimore, Maryland).<sup>17</sup> After diagonalization, 3 eigenvalues and eigenvectors, as well as FA, MD, DA, and DR, were obtained. A 2-step image transformation was used to warp the individual data to a standard template, JHU-MNI-ss (Johns Hopkins University,

www.mristudio.org) in the ICBM-152/ICBM-DTI-81 space. First, affine transformation was used to globally adjust the brain position, rotation, and size. Next, a nonlinear transformation with large deformation diffeomorphic metric mapping<sup>18</sup> was applied to accurately warp the local structures. The dual-contrast large deformation diffeomorphic metric mapping, in which both the B0 image and the FA map were applied simultaneously, was used. These procedures are reciprocal and provide forward (subject to atlas) and backward (atlas to subject) transformation matrices. FA, MD, DA, and DR images then were transformed to template space by using the forward matrix. After the registration, all images were smoothed using statistical parametric mapping by setting the full width at half maximum = [4 4 4].

### Statistical Analysis

The 2-tailed Student *t* test was performed to test for differences in age, education levels, and PTA between patients with presbycusis and healthy controls. The differences in sex were evaluated by a 2-tailed Pearson  $\chi^2$  test. The threshold of significance was set at  $P = .05$ . Statistical analyses were performed by using the SPSS version 18.0 software package (IBM, Armonk, New York).

Intergroup statistics were implemented (voxel by voxel) to several DTI indices, including FA, MD, DA, and DR, which had been transformed to the standard space. The results were obtained from SPM8 (<http://www.fil.ion.ucl.ac.uk/spm/>) by the application of multiple comparisons and the setting of thresholds of  $P < .001$  (uncorrected) at voxel level and  $P < .05$  (family-wise error–corrected) at cluster level. The minimum cluster size was 100 voxels. The results were visualized by using a Matlab (MathWorks, Natick, Massachusetts) toolbox named *xjview* (<http://www.alivelearn.net/xjview>).

### RESULTS

All patients had a type-A curve on tympanometry, which indicated normal middle-ear function. There was no significant difference in PTA between the left and right ears in the presbycusis group ( $P = .49$ ) or the control group ( $P = .10$ ); therefore, the thresholds of both ears were averaged in each group. The PTA was significantly higher in patients with presbycusis than in healthy patients ( $P < .001$  [Table]). In the control group, the mean hearing thresholds were  $<20$  dB HL at all frequencies; in the presbycusis group, the mean hearing thresholds were  $>20$  dB HL at 1 kHz and reached 46.8 dB HL at 4 kHz and 55.2 dB HL at 8 kHz (Fig 1).

The results of voxel-based analyses are shown in Fig 2. The presbycusis group showed increased DA near the right-side Heschl gyrus and increased DR near the right-side Heschl gyrus and the left-side inferior frontal gyrus. The presbycusis group showed decreased FA near the right-side angular gyrus and inferior frontal gyrus and decreased FA near the right-side temporal pole and middle temporal gyrus, which were partly overlapped with acoustic radiation. The presbycusis group also showed increased MD near the right-side Heschl gyrus and the left-side inferior frontal gyrus. The On-line Table specifies the above-mentioned areas distributed in the brain image as voxel clusters with detailed information, including the peak coordinates in the Montreal Neuro-

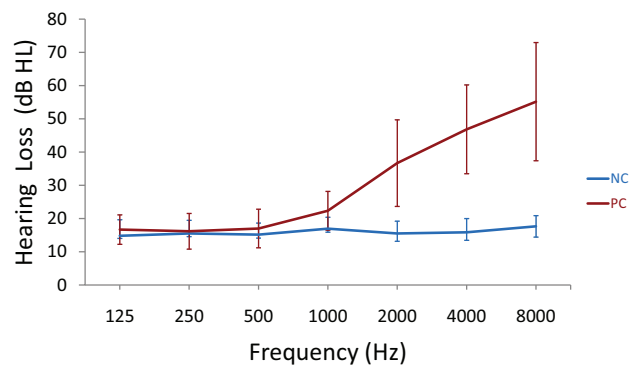


**FIG 1.** Results of pure-tone audiometry from 125 Hz to 8000 Hz (air conduction). Hearing thresholds from both ears are averaged (mean  $\pm$  standard deviation) in the presbycusis (PC) and healthy control (NC) groups.

logical Institute space, cluster-level *P* value, and peak T-value of each cluster.

### DISCUSSION

Our study demonstrated altered DA, DR, FA, and MD near the right-side hearing-related areas of patients with presbycusis compared with age- and sex-matched healthy controls. Increased DR and MD were also observed in a language-related area (Broca area) of patients with presbycusis. To our knowledge, this is the first in vivo demonstration of presbycusis-related changes over the entire brain in a DTI fashion by using a voxel-based analysis.

The scalar measurements of DTI were capable of characterizing various white matter pathologies. Among all of these measurements, FA was sensitive to various microstructural changes<sup>19</sup>; MD was considered the inverse measure of the membrane attenuation and fluid viscosity<sup>20</sup>; DA was considered highly sensitive to axonal degeneration; and DR was sensitive to demyelination.<sup>21</sup> DTI technique was introduced to study the macroscopic architecture of white matter. However, several animal studies have shown changes of DTI parameters, including MD, DA, and DR, in gray matter areas because of neuron loss. FA did not account for those contributions because the dendrites are only partially coherently organized and the axons are not homogeneously distributed and might be myelinated or unmyelinated in gray matter.<sup>22,23</sup> When overlaid to the statistical parametric mapping–integrated T1 template, the changes were seen mostly within the subcortical white matter areas with a small portion of voxels overlapped with cortex. Because it is difficult to separate the white matter and gray matter with DTI contrast, the results are elaborated with “gyrus” (which contain both subcortical white matter and cortex) as its units. In our study, increased DA, DR, and MD were found near the right-side Heschl gyrus in patients with presbycusis; decreased FA was also seen in white matter areas that partly overlapped with the right-side acoustic radiation. To further examine the functional representation of the clusters shown in the On-line Table, we overlaid the Brodmann atlas to our results and found that changes overlapped with superior temporal gyrus and angular gyrus were close to Brodmann area 41, which refers to the auditory cortex. These results could indicate a dysfunctional auditory pathway in presbycusis. This is consistent with previous studies where the DTI-based parameters were changed at the Heschl

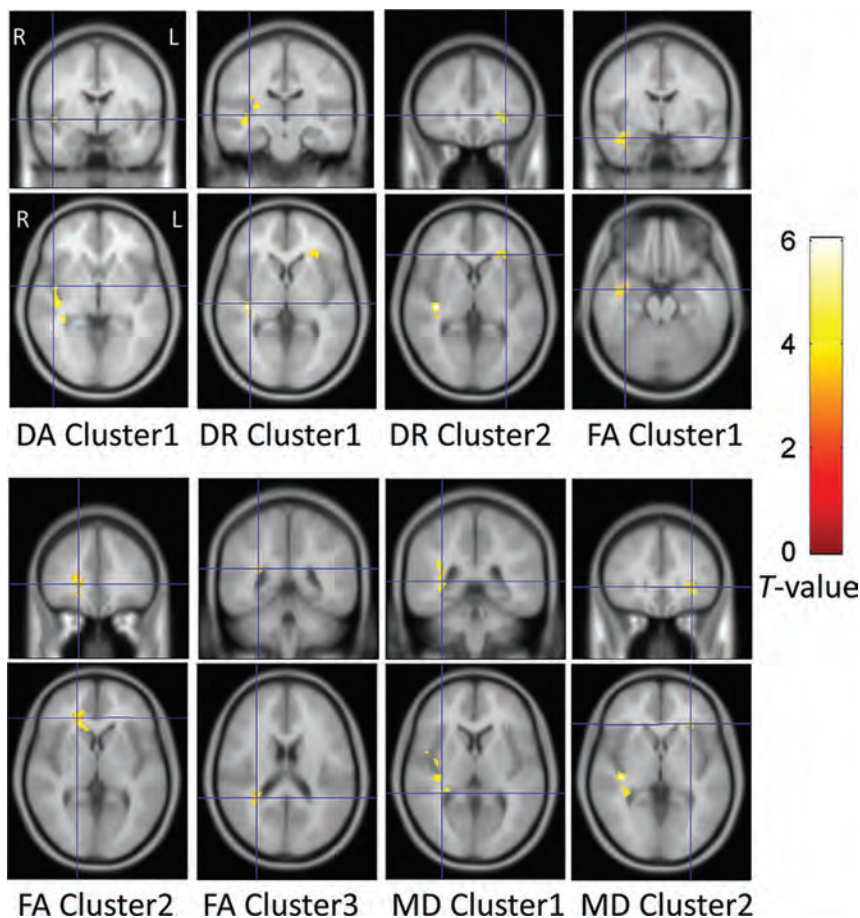


**FIG 2.** Voxel-based analysis results. The DA, DR, and MD were significantly increased and the FA was significantly decreased in the presbycusis group compared with the healthy control group ( $P < .001$  at voxel level, uncorrected;  $P < .05$  at cluster level, family-wise error-corrected). Each cluster contains more than 100 adjacency voxels that show significant variation of those diffusion parameters. For example, DA cluster 1 denotes the first group of voxels that show significant intergroup difference of DA, whereas DR cluster 1 denotes the first group of voxels that show significant intergroup difference of DR. The significant voxels are displayed with their T-values. The ascending T-values are shown from darkness to brightness. Each panel displays a single cluster with its location indicated by a blue section marker.

gyrus, superior temporal gyrus, lateral lemniscus, auditory radiation, and inferior colliculus in patients with sensorineural hearing loss.<sup>9,24,25</sup> Two possible explanations for the alteration shown in the right-side hearing-related areas are as follows: 1) Presbycusis is most often characterized by a decline in frequency audibility toward high frequencies, which is crucial for pitch perception. One study has demonstrated that the right hemisphere was the dominant hemisphere involved in pitch perception<sup>26</sup>; and 2) Another study found a clear rightward asymmetry in the white matter under the auditory cortex in patients with presbycusis.<sup>6</sup>

To our knowledge, only 1 study has used a DTI-based technique to investigate microstructural changes in the white matter of patients with presbycusis.<sup>6</sup> In that study, the DA value was increased in the right-side auditory pathway of patients with mild presbycusis compared with young healthy controls. Therefore, the altered integrity of the auditory pathway might be mainly caused by aging. In our study, age-matched healthy patients served as controls, so we determined the altered integrity of the white matter in the right-side Heschl gyrus is mainly driven by hearing loss. However, there were no differences in any measured

DTI parameters between patients with mild presbycusis and expressed presbycusis in the previous study.<sup>6</sup> Except for the selection of ROI sizes (the minimal size of an ROI is a single voxel), as mentioned in the introduction, the contradiction in results might be explained by differences in the patient populations.

Apart from the findings along the auditory pathway, our results also showed changes in a language-related area within the inferior frontal gyrus (near the Broca area). This finding is consistent with previous studies: decreased audibility in patients with presbycusis influences speech processing, especially in noisy environments.<sup>3</sup> The inability to clearly detect temporal cues is a possible reason for decreased speech understanding in patients with presbycusis.<sup>2,27</sup> The processing of temporal cues, which mainly occurs in the auditory cortex,<sup>28</sup> might be influenced by age-related changed inhibition.<sup>29,30</sup> Gamma-aminobutyric acid is the main inhibitory neurotransmitter in the central auditory system. One MR spectroscopy study demonstrated that gamma-aminobutyric acid concentrations were reduced in the auditory cortex of patients with presbycusis.<sup>31</sup> The inhibition-deficit hypothesis is also considered the reason for the decline in several other cognitive domains, such as reading.<sup>32</sup> Altered DTI parameters were also found near the insula in patients with presbycusis. This is consistent with functional imaging studies that have shown that the insula

plays an important role in auditory processing.<sup>33</sup>

Voxel-based analysis, which is capable of localizing very subtle anatomic changes, suffers from 2 major limitations. First, it searches for the group differences in a hypothesis-independent way.<sup>34</sup> However, disease-related changes can be distributed in a complex fashion. Therefore, the voxel-based analysis is not sensitive for the detection of small and widely distributed changes in image intensities. Second, voxel-based analysis is sensitive to registration accuracy, which is not reliable enough when based on DTI. This is because DTI does not contain enough structural information compared with T1WI. The registration errors could be reduced by using a more sophisticated approach to further improve accuracy of voxel-based analysis. In addition, DTI is itself limited because it often has to pay a penalty of a higher SNR and higher sensitivity to measurement artifacts such as patient motion and eddy current.<sup>35,36</sup> Finally, our study was further limited by the small sample size; hence, it should be viewed as a preliminary study and requires confirmation in larger samples.



## CONCLUSIONS

Using a voxel-based analysis, this study revealed presbycusis-related changes of DTI parameters along the auditory pathway and a language-related area. Our findings could be important for exploring more reliable imaging evidence of presbycusis and could complement the ROI-based approach or studies by using different patient populations.

## REFERENCES

1. Schuknecht HF, Gacek MR. **Cochlear pathology in presbycusis.** *Ann Otol Rhinol Laryngol* 1993;102(1 Pt 2):1–16 Medline
2. Mazelová J, Popelar J, Syka J. **Auditory function in presbycusis: peripheral vs. central changes.** *Exp Gerontol* 2003;38:87–94 CrossRef Medline
3. Snell KB, Frisina DR. **Relationships among age-related differences in gap detection and word recognition.** *J Acoust Soc Am* 2000;107:1615–26 CrossRef Medline
4. Suta D, Rybalko N, Pelánová J, et al. **Age-related changes in auditory temporal processing in the rat.** *Exp Gerontol* 2011;46:739–46 CrossRef Medline
5. Ouda L, Druga R, Syka J. **Changes in parvalbumin immunoreactivity with aging in the central auditory system of the rat.** *Expl Gerontol* 2008;43:782–89 CrossRef Medline
6. Profant O, Škoch A, Balogová Z, et al. **Diffusion tensor imaging and MR morphometry of the central auditory pathway and auditory cortex in aging.** *Neuroscience* 2014;260:87–97 CrossRef Medline
7. Profant O, Tintěra J, Balogová Z, et al. **Functional changes in the human auditory cortex in ageing.** *PloS One* 2015;10:e0116692 CrossRef Medline
8. Wu CM, Ng SH, Liu TC. **Diffusion tensor imaging of the subcortical auditory tract in subjects with long-term unilateral sensorineural hearing loss.** *Audiol Neurootol* 2009;14:248–53 CrossRef Medline
9. Lin Y, Wang J, Wu C, et al. **Diffusion tensor imaging of the auditory pathway in sensorineural hearing loss: changes in radial diffusivity and diffusion anisotropy.** *J Magn Reson Imaging* 2008;28:598–603 CrossRef Medline
10. Miller MI, Faria AV, Oishi K, et al. **High-throughput neuro-imaging informatics.** *Front Neuroinform* 2013;7:31 CrossRef Medline
11. Oishi K, Mielke MM, Albert M, et al. **DTI analyses and clinical applications in Alzheimer's disease.** *J Alz Dis* 2011;26 Suppl 3:287–96 CrossRef
12. Lin FR, Thorpe R, Gordon-Salant S, et al. **Hearing loss prevalence and risk factors among older adults in the United States.** *J Gerontol A Biol Sci Med Sci* 2011;66:582–90 CrossRef Medline
13. Van Eyken E, Van Laer L, Franssen E, et al. **KCNQ4: a gene for age-related hearing impairment?** *Hum Mutat* 2006;27:1007–16 CrossRef Medline
14. Gong G, Jiang T, Zhu C, et al. **Side and handedness effects on the cingulum from diffusion tensor imaging.** *Neuroreport* 2005;16:1701–05 CrossRef Medline
15. Hatta T. **Handedness and the brain: a review of brain-imaging techniques.** *Magn Reson Med Sci* 2007;6:99–112 CrossRef Medline
16. Woods RP, Grafton ST, Holmes CJ, et al. **Automated image registration. I. General methods and intrasubject, intramodality validation.** *J Comput Assist Tomogr* 1998;22:139–52 CrossRef Medline
17. Jiang H, van Zijl PC, Kim J, et al. **DtiStudio: resource program for diffusion tensor computation and fiber bundle tracking.** *Comput Methods Programs Biomed* 2006;81:106–16 CrossRef Medline
18. Ceritoglu C, Oishi K, Li X, et al. **Multi-contrast large deformation diffeomorphic metric mapping for diffusion tensor imaging.** *Neuroimage* 2009;47:618–27 CrossRef Medline
19. Beaulieu C. **The basis of anisotropic water diffusion in the nervous system - a technical review.** *NMR Biomed* 2002;15:435–55 CrossRef Medline
20. Alexander AL, Hurley SA, Samsonov AA, et al. **Characterization of cerebral white matter properties using quantitative magnetic resonance imaging stains.** *Brain Connect* 2011;1:423–46 CrossRef Medline
21. Alexander AL, Lee JE, Lazar M, et al. **Diffusion tensor imaging of the brain.** *Neurotherapeutics* 2007;4:316–29 CrossRef Medline
22. Song SK, Kim JH, Lin SJ, et al. **Diffusion tensor imaging detects age-dependent white matter changes in a transgenic mouse model with amyloid deposition.** *Neurobiol Dis* 2004;15:640–47 CrossRef Medline
23. Zerbi V, Kleinnijenhuis M, Fang X, et al. **Gray and white matter degeneration revealed by diffusion in an Alzheimer mouse model.** *Neurobiol Aging* 2013;34:1440–50 CrossRef Medline
24. Lutz J, Hemminger F, Stahl R, et al. **Evidence of subcortical and cortical aging of the acoustic pathway: a diffusion tensor imaging (DTI) study.** *Acad Radiol* 2007;14:692–700 CrossRef Medline
25. Chang Y, Lee SH, Lee YJ, et al. **Auditory neural pathway evaluation on sensorineural hearing loss using diffusion tensor imaging.** *Neuroreport* 2004;15:1699–703 CrossRef Medline
26. Zatorre RJ, Evans AC, Meyer E, et al. **Lateralization of phonetic and pitch discrimination in speech processing.** *Science* 1992;256:846–49 CrossRef Medline
27. Góndon-Salant S, Fitzgibbons PJ. **Temporal factors and speech recognition performance in young and elderly listeners.** *J Speech Hear Res* 1993;36:1276–85 CrossRef Medline
28. Bao S, Chang EF, Woods J, et al. **Temporal plasticity in the primary auditory cortex induced by operant perceptual learning.** *Nat Neurosci* 2004;7:974–81 CrossRef Medline
29. Caspary DM, Schatteman TA, Hughes LF. **Age-related changes in the inhibitory response properties of dorsal cochlear nucleus output neurons: role of inhibitory inputs.** *J Neurosci* 2005;25:10952–59 CrossRef Medline
30. Burkard RF, Sims D. **The human auditory brainstem response to high click rates: aging effects.** *Am J Audiol* 2001;10:53–61 CrossRef Medline
31. Gao F, Wang G, Ma W, et al. **Decreased auditory GABA+ concentrations in presbycusis demonstrated by edited magnetic resonance spectroscopy.** *Neuroimage* 2015;106:311–16 CrossRef Medline
32. Manly JJ, Touradji P, Tang MX, et al. **Literacy and memory decline among ethnically diverse elders.** *J Clin Exp Neuropsychol* 2003;25:680–90 CrossRef Medline
33. Bamiou DE, Musiek FE, Luxon LM. **The insula (Island of Reil) and its role in auditory processing. Literature review.** *Brain Res Brain Res Rev* 2003;42:143–54 CrossRef Medline
34. Qin YY, Li MW, Zhang S, et al. **In vivo quantitative whole-brain diffusion tensor imaging analysis of APP/PS1 transgenic mice using voxel-based and atlas-based methods.** *Neuroradiology* 2013;55:1027–38 CrossRef Medline
35. Jones DK, Cercignani M. **Twenty-five pitfalls in the analysis of diffusion MRI data.** *NMR Biomed* 2010;23:803–20 CrossRef Medline
36. Tournier JD, Mori S, Leemans A. **Diffusion tensor imaging and beyond.** *Magn Reson Med* 2011;65:1532–56 CrossRef Medline

# Disrupted Brain Connectivity Patterns in Patients with Type 2 Diabetes

Y. Cui, S.-F. Li, H. Gu, Y.-Z. Hu, X. Liang, C.-Q. Lu, Y. Cai, C.-X. Wang, Y. Yang, and G.-J. Teng



## ABSTRACT

**BACKGROUND AND PURPOSE:** Type 2 diabetes is associated with an increased risk of dementia. This study investigated the global connectivity patterns in the brains of patients with type 2 diabetes by using a functional MR imaging technique.

**MATERIALS AND METHODS:** Forty patients and 43 age-, sex-, and education-matched healthy controls underwent resting-state functional imaging in a 3T MR imaging unit. Degree centrality, a commonly used measurement of global connectivity, was computed for a full-brain exploration of the regions influenced by type 2 diabetes. We then examined the functional connectivity of each region by using the seed-based approach. Finally, voxelwise correlation analyses were performed to explore the relationship among the connectivity changes, cognitive performance, and diabetes-related variables.

**RESULTS:** Patients exhibited decreased degree centrality in the left lingual gyrus and increased centrality in the right insula and dorsal anterior cingulate cortex (corrected  $P < .05$ ). The occipital network anchored in the lingual gyrus showed extensively reduced connectivity, while the network connectivity of the insula and cingulate cortex (mostly included in the salience network) was significantly elevated (corrected  $P < .05$ ). Correlational analyses revealed that in the diabetic group, impaired visual memory and executive function performance were correlated with occipital hypoconnectivity, while higher fasting plasma glucose levels and better executive functioning were related to anterior cingulate cortex hyperconnectivity (all corrected  $P$  values  $< .05$ ). Similar effects were not detected in the controls.

**CONCLUSIONS:** This preliminary study shows that network connectivity is altered in patients with type 2 diabetes, which may provide critical insight into the neural substrate of diabetes-related cognitive decline.

**ABBREVIATIONS:** CFT = Complex Figure Test; dACC = dorsal anterior cingulate cortex; DC = degree centrality; FC = functional connectivity; FPG = fasting plasma glucose; HbA1c = glycosylated hemoglobin; HC = healthy control; T2DM = type 2 diabetes mellitus; TMT = Trail-Making Test

It has been suggested that type 2 diabetes mellitus (T2DM) is associated with cognitive dysfunction and a higher risk of dementia, especially in elderly subjects.<sup>1,2</sup> However, the neural substrate of T2DM-related cognitive impairment remains elusive. Because brain pathologies may precede clinically measurable cognitive deficits,<sup>3</sup> identifying vulnerable brain regions might be advantageous for tracking the early effects of T2DM on cognitive functioning.

The human brain consists of spatially distributed but functionally interacting regions that form an efficient functional connectome to support normal cognitive functioning.<sup>4</sup> Recent studies on patients with Alzheimer disease suggest that altered functional connectivity (FC) between regions may represent early deleterious outcomes that occur before structural changes and clinical manifestations.<sup>5</sup> However, only a limited number of studies have explored FC changes in relation to T2DM so far: One study reported a decreased FC of the hippocampus, while another study observed alterations in thalamocortical connections.<sup>6,7</sup> Other studies on this topic focused on the changes either within the default mode network<sup>8-10</sup> or in the attentional network.<sup>11</sup> Notably, these studies relied on seed-based approaches or an in-

Received September 24, 2015; accepted after revision May 11, 2016.

From the Department of Radiology (Y.Cui, C.-Q.L., Y.Cai, C.-X.W., G.-J.T.), Jiangsu Key Laboratory of Molecular and Functional Imaging, Zhongda Hospital, Medical School of Southeast University, Nanjing, China; and Neuroimaging Research Branch (Y.Cui, S.-F.L., H.G., Y.-Z.H., X.L., Y.Y.), National Institute on Drug Abuse, National Institutes of Health, Baltimore, Maryland.

This work was supported by grants from the Major State Basic Research Development Program of China (973 Program) (Nos. 2013CB733800, 2013CB733803), the Key Project of Jiangsu Province Natural Science Foundation of China (BK20130057), and the National Natural Science Foundation of China General Projects (Nos. 81230034, 81271739). S.-F.L., H.G., Y.-Z.H., X.L., and Y.Y. were supported by the Intramural Research Program of the National Institute on Drug Abuse, the National Institutes of Health.

Please address correspondence to Gao-Jun Teng, MD, 87 Dingjiaqiao Rd, Nanjing 210009, Jiangsu, China; e-mail: giteng@vip.sina.com

Indicates open access to non-subscribers at www.ajnr.org

Indicates article with supplemental on-line table.

Indicates article with supplemental on-line photos.

<http://dx.doi.org/10.3174/ajnr.A4858>

**Table 1: Demographics and clinical characteristics for T2DM and control groups<sup>a</sup>**

Measures	T2DM (n = 40)	Control (n = 43)	P Value
Age (yr)	60.5 ± 6.9	57.6 ± 6.6	.08
Sex (male/female) <sup>a</sup>	24:21	16:30	.09
Education (yr)	10.0 ± 3.4	10.2 ± 2.3	.46
Head motion (FD) (mm)	0.09 ± 0.07	0.08 ± 0.05	.35
Diabetes duration (yr)	8.9 ± 5.0	—	—
Insulin treatment (No.) (%)	8 (20)	—	—
HbA1c (%) (mmol/mol)	7.8 ± 1.6 (62 ± 17.5)	5.6 ± 0.3 (37 ± 3.3)	<.001 <sup>b</sup>
FPG (mmol/L)	7.8 ± 2.1	5.5 ± 0.4	<.001 <sup>b</sup>
HOMA-IR	3.1 ± 1.9	2.4 ± 1.1	.02 <sup>b</sup>
BMI (kg/m <sup>2</sup> )	24.4 ± 2.7	23.8 ± 2.7	.22
Systolic BP (mm Hg)	136.6 ± 14.8	132.7 ± 14.8	.18
Diastolic BP (mm Hg)	86.0 ± 11.1	86.6 ± 11.2	.81
Hypertension (No.) (%) <sup>c</sup>	21 (53)	12 (28)	
Antihypertensive treatment (No.) (%) <sup>c</sup>	17 (43)	8 (19)	
Total cholesterol (mmol/L)	5.5 ± 1.2	5.3 ± 0.9	.46
Triglyceride (mmol/L)	1.5 ± 0.8	1.4 ± 0.8	.69
HDL cholesterol (mmol/L)	1.4 ± 0.3	1.3 ± 0.7	.57
LDL cholesterol (mmol/L)	3.3 ± 0.8	3.1 ± 0.6	.30
White matter lesions (range)	0–6	0–7	.26
Lacunar infarcts (No.) (%) <sup>a</sup>	9	5	.11

**Note:**—FD indicates frame-wise displacement; HOMA-IR, homeostasis model assessment of insulin resistance; BP, blood pressure; BMI, body mass index; LDL, low-density lipoprotein; HDL, high-density lipoprotein.

<sup>a</sup>Data are mean and number or range.

<sup>b</sup>P value < .05.

<sup>c</sup>Statistical analyses were performed by  $\chi^2$  tests.

dependent component analysis, focusing their examinations within specific brain networks. Based on pathologic evidence, neural degeneration in the brains of those with diabetes is diffusely distributed.<sup>12</sup> Therefore, a voxelwise whole-brain FC analysis may yield a more comprehensive understanding of the functional alterations related to the disease.

Degree centrality (DC) is a commonly used graph theory-based measurement of global connectivity. It computes the correlation of each voxel with all other voxels in the entire brain, resulting in a connectivity map that represents the sum (attenuation) of connections at each voxel.<sup>13</sup> Recent studies from our group have demonstrated that DC is highly associated with regional cerebral blood flow and metabolism, which establish the physiologic basis of this topologic measurement.<sup>14</sup> So far, DC analyses have been applied to various mental disorders, such as Alzheimer disease, schizophrenia, and autism.<sup>15–17</sup> In this study, we used DC measurements to perform a full-brain exploration of brain regions with altered connectivity density. The FC pattern of each region was subsequently examined by using a seed-based approach. Finally, correlations among the connectivity in each brain circuit, cognitive performance, and T2DM-relevant variables were explored to better understand the link between network dysfunction and cognitive deficits.

## MATERIALS AND METHODS

### Participants

The current study was approved by the ethics committee of the institutional review board of Zhongda Hospital, Southeast University. Written informed consent was obtained from all subjects before their participation. Patients with T2DM and age-, sex-, and education-matched healthy controls (HCs) were recruited via advertisement in the local community. All subjects were between 50 and 75 years of age, with a minimum education of 6 years. The exclusion criteria were as follows: a history of alcohol or sub-

stance abuse, Mini-Mental State Examination score of <24,<sup>18</sup> a Hamilton Depression Rating Scale score of  $\geq 7$ ,<sup>19</sup> a history of brain lesions such as tumor or stroke, an unrelated psychiatric or neurologic disorder, or MR imaging contraindications.

The diagnosis of T2DM was made on the basis of medical histories, medication used, or fasting plasma glucose (FPG) levels ( $\geq 7$  mmol/L).<sup>20</sup> None of the patients reported any history of hypoglycemic episodes or had been diagnosed with clinically detectable complications such as retinopathy, nephropathy, and peripheral neuropathy. HCs underwent an oral glucose tolerance test (75 g of dextrose monohydrate in 250 mL of water). HCs with fasting blood glucose levels of  $\geq 7.0$  mmol/L or post-oral glucose tolerance test glucose levels of  $\geq 7.8$  mmol/L were excluded.

Information on medical histories and medication use was collected, and

weight, height, and waist circumferences were carefully recorded for all subjects. Hypertension was defined as previously described.<sup>21</sup> Blood samples were collected after an 8-hour fast to assess FPG, glycosylated hemoglobin (HbA1c), fasting insulin, and cholesterol levels. The homeostasis model assessment of insulin resistance was used to assess the degree of insulin resistance for all HCs and patients who were not treated with insulin.<sup>22</sup>

The final study sample included 40 patients with T2DM (mean age, 60.5 ± 6.9 years; 21 women) and 43 HCs (57.6 ± 6.6 years, 30 women) (Table 1), who were 50–75 years of age. Among the patients, disease duration ranged from 2 to 17 years (mean duration, 8.9 ± 5.0 years). Eight patients with T2DM received insulin treatment, while the others were treated with either oral hypoglycemic agents ( $n = 22$ ) or dietary restrictions ( $n = 10$ ).

### Neuropsychological Tests

All participants were subjected to a detailed battery of neuropsychological tests, which covered multiple cognitive domains. Episodic memory regarding verbal and visual information was assessed via the Auditory Verbal Learning Test and the Rey-Osterrieth Complex Figure Test (CFT) delayed recall trial, respectively. Working memory was measured via the forward and backward trials of the Digit Span Test. Attention was evaluated via the Trail-Making Test part A, and executive functioning was assessed via Trail-Making Test part B (TMT-B). Spatial processing ability was assessed via the Clock Drawing Test and the CFT copy trial. Language processing ability was assessed via the Verbal Fluency Test. The total time required to complete all tests was approximately 60 minutes.

### MR Imaging Data Acquisition

The resting-state fMRI data were acquired in a 3T Magnetom Trio scanner (Siemens, Erlangen, Germany). Foam padding and ear-

plugs were used to reduce head motion and scanner noise. Subjects were instructed to keep their eyes closed, remain awake, and avoid specific thoughts during the scanning, which was later confirmed by using a questionnaire. A 6-minute whole-brain fMRI dataset based on blood oxygen level–dependent signals was acquired for each subject by using a gradient-echo EPI sequence (volume = 240, sections = 36, TR/TE = 2000/25 ms, section thickness = 4 mm, flip angle = 90°, FOV = 240 mm, acquisition matrix = 64 × 64). High-resolution (1-mm<sup>3</sup>) T1-weighted images were acquired by using a whole-brain 3D MPRAGE sequence (sections = 176, TR/TE = 1900/2.48 ms, section thickness = 1.0 mm, flip angle = 9°, FOV = 250 mm, acquisition matrix = 256 × 256). FLAIR images were also obtained (TR/TE = 8500/94 ms, sections = 20, section thickness = 5 mm, each with a voxel size of 1.3 × 0.9 × 5 mm<sup>3</sup>).

To assess small-vessel disease, we evaluated the white matter lesions and lacunar infarcts on FLAIR images.<sup>23</sup> The brain was divided into 5 regions in each hemisphere, and the WM lesion score was determined separately for each region on a 4-point scale (from 0 to 3), resulting in final scores ranging from 0 to 30.<sup>23</sup> Participants with a score of 3 in any region were considered to have severe small-vessel disease and were thus excluded. The final results indicated that none of the participants met the white matter lesion exclusion criteria.

### Data Preprocessing

Functional MR imaging data were preprocessed by using Data Processing Assistant for Resting-State fMRI software (<http://www.restfmri.net/forum/DPARSF>) and SPM8 (<http://www.fil.ion.ucl.ac.uk/spm/>). After discarding the first 10 functional volumes, section-timing correction and realignment were subsequently performed (subjects with head motion of >2.0 mm of translation or >2.0° of rotation were excluded). Structural and functional images were then coregistered and normalized to the standard Montreal Neurological Institute space. Afterward, nuisance covariates, including 6 motion parameters, white matter, and CSF signals, were regressed out, followed by detrending and bandpass filtering (0.01–0.1 Hz) procedures. To minimize motion-induced artificial correlations, we cleaned functional images by applying a scrubbing procedure that removed images (frames) with >0.5-mm frame-wise displacement, along with the 2 frames immediately before and after the removed images.<sup>24</sup> The number of scrubbed imaging volumes for each individual is summarized in On-line Fig 1. The mean frame-wise displacement of each subject was included as a motion covariate in the statistical analyses.

### DC Analyses

DC maps can be represented as either weighted or binarized graphs, with the former focusing on the sum of weights from edges connecting to a node and the latter, on the number of the connected edges.<sup>13</sup> Here, both graphs were computed to obtain more comprehensive information. The DC maps were generated by using Pearson correlations in Matlab (MathWorks, Natick, Massachusetts). Specifically, the time course of each voxel within a gray matter mask (obtained from the overlap of all subjects' segmented GM) was extracted and correlated with that of every other voxel within the mask to generate a correlation matrix. After

thresholding each correlation at  $R > 0.25$ , we computed DC as either the sum of connections (binarized) or the sum of the weights of connections (weighted) for each voxel. The resulting voxelwise DC map was subsequently converted into a  $z$  score map by subtracting the global mean DC and dividing by the SD of the whole-brain DC.<sup>13</sup> Finally, the DC maps were smoothed with a Gaussian kernel of 4 mm to obtain the individual DC maps for each subject.

Further analyses for DC maps were performed by using the Analysis of Functional Neuro Images software (AFNI; <http://afni.nimh.nih.gov/afni>).<sup>25</sup> The smoothed individual DC maps of all subjects in each group were analyzed by using a 1-sample  $t$  test to identify the spatial distribution of the DC values in each group. The statistical threshold was set at  $P < .05$ , with a family-wise correction. Independent 2-sample  $t$  tests were also performed on the basis of the individual DC maps to examine the differences in DC between groups. Age, sex, years of education, and head motion (mean frame-wise displacement) were included as covariates. To further exclude the confounding effects of small-vessel disease, we also controlled for the WM lesion score and the existence of hypertension during the comparison. The  $P_{\text{uncorrected}}$  value was set at .01, with a cluster size of 30 voxels (determined via Monte Carlo simulation) corresponding to a  $P_{\text{corrected}}$  of .05.

### Seed-Based FC Analyses

The identified brain regions with altered DC were chosen as the seeds to examine their FC changes. The time-series of each region was averaged and correlated with that of every other voxel within the GM mask. Correlation coefficients between the seed and every other voxel were then converted by using the Fisher  $r$ -to- $z$  transform, yielding variates that were approximately normally distributed. One-sample  $t$  tests were performed on the individual  $z$ -transformed FC maps in each group to identify the spatial distribution of each brain circuit ( $P < .05$  with family-wise error correction). Voxelwise group comparisons on each  $z$ -transformed FC map were then performed, which were confined to a mask obtained by combining the results of the within-group analyses in each group. Statistical significance was determined on the basis of  $P_{\text{uncorrected}} < .01$  and  $P_{\text{corrected}} < .05$ . The same covariates used during the DC analyses were included.

### Statistical Analyses

**Clinical Data.** Statistical analyses were performed by using SPSS software (Version 18.0; IBM, Armonk, New York). Normal distributions were tested by using the Kolmogorov-Smirnov test. Group comparisons of clinical parameters were explored by using independent 2-sample  $t$  tests for normally distributed variables; the nonparametric Mann-Whitney  $U$  test, for asymmetrically distributed variables; and  $\chi^2$  tests, for categorical variables. A  $P$  value  $\leq .05$  was considered statistically significant.

**Relationship between FC and Clinical Variables.** The correlations between the FC of each seed-relevant network and the clinical variables, including neurocognitive performance (those tasks performed significantly worse by patients than by HCs) and T2DM-related parameters (HbA1c, FPG, and homeostasis model assessment of insulin resistance), were explored in a whole-brain linear

regression model by using the 3dLME command in AFNI. The FC maps and clinical variables in both groups were entered into the models along with age, sex, education, head motion, and small-vessel disease parameters as covariates of no interest. To identify the regions where the FC was differentially correlated with clinical variables in patients versus HCs, we focused on the group  $\times$  variable statistical interaction maps ( $P_{\text{corrected}} < .05$ ,  $P_{\text{voxelwise}} < .01$ ). Brain regions with significant interaction effects were considered important in contributing to T2DM-related cognitive impairment.

## RESULTS

### Demographic and Clinical Parameters

All clinical parameters are summarized in Table 1. The 2 groups were matched in terms of age, sex, education, and their frame-wise displacement measurement. As expected, patients exhibited

**Table 2: Cognitive test results for the T2DM and control groups<sup>a</sup>**

Measures	T2DM (n = 40)	Control (n = 43)	P Value
General cognitive status			
MMSE	28.3 $\pm$ 1.2	28.7 $\pm$ 1.2	.26
Episodic memory			
AVLT	5.9 $\pm$ 1.3	6.3 $\pm$ 1.8	.11
AVLT, delay	5.8 $\pm$ 2.3	6.3 $\pm$ 2.1	.31
CFT, delay	13.9 $\pm$ 5.8	17.5 $\pm$ 5.8	<.01 <sup>b</sup>
Working memory			
DST (forward)	6.8 $\pm$ 1.3	7.3 $\pm$ 1.5	.11
DST (backward)	4.1 $\pm$ 1.0	4.5 $\pm$ 1.3	.16
Attention			
TMT, part A	64.5 $\pm$ 19.0	63.3 $\pm$ 14.8	.76
Executive functioning			
TMT, part B	182.2 $\pm$ 62.8	152.0 $\pm$ 50.6	.02 <sup>b</sup>
Spatial processing			
CFT, copy	34.3 $\pm$ 1.8	34.8 $\pm$ 1.5	.16
CDT	3.3 $\pm$ 0.6	3.5 $\pm$ 0.6	.07
Language processing			
VFT	16.5 $\pm$ 3.6	17.6 $\pm$ 3.0	.52

**Note:**—MMSE indicates Mini-Mental State Examination; AVLT, Auditory Verbal Learning Test; DST, Digit Span Test; CDT, Clock Drawing Test; VFT, Verbal Fluency Test.

<sup>a</sup>Data are represented as means.

<sup>b</sup>P value < .05.

significantly higher FPG, HbA1c, and homeostasis model assessment of insulin resistance values than the HCs. No differences were observed in blood pressure, lipid levels, or degree of small-vessel disease. Patients performed significantly worse on CFT delay and TMT-B than HCs (Table 2), which mainly involve visual memory and executive functioning domains. Among the diabetes-related variables, disease duration was significantly correlated with the scores in 2 tasks after controlling for age (CFT copy,  $R = -0.45$ ,  $P < .01$ ; CFT delay,  $R = -0.40$ ,  $P = .02$ ), while the HbA1c level was associated with the CFT copy score ( $R = -0.35$ ,  $P = .02$ ).

### DC Results

Due to the highly consistent results of the weighted and binarized measurements, the present findings are primarily based on the weighted maps.

The spatial distribution of the weighted DC maps is shown in Fig 1. In both groups, the DC in the posterior cingulate cortex, cuneus, visual cortex, medial prefrontal cortex, and insula was significantly higher than the global mean value. The binarized map shows a similar pattern (On-line Fig 2).

Patients with T2DM exhibited decreased DC in the left lingual gyrus and increased DC in the right anterior insula and dorsal anterior cingulate cortex (dACC) (Fig 2). The results shown in the binarized DC map are highly consistent with the results in the weighted map (On-line Fig 3). Detailed information for the identified brain regions are summarized in Table 3 and the On-line Table.

### Seed-Based FC Analyses

The FC pattern of each region (ie, dACC, right anterior insula, and left lingual gyrus) is shown in Fig 3. Specifically, the dACC was connected with the cingulate cortex, anterior insula, and sensorimotor cortex, while the right anterior insula was connected with the entire insula, dACC, and the adjacent frontal, temporal, and sensorimotor cortices. Meanwhile, the lingual gyrus was mainly connected with the visual cortex and the superior/middle temporal and sensorimotor cortices.

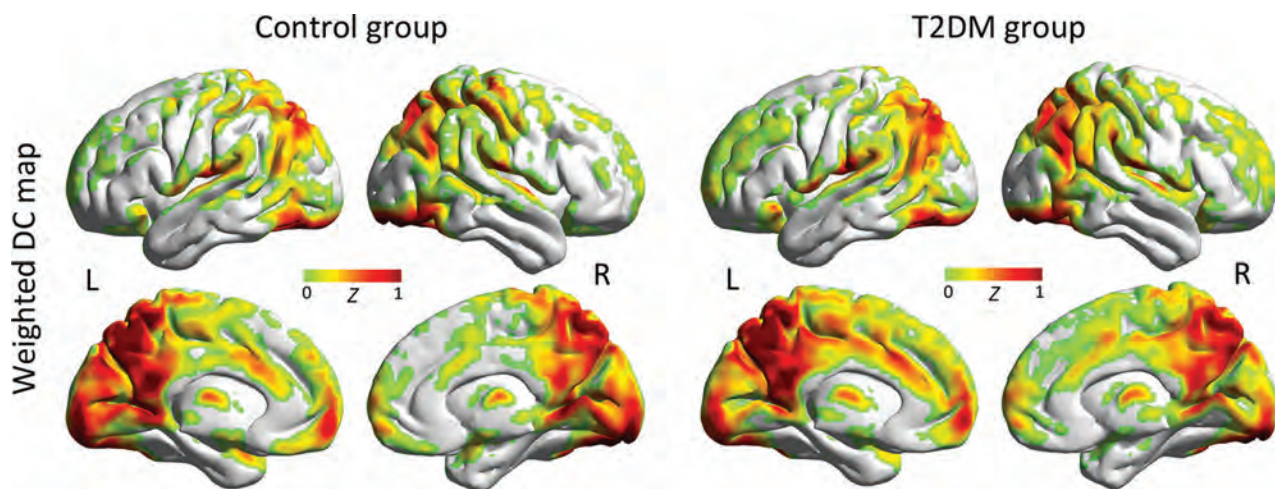


**FIG 1.** Spatial distribution of weighted DC maps in patients with T2DM and HCs ( $P < .05$ , family-wise error–corrected). In the weighted DC map, standardized DC in the posterior cingulate, visual cortex, medial prefrontal cortex, insula, and thalamus was significantly higher than the global mean values in both groups. Color scale denotes the z score. R indicates right; L, left.

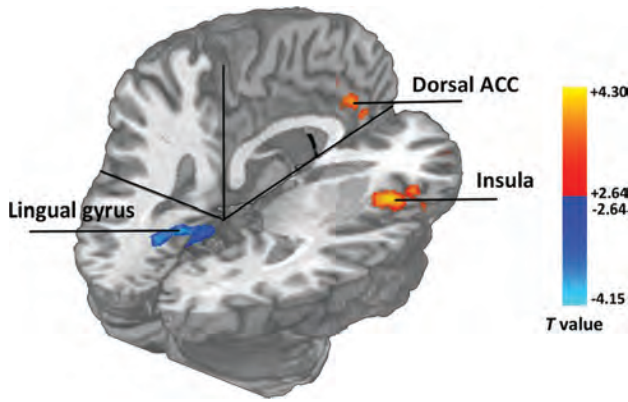


**FIG 2.** Group differences of weighted DC maps between patients with T2DM and HCs ( $P < .05$ ; AlphaSim-corrected; [https://afni.nimh.nih.gov/pub/dist/doc/program\\_help/AlphaSim.html](https://afni.nimh.nih.gov/pub/dist/doc/program_help/AlphaSim.html)). In the weighted DC map, patients with T2DM showed significantly decreased value (cool color) in the left lingual gyrus and increased values (warm color) in the dACC and the right anterior insula. The color scale denotes the  $t$ -value.

**Table 3: Brain regions with significant differences in weighted DC maps between patients with T2DM and HCs<sup>a</sup>**

Brain Regions	MNI			Voxels	Peak $t$ -Value
	X	Y	Z		
RAI	+42	+15	+0	51	+4.30
dACC	+6	+30	+24	31	+4.03
L lingual gyrus	-15	-51	-3	37	-3.51

**Note:**—MNI indicates Montreal Neurological Institute; RAI, right anterior insula; L, left.

<sup>a</sup> Comparisons were performed at  $P < .05$ , corrected by AlphaSim multiple comparisons. X, y, and z are coordinates of primary peak locations in the MNI space. Positive  $t$  values are T2DM > control subjects. Negative  $t$  values are T2DM < control subjects.

In the subjects with diabetes, the dACC showed stronger connectivity with the bilateral ventral dorsal anterior cingulate cortex/medial prefrontal cortex (Fig 4, first row), while the right anterior insula had increased interactions with the right posterior insula and left superior temporal gyrus (Fig 4, second row). In contrast, diffusely decreased connectivity was observed in the lingual gyrus-related visual network, especially in the higher order visual cortex and the sensory areas (Fig 4, third row).

Voxelwise correlation analyses identified significant effects of the clinical variables on several brain regions in the T2DM group (Fig 5). The occipital connectivity was positively correlated with the CFT delay score (Fig 5A,  $R = 0.48$ ,  $P = .002$ ; group  $\times$  performance interaction,  $P = .001$ ) and negatively correlated with the time spent on the TMT-B (Fig 5C,  $R = -0.46$ ,  $P = .003$ ; group  $\times$  performance interaction,  $P = .87$ ). The hyperconnectivity of the dACC was correlated with higher FPG levels (Fig 5B,  $R = 0.65$ ,  $P < .001$ ; group  $\times$  FPG interaction,  $P = .001$ ) and better TMT-B performance (Fig 5D,  $R = -0.52$ ,  $P = .001$ ; group  $\times$  performance interaction,  $P = .04$ ). Due to the significant correlation between disease duration and neurocognitive performance, we further controlled for disease duration and reanalyzed the correlations. This reanalysis did not significantly affect our findings (data not shown). Similar effects were not detected in the HCs.

## DISCUSSION

Using graph theory-based analyses, the present study provides the initial evidence of altered global connectivity in the brains of patients with T2DM. Patients showed decreased DC in the occipital region and increased DC in the higher order cognitive control regions. Seed-based analytic approaches revealed that the brain

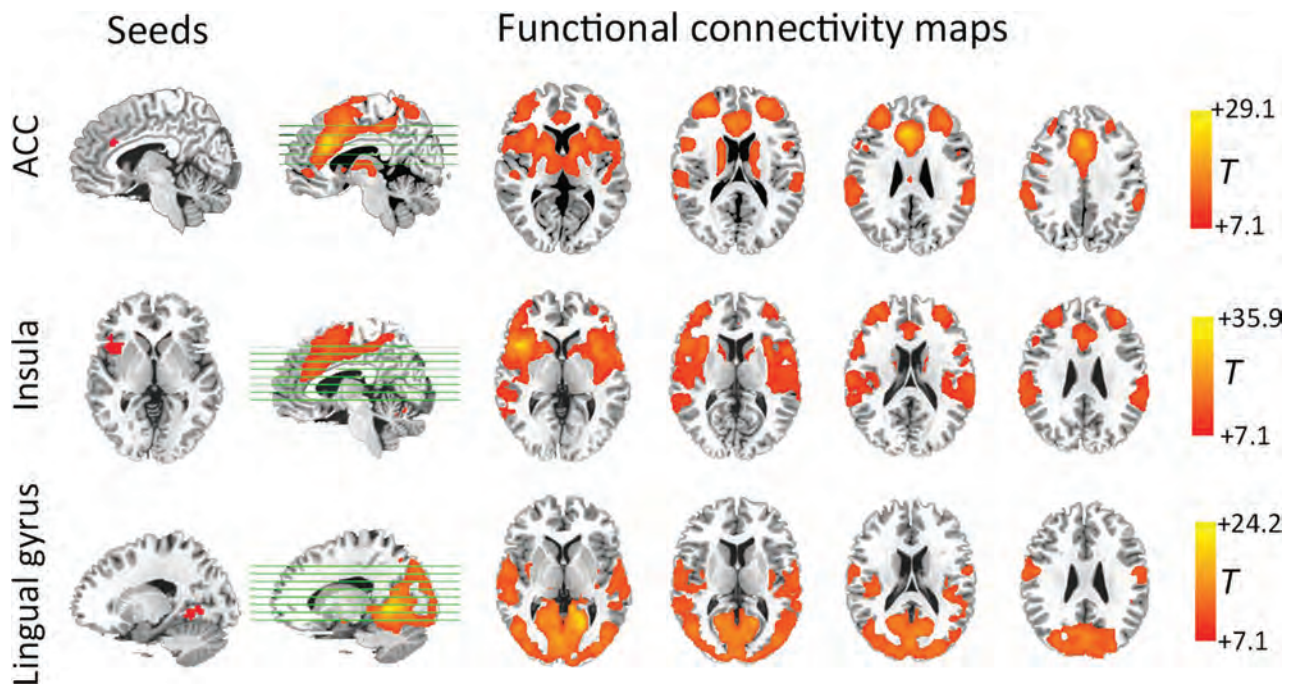


**FIG 3.** Spatial pattern of the network anchored in the regions with altered DC ( $P < .05$ , family-wise error-corrected). The dACC and right anterior insula (AI) exhibit similar connectivity patterns, which are largely included in the salience network. Specifically, the dACC is connected to the cingulate cortex, anterior insula, and sensorimotor cortex (first row). The AI is functionally connected to the entire insula, dACC, and adjacent frontal, temporal, and sensorimotor areas (second row). The lingual gyrus is mainly connected to the visual cortex and adjacent superior middle temporal and sensorimotor cortices (third row). The color scale denotes the  $t$ -value.

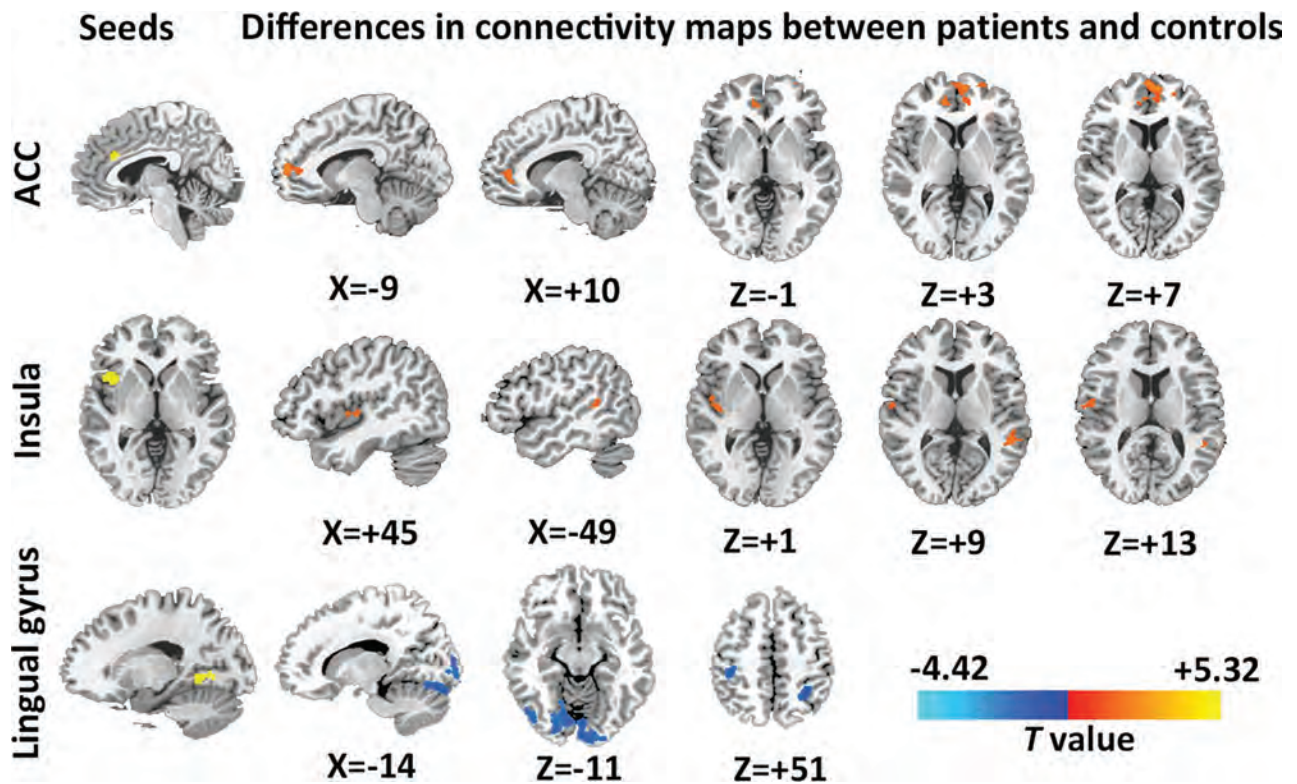


**FIG 4.** Group differences of network connectivity based on the seed regions identified in the DC comparison ( $P < .05$ , AlphaSim-corrected). Regions with significant connectivity differences in networks anchored in hubs with altered DC (ie, dACC, anterior insula [AI], and lingual gyrus). In dACC-relevant network, increased connectivity was found in the medial prefrontal cortex (first row); in the AI-relevant network, increased connectivity was mainly located in the right insula and left superior temporal gyrus (second row). In the lingual gyrus-relevant network, decreased connectivity was diffusely distributed in the visual cortex and the sensory area and superior parietal lobule (third row). Coordinates are all in Montreal Neurological Institute space. The color bar denotes the  $t$ -value.

circuits anchored in these regions were also affected, which was correlated with altered neurocognitive performance, suggesting that brain connectivity might be a potential imaging marker for T2DM-associated cognitive impairment.

Decreased DC and within-network connectivity were observed in the lingual gyrus. Consistent with these results, previous imaging studies on patients with T2DM have also reported occipital alterations. For example, the occipital lobe has been shown to have not only impaired cerebrovascular reactivity but also decreased overall volume.<sup>26,27</sup> Studies on a similar diabetic population also reported a decrease in neural intensity and coherence around the lingual gyrus.<sup>28,29</sup> The lingual gyrus and its associated occipital regions are linked to processing vision-related information and encoding visual memories.<sup>30</sup> Given the positive correlations of occipital connectivity with visual memory and executive performance demonstrated in the current results, we suggest that decreased occipital connectivity might play an important role in the reduced performance in vision-dependent tasks in patients with T2DM. However, due to the small sample size and the lack of visual measurements, it is difficult to determine whether the hypoconnectivity is a neural alteration before or is a reflection of reduced visual input induced by potential diabetic retinopathy. Future studies are warranted to clarify the underlying neuropathology of these findings.

In the T2DM group, increased DC was observed in 2 critical brain hubs, the right anterior insula and dACC. Moreover, the connectivity of the networks anchored in these 2 regions was also

elevated. The right anterior insula and dACC have strong reciprocal connectivity, forming the core of the salience network, which facilitates higher order cognitive control and behavioral adaption via the “bottom-up” signal detection and the “top-down” transmission of control signals.<sup>31</sup> Although cognitive functions are often affected in patients with T2DM, the effect sizes are smaller in middle-aged adults compared with the effects in those older than 65 years.<sup>2</sup> This finding is probably due to a greater brain reserve capacity in younger subjects, reflected by an increased neuronal interconnection.<sup>32</sup> Moreover, longer diabetes duration in elder patients is often associated with a higher prevalence and severity of diabetic complications and comorbidities, which may further contribute to the worsening of cognitive function. Therefore, the increased connectivity in hub regions probably represents a compensatory mechanism in the younger diabetic population, in cases in which more neural resources were required to successfully accomplish relevant tasks. Our results showing a significant correlation between dACC hyperconnectivity and executive performance in the TMT-B task may also support such an assumption. However, whether this compensatory role ceases to be effective in elderly populations needs to be examined in future studies.

Previous fMRI studies primarily focused on the changes within the default mode network, attentional network, and thalamocortical connections have also identified differences in FC between patients with T2DM and HCs.<sup>6-8,10,11</sup> Unlike the seed-based analysis or independent component analysis, the graph the-

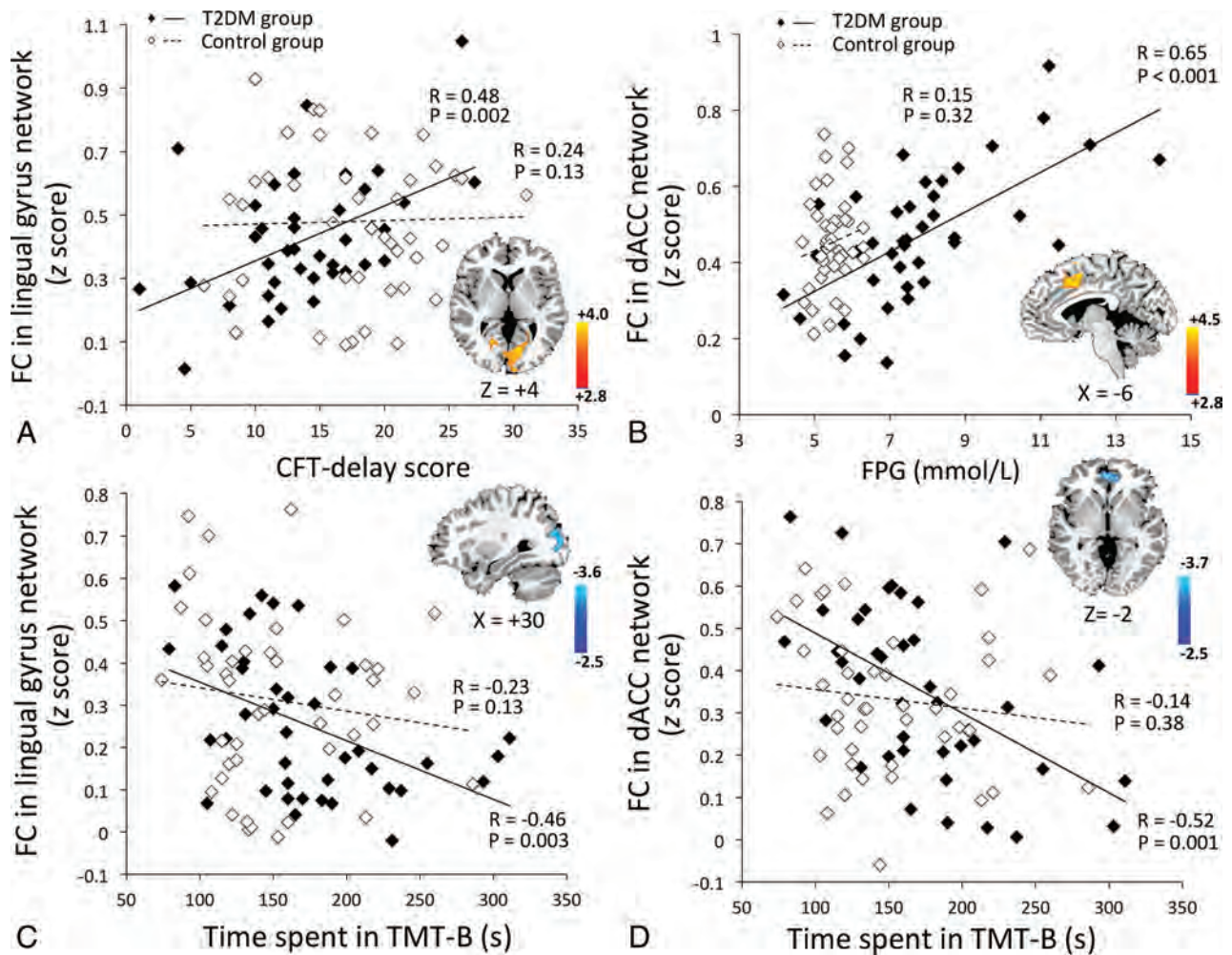


**FIG 5.** Voxelwise correlation between network connectivity (z score) and clinical variables. Correlations in the T2DM group are represented by *black diamonds*, while correlations in the control group are represented by *white diamonds*. The T2DM group: A, CFT-delay performance was positively correlated with the occipital connectivity in the lingual gyrus–relevant network (group  $\times$  performance interaction,  $P = .001$ ). B, FPG was positively correlated with the connectivity of dACC–relevant network, especially in the medial frontal cortex (group  $\times$  FPG interaction,  $P = .001$ ). C and D, Longer time spent on TMT-B was correlated with lower connectivity in the lingual gyrus–relevant network (C, group  $\times$  performance interaction,  $P = .87$ ) and lower connectivity in dACC–relevant network (D, group  $\times$  performance interaction,  $P = .04$ ). No such correlations were observed in the control group.

ory–based approach adopted in the current study takes into account the entire functional connectome instead of relying on a priori seeds or blind source separation.<sup>13</sup> The discrepancies in the methods used and the brain regions observed might be the cause of the differences in the findings between the current study and previous studies. In addition, our results suggest more prominent alterations in the occipital and salience network–related regions in relation to whole-brain functional interactions. Nevertheless, such results remain to be confirmed by future studies with a larger sample size.

As in many cross-sectional clinical studies, the current study has several limitations in addition to the relatively small sample size. First, the medications and the duration of diabetes of the included patients were quite variable, which could exert confounding effects on the DC measurement. Treatment-naïve patients from a narrower disease-duration range should be recruited in future studies. Second, we did not adjust for visual acuity during the vision-dependent cognitive tasks. The inclusion of such measurements is crucial for understanding potential impairment

of occipital connectivity, and this should be considered in future studies. Third, a questionnaire was used to confirm the state of the subjects during MR imaging. More objective and rigorous methods, such as visual fixation on a screen, should be performed to avoid such confounding effects. Finally, other FC measurements, such as dynamic and Granger causality connectivity, should be included to obtain more comprehensive information about the network changes in patients with T2DM.

## CONCLUSIONS

This preliminary study suggests that in patients with T2DM, the connectivity density is altered in several brain regions. Decreased DC was primarily found in the occipital lobe, which was correlated with impaired visual memory and executive performance. Hyperconnectivity was found in key nodes (dACC and anterior insula) of the salience network, which is responsible for higher order cognitive control, and this was correlated with better executive performance. The current results suggest the importance of network connectivity as a potential imaging marker of cognitive



decline in T2DM and may provide valuable insight into the neuropathologic process of T2DM-related brain alterations.

## ACKNOWLEDGMENTS

We thank Shaohua Wang and Dr Wenqing Xia, Department of Endocrinology, Affiliated Zhongda Hospital of Southeast University, for their assistance with the data collection.

Disclosures: Yihong Yang—*RELATED: Other:* Intramural Research Program of the National Institute on Drug Abuse, *Comments:* Yihong Yang is an employee of the Intramural Research Program of the National Institute on Drug Abuse, the National Institutes of Health.

## REFERENCES

1. Geijselaers SL, Sep SJ, Stehouwer CD, et al. **Glucose regulation, cognition, and brain MRI in type 2 diabetes: a systematic review.** *Lancet Diabetes Endocrinol* 2015;3:75–89 CrossRef Medline
2. Biessels GJ, Deary IJ, Ryan CM. **Cognition and diabetes: a lifespan perspective.** *Lancet Neurol* 2008;7:184–90 CrossRef Medline
3. Roberts RO, Knopman DS, Przybelski SA, et al. **Association of type 2 diabetes with brain atrophy and cognitive impairment.** *Neurology* 2014;82:1132–41 CrossRef Medline
4. van den Heuvel MP, Hulshoff Pol HE. **Exploring the brain network: a review on resting-state fMRI functional connectivity.** *Eur Neuropsychopharmacol* 2010;20:519–34 CrossRef Medline
5. Sheline YI, Raichle ME. **Resting state functional connectivity in preclinical Alzheimer's disease.** *Biol Psychiatry* 2013;74:340–47 CrossRef Medline
6. Zhou H, Lu W, Shi Y, et al. **Impairments in cognition and resting-state connectivity of the hippocampus in elderly subjects with type 2 diabetes.** *Neurosci Lett* 2010;473:5–10 CrossRef Medline
7. Chen YC, Xia W, Qian C, et al. **Thalamic resting-state functional connectivity: disruption in patients with type 2 diabetes.** *Metab Brain Dis* 2015;30:1227–36 CrossRef Medline
8. Musen G, Jacobson AM, Bolo NR, et al. **Resting-state brain functional connectivity is altered in type 2 diabetes.** *Diabetes* 2012;61:2375–79 CrossRef Medline
9. Hoogenboom WS, Marder TJ, Flores VL, et al. **Cerebral white matter integrity and resting-state functional connectivity in middle-aged patients with type 2 diabetes.** *Diabetes* 2014;63:728–38 CrossRef Medline
10. Cui Y, Jiao Y, Chen HJ, et al. **Aberrant functional connectivity of default-mode network in type 2 diabetes patients.** *Eur Radiol* 2015;25:3238–46 CrossRef Medline
11. Xia W, Wang S, Rao H, et al. **Disrupted resting-state attentional networks in T2DM patients.** *Sci Rep* 2015;5:11148 CrossRef Medline
12. Nelson PT, Smith CD, Abner EA, et al. **Human cerebral neuropathology of type 2 diabetes mellitus.** *Biochim Biophys Acta* 2009;1792:454–69 CrossRef Medline
13. Zuo XN, Ehmke R, Mennes M, et al. **Network centrality in the human functional connectome.** *Cereb Cortex* 2012;22:1862–75 CrossRef Medline
14. Liang X, Zou Q, He Y, et al. **Coupling of functional connectivity and regional cerebral blood flow reveals a physiological basis for network hubs of the human brain.** *Proc Natl Acad Sci U S A* 2013;110:1929–34 CrossRef Medline
15. Buckner RL, Sepulcre J, Talukdar T, et al. **Cortical hubs revealed by intrinsic functional connectivity: mapping, assessment of stability, and relation to Alzheimer's disease.** *J Neurosci* 2009;29:1860–73 CrossRef Medline
16. Di Martino A, Zuo XN, Kelly C, et al. **Shared and distinct intrinsic functional network centrality in autism and attention-deficit/hyperactivity disorder.** *Biol Psychiatry* 2013;74:623–32 CrossRef Medline
17. Rubinov M, Knock SA, Stam CJ, et al. **Small-world properties of nonlinear brain activity in schizophrenia.** *Hum Brain Mapp* 2009;30:403–16 CrossRef Medline
18. Galea M, Woodward M. **Mini-Mental State Examination (MMSE).** *Aust J Physiother* 2005;51:198 CrossRef Medline
19. Hamilton M. **A rating scale for depression.** *J Neurol Neurosurg Psychiatry* 1960;23:56–62 CrossRef Medline
20. American Diabetes Association. **Diagnosis and classification of diabetes mellitus.** *Diabetes Care* 2014;37(suppl 1):S81–90 CrossRef Medline
21. van den Berg E, Reijmer YD, de Bresser J, et al; Utrecht Diabetic Encephalopathy Study Group. **A 4 year follow-up study of cognitive functioning in patients with type 2 diabetes mellitus.** *Diabetologia* 2010;53:58–65 CrossRef Medline
22. Matthews DR, Hosker JP, Rudenski AS, et al. **Homeostasis model assessment: insulin resistance and beta-cell function from fasting plasma glucose and insulin concentrations in man.** *Diabetologia* 1985;28:412–19 CrossRef Medline
23. Wahlund LO, Barkhof F, Fazekas F, et al; European Task Force on Age-Related White Matter Changes. **A new rating scale for age-related white matter changes applicable to MRI and CT.** *Stroke* 2001;32:1318–22 CrossRef Medline
24. Jenkinson M, Bannister P, Brady M, et al. **Improved optimization for the robust and accurate linear registration and motion correction of brain images.** *Neuroimage* 2002;17:825–41 CrossRef Medline
25. Cox RW. **AFNI: software for analysis and visualization of functional magnetic resonance neuroimages.** *Comput Biomed Res* 1996;29:162–73 CrossRef Medline
26. Tchistiakova E, Anderson ND, Greenwood CE, et al. **Combined effects of type 2 diabetes and hypertension associated with cortical thinning and impaired cerebrovascular reactivity relative to hypertension alone in older adults.** *Neuroimage Clin* 2014;5:36–41 CrossRef Medline
27. Espeland MA, Bryan RN, Goveas JS, et al; WHIMS-MRI Study Group. **Influence of type 2 diabetes on brain volumes and changes in brain volumes: results from the women's health initiative magnetic resonance imaging studies.** *Diabetes Care* 2013;36:90–97 CrossRef Medline
28. Cui Y, Jiao Y, Chen YC, et al. **Altered spontaneous brain activity in type 2 diabetes: a resting-state functional MRI study.** *Diabetes* 2014;63:749–60 CrossRef
29. Chen YC, Jiao Y, Cui Y, et al. **Aberrant brain functional connectivity related to insulin resistance in type 2 diabetes: a resting-state fMRI study.** *Diabetes Care* 2014;37:1689–96 CrossRef Medline
30. Machielsen WC, Rombouts SA, Barkhof F, et al. **fMRI of visual encoding: reproducibility of activation.** *Hum Brain Mapp* 2000;9:156–64 Medline
31. Ham T, Leff A, de Boissezon X, et al. **Cognitive control and the salience network: an investigation of error processing and effective connectivity.** *J Neurosci* 2013;33:7091–98 CrossRef Medline
32. Mortimer JA. **Brain reserve and the clinical expression of Alzheimer's disease.** *Geriatrics* 1997;52(suppl 2):S50–53 Medline

# Orbital Fat Volumetry and Water Fraction Measurements Using T2-Weighted FSE-IDEAL Imaging in Patients with Thyroid-Associated Orbitopathy

Y. Kaichi, K. Tanitame, H. Itakura, H. Ohno, M. Yoneda, Y. Takahashi, Y. Akiyama, and K. Awai

## ABSTRACT

**BACKGROUND AND PURPOSE:** The quantitative evaluation of orbital fat proliferation and edema and the assessment of extraocular muscles are useful for diagnosing and monitoring thyroid-associated orbitopathy. To evaluate therapy-induced quantitative changes in the orbital fat of patients with thyroid-associated orbitopathy, we performed volumetric and water fraction measurements by using T2-weighted FSE iterative decomposition of water and fat with echo asymmetry and least-squares estimation (FSE-IDEAL) imaging.

**MATERIALS AND METHODS:** Orbital FSE-IDEAL images of 30 volunteers were acquired twice within 1 week. Nine patients with thyroid-associated orbitopathy underwent FSE-IDEAL imaging before and after methylprednisolone pulse therapy, and the treatment results were assessed by using their pre- and post-methylprednisolone pulse therapy clinical activity scores. We performed volumetric and water fraction measurements of orbital fat by using FSE-IDEAL imaging and evaluated interscan differences in the volunteers. In patients with thyroid-associated orbitopathy, we compared pre- and posttherapy orbital fat measurements and assessed the correlation between the pretherapy values and clinical activity score improvement.

**RESULTS:** The reproducibility of results obtained by the quantitative evaluation of orbital fat in volunteers was acceptable. After methylprednisolone pulse therapy, the water fraction in the orbital fat of patients with thyroid-associated orbitopathy was significantly decreased ( $P < .001$ ). There was a significant positive correlation between the pretherapy water fraction and clinical activity score improvement (right,  $r = 0.82$ ; left,  $r = 0.79$ ) and a significant negative correlation between the pretherapy volume and clinical activity score improvement (bilateral,  $r = -0.84$ ).

**CONCLUSIONS:** Volumetric and water fraction measurements of orbital fat by using FSE-IDEAL imaging are feasible and useful for monitoring the effects of therapy and for predicting the response of patients with thyroid-associated orbitopathy to methylprednisolone pulse therapy.

**ABBREVIATIONS:** CAS = clinical activity score; FSE-IDEAL = FSE iterative decomposition of water and fat with echo asymmetry and least-squares estimation; MPPT = methylprednisolone pulse therapy; SI = signal intensity; TAO = thyroid-associated orbitopathy

Thyroid-associated orbitopathy (TAO) is the most common extrathyroid manifestation of Graves disease. The enlargement of orbital fat and extraocular muscles in the relatively fixed volume space imposed by the bony orbit may produce proptosis, ocular motility loss, and decreased visual acuity.<sup>1</sup> Histologic studies showed lymphocytic infiltration and edema due to the accu-

mulation of hydrophilic, interstitial glycosaminoglycans in the orbital fat and extraocular muscles,<sup>2,3</sup> attributable to antigenic cross-reactivity between thyroid proteins and orbital fibroblasts.<sup>4</sup>

The course of TAO can be divided into the active, regressing, and a burnt-out phase.<sup>5</sup> Early active disease is treated with combined immunosuppression.<sup>6,7</sup> The identification of patients who stand to benefit from this therapy is important but clinically difficult, despite the availability of activity scoring systems. Consequently, objective methods are needed.

CT has been used to quantify the volume of extraocular muscles and orbital fat in TAO.<sup>8-11</sup> However, ocular radiation exposure limits its clinical use. Because MR imaging without ionizing radiation yields orbital images with excellent soft-tissue contrast in any plane, it has been used for evaluating TAO.<sup>12-15</sup>

The quantitative evaluation of the orbital fat volume on T1-weighted images was reported useful for assessing the severity of TAO and for monitoring the treatment response.<sup>12,16</sup> Recently,

Received January 28, 2016; accepted after revision May 8.

From the Department of Diagnostic Radiology (Y.K., K.A.), Graduate School and Institute of Biomedical and Health Sciences, Hiroshima University, Hiroshima, Japan; Department of Radiology (K.T.), Chugoku Rosai Hospital, Kure, Japan; Department of Ophthalmology and Visual Science (H.I.) and Department of Molecular and Internal Medicine (H.O., M.Y.), Institute of Biomedical and Health Sciences, Hiroshima University, Hiroshima, Japan; and Department of Clinical Radiology (Y.T., Y.A.), Hiroshima University Hospital, Hiroshima, Japan.

Please address correspondence to Yoko Kaichi, MD, Diagnostic Radiology, Graduate School of Biomedical and Health Sciences, Hiroshima University, Kasumi 1-2-3, Minami-ku, Hiroshima 734-8551, Japan; e-mail: kaichi@hiroshima-u.ac.jp

<http://dx.doi.org/10.3174/ajnr.A4859>

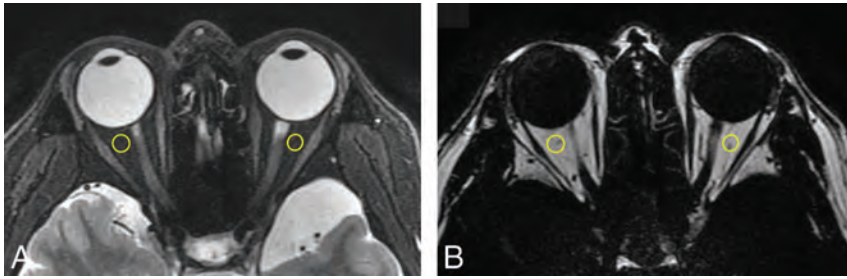


**FIG 1.** Axial water (A) and fat (B) images of a healthy volunteer. The ROIs are encircled in yellow.

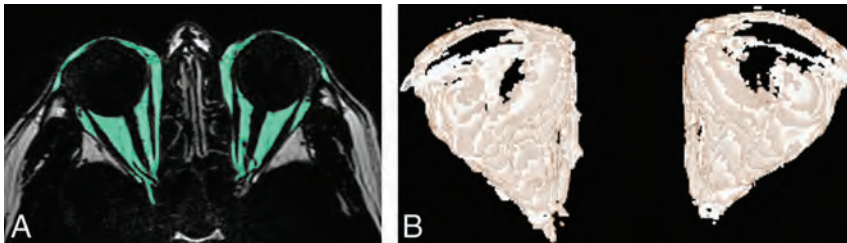


**FIG 2.** Axial fat image (A) of a healthy volunteer. The selected orbital fat is light green. We separated fat tissue by using an adequate signal-intensity threshold and manually removed extraorbital fat. In this volunteer, the internal rectus muscle showed an average SI of 207 and an SD of 112, whereas the orbital fat showed an average SI of 1636 and an SD of 88. Therefore the threshold value was  $[(207 + 112) + (1636 - 88) / 2 = 933]$ . Using FSE-IDEAL images, we then produced 3D reconstruction images of the bilateral orbital fat (B) and measured the orbital fat volume on a workstation.

Higashiyama et al<sup>17</sup> demonstrated that after methylprednisolone pulse therapy (MPPT), the orbital fat volume was unchanged, while the total volume of extraocular muscles was decreased on T2-weighted images. However, in our search of the literature, we found no reports on quantitative changes in orbital fat edema after MPPT or orbital irradiation. Consequently, the correlation between the volume and edema of orbital fat and the treatment response of patients with TAO remains to be elucidated.

FSE iterative decomposition of water and fat with echo asymmetry and least-squares estimation (FSE-IDEAL), a novel 3-point Dixon method, is useful for separating the fat signal from the water signal<sup>18,19</sup> but has not been used to quantify the orbital structures in TAO. To evaluate the feasibility of FSE-IDEAL imaging for the precise quantitative evaluation of orbital fat, we subjected healthy volunteers to 2 FSE-IDEAL imaging studies performed during 1 week. We measured the volume and the water fraction of their orbital fat and ascertained the reproducibility of the measurement results. We also acquired FSE-IDEAL images in patients with TAO to assess MPPT-induced changes in the volume and water fraction of their orbital fat and evaluated the correlation between the quantitative values of orbital fat and the improvement in their symptoms.

## MATERIALS AND METHODS

### Subjects

This prospective study was approved by the Ethics Committee of Hiroshima University. Informed consent was obtained from all participants before entry into the study.

We recruited 30 healthy volunteers (15 men, 15 women; median age,  $29 \pm 7.6$  years). They underwent orbital FSE-IDEAL imaging twice within 1 week to evaluate the reproducibility of the water fraction and the volume measurements of the orbital fat.

We also recruited 16 patients older than 20 years of age who had a clinical diagnosis of TAO between December 2013 and November 2015. The recorded activity of their TAO was based on their clinical activity score (CAS), including pain, eyelid erythema or edema, conjunctival hyperemia and chemosis, and a swollen caruncle.<sup>20</sup> All 16 patients underwent orbital FSE-IDEAL imaging. Two of them underwent local injection of triamcinolone acetonide into the orbit, and 5 of them followed a conservative wait-and-see approach because their TAO was slight and the risk of MPPT would exceed the benefit. Consequently, the 9 patients (2 men, 7 women; median age,  $57 \pm 12.5$  years; 18 eyes) who received MPPT (500 mg of methylprednisolone administered intravenously once a day for 3 consecutive days) were included in this study and underwent FSE-IDEAL imaging again  $1.6 \pm 0.7$  months thereafter. Re-evaluation of the TAO activity was based on the latest CAS obtained around the time of

the second MR imaging study (the interval, 1–15 days; median, 6.5 days).

### MR Imaging

All images were acquired on a 3T scanner (Signa Excite HD 3.0; GE Healthcare, Milwaukee, Wisconsin; gradient strength, 40 mT/m; slew rate, 150 T/m/s) by using an 8-channel phased array brain coil. We optimized the T2-weighted FSE-IDEAL sequence (TR/TE, 6000/100 ms; flip angle, 90°; image matrix,  $288 \times 160$ ; FOV,  $160 \times 160$  mm; section thickness/gap, 2/0 mm; asymmetric echo shifts,  $-\pi/6, \pi/2, 7\pi/6$ ; number of acquisitions, 3; number of sections, 32; scan time, 2 minutes 42 seconds) and obtained orbital water and fat images for all subjects.

### Orbital Fat Water Fraction and Volume Measurements

We placed an ROI in the orbital fat on FSE-IDEAL images of water and fat and measured the average signal intensity (SI) in the ROIs. Next, we defined and calculated the water fraction of the orbital fat as  $[SI \text{ Water} / (SI \text{ Water} + SI \text{ Fat})]$  to assess the orbital fat edema on the basis of the fat fraction  $(SI \text{ Fat} / [SI \text{ Water} + SI \text{ Fat}])$ ,<sup>18</sup> defined to quantify fatty infiltration (Fig 1). The orbital fat volume of both eyes was measured on a workstation (Virtual Place Raijin; AZE Ltd, Tokyo, Japan). We first separated fat tissue from other structures by using the threshold value, recorded as the mean value between the average SI plus the SD of the ROI in the internal rectus muscle and the average SI minus the SD of the ROI in the orbital fat, considering some dispersion of signal intensities in the ROIs. Then we manually removed the fatty marrow of the orbital bone and outer fat; the orbital fat volume was automatically measured on the workstation (Fig 2).

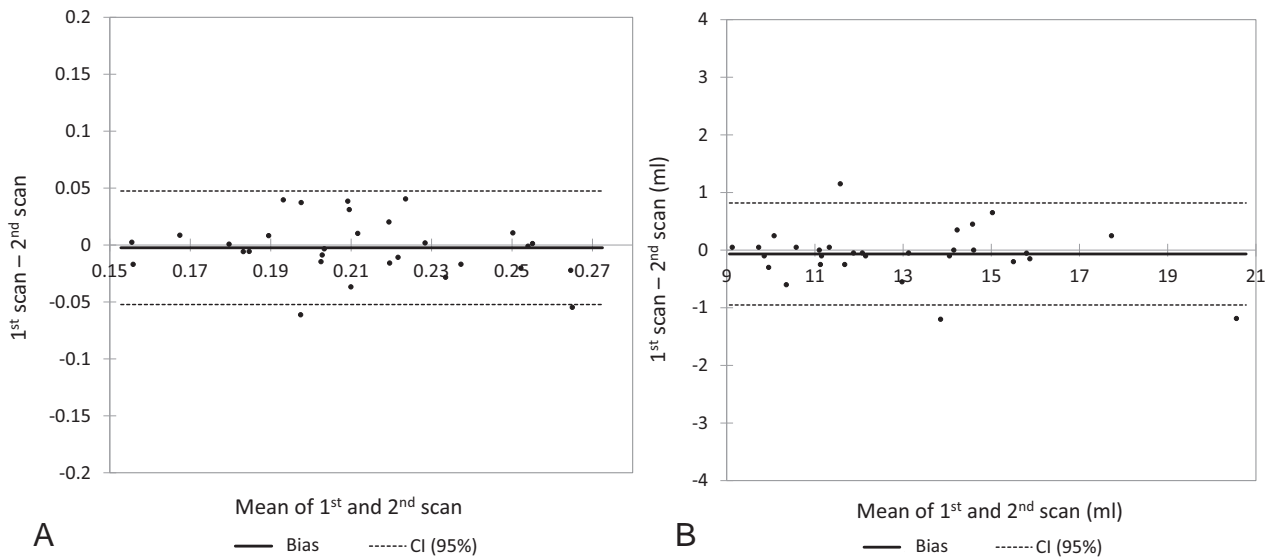


**FIG 3.** Bland-Altman analysis confirming the interscan reproducibility of the water fraction (A) and the volume of orbital fat (B) on FSE-IDEAL images of the volunteers.

### Statistical Analyses

All statistical analyses were performed with commercially available software (XLSTAT, version 2015.6.01.244, Addinsoft; <https://www.xlstat.com/en/company/about-us>) and Excel 2010 (Microsoft, Redmond, Washington).

We used Bland-Altman analysis and the Pearson correlation coefficient to evaluate interscan differences in the volunteers and used the mean value of the water fraction and the volume of the bilateral orbit in our analyses.

In patients with TAO, we performed paired-sample *t* tests to compare the water fraction and the volume of orbital fat before and after MPPT. The right and left orbits were examined separately because patients with unilateral TAO manifested unilateral excess fat exophthalmos.<sup>10</sup> To ascertain that the values obtained before and after treatment were significantly different, we applied the 2-sample *t* test to compare the therapy-induced changes with the values obtained in the volunteers. We defined the therapeutic effect of MPPT as the following formula: [CAS Improvement Ratio = (Pretherapy CAS – Posttherapy CAS) / Pretherapy CAS] and determined the correlation between the measured values before MPPT and the CAS improvement ratio with the Pearson correlation coefficient test. Differences of  $P < .05$  were considered statistically significant.

## RESULTS

### Volunteers

The difference in the water fraction and the volume of orbital fat on the first and second scans was  $1.1\% \pm 11.9\%$  and  $0.5\% \pm 3.6\%$ , respectively. Bland-Altman analysis of the measurement results showed that their reproducibility was adequate (water fraction:  $r = 0.71$ , bias =  $-0.002$ ; 95% CI bias,  $-0.012$ – $0.007$ ; 95% CI,  $-0.052$ – $0.047$ ; volume:  $r = 0.99$ , bias =  $-0.066$ ; 95% CI bias,  $-0.235$ – $0.102$ ; 95% CI,  $-0.951$ – $0.819$ ) (Fig 3).

### Patients

The clinical characteristics of the 9 patients with TAO are summarized in the Table. After MPPT, the water fraction in the orbital fat on both sides was significantly decreased (right,

### Patient profiles

Characteristics	
Median age (yr) (range)	57 (43–82)
Sex: male/female	2/7
Median duration of the treatment for GD (mo) (range)	11 (1–168)
Median duration from the onset of TAO (mo) (range)	4 (1–8)
Smoking: yes/no	3/6
Median pretherapy CAS (range)	2 (1–4)
Involvement of extraocular muscle: yes/no	7/2

**Note:**—GD indicates Graves disease.

$12.4\% \pm 3.8\%$ ,  $P < .001$ ; left,  $13.6\% \pm 6.5\%$ ,  $P < .001$ ; Fig 4A). The treatment-induced reduction in the water fraction was significantly larger than the interscan difference observed in the volunteers (right,  $P = .002$ ; left,  $P = .001$ ). There was no significant difference in the orbital fat volume pre- and posttreatment (right,  $2.0\% \pm 7.8\%$ ,  $P = .37$ ; left,  $1.9\% \pm 3.8\%$ ,  $P = .17$ , Fig 4B).

The pre- and posttreatment CAS fell by 3 points in 2 patients, by 2 points in 1 patient, and by 1 point in 3 patients. In the other 3, there was no change. The positive correlation between the pretreatment water fraction and the CAS improvement rate (right,  $r = 0.82$ ,  $P = .007$ ; left,  $r = 0.79$ ,  $P = .012$ ) showed that the higher the pretreatment water fraction, the greater was the posttreatment CAS improvement. On the other hand, there was a negative correlation between the fat volume and CAS improvement (right,  $r = -0.84$ ,  $P = .005$ ; left,  $r = -0.84$ ,  $P = .005$ ), indicating that the larger the pretreatment orbital fat volume, the lower the posttreatment CAS improvement rate.

## DISCUSSION

To the best of our knowledge, this is the first quantitative evaluation of orbital fat by using FSE-IDEAL imaging. We document an MPPT-induced reduction in the water fraction of orbital fat in patients with TAO and report the positive correlation between the pretreatment water fraction and the

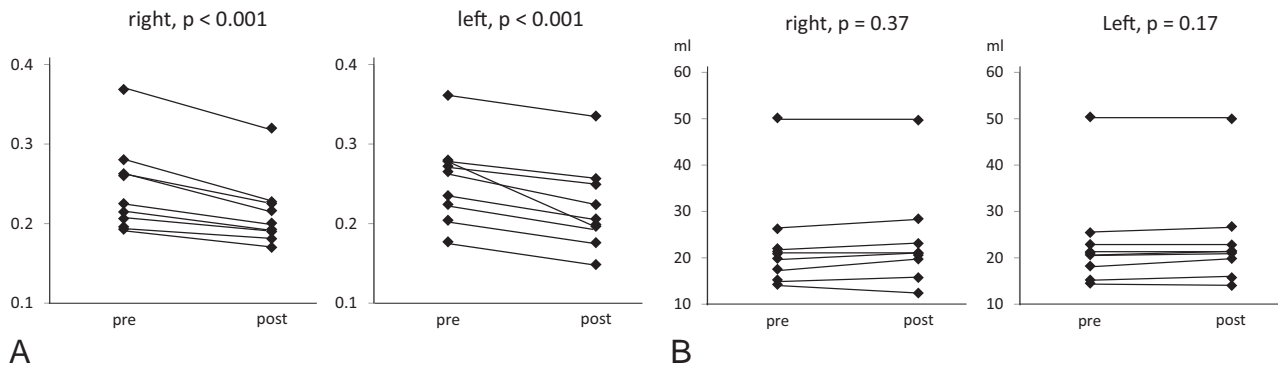


**FIG 4.** Comparison of the pre- and posttreatment water fraction (A) and the volume of orbital fat (B) in patients with TAO. Methylprednisolone pulse therapy significantly decreased the water fraction. The volume was unchanged.

CAS improvement rate and the negative correlation between the pretreatment orbital fat volume and the CAS improvement rate.

We used FSE-IDEAL imaging to acquire axial images of the bilateral orbits and measured the water fraction and the volume of orbital fat in healthy volunteers and patients with TAO. Although many images contained motion artifacts due to voluntary and involuntary eye movements, it was possible to differentiate the SI of orbital fat and other intraorbital structures by applying an adequate threshold in the orbital fat volumetry. To measure the water fraction in orbital fat, we placed ROIs on the intraorbital fat; measurement of the SI was not hampered by motion artifacts. The reproducibility of water fraction and fat volume measurements on all iteratively acquired FSE-IDEAL images was sufficient.

Others<sup>12,21</sup> used a 1.5T MR imaging scanner and a receiver surface coil to measure orbital fat volumes. Although surface coils can yield orbital images with high spatial resolution, the signal strength decreases as the distance from the coil increases. Our use of a 3T MR imaging scanner and an 8-channel brain coil resulted in orbital images with a high enough signal-to-noise ratio for the estimation of the orbital fat volume and the water fraction.

Orbital images with high spatial and temporal resolution and fewer motion artifacts due to eye movement can be acquired on multidetector row CT scanners.<sup>11</sup> However, the low soft-tissue contrast on multidetector row CT images makes it difficult to separate out orbital fat. In addition, ocular radiation exposure is a serious concern. Therefore, MR imaging with high soft-tissue contrast is safer for orbital imaging.

We found that MPPT reduced the water fraction in the orbital fat of patients with TAO, possibly because it decreased the severity of edema. Earlier studies<sup>7,22-25</sup> reported that the SI of extraocular muscles on short  $\tau$  inversion recovery sequences correlated well with the disease activity assessed with clinical methods. The correlation was maintained as disease activity changed. Although the reversibility of the relaxation time in muscles with prolonged T2 values was explained as a therapy-induced decrease in the water content,<sup>8</sup> treatment-induced changes in orbital fat have not been documented.

Like Higashiyama et al,<sup>17</sup> we detected no significant difference in the pre- and posttreatment orbital fat volume. Others<sup>26-28</sup>

found no difference in the degree of exophthalmos, which is related to an increase in orbital fat, in patients with TAO who had undergone MPPT. Expansion of the adipose tissue volume is elicited by glycosaminoglycan-related edema and the emergence of a population of newly differentiated fat cells in these tissues.<sup>29</sup> Although MPPT can reduce orbital fat edema, the increase in the number of fat cells may persist after therapy.

In Japan, MPPT is generally applied in patients with TAO with low CAS scores because the Japanese patients with TAO often have orbital inflammation despite low CAS scores.<sup>30</sup> We found that the higher the pretreatment water fraction, the greater the posttreatment decrease in the CAS, despite the low pretreatment CAS scores of our study patients. An increase in the water fraction is indicative of an increase in the tissue water content and may reflect acute inflammatory changes. Earlier studies on extraocular muscles found a correlation between the SI increase on pretreatment STIR images and a good therapeutic response<sup>31-33</sup> and between prolonged pretreatment T2 values and a good response to systemic corticosteroids or orbital radiation therapy.<sup>33</sup> These findings indicate that treatment at an early and immunologically active stage of orbitopathy is important.<sup>11,34,35</sup> Our quantitative MR imaging study by using the FSE-IDEAL sequence showed that MPPT was useful in patients with TAO whose orbital fat contained an elevated water fraction. On the other hand, the larger the pretreatment orbital fat volume, the lower the posttreatment CAS improvement rate. Because a longer duration of TAO is associated with a larger orbital fat mass and fibrosis,<sup>36</sup> we think that a response to steroids is less likely when the disease is in its late, inactive stage with more fibrosis.<sup>33,34</sup>

Our study has several limitations. The number of patients with TAO who underwent MPPT was small, and the lack of age-matched controls limits the comparison between patients with TAO and healthy individuals. In addition, we used the T2-weighted FSE-IDEAL sequence provided by GE Healthcare. It is a novel, 3-point Dixon method that applies iterative algorithms and the region-growing technique to estimate local field inhomogeneities.<sup>37-39</sup> Application of the 3-point Dixon method developed by different vendors may result in significantly different measurement results with respect to the water fraction of orbital fat. In addition, the demarcation between orbital and upper or lower

eyelid fat is ambiguous, and this feature may introduce some interobserver variability in the orbital fat volume. Last, the correct cutoff value for the water fraction and the volume of the orbital fat between patients with TAO and their controls remains to be determined.

## CONCLUSIONS

The estimation of the water fraction and the volume of orbital fat on FSE-IDEAL images is feasible, and the reproducibility of these measurements is adequate. FSE-IDEAL imaging is useful for monitoring the effects of therapy and for predicting the response of patients with TAO to methylprednisolone pulse therapy.

Disclosures: Kazuo Awai—UNRELATED: Consultancy: GE Healthcare; Grants/Grants Pending: Toshiba Medical Systems,\* Hitachi Medical Corporation,\* Bayer Yakuin,\* Eisai,\* Daiichi Sankyo,\* Comments: research grants. \*Money paid to the institution.

## REFERENCES

- Kendler DL, Lipka J, Rootman J. **The initial clinical characteristics of Graves' orbitopathy vary with age and sex.** *Arch Ophthalmol* 1993; 111:197–201 CrossRef Medline
- Winand RJ, Cornet G, Etienne-Decerf J, et al. **Original acquisition in the pathogenesis and the treatment of endocrine ophthalmopathy.** *Metab Pediatr Syst Ophthalmol* 1988;11:126–32 Medline
- Kahaly G, Hansen C, Beyer J, et al. **Plasma glycosaminoglycans in endocrine ophthalmopathy.** *J Endocrinol Invest* 1994;17:45–50 CrossRef Medline
- Ludgate M, Baker G. **Unlocking the immunological mechanisms of orbital inflammation in thyroid eye disease.** *Clin Exp Immunol* 2002; 127:193–98 CrossRef Medline
- Rundle FF, Wilson CW. **Development and course of exophthalmos and ophthalmoplegia in Graves' disease with special reference to the effect of thyroidectomy.** *Clin Sci* 1945;5:177–94 Medline
- Claridge KG, Ghabrial R, Davis G, et al. **Combined radiotherapy and medical immunosuppression in the management of thyroid eye disease.** *Eye* 1997;11:717–22 CrossRef Medline
- Mayer EJ, Herdman G, Burnett C, et al. **Serial STIR magnetic resonance imaging correlates with clinical score of activity in thyroid disease.** *Eye* 2001;15:313–18 CrossRef Medline
- Kahaly GJ. **Imaging in thyroid-associated orbitopathy.** *Eur J Endocrinol* 2001;145:107–18 CrossRef Medline
- Feldon SE, Lee CP, Muramatsu SK, et al. **Quantitative computed tomography of Graves' ophthalmopathy: extraocular muscle and orbital fat in development of optic neuropathy.** *Arch Ophthalmol* 1985;103:213–15 CrossRef Medline
- Peyster RG, Ginsberg F, Silber JH, et al. **Exophthalmos caused by excessive fat: CT volumetric analysis and differential diagnosis.** *AJR Am J Roentgenol* 1986;146:459–64 CrossRef Medline
- Fang ZJ, Zhang JY, He WM. **CT features of exophthalmos in Chinese subjects with thyroid-associated ophthalmopathy.** *Int J Ophthalmol* 2013;6:146–49 CrossRef Medline
- Nishida Y, Tian S, Isberg B, et al. **Significance of orbital fatty tissue for exophthalmos in thyroid-associated ophthalmopathy.** *Graefes Arch Clin Exp Ophthalmol* 2002;240:515–20 CrossRef Medline
- Kvetny J, Puhakka KB, Rohl L. **Magnetic resonance imaging determination of extraocular eye muscle volume in patients with thyroid-associated ophthalmopathy and proptosis.** *Acta Ophthalmol Scand* 2006;84:419–23 CrossRef Medline
- Prummel MF, Gerding MN, Zonneveld FW, et al. **The usefulness of quantitative orbital magnetic resonance imaging in Graves' ophthalmopathy.** *Clin Endocrinol (Oxf)* 2001;54:205–09 CrossRef Medline
- Mayer EJ, Fox DL, Herdman G, et al. **Signal intensity, clinical activity and cross-sectional areas on MRI scans in thyroid eye disease.** *Eur J Radiol* 2005;56:20–24 CrossRef Medline
- Comerci M, Elefante A, Strianese D, et al. **Semiautomatic regional segmentation to measure orbital fat volumes in thyroid-associated ophthalmopathy: a validation study.** *Neuroradiol J* 2013;26:373–79 CrossRef Medline
- Higashiyama T, Nishida Y, Ohji M. **Changes of orbital tissue volumes and proptosis in patients with thyroid extraocular muscle swelling after methylprednisolone pulse therapy.** *Jpn J Ophthalmol* 2015;59:430–35 CrossRef Medline
- Hu HH, Kim HW, Nayak KS, et al. **Comparison of fat-water MRI and single-voxel MRS in the assessment of hepatic and pancreatic fat fractions in humans.** *Obesity (Silver Spring)* 2010;18:841–47 CrossRef Medline
- Takasu M, Tani C, Sakoda Y, et al. **Iterative decomposition of water and fat with echo asymmetry and least-squares estimation (IDEAL) imaging of multiple myeloma: initial clinical efficiency results.** *Eur Radiol* 2012;22:1114–21 CrossRef Medline
- Bartalena L, Baldeschi L, Dickinson A, et al; European Group on Graves' Orbitopathy (EUGOGO). **Consensus statement of the European Group on Graves' Orbitopathy (EUGOGO) on management of GO.** *Eur J Endocrinol* 2008;158:273–85 CrossRef Medline
- Tian S, Nishida Y, Isberg B, et al. **MRI measurements of normal extraocular muscles and other orbital structures.** *Graefes Arch Clin Exp Ophthalmol* 2000;238:393–404 CrossRef Medline
- Hoh HB, Laitt RD, Wakely C, et al. **The STIR sequence MRI in the assessment of extraocular muscles in thyroid eye disease.** *Eye* 1994; 8:506–10 CrossRef Medline
- Laitt RD, Hoh B, Wakeley C, et al. **The value of the short tau inversion recovery sequence in magnetic resonance imaging of thyroid eye disease.** *Br J Radiol* 1994;67:244–47 CrossRef Medline
- Bailey CC, Kabala J, Laitt R, et al. **Magnetic resonance imaging in thyroid eye disease.** *Eye* 1996;10:617–19 CrossRef Medline
- Higashiyama T, Nishida Y, Morino K, et al. **Use of MRI signal intensity of extraocular muscles to evaluate methylprednisolone pulse therapy in thyroid-associated ophthalmopathy.** *Jpn J Ophthalmol* 2015;59:124–30 CrossRef Medline
- Bartalena L, Baldeschi L, Dickinson AJ, et al. **Consensus statement of the European Group on Graves' Orbitopathy (EUGOGO) on management of Graves' orbitopathy.** *Thyroid* 2008;18:333–46 CrossRef Medline
- Kauppinen-Mäkelin R, Karma A, Leinonen E, et al. **High dose intravenous methylprednisolone pulse therapy versus oral prednisone for thyroid-associated ophthalmopathy.** *Acta Ophthalmol Scand* 2002;80:316–21 CrossRef Medline
- van Geest RJ, Sasim IV, Koppeschaar HP, et al. **Methylprednisolone pulse therapy for patients with moderately severe Graves' orbitopathy: a prospective, randomized, placebo-controlled study.** *Eur J Endocrinol* 2008;158:229–37 CrossRef Medline
- Bahn RS, Heufelder AE. **Pathogenesis of Graves' ophthalmopathy.** *N Engl J Med* 1993;329:1468–75 CrossRef Medline
- Watanabe N, Noh JY, Kozaki A, et al. **Radioiodine-associated exacerbation of Graves' orbitopathy in the Japanese population: randomized prospective study.** *J Clin Endocrinol Metab* 2015;100: 2700–08 CrossRef Medline
- Hirohata Y, Kojima K, Ishisaka N, et al. **Role of magnetic resonance imaging in thyroid-associated ophthalmopathy: its predictive value for therapeutic outcome of immunosuppressive therapy.** *Thyroid* 1992;2:299–305 CrossRef Medline
- Just M, Kahaly GJ, Higer HP, et al. **Graves ophthalmopathy: role of MR imaging in radiation therapy.** *Radiology* 1991;179:187–90 CrossRef Medline
- Ohnishi T, Noguchi S, Murakami N, et al. **Extraocular muscles in**

- Graves ophthalmopathy: usefulness of T2 relaxation time measurements.** *Radiology* 1994;190:857–62 CrossRef Medline
34. Kendall-Taylor P, Crombie AL, Stephenson AM, et al. **Intravenous methylprednisolone in the treatment of Graves' ophthalmopathy.** *BMJ* 1988;297:1574–78 CrossRef Medline
35. Bartalena L, Marcocci C, Bogazzi F, et al. **Use of corticosteroids to prevent progression of Graves' ophthalmopathy after radioiodine therapy for hyperthyroidism.** *N Engl J Med* 1989;321:1349–52 CrossRef Medline
36. Potgieser PW, Wiersinga WM, Regensburg NI, et al. **Some studies on the natural history of Graves' orbitopathy: increase in orbital fat is a rather late phenomenon.** *Eur J Endocrinol* 2015;173:149–53 CrossRef Medline
37. Costa DN, Pedrosa I, McKenzie C, et al. **Body MRI using IDEAL.** *AJR Am J Roentgenol* 2008;190:1076–84 CrossRef Medline
38. Gerdes CM, Kijowski R, Reeder SB. **IDEAL imaging of the musculoskeletal system: robust water fat separation for uniform fat suppression, marrow evaluation, and cartilage imaging.** *AJR Am J Roentgenol* 2007;189:284–91 Medline
39. Humbert IA, Reeder SB, Porcaro EJ, et al. **Simultaneous estimation of tongue volume and fat fraction using IDEAL-FSE.** *J Magn Reson Imaging* 2008;28:504–08 CrossRef Medline

# Migration of Bone Wax into the Sigmoid Sinus after Posterior Fossa Surgery

K. Byrns, A. Khasgiwala, and S. Patel



## ABSTRACT

**BACKGROUND AND PURPOSE:** Bone wax is a hemostatic agent that has been reported in some instances to migrate into the sigmoid sinus following posterior fossa surgery. The purpose of this study was to characterize the CT and MR imaging findings of this entity.

**MATERIALS AND METHODS:** The study included 212 consecutive patients who underwent posterior fossa surgery and postoperative CT and contrast-enhanced MR imaging. The presence of sigmoid sinus bone wax migration was determined with the following criteria: sigmoid sinus filling defect showing low signal on all MR imaging pulse sequences; sigmoid sinus filling defect showing low CT attenuation, similar to fat attenuation; and clinical confirmation that bone wax was used intraoperatively. CT and MR imaging of an in vitro bone wax sample was also performed.

**RESULTS:** We identified 6 cases of sigmoid sinus bone wax migration. In each case, a low-signal-intensity, low-attenuation filling defect was noted in the sigmoid sinus. The morphology was linear ( $n = 3$ ) or globular ( $n = 3$ ). In patients with serial imaging, the appearance of migrated bone wax remained stable over time. No adverse outcomes related to sigmoid sinus bone wax migration were encountered. In vitro imaging of bone wax confirmed low CT attenuation and low MR imaging signal intensity on T1WI and T2WI.

**CONCLUSIONS:** Bone wax migration into the sigmoid sinus is a recognizable imaging finding after posterior fossa surgery that appears to have a benign clinical course. The finding should be distinguished from more serious complications, such as venous sinus thrombosis.

**ABBREVIATIONS:** HU = Hounsfield units; VIBE = volumetric interpolated breath-hold examination

Bone wax is commonly used during the course of posterior fossa craniotomy to control bleeding from emissary veins or to pack violated mastoid air cells. The mastoid emissary vein often lies close to or within the retrosigmoid or suboccipital craniotomy bed and represents a channel in direct communication with the sigmoid sinus.<sup>1</sup> Awareness of the use of this agent is important in assessing postoperative imaging because its presence within a dural venous sinus might be mistaken for air, fat, or thrombus. The particular imaging characteristics of this agent can aid appropriate diagnosis. The appearance has been reported in the literature as low attenuation on CT (intermediate between fat and simple fluid) and as a signal void on MR imaging (attributable to its semicrystalline solid nature).<sup>2</sup> To our knowledge, only 2 prior

studies of sigmoid sinus bone wax migration (including 8 total cases) have been reported in the literature, and conventional MR imaging features of the migrated bone wax were reported in only 1 of these cases.<sup>3,4</sup> The purpose of our study was to describe the CT and MR imaging features of sigmoid sinus bone wax migration after posterior fossa surgery. We also sought to assess the CT and MR imaging features of an in vitro bone wax sample.

## MATERIALS AND METHODS

This Health Insurance Portability and Accountability Act–compliant retrospective study was reviewed and approved by our institutional review board.

To compile a set of patients who underwent posterior fossa surgery, a query of our radiology report data base was used to identify reports containing the terms “suboccipital,” “retrosigmoid,” or “mastoidectomy” generated over a 6-month period. Scans of the resultant patients were reviewed to identify those who had in fact undergone surgery. The patient list was further refined by including only those patients who underwent both CT and contrast-enhanced MR imaging postoperatively. A neuroradiologist with a Certificate of Added Qualification reviewed this subset of patients to identify cases of sigmoid sinus bone wax migration.

Received March 4, 2016; accepted after revision May 15.

From the Department of Neuroradiology (K.B., A.K.), NYU Langone Medical Center, New York, New York; and Division of Neuroradiology (S.P.), University of Virginia Health System, Charlottesville, Virginia.

Please address correspondence to Kory A. Byrns, MD, Department of Neuroradiology, NYU Langone Medical Center, 660 1st Ave, New York, NY 10016; e-mail: kory.byrns@gmail.com

Indicates article with supplemental on-line table.

<http://dx.doi.org/10.3174/ajnr.A4871>



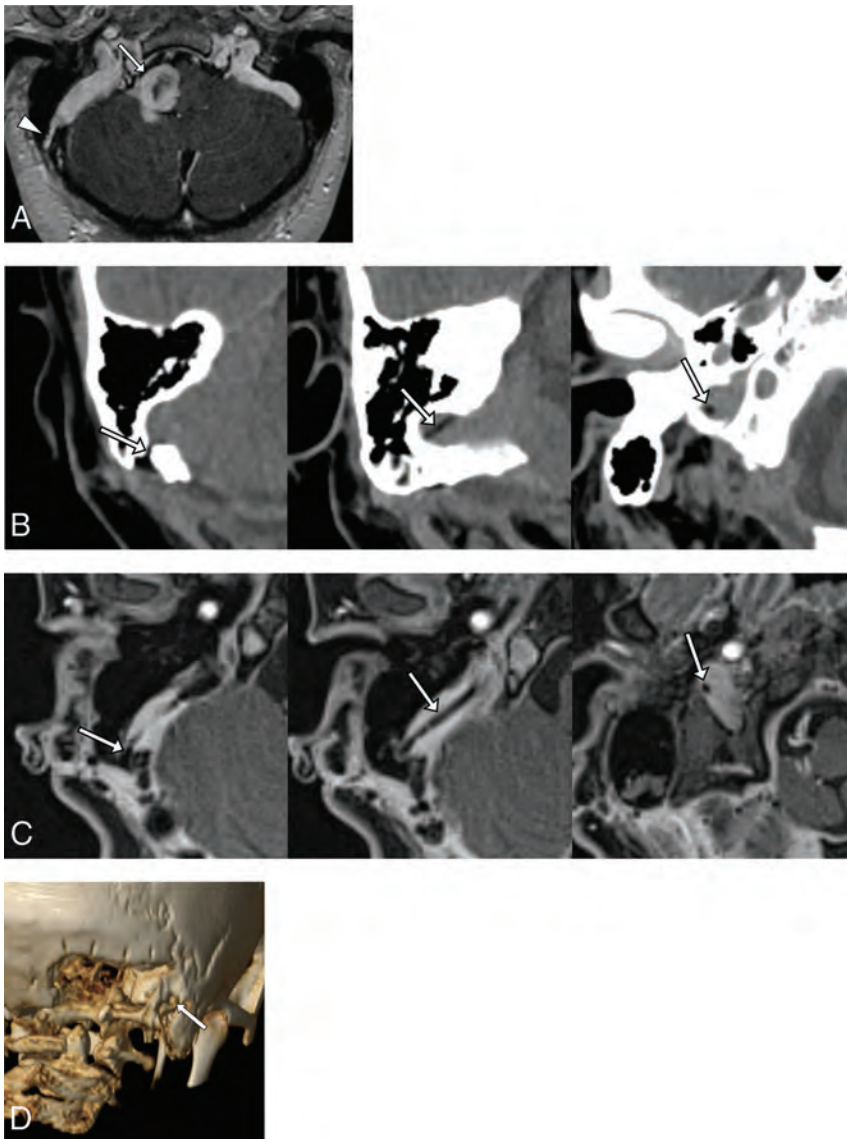


**FIG 1.** A, Axial contrast-enhanced T1WI demonstrates a lobulated enhancing lesion in the right perimedullary space exhibiting mass effect upon the medulla and right cerebellar hemisphere (arrow). A right mastoid emissary vein communicating with the sigmoid sinus is also visible (arrowhead). B, Sequential axial nonenhanced CT images obtained postoperatively demonstrate a linear low-attenuation (−49 HU) stringlike structure traversing the mastoid canal and extending along the course of the sigmoid sinus to terminate at the level of the jugular foramen. C, Axial contrast-enhanced T1WI with fat suppression performed postoperatively demonstrates a linear low-signal filling defect within the sigmoid sinus following the course of the low-attenuation structure identified on CT. D, Volume-rendering technique of the CT viewed posteriorly demonstrates the location of the foramen of the mastoid emissary vein just lateral to the craniectomy (arrow).

The criteria for sigmoid sinus bone wax migration were: 1) sigmoid sinus filling defect showing low signal intensity on all MR imaging pulse sequences; 2) sigmoid sinus filling defect showing low CT attenuation, similar to fat attenuation; and 3) confirmation via review of the medical record that bone wax was used intraoperatively. The demographic data, lesion treated, interval between surgery and imaging, and the morphology, location, and attenuation in Hounsfield units (HU) of the filling defect were recorded. All available postoperative imaging studies were reviewed to determine any change in the appearance of the migrated bone wax. Medical records of each patient were reviewed for any adverse clinical outcome related to bone wax migration.

The protocol used at our institution for postoperative MR imaging of the temporal bones and posterior fossa is as follows: whole brain sequences including axial T2WI (TR/TE 3800/116 ms, matrix = 320 × 224, section thickness = 5 mm), axial FLAIR (TR/TE/TI = 9000/81/2500 ms, matrix = 320 × 224, section thickness = 5 mm), axial DWI (TR/TE = 7800/83 ms; *b* = 0, 500, 1000; matrix = 150 × 150; section thickness = 5 mm), and postcontrast axial T1WI (TR/TE = 550/6.7 ms, matrix = 320 × 224, section thickness = 5 mm); precontrast temporal bone sequences including axial T1WI (TR/TE = 550/6.7 ms, matrix = 320 × 224, section thickness = 3 mm) and axial CISS (TR/TE = 1000/136 ms, matrix = 320 × 317, section thickness = 0.44-mm); and postcontrast temporal bone sequences including axial radial volumetric interpolated breath-hold examination (radial VIBE) (TR/TE = 4.42/2.08 ms, matrix = 224 × 224, section thickness = 0.8 mm), axial T1WI with fat saturation (TR/TE = 550/6.7 ms, matrix = 320 × 224, section thickness = 3 mm), and coronal T1WI (TR/TE = 538/6.7 ms, matrix = 320 × 224, section thickness = 3 mm). For several patients, a volumetric T1-weighted MPR sequence (TR/TE/TI 2730/1000/3.31 ms, matrix = 256 × 216, section thickness = 1.10 mm) was performed rather than the radial VIBE sequence. There was no intersection gap in any sequences performed.

In vitro imaging evaluation of bone wax obtained from our hospital's surgical supply was performed by using a 1-g sample suspended within a 10-mL plastic syringe containing sterile water. The sample was evaluated with CT and MR, including T2-weighted (TR/TE = 3000/68 ms, matrix = 256 × 218, section thickness = 2 mm) and T1-weighted (TR/TE = 450/11, matrix = 320 × 282, section thickness = 3 mm) sequences. After adding a small amount of Gadavist (Bayer Schering Pharma, Berlin, Germany) gadolinium-based contrast to the syringe, an additional T1-weighted sequence (TR/TE = 613/11, matrix = 320 × 282, section thickness = 3 mm) was performed.

## RESULTS

The initial data base query yielded 451 patients. Review of the available imaging for these patients yielded a total of 212 for whom surgery involving the posterior fossa had been performed and appropriate postoperative CT and MR imaging was available. Finally, review of this subset of patients yielded 6 patients who met

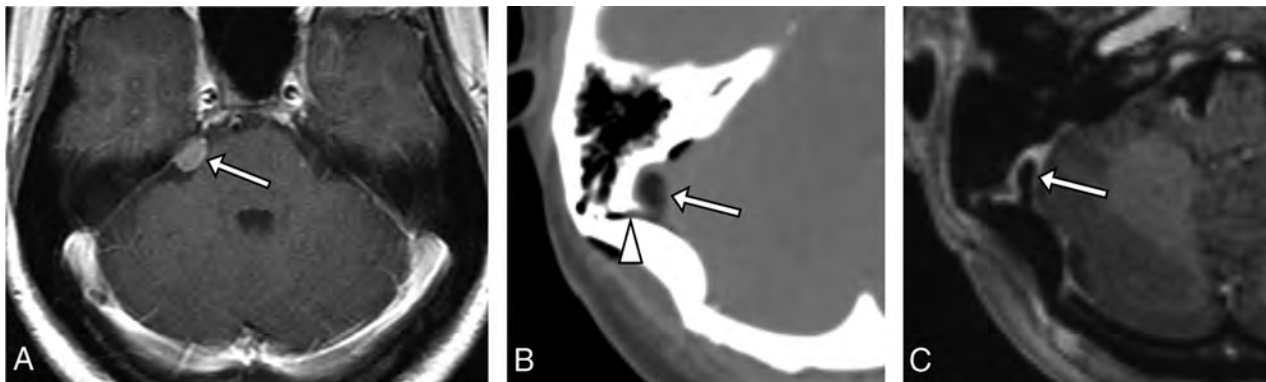


**FIG 2.** A, Axial contrast-enhanced T1WI demonstrates a small meningioma arising from the petrous ridge (arrow). B, Postoperative axial nonenhanced CT demonstrates a globular focus of low attenuation ( $-162$  HU) within the sigmoid sinus (arrow) adjacent to the craniotomy bed, which is noted to extend to the canal for the mastoid emissary vein (arrowhead). C, Postoperative axial contrast-enhanced T1WI shows that the filling defect is low signal (arrow), consistent with migrated bone wax. Note that the material is low signal even in the absence of fat-suppression techniques.

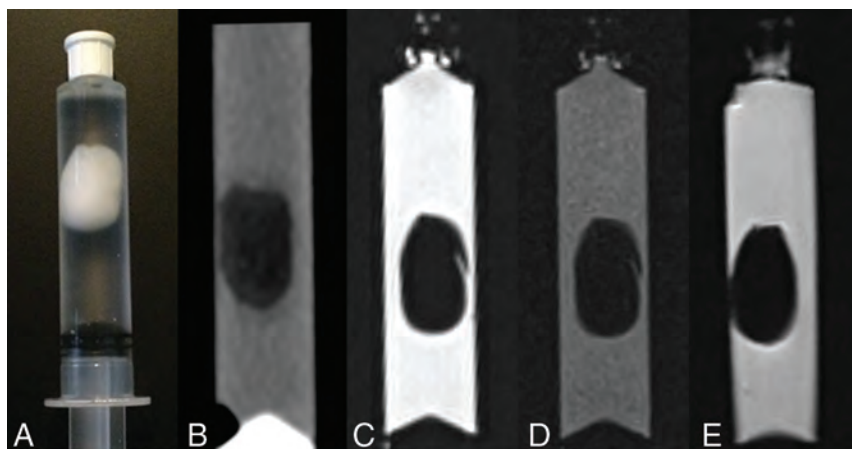


**FIG 3.** A, Photograph of a 1-g sample of bone wax suspended in sterile water within a 10-mL plastic syringe. B, CT of the sample illustrates the low attenuation of the material ( $-104$  HU). There is uniformly low MR signal intensity on T2WI (C), T1WI (D), and T1WI performed after adding a small amount of gadolinium-based contrast to the solution (E).

all criteria for a presumed diagnosis of migrated bone wax within the sigmoid sinus. A seventh patient met 2 of 3 criteria, though CT imaging was not available to confirm low attenuation of the filling defect that otherwise resembled migrated bone wax. A summary of our findings is presented in the On-line Table. For the 6 cases meeting all criteria, patient ages ranged from 30 to 78 years, and the group consisted of 5 women and 1 man. The lesions treated included a vestibular schwannoma, a spinal accessory nerve schwannoma, a clival meningioma, a petrous apex meningioma, a cerebellar hemangioblastoma, and an arachnoid cyst of the posterior fossa. The filling defects were nonocclusive and appeared globular in 3 cases and linear in the remaining 3. The material extended caudally into the jugular bulb or internal jugular vein in 3 of the cases. Measured attenuation ranged from  $-162$  to  $-39$  HU.

The interval between the initial operation and the most recent imaging varied from immediately postoperative to over 3 years, with a mean interval of 414 days. No appreciable change in the finding was observed for the cases with long-term follow-up available. Review of the medical records did not indicate any negative clinical outcome attributed to bone wax migration or reoperation

performed for this reason. The interval between the patient's surgery and most recent clinical evaluation varied from 17 to 1213 days, with a mean interval of 475 days. One patient (case 3) presented 9 months postoperatively with seizures characteristic of known epilepsy. Imaging was stable at this time and no neurosurgical intervention was recommended. Another patient (case 5) presented 2 months postoperatively with drainage near the wound site, which was attributed to a small pustule, and no repeat imaging was recommended.

A representative case of linear migrated bone wax (case 3) is presented in Fig 1. Preoperative MR imaging demonstrates the excised lesion (a perimedullary schwannoma discovered to arise from the spinal accessory nerve) as well as a patent, well-developed mastoid emissary vein.

Selected images after suboccipital craniotomy reveal a linear low-attenuation, low-signal filling defect traversing the emissary venous channel and coursing into the sigmoid sinus. Volumetric rendering of the CT demonstrates the proximity of the mastoid emissary foramen to the craniotomy site.

A case exemplifying globular migrated bone wax (case 4) is presented in Fig 2. Preoperative contrast-enhanced MR imaging demonstrates a small petrous ridge meningioma projecting into the cerebellopontine angle cistern. Immediate postoperative CT demonstrates a globular low-attenuation filling defect within the sigmoid sinus adjacent to the craniotomy bed, which extends into the nearby mastoid emissary vein channel. Contrast-enhanced MR performed 3 months later reveals a low-signal filling defect in a stable location and configuration.

Figure 3 shows a photograph of an in vitro sample of bone wax suspended in sterile water along with corresponding CT and MR images. The sample demonstrated low attenuation on CT ( $-104$  HU), and low signal intensity on T1WI and T2WI.

## DISCUSSION

The neurosurgical approach to deep posterior fossa lesions often necessitates extension of the craniotomy/craniectomy to include emissary venous foramina. In particular, the opening of the mastoid canal, which transmits the mastoid emissary vein, can be exposed or otherwise instrumented. The vein is an example of several variably present channels that act as an extracranial drainage conduit for the dural venous sinuses. This connection functions as an alternate pathway if the internal jugular vein is occluded or otherwise compromised.<sup>1</sup>

In the event of excessive venous bleeding encountered while instrumenting the region of the mastoid canal, a common method of achieving hemostasis is to apply bone wax. The bone wax used in our institution is a sterile mixture of beeswax, paraffin, and isopropyl palmitate (a wax-softening agent) that functions as a mechanical barrier to tamponade bleeding from divided, drilled, or chipped edges of bone.<sup>5</sup> Bone wax is also used to seal off visible mastoid air cells after retrosigmoid craniotomy to prevent postoperative CSF leaks.<sup>6</sup> This agent has remained in common use because it is inexpensive, biochemically inert, and nonabsorbable.

Reported complications related to bone wax application are varied but uncommon. These include granulomatous reaction,<sup>7-10</sup> mass effect,<sup>2</sup> saphenous vein graft thrombosis,<sup>11</sup> epistaxis,<sup>12</sup> calvarial osteohypertrophy,<sup>13</sup> and infection.<sup>14</sup> Retained, excessive, or migrated bone wax might simulate a mass.<sup>15</sup> Bone wax has been used in the treatment of superior semicircular canal dehiscence and, in these cases, excessive wax application might migrate along the lumen to adversely affect the sensory neuroepithelium of the vestibular end organs.<sup>16</sup> There is at least a theoretic risk of bone wax embolization when applied to the marrow space, as postulated in an animal study in which deposits were found in the lungs after application of radioactive bone wax to canine sternotomy incisions.<sup>17</sup> Additional potential hazards noted by the manufacturer include inhibition of osteogenesis and the possibility of potentiating an infection, as with any foreign body. Instructions for use specifically warn that bone wax should be used sparingly and any excess should be removed from the operative site.<sup>5</sup>

Review of the neurosurgical literature revealed a single case series of migration of bone wax into the sigmoid sinus. Hadeishi et al<sup>3</sup> reported 7 cases after retrosigmoid craniotomy from a series of 161 patients. Postoperative CT and time-of-flight MRV were reported in each case, though conventional MR imaging sequences were not described. Of the 7 reported patients, none demonstrated any sign of neurologic deterioration postoperatively. A single case report of symptomatic sigmoid sinus occlusion by bone wax was reported by Crocker et al.<sup>4</sup> The patient developed acute exacerbation of headaches as well as transient hemiparesis on day 6 after retrosigmoid craniectomy for resection of a vestibular schwannoma. In this instance, the patient was anticoagulated and discharged on postoperative day 9 without further symptoms or additional surgical intervention. Of note, the imaging in this case revealed the lumen to be totally occluded by bone wax, with absence of flow in the ipsilateral transverse and sigmoid sinuses. In our series, the filling defects were uniformly nonocclusive, and review of medical

records did not reveal any adverse outcome attributed to migrated bone wax.

There are several limitations of this investigation that should be noted. Pathologic confirmation of the diagnosis was not available because no additional surgical interventions were performed. The data base search method is inherently limited by variations in terminology and reporting. Thus, all instances of posterior fossa surgery that can lead to sigmoid sinus bone wax migration may not have been captured for the time period investigated. Moreover, we restricted our patient cohort to those who underwent both postoperative CT and MR imaging scans. Given these caveats, we are unable to report the true incidence of this finding after posterior fossa surgery.

## CONCLUSIONS

The sigmoid sinus should be routinely inspected when interpreting postoperative imaging after postoperative craniotomy because thrombosis is a rare but reported complication of this approach.<sup>18,19</sup> However, as illustrated by the cases presented here, detection of a filling defect should prompt careful evaluation of the attenuation and signal characteristics of the abnormality on all available modalities. The course, morphology, and extent of occlusion should be assessed, and consultation with the surgical team is suggested to determine what foreign materials were introduced into the surgical field. Migration of bone wax into the dural venous sinuses is a rare result of posterior fossa surgery that radiologists should be prepared to differentiate from more serious complications. The finding may persist for many years postoperatively and, as in our series, may not have any associated negative clinical outcome.

## REFERENCES

1. Ginsberg L. **The posterior condylar canal.** *AJNR Am J Neuroradiol* 1994;15:969–72 Medline
2. Stein JM, Eskey CJ, Mamourian AC. **Mass effect in the thoracic spine from remnant bone wax: an MR imaging pitfall.** *AJNR Am J Neuroradiol* 2010;31:844–46 CrossRef Medline
3. Hadeishi H, Yasui N, Suzuki A. **Mastoid canal and migrated bone wax in the sigmoid sinus: technical report.** *Neurosurgery* 1995;36:1220–23; discussion 1223–24 Medline
4. Crocker M, Nesbitt A, Rich P, et al. **Symptomatic venous sinus thrombosis following bone wax application to emissary veins.** *Brit J Neurosurg* 2008;22:798–800 CrossRef Medline
5. Bone Wax [package insert]. Bridgewater, New Jersey: Ethicon; 2015
6. Ling PY, Mendelson ZS, Reddy RK, et al. **Reconstruction after retrosigmoid approaches using autologous fat graft-assisted Medpor Titan cranioplasty: assessment of postoperative cerebrospinal fluid leaks and headaches in 60 cases.** *Acta Neurochir (Wien)* 2014;156:1879–88 CrossRef Medline
7. Ateş O, Cayli SR, Gürses I. **Bone wax can cause foreign body granuloma in the medulla oblongata.** *Br J Neurosurg* 2004;18:538–40 CrossRef Medline
8. Leprovost N, Taupin A, Soubeyrand E, et al. **Foreign body granuloma due to Horsley wax** [in French]. *Rev Stomatol Chir Maxillofac* 2011;112:117–20 CrossRef Medline
9. Low WK, Sim CS. **Bone wax foreign body granuloma in the mastoid.** *ORL J Otorhinolaryngol Relat Spec* 2002;64:38–40 CrossRef Medline
10. Wolvius EB, van der Wal KG. **Bone wax as a cause of a foreign body granuloma in a cranial defect: a case report.** *Int J Oral Maxillofacial Surgery* 2003;32:656–58 CrossRef Medline
11. Chun PK, Virmani R, Mason TE, et al. **Bone wax granuloma causing**

- saphenous vein graft thrombosis. *Am Heart J* 1988;115:1310–13 CrossRef Medline
12. Tay HL, Tan LK. **Surgical bone wax causing epistaxis.** *J Laryngol Otol* 1996;110:267–68 Medline
  13. Kamide T, Nakada M, Hirota Y, et al. **Skull osteohypertrophy as a complication of bone wax.** *J Clin Neuroscience* 2009;16:1658–60 CrossRef
  14. Gibbs L, Kakis A, Weinstein P, et al. **Bone wax as a risk factor for surgical-site infection following neurospinal surgery.** *Infect Control Hosp Epidemiol* 2004;25:346–48 CrossRef Medline
  15. Karabekir HS, Korkmaz S. **Residue bone wax simulating spinal tumour: a case report.** *Turk Neurosurg* 2010;20:524–26 CrossRef Medline
  16. Cheng YS, Kozin ED, Remenschneider AK, et al. **Characteristics of wax occlusion in the surgical repair of superior canal dehiscence in human temporal bone specimens.** *Otol Neurotol* 2016;37:83–88 CrossRef Medline
  17. Robicsek F, Masters TN, Littman L, et al. **The embolization of bone wax from sternotomy incisions.** *Annals Thorac Surg* 1981;31:357–59 CrossRef
  18. Keiper GL Jr., Sherman JD, Tomsick TA, et al. **Dural sinus thrombosis and pseudotumor cerebri: unexpected complications of suboccipital craniotomy and translabyrinthine craniectomy.** *J Neurosurg* 1999;91:192–97 CrossRef Medline
  19. Lega BC, Yoshor D. **Postoperative dural sinus thrombosis in a patient in a hypercoagulable state. Case report.** *J Neurosurg* 2006;105:772–74 CrossRef Medline

# Imaging Features of Malignant Lacrimal Sac and Nasolacrimal Duct Tumors

V.A. Kumar, B. Esmaeli, S. Ahmed, B. Gogia, J.M. Debnam, and L.E. Ginsberg



## ABSTRACT

**SUMMARY:** The purpose of this study was to present the imaging features of primary and secondary malignant lacrimal sac and nasolacrimal duct tumors and their pattern of tumor spread in 18 patients. The most common tumor histology in our series was squamous cell carcinoma. In 15/18 patients, tumor involved both the lacrimal sac and duct at the time of diagnosis. In 11/16 patients on CT, the nasolacrimal bony canal was smoothly expanded without erosive changes. The medial canthus region (16/18) was a frequent site of direct tumor spread. Two patients had intraconal orbital spread of tumor. Tumor spread to the sinus or nasal cavity was observed in 5/13 primary tumors. Only 1 patient presented with nodal metastasis. There was no intracranial tumor extension, perineural tumor spread along the infraorbital nerve, distant metastasis, or dacryocystocele formation in any of the patients at the time of diagnosis.

**ABBREVIATION:** SCCA = squamous cell carcinoma

The lacrimal drainage apparatus consists of the superior and inferior canaliculi, common canaliculus, lacrimal sac, and nasolacrimal duct (Fig 1).<sup>1</sup> Tears collect in the lacrimal sac before draining into the nasolacrimal duct and the inferior meatus of the nasal cavity.<sup>2</sup> Lacrimal sac and duct tumors are rare.<sup>3</sup> The most common presenting clinical symptoms of lacrimal sac and duct tumors are epiphora, recurrent dacryocystitis, epistaxis, and/or a lacrimal sac mass.<sup>3</sup> These tumors present with nonspecific symptoms suggestive of chronic dacryocystitis; often diagnosis and treatment are delayed.<sup>4</sup> Early diagnosis and treatment are often curative and can prevent tumor recurrence and loss of the eye and visual function.<sup>4,5</sup> The tumors are divided into epithelial and non-epithelial neoplasms. Benign epithelial tumors include squamous and transitional cell papillomas and oncocytomas. The malignant epithelial neoplasms include squamous cell carcinoma (SCCA), transitional cell carcinoma, adenocarcinoma, adenoid cystic carcinoma, poorly differentiated carcinoma, and, rarely, primary melanomas.<sup>5</sup> Secondary involvement of the lacrimal sac and duct can occur from any cutaneous lesion that involves the eyelid and/or conjunctiva, including SCCA, basal cell carcinoma, and sebaceous cell carcinoma, and from any neoplastic process in-

volving the paranasal sinuses. Metastatic lesions to the lacrimal sac can originate from any distant site and may include carcinomas or melanomas.

The purpose of this study was to review the CT and MR imaging features of malignant lacrimal sac and nasolacrimal duct tumors. We investigated the extent of tumor involvement of the lacrimal sac and duct and the extent of bony expansion or destruction of the nasolacrimal duct bony canal. We characterized the malignant lacrimal sac and duct tumors by the degree of enhancement, signal characteristics on MR imaging, and local/regional spread. We also sought to determine whether dacryocystocele formation was a feature associated with these tumors and whether nodal metastasis, distant metastasis, perineural tumor spread along the infraorbital nerve, or intracranial tumor extension was present on imaging at the time of the initial evaluation.

## MATERIALS AND METHODS

### Case Series

Approval for this retrospective Health Insurance Portability and Accountability Act–compliant study was obtained from the institutional review board, with a waiver of informed consent. A retrospective analysis was performed on 18 patients, 11 women and 7 men, 45–86 years of age (mean, 64 years), who had been treated for malignant lacrimal sac and nasolacrimal duct tumors at our institution. Thirteen patients had primary malignant tumors of the lacrimal sac and/or nasolacrimal duct, 4 patients had contiguous malignant tumor spread to the lacrimal sac and/or duct from a neighboring site, and 1 patient had a metastatic melanoma to the lacrimal sac and duct. The tumor histology consisted of the

Received February 10, 2016; accepted after revision June 2.

From the Department of Diagnostic Radiology (V.A.K., S.A., B.G., J.M.D., L.E.G.), and Orbital Oncology and Ophthalmic Plastic Surgery Program, Department of Plastic Surgery (B.E.), University of Texas MD Anderson Cancer Center, Houston, Texas.

Please address correspondence to Vinodh A. Kumar, MD, Department of Diagnostic Radiology, Unit 1482, University of Texas MD Anderson Cancer Center, 1400 Pressler St, Houston, TX 77030; e-mail: vakumar@mdanderson.org

<http://dx.doi.org/10.3174/ajnr.A4882>

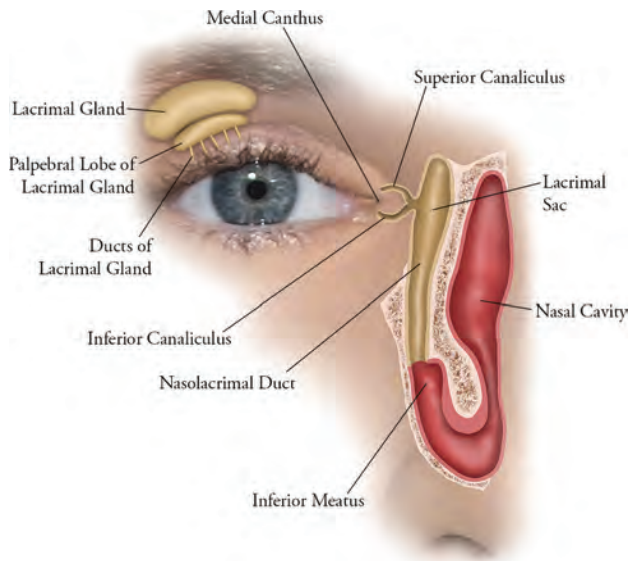


**FIG 1.** Normal anatomy of the lacrimal drainage system apparatus, which includes the canaliculi, lacrimal sac, and nasolacrimal duct.

following: SCCA ( $n = 7$ ), poorly differentiated sebaceous carcinomas ( $n = 3$ ), melanomas ( $n = 3$ ), adenocarcinomas ( $n = 2$ ), adenoid cystic carcinoma ( $n = 1$ ), small cell undifferentiated carcinoma ( $n = 1$ ), and papillary transitional carcinoma ( $n = 1$ ).

CT was performed on HD 750 scanners (GE Healthcare, Milwaukee, Wisconsin) after the administration of intravenous contrast by using the following parameters: 120–140 kV(peak); 180–220 mA; section thickness, 1.25 mm; FOV, 180 to 250. MR imaging studies were performed on 1.5T MR imaging scanners (Excite HDxt; GE Healthcare) with the following pulse sequences: T1WI, T2WI, and postcontrast T1WI. The images were reviewed by 2 head and neck radiologists (V.A.K. and L.E.G.).

The degree of contrast enhancement of the malignant lacrimal sac and nasolacrimal duct tumors on CT and MR imaging was graded relative to the degree of contrast enhancement of the normal lacrimal glands. For this study, a normal lacrimal gland demonstrated moderate enhancement on postcontrast CT and intense contrast enhancement on postcontrast T1WI.

## RESULTS

The results of this study are summarized in the Table. In 15/18 patients, malignant tumor involved both the lacrimal sac and nasolacrimal duct at the time of diagnosis. Only 3 patients had tumor confined to the lacrimal sac. Tumor was not observed solely within the nasolacrimal duct in any patient. In 16/18 patients, tumor had spread from the lacrimal sac into the medial canthus region (Figs 2 and 3). Two patients had intraconal orbital tumor spread (Fig 4A).

In 11/16 patients who had undergone CT, the nasolacrimal bony canal was smoothly expanded without erosive changes (Fig 5B). In 2 patients, there were erosive changes to the nasolacrimal duct bony canal. One patient with possible erosive changes had undergone a prior dacryocystorhinostomy; therefore, the findings were iatrogenic. In 2 patients, there was no nasolacrimal duct dilation or erosion because these tumors were diagnosed at an early stage.

## Imaging features and regional spread of malignant lacrimal sac and nasolacrimal duct tumors

Features	No. of Patients
Tumor location along lacrimal system on CT and MRI ( $n = 18$ )	
Lacrimal sac only	3
Nasolacrimal duct only	0
Involving lacrimal sac and nasolacrimal duct	15
Tumor involvement of the nasolacrimal duct bony canal on CT ( $n = 16$ )	
No duct dilation	2
Smoothly expanded duct	11
Erosive/lytic changes to duct	2
Iatrogenic changes to duct from prior dacryocystorhinostomy	1
Orbit involvement by tumor ( $n = 18$ )	
Medial canthus/extraconal space of orbit	16
Intraconal space of orbit	2
Sinonasal involvement by tumor in primary malignant tumors of the lacrimal sac or duct ( $n = 5$ ) <sup>a</sup>	
Ethmoid sinus	4
Maxillary sinus	3
Nasal cavity	5
Other findings ( $n = 18$ )	
Nodal metastasis	1
Distant metastasis	0
Perineural tumor spread along the infraorbital nerve	0
Intracranial extension	0
Dacryocystocele formation	0

<sup>a</sup>Please note that some patients had >1 subsite of sinonasal tumor extension.



**FIG 2.** A 46-year-old woman with moderately differentiated invasive SCCA of the right lacrimal sac and nasolacrimal duct. Post-contrast-enhanced CT shows tumor extension from the lacrimal sac into the medial canthus region (arrow), which is a common site of tumor spread.

Of the 16 cases of malignant lacrimal sac and duct tumors evaluated with CT, 3 demonstrated mild contrast enhancement, 9 showed moderate contrast enhancement, and 4 exhibited intense enhancement. In the 12/13 patients who had undergone MR imaging, the lacrimal sac and duct tumors were isointense on T1WI, with the exception of 1 patient with nasal melanoma, which demonstrated high intensity on T1WI. In all 13 patients, the tumors showed isointense signal on T2WI (Fig 3B). On MR imaging, 3 cases demonstrated mild contrast enhancement, 7 cases had moderate contrast enhancement, and 3 exhibited intense contrast enhancement.

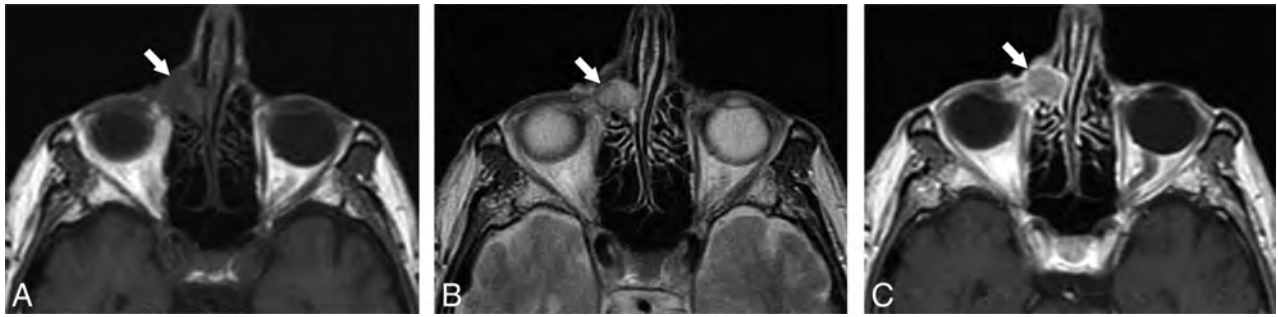


**FIG 3.** An 85-year-old man with metastatic melanoma to the lacrimal sac and nasolacrimal duct with extension into the medial canthus region. Axial MR imaging demonstrates an isointense mass in the right medial canthus on T1WI (A), isointensity on T2WI (B), and enhancement on postcontrast T1WI (C).

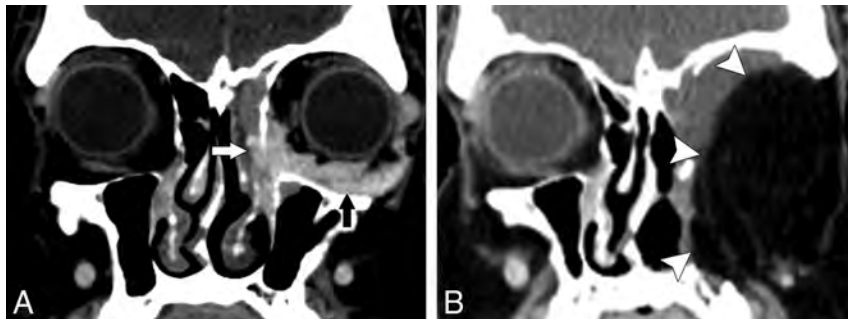


**FIG 4.** A 50-year-old man with adenocarcinoma of the left lacrimal sac and nasolacrimal duct. A, Postcontrast thin-section coronal CT reformatted images demonstrate tumor in the lacrimal sac and duct (white arrow) with direct extension into the inferior intraconal orbital space (black arrow). B, Due to the extent of tumor spread, the patient underwent left orbital exenteration, maxillectomy, and free flap reconstruction (white arrowheads) with adjuvant radiation therapy and has been disease-free for 3 years.

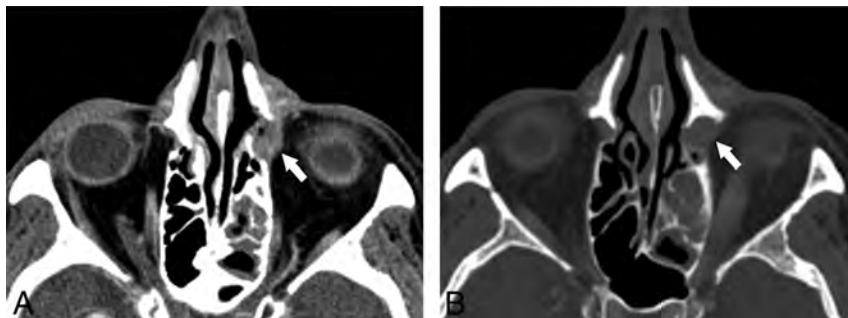


**FIG 5.** A 73-year-old woman with well-differentiated SCCA of the lacrimal sac and nasolacrimal duct. A, Post-contrast-enhanced CT demonstrates an enhancing tumor within the left lacrimal sac (arrow). B, At a slightly more inferior level (bone window), note the mild expansion of the lacrimal bony canal by tumor (arrow).

Five of 13 patients with primary malignant lacrimal sac and duct tumors had disease spread to the sinus or nasal cavity. Four had ethmoid sinus tumor extension, and 3 had maxillary sinus tumor involvement. Five had nasal cavity tumor extension, with 4 specifically involving the inferior meatus of the nasal cavity. Note that some patients had >1 subsite of sinonasal tumor extension. Postobstructive sinus secretions were noted in 3 patients.

One patient presented with an ipsilateral jugulodiaphragmatic (level IIA) nodal metastasis at the time of initial diagnosis. Dacryocystocele formation, perineural tumor spread along the infraorbital nerve, intracranial extension of tumor or distant metastases were not seen in any of the patients at the time of initial diagnosis.

## DISCUSSION

To our knowledge, no large imaging series has assessed malignant lacrimal sac and nasolacrimal duct tumors. This report highlights the CT and MR imaging features and spread pattern of these tumors. In our series, the most common tumor histology was SCCA (39%), which has also been reported in other studies.<sup>5,6</sup> Eighty-three percent of primary and secondary tumors in our study involved both the lacrimal sac and nasolacrimal duct at the time of initial imaging. The medial canthus region (Figs 2 and 3) was commonly involved by malignant tumors (89%) because of direct tumor spread from the lacrimal sac; intraconal orbital extension of tumor was less common (11%). The differential diagnosis of masses in the medial canthus includes lacrimal sac and duct neoplasms, but more commonly, dacryocystitis or idiopathic nasolacrimal duct blockage is a cause.<sup>5</sup> In our series, 38% of the primary malignant nasolacrimal sac or nasolacrimal duct tumors demonstrated spread to either the sinus or nasal cavity.

Tumor abutted the infraorbital foramen in 2 patients with advanced disease. However, perineural tumor spread along the infraorbital nerve was not seen on imaging or on histology. Intracranial tumor extension or distant metastases were not observed in any patient at the time of diagnosis. Nodal metastasis was seen in only 1 patient in our series. In a large ophthalmology study, Ni et al<sup>7</sup> found distant metastases from malignant lacrimal sac tumors in only 6/74 patients and intracranial tumor spread in 1/74 patients. They found nodal metastasis in 28% of patients, generally months to years after the initial diagnosis.<sup>7</sup> When present, nodal metastases from malignant lacrimal sac and duct tumors generally involve the preauricular, submandibular, and cervical lymph nodes.<sup>7,8</sup>

In 69% our cases imaged with CT, the malignant lacrimal sac and duct tumors expanded the lacrimal bony canal (Fig 5B) without erosion. CT was superior to MR imaging in the delineation of

the lacrimal bony canal and in evaluating expansion versus erosion of the canal. Thin-section coronal imaging was very helpful on both CT and MR imaging in the interpretation of the study because it nicely displayed the entirety of the lacrimal sac and duct and regional tumor spread (Fig 4A). When postobstructive sinus secretions were present (3 cases), MR imaging was superior to CT in distinguishing tumor from secretions within the sinonasal cavity. In 2 cases, MR imaging and CT were equivalent in the diagnostic evaluation of intraconal tumor spread. We found that the lacrimal canaliculi were not easily identifiable on MR imaging and CT, due to the small size of these anatomic structures. In cases of locally advanced malignant lacrimal sac and duct tumors, we found it difficult to distinguish primary tumors from secondary tumors by imaging. We anticipated seeing dacryocystocele formation secondary to tumor obstruction of the nasolacrimal duct more frequently; however, this was not seen in any case.

In most cases in this study, the malignant lacrimal sac and nasolacrimal sac tumors demonstrated moderate contrast enhancement on CT and MR imaging and demonstrated isointense signal intensity on T1-weighted and T2-weighted MR imaging. Contrast enhancement and MR imaging signal intensity were not helpful in distinguishing tumor histology, except in 1 case of recurrent nasal cavity melanoma, which spread to the nasolacrimal duct and demonstrated high T1WI signal intensity. Primary malignant melanoma of the lacrimal sac is rare, accounting for only 5% of lacrimal sac tumors.<sup>9</sup> Due to the paramagnetic properties of melanin, melanoma may appear hyperintense on T1WI and hypointense on T2WI.<sup>6</sup> According to Billing et al,<sup>9</sup> melanoma may also demonstrate isointense T1WI and T2WI signal on MR imaging (Fig 3A, -B).

Treatment of primary malignant lacrimal sac and nasolacrimal duct tumors typically involves wide local resection, followed by radiation and/or chemotherapy. In our series, surgical excision of the lacrimal sac was complemented by a medial maxillectomy to allow complete resection of the nasolacrimal duct. Judicious use of postoperative adjuvant proton radiation therapy or concurrent chemoradiation therapy can yield good local/regional control, and a globe-sparing surgery can be achieved in most cases with reasonable visual outcomes.<sup>5</sup> Bony erosion of the nasolacrimal bony canal does not portend a worse prognosis, but it may dictate the size of the planned bony resection, which, in addition to a medial maxillectomy, may also include an ethmoidectomy. Larger tumor diameter (generally >30 mm) at the time of presentation<sup>5</sup> and tumor invasion of the intraconal space of the orbit may necessitate orbital exenteration (Fig 4A, -B).

Imaging surveillance of the head and neck is recommended every 3 months for the first year, every 6 months the second year, and annually in the third year and beyond.<sup>5</sup> On the basis of the

results of this study, the authors recommend performing a thin-section (1.25 mm) CT with contrast as the first-line imaging study to evaluate malignant lacrimal sac and nasolacrimal duct tumors at the time of initial staging. MR imaging can be performed if CT cannot distinguish sinonasal tumor extension from postobstructive secretions.

## CONCLUSIONS

Malignant lacrimal sac and nasolacrimal duct tumors tend to expand the nasolacrimal bony canal, rather than erode it. CT was superior to MR imaging in characterizing expansion versus erosion of the nasolacrimal bony canal. In most cases, tumor involved both the lacrimal sac and nasolacrimal duct at initial diagnosis. The medial canthus region was a frequent site of tumor spread. Tumor spread to the sinus or nasal cavity was observed in less than half of the primary tumor cases. Nodal metastasis was seen in only 1 patient. There was no intracranial tumor extension, perineural tumor spread along the infraorbital nerve, distant metastasis, or dacryocystocele formation in any of the cases at the time of initial imaging. The most common tumor histology in our series was SCAA.

Disclosures: Bitu Esmaeli—UNRELATED: Other: Roche; I served on their Data Safety Monitoring Board last year.

## REFERENCES

1. Debnam JM, Esmaeli B, Ginsberg LE. **Imaging characteristics of dacryocystocele diagnosed after surgery for sinonasal cancer.** *AJNR Am J Neuroradiol* 2007;28:1872–75 CrossRef Medline
2. Russell EJ, Czervionke L, Huckman M, et al. **CT of inferomedial orbit and lacrimal drainage apparatus: normal and pathologic anatomy.** *AJR Am J Roentgenol* 1985;145:1147–54 CrossRef Medline
3. Stefanyshyn MA, Hidayat AA, Pe'er JJ, et al. **Lacrimal sac tumors.** *Ophthalm Plast Reconstr Surg* 1994;10:169–84 CrossRef Medline
4. De Stefani A, Lerda W, Usai A, et al. **Squamous cell carcinoma of lacrimal drainage system: case report and literature review.** *Tumori* 1998;84:506–10 Medline
5. El-Sawy T, Frank SJ, Hanna E, et al. **Multidisciplinary management of lacrimal sac/nasolacrimal duct carcinomas.** *Ophthalm Plast Reconstr Surg* 2013;29:454–57 CrossRef Medline
6. Weber AL, Rodriguez-DeVelasquez A, Lucarelli MJ, et al. **Normal anatomy and lesions of lacrimal sac and duct: evaluated by dacryocystography, computed tomography, and MR imaging.** *Neuroimaging Clin N Am* 1996;6:199–217 Medline
7. Ni C, D'Amico DJ, Fan CQ, et al. **Tumors of lacrimal sac: a clinicopathological analysis of 82 cases.** *Int Ophthalmol Clin* 1982;22:121–40 CrossRef Medline
8. Rahangdale SR, Castillo M, Shockley W. **MR in squamous cell carcinoma of the lacrimal sac.** *AJNR Am J Neuroradiol* 1995;16:1262–64 Medline
9. Billing K, Malhotra R, Selva D, et al. **Magnetic resonance imaging findings in malignant melanoma of the lacrimal sac.** *Br J Ophthalmol* 2003;87:1187–88 CrossRef Medline



# Is Hypoglossal Nerve Palsy Caused by Craniocervical Junction Degenerative Disease an Underrecognized Entity?

 S.M. Weindling,  R.D. Goff,  C.P. Wood,  D.R. DeLone, and  J.M. Hoxworth



## ABSTRACT

**SUMMARY:** Isolated hypoglossal nerve palsy is uncommon, and underlying craniocervical junction degenerative disease has rarely been reported as an underlying cause. To improve understanding of this entity, we present a retrospective series of 18 patients with hypoglossal palsy in whom twelfth cranial nerve compression within the premedullary cistern or hypoglossal canal, or both, was found secondary to craniocervical junction juxta-articular cysts, retro-odontoid fibrous pseudotumors, and osteophytes. The imaging techniques and characteristic craniocervical junction degenerative disease lesion imaging findings presented here might help clinicians interpreting hypoglossal palsy imaging studies avoid perceptual and interpretive errors commonly found in the present series.

**ABBREVIATIONS:** CCJ = craniocervical junction; CCJDD = craniocervical junction degenerative disease; JAC = juxta-articular cyst; ROFP = retro-odontoid fibrous pseudotumor

**H**ypoglossal nerve palsy is an infrequent clinical presentation, most commonly occurring in combination with other lower cranial nerve palsies. By using a segmental approach,<sup>1</sup> the underlying etiologic factors can be subdivided by location as involving the brain stem, premedullary cistern, skull base, nasopharynx or oropharynx, or sublingual regions. Hypoglossal nerve palsy secondary to craniocervical junction (CCJ) juxta-articular (synovial and ganglion) cysts<sup>2-8</sup> and osteophytes<sup>9,10</sup> has been described in isolated case reports; yet, these pathologies are not classically included in the differential diagnosis for hypoglossal palsy. Distinguishing CCJ degenerative lesions from other hypoglossal nerve pathologies might have important diagnostic and treatment implications. To improve understanding of this disorder, a case series of 18 patients with hypoglossal palsy and ipsilateral twelfth cranial nerve compression secondary to CCJ juxta-articular cysts

(JACs), retro-odontoid fibrous pseudotumors (ROFPs), and osteophytes is presented.

## CASE SERIES

### Patients


This Health Insurance Portability and Accountability Act–compliant retrospective case series was approved by the Mayo Clinic Institutional Review Board. Initially, 4 neuroradiologists (S.M.W., C.P.W., D.R.D., J.M.H.) provided 7 known cases of hypoglossal palsy secondary to craniocervical junction degenerative disease (CCJDD) from their teaching files. Next, a retrospective Boolean search of radiology reports from 3 affiliated tertiary medical centers between January 1, 2005, and December 31, 2014, was performed, combining the words “hypoglossal” or “tongue” and “palsy,” “atrophy,” or “denervation.” From this list, patients were excluded if hypoglossal palsy could not be confirmed through review of the electronic health record. Patients with prior head and neck or skull base tumor, radiation therapy, or surgery also were excluded. For the remaining patients with hypoglossal palsy, imaging studies that included the CCJ were reviewed for possible twelfth cranial nerve compression by an underlying CCJDD lesion (JAC, ROFP, or osteophyte). Eleven additional cases were discovered from this 10-year multicenter retrospective review. Three physicians with neuroradiology subspecialty board certification (S.M.W., C.P.W., J.M.H.) performed a consensus imaging review for all patients with hypoglossal palsy believed secondary to CCJDD to confirm and characterize the offending lesions. For

Received March 11, 2016; accepted after revision May 30.

From the Department of Radiology (S.M.W., R.D.G.), Mayo Clinic, Jacksonville, Florida; Department of Radiology (C.P.W., D.R.D.), Mayo Clinic, Rochester, Minnesota; and Department of Radiology (J.M.H.), Mayo Clinic Hospital, Phoenix, Arizona.

Paper previously presented at: Annual Meeting of the American Society of Head and Neck Radiology, September 9–13, 2015; Naples, Florida.

Please address correspondence to Steven M. Weindling, MD, Department of Radiology, Mayo Clinic, 4500 San Pablo Rd, Jacksonville, FL 32224; e-mail: weindling.steven@mayo.edu

 Indicates article with supplemental on-line tables.

<http://dx.doi.org/10.3174/ajnr.A4885>

each patient with hypoglossal palsy caused by CCJDD, our institution's first MR imaging or CT report was reviewed to ascertain whether the initial differential diagnosis included the consensus diagnosis.

### Clinical Findings

A total of 18 patients with hypoglossal palsy related to CCJDD were included in this case series (12 women and 6 men; mean age, 74 years; range, 52–89 years). Symptoms at presentation to our institutions most commonly included tongue weakness or deviation (13/18), dysarthria (12/18), and dysphagia (6/18) (On-line Table 1). Neurologic examination confirmed hypoglossal palsy in all patients. Among the 4 patients in whom the underlying lesion was addressed surgically, the duration between symptom onset and surgery was 3 months ( $n = 1$ ), 11 months ( $n = 2$ ), and 7 years ( $n = 1$ ), respectively. In the final patient, surgical delay was due to lesion misdiagnosis as a hypoglossal schwannoma until the correct diagnosis of JAC was rendered 1 month before surgery. New-onset or worsening headache or suboccipital pain was an associated concern for 13 patients. No patient had a history of rheumatoid arthritis, psoriatic arthritis, gout, or calcium pyrophosphate deposition disease.

### Imaging Findings

For the 18 patients with CCJDD hypoglossal palsy, the brain, head and neck, and cervical spine imaging studies from our institution and outside facilities spanning 12 years included 17 MR imaging (15 with contrast medium) and 12 CT scans using diverse techniques. Underlying CCJDD lesions included atlanto-occipital JACs ( $n = 10$ ), atlantoaxial JACs ( $n = 2$ ), ROFPs ( $n = 4$ ), and

C1-occipital osteophytes ( $n = 2$ ) (On-line Table 2). All 18 patients had cranio-occipital and/or upper cervical degenerative disease on imaging studies. Altered cervical biomechanics in 4 of 18 patients was secondary to congenital nonsegmentation in 2 patients (C1-occipital and C2–C3) and prior surgical fusion in 2 patients (C2–C5 dorsal fixation and C6–C7 anterior cervical discectomy and fusion).

CCJ JACs appeared as well-circumscribed extradural lesions extending cephalad into the foramen magnum to encroach on the hypoglossal canal internal ostium. They showed lobular projections that were at least partially divergent from the expected twelfth cranial nerve course (Fig 1). On MR imaging, all 12 JACs were T1-hypointense and T2-hyperintense relative to the brain stem and lacked central contrast enhancement. On CT, cysts typically appeared predominantly hypoattenuated (5/6). In 4 of 12 JACs, twelfth cranial nerve compression was limited to the hypoglossal canal internal ostium, where 50% or more of the ostium was covered by JAC in every case. More commonly (8/12), CCJ JACs extended into the hypoglossal canal and caused focal smooth canal widening on CT in 3 of 8 patients (Fig 2). On axial T2-weighted images, the mean CCJ JAC size was 12.3 mm in maximal dimension (range, 7–19 mm). For the 10 patients with CCJ JAC and MR imaging follow-up (mean, 542 days; SD, 855), 4 cysts had decreased in size, 2 were stable, and 4 were enlarged. In 2 of 12 cases, the JAC was not described in the initial radiology report. More often (6/12), the JAC was seen but not correctly identified in the initial radiology report differential diagnosis. In these cases, the correct diagnosis was made at follow-up imaging or at prior examination review.

ROFPs ( $n = 4$ ) uniformly appeared hyperattenuated on unenhanced CT (3/3) and often extended into the hypoglossal canal (3/4), causing focal irregular bony erosion (2/3) or smooth remodeling (1/3) (Fig 3). On MR imaging, relative to the adjacent brain stem, these masses were T1 iso-hypointense (3/3), T2 hypointense (2/3), or T2 iso-hyperintense (1/3) and showed some internal enhancement in 3 of 4 cases. The ROFP was correctly included in the initial radiology report differential diagnosis in 3 cases. In the fourth case, the offending ROFP was not seen despite radiologist identification of ipsilateral hypoglossal atrophy.

Two patients with hypoglossal



**FIG 1.** C1-occipital JAC encroaching on the hypoglossal canal internal ostium of patient 1. The patient was a 56-year-old man with a 3-month history of tongue weakness. The T2-hyperintense JAC (*large arrows*) encroachment of the hypoglossal canal internal ostium (*arrowhead*) and lobular cyst projections (*small arrows*) from the C1-occipital joint are best seen on T2-weighted coronal (A) and sagittal (B) images. C, Postcontrast T1-weighted coronal image shows JAC thin rim enhancement (*large arrow*).

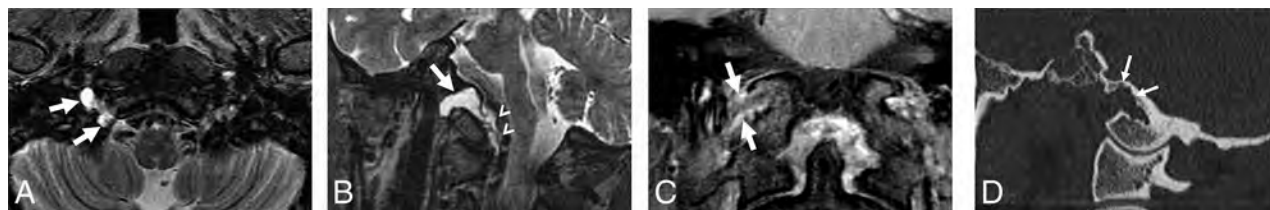


**FIG 2.** C1-occipital JAC extending into hypoglossal canal of patient 12. The patient was a 64-year-old man with a 9-month history of tongue weakness, dysarthria, and dysphagia. A, MR T2-weighted axial image shows an extradural hyperintense JAC with a thin hypointense rim extending through the hypoglossal canal (*large arrows*). B, Oblique T2-weighted image parallel to the hypoglossal canal shows the JAC extension through the hypoglossal canal (*large arrow*) and contiguity with the C1-occipital joint through a thin lobular extradural projection (*arrowheads*). C, Postcontrast T1-weighted coronal image shows cyst rim enhancement (*large arrows*). D, CT sagittal bone reconstruction at the hypoglossal canal external ostium shows secondary canal widening (*arrows*).

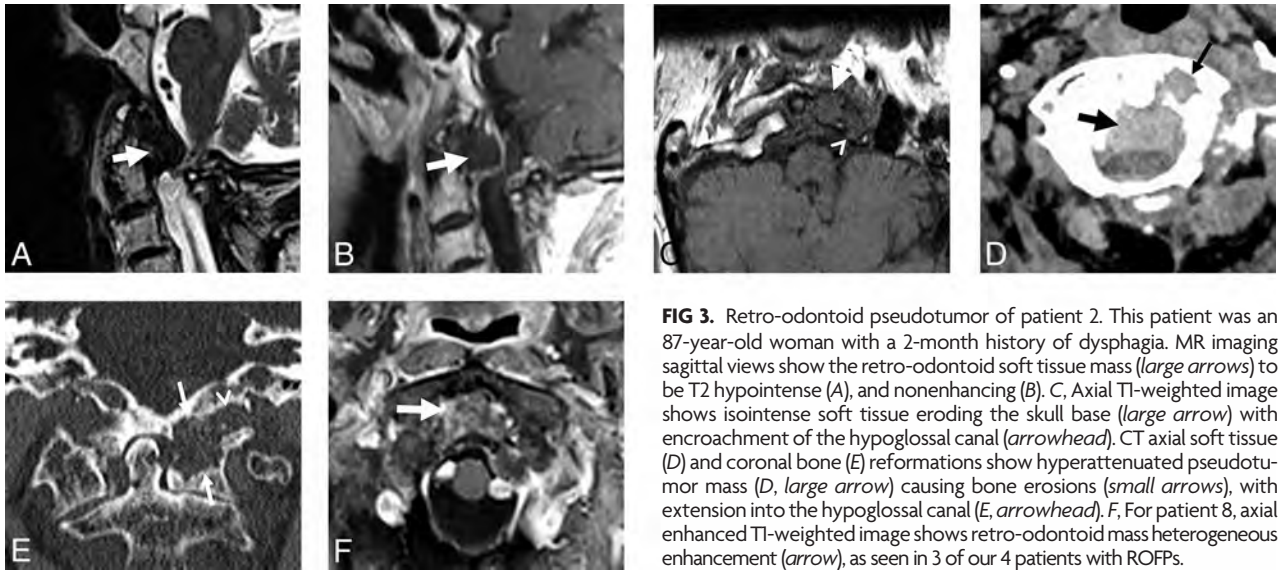


**FIG 3.** Retro-odontoid pseudotumor of patient 2. This patient was an 87-year-old woman with a 2-month history of dysphagia. MR imaging sagittal views show the retro-odontoid soft tissue mass (*large arrows*) to be T2 hypointense (*A*), and nonenhancing (*B*). *C*, Axial T1-weighted image shows isointense soft tissue eroding the skull base (*large arrow*) with encroachment of the hypoglossal canal (*arrowhead*). CT axial soft tissue (*D*) and coronal bone (*E*) reformations show hyperattenuated pseudotumor mass (*D, large arrow*) causing bone erosions (*small arrows*), with extension into the hypoglossal canal (*E, arrowhead*). *F*, For patient 8, axial enhanced T1-weighted image shows retro-odontoid mass heterogeneous enhancement (*arrow*), as seen in 3 of our 4 patients with ROFPs.

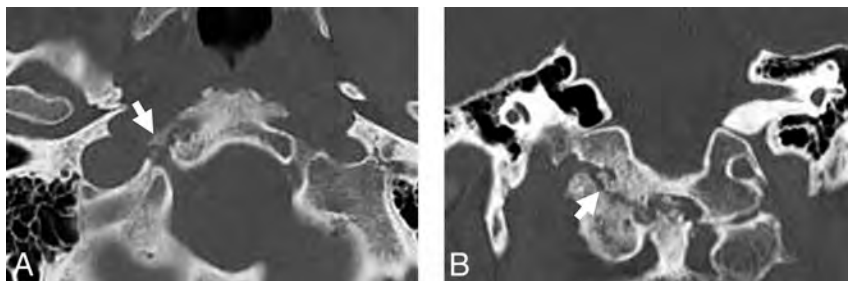


**FIG 4.** C1-occipital osteophyte of patient 7. This patient was a 77-year-old man with a 3-month history of tongue weakness and dysarthria. CT axial (*A*) and coronal (*B*) images show severe C1-occipital arthrosis with osteophyte encroachment at the hypoglossal canal external ostium (*arrows*).

palsy with advanced CCJDD had C1-occipital joint osteophyte encroachment on the ipsilateral hypoglossal canal external ostia. In these patients, C1-occipital arthrosis and osteophytes narrowed the hypoglossal canal and caused erosions of its walls. The osteophytes appeared hypointense on T1- and T2-weighted MR imaging, and hyperattenuated on CT (Fig 4). Degenerative osteophyte encroachment on the hypoglossal canal was correctly identified within the initial radiology report for 1 patient. For the other patient, the offending osteophyte was not seen, though tongue hemiatrophy was noted in the radiology report.

#### Surgical Correlation

Four patients underwent surgical treatment for hypoglossal nerve compression by CCJ JACs. Two patients had atlanto-occipital JAC resection, with pathologic evaluation confirming synovial cysts. In another 2 patients with CCJ JAC, the hypoglossal palsy was considered irreversible, and occipital-C2 posterior fusion was performed to prevent additional cranial nerve injury by potential cyst enlargement. Postfusion MRI demonstrated resolution of 1 atlanto-occipital JAC and decreased size for the other. Surgery was not performed in patients with hypoglossal palsy caused by underlying ROFPs or osteophytes.

#### DISCUSSION

Hypoglossal nerve palsy is uncommon, and diagnosis of the underlying cause can be problematic for clinicians and radiologists. High-resolution imaging and a detailed understanding of twelfth cranial nerve anatomy are critical to the identification of causative lesions and to formulating an educated differential diagnosis. Overall, tumors are the most common cause of hypoglossal nerve palsy, accounting for nearly 50% of cases.<sup>1</sup> Hypoglossal nerve palsy secondary to premedullary cistern or hypoglossal

canal pathology is most frequently caused by hematogenous skull base metastasis. Skull base invasion of nasopharyngeal carcinoma, radiation-induced neuropathy, hypoglossal neuritis, and schwannomas or secondary nerve compression by meningioma, aneurysm, arachnoid cyst, and occipital condyle fracture are also commonly included in the differential diagnosis.<sup>1,2,4,5,8-10</sup> Our series of 18 patients with hypoglossal palsy secondary to JACs, ROFPs, and osteophytes is, to our knowledge, the largest series with underlying CCJDD pathologic causes. In this retrospective series, perceptual and interpretive errors in diagnosis led to an underreporting of these lesions as the cause for hypoglossal palsy.

#### Juxta-Articular Cysts

Isolated case reports have described hypoglossal palsy resulting from CCJ juxta-articular synovial<sup>2,4,5</sup> and ganglion<sup>3,6-8</sup> cysts arising from either the atlanto-occipital<sup>2-4,8</sup> or the atlantoaxial<sup>5</sup> joints. Although synovial and ganglion cysts can be distinguished histologically, differentiation by imaging is neither feasible nor clinically important. Therefore, it is practical to adhere to the convention proposed by Kao et al<sup>11</sup> and simply identify either synovial or ganglion cysts as JACs. Spinal degeneration and segmental instability are thought to have an im-

portant role in JAC development, having a predilection for the most mobile levels in the cervical spine.<sup>12</sup> Our series included 1 patient with developmental occipitalization of C1, which might have contributed to the patient's atlantoaxial JAC formation.

Most of our patients with CCJ JAC (8/12) were women (mean age, 70.2 years; range, 52–89 years). Our findings are consistent with the female predilection<sup>13</sup> and higher seventh-decade prevalence<sup>12,13</sup> previously reported for lumbar spinal JACs. Of interest, though the association of headache and JAC was noted previously in a case report,<sup>5</sup> 10 of 12 patients with CCJ JAC reported new or worsening ipsilateral headache or suboccipital pain initiating in close relation to their hypoglossal palsy onset.

CCJ JACs appeared as well-defined extradural lesions with extension into the hypoglossal canal and narrow connections with the parent atlanto-occipital or atlantoaxial joint best visualized on thin-section, coronal T2-weighted images and oblique 2D or 3D reformations parallel to the hypoglossal canal. JACs were most conspicuous on T2-weighted images, where they uniformly showed a thin hypointense cyst wall and central hyperintensity. On postcontrast T1-weighted images, cysts showed only peripheral rim enhancement. These findings are consistent with those reported in a large imaging review of lumbar synovial cysts.<sup>13</sup> On CT, CCJ JACs were mostly hypoattenuated (6/7). All CCJ JACs encroached on the hypoglossal canal internal ostium by 50% or more, with most (8/12) extending into or through the hypoglossal canal. Secondary hypoglossal canal smooth remodeling, as previously reported in lumbar JACs,<sup>13</sup> was seen in 3 of 8 patients. Ten patients had follow-up MR imaging without intervening surgery, revealing JAC size to be enlarged in 4, unchanged in 2, and decreased in 4. Synovial cyst size variation has been reported previously in the lumbar spine, where decreased size<sup>13</sup> or complete resolution<sup>14</sup> might be attributed to diminished synovial inflammatory fluid production or spontaneous cyst rupture.

CCJ JACs that cause hypoglossal palsy can be treated with surgical resection via a lateral suboccipital craniotomy,<sup>2-4,7,8</sup> posterior fusion, or conservative management.<sup>5</sup> Most of our 12 patients with hypoglossal palsy caused by CCJ JAC chose conservative management because the hemiglossal palsy was clinically tolerable and considered likely irreversible. Four patients with CCJ JAC underwent surgery. Two patients with cyst resection had no change in hypoglossal palsy, though suboccipital headache decreased for 1 patient. For 2 patients who underwent occipital-C2 fusion, postoperative MRI showed that the JACs either resolved or decreased in size, though neither patient reported improvement in hypoglossal palsy symptoms or suboccipital headache. The CCJ JAC decreased size or resolution after occipital-C2 fusion supports the theory that spinal instability strongly contributes to synovial cyst formation because increased motion causes synovial inflammation and secondary fluid production.

#### **Retro-Odontoid Fibrous Pseudotumor**

Retro-odontoid soft tissue masses causing cervicomedullary compression can result from numerous diseases, including rheumatoid arthritis<sup>15</sup> and calcium pyrophosphate deposition disease.<sup>16</sup> Some investigators have theorized that in noninflammatory

ROFP, also known as degenerative pseudopannus, soft tissue masses composed of benign fibrous granulation tissue form in response to chronic atlantoaxial subluxation.<sup>17,18</sup> Other investigators have reported ROFP formation in patients without overt atlantoaxial subluxation<sup>19,20</sup> and proposed that altered biomechanics attributable to adjacent segment ankyloses cause repeated transverse ligament injury with resulting hypertrophy. None of our 4 patients with ROFP had a systemic arthritic condition. Two had previously undergone surgical cervical fixation, with resulting altered biomechanics likely contributing to chronic, excessive atlantoaxial stress.

Although most of the previously reported patients with ROFP were men, most patients in our series were women. Our mean patient age of 82 years (range, 70–87 years) is higher than previously reported by Chikuda et al<sup>19</sup> (mean, 72 years) and Kakutani et al<sup>20</sup> (mean, 76 years). The most common clinical manifestation of ROFP is myelopathy secondary to ventral cervicomedullary compression.<sup>18-20</sup> To the best of our knowledge, ROFP has not been previously reported as a cause of hypoglossal palsy. Of interest, none of our 4 patients with CCJ ROFP hypoglossal palsy had myelopathy on neurologic examination, though imaging showed ventral cervicomedullary compression in 2 of the 4 patients.

ROFPs in our series showed variable MR imaging characteristics on T1- (hypointense, 2/3; isointense, 1/3) and T2-weighted (hypointense, 2/3; mixed iso-hyperintense, 1/3) sequences. Most ROFPs have been reported as iso-hypointense on T1-weighted images and hypointense on T2-weighted images,<sup>17,19</sup> consistent with a predominant fibrous composition. Alternatively, some ROFPs have been described on T2-weighted images as an admixture of iso-hyperintensity,<sup>18,20</sup> perhaps reflecting a larger component of vascular granulation tissue. ROFP enhancement, variably described as “absent” and “present” in previous reports,<sup>18,20</sup> was seen in 3 of our 4 patients. Prior studies have shown that CCJ pseudotumor mass volume can decrease after direct resection,<sup>17</sup> occipital-cervical fusion,<sup>18,19</sup> or C1 laminectomy,<sup>20</sup> with secondary myelopathy commonly improved after either surgical approach.<sup>18-20</sup>

#### **Atlanto-Occipital Osteophytes**

Hypoglossal palsy secondary to atlanto-occipital osteophytes has been previously described in single-case reports.<sup>9,10</sup> In our 2 patients with hypoglossal palsy secondary to C1-occipital osteophytes, osteophyte encroachment and secondary hypoglossal canal wall erosions were observed at the external ostium. This external canal encroachment is in contrast to ROFPs and CCJ JACs, which encroach on the internal ostium, and commonly extended within and/or through the hypoglossal canal. One of our 2 patients with C1-occipital osteophytes had underlying congenital C2–C3 vertebral body nonsegmentation. Both patients were treated conservatively because unilateral hypoglossal palsy is reasonably well tolerated, requires complex surgery with substantial morbidity, and is unlikely to regress postoperatively.

#### **Improving CCJDD Lesion Recognition and Differentiating JACs from Hypoglossal Schwannomas**

In our series, CCJDD lesions causing hypoglossal palsy were often undiagnosed at initial imaging interpretation because of percep-

tual or interpretive errors. Among the 18 patients, perceptual errors—in which the underlying CCJ lesion was not described in the initial imaging interpretation despite radiologist notation of ipsilateral hemiglossal atrophy—were found in 4 patients (2 of 12 patients with JACs; 1 of 3 with ROFPs; 1 of 2 with osteophytes). Interpretive errors—in which the lesion was described in the initial imaging report, yet was not correctly specified within the differential diagnosis—occurred in 6 of the 12 patients with CCJ JAC. Therefore, hypoglossal palsy causative JAC was correctly included in the initial radiology report in only 33% (4/12) of our patients with JAC. The underlying lesion was correctly included in the initial radiology report's differential diagnosis in 3 of 4 ROFP cases and 1 of 2 cases of hypoglossal canal osteophyte encroachment.

Diverse MR imaging and CT techniques used at outside institutions and our tertiary medical centers during this 10-year retrospective period were seldom optimized for evaluation of twelfth cranial nerve pathologies. Contrast-enhanced CT is the most common initial imaging study for evaluating patients with hypoglossal palsy. Helical acquisition from the posterior fossa to the hyoid bone allows evaluation from the medullary hypoglossal nuclei to the end-organ intrinsic tongue, styloglossus, hyoglossus, and genioglossus muscles. Demonstration of hypoglossal canal encroachment by CCJDD lesions can be aided by small field of view, thin-section ( $\leq 2$  mm) axial, coronal, and sagittal soft tissue and bone reconstructions centered at the hypoglossal canal. Oblique reformations parallel to the hypoglossal canal can be helpful in assessing intracranial extension and bony erosion. In our series, CCJ JACs, the most common CCJDD lesion to cause hypoglossal palsy, were more conspicuous on MR imaging than CT. A dedicated posterior fossa–skull base MR imaging protocol, including thin-section ( $\leq 3$  mm), small field of view sequences, should be used to evaluate patients with hypoglossal palsy in whom initial enhanced neck CT is unrewarding or in whom hemiglossal atrophy is noted on routine MR imaging. Besides postcontrast T1-weighted images, T2-weighted sequences are particularly helpful in evaluating CCJ degenerative lesions. Their inclusion in all 3 planes, ideally as a high-resolution volumetric sequence, is strongly recommended.

Among our 12 patients with CCJ JACs, cystic hypoglossal schwannoma was listed within the report differential 5 times. Differentiating CCJ JACs from “cystic” hypoglossal schwannomas is challenging. In a series of 44 surgically treated hypoglossal schwannomas, Nonaka et al<sup>21</sup> found clinical presentations similar to CCJ JACs, with a female predominance, mean patient age of 45.8 years, and symptoms including ipsilateral tongue atrophy (92%), headache (61%), and dysphagia (32%). Hypoglossal schwannomas can be characterized as intracranial (31.5%), extra- and intracranial “dumbbell” (50%), or extracranial (18.5%),<sup>22</sup> with secondary hypoglossal canal enlargement reported in up to 83%.<sup>21</sup> So-called cystic hypoglossal schwannomas are uncommon, with cystic foci most often developing within large tumors with necrosis or spontaneous intratumoral hemorrhage.<sup>23,24</sup> In a previous cystic hypoglossal schwannoma case report, preoperative MR imaging showed peripheral enhancement surrounding cystic regions, whereas the tumor solid component enhanced uniformly.<sup>23</sup> Thus, hypoglossal schwannomas and CCJ JACs share

identical clinical presentations, might extend into and remodel the hypoglossal canal, and appear T1 hypointense and T2 hyperintense on MR imaging. However, an extradural location at the premedullary cistern, contiguity with the atlanto-occipital or atlantoaxial joints, lobular projections inconsistent with the hypoglossal nerve course, and thin peripheral contrast enhancement without solid enhancing component are helpful in distinguishing CCJ JACs from cystic hypoglossal schwannomas. This distinction is imperative because CCJ JAC misdiagnosis as a hypoglossal schwannoma can result in mistreatment and potential morbidity of stereotactic radiosurgery or in an unwarranted intradural surgical approach with possible cranial nerve injury.<sup>4</sup>

The present study has several limitations. It is a retrospective review of a rare entity and is limited as such. Based on our method for identifying patients for review, the potential exists for missing cases in which the neuroradiologist did not include “hypoglossal palsy” or “tongue atrophy” in the radiology report. A referral bias might be present because our institution is a tertiary care center. In addition, at our large referral center, many patients had limited or no long-term follow-up after their initial evaluation. Most patients were conservatively treated, limiting surgical confirmation.

## CONCLUSIONS

Though degenerative disease at the craniocervical junction is commonly seen on imaging studies, it has been rarely reported as a cause of hypoglossal palsy. JACs were a more common CCJDD causative lesion than ROFPs and osteophytes. CCJDD should be added to the list of potential hypoglossal palsy causes, and familiarity with each type of CCJ degenerative lesion and its characteristic imaging appearance should improve the diagnosis and treatment of these disorders.

## REFERENCES

1. Thompson EO, Smoker WR. **Hypoglossal nerve palsy: a segmental approach.** *Radiographics* 1994;14:939–58 CrossRef Medline
2. Mujic A, Hunn A, Liddell J, et al. **Isolated unilateral hypoglossal nerve paralysis caused by an atlanto-occipital joint synovial cyst.** *J Clin Neurosci* 2003;10:492–95 CrossRef Medline
3. Baldauf J, Junghans D, Schroeder HW. **Endoscope-assisted microsurgical resection of an intraneural ganglion cyst of the hypoglossal nerve.** *J Neurosurg* 2005;103:920–22 CrossRef Medline
4. Elhammady MS, Farhat H, Aziz-Sultan MA, et al. **Isolated unilateral hypoglossal nerve palsy secondary to an atlantooccipital joint juxtafacet synovial cyst.** *J Neurosurg Spine* 2009;10:234–39 CrossRef Medline
5. Mendes-Araújo L, Rangel C, Domingues RC, et al. **Case report: atlantoaxial synovial cyst causing isolated unilateral hypoglossal nerve paralysis.** *Br J Radiol* 2010;83:e35–38 CrossRef Medline
6. Nonaka Y, Grossi PM, Filomena CA, et al. **Unilateral hypoglossal nerve palsy caused by an intraneural ganglion cyst.** *J Neurosurg* 2010;113:380–83 CrossRef Medline
7. Gambhir S, Mujic A, Hunn A. **An intraneural ganglion cyst causing unilateral hypoglossal nerve palsy.** *J Clin Neurosci* 2011;18:1114–15 CrossRef Medline
8. Bilgin-Freiert A, Fugleholm K, Poulsgaard L. **Case report: intraneural intracanalicular ganglion cyst of the hypoglossal nerve treated by extradural transcondylar approach.** *J Neurol Surg Rep* 2015;76:e180–82 CrossRef Medline
9. Patron V, Roudaut PY, Lerat J, et al. **Isolated hypoglossal palsy due to cervical osteophyte.** *Eur Ann Otorhinolaryngol Head Neck Dis* 2012;129:44–46 CrossRef Medline
10. Patro SN, Torres C, Riasco R. **An unusual case of isolated hypoglos-**

- sal nerve palsy secondary to osteophytic projection from the atlanto-occipital joint. *Neuroradiol J* 2014;27:361–64 CrossRef Medline
11. Kao CC, Winkler SS, Turner JH. **Synovial cyst of spinal facet: case report.** *J Neurosurg* 1974;41:372–76 CrossRef Medline
  12. Boviatsis EJ, Stavrinou LC, Kouyialis AT, et al. **Spinal synovial cysts: pathogenesis, diagnosis and surgical treatment in a series of seven cases and literature review.** *Eur Spine J* 2008;17:831–37 CrossRef Medline
  13. Apostolaki E, Davies AM, Evans N, et al. **MR imaging of lumbar facet joint synovial cysts.** *Eur Radiol* 2000;10:615–23 CrossRef Medline
  14. Swartz PG, Murtagh FR. **Spontaneous resolution of an intraspinal synovial cyst.** *AJNR Am J Neuroradiol* 2003;24:1261–63 Medline
  15. Casey AT, Crockard HA, Pringle J, et al. **Rheumatoid arthritis of the cervical spine: current techniques for management.** *Orthop Clin North Am* 2002;33:291–309 CrossRef Medline
  16. Patel NP, Wright NM, Choi WW, et al. **Forestier disease associated with a retroodontoid mass causing cervicomedullary compression.** *J Neurosurg* 2002;96(2 suppl):190–96 CrossRef Medline
  17. Sze G, Brant-Zawadzki MN, Wilson CR, et al. **Pseudotumor of the craniovertebral junction associated with chronic subluxation: MR imaging studies.** *Radiology* 1986;161:391–94 CrossRef Medline
  18. Yamaguchi I, Shibuya S, Arima N, et al. **Remarkable reduction or disappearance of retroodontoid pseudotumors after occipitocervical fusion: report of three cases.** *J Neurosurg Spine* 2006;5:156–60 CrossRef Medline
  19. Chikuda H, Seichi A, Takeshita K, et al. **Radiographic analysis of the cervical spine in patients with retro-odontoid pseudotumors.** *Spine (Phila Pa 1976)* 2009;34:E110–14 CrossRef Medline
  20. Kakutani K, Doita M, Yoshikawa M, et al. **C1 laminectomy for retro-odontoid pseudotumor without atlantoaxial subluxation: review of seven consecutive cases.** *Eur Spine J* 2013;22:1119–26 CrossRef Medline
  21. Nonaka Y, Grossi PM, Bulsara KR, et al. **Microsurgical management of hypoglossal schwannomas over 3 decades: a modified grading scale to guide surgical approach.** *Neurosurgery* 2011;69(2 suppl operative):ons121–40; discussion ons140 CrossRef Medline
  22. Hoshi M, Yoshida K, Ogawa K, et al. **Hypoglossal neurinoma: two case reports.** *Neurol Med Chir (Tokyo)* 2000;40:489–93 CrossRef Medline
  23. Li WC, Hong XY, Wang LP, et al. **Large cystic hypoglossal schwannoma with fluid-fluid level: a case report.** *Skull Base* 2010;20:193–97 CrossRef Medline
  24. Takahashi T, Tominaga T, Sato Y, et al. **Hypoglossal neurinoma presenting with intratumoral hemorrhage.** *J Clin Neurosci* 2002;9:716–19 CrossRef Medline

# Variability of Cerebral Deep Venous System in Preterm and Term Neonates Evaluated on MR SWI Venography

 D. Tortora,  M. Severino,  M. Malova,  A. Parodi,  G. Morana,  L.A. Ramenghi, and  A. Rossi

## ABSTRACT

**BACKGROUND AND PURPOSE:** The anatomy of the deep venous system is characterized by a great variability that might play an important role in the pathogenesis of brain lesions in the preterm brain. The aim of this study was to compare the anatomy of cerebral subependymal veins evaluated on SWI venography in 3 groups of neonates with normal brain MR imaging (very preterm [gestational age <32 weeks], moderate-to-late preterm [gestational age  $\geq 32$  to  $\leq 37$  weeks], and term neonates [gestational age >37 weeks]) and to evaluate the influence of preterm birth on development of subependymal veins.

**MATERIALS AND METHODS:** SWI venographies of 84 very preterm, 31 moderate-to-late preterm, and 50 term neonates were retrospectively evaluated. Subependymal vein anatomy was classified into 6 different patterns: type 1 represented the classic pattern and types 2–6 were considered anatomic variants. A  $\chi^2$  test was used to evaluate differences between the distributions of subependymal vein patterns.

**RESULTS:** A significant difference ( $P = .011$ ) was noticed between the 6 patterns based on gestational age. Type 1 was more frequent in term neonates (68%) than in both very preterm (41.7%) and moderate-to-late preterm neonates (56.5%). Anatomic variants were more common in very preterm neonates (66%) than in both moderate-to-late preterm (41%) and term neonates (36%). Interhemispheric asymmetry was more frequent in very preterm (59.5%) and moderate-to-late preterm neonates (51.6%) than in term neonates (34%;  $P = .017$ ). Sex and monozygotic twin birth did not significantly affect the frequency of subependymal vein patterns ( $P = .0962$ ).

**CONCLUSIONS:** The deep venous system of the neonatal brain shows a large spectrum of anatomic variants with higher variability of subependymal vein anatomy in preterm than term neonates, likely related to the influence of the preterm birth and epigenetic factors on subependymal vein development.

**ABBREVIATIONS:** ASV = anterior septal vein; TSV = thalamostriate vein; DLV = direct lateral vein; ICV = internal cerebral vein; SV = subependymal veins

The cerebral deep venous system includes veins that course into the lateral ventricles from the surrounding white matter and basal ganglia and then exit into the transverse fissure, draining into the internal cerebral veins (ICVs).<sup>1</sup> These veins are characterized by their subependymal location in the lateral ventricles and by their centripetal direction of blood flow. In 1964, Wolf and Huang<sup>2</sup> classified the deep venous system into 2 main groups: the deep medullary veins and the subependymal veins (SV). The deep medullary veins are small vessels, arranged in wedge-shaped patterns within the white matter of the cerebral hemispheres, directly participating in the drainage of white matter via the SV into the

ICVs. The SV bilaterally surround the medial and lateral edges of lateral ventricles and are classified based on the portion of the lateral ventricles in which they lie (Fig 1).

The first anatomic studies described the cerebral deep venous system based on ex vivo angiographic planes.<sup>3</sup> Today, MR imaging can be used as an alternative, noninvasive method to characterize the anatomy of cerebral arteries and veins. Several types of angiographic sequences have been developed to unravel the signal of the blood flow in the arteries (arterial MRA) and in the veins (venous MRA). Venous MRA techniques demonstrate the anatomy of larger vessels, such as the cerebral dural veins, but often fail to depict the blood-flow signal in the smaller veins of the deep venous system.<sup>4</sup> However, a relatively new sequence, SWI, can depict small vessels and venous structures rich in deoxygenated blood.<sup>5</sup> Indeed, this 3D, fully velocity-compensated gradient recalled–echo sequence uses deoxyhemoglobin as an intrinsic contrast agent, therefore affording in vivo assessment of even smaller cerebral veins.<sup>6</sup>

Received April 12, 2016; accepted after revision May 23.

From the Neuroradiology Unit (D.T., M.S., G.M., A.R.) and Neonatal Intensive Care Unit (M.M., A.P., L.A.R.), Istituto Giannina Gaslini, Genoa, Italy.

Please address correspondence to Domenico Tortora, MD, Neuroradiology Unit, Istituto Giannina Gaslini, Via Gerolamo Gaslini 5, 16147 Genoa, Italy; e-mail: domenicotortora@gaslini.org

<http://dx.doi.org/10.3174/ajnr.A4877>

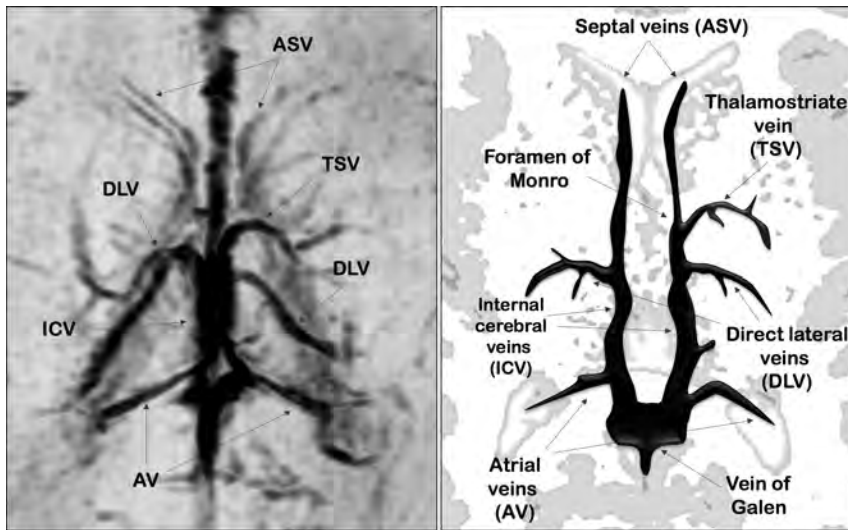


**FIG 1.** Axial-reformatted SWI venography and corresponding schematic representation of SV.

**Table 1: MRI sequence parameters**

Sequence	Section		Intersection (mm)	TR (msec)	TE (msec)	FA (deg)	SAR (W/kg)	Bandwidth
	Thickness (mm)	Matrix						
Axial T1-SE	3	232 × 110	1	780	16	NA	<2.6	8.2
Axial T2-TSE	3	308 × 171	1	6923	140	NA	3.1	5.6
Coronal T2-TSE	3	232 × 171	1	6782	140	NA	<3	6.7
3D T1 TFE	1	200 × 150	NA	9.8	4.6	10	<0.2	2.3
Axial DWI	4	108 × 104	0.4	2530	74	NA	0.3	12.9

**Note:**—FA indicates flip angle; NA, not available; SAR, specific absorption rate; SE, spin echo; TFE, turbo-field echo.

The anatomy of the deep venous system is characterized by a great variability<sup>4,7</sup> that has been ascribed to rearrangement of the main venous drainage of the primitive choroid plexus occurring in the late period of fetal life.<sup>3,8</sup> This anatomic variability might play an important role in the pathogenesis of brain lesions in the preterm brain. In particular, germinal matrix-intraventricular hemorrhage, the most frequent brain lesion and leading cause of poor neurodevelopmental outcome and motor disability in preterm neonates,<sup>9</sup> has been associated with acquired and congenital risk factors,<sup>10</sup> including peculiarities in the venous drainage through the brain deep venous vessels.<sup>11-13</sup> The aim of this study was to describe the anatomy of SV evaluated on SWI venography in 3 groups of neonates with normal brain MR imaging (very preterm [gestational age <32 weeks], moderate-to-late preterm [gestational age ≥32 to ≤37 weeks], and term neonates [gestational age >37 weeks]) and to evaluate the influence of preterm birth on SV development.

## MATERIALS AND METHODS

### Patients

Our institutional review board approved this retrospective study and waived informed consent.

The brain MR imaging studies of 248 consecutive preterm neonates and 83 term neonates acquired from January 2012 to December 2015 were retrospectively evaluated. In preterm neonates, MR imaging was performed at term-equivalent age as a part of a screening program for identification of prematurity-related lesions. Term neonates (gestational age >37 weeks) underwent brain MR imaging within 5 days of birth to rule out suspected

brain lesions detected at early cranial sonography or to evaluate brain involvement after perinatal asphyxia.

Four exclusion criteria were used in this study: presence of brain lesions at MR imaging, history of perinatal asphyxia or any other clinical adverse event, absence of SWI venography in the study protocol, and poor quality of MR images.

Preterm neonates were then classified based on gestational age as very preterm (<32 weeks) and moderate-to-late preterm (≥32 to ≤37 weeks).<sup>14</sup> Among all groups of neonates, the pairs of monozygotic twins were selected, and their SV patterns were compared to identify possible differences in SV anatomy among neonates with identical genes.

### Imaging

MR imaging was performed with a 1.5T whole-body system (Achieva 1.5T X-Series; Philips Healthcare, Best, the Netherlands) using an 8-channel dedicated neonatal head array coil. The parents of the neonates provided written informed consent before acquisitions.

All patients were fed before MR imaging examination to achieve spontaneous sleep and were spontaneously breathing during examination. The need for sedation to prevent head movement was verified with the neuroradiologist based on the infant's state of arousal and the quality of images after the first sequence. Hearing protection was used in all patients. Heart rate and oxygen saturation were noninvasively monitored by pulse oximetry during examination.

All neonates underwent the same MR imaging protocol (Table 1). SWI data were collected with a 3D, fully flow-compensated fast-field echo sequence by using the following parameters: TE = 48 ms, TR = 33 ms, 96 sections, flip angle = 15°, bandwidth = 140 Hz/px, field of view = 120 × 120, acquisition matrix = 512 × 512, acquisition voxel size = 0.78 × 0.88 × 1.5 mm, and reconstructed voxel size = 0.7 × 0.8 × 1 mm. Parallel imaging (sensitivity encoding) with an acceleration factor of 2 resulted in a total acquisition time of 2 minutes and 57 seconds.

### Qualitative Analysis of Subependymal Veins

**Phase 1.** A pediatric neuroradiologist with 20 years' experience in neonatal neuroimaging first reviewed all the MR imaging studies by using a workstation equipped with a professional DICOM viewer (OsiriX Imaging Software; <http://www.osirix-viewer.com>) to exclude neonates with brain lesions. Furthermore, image quality of the acquired SWI sequences was assessed by evaluating the general image quality, noise, venous contrast, and presence of motion artifacts. The selected SWI sequences were translated and rotated into the anterior/posterior commissure



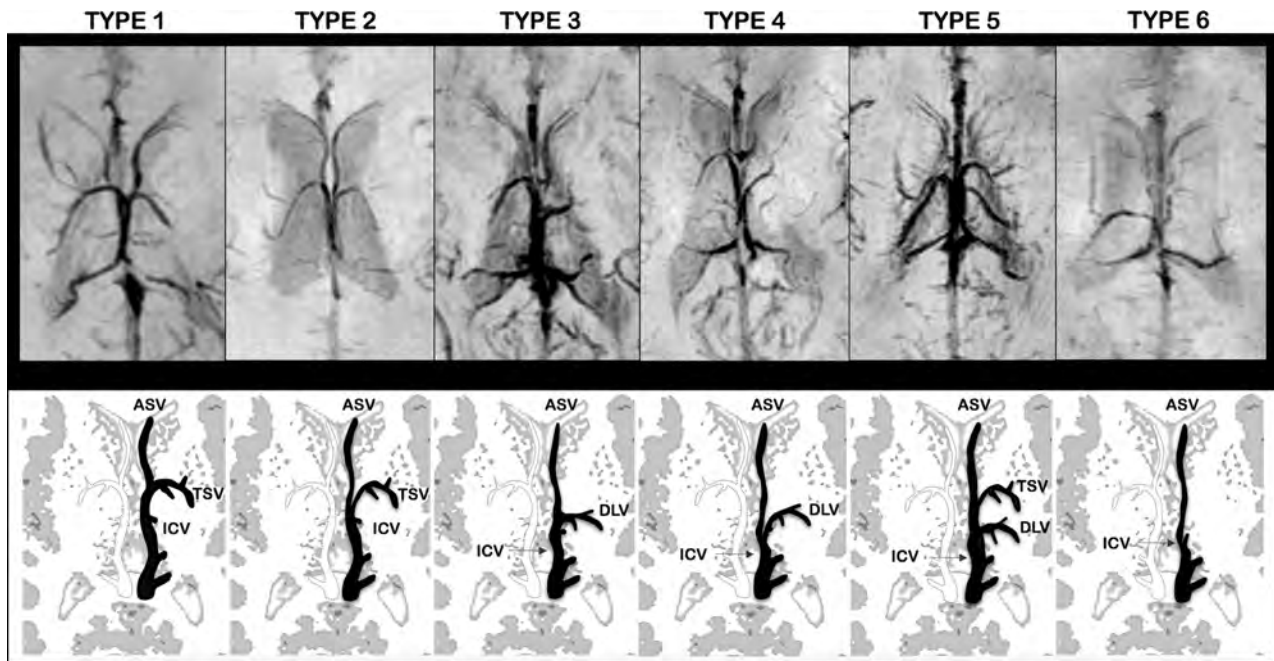


**FIG 2.** Axial-reformatted SWI venography and corresponding schematic representation of SV patterns. The left side of SWI venography and the black schematic vein represent the anatomic pattern. Type 1: The ASV joined the ICV at the level of the foramen of Monro and the TSV-ICV junction. The DLV was absent. Type 2: The ASV joined the ICV posterior to both the TSV-ICV junction and the foramen of Monro. The DLV was absent. Type 3: The ASV joined the ICV close to the site of DLV-ICV junction, posterior to the foramen of Monro. The TSV was absent. Type 4: The ASV joined the ICV posterior to both the foramen of Monro and DLV-ICV junction. The TSV was absent. Type 5: Both the TSV and DLV were present. Type 6: Both the TSV and DLV were absent. Atrial veins were not included in schematic representations.

Talairach baseline<sup>15</sup> to standardize the spatial orientation of each brain.

**Phase 2.** Two neuroradiologists (with 9 and 6 years' experience, respectively), blinded to neonate identity, independently reviewed the SWI sequences selected in phase 1. They identified the SV on the basis of their anatomic location on axial-reformatted SWI sections. The evaluated SV were the anterior septal vein (ASV), thalamostriate vein (TSV), direct lateral vein (DLV), atrial vein, and ICV (Fig 1).

Subsequently, they evaluated the location of the junction between the ASV and ICV and classified it into 2 categories: 1) at the level of the foramen of Monro and 2) posterior to the foramen of Monro.

**Phase 3.** Based on the results of the phase 2 evaluation, readers independently assigned 1 of 6 patterns of subependymal vein anatomy for each brain hemisphere (Fig 2):

- Type 1: The ASV joined the ICV at the level of the foramen of Monro and the TSV-ICV junction. The DLV was absent. According to Stein and Rosenbaum<sup>3</sup>, this pattern describes the classic anatomy of SV.
- Type 2: The ASV joined the ICV posterior to both the TSV-ICV junction and the foramen of Monro. The DLV was absent.
- Type 3: The ASV joined the ICV close to the site of DLV-ICV junction, posterior to the foramen of Monro. The TSV was absent.
- Type 4: The ASV joined the ICV posterior to both the foramen of Monro and DLV-ICV junction. The TSV was absent.
- Type 5: Both the TSV and DLV were present.
- Type 6: Both the TSV and DLV were absent.

In all SV patterns, the atrial vein was present and had the same course below the splenium of the corpus callosum, joining the posterior end of the ICV.

Furthermore, the SV pattern of each hemisphere was compared with the contralateral to classify each neonate into a symmetric or asymmetric venous pattern group. Finally, the SV anatomic pattern of each pair of monozygotic twins was evaluated to assess if a venous "intertwin" anatomic variability existed.

**Phase 4.** The same 2 neuroradiologists jointly reviewed the SWI venography of neonates with phase 3 discordant evaluation and were asked to reach a consensus on the SV pattern and interhemispheric symmetry definitions.

### Statistical Analysis

Statistical analysis was performed using SPSS Statistics for Mac, Version 21.0 (IBM, Armonk, New York). The level of significance was set at  $P < .05$ .

The frequencies and percentages of different SV patterns were calculated for all neonates and separately for the 3 different gestational age groups and for each pair of monozygotic twins. Significant gestational age and sex differences were assessed by a  $\chi^2$  test. The same test was also used to evaluate significant differences in the distribution of the symmetric and asymmetric SV pattern among the 3 gestational age groups.

## RESULTS

### Patients

The MR imaging studies of 166 patients (133 of 248 [54%] preterm neonates and 33 of 83 [40%] term neonates) were excluded from this study based on the exclusion criteria. In particular, 56

**Table 2: Overall frequencies and percentages of SV patterns for each brain hemisphere in the 3 groups of neonates<sup>a</sup>**

Pattern	VP		MLP		TN		Total Hemispheres
	Left	Right	Left	Right	Left	Right	
Type 1	28 (33.3%)	42 (50%)	15 (48.4%)	20 (64.5%)	36 (72%)	32 (64%)	173
Type 2	4 (4.8%)	6 (7%)	4 (12.9%)	0 (0%)	2 (4%)	3 (6%)	19
Type 3	36 (42.9%)	25 (29.8)	9 (29%)	7 (22.6%)	10 (20%)	13 (26%)	100
Type 4	7 (8.2%)	4 (4.8%)	3 (9.7%)	1 (3.2%)	2 (4%)	2 (4%)	19
Type 5	5 (6%)	2 (2.4%)	0 (0%)	2 (6.5%)	0 (0%)	0 (0%)	9
Type 6	4 (4.8%)	5 (6%)	0 (0%)	1 (3.2%)	0 (0%)	0 (0%)	10

Note:—MLP indicates moderate-to-late preterm neonates; TN, term neonates; VP, very preterm neonates.

<sup>a</sup> 84 VP neonates; 31 MLP neonates; 50 TN neonates.

**Table 3: Frequencies and percentages of interhemispheric symmetry and asymmetry patterns in the 3 groups of neonates**

Pattern	VP	MLP	TN	Total Neonates
Interhemispheric symmetry	34 (40.5%)	15 (48.4%)	33 (66%)	82
Interhemispheric asymmetry	50 (59.5%)	16 (51.6%)	17 (34%)	83
Total neonates	84	31	50	165

Note:—MLP indicates moderate-to-late preterm neonates; TN, term neonates; VP, very preterm neonates.

neonates presented brain lesions and a pathologic clinical history, 37 MR images were affected by motion artifacts, and the remaining 73 neonates lacked SWI venography.

Thus, MR imaging studies of 115 of 248 (46%) preterm neonates and 50 of 83 (60%) term neonates (13 females; average gestational age, 39 weeks; range 37–41 weeks) were included in this study. Eighty-four of 115 (73%) preterm neonates were very preterm (40 females; average gestational age, 28 weeks; range, 23–32 weeks), and 31 of 115 (27%) were moderate-to-late preterm neonates (19 females; average gestational age, 34 weeks; range, 32–36 weeks). Six pairs of female monozygotic twins were identified among the selected neonates; 1 pair was very preterm (gestational age, 26 weeks) and 5 pairs were moderate-to-late preterm (average gestational age, 34 weeks; range 32–36 weeks).

### Qualitative Analysis of SV

The consensus reading was necessary in 11 of 165 (6.6%) neonatal hemispheres (3 very preterm, 4 moderate-to-late preterm, and 4 term). In all discordant cases, the consensus reading was necessary to define the site of ASV–ICV junction to distinguish type 3 and type 4 patterns (9 of 11 hemispheres were finally assigned to the type 3 pattern).

No gestational-age difference was observed between the group of males ( $n = 91$ ) and females ( $n = 74$ ;  $P = .653$ ). Moreover, no significantly different frequencies of SV patterns were observed between male and female neonates ( $P = .962$ ).

The frequencies and percentages of each SV anatomic pattern for the 3 groups of neonates are reported in Table 2. A significant difference was noticed between the 6 anatomic patterns according to gestational age at birth ( $\chi^2 = 22.977$ ;  $P = .011$ ). The classic anatomic pattern (type 1) was more frequent in term neonates (68%) than in both very preterm (41.7%) and moderate-to-late preterm neonates (56.5%). The type 3 pattern was the most fre-

quent anatomic variant and was more frequent in very preterm (36.3%) and moderate-to-late preterm (25.8%) neonates. The type 5 and type 6 anatomic patterns were the least frequent and were exclusively observed in very preterm and moderate-to-late preterm neonates.

Table 3 provides frequencies and percentages of interhemispheric asymmetry of SV pattern for the 3 groups of neonates. A significant age difference

was observed between the symmetric and asymmetric pattern ( $\chi^2 = 8.194$ ;  $P = .017$ ). The asymmetric pattern was observed more frequently in very preterm (59.5%) and moderate-to-late preterm neonates (51.6%) than in term neonates (34%). Furthermore, the right hemisphere of very preterm and moderate-to-late preterm neonates more frequently presented the classic SV pattern (type 1) than the left hemisphere. Accordingly, the left hemisphere commonly showed variations from the classic patterns.

The analysis of the SV pattern performed on the 6 pairs of monozygotic twins identified different SV patterns between siblings in 5 of 6 pairs (83.3%).

### DISCUSSION

The anatomy of the cerebral deep venous system is highly variable in humans. In adults, a systematic observation of the cerebral venous system on MR images has revealed a great anatomic variability of the deep venous system.<sup>4,7</sup> Four types of deep venous anatomic variants, according to the locations of the ASV–ICV and TSV–ICV junctions in adult brains (types 1–4), have been described to date.<sup>4,16</sup> The present study with SWI venography demonstrates that the deep venous system of the neonatal brain shows an even larger spectrum of anatomic variants. In particular, the present classification included 2 additional patterns characterized by the simultaneous presence or absence of both TSV and DLV (types 5 and type 6, respectively). Furthermore, in this classification, the posterior location of the ASV–ICV junction relative to the foramen of Monro (types 3 and 4) was not related to an abnormal course of the TSV, but it was considered an anatomic marker of a prominent DLV.

The presence of so many possible anatomic variants likely reflects the complexity of the development of the deep venous system. Indeed, the evolution of cranial veins falls into an orderly sequence related to the changing environment of the fetal brain. The venous drainage in early stages of brain development occurs through the superficial pial venous network in a centrifugal direction. The appearance of the deep venous system is concomitant with the expansion of the cerebral hemispheres and seems to be a necessary circulatory adjustment to the thickening of the periventricular white matter, which encourages an additional centripetal blood flow.<sup>1</sup> SV are thought to be derivatives of the primitive choroid veins (superior and inferior) that are tributaries of the ICV. As the hemispheres expand, complex mechanisms of integration between the venous structures of the primitive choroid plexus occur, determining the relatively high frequency of variation of SV in the normal neonatal brain.<sup>17</sup>

To our knowledge, this is the first study using SWI venography to identify and characterize the venous phenotype associated with preterm birth. The analysis of the SV anatomy of preterm and term neonates revealed significant differences. As expected, the most frequent pattern of SV anatomy matched its classic definition (type 1) in all groups of neonates (ie, the SV were symmetric in both hemispheres, and the TSV was present bilaterally with the ASV–ICV junction located near the foramen of Monro). Conversely, we demonstrated that preterm neonates more frequently presented variations from this pattern. In particular, in very preterm neonates, the DLV replaced a hypoplastic TSV (type 3) with higher frequency than in both moderate-to-late preterm and term neonates (36.3%, 25.8%, and 23%, respectively).

The increased variability of the SV pattern in association with preterm delivery might be explained by the modifications of the environment and angiogenetic factors affecting vascular development after birth. In fact, cerebral vessel development is highly influenced by oxygen levels and fatty acid concentrations.<sup>18–22</sup> Preterm neonates are delivered into a relatively hyperoxic environment compared with the oxygen levels in the uterus, where relative hypoxia stimulates vessel growth and development. In addition, preterm neonates are deficient in numerous factors normally passed over the placenta during the third trimester of pregnancy, including the essential fatty acids, which are structural and functional constituents of cell membranes and play a fundamental role in vascular development and function.<sup>23</sup>

Intriguingly, in the present study, the proportions of anatomic variants of SV were equally spread among male and female neonates. Sex differences in brain anatomy are known to be present already at birth. In particular, males have greater intracranial and cortical gray-matter volumes than females, and they present larger cranial circumference.<sup>24</sup> The absence of sex differences in the anatomic pattern of SV in the present study further suggests that brain venous development is not only genetically determined, but also might be influenced by perinatal environmental factors. This hypothesis is also supported by the presence of different SV patterns in almost all pairs of monozygotic twins (83.3%). Similarly, previous MR studies on monozygotic twins showed high variability in the cortical pattern, thus underlying the strong influence of epigenetic factors on CNS development.<sup>25,26</sup>

We also found a high age-dependent interhemispheric variability of the SV patterns, with very preterm and moderate-to-late preterm neonates presenting an asymmetric SV pattern with higher frequency than term neonates. Hemispheric anatomic asymmetries were first observed in postmortem studies on the fetal and premature cortex, showing that some areas of the right hemisphere mature quicker than the corresponding areas in the left hemisphere.<sup>27,28</sup> More recent MR imaging studies demonstrated that left–right hemispheric asymmetries in infants are region-specific. For instance, the superior temporal sulcus develops earlier in the right hemisphere,<sup>29</sup> and the Broca area develops earlier in the left hemisphere.<sup>30</sup> Recently, Lin et al<sup>31</sup> demonstrated hemispheric asymmetries and regional differences in cerebral oxygen metabolism, blood flow, and blood volume with near-infrared spectroscopy in premature and term neonates. In particular, they found a higher metabolism and perfusion in the right hemisphere, especially in preterm neonates, supporting current theo-

ries about the delay in maturation of the left hemisphere at birth.<sup>32,33</sup> Interestingly, in the present study, preterm neonates presented the classic SV pattern (type 1) with higher frequency in the right than in the left hemisphere. Considering that the left hemisphere matures later and, thus, is more exposed to the influence of postnatal epigenetic factors, we hypothesize that the variations from the classic SV pattern might represent different forms of a delayed venous development, whereas the type 1 SV pattern might be considered a marker of maturation of the brain structures. Nevertheless, the relationship between development, morphology, and function of the SV itself remains speculative and is worthy of future investigation. In particular, because the degree of prematurity remains a main risk factor for hemorrhagic brain injury,<sup>14</sup> further studies are needed to explore if the wider variability of SV patterns in very preterm neonates have implications for the development of these lesions.

## CONCLUSIONS

MR SWI venography represents an in vivo, noninvasive method able to describe morphologic, positional, and numeric variants of SV in neonates. In this study, we provided the frequencies of 6 different anatomic patterns in very preterm, moderate-to-late preterm, and term neonates with normal brain MR imaging and demonstrated a significant age difference in SV pattern distribution, likely related to the influence of preterm birth and epigenetic factors on deep venous system development.

## REFERENCES

1. Stephens RB, Stilwell DL. *Arteries and Veins of the Human Brain*. Springfield, Illinois: C.C. Thomas; 1969
2. Huang YP, Wolf BS. **Veins of the white matter of the cerebral hemispheres (the medullary veins)**. *Am J Roentgenol Radium Ther Nucl Med* 1964;92:739–55 Medline
3. Stein RL, Rosenbaum AE. **Deep supratentorial veins. Section I. Normal deep cerebral venous system**. In: Newton TH, Potts DG, eds. *Radiology of the Skull and Brain, vol 2. (angiography), book 3 (veins)*. St. Louis: Mosby; 1974:1903–98
4. Cimşit NC, Türe U, Ekinci G, et al. **Venous variations in the region of the third ventricle: the role of MR venography**. *Neuroradiology* 2003; 45:900–04 CrossRef Medline
5. Haacke EM, Xu Y, Cheng YC, et al. **Susceptibility weighted imaging (SWI)**. *Magn Reson Med* 2004;52:612–18 CrossRef Medline
6. Parodi A, Morana G, Severino MS, et al. **Low-grade intraventricular hemorrhage: is ultrasound good enough?** *J Matern Fetal Neonatal Med* 2015;28(suppl 1):2261–64 CrossRef Medline
7. Fujii S, Kanasaki Y, Matsusue E, et al. **Demonstration of cerebral venous variations in the region of the third ventricle on phase-sensitive imaging**. *AJNR Am J Neuroradiol* 2010;31:55–59 CrossRef Medline
8. Mokrohisky JF, Paul RE, Lin PM, et al. **The diagnostic importance of normal variants in deep cerebral phlebography, with special emphasis on the true and false venous angles of the brain and evaluation of venous angle measurements**. *Radiology* 1956;67:34–47 CrossRef Medline
9. Marlow N, Wolke D, Bracewell MA, et al. **Neurologic and developmental disability at six years of age after extremely preterm birth**. *N Engl J Med* 2005;352:9–19 CrossRef Medline
10. Ramenghi LA, Fumagalli M, Groppo M, et al. **Germinal matrix hemorrhage: intraventricular hemorrhage in very-low-birth-weight infants: the independent role of inherited thrombophilia**. *Stroke* 2011;42:1889–93 CrossRef Medline
11. Anstrom JA, Brown WR, Moody DM, et al. **Subependymal veins in**

- premature neonates: implications for hemorrhage. *Pediatr Neuro* 2004;30:46–53 CrossRef Medline
12. Ramenghi LA, Gill BJ, Tanner SF, et al. **Cerebral venous thrombosis, intraventricular haemorrhage and white matter lesions in a preterm newborn with factor V (Leiden) mutation.** *Neuropediatrics* 2002;33:97–99 CrossRef Medline
  13. Volpe JJ. **Intracranial hemorrhage: germinal matrix-intraventricular hemorrhage of the premature infant.** In: Volpe JJ, ed. *Neurology of the Newborn*. 5th ed. Philadelphia: Saunders Elsevier; 2008:517–88
  14. Sannia A, Natalizia AR, Parodi A, et al. **Different gestational ages and changing vulnerability of the premature brain.** *J Matern Fetal Neonatal Med* 2015;28(suppl 1):2268–72 CrossRef
  15. Talairach J, Tournoux P. *Co-Planar Stereotaxic Atlas of the Human Brain*. New York: Thieme; 1988
  16. Türe U, Yaşargil MG, Al-Mefty O. **The transcallosal-transforaminal approach to the third ventricle with regard to the venous variations in this region.** *J Neurosurg* 1997;87:706–15 CrossRef Medline
  17. Padget DH. **The cranial venous system in man in reference to development, adult configuration, and relation to the arteries.** *Am J Anat* 1956;98:307–55 CrossRef Medline
  18. Malamateniou C, Counsell SJ, Allsop JM, et al. **The effect of preterm birth on neonatal cerebral vasculature studied with magnetic resonance angiography at 3 Tesla.** *Neuroimage* 2006;32:1050–59 CrossRef Medline
  19. Risau W. **Mechanisms of angiogenesis.** *Nature* 1997;386:671–74 CrossRef Medline
  20. Plate KH. **Mechanisms of angiogenesis in the brain.** *J Neuropathol Exp Neurol* 1999;58:313–20 CrossRef Medline
  21. Breier G. **Angiogenesis in embryonic development—a review.** *Placenta* 2000;21(suppl A):S11–15 Medline
  22. Ferrara N, Gerber HP, LeCouter J. **The biology of VEGF and its receptors.** *Nat Med* 2003;9:669–76 CrossRef Medline
  23. Crawford MA, Costeloe K, Ghebremeskel K, et al. **Are deficits of arachidonic and docosahexaenoic acids responsible for the neural and vascular complications of preterm babies?** *Am J Clin Nutr* 1997;66(suppl):1032S–1041S Medline
  24. Gilmore JH, Lin W, Prastawa MW, et al. **Regional gray matter growth, sexual dimorphism, and cerebral asymmetry in the neonatal brain.** *J Neurosci* 2007;27:1255–60 CrossRef Medline
  25. Bartley AJ, Jones DW, Weinberger DR. **Genetic variability of human brain size and cortical gyral patterns.** *Brain* 1997;120(Pt 2):257–69 CrossRef Medline
  26. Steinmetz H, Hergoz A, Huang Y, et al. **Discordant brain-surface anatomy in monozygotic twins.** *N Engl J Med* 1994;331:951–52 Medline
  27. Chi JG, Dooling EC, Gilles FH. **Left-right asymmetries of the temporal speech areas of the human fetus.** *Arch Neurol* 1977;34:346–48 CrossRef Medline
  28. Simonds RJ, Scheibel AB. **The postnatal development of the motor speech area: a preliminary study.** *Brain Lang* 1989;37:42–58 CrossRef Medline
  29. Dubois J, Benders M, Cachia A, et al. **Mapping the early cortical folding process in the preterm newborn brain.** *Cereb Cortex* 2008;18:1444–54 CrossRef Medline
  30. Dubois J, Benders M, Lazeyras F, et al. **Structural asymmetries of perisylvian regions in the preterm newborn.** *Neuroimage* 2010;52:32–42 CrossRef Medline
  31. Lin PY, Roche-Labarbe N, Dehaes M, et al. **Regional and hemispheric asymmetries of cerebral hemodynamic and oxygen metabolism in newborns.** *Cerebral Cortex* 2013;23:339–48 CrossRef Medline
  32. Sun T, Collura RV, Ruvolo M, et al. **Genomic and evolutionary analyses of asymmetrically expressed genes in human fetal left and right cerebral cortex.** *Cereb Cortex* 2006;16(suppl 1):i18–25 Medline
  33. Sun T, Patoine C, Abu-Khalil A, et al. **Early asymmetry of gene transcription in embryonic human left and right cerebral cortex.** *Science* 2005;308:1794–98 CrossRef Medline

# Diffusion Tensor Imaging of the Normal Cervical and Thoracic Pediatric Spinal Cord

S. Saksena, D.M. Middleton, L. Krisa, P. Shah, S.H. Faro, R. Sinko, J. Gaughan, J. Finsterbusch, M.J. Mulcahey, and F.B. Mohamed



## ABSTRACT

**BACKGROUND AND PURPOSE:** DTI data of the normal healthy spinal cord in children are limited compared with adults and are typically focused on the cervical spinal cord. The purpose of this study was the following: to investigate the feasibility of obtaining repeatable DTI parameters along the entire cervical and thoracic spinal cord as a function of age in typically developing pediatric subjects; to analyze the DTI parameters among different transverse levels of the cervical and thoracic spinal cord; and to examine the sex differences in DTI parameters along the cervical and thoracic spinal cord.

**MATERIALS AND METHODS:** Twenty-two subjects underwent 2 identical scans by using a 3T MR imaging scanner. Axial diffusion tensor images were acquired by using 2 overlapping slabs to cover the cervical and thoracic spinal cord. After postprocessing, DTI parameters were calculated by using ROIs drawn on the whole cord along the entire spinal cord for both scans.

**RESULTS:** An increase in fractional anisotropy and a decrease in mean diffusivity, axial diffusivity, and radial diffusivity were observed with age along the entire spinal cord. Significantly lower fractional anisotropy and higher mean diffusivity values were observed in the lower cervical cord compared with the upper cervical cord. Axial diffusivity values in the cervical cord were higher compared with the thoracic cord. No statistically significant sex differences were observed for all DTI parameters. There was a moderate-to-strong repeatability for all DTI parameters.

**CONCLUSIONS:** This study provides an initial understanding of DTI values of the spinal cord relevant to age and sex and shows that obtaining repeatable DTI values of the entire cord in children is feasible.

**ABBREVIATIONS:** AD = axial diffusivity; FA = fractional anisotropy; MD = mean diffusivity; RD = radial diffusivity; SC = spinal cord

DTI is a valuable technique that measures the diffusivity of water molecules in tissues and provides in vivo information about tissue integrity and structure that is not apparent with conventional MR imaging. The commonly used DTI measures are fractional anisotropy (FA), which describes the degree of directional dependence; mean diffusivity (MD), which expresses the magnitude of the diffusion; axial diffusivity (AD), which repre-

sents water diffusivity parallel to the axonal fibers; and radial diffusivity (RD), which represents water diffusivity perpendicular to the axonal fibers.<sup>1</sup> DTI studies have investigated the cervical spinal cord (SC) in healthy adult subjects and have shown that DTI parameters are sensitive to age-related microstructural changes.<sup>2,3</sup> In contrast to the studies in adults, 1 study has evaluated the age-dependent evolution of FA and ADC values of the pediatric cervical SC.<sup>4</sup> There are no studies, to date to our knowledge, describing the age-related changes in the DTI parameters along the entire cervical and thoracic SC in pediatric subjects.

The usefulness of DTI has been shown for examining the cervical SC in pediatric subjects.<sup>5-7</sup> However, a comprehensive study examining the diffusion characteristics and repeatability of DTI along the cervical and thoracic SC in pediatric subjects has not been reported. On the basis of the promising outcomes of previous pediatric studies and owing to the growing practice of obtaining DTI in clinical patients,<sup>7,8</sup> it is essential to establish normative pediatric DTI values along the cervical and thoracic SC to aid in the clinical interpretation of the injured SC.

The purpose of this study was 3-fold: to investigate the feasi-

Received February 11, 2016; accepted after revision May 23.

From the Departments of Radiology (S.S., F.B.M.) and Occupational Therapy (L.K., R.S., M.J.M.), Thomas Jefferson University, Philadelphia, Pennsylvania; Department of Radiology (D.M.M., P.S., S.H.F.), Temple University, Philadelphia, Pennsylvania; Biostatistics Consulting Center (J.G.), Temple University School of Medicine, Philadelphia, Pennsylvania; and Department of Systems Neuroscience (J.F.), University Medical Center Hamburg-Eppendorf, Hamburg, Germany.

This work was supported by National Institute of Neurological Disorders of the National Institutes of Health under award No. R01NS079635 (F.B. Mohamed and M.J. Mulcahey, Principal Investigator).

Please address correspondence to Feroze B. Mohamed, PhD, Department of Radiology, Thomas Jefferson University, 909 Walnut St, Philadelphia, PA 19107; e-mail: Feroze.Mohamed@jefferson.edu

Indicates open access to non-subscribers at [www.ajnr.org](http://www.ajnr.org)

<http://dx.doi.org/10.3174/ajnr.A4883>

bility of obtaining repeatable DTI parameters along the entire cervical and thoracic SC as a function of age in typically developing pediatric subjects by using an inner FOV DTI sequence; to analyze the DTI parameters among different levels of the cervical and thoracic SC; and to examine the sex differences in the DTI parameters along the cervical and thoracic SC.

## MATERIALS AND METHODS

### Study Design

This initial study was part of a larger research effort to develop and validate DTI as a method for assessing the SC in children, similar to others that are working to validate DTI of the brain. The validation requires examining a population of subjects that have core variables such as age, sex, race, ethnicity, handedness, and education levels for any normative data base.<sup>9</sup> Twenty-two typically developing subjects (mean age,  $11.44 \pm 3.07$  years) were recruited. There were 8 males (mean age,  $10.51 \pm 3.31$  years) and 14 females (mean age,  $11.97 \pm 2.92$  years). These subjects were recruited mostly through our colleagues or family members. A few typically developing children were recruited as siblings of some of our spinal cord injury population. Thirteen subjects were excluded during the recruitment for the following reasons: Three declined, 7 had scheduling conflicts, and 3 had metal piercings or permanent retainers. Subjects were included in the study if they had no evidence of spinal cord injury or pathology, as assessed by performing a neurologic screen (a questionnaire about their medical history associated with neurologic injuries and a brief assessment of motor and sensory function and reflexes). Subjects were excluded from the study if they were unable to tolerate MR imaging without sedation or had infantile, juvenile, or adolescent idiopathic scoliosis or any abnormality of the nervous and/or musculoskeletal system. No subjects with orthodontic hardware were included in this study. Written informed assent (child) and consent (parent) were obtained under the protocol approved by the Temple University institutional review board.

### MR Imaging Protocol

The scans were performed by using a 3T Verio MR imaging scanner (Siemens, Erlangen, Germany) with a 4-channel neck matrix and an 8-channel spine matrix coil. The protocol consisted of an initial gradient-echo T2WI scout sagittal scan of the cervical and thoracic SC. The sagittal images were used to prescribe axial sections of the cervical and thoracic SC. Next, axial gradient-echo T2WI; a sagittal T2WI 3D SPACE sequence (sampling perfection with application-optimized contrasts by using different flip angle evolution; Siemens, Erlangen, Germany); sagittal TSE T1WI; sagittal TSE T2WI; and axial DTI scans were obtained.

DTI was performed by using an inner FOV sequence. The inner FOV sequence was based on a single-shot echo-planar imaging sequence for DWI with 2D-selective radiofrequency excitations, which improve the SNR and reduce geometric distortions in SC imaging, described in detail elsewhere.<sup>5,10</sup> Manual shim volume adjustments were also performed before data acquisition to restrict the adjustment volume to the anatomy of interest as much as possible.

Diffusion tensor images were acquired axially by using 2 over-

lapping slabs, in the same anatomic location prescribed for the T2 gradient-echo images, to cover the cervical (C1-upper thoracic region) and thoracic (upper thoracic-L1) SC (Fig 1). The imaging parameters for each slab of DTI acquisition included the following: FOV = 164 mm, phase FOV = 28.4% (47 mm), 3 averages of 20 diffusion directions, 6 B0 acquisitions,  $b=800$  s/mm<sup>2</sup>, voxel size =  $0.8 \times 0.8 \times 6$  mm<sup>3</sup>, axial sections = 40, TR = 7900 ms, TE = 110 ms, acquisition time = 8:49 minutes. To test the repeatability of DTI, we imaged all subjects twice by using the same protocol within 2 hours following the initial scan. Anesthesia was not administered. Cardiac and respiratory gating was not used, to keep scan times as short as possible.

### Image Preprocessing and Analysis

Initially, a central mask was applied to the raw DTI to eliminate the anatomy outside the SC. A mean B0 image was calculated, generated from the coregistration of all 6 B0 acquisitions. The diffusion-weighted images were corrected for motion by using a rigid-body-correction algorithm.<sup>11</sup> After motion correction, tensor estimation was done on a voxel-by-voxel basis from the axial DTI. All processing was performed by using in-house software developed in Matlab (MathWorks, Natick, Massachusetts). For robust diffusion tensor estimation, a nonlinear fitting algorithm implemented in RESTORE technique was used.<sup>12</sup>

Each ROI was manually drawn on the whole cord on grayscale FA maps at every axial section, on the basis of the methodology from the previous article,<sup>5</sup> along the cervical and thoracic SC for both scans. For drawing the ROI, sections corresponding to the anatomic regions with accurate vertebral levels were defined for the cervical and thoracic SC by a board-certified pediatric neuroradiologist. The placement of ROIs was performed by a neuroscientist (S.S.) and confirmed by a neuroradiologist (S.H.F). There was a consistent sparing of the outer margin of the cervical and thoracic SC of approximately 1-voxel width to minimize volume averaging with the CSF.

In this study, the 22 subjects were divided into the following age groups: 6–11 years ( $n = 12$ ) and 12–16 years ( $n = 10$ ) based on similar standards and age definitions used for reporting spinal cord injury in the pediatric population.<sup>13</sup> DTI parameters were quantified at each intervertebral disc level and at the mid-vertebral body level of the cervical and thoracic SC in all subjects. DTI parameters were compared for the cervical and thoracic SC as a function of age and among different levels of the cervical and thoracic SC. To study the changes in diffusion parameters among different levels of the cervical and thoracic SC, we averaged DTI values across the following levels per subject: upper cervical cord (C1, mid-dens, base dens, mid-C2, C2–C3, mid-C3), middle cervical cord (C3–C4, mid-C4, C4–C5, mid-C5), and lower cervical cord (C5–C6, mid-C6, C6–C7, mid-C7, C7–T1), upper thoracic cord (mid-T1, T1–T2, mid-T2, T2–T3, mid-T3, T3–T4, mid-T4, T4–T5), middle thoracic cord (mid-T5, T5–T6, mid-T6, T6–T7, mid-T7, T7–T8, mid-T8, T8–T9), and lower thoracic cord (mid-T9, T9–T10, mid-T10, T10–T11, mid-T11, T11–T12, mid-T12, T12–L1, mid-L1). The mean values were used for comparison among the upper, middle, and lower cervical and thoracic SC across all subjects.

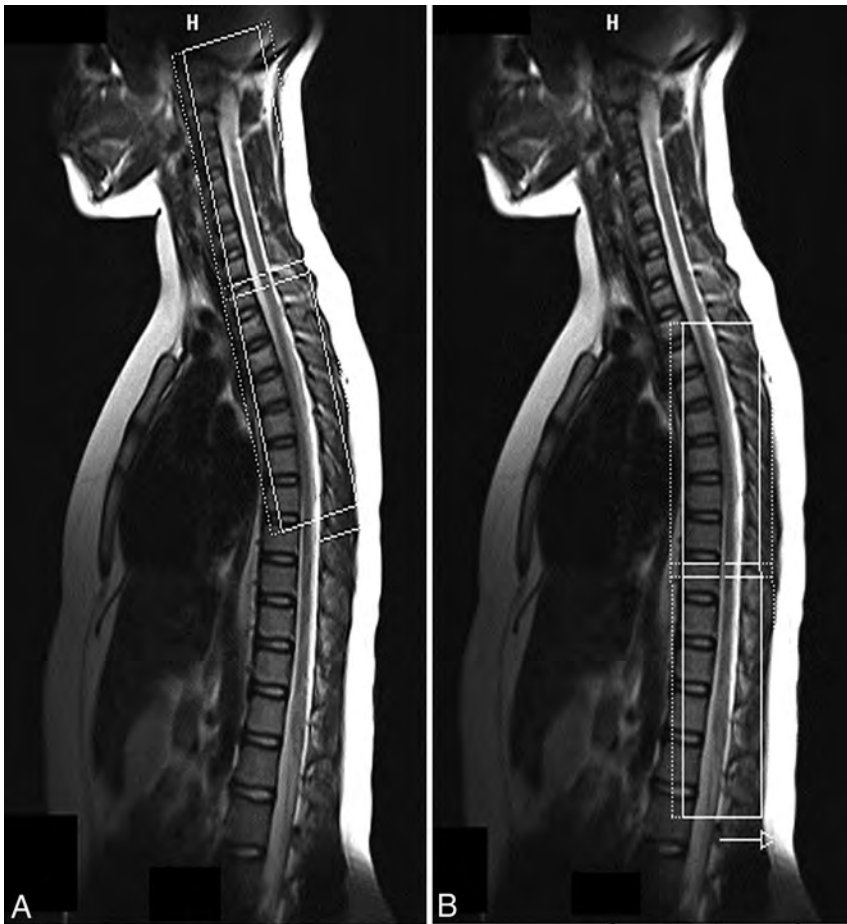


**FIG 1.** Localization image from which the axial cervical (A) and thoracic (B) SC sections are prescribed. The inner solid white rectangular line represents the inner FOV, which was oversampled (dotted white line) to avoid aliasing.

### Statistical Analysis

Means with SD were calculated for DTI parameters according to age groups, cord levels, and sex. The coefficient of variation was calculated as an additional measure of variability. Because the DTI parameters failed the Shapiro-Wilk test for normality, the data were transformed into “normalized ranks” to allow parametric testing.<sup>14</sup> The ANOVA for repeated measures and linear regression was used to compare scans, cord levels, and age. A *P* value of .05 was used throughout to determine statistical significance. Test-retest repeatability was calculated by using the intraclass correlation coefficient according to the method of Shrout and Fleiss.<sup>15</sup> All statistical analyses were performed with SAS, Version 9.4 (SAS Institute, Cary, North Carolina).

### RESULTS

All 22 subjects tolerated 2 repeat imaging sessions. Each session was 40–45 minutes in duration with a 2-hour delay between sessions. Imaging with the inner FOV sequence with 2D-selective radiofrequency excitations resulted in DTI with high spatial resolution. Better distinction between WM and GM structures was observed throughout the cord; however, in general, the GM-WM differentiation was better in the cervical and upper thoracic cord (Fig 2). In Fig 2, the green anisotropy in the fourth row might represent some spurious voxels; and in the eighth row, the

conus is present in the imaging volume and the artifacts seen are largely due to partial volume averaging and complex CSF flow. Figure 3 shows the sagittal reconstruction of FA color maps of 2 overlapping slabs of the same subject in Fig 2. Figure 3A shows the cervical and upper thoracic region (C1 to T5), and Fig 3B shows the upper thoracic through the conus region (T4 to L1).

### DTI Parameters along the Cervical and Thoracic SC According to Age

Table 1 summarizes the DTI values for 2 age groups. FA values were low in subjects 6–11 years of age, while they were high in subjects 12–16 years of age along the cervical and thoracic SC. MD, AD, and RD values followed an opposite trend and were high in subjects 6–11 years of age and low in subjects 12–16 years of age. The increase in FA values from age groups 6–11 years to 12–16 years was statistically significant (*P* = .0193).

As shown in Table 1, MD decreased significantly from age groups 6–11 years to 12–16 years (*P* < .0001). There was a significant decrease in AD from age groups 6–11 years to 12–16 years (*P* < .0001). Similarly, RD decreased significantly from age groups 6–11 years to 12–16 years (*P* < .0001) (Table 1).

A simple linear regression analysis was used to measure the effect of age on

DTI parameters. As seen from Fig 4, an increase in FA was observed; however, MD, AD, and RD showed a decrease along the cervical and thoracic SC with age.

### DTI Parameters According to Cord Levels

Table 2 shows that FA values in the upper cervical cord and middle cervical cord were significantly higher compared with the lower cervical cord (*P* < .0001). No statistically significant difference in FA values was observed in the upper cervical cord compared with the middle cervical cord (*P* = .3732). In the upper thoracic cord, FA values were significantly lower compared with the middle thoracic cord (*P* < .0001), while they were significantly higher compared with the lower thoracic cord (*P* < .0001). FA values in the middle thoracic cord were significantly higher compared with the lower thoracic cord (*P* < .0001) (Table 2).

A significant decrease in MD values was observed in the upper cervical cord and middle cervical cord compared with the lower cervical cord (*P* < .0001, *P* = .0265). No statistically significant difference in MD values was observed in the upper cervical cord compared with the middle cervical cord (*P* = .1357). In the middle thoracic cord, a significant increase in MD values was observed compared with the upper thoracic cord and lower thoracic cord (*P* < .0001). No statistically significant difference was ob-

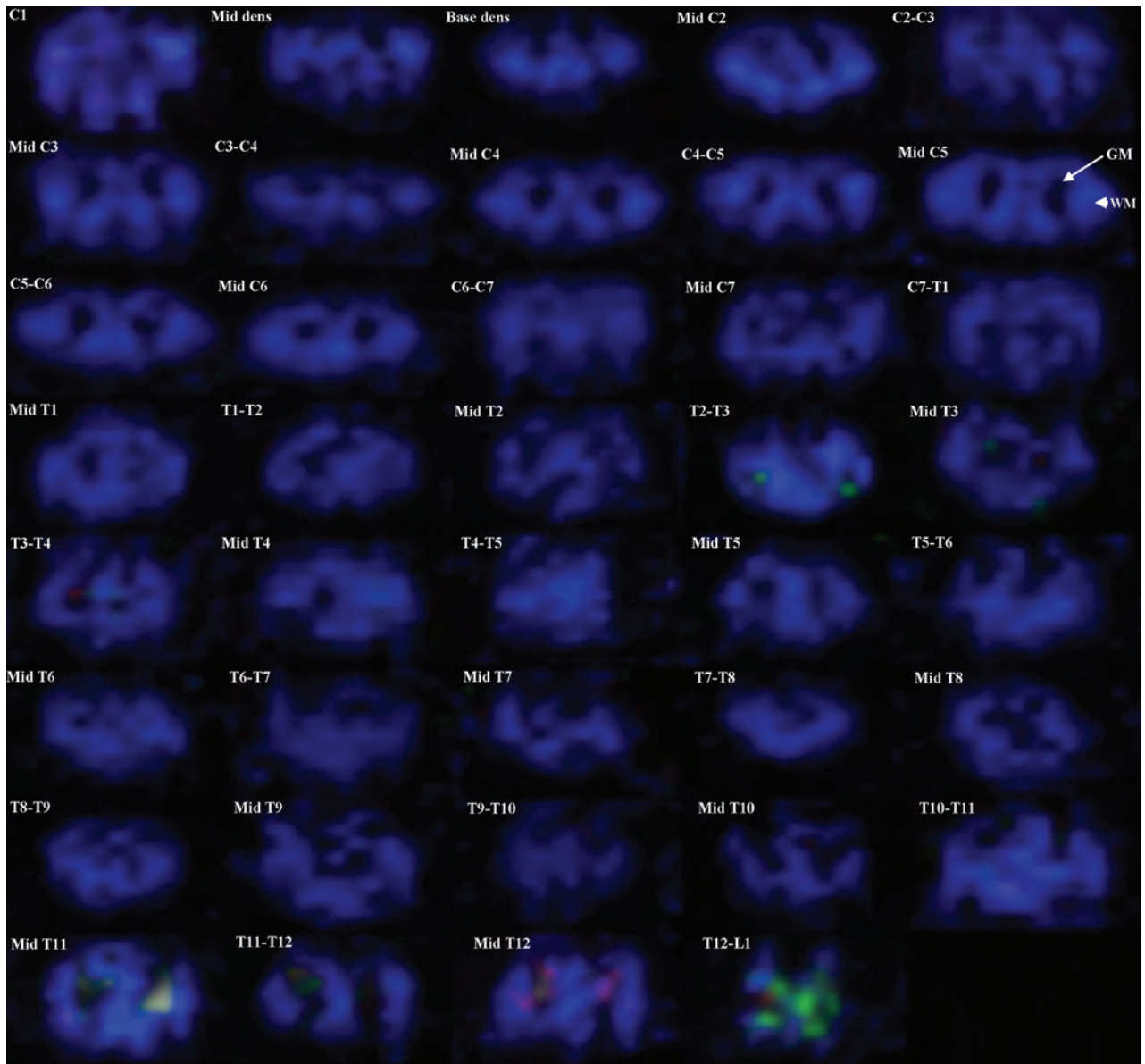


**FIG 2.** Axial FA color maps of each intervertebral disc level and within the mid-vertebral body level along the entire cervical and thoracic SC in a typically developing subject (C1 to T12–L1 level). An example of GM at the mid-C5 level is shown with an *arrow*, and WM, with an *arrowhead*.

served in the upper thoracic cord compared with lower thoracic cord ( $P = .2665$ ) (Table 2).

AD values in the upper cervical cord were significantly higher compared with the upper thoracic cord ( $P < .0001$ ) and lower thoracic cord ( $P < .0001$ ). No significant difference was observed in the upper cervical cord compared with middle thoracic cord ( $P = .1485$ ). In the middle cervical cord, AD values were significantly higher compared with the upper thoracic cord ( $P < .0001$ ), middle thoracic cord ( $P = .0033$ ), and lower thoracic cord ( $P < .0001$ ). AD values in the lower cervical cord were significantly higher compared with the upper thoracic cord ( $P < .0001$ ), middle thoracic cord ( $P = .0158$ ), and lower thoracic cord ( $P < .0001$ ) (Table 2).

RD values in the upper cervical cord were not statistically significant compared with the upper thoracic cord ( $P = .2707$ ), mid-

dle thoracic cord ( $P = .1044$ ), and lower thoracic cord ( $P = .9320$ ). Significant differences in RD values were observed in the middle cervical cord compared with the upper thoracic cord ( $P = .0198$ ) and middle thoracic cord ( $P = .0048$ ). No statistically significant difference was observed in the middle cervical cord compared with lower thoracic cord ( $P = .1774$ ). A significant increase in RD values was observed in the lower cervical cord compared with the upper ( $P < .0001$ ), middle ( $P < .0001$ ), and lower thoracic cord ( $P < .0001$ ) (Table 2).

#### **Coefficient of Variation**

The coefficient of variation represents the SD as a percentage of the mean and is an additional indication of the variability of the DTI measurements. The coefficient of variation showed that the variability of the DTI parameters was very good for both age



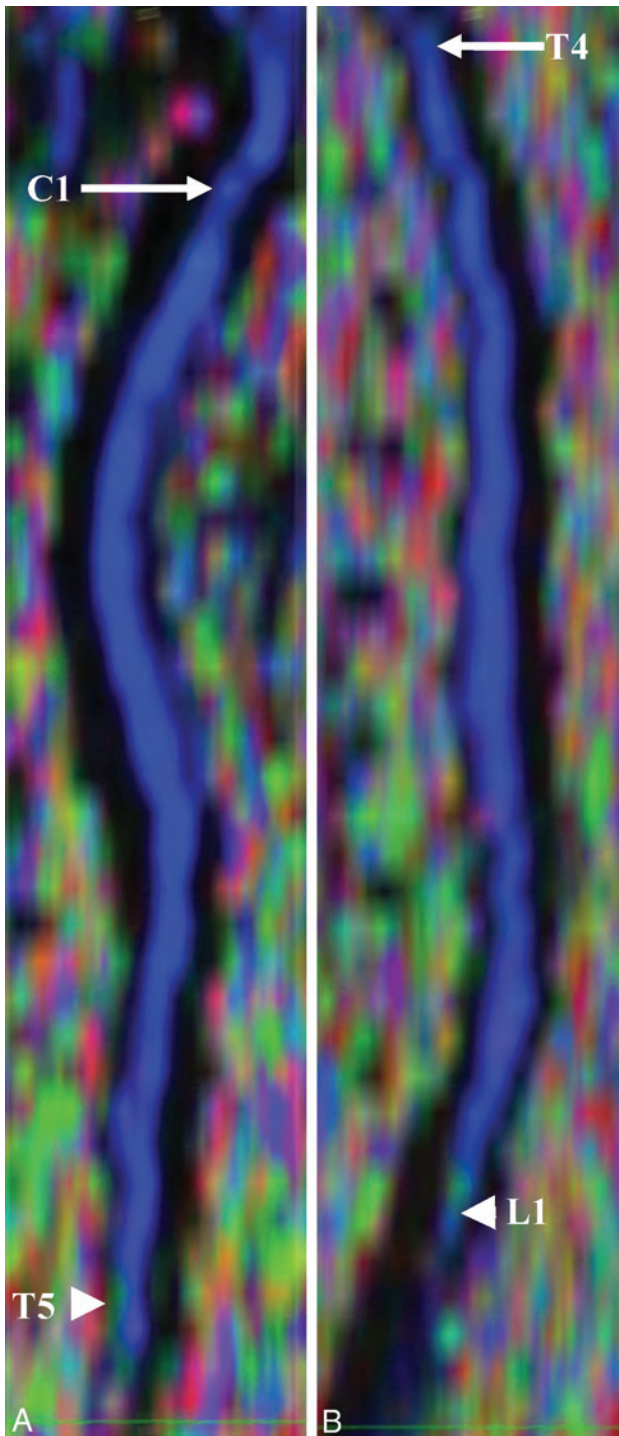


**FIG 3.** Sagittal reconstruction of FA color maps of 2 overlapping slabs of the same subject as shown in Fig 2. A, The cervical and upper thoracic regions (C1, arrow, to T5, arrowhead). B, The upper thoracic-through-conus regions (T4, arrow, to L1, arrowhead).

groups and similar to other reports of DTI measurement variability.<sup>16</sup> Overall, FA showed the least variability (6–11 years, 16.66%; 12–16 years, 17.24%).

#### **DTI Parameters and Sex**

DTI parameters did not show any statistically significant difference between males (FA:  $0.56 \pm 0.09$ ; MD:  $1.07 \pm 0.29$ ; AD:

**Table 1: Means of FA, MD, AD, and RD along the cervical and thoracic SC according to age groups**

DTI Parameters	Age Groups (yr)		P Values
	6–11	12–16	
FA	$0.54 \pm 0.09$	$0.58 \pm 0.10$	.0193
MD	$1.14 \pm 0.26$	$0.91 \pm 0.21$	<.0001
AD	$1.88 \pm 0.38$	$1.58 \pm 0.38$	<.0001
RD	$0.77 \pm 0.23$	$0.58 \pm 0.17$	<.0001

$1.80 \pm 0.43$ ; RD:  $0.71 \pm 0.25$ ) and females (FA:  $0.56 \pm 0.10$ ; MD:  $1.01 \pm 0.25$ ; AD:  $1.71 \pm 0.39$ ; RD:  $0.66 \pm 0.22$ ) along the cervical and thoracic SC.

#### **Test-Retest Repeatability**

Table 3 shows the intraclass correlation coefficient and 95% CIs for test-retest repeatability of DTI values for the cervical and thoracic SC. There was a moderate-to-strong repeatability for DTI values for the cervical and thoracic SC (Table 3).

#### **DISCUSSION**

In this study, the entire SC of 22 typically developing children was successfully scanned to obtain DTI parameters (FA, MD, AD, and RD) that revealed location and age- and sex-related trends and moderate-to-strong repeatability. To the best of our knowledge, this study is the first to examine developmental and sex differences in DTI parameters of the entire pediatric SC. One previous study did examine FA and ADC changes in the pediatric cervical spine,<sup>4</sup> with findings similar to those in our study.

The results of this study showed that with increasing age, FA increased along the cervical and thoracic SC. Studies in the brain have reported age-related changes in the DTI parameters to describe the normal developmental characteristics from infancy to adulthood.<sup>17</sup> In addition, it is proposed that changes in DTI parameters in the brain as a function of age may result from decreasing water content, myelination of fiber tracts, and the thickening diameter of fiber tracts.<sup>18</sup> The SC is an extension of the brain, transmitting messages from the brain to the periphery and vice versa; and similar physiologic processes may occur in the SC. It has been reported that myelination in the SC starts during the second half of fetal life, peaks during the first year postnatally, and continues until 20 years of age.<sup>19</sup> In our study, an increase in FA with age in the SC was observed, similar to the FA findings in the brain, which suggests the ongoing process of myelination.

In our study, MD, AD, and RD decreased with age along the cervical and thoracic SC. MD is the average of all 3 eigenvalues and represents a variety of physiologic processes that include continuing myelination, increased organization, and compactness of the axonal bundles. It has been demonstrated that there is a strong correlation between AD/RD and histology in animal studies.<sup>20</sup> AD in the WM tracts correlates well with the integrity of axons in these tracts, while RD in the WM tracts correlates with the amount of myelin.<sup>20</sup> Decreased AD with age may result from increased axonal density or axonal caliber, leading to an addition of diffusion barriers parallel to the axon due to reduced interaxonal space. Decreased RD with age may be due to continuing myelination because thickening of the myelin sheath will reduce perpendicular water diffusion.

In addition to age-related changes, our study demonstrated

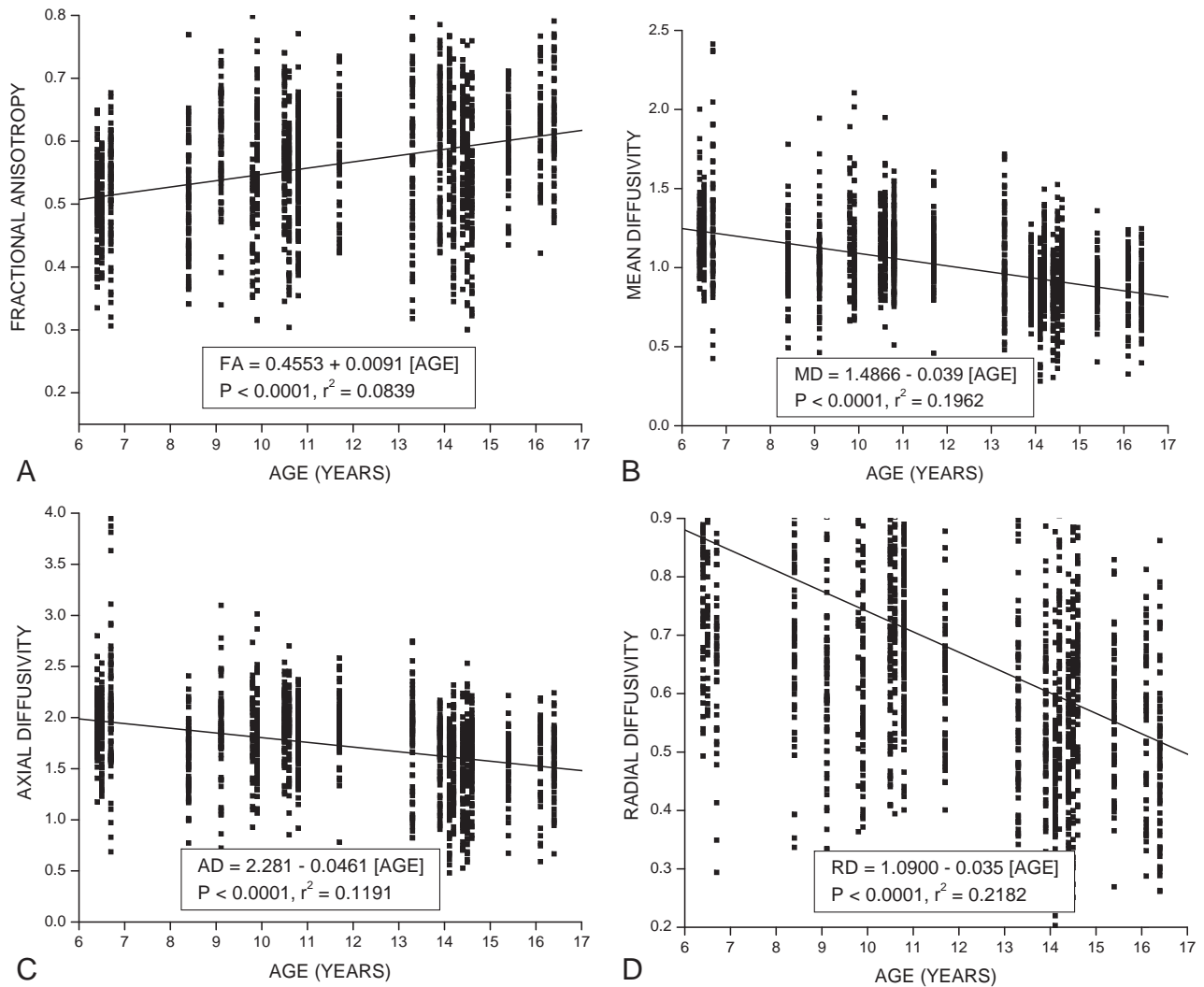


**FIG 4.** Linear fit plots showing the relationship among FA (A), MD (B), AD (C), and RD (D) and age along the cervical and thoracic SC (C1 to mid-L1) in typically developing pediatric subjects.

**Table 2: Means of FA, MD, AD, and RD according to different levels of the cervical and thoracic SC**

DTI Parameters	Cord Divisions					
	CUP	CMID	CLOW	TUP	TMID	TLOW
FA <sup>a</sup>	0.60 ± 0.08	0.59 ± 0.07	0.54 ± 0.08	0.53 ± 0.09	0.60 ± 0.10	0.49 ± 0.09
MD <sup>b</sup>	1.06 ± 0.20	1.08 ± 0.15	1.15 ± 0.24	0.98 ± 0.32	1.05 ± 0.26	0.93 ± 0.27
AD <sup>c</sup>	1.85 ± 0.30	1.90 ± 0.20	1.89 ± 0.33	1.58 ± 0.50	1.83 ± 0.35	1.45 ± 0.41
RD <sup>d</sup>	0.66 ± 0.18	0.67 ± 0.15	0.78 ± 0.23	0.67 ± 0.26	0.66 ± 0.24	0.66 ± 0.23

**Note:**—CUP indicates upper cervical cord; CMID, middle cervical cord; CLOW, lower cervical cord; TUP, upper thoracic cord; TMID, middle thoracic cord; TLOW, lower thoracic cord.

<sup>a</sup> FA = CUP vs CMID:  $P = .3732$ ; CUP vs CLOW:  $P < .0001$ ; CMID vs CLOW:  $P < .0001$ ; TUP vs TMID:  $P < .0001$ ; TUP vs TLOW:  $P < .0001$ ; TMID vs TLOW:  $P < .0001$ .

<sup>b</sup> MD = CUP vs CMID:  $P = .1357$ ; CUP vs CLOW:  $P < .0001$ ; CMID vs CLOW:  $P = .0265$ ; TUP vs TMID:  $P < .0001$ ; TUP vs TLOW:  $P = .2665$ ; TMID vs TLOW:  $P < .0001$ .

<sup>c</sup> AD = CUP vs TUP:  $P < .0001$ ; CUP vs TLOW:  $P < .0001$ ; CUP vs TMID:  $P = .1485$ ; CMID vs TUP:  $P < .0001$ ; CMID vs TMID:  $P = .0033$ ; CMID vs TLOW:  $P < .0001$ ; CLOW vs TUP:  $P < .0001$ ; CLOW vs TMID:  $P = .0158$ ; CLOW vs TLOW:  $P < .0001$ .

<sup>d</sup> RD = CUP vs TUP:  $P = .2707$ ; CUP vs TLOW:  $P = .9320$ ; CUP vs TMID:  $P = .1044$ ; CMID vs TUP:  $P = .0198$ ; CMID vs TMID:  $P = .0048$ ; CMID vs TLOW:  $P = .1774$ ; CLOW vs TUP:  $P < .0001$ ; CLOW vs TMID:  $P < .0001$ ; CLOW vs TLOW:  $P < .0001$ .

that diffusion characteristics are not consistent throughout the SC and are dependent on the cord level. The SC is greater in width and diameter in the cervical and lumbosacral regions, forming the cervical plexus and the lower thoracic lumbar–sacral plexus, the site of neurons that primarily supply the extremities.<sup>21</sup> These neurons represent GM that is higher in concentration compared with the remainder of the cord.<sup>21</sup> In the SC, the GM is a central but-

terfly-shaped structure surrounded by the WM. Additionally, the volume of WM and GM is different depending on the location within the SC. Goto and Otsuka<sup>22</sup> reported that the GM volume, on average, represents 18% of the SC at the anatomic level at the origin of the C2-through-C8 nerve root (the cervical region). The volume of GM represents 13.2% of the SC at the anatomic level at the origin of the T1-through-T12 nerve root (the tho-

**Table 3: Test-retest repeatability for each DTI parameter per the cervical and thoracic SC**

DTI Parameters	Level	ICC (95% CI)
FA	Cervical	0.86 (0.86–0.70)
	Thoracic	0.85 (0.85–0.67)
MD	Cervical	0.91 (0.91–0.79)
	Thoracic	0.89 (0.90–0.73)
AD	Cervical	0.91 (0.91–0.79)
	Thoracic	0.80 (0.83–0.55)
RD	Cervical	0.90 (0.90–0.77)
	Thoracic	0.92 (0.93–0.82)

**Note:**—ICC indicates intraclass correlation coefficient.

racic region). The amount of WM decreases gradually in the caudal direction because the long ascending and descending pathways contain fewer axons at successively more caudal levels of the SC.<sup>21</sup>

When comparing DTI parameters at different locations of the cervical and lower thoracic regions, our study demonstrated significantly lower FA and higher MD values in the lower cervical cord compared with the upper cervical cord. Another study demonstrated that at the upper cervical cord, the right-to-left diameter of the SC and the area of the central GM are smaller compared with the lower cervical cord.<sup>23</sup> The relative lower cervical cord enlargement, which corresponds to the cervical plexus, is due to an increase in the GM/WM ratio. It has been reported that in adults, the central GM of the SC has lower FA and higher MD compared with the WM.<sup>24</sup> In our study, the larger central GM area in the lower cervical cord may be responsible for decreased FA and increased MD compared with the upper cervical cord. Decreased FA values in the lower thoracic cord compared with the upper thoracic cord may be due to the variations in the percentage of GM within different levels of the thoracic cord.

Diffusion in the healthy SC is highly anisotropic with transverse ADC values less than longitudinal ADC values.<sup>25</sup> Anisotropy in the SC is due to diffusion barriers encountered as water moves perpendicular to the fibers. These barriers, such as the cell membrane and myelin sheath, result in low transverse ADC values. As water diffuses longitudinally in the SC, these diffusion barriers are not encountered and hence longitudinal ADC is higher.<sup>25</sup> Our study also demonstrated higher AD values in the cervical and thoracic cord compared with RD values. It has been reported that the density and integrity of cytoskeletal proteins (microtubules and neurofilaments) affect longitudinal water diffusion.<sup>26</sup> Schwartz et al<sup>27</sup> demonstrated a positive correlation of longitudinal ADC with axon diameter in the normal rat cervical cord and explained that this was due to the inverse relationship between axon caliber and cytoskeletal protein density. These findings may explain our results of increased AD values in the upper, middle, and lower cervical cord, which may contain a higher percentage of large-diameter axons compared with the upper, middle, and lower thoracic cord. Because large axons have a decreased density of microtubules and neurofilaments, this may result in increased longitudinal water diffusion in the cervical cord. It has been observed in ex vivo studies that increased axonal diameter and decreased axonal density correlate with increased transverse diffusion in SC tracts.<sup>28</sup> In our study, larger axons in the lower cervical cord may explain the increased RD values compared with the thoracic cord.

DTI has proved to be a useful tool for examining sex differences in the brain WM during childhood and adolescence<sup>29</sup>; however, in the SC, these are not well-studied. We found no significant sex differences, when comparing males and females, along the cervical and thoracic SC. Our results are consistent with the findings of previous DTI studies of the maturing cervical SC<sup>4</sup> and brain maturation,<sup>30</sup> which also did not show any sex differences. These sex-related DTI findings in the SC need to be further investigated to determine whether they hold up with larger sample sizes and, if so, to produce normative data for males and females of different ages.

As we have shown previously in the cervical SC, there was good-to-strong repeatability in DTI values.<sup>5,8</sup> It has also been reported that in adult cervical SC DTI, there is good intra- and interobserver variability.<sup>16</sup> In our current study, we have shown that within the cervical and thoracic SC, DTI values showed moderate-to-strong repeatability. These findings add to the existing evidence that DTI values for the normal SC are repeatable.

One of the limitations of the study was the use of manual ROI selection, which may have introduced partial volume contamination from the CSF surrounding the cord. The ROIs drawn were conservative, to minimize this volume-averaging effect. In our study, because the DTI measurements were performed on the whole cord, the inclusion of GM and WM in the analysis might have affected the DTI values.<sup>31</sup> Currently, no automatic methods exist for delineating WM and GM from DTI SC images, and manual segmentation is cumbersome and time-consuming. Therefore, for future analysis, an automated or semiautomated segmentation method is required for accurately delineating the GM and WM in the SC. Another limitation of this study is the low number of subjects within different age groups and sex. Future work with more subjects is needed in these subgroups to establish normative DTI data of the pediatric cord. There was also heterogeneity of the signal in many subjects at the edge of the coil and in the lower thoracic region, which potentially can be reduced with improved imaging techniques. In addition, we chose a section thickness of 6 mm to allow a maximal SNR of the imaging voxel while balancing the in-plane resolution and the number of sections needed to scan the subject within a clinically acceptable time of acquisition per slab. This limitation could be overcome in the future by imaging the SC at a higher field strength, with improved radiofrequency coils and multiband DTI techniques, which will allow imaging small voxels while still maintaining a relatively short imaging time.

## CONCLUSIONS

This study provides an initial understanding of DTI values of the SC relevant to age and sex and shows that obtaining repeatable DTI values of the entire cervical and thoracic cord in children is feasible.

## ACKNOWLEDGMENTS

We thank Mahdi Alizadeh for helping with the manuscript preparation.

Disclosures: Scott H. Faro—*RELATED: Grant:* National Institutes of Health—National Institute of Neurological Disorders and Stroke.\* John Gaughan—*RELATED: Consulting Fee or Honorarium:* Temple University, National Institutes of Health R01

NS079635 (statistical consulting). Mary Jane Mulcahey—RELATED: Grant: National Institute of Neurological Disorders and Stroke\*; Support for Travel to Meetings for the Study or Other Purposes: National Institute of Neurological Disorders and Stroke\*; UNRELATED: Board Membership: President, American Spinal Injury Association, no payment; Vice President, Pediatric Spine Foundation, no payment; Consultancy: Topics in Spinal Cord Rehabilitation, Comments: Associate Editor; Grants/Grants Pending: Community Health Network Foundation,\* Department of Defense,\* Shriners Hospitals\*; Royalties: Mac Keith Press (editor, book); Travel/Accommodations/Meeting Expenses Unrelated to Activities Listed: Boston Rehabilitation Outcomes Center (Visiting Scientist, 2015–2016). Feroze B. Mohamed—RELATED: Grant: National Institutes of Health—National Institute of Neurological Disorders and Stroke.\* \*Money paid to the institution.

## REFERENCES

1. Basser PJ. **Inferring microstructural features and the physiological state of tissues from diffusion-weighted images.** *NMR Biomed* 1995; 8:333–44 CrossRef Medline
2. Van Hecke W, Leemans A, Sijbers J, et al. **A tracking-based diffusion tensor imaging segmentation method for the detection of diffusion-related changes of the cervical spinal cord with aging.** *J Magn Reson Imaging* 2008;27:978–91 CrossRef Medline
3. Wang K, Song Q, Zhang F, et al. **Age-related changes of the diffusion tensor imaging parameters of the normal cervical spinal cord.** *Eur J Radiol* 2014;83:2196–202 CrossRef Medline
4. Singhi S, Tekes A, Thurnher M, et al. **Diffusion tensor imaging of the maturing paediatric cervical spinal cord: from the neonate to the young adult.** *J Neuroradiol* 2012;39:142–48 CrossRef Medline
5. Barakat N, Mohamed FB, Hunter LN, et al. **Diffusion tensor imaging of the normal pediatric spinal cord using an inner field of view echo-planar imaging sequence.** *AJNR Am J Neuroradiol* 2012;33: 1127–33 CrossRef Medline
6. Mohamed FB, Hunter LN, Barakat N, et al. **Diffusion tensor imaging of the pediatric spinal cord at 1.5T: preliminary results.** *AJNR Am J Neuroradiol* 2011;32:339–45 CrossRef Medline
7. Mulcahey MJ, Samdani AF, Gaughan JP, et al. **Diagnostic accuracy of diffusion tensor imaging for pediatric cervical spinal cord injury.** *Spinal Cord* 2013;51:532–37 CrossRef Medline
8. Mulcahey M, Samdani AF, Gaughan J, et al. **Diffusion tensor imaging in pediatric spinal cord injury: preliminary examination of reliability and clinical correlation.** *Spine (Phila Pa 1976)* 2012;37: E797–803 CrossRef Medline
9. Wintermark M, Coombs L, Druzgal TJ, et al; American College of Radiology Head Injury Institute. **Traumatic brain injury imaging research roadmap.** *AJNR Am J Neuroradiol* 2015;36:E12–23 CrossRef Medline
10. Finsterbusch J. **Improving the performance of diffusion-weighted inner field-of-view echo-planar imaging based on 2D-selective radiofrequency excitations by tilting the excitation plane.** *J Magn Reson Imaging* 2012;35:984–92 CrossRef Medline
11. Middleton DM, Mohamed FB, Barakat N, et al. **An investigation of motion correction algorithms for pediatric spinal cord DTI in healthy subjects and patients with spinal cord injury.** *Magn Reson Imaging* 2014;32:433–39 CrossRef Medline
12. Chang LC, Jones DK, Pierpaoli C. **RESTORE: robust estimation of tensors by outlier rejection.** *Magn Reson Med* 2005;53:1088–95 CrossRef Medline
13. DeVivo MJ, Vogel LC. **Epidemiology of spinal cord injury in children and adolescents.** *J Spinal Cord Med* 2004;27(suppl 1):S4–10 Medline
14. Conover WJ, Iman RL. **Rank transformations as a bridge between parametric and nonparametric statistics.** *The American Statistician* 1981;35:124–29 CrossRef
15. Shrout PE, Fleiss JL. **Intraclass correlations: uses in assessing rater reliability.** *Psychol Bull* 1979;86:420–28 CrossRef Medline
16. Brander A, Koskinen E, Luoto TM, et al. **Diffusion tensor imaging of the cervical spinal cord in healthy adult population: normative values and measurement reproducibility at 3T MRI.** *Acta Radiol* 2014; 55:478–85 CrossRef Medline
17. Uda S, Matsui M, Tanaka C, et al. **Normal development of human brain white matter from infancy to early adulthood: a diffusion tensor imaging study.** *Dev Neurosci* 2015;37:182–94 CrossRef Medline
18. Yoshida S, Oishi K, Faria AV, et al. **Diffusion tensor imaging of normal brain development.** *Pediatr Radiol* 2013;43:15–27 CrossRef Medline
19. Baumann N, Pham-Dinh D. **Biology of oligodendrocyte and myelin in the mammalian central nervous system.** *Physiol Rev* 2001;81:871–927 Medline
20. Budde MD, Kim JH, Liang HF, et al. **Toward accurate diagnosis of white matter pathology using diffusion tensor imaging.** *Magn Reson Med* 2007;57:688–95 CrossRef Medline
21. Campbell WW, DeJong RN. **The spinal cord level.** In: *DeJong's the Neurologic Examination*. 6th ed. Philadelphia: Lippincott Williams Wilkins; 2005:314–24
22. Goto N, Otsuka N. **Development and anatomy of the spinal cord.** *Neuropathology* 1997;17:25–31 CrossRef
23. Barker GJ. **Diffusion-weighted imaging of the spinal cord and optic nerve.** *J Neurol Sci* 2001;186(suppl 1):S45–49 CrossRef Medline
24. Bosma RL, Stroman PW. **Characterization of DTI indices in the cervical, thoracic, and lumbar spinal cord in healthy humans.** *Radiol Res Pract* 2012;2012:143705 CrossRef Medline
25. Schwartz ED, Hackney DB. **Diffusion-weighted MRI and the evaluation of spinal cord axonal integrity following injury and treatment.** *Exp Neurol* 2003;184:570–89 CrossRef Medline
26. Kinoshita Y, Ohnishi A, Kohshi K, et al. **Apparent diffusion coefficient on rat brain and nerves intoxicated with methylmercury.** *Environ Res* 1999;80:348–54 CrossRef Medline
27. Schwartz ED, Cooper ET, Fan Y, et al. **MRI diffusion coefficients in spinal cord correlate with axon morphometry.** *Neuroreport* 2005;16: 73–76 CrossRef Medline
28. Takahashi M, Hackney DB, Zhang G, et al. **Magnetic resonance microimaging of intraaxonal water diffusion in live excised lamprey spinal cord.** *Proc Natl Acad Sci U S A* 2002;99:16192–96 CrossRef Medline
29. Hermoye L, Saint-Martin C, Cosnard G, et al. **Pediatric diffusion tensor imaging: normal database and observation of the white matter maturation in early childhood.** *Neuroimage* 2006;29:493–504 CrossRef Medline
30. Perrin JS, Leonard G, Perron M, et al. **Sex differences in the growth of white matter during adolescence.** *Neuroimage* 2009;45:1055–66 CrossRef Medline
31. Carabelli E, Shah P, Faro S, et al. **DTI indices as defined by various ROI analysis in the typically developing pediatric cervical spinal cord: a comparison of gray matter, white matter and whole cord ROI analysis and its effects on DTI metrics.** In: *Proceedings of the Annual Meeting of the American Society of Neuroradiology and the Foundation of the ASNR Symposium*, Chicago, Illinois. April 25–30, 2015

# 3D MR Neurography of the Lumbosacral Plexus: Obtaining Optimal Images for Selective Longitudinal Nerve Depiction

G. Cho Sims, E. Boothe, R. Joodi, and A. Chhabra

## ABSTRACT

**BACKGROUND AND PURPOSE:** The number of centers currently performing 3D fat-suppressed isotropic imaging is limited. If the angular orientations of the major lumbosacral plexus nerves on 3D isotropic MR neurography could be determined, similar planes could be prescribed during acquisition of 2D or 3D nonisotropic techniques for optimal depiction of various nerves. Our aim was to determine oblique sagittal and coronal angular measurements for longitudinal depiction of lumbosacral plexus nerves. Interobserver and intraobserver performance and mean calibers of sciatic and femoral nerves were also determined.

**MATERIALS AND METHODS:** A consecutive series of lumbosacral plexus MR neurography examinations with 3D nerve-selective imaging performed during a 10-month period on a 3T scanner were evaluated. Two observers performed reconstructions and angular measurements. Sciatic and femoral nerve diameters were measured. Descriptive statistics and intraclass correlation coefficient correlations were used.

**RESULTS:** There were 52 subjects, 11 men and 41 women. Mean sagittal thecal sac angles for coronal demonstration of lumbosacral plexus nerve roots from L1 to S1 for 2 independent observers measured  $13.58^\circ \pm 2.87^\circ$  and  $13.61^\circ \pm 2.18^\circ$ . Mean sagittal femoral nerve angles were  $27.78^\circ \pm 4.81^\circ$  and  $28.94^\circ \pm 4.49^\circ$ , and mean sagittal sciatic nerve angles were  $-10.7^\circ \pm 3.75^\circ$  and  $-11.82^\circ \pm 2.87^\circ$ . Coronal angular measurements of the femoral and sciatic nerves were similar. The intraclass correlation coefficient was moderate (0.582–0.671) for interobserver performance. For intraobserver performance among various angular measurements, the intraclass correlation coefficient was moderate to good (0.586–0.788). Femoral nerve caliber on MR imaging was almost half that of the sciatic nerve. Mean right femoral nerve thickness was  $4.52 \pm 1.11$  mm and  $4.85 \pm 0.64$  mm for the 2 observers, and mean left femoral nerve thickness was  $4.48 \pm 0.97$  mm and  $4.94 \pm 0.57$  mm. Mean right sciatic nerve thickness was  $9.71 \pm 1.76$  mm and  $9.94 \pm 0.83$  mm, and mean left sciatic nerve thickness was  $10.03 \pm 1.71$  mm and  $9.98 \pm 0.99$  mm.

**CONCLUSIONS:** Angular lumbosacral plexus measurements aid in the prescription of different planes on MR imaging for the optimal longitudinal demonstration of nerves.

**ABBREVIATIONS:** ICC = intraclass correlation coefficient; LS = lumbosacral; SHINKEI = nerve-SHeath signal increased with INKed rest-tissue rArE Imaging

The lumbosacral (LS) plexus is a complex network of nerves, which provides both motor and sensory innervation to most structures of the pelvis and lower extremities. Most anatomy illustrations in the text books and Internet Web sources depict coronal views of the LS plexus and its branch nerves to demonstrate their longitudinal extent. Some surgeons and physicians prefer to visualize the LS plexus in the coronal

plane, and this plane may be beneficial for patient consultations. MR imaging provides the best soft-tissue contrast for the evaluation of deep soft-tissue structures, including the nerves.<sup>1</sup> With increasing frequency, MR neurography is playing a prominent role in the diagnosis, characterization, localization, and determination of the extent of pathology in patients with symptoms of lumbar plexopathy.<sup>2,3</sup> Due to the complex anatomy and oblique course of the plexus branches, however, the longitudinal extent of pathology is difficult to determine on direct coronal or sagittal MR images. 3D isotropic MR images can be reconstructed in various arbitrary planes to depict the peripheral nerves in their entirety.<sup>4</sup> However, the number of centers currently performing 3D fat-suppressed isotropic imaging is limited due to various hardware and software limitations. If the angular orientations of the major LS plexus nerves

Received April 13, 2016; accepted after revision May 25.

From the Department of Musculoskeletal Radiology, University of Texas Southwestern Medical Center, Dallas, Texas.

Please address correspondence to Avneesh Chhabra, MD, Department of Musculoskeletal Radiology, UT Southwestern Medical Center, 5323 Harry Hines Blvd, Dallas, TX 75390-9178; e-mail: avneesh.chhabra@utsouthwestern.edu

<http://dx.doi.org/10.3174/ajnr.A4879>

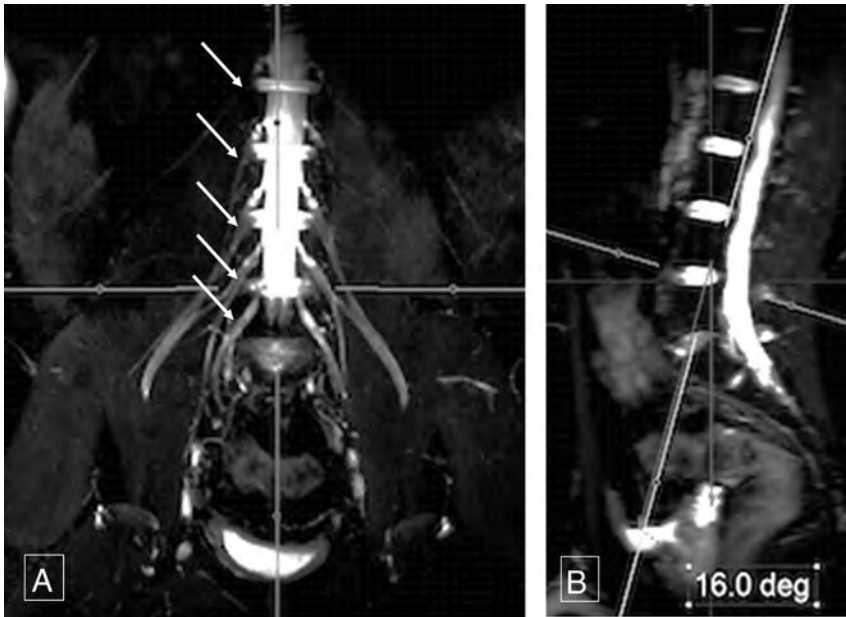


**FIG 1.** Sagittal thecal sac angle. Thick-slab 20-mm coronal MIP image from a 3D SHINKEI acquisition (A) obtained at a sagittal angle of 16° (B) optimally demonstrates all the lumbar nerve roots (arrows, A) from their origin to the maximum length. Deg indicates degree.

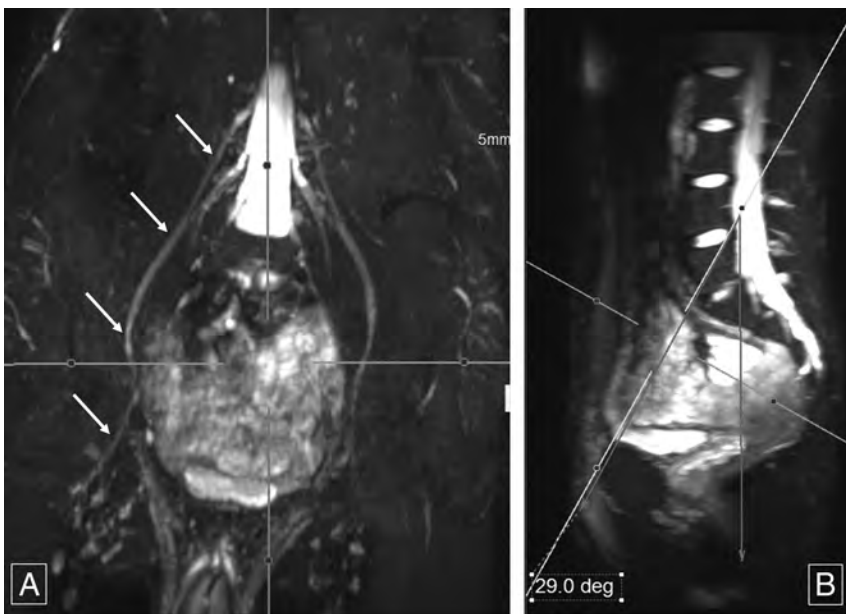


**FIG 2.** Sagittal femoral nerve angle. Thick-slab 20-mm coronal MIP image from a 3D SHINKEI acquisition (A) obtained at a sagittal angle of 29° (B) optimally demonstrates bilateral femoral nerves (arrows, A) from their origin to the maximum length across the inguinal ligaments. Deg indicates degree.

on 3D isotropic MR neurography could be determined, similar planes could be prescribed during acquisition of 2D or 3D nonisotropic techniques for optimal depiction of various nerves, depending on the clinical suspicion of different neuropathies. This added oblique imaging plane/sequence would help the radiologists and referring physicians precisely assess the location and extent of the pathology while facilitating multidisciplinary communication.

The primary aim of the study was to determine oblique sagittal and coronal angular measurements for the optimal longitudinal depiction of lumbosacral plexus nerve roots and sciatic and femoral

nerves from their origin to the most distal extent without a break in continuity. As secondary aims, interobserver and intraobserver performance was assessed and the average calibers of sciatic and femoral nerves were measured to generate normative data.

## MATERIALS AND METHODS

Informed consent for this retrospective evaluation was waived, and anonymized data were evaluated. A consecutive series of LS plexus MR neurography examinations for pelvic pain performed during a 10-month period (November 2013 to August 2014) on a 3T scanner (Achieva; Philips Healthcare, Best, the Netherlands) were evaluated. The inclusion criteria were consecutive examinations with no distortion of images by metal, motion, or poor fat suppression. The exclusion criteria were incomplete imaging or evidence of any major nerve pathology, which could cause abnormal thickening in the evaluated nerves. All the MR imaging examinations were performed on nerve-SHeath signal increased with INKed rest-tissue rare Imaging (SHINKEI; Philips Healthcare) acquisitions, which were obtained as part of the LS plexus MR neurography examination. This sequence uses adiabatic inversion recovery fat suppression for uniform fat saturation and a motion-sensitive driven equilibrium pulse for vascular signal suppression for selective demonstration of the LS plexus nerves.<sup>5</sup> The SENSE XL Torso coil (Philips Healthcare) combined with spine elements was used for imaging. The parameters of the sequence included the following: TR, 2000 ms; TE, 78 ms; voxels, 1.5 mm isotropic; acquisition time, 7–8 minutes; fat suppression, spectral adiabatic inversion recovery. The source data were manipulated on independent Aquarius iNtuition software (TeraRecon, San Mateo, California).

Two observers (E.B. and R.J., second- and third-year radiology residents) performed the reconstructions and measurements independently, following training on an initial set of 10 cases. Sagittal and coronal oblique 20-mm-thick-slab maximum-intensity reconstructions were performed, which allowed maximum longitudinal visualization of the LS plexus nerve roots and sciatic and femoral nerves from their origin to termination without a break in continuity (ie, the distal-to-inguinal ligament in the case of femoral nerves). Thinner slab MIP reconstructions did not show the maximum longitu-

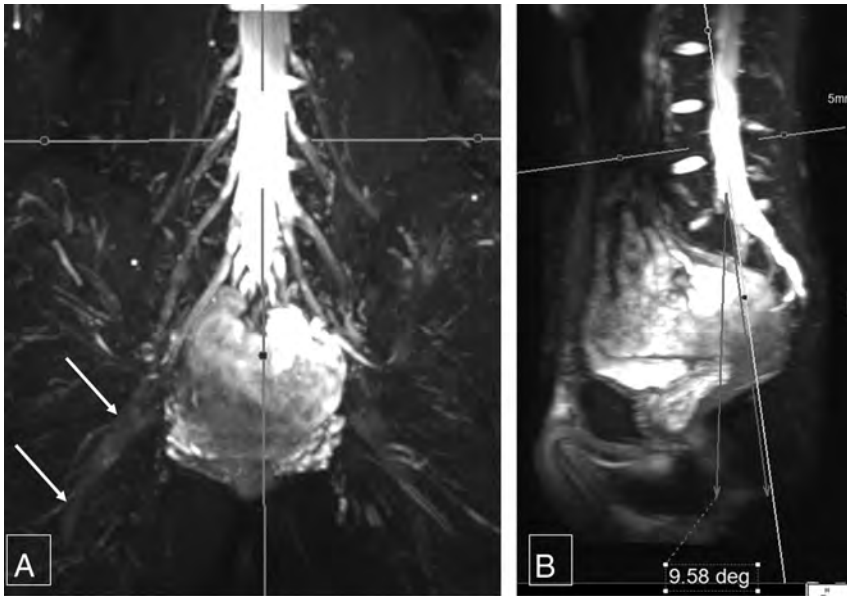


**FIG 3.** Sagittal sciatic nerve angle. Thick-slab 20-mm coronal MIP image from a 3D SHINKEI acquisition (A) obtained at a sagittal angle of  $-9.6^\circ$  (B) optimally demonstrates the bilateral sciatic nerves (arrows, A) from their origin to the maximum length. Deg indicates degree.

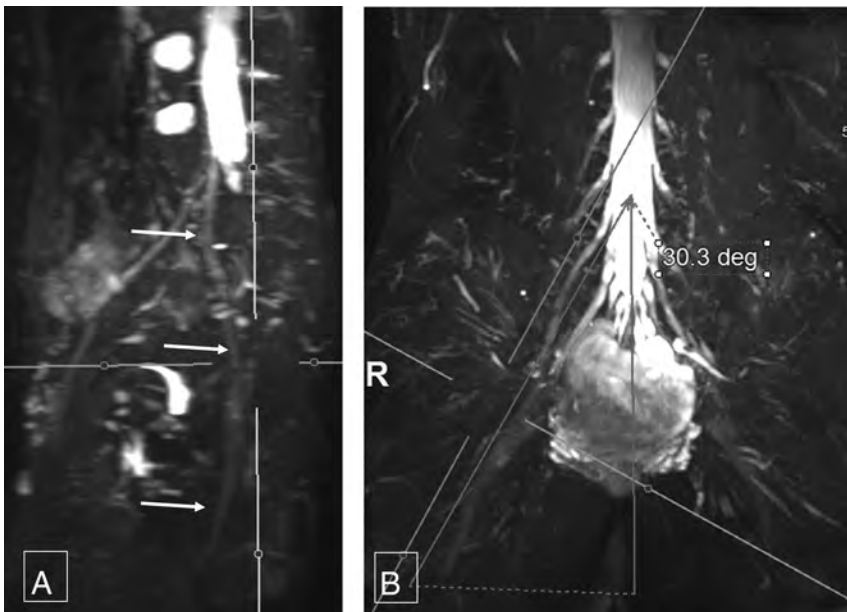


**FIG 4.** Coronal sciatic nerve angle. Thick-slab 20-mm sagittal MIP image from a 3D SHINKEI acquisition (A) obtained at a coronal angle of  $30.3^\circ$  (B) optimally demonstrates the right sciatic nerve (arrows, A) from its origin to the maximum length. Deg indicates degree.

dinal course of the nerves, while thicker slab MIP reconstructions resulted in blurring of the nerves due to overlapping of adjacent structures. In our initial testing, 20-mm-thick slabs provided the optimal longitudinal depiction of the nerves; MIP parameters would not be expected to change substantially in patients with conditions such as chronic inflammatory demyelinating polyneuropathy, or neurofibromatosis, though parameters could be optimized for each patient.

The sagittal plane measurements for the angle ventral to the thecal sac were denoted by positive numbers and dorsal to the thecal sac, by negative numbers. Femoral and sciatic nerve calibers were measured in their midportions in the abdomen and

pelvis, respectively, at the site of optimal nerve visualization and maximum thickness (ie, immediately below the piriformis muscle and sciatic notch for the sciatic nerve and adjacent to the iliopsoas crotch for the femoral nerve). Descriptive statistics were performed, and data were expressed as mean  $\pm$  SD. Interobserver variance was evaluated by using the intraclass correlation coefficient (ICC), with values of  $\geq 0.65$  considered good;  $<0.65$  to  $\geq 0.50$ , moderate;  $<0.50$  to  $\geq 0.40$ , fair; and  $<0.40$ , poor correlations. Intraobserver performance was also assessed by using the ICC for the reader E.B., who obtained repeat measurements approximately 25 weeks following the initial measurements.

## RESULTS

There were 62 examinations with full abdomen and pelvis MR neurography imaging, though 10 were excluded due to hardware artifacts ( $n = 3$ ) and motion and suboptimal fat suppression and incomplete imaging ( $n = 7$ ). Final samples included 52 subjects, 11 men (mean age,  $45.73 \pm 18.4$  years) and 41 women (mean age,  $48.85 \pm 12.65$  years). All reconstructions were successfully obtained in  $<7$  minutes.

Mean sagittal thecal sac angles for the coronal demonstration of LS plexus nerve roots from L1 to S1 for the 2 independent observers measured  $13.58^\circ \pm 2.87^\circ$  and  $13.61^\circ \pm 2.18^\circ$  (Fig 1). For complete longitudinal nerve course depiction bilaterally in the coronal plane, the mean sagittal angular measurements of the femoral nerve were  $27.78^\circ \pm 4.81^\circ$  and  $28.94^\circ \pm 4.49^\circ$  (Fig 2). Similarly, mean sagittal sciatic nerve angle measurements for coronal depiction were  $-10.7^\circ \pm 3.75^\circ$  and  $-11.82^\circ \pm 2.87^\circ$  (Fig 3).

The mean coronal angular measurements for the sagittal long axis demonstration of the right femoral nerve were  $33.54^\circ \pm 4.55^\circ$  and  $33.87^\circ \pm 3.57^\circ$ ; and for the left femoral nerve,  $32.85^\circ \pm 4.24^\circ$  and  $34.29^\circ \pm 3.75^\circ$ , respectively (Fig 4). The mean coronal angular measurements for the sagittal long axis demonstration of the right sciatic nerve were  $33.01^\circ \pm 4.41^\circ$  and  $34.53^\circ \pm 3.8^\circ$  and, for the left sciatic nerve,  $32.75^\circ \pm 3.72^\circ$  and  $34.37^\circ \pm 3.5^\circ$ , respectively (Fig 5). The interobserver ICC was moderate (0.582–0.671) for various angular measurements. For intraobserver performance among various angular measurements, the ICC was moderate to good (0.586–0.788).

Femoral nerve caliber on MR imaging was almost half that of

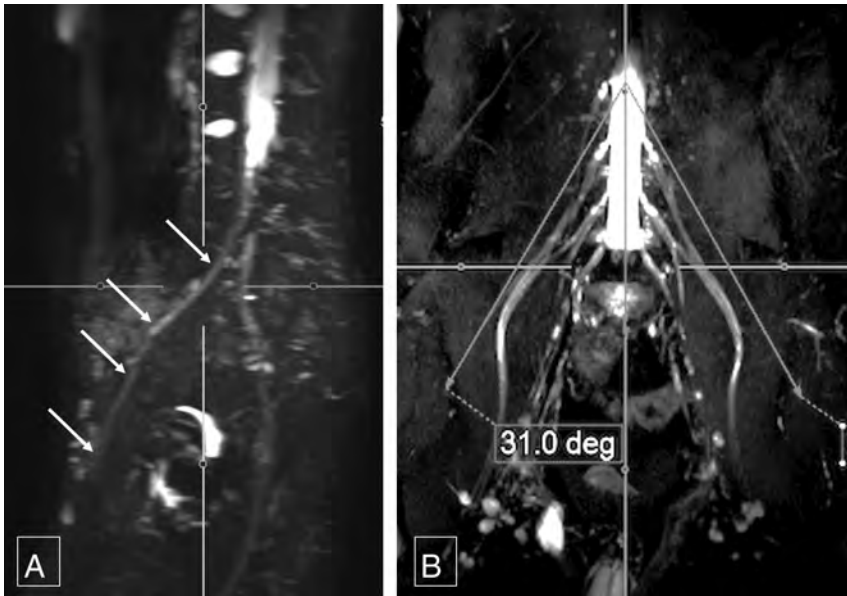


**FIG 5.** Coronal femoral nerve angle. Thick-slab 20-mm sagittal MIP image from a 3D SHINKEI acquisition (A) obtained at a coronal angle of 31° (B) optimally demonstrates the right femoral nerve (arrows, A) from its origin to the maximum length. Deg indicates degree.

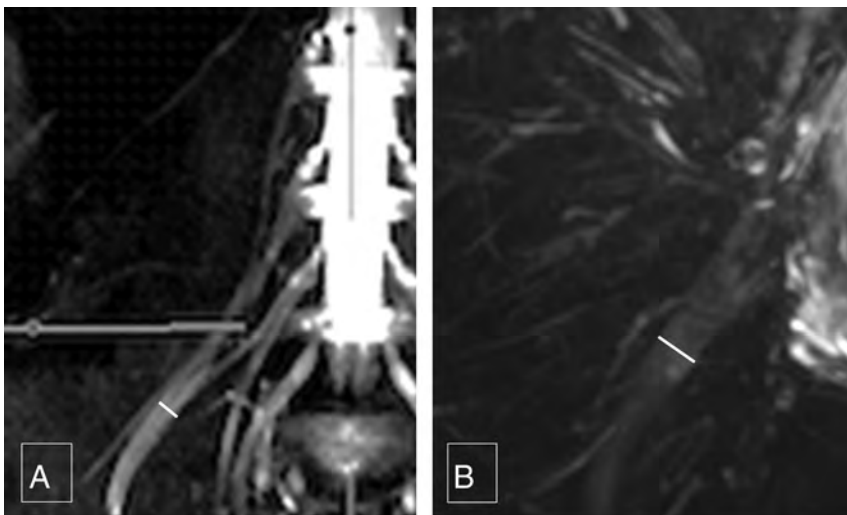


**FIG 6.** Femoral and sciatic nerve calibers. Thick-slab 20-mm sagittal MIP images from a 3D SHINKEI acquisition through the abdomen (A) and pelvis (B) show the femoral nerve diameter (4.8 mm), which is almost one-half of sciatic nerve diameter (9.7 mm).

**ICC: intraobserver performance**

Variable	Intraobserver ICC
Fem cor Lt	0.75146
Fem cor Rt	0.69077
Fem sag	0.78773
Fem width Lt	0.64571
Fem width Rt	0.75638
L plexus sag	0.67175
Sciatic width Lt	0.39228
Sciatic width Rt	0.73182
Sciatic cor Lt	0.58572
Sciatic cor Rt	0.61695
Sciatic sag	0.72101

**Note:**—Fem indicates femoral; cor, coronal; Lt, left; Rt, right; L, lumbrosacral; sag, sagittal.

the sciatic nerve. Mean right femoral nerve thickness was  $4.52 \pm 1.11$  mm and  $4.85 \pm 0.64$  mm for the 2 observers, and mean left femoral nerve thickness was  $4.48 \pm 0.97$  mm and  $4.94 \pm 0.57$  mm, respectively. Mean right sciatic nerve thickness was  $9.71 \pm 1.76$  mm and  $9.94 \pm 0.83$  mm, and mean left sciatic nerve thickness was  $10.03 \pm 1.71$  mm and  $9.98 \pm 0.99$  mm, respectively (Fig 6). The interobserver ICC was moderate to good (0.557–0.737) for the above thicknesses except for the right femoral nerve thickness, which was poor (0.343). Intraobserver performance for nerve thickness was moderate to good (0.646–0.756), except for the left sciatic nerve thickness, which was poor (0.392) (Table).

**DISCUSSION**

3D SHINKEI allows excellent vascular and fat signal suppression, leading to selective nerve depiction.<sup>6,7</sup> This sequence uses adiabatic inversion recovery for uniform fat suppression and a motion-sensitive driven equilibrium pulse for vascular signal suppression, thereby enabling selective demonstration of the LS plexus nerves.<sup>5</sup> The variable turbo spin-echo component limits the acquisition time to 7–8 minutes.

This imaging technique allows ready depiction of the nerves in various arbitrary planes. Thus, the angular prescriptions could be easily and confidently measured<sup>8,9</sup>; these results are reflected in nearly good interobserver and intraobserver performance in angular measurements.

The femoral nerve calibers were ~4–5 mm, the sciatic nerve calibers were ~8–11 mm, and the interobserver performance was moderate to good ex-

cept for the right femoral nerve, due to the relatively smaller size of the femoral nerve. The normative data can be used for identification of pathologies that frequently cause abnormal nerve thickening, such as chronic demyelinating polyneuropathy, diabetic polyneuropathy, perineurioma, or Charcot-Marie-Tooth disease and so forth.<sup>10–12</sup> The nerve-caliber measurements are also reproducible, as shown by moderate-to-good ICC results for intraobserver performance, except for the left sciatic nerve caliber, which was poor (0.392).

Although this is the first study depicting angular and nerve-caliber measurements, there are some limitations. We did not obtain surgical or cadaveric correlation because it would not be practical to obtain such correlations for a large sample. In addi-



tion, no correlations with diffusion imaging were obtained, which is also shown to produce nerve-selective images. The observers felt confident in nerve identification on 3D SHINKEI during the evaluation of the initial training set due to excellent vascular signal suppression and nerve depiction by this technique. It was therefore decided that diffusion imaging evaluation can be avoided and left as the subject of another article. Another limitation is that we evaluated only patients with normal nerves. Patients with significant nerve pathology/known mass lesions were excluded from our patient population. Patients with significant nerve pathology may require different angles to optimize the longitudinal display of the nerves, due to distortion of nerve course. Nerve caliber in these patients would also be expected to differ from that of patients with normal nerves. Finally, we did not measure obturator nerve angles. Because this nerve has been shown to travel in a straight coronal plane, it was thought that further study would not yield a significant angle.<sup>13</sup>

## CONCLUSIONS

The study fills a gap in the literature regarding angular LS plexus nerve measurements for their maximum length depiction and nerve thickness. It will aid in prescription of predictable nerve planes on MR imaging for their optimal longitudinal demonstration.

## ACKNOWLEDGMENTS

The authors would like to acknowledge Dr Vibhor Wadhwa for help with image formatting.

Disclosures: Avneesh Chhabra—UNRELATED: Consultancy: Siemens (CAD Consulting); Royalties: Jaypee, Wolters Kluwer, Elsevier, Comments: book royalties; Payment for Development of Educational Presentations: educational symposia; OTHER: A. Chhabra has received research grants from GE-Radiology Research Academic Fellowship, Siemens, Gatewood Fellowship Award, and Integra Life Sciences.

## REFERENCES

1. Neufeld EA, Shen PY, Nidecker AE, et al. **MR imaging of the lumbosacral plexus: a review of techniques and pathologies.** *J Neuroimaging* 2015;25:691–703 CrossRef Medline
2. Soldatos T, Andreisek G, Thawait GK, et al. **High-resolution 3-T MR neurography of the lumbosacral plexus.** *Radiographics* 2013;33:967–87 CrossRef Medline
3. Delaney H, Bencardino J, Rosenberg ZS. **Magnetic resonance neurography of the pelvis and lumbosacral plexus.** *Neuroimaging Clin N Am* 2014;24:127–50 CrossRef Medline
4. Vargas MI, Gariani J, Delattre BA, et al. **Three-dimensional MR imaging of the brachial plexus.** *Semin Musculoskelet Radiol* 2015;19:137–48 CrossRef Medline
5. Kasper JM, Wadhwa V, Scott KM, et al. **SHINKEI—a novel 3D isotropic MR neurography technique: technical advantages over 3DIRTSE-based imaging.** *Eur Radiol* 2015;25:1672–77 CrossRef Medline
6. Yoneyama M, Takahara T, Kwee TC, et al. **Rapid high resolution MR neurography with a diffusion-weighted pre-pulse.** *Magn Reson Med* 2013;12:111–19 CrossRef Medline
7. Huisman M, Staruch RM, Ladouceur-Wodzak M, et al. **Non-invasive targeted peripheral nerve ablation using 3D MR neurography and MRI-guided high-intensity focused ultrasound (MR-HIFU): pilot study in a swine model.** *PLoS One* 2015;14;10:e0144742 CrossRef Medline
8. Burge AJ, Gold SL, Kuong S, et al. **High-resolution magnetic resonance imaging of the lower extremity nerves.** *Neuroimaging Clin N Am* 2014;24:151–70 CrossRef Medline
9. Chhabra A, Rozen S, Scott K. **Three-dimensional MR neurography of the lumbosacral plexus.** *Semin Musculoskelet Radiol* 2015;19:149–59 CrossRef Medline
10. Ellegala DB, Monteith SJ, Haynor D, et al. **Characterization of genetically defined types of Charcot-Marie-Tooth neuropathies by using magnetic resonance neurography.** *J Neurosurg* 2005;102:242–45 CrossRef Medline
11. Mauermann ML, Amrami KK, Kuntz NL, et al. **Longitudinal study of intraneural perineurioma: a benign, focal hypertrophic neuropathy of youth.** *Brain* 2009;132(pt 8):2265–76 CrossRef Medline
12. Lozeron P, Lacour MC, Vandendries C, et al. **Contribution of plexus MRI in the diagnosis of atypical chronic inflammatory demyelinating polyneuropathies.** *J Neurol Sci* 2016;360:170–75 CrossRef Medline
13. Petchprapa CN, Rosenberg ZS, Sconfienza LM, et al. **MR imaging of entrapment neuropathies of the lower extremity, Part 1: the pelvis and hip.** *Radiographics* 2010;30:983–1000 CrossRef Medline

# Cervical Spinal Cord DTI Is Improved by Reduced FOV with Specific Balance between the Number of Diffusion Gradient Directions and Averages

A. Crombe, N. Alberti, B. Hiba, M. Uettwiller, V. Dousset, and T. Tourdias



## ABSTRACT

**BACKGROUND AND PURPOSE:** Reduced-FOV DTI is promising for exploring the cervical spinal cord, but the optimal set of parameters needs to be clarified. We hypothesized that the number of excitations should be favored over the number of diffusion gradient directions regarding the strong orientation of the cord in a single rostrocaudal axis.

**MATERIALS AND METHODS:** Fifteen healthy individuals underwent cervical spinal cord MR imaging at 3T, including an anatomic 3D-Multi-Echo Recombined Gradient Echo, high-resolution full-FOV DTI with a NEX of 3 and 20 diffusion gradient directions and 5 sets of reduced-FOV DTIs differently balanced in terms of NEX/number of diffusion gradient directions: (NEX/number of diffusion gradient directions = 3/20, 5/16, 7/12, 9/9, and 12/6). Each DTI sequence lasted 4 minutes 30 seconds, an acceptable duration, to cover C1–C4 in the axial plane. Fractional anisotropy maps and tractograms were reconstructed. Qualitatively, 2 radiologists rated the DTI sets blinded to the sequence. Quantitatively, we compared distortions, SNR, variance of fractional anisotropy values, and numbers of detected fibers.

**RESULTS:** Qualitatively, reduced-FOV DTI sequences with a NEX of  $\geq 5$  were significantly better rated than the full-FOV DTI and the reduced-FOV DTI with low NEX ( $N = 3$ ) and a high number of diffusion gradient directions ( $D = 20$ ). Quantitatively, the best trade-off was reached by the reduced-FOV DTI with a NEX of 9 and 9 diffusion gradient directions, which provided significantly fewer artifacts, higher SNR on trace at  $b = 750$  s/mm<sup>2</sup> and an increased number of fibers tracked while maintaining similar fractional anisotropy values and dispersion.

**CONCLUSIONS:** Optimized reduced-FOV DTI improves spinal cord imaging. The best compromise was obtained with a NEX of 9 and 9 diffusion gradient directions, which emphasizes the need for increasing the NEX at the expense of the number of diffusion gradient directions for spinal cord DTI contrary to brain DTI.

**ABBREVIATIONS:** CSC = cervical spinal cord; FA = fractional anisotropy; f-FOV = full-FOV; MERGE = Multi-Echo Recombined Gradient Echo; NDGD = number of diffusion gradient directions; r-FOV = reduced-FOV

Cervical spinal cord (CSC) assessment in daily clinical routines still essentially relies on a qualitative evaluation of conventional MR imaging sequences. Nonetheless, additional sequences could provide more sensitive information about CSC alterations,

notably in inflammatory, traumatic, and neurodegenerative diseases.<sup>1–5</sup> Among the sequences, diffusion tensor imaging, classically based on single-shot echo-planar imaging, could provide valuable qualitative information and quantitative surrogate biomarkers.

While DTI has been widely investigated in the brain, its use for CSC imaging is still challenging and is restricted to preclinical and monocentric clinical studies. Several reasons for these limitations include the CSC being a small structure, prone to distortions;

Received February 23, 2016; accepted after revision April 25.

From the Centre Hospitalier Universitaire de Bordeaux (A.C., V.D., T.T.), Service de Neuroimagerie Diagnostique de Thérapeutique, Bordeaux, France; Institut National de la Santé et de la Recherche Médicale U1215 (A.C., V.D., T.T.), Physiopathologie de la Plasticité Neuronale, Bordeaux, France; Institut de Bio-Imagerie de Bordeaux (A.C., N.A., B.H., V.D., T.T.), Université de Bordeaux, Bordeaux, France; Centre de Résonance Magnétique des Systèmes Biologiques (N.A., B.H.), Centre National de la Recherche Scientifique Unité Mixte de Recherche 5536, Bordeaux, France; Institut de Neurosciences Cognitives et Intégratives d'Aquitaine (B.H.), Centre National de la Recherche Scientifique Unité Mixte de Recherche 5287, Bordeaux, France; and GE Healthcare (M.U.), Vélizy–Villacoublay, France.

The work was supported by public grants from the French Agence Nationale de la Recherche within the context of the Investments for the Future program referenced ANR-10-LABX-57 named TRAIL (Translational Research and Advanced Imaging Laboratory) and ANR-10-LABX-43 named BRAIN (Bordeaux Region Aquitaine Initiative for Neurosciences).

Paper previously presented in part at: Annual Meeting of the French Society of Radiology, October 19, 2014; Paris, France; and Annual Meeting of the French Society of Neuroradiology, April 8, 2015; Paris, France.

Please address correspondence to Amandine Crombe, Service de Neuroimagerie Diagnostique et Thérapeutique, Hôpital Pellegrin, CHU de Bordeaux, Place Amélie Raba-Leon, 33076 Bordeaux cedex, France; e-mail: amandine.crombe@ens-lyon.fr

Indicates open access to non-subscribers at [www.ajnr.org](http://www.ajnr.org)

<http://dx.doi.org/10.3174/ajnr.A4850>

susceptibility artifacts, especially with a long echo-planar readout train; flow artifacts; and physiological motion artifacts.

Among the various methods that have been implemented on MR imaging systems to improve DTI quality, reduced field-of-view (r-FOV) is particularly promising. It consists of reducing the FOV in the phase- or frequency-encoding direction to shorten the echo-planar readout train and attenuate susceptibility- and motion-related artifacts.<sup>6-11</sup> Because the CSC is a small longitudinal structure, r-FOV is especially suitable for its exploration. One of the r-FOV techniques uses a 2D echo-planar radiofrequency pulse to excite a rectangular FOV, with contiguous multisections. The *k*-space is then more rapidly acquired for the same spatial resolution, which decreases single-shot EPI artifacts together with inherent fat suppression.<sup>6</sup>

On qualitative analysis, this CSC r-FOV diffusion-weighted imaging method obtained from 3 orthogonal diffusion gradient directions has already demonstrated its ability to better detect anatomic details, with fewer ghosting and blurring artifacts,<sup>12</sup> while apparent diffusion coefficient values were stable compared with conventional full-FOV CSC DWI (f-FOV).

However, there is no recommendation regarding the optimal set of parameters to perform r-FOV DTI in CSC. Some consensus has been reached (regarding the *b*-value, voxel size, number of excitations, number of diffusion gradient directions [NDGD], and bandwidth<sup>13</sup>), but these recommendations concern f-FOV DTI with parallel imaging, whose sequence scheme is different from the r-FOV scheme. The smaller voxel size in r-FOV inherently leads to a decrease of the signal-to-noise ratio. Classic strategies to recover SNR consist of increasing the NEX and/or the NDGD. Unlike brain DTI, for which the NDGD should be preferred over the NEX, there is no consensus about the best pair of NEX/NDGD for CSC DTI to handle with the complex fiber orientation. One might even hypothesize that the best trade-off of NEX/NDGD could be obtained by favoring NEX (unlike for brain DTI) because the CSC is particularly affected by artifacts and presents a single prominent orientation. It is difficult to rely on phantom studies or theoretic analyses for such optimization in the CSC, which could not take into account CSF pulsations, heartbeats, or patient respiratory motions.

Therefore, the purpose of this study was to compare different sets of r-FOV CSC DTI, depending on different pairs of NEX and NDGD, and a standard f-FOV DTI. To do so, we used an empiric nonsequential optimization approach, in which both NEX and NDGD were modified simultaneously, with the only constraint being maintaining the same clinically acceptable scan duration. To evaluate image quality, we proposed a practical clinical approach with a standardized bench test for qualitative and quantitative evaluations derived from ROIs and tractography.

## MATERIALS AND METHODS

### Patient Population

Fifteen healthy volunteers (6 women, 9 men; age range, 22–30 years) were prospectively included at Bordeaux University Hospital after written informed consent was obtained. This study was approved by the local ethics committee review board.

### Imaging Methods

All scans were obtained on a 3T MR imaging scanner (Discovery MR750W; GE Healthcare, Milwaukee, Wisconsin) equipped with high-performance gradients (maximum slew rate of 200 mT/m/ms and maximum strength of 44 mT/m) and a dedicated posterior coil with 40 elements and a 19-channel phased array head-neck spine coil.

Subjects were asked to breathe normally and not to swallow or cough during the acquisition. They were positioned with a slight flexion of the head and with well immobilized to reduce involuntary movements.

All sequences were performed in the axial plane with an anteroposterior phase-encoding direction and used similar geometry to perform fair comparisons. Pulse triggering was not used, to limit the scan time.

**Conventional Imaging.** The protocol included an anatomic sagittal T2-weighted spin-echo and a 3D Multi-Echo Recombined Gradient Echo sequence (MERGE; GE Healthcare) acquired in the same axial plane as the DTI sequences (ie, perpendicular to the long axis of the upper cervical spine). 3D-MERGE provides good white and gray matter differentiation with good SNR and was considered the anatomic reference. One hundred eight sections with a resolution of  $0.8 \times 0.8 \times 0.8 \text{ mm}^3$  covering a  $140 \times 140 \text{ mm}^2$  FOV were acquired in 8 minutes. Other sequence parameters were the following: TR/TE, 10/5 ms; flip angle, 7°; turbo factor, 36.

**f-FOV DTI.** Conventional CSC DTI corresponded to the DTI usually performed at our institutions,<sup>14</sup> which was optimized beforehand according to the literature.<sup>15,16</sup> Parallel imaging was used (array spatial sensitivity encoding technique) with an acceleration factor of 2. The single-shot EPI parameters were the following: NDGD, 20 directions;  $b=0 \text{ s/mm}^2$  and  $b=750 \text{ s/mm}^2$ ; matrix,  $96 \times 96$ ; FOV,  $120 \times 120 \text{ mm}^2$ ; in-plane resolution,  $1.25 \times 1.25 \text{ mm}^2$ ; section thickness, 5 mm; TR/TE, 5600/75 ms; and NEX, 3. This sequence covered the CSC from C1 to C7 within 6 minutes 50 seconds.

**r-FOV DTI.** For each subject, r-FOV DTI was acquired by using 5 schemes with different combinations of NDGD and NEX for each direction, starting from a sequence with many directions (NDGD = 20) and few excitations (NEX = 3) up to an opposite scenario obtained with the minimum number of directions to calculate a diffusion tensor (NDGD = 6) and a maximum number of excitations (NEX = 12). Each scheme lasted about 4 minutes 30 seconds, to cover the upper cervical spine from C1 to C4. The 5 schemes of the single-shot EPI sequence were as follows in terms of NEX/NDGD: 3N/20D, 5N/16D, 7N/12D, 9N/9D, 12N/6D. The directions were noncollinear and generated according to the recommendations of Jones et al<sup>17</sup> for the optimization of gradient vector orientations (TR/TE, 3600/75 ms). The other parameters were fixed and corresponded to those applied for the f-FOV sequence to compare r-FOV and f-FOV, notably regarding voxel size (r-FOV was  $96 \times 48$  with a matrix of  $120 \times 60 \text{ mm}^2$ ; in-plane resolution was  $1.25 \times 1.25 \text{ mm}^2$ , with a 5-mm section thickness).

The entire protocol was performed during the same session and lasted 40 minutes.

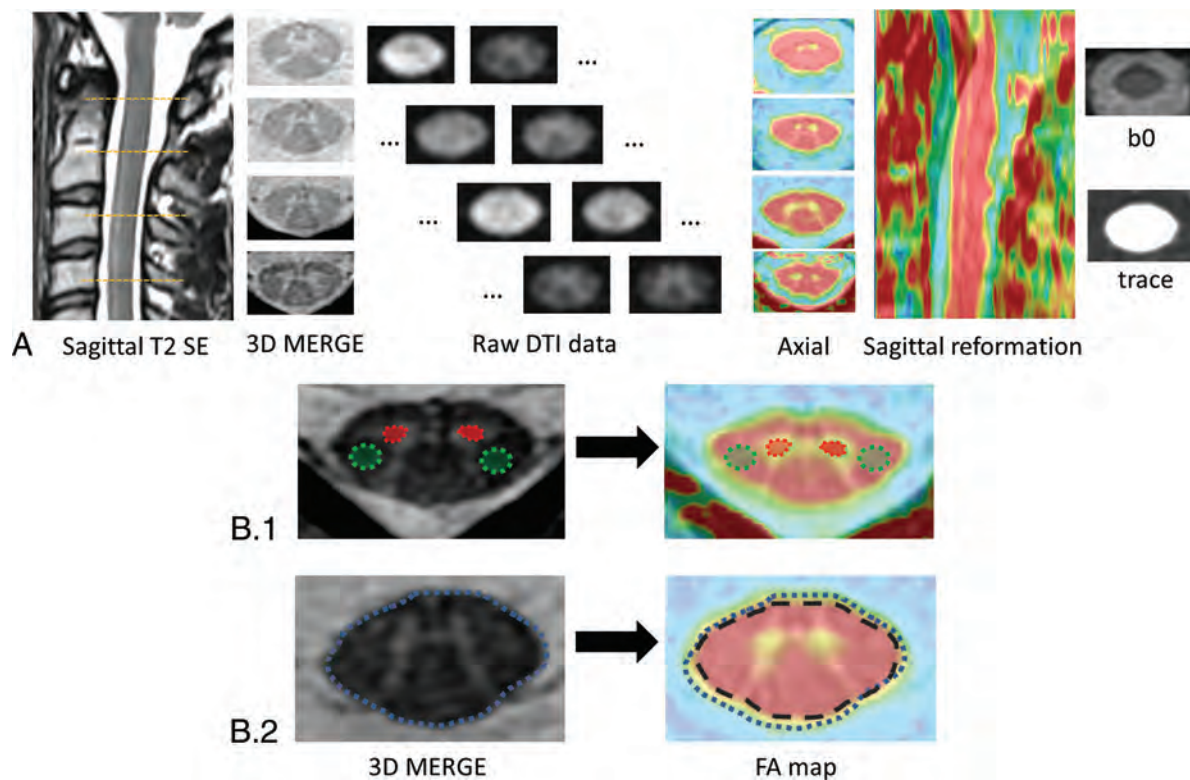


**FIG 1.** Postprocessing pipeline and analyses. *A*, Four sections were analyzed in detail: C1, C2, C3, and C4. Raw data diffusion-weighted images were treated for eddy current correction before generation of DTI parameters. We focused on FA because this parameter is the most commonly used. Fusions of FA and 3D-MERGE were created at these 4 levels as well as reconstructed on the sagittal orientation to facilitate the identification of distortions and pixel misregistration. *B*, ROI positioning: ROIs (B1) were manually delineated on 3D-MERGE, on the right and left anterior horns of the cord (red area) for gray matter, and on the right and left corticospinal tract (green area) for white matter, and then propagated on the coregistered FA map. B2, If needed, ROIs were manually adjusted to account for FA map distortion. Furthermore, because of the partial volume effect at the interface between CSF and the FA map, ROIs of the full section (blue dotted line, whose surface corresponded to  $S_{[Full\ Section - Merge]}$ ) were adjusted to remove the pixels subject to artifacts at the periphery of the ROI (black dashed line, whose area corresponded to  $S_{[Full\ Section - FA]}$ ).

**Postprocessing.** Because our goal was to identify the best set of parameters for a DTI sequence used for clinical applications, we postprocessed the images with the tools that are accessible on clinical systems. Therefore, the DTI dataset processing and the qualitative and ROI-based analyses were performed on an AW server Workstation 5 (GE Healthcare). Tractography-based analyses were performed with Olea Sphere software (Olea Medical, La Ciotat, France).

All the raw images were corrected for motion artifacts and eddy current distortion with the algorithm implemented on the DTI analysis software (GE Healthcare).

### Radiologic Assessment

**Qualitative Analysis.** Two radiologists (A.C. and N.A., with, respectively, 4 and 7 years of experience in MR imaging) randomly evaluated the quality of each of the 6 DTI sequences (f-FOV, r-FOV 3N/20D, r-FOV 5N/16D, r-FOV 7N/12D, r-FOV 9N/9D, r-FOV 12N/6D) blinded to the nature of the sequence. They determined a score based on a 4-point scale, adapted from Zaharchuk et al<sup>12</sup> as follows: 1 = nondiagnostic, 2 = poor, 3 = moderate, 4 = good. This score was based on anatomic details, artifacts, distortion, and perceived SNR from fractional anisotropy (FA) maps alone and fused with 3D-MERGE. In case of disagreement between the 2 radiologists, consensus was obtained

after discussion with a third experienced neuroradiologist (T.T., with 14 years of experience).

**Number of Sections with Artifacts.** The number and the types of artifacts or nondiagnostic sections for each DTI sequence (flow artifacts, motion artifacts, susceptibility artifacts, major distortion) were reported and expressed as the percentage of sections with artifacts of the total number of sections.

**Quantitative Comparisons of FA Values Based on ROI Analysis.** For this part of the study, 1 neuroradiologist (A.C.), still blinded to the sequence, manually delineated ROIs on 4 sections passing through the middle of the vertebral bodies C1, C2, C3, and C4. ROIs were positioned twice with good reproducibility (intraclass correlation coefficient, 0.788; 95% CI, 0.353–0.943).

Measurements were obtained on the following areas: 1) gray matter: left and right anterior horn of the cord (GM); 2) white matter: left and right corticospinal tract (WM); and 3) a full section of the cervical spinal cord (Fig 1). ROIs were initially placed on the axial 3D-MERGE image and then propagated on coregistered FA maps. If needed, ROIs were slightly manually adjusted to account for FA map distortion. Because of partial volume effects at the interface between the CSF and spinal cord with about 2 pixels showing intermediate FA values, measurements on the full section of the spinal cord were

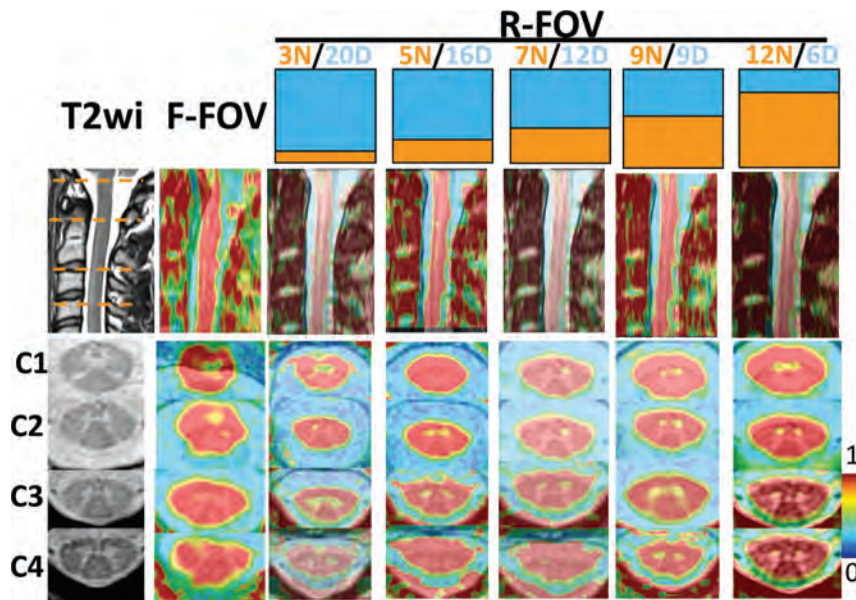


**FIG 2.** Examples of MR images available for qualitative analysis. All the images came from the same subject. Cervical levels are located on 3D T2-MERGE and sagittal T2-spin echo. Fusion of FA – 3D MERGE clearly shows that f-FOV DTI and r-FOV 3N/20D are more distorted and more blurred with less anatomic precision than the other r-FOV images.

conducted on a smaller ROI eroded by 2 pixels. The FA values of each ROI were extracted, with right and left measurements being averaged (Fig 1B).

1) Quantifications of residual distortion: The residual distortion after eddy current correction was quantified by a ratio that we called the “distortion ratio” calculated as follows:

Distortion Ratio =

$$\frac{|(S(\text{Full Section} - \text{Merge}) - S(\text{Full Section} - \text{FA}))|}{S(\text{Full Section} - \text{Merge})} \times 100,$$

where  $S$  is the surface of the full section of the cervical spinal cord. The distortion ratio was calculated at the 4 cervical levels and then averaged to obtain 1 single distortion ratio value per patient for each sequence. It ranges from zero when there is no distortion in the FA map compared with the reference anatomic MERGE sequence, and it increases when distortions are more pronounced.

2) Signal-to-noise ratio: Because multichannel coil and parallel imaging were used to collect DTI data, SNR cannot be exactly assessed.<sup>18</sup> In addition, background noise was not always included within the r-FOV DTI acquisition. Therefore, we estimated spinal cord SNR at B0 and  $b=750$  s/mm<sup>2</sup> as the ratio between the signal of the full section of the cord and the SD measured within the same neck muscle (longissimus capitis). SNR<sub>B0</sub> and SNR<sub>b750</sub> were assessed at the 4 cervical levels and then averaged to obtain single SNR<sub>B0</sub> and SNR<sub>b750</sub> values per patient and per DTI sequence.

3) Variability of FA measurements: Because a current issue with CSC DTI is its lack of precision and its variability, even among healthy subjects, we aimed at estimating variations among healthy volunteers. For this purpose, we measured FA on the full section and WM and GM at the 4 levels, and we calculated the mean and SD of these 4 values.

4) Quantitative comparisons based on tractography analysis:

Raw data were postprocessed with Olea Sphere software. Motion correction was performed. We drew 2 seed ROIs that included the entire section of the spine at the C1 and C3 levels. We measured the number of fibers detected between these 2 ROIs, per patient and per DTI sequence. The following parameters were used for stopping the tractography: FA minimum = 0.25, maximum angle = 41.4°, fiber minimum length = 20 mm.

### Statistical Analyses

All statistical analyses were performed with GraphPad Prism Software, Version 6 (GraphPad Software, San Diego, California). Gaussian distributions were tested with a Shapiro-Wilk normality test. To compare the qualitative scores, distortion ratio, SNR<sub>B0</sub>, SNR<sub>b750</sub>, mean FA values per topography, and number of detected fibers by tractography, we used 1-way ANOVA (with a post hoc  $t$

test) or the Kruskal-Wallis test (with a post hoc Dunn test), depending on the distribution of the variables. For artifact comparisons, contingency tables were built, and we compared sequences with the Fisher exact test to account for the small size of the sample. We performed a Bartlett test to assess whether the FA values of each DTI set had equal variance, after verification of the Gaussian distribution.  $P < .05$  was significant.

## RESULTS

No incidental pathologic finding was observed in these young subjects, notably, no degenerative disc disease.

### Qualitative Analysis

Figure 2 shows the superimposition of the FA map with the anatomic reference 3D-T2-MERGE at the 4 levels of interest (C1–C4) and a sagittal reconstruction for the f-FOV and the 5 r-FOV schemes, with the same FA color scale.

On qualitative radiologic assessment, the 5 r-FOV DTI sequences with a NEX of  $\geq 5$  were not scored differently from each other but were significantly better evaluated than the f-FOV images (3N/20D) ( $1.1 \pm 0.8$ ) or the r-FOV images (3N/20D) ( $1.8 \pm 0.56$ ). There was no qualitative difference between the f-FOV sequence and the r-FOV 3N/20D sequence (Fig 3).

Specifically, the 2 radiologists consistently observed fewer distortions, less misregistration in the anteroposterior direction, and less blurring for the r-FOV sequences with a NEX of  $> 5$  than for the 2 other sequences. The r-FOV images obtained with 5N/16D, 7N/12D, 9N/9D, and 12N/6D provided CSC morphology closer to the anatomic reference as opposed to the f-FOV or the r-FOV 3N/20D images (Figs 2 and 3).

### Number of Sections with Artifacts

The dataset with the highest number of sections with artifacts was r-FOV 3N/20D (31.6%) followed by f-FOV (22.7%), while the

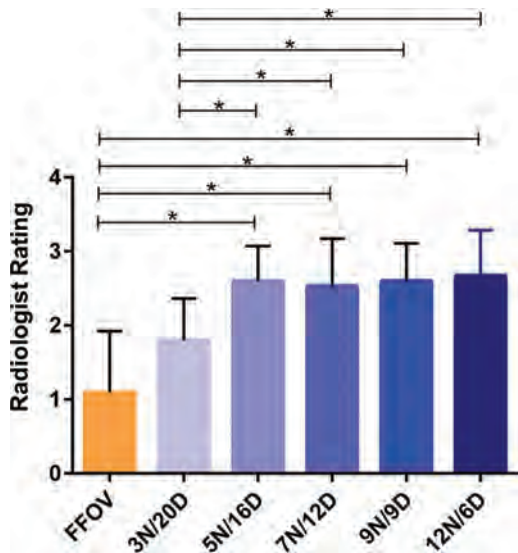


**FIG 3.** Qualitative analysis. Radiologists determined a rate for each sequence, for each subject, from 1 (nondiagnostic) to 4 (good). Mean rates  $\pm$  SDs for the sequence are represented. Superimposed black lines indicate which sequences are statistically different with  $P < .05$  (asterisk).

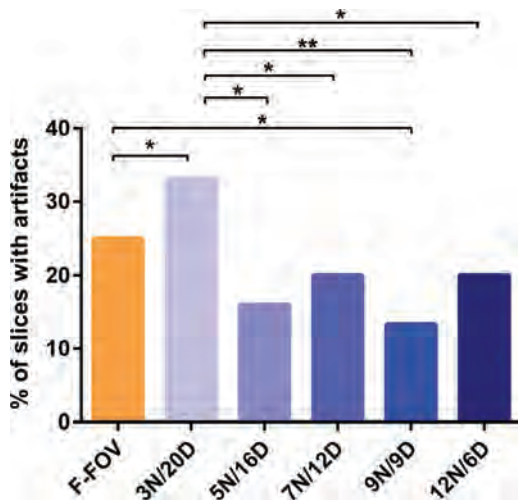


**FIG 4.** Percentages of sections with artifacts unusable for DTI analysis due to susceptibility artifacts or poor SNR. Superimposed black lines indicate which sequences are statistically different with  $P < .05$  (asterisk) and  $P < .005$  (double asterisks).

r-FOV sequences with a NEX of  $\geq 5$  were significantly better; the r-FOV 9N/9D was the one with fewest artifacts (13.3%) (Fig 4).

Artifacts were mainly due to CSF flow on B0 images and residual distortions after eddy current correction (the latter being particularly seen on f-FOV and r-FOV 3N/20D), notably at the lower level of the acquisition volume (C4).

#### Quantitative Comparisons Based on ROI Analysis

The distortion ratio decreased continuously while increasing the NEX (and, in turn, decreasing the NDGD), even though this effect did not reach statistical significance (Fig 5A). Thus, the distortion ratios for r-FOV 3N/20D and r-FOV 12N/6D were  $13.14 \pm 6.6\%$  and  $9.25 \pm 5.5\%$ , respectively.

SNR on the B0 map did not show significant differences be-

tween the sequences ( $P > .05$ ). At  $b=750 \text{ s/mm}^2$ , no significant difference was observed among the DTI sets, except for the comparison between r-FOV 3N/20D and r-FOV 9N/9D, which had, respectively, the lowest and the highest SNR ( $23.95 \pm 4$  versus  $36.04 \pm 5.8$ ,  $P = .0182$ ) (Fig 5B). Considering that a critical threshold of SNR below 8 should lead to section rejection, 10% of the sections had to be rejected because of a signal below this threshold on f-FOV; 6.7%, on r-FOV 3N/20D; and 5%, on r-FOV 7N/12D and r-FOV 12N/6D. The SNR was always above 8 for r-FOV sections acquired with 5N/16D and with 9N/9D.

Whatever the location (full section, GM, and WM) and sequences, comparisons of the distributions of FA values did not reveal a significant difference (Fig 5C). Furthermore, there was no significant difference between the FA values, depending on the acquisition pulse sequence. For instance, FA values of the full section were the following:  $0.70 \pm 0.04$  for f-FOV,  $0.74 \pm 0.04$  for r-FOV 3N/20D,  $0.71 \pm 0.05$  for r-FOV 5N/16D,  $0.7 \pm 0.04$  for r-FOV 7N/12D,  $0.074 \pm 0.03$  for r-FOV 9N/9D, and  $0.74 \pm 0.04$  for r-FOV 12N/6D. The FA values that we obtained were consistent with those in the literature,<sup>19-22</sup> with lower and more dispersed measures within the GM and higher and less dispersed measures within the WM.

#### Quantitative Comparisons Based on Tractography Analysis

Figure 6A represents tractograms derived from the 2 seeds superimposed on the corresponding trace at  $b=750 \text{ s/mm}^2$ . R-FOV 7N/12D, 9N/9D, and 12N/6D qualitatively exhibited a more realistic anatomy of the cord than f-FOV, r-FOV 3N/20D, and r-FOV 5N/16D, with more fibers and longer tracts.

Quantitatively, r-FOV 9N/9D detected the highest number of tracts without abnormal tract findings on tractograms ( $4587 \pm 1743$ ), closely followed by r-FOV 12N/6D ( $4290 \pm 1206$ ), with findings not significantly different from the previous ones. The best sequence (r-FOV 9N/9D) detected significantly more fibers than f-FOV ( $P < .0001$ ), r-FOV 5N/16D ( $P = .0004$ ), and r-FOV 3N/20D ( $P < .05$ ) (Fig 6B).

#### DISCUSSION

Our study did not show any significant difference between CSC DTI obtained with f-FOV or r-FOV when using a protocol favoring NDGD over NEX. However, we showed real benefits of the r-FOV by balancing the NDGD and the NEX, the best trade-off being 9N/9D, in terms of qualitative aspects, reduction of artifacts, SNR, and detection of fibers, while maintaining identical FA values.

This study demonstrates that optimized parameters for CSC DTI in clinical conditions are different from those for brain DTI, which requires a high number of directions, ideally at least 31 while the NEX can be reduced.<sup>23</sup> Here, we demonstrated that CSC DTI does not require such a high number of gradient directions. In theory, high NDGD leads to more precise DTI information. In the CSC, FA values and their variations were similar with 6, 9, 12, 16, or 20 NDGD in a set of healthy subjects; this finding might be explained by the strong orientation of the cord in the rostrocaudal axis. However, we recommend increasing the number of averages

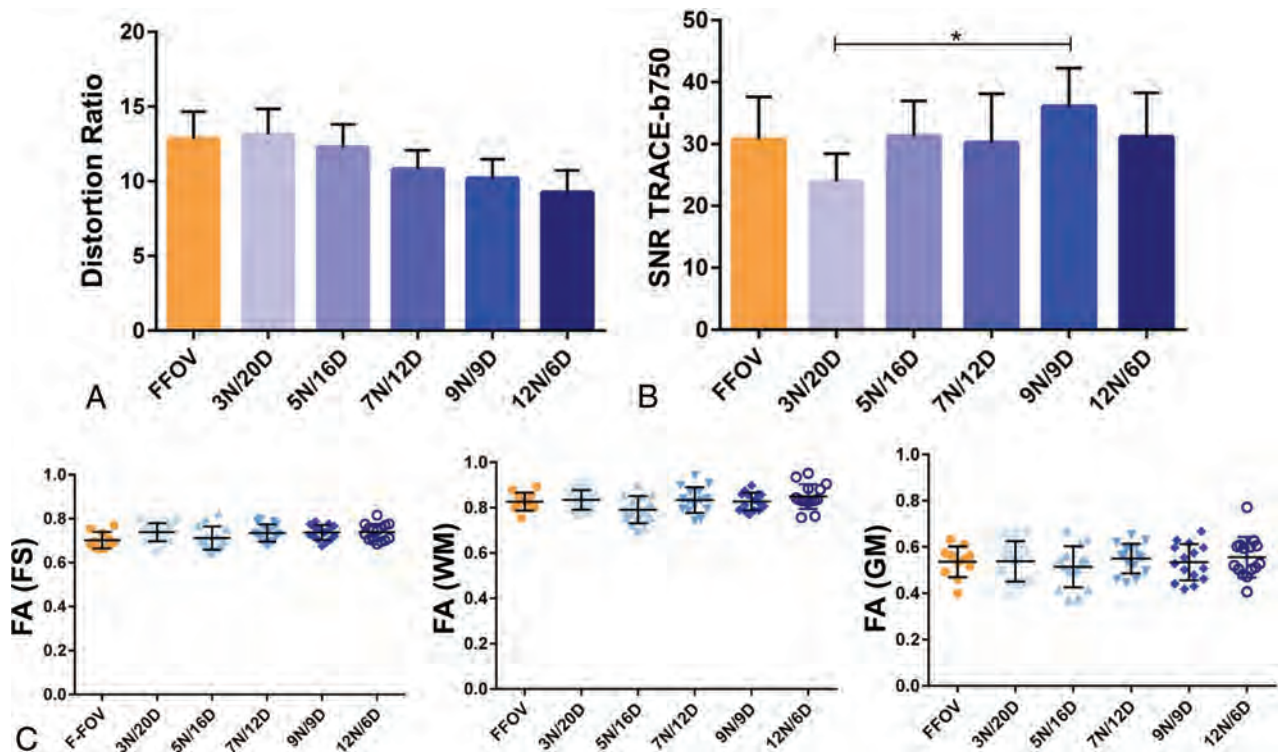


**FIG 5.** Quantitative comparisons on ROI-based analyses. *A*, The distortion ratio. *B*, The SNR on the trace image at  $b=750$  s/mm<sup>2</sup>. *C*, Representation of the dispersion of FA values, depending on the DTI sequence and, successively, a full section of the spinal cord (FS), WM, and GM. Mean rates  $\pm$  SDs for the sequence are represented. Superimposed *black lines* indicate which sequences are statistically different with  $P < .05$  (asterisk).

because the CSC has low intrinsic signal and is prone to artifacts that can be averaged and canceled (such as flow artifacts) with several excitations. Altogether, we recommend choosing NEX over NDGD when time is limited as opposed to standard recommendation for brain exploration. These results might be particularly important when axial sections are used because the axial section is prone to flow artifacts. Other strategies could be adopted and associated in the future to further limit the flow artifacts: 1) Many B0s could be acquired to select the one with the fewest artifacts; 2) cardiac gating could be added but at the cost of increasing scan time; 3) 2 B0 acquisitions could be averaged, in phase and in reversed phase; and 4) the tensor could be estimated from the  $b=50$  s/mm<sup>2</sup> and  $b=750$  s/mm<sup>2</sup> acquisition without requiring B0.

In line with this conclusion, previous studies dealing with the optimization of DTI parameters for CSC have also demonstrated, in a similar sequential approach, that there was no need to drastically increase NDGD (15 was satisfying compared with 32), while the NEX had to be increased.<sup>13</sup> However, these results were obtained with a f-FOV sequence, and their relevance might be still more important with a r-FOV strategy.

Other kinds of r-FOV sequences exist, depending on the MR imaging system, but all of them rely on the same principle. Reducing the excited region in the phase-encoding direction enables a shorter echo train, increased blip moment, and, thus, reduced susceptibility effects.<sup>24</sup> Spatial definition can be improved. SNR and scan time are supposed to remain stable. Among the r-FOV methods, the most popular are the following: 1) Zonal Oblique Multislice-EPI,<sup>11</sup> an inner volume technique, in which a refocus-

ing pulse in an orthogonal or oblique plane to the excitation plane is applied, but with the creation of section gaps; 2) inner volume excitation and outer volume suppression<sup>10</sup>; and 3) the r-FOV.<sup>6</sup> As a consequence of the increased image quality, applications of r-FOV sequences are increasingly used not only for the CSC but also to explore the midbrain, optic nerves, or hippocampi for neuro-radiology, and also the pancreas and prostate.<sup>25,26</sup>

Currently, there is no validated method for CSC DTI quality control. The CSC and its environment are too complex for mathematic<sup>15</sup> or phantom simulations. The method that we proposed here can be viewed as a realistic bench test that can be performed by any radiologist and that covers all aspects of quality control.

Finally, as additional techniques are being developed, we can expect further improvement: 1) The combination of parallel imaging and r-FOV, which has already been performed for the pons at 7T<sup>27</sup>, can still increase DTI quality; 1) multisegmented 3D-EPI could increase the SNR and could be associated with r-FOV and parallel imaging to reduce the echo train<sup>28</sup>; 3) a more accurate diffusion model could be used such as neurite orientation dispersion and density imaging,<sup>29</sup> which might provide more accurate quantitative diffusion metrics, especially for anisotropic structures like gray matter; and 4) improved postprocessing methods are being developed,<sup>30</sup> with improved eddy current and motion corrections.

Our study has limitations. We did not investigate other important parameters such as b-value, section thickness, bandwidth, cardiac gating, respiratory gating, and different designs of diffusion vectors. However, these parameters were set regardless of the

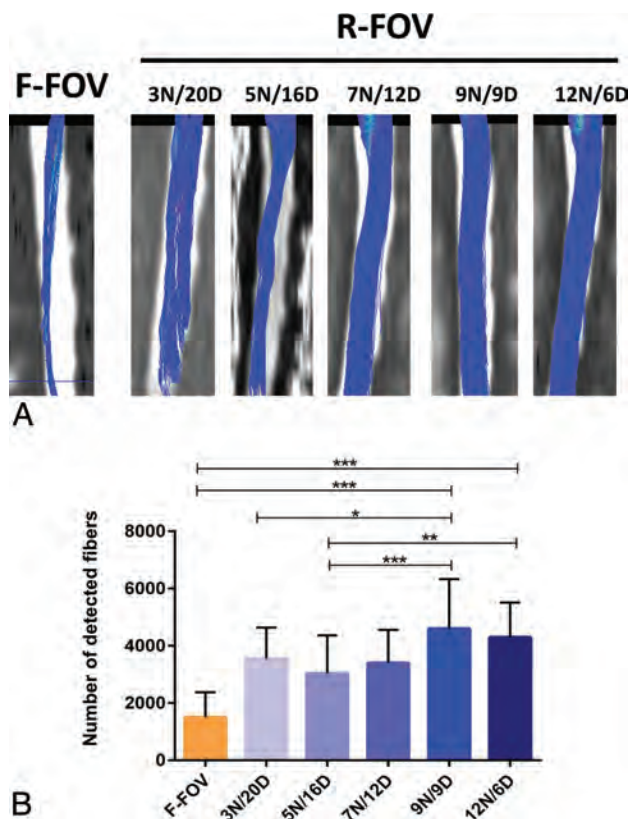


**FIG 6.** Tractography-based analyses. *A*, The reconstructed tractograms for the whole DTI dataset. For each DTI sequence, 2 similar seed ROIs were placed on the anatomic sequence, at the C1 and C3 levels, and then propagated on diffusion data. Care was taken to exclude abnormal fiber detection (ie, in the CSF). Qualitatively, r-FOV sequences clearly exhibit better tractogram definitions. *B*, The number of detected fibers between the 2 seeds.  $P < .05$  (asterisk),  $P < .005$  (double asterisks),  $P < .0005$  (triple asterisks).

sequence. The values we used ranged among those classically recommended,<sup>31</sup> notably by MR imaging constructors. Furthermore, all our acquisitions were performed on the same 3T MR imaging system. Further studies are required to investigate whether our results could be translated to 1.5T. The current literature suggests that 1.5T and 3T should provide similar DTI results, though a direct comparison has not been conducted for CSC DTI, to our knowledge. Phantom studies with classic diffusion have shown that the increased SNR inherent at higher magnetic fields was counterbalanced by increased distortions or susceptibility artifacts.<sup>32</sup> For brain DTI, Grech-Sollars et al<sup>33</sup> recently concluded that no significant difference was observed in the inter-scanner coefficient of variation for mean diffusivity and FA when 1.5T and 3T systems were compared with similar brain DTI protocols. Therefore, the parameter adjustments that we suggest at 3T might translate to 1.5T, but a formal comparison will be needed to validate this statement. In addition, our patient population consisted of only healthy young adults without significant medical histories, which might have led to better quality than what can be encountered in clinical routine. Degenerative, inflammatory, traumatic, metabolic, or tumoral spinal diseases can modify diffusivity parameters.<sup>1-5</sup> Consequently, even though our study design compared the DTI sequences, the values of our judgment criteria cannot be translated directly into clinical practice.

Another limitation is that we studied only 15 healthy subjects, which might not provide the statistical power to detect subtle differences. Nonetheless, this sample already reveals a better set of parameters, namely r-FOV 9N/9D.

## CONCLUSIONS

R-FOV CSC DTI is clinically feasible and provides significant qualitative and quantitative improvement when optimized. Contrary to brain imaging, we recommend limiting NDGD and increasing NEX because the CSC is a small highly oriented structure generating low signal and is subject to artifacts. The best compromise in a clinically acceptable scan time of 4 minutes 30 seconds is r-FOV with a NEX of 9 and 9 NDGD.

## ACKNOWLEDGMENTS

We thank Gerard Raffard for his help with image analyses in this study.

Disclosures: Thomas Tourdias—UNRELATED: Grants/Grants Pending: ANR-10-LABX-57 named TRAIL and ANR-10-LABX-43 named BRAIN.\* Marion Uettwiller—I am a General Electric Healthcare employee working as an application specialist. The system used for this study was a General Electric system. I assisted in establishing the acquisition protocol and provided technical information included in the article. \*Money paid to the institution.

## REFERENCES

- Shanmuganathan K, Gullapalli R, Zhuo J, et al. Diffusion tensor MR imaging in cervical spine trauma. *AJNR Am J Neuroradiol* 2008;29:655–59 CrossRef Medline
- Facon D, Ozanne A, Fillard P, et al. MR diffusion tensor imaging and fiber tracking in spinal cord compression. *AJNR Am J Neuroradiol* 2005;26:1587–94 Medline
- Renoux J, Facon D, Fillard P, et al. MR diffusion tensor imaging and fiber tracking in inflammatory diseases of the spinal cord. *AJNR Am J Neuroradiol* 2006;27:1947–51 Medline
- van Hecke W, Nagels G, Emonds G, et al. A diffusion tensor imaging group study of the spinal cord in multiple sclerosis patients with and without T2 spinal cord lesions. *J Magn Reson Imaging* 2009;30:25–34 CrossRef Medline
- Budzik JF, Balbi V, Le Thuc V, et al. Diffusion tensor imaging and fibre tracking in cervical spondylotic myelopathy. *Eur Radiol* 2011;21:426–33 CrossRef Medline
- Saritas EU, Cunningham CH, Lee JH, et al. DWI of the spinal cord with reduced FOV single-shot EPI. *Magn Reson Med* 2008;60:468–73 CrossRef Medline
- Kim TH, Zollinger L, Shi XF, et al. Quantification of diffusivities of the human cervical spinal cord using a 2D single-shot interleaved multisection inner volume diffusion-weighted echo-planar imaging technique. *AJNR Am J Neuroradiol* 2010;31:682–87 CrossRef Medline
- Finsterbusch J. High-resolution diffusion tensor imaging with inner field-of-view EPI. *J Magn Reson Imaging* 2009;29:987–93 CrossRef Medline
- Jeong EK, Kim SE, Guo J, et al. High-resolution DTI with 2D interleaved multisection reduced FOV single-shot diffusion-weighted EPI (2D ss-rFOV-DWEPI). *Magn Reson Med* 2005;54:1575–79 CrossRef Medline
- Wilm BJ, Svensson J, Henning A, et al. Reduced field-of-view MRI using outer volume suppression for spinal cord diffusion imaging. *Magn Reson Med* 2007;57:625–30 CrossRef Medline
- Wheeler-Kingshott CA, Hickman SJ, Parker GJ, et al. Investigating cervical spinal cord structure using axial diffusion tensor imaging. *Neuroimage* 2002;16:93–102 CrossRef Medline
- Zaharchuk G, Saritas EU, Andre JB, et al. Reduced field-of-view diffusion imaging of the human spinal cord: comparison with conven-



- tional single-shot echo-planar imaging. *AJNR Am J Neuroradiol* 2011;32:813–20 CrossRef Medline
13. Lee JW, Kim JH, Kang HS, et al. **Optimization of acquisition parameters of diffusion-tensor magnetic resonance imaging in the spinal cord.** *Invest Radiol* 2006;41:553–59 CrossRef Medline
  14. Crombe A, Menegon P, Tourdias T, et al. **Diffusion tensor imaging of cervical spinal cord at 3T: normal values of radial, axial, mean diffusivities and fractional anisotropy in anterior horn, dorsal funiculus and pyramidal tract at each cervical level.** In: *Proceedings of the International Society for Magnetic Resonance in Medicine and the European Society for Magnetic Resonance in Medicine Joint Annual Meeting*, Milan, Italy. May 10–16, 2014
  15. Gao W, Zhu H, Lin W. **A unified optimization approach for diffusion tensor imaging technique.** *Neuroimage* 2009;44:729–41 Medline
  16. Mukherjee P, Chung SW, Berman JL, et al. **Diffusion tensor MR imaging and fiber tractography: technical considerations.** *AJNR Am J Neuroradiol* 2008;29:843–52 CrossRef Medline
  17. Jones DK, Horsfield MA, Simmons A. **Optimal strategies for measuring diffusion in anisotropic systems by magnetic resonance imaging.** *Magn Reson Med* 1999;42:515–25 Medline
  18. Dietrich O, Raya JG, Reeder SB, et al. **Measurement of signal-to-noise ratios in MR images: influence of multichannel coils, parallel imaging, and reconstruction filters.** *J Magn Reson Imaging* 2007;26:375–85 CrossRef Medline
  19. Brander A, Koskinen E, Luoto TM, et al. **Diffusion tensor imaging of the cervical spinal cord in healthy adult population: normative values and measurement reproducibility at 3T MRI.** *Acta Radiol* 2014;55:478–85 CrossRef Medline
  20. Xu J, Shimony JS, Klawiter EC, et al. **Improved in vivo diffusion tensor imaging of human cervical spinal cord.** *Neuroimage* 2013;67:64–76 CrossRef Medline
  21. Tang L, Wen Y, Zhou Z, et al. **Reduced field-of-view DTI segmentation of cervical spine tissue.** *Magn Reson Imaging* 2013;31:1507–14 CrossRef Medline
  22. Ellingson B, Ulmer JL, Kurpad SN, et al. **Diffusion tensor MR imaging of the neurologically intact human spinal cord.** *AJNR Am J Neuroradiol* 2008;29:1279–84 CrossRef Medline
  23. Ni H, Kavcic V, Zhu T, et al. **Effects of number of diffusion gradient directions on derived diffusion tensor imaging indices in human brain.** *AJNR Am J Neuroradiol* 2006;27:1776–81 Medline
  24. Viallon M, Cuvinciuc V, Delattre B, et al. **State-of-the-art MRI techniques in neuroradiology: principles, pitfalls, and clinical applications.** *Neuroradiology* 2015;57:441–67 CrossRef Medline
  25. Ma C, Li YJ, Pan CS, et al. **High resolution diffusion weighted magnetic resonance imaging of the pancreas using reduced field of view single-shot echo-planar imaging at 3 T.** *Magn Reson Imaging* 2014;32:125–31 CrossRef Medline
  26. Korn N, Kurhanewicz J, Banerjee S, et al. **Reduced-FOV excitation decreases susceptibility artifact in diffusion-weighted MRI with endorectal coil for prostate cancer detection.** *Magn Reson Imaging* 2015;33:56–62 CrossRef Medline
  27. Wargo CJ, Gore JC. **Localized high-resolution DTI of the human midbrain using single-shot EPI, parallel imaging, and outer-volume suppression at 7T.** *Magn Reson Imaging* 2013;31:810–19 CrossRef Medline
  28. Engström M, Skare S. **Diffusion-weighted 3D multislab echo planar imaging for high signal-to-noise ratio efficiency and isotropic image resolution.** *Magn Reson Med* 2013;70:1507–14 CrossRef Medline
  29. Grussu F, Schneider T, Zhang H, et al. **Neurite orientation dispersion and density imaging of the healthy cervical spinal cord in vivo.** *Neuroimage* 2015;111:590–601 CrossRef Medline
  30. Mohammadi S, Freund P, Feiweier T, et al. **The impact of post-processing on spinal cord diffusion tensor imaging.** *Neuroimage* 2013;70:377–85 CrossRef Medline
  31. Jones D. *Diffusion MRI: Theory, Methods, and Applications*. New York: Oxford University Press; 2011
  32. Lavdas I, Miquel ME, McRobbie DW, et al. **Comparison between diffusion-weighted MRI (DW-MRI) at 1.5 and 3 Tesla: a phantom study.** *J Magn Reson Imaging* 2014;40:682–90 CrossRef Medline
  33. Grech-Sollars M, Hales PW, Miyazaki K, et al. **Multi-centre reproducibility of diffusion MRI parameters for clinical sequences in the brain.** *NMR Biomed* 2015;28:468–85 CrossRef Medline

# Dorsal Lumbar Disc Migrations with Lateral and Ventral Epidural Extension on Axial MRI: A Case Series and Review of the Literature

M.M. Zarrabian, F.E. Diehn, A.L. Kotsenas, J.T. Wald, E. Yu, and A. Nassr

## ABSTRACT

**SUMMARY:** Dorsal epidural migration of lumbar disc extrusion is rare and commonly misdiagnosed. Our purpose was to retrospectively analyze soft-tissue abnormalities on axial MR imaging in both the ventral and lateral epidural space in such dorsal epidural migrations. The presence of each component required complete concordance by 3 independent neuroradiologist readers. In a case series ( $n = 6$ ) of surgically proved dorsal lumbar disc migrations, in which the radiologist's favored prospective diagnosis had not been correct, each case demonstrated epidural soft-tissue abnormality that had components both laterally and ventrally, abutting the parent disc. Similarly, in previously published cases for which axial MR imaging was available, the lateral component was demonstrated in 23/24 cases (96%). Ventral abutment of the parent disc was evident, in addition, in 17/18 cases (94%) with available disc-level axial images. Both ventral and lateral epidural soft-tissue abnormalities are typically present in dorsal lumbar disc herniations and may help radiologists suggest this rare diagnosis in appropriate cases.

Per the second version of lumbar disc nomenclature derived by multisociety task forces, a disc extrusion is defined as a disc herniation that is displaced “beyond the outer annulus of the disc material with any distance between its edges greater than the distance between the edges of the base...”; the term “migration” refers to “displacement of disc material away from the site of extrusion...regardless of continuity with the disc...in either the sagittal or axial plane.”<sup>1</sup> Lumbar disc extrusions are common, with disc material typically migrating superiorly, inferiorly, or laterally.<sup>2</sup> Migration into the dorsal epidural space (Fig 1), however, is rare. This was first described by Lombardi<sup>3</sup> in 1973 as a “posterior rotation of the annulus fibrosis.” Posterior migration of the disc is thought to be anatomically inhibited by the posterior longitudinal ligament and the peridural membrane, midline septum, epidural fat/venous plexus, dura, and nerve root.<sup>4-6</sup>

Dorsal disc migrations are uncommon, with fewer than 100 reported cases, and a diagnostic challenge for several other reasons.<sup>7,8</sup> They can present with atypical clinical features, including a relatively

high prevalence (55%) of cauda equina syndrome.<sup>7</sup> In addition, their MR imaging findings overlap much more common differential considerations, such as synovial cyst and epidural abscess. Neither signal characteristics nor enhancement pattern of dorsal disc migrations allow a confident diagnosis on MR imaging. Previous reviews of the literature have shown that standard MR imaging features such as T1 and T2 signal characteristics are variable and nonspecific.<sup>5,7,9</sup> Like other disc herniations, the gadolinium-enhancement pattern is typically peripheral,<sup>6</sup> but this is also nonspecific, and intravenous contrast is often not administered in routine cases.

Morphologically, the phenomenon of dorsal epidural disc migration has often been referred to as a “posterior sequestered disc fragment” in prior articles. However, we have anecdotally observed, in our clinical practice, that in at least some cases of dorsal disc migration, the abnormal epidural soft tissue on MR imaging is typically not purely located in the dorsal epidural space. Rather, as noted in a prior single case report,<sup>6</sup> the abnormality contacts the parent disc in the ventral epidural space and from there asymmetrically involves the lateral epidural space to reach a posterior location. The purpose of the present clinical report was to analyze this morphology on axial MR imaging in dorsal lumbar disc herniations, both in a retrospective case series and in images of previously published cases.

## Case Series

Institutional review board approval with waived consent was obtained for this Health Insurance Portability and Accountability Act-compliant retrospective clinical report. The study took place

Received March 17, 2016; accepted after revision May 15.

From the Departments of Orthopedic Surgery (M.M.Z., A.N.) and Radiology (F.E.D., A.L.K., J.T.W.), Division of Neuroradiology, Mayo Clinic, Rochester, Minnesota; and Department of Orthopaedics (E.Y.), Division of Spine, Ohio State University, Comprehensive Spine Center, Columbus, Ohio.

Please address correspondence to Felix E. Diehn, MD, Division of Neuroradiology, Department of Radiology, Mayo Clinic, 200 1st St SW, Rochester, MN 55905; e-mail: diehn.felix@mayo.edu

<http://dx.doi.org/10.3174/ajnr.A4875>

at Mayo Clinic in Rochester, Minnesota. Between 2006 and 2015, 6 patients from our spine surgery practice with surgically and pathologically proved diagnoses of dorsal lumbar disc migration were identified through a search of the electronic medical record, including radiologic, surgical, and pathologic data bases. The relevant clinical, imaging, and surgical features were reviewed. We searched PubMed for published reports of dorsal lumbar disc herniation, during 2000–2015. Search terms included “dorsal/posterior epidural disc/disk herniation,” “extrusion,” “migration,” and “sequestration.” Relevant references from identified articles were reviewed. For all cases (series and literature), a staff

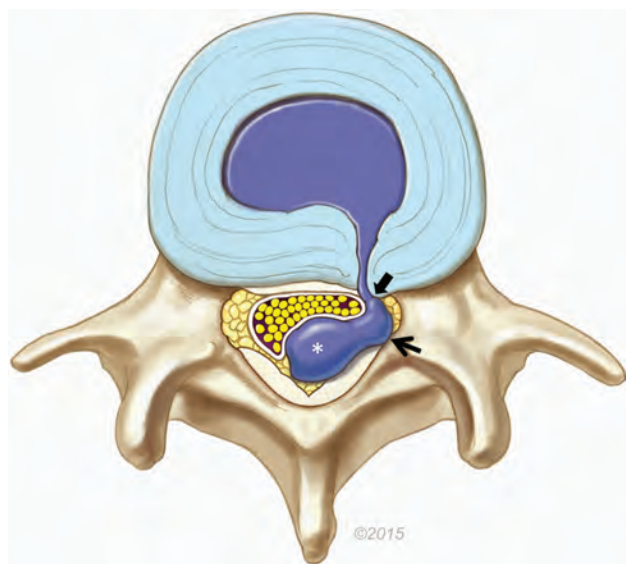


**FIG 1.** Illustration of a dorsal lumbar disc herniation. The bulk of the herniated disc material is located in the dorsal epidural space (*asterisk*), causing mass effect on the thecal sac and cauda equina. However, a lateral epidural component is also present (*arrow*). In this example, disc material extends into the ventrolateral epidural space directly to a rent in the annulus, contiguous with the parent disc (*block arrow*). On MR imaging, the soft tissue ventrally/laterally can represent disc material and/or granulation tissue. Reproduced with permission from the Mayo Foundation for Medical Education and Research.

neuroradiologist with American Board of Radiology certification and a Certificate of Added Qualification in neuroradiology (F.E.D., with 6 years of postfellowship experience) recorded the cases that had available axial MR images of sufficient quality to evaluate 2 specific morphologic features: 1) epidural soft tissue wrapping laterally around the thecal sac from ventrolateral to dorsolateral/dorsal, and 2) apparent abutment with the parent disc in the ventral epidural space at disc-level axial images, when available (Fig 1). These 2 features on axial images only were evaluated at an electronic workstation independently by 3 staff neuroradiologists with the same qualifications (F.E.D., A.L.K., and J.T.W., with 6, 17, and 20 years of postfellowship experience, respectively). The features were considered present only if all 3 neuroradiologists graded them as evident. Because most cases did not include postcontrast imaging, no attempt was made to discriminate whether the ventral/lateral epidural soft tissue, if present, represented either actual disc material and/or granulation tissue extending to the dorsally migrated disc material.

The clinical and relevant MR imaging features of the 6 cases are shown in the Table. The interpreting radiologist’s clinical report was available in 5 cases (1 outside MR imaging was not formally interpreted; each interpreting radiologist had American Board of Radiology certification and a Certificate of Added Qualification in neuroradiology); in no case was the dorsal disc herniation the favored diagnosis (Table). On independent analysis by all 3 reviewing neuroradiologists, all 6 of these dorsally migrated disc herniations demonstrated the epidural soft-tissue abnormality both wrapping laterally around the thecal sac and abutting the parent disc. In case 1, MR imaging (Fig 2) demonstrated a 3.5-cm peripherally enhancing (Fig 2C, -F) left dorsal epidural mass, extending from the L4 to the lower L5 body levels. At the operation, a large, flat, adherent, and firm left dorsal mass of disc material (pathologically confirmed) was resected (Fig 3). This tracked from L3 to L5, enveloping the L5 nerve circumferentially. The patient obtained relief of the leg pain and was discharged on postoperative day 3.

In case 2, MR imaging (Fig 4) demonstrated a 1.9-cm dorsal epidural mass at L3–4, contributing to severe spinal stenosis. The

#### Clinical and MRI features of 5 patients with dorsal epidural disc herniations

Case No./Age (yr)/Sex	Symptoms	Side/Level	Ventral Soft Tissue, Abutting Disc			Radiologist’s Favored Diagnosis
			Lateral Soft Tissue	Gadolinium Enhancement		
1/48/M	3-Week back pain, radiating to right lower extremity, paresthesias on dorsum of right foot, urinary hesitancy	Left/L4–5	Yes	Yes	Peripheral	Epidural abscess
2/77/M	4-Month low back pain, intermittent radiation into right > left lower extremities, weakness; acutely unable to ambulate	Right/L3–4	Yes	Yes	NA	Epidural hematoma
3/69/M	2-Week low back pain radiating into thighs, progressive right lower extremity weakness	Left/L2–3	Yes	Yes	NA	Synovial cyst
4/61/M	5-Day low back pain, 2-day progressive right lower extremity weakness	Left/L3–4	Yes	Yes	NA	Epidural hematoma
5/35/M	1-Week back and bilateral lower extremity pain, weakness	Left/L4–5	Yes	Yes	Peripheral	NA
6 <sup>a</sup> /60/M	3-Week progressive severe right lower extremity radicular pain, resulting in hospital admission for pain control	Right/L4–5	Yes	Yes	Peripheral	Epidural abscess

**Note:**—NA indicates not applicable.

<sup>a</sup>Images from case 6 appear in Diehn et al.<sup>8</sup>

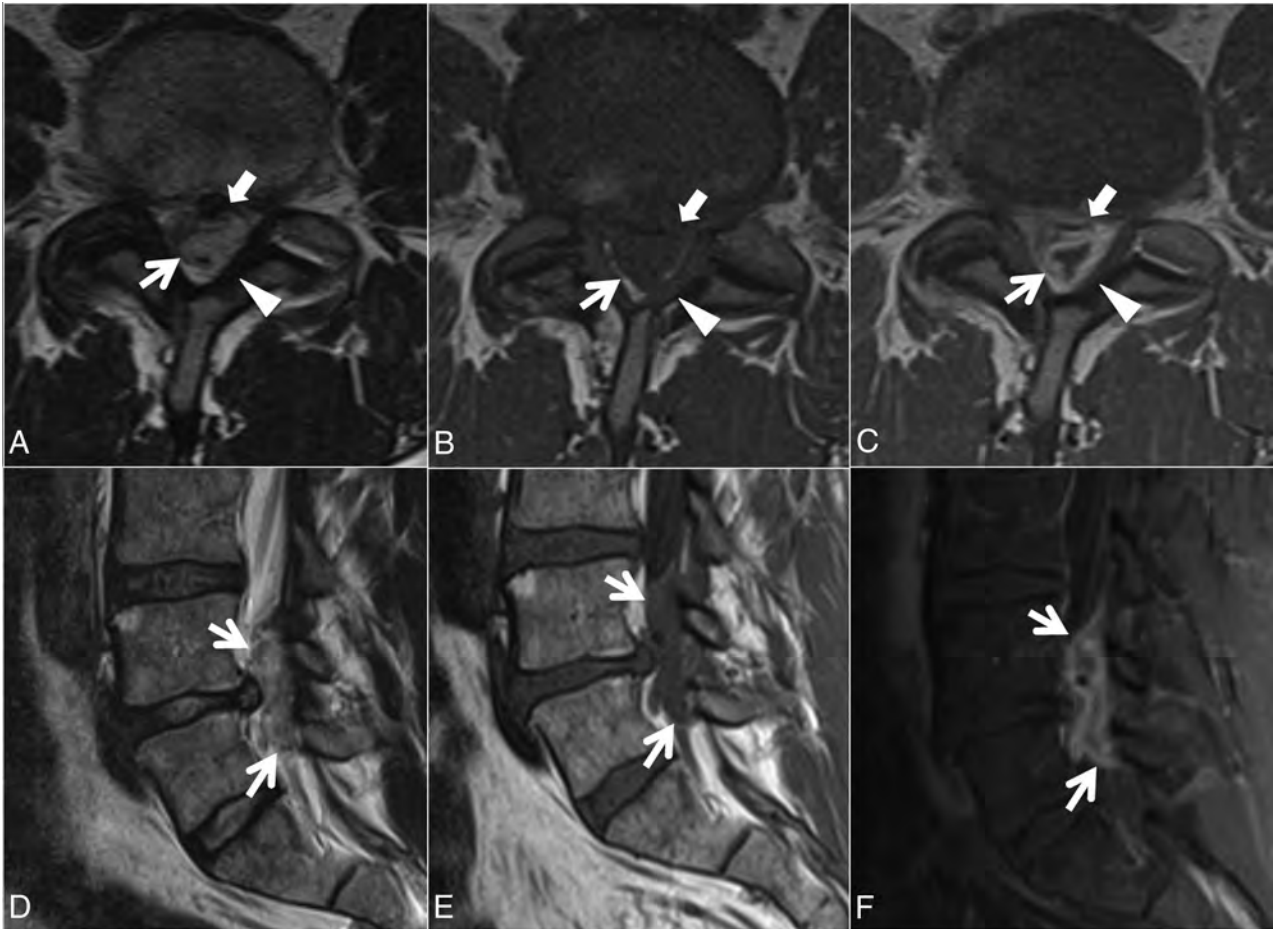


**FIG 2.** Case 1. A 48-year-old man with 3 weeks of back pain radiating to the right lower extremity and paresthesias on the dorsum of the right foot. Axial T2- (A), T1- (B), and postcontrast T1-weighted (C) and sagittal T2- (D), T1- (E), and postcontrast fat-suppressed T1-weighted (F) images. A heterogeneous predominantly T1-isointense, T2-hyperintense 3.5-cm maximal dimension mass (white arrows, A–F) in the dorsal and left lateral epidural fat partially abutting the left ligamentum flavum (arrowheads, A–C) contributes to severe L4–5 spinal stenosis, with rightward displacement and effacement of the thecal sac. There is no definite connection to the left L4–5 facet joint. The left lateral epidural fat is effaced, and the dorsal mass is contiguous with the dorsal margin of the L4–5 disc (white block arrow in A–C). The mass peripherally enhances (C and F). The radiologist’s interpretation favored epidural abscess. At the operation, the dorsal disc herniation was an inflammatory-appearing mass with considerable adhesion to the undersurface of the lamina. Also contributing to the L4–5 stenosis are a disc protrusion and ligamentum flavum redundancy.

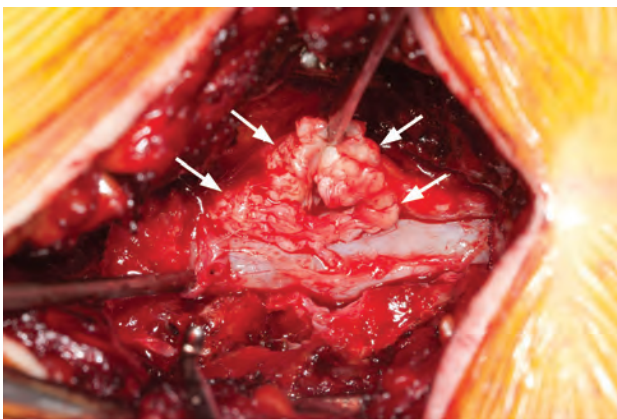


**FIG 3.** Case 1. Intraoperative photo after an L4–5 laminectomy demonstrates a left-sided mass (arrows) pathologically proved to be disc material.

radiologist’s differential diagnosis favored focal epidural hematoma and included dorsal disc migration, a synovial cyst, or sequela of a recent epidural injection. At the operation, a 2-cm

dorsal disc fragment (pathologically confirmed) adherent to the dura at L3–4 was resected. This disc fragment was followed laterally to the right aspect of the L3–4 disc, where a rent in the annulus was detected in the foraminal zone. The patient was discharged on postoperative day 2 with noted improvement in pain, ambulation, and strength.

In case 3, MR imaging (Fig 5) showed severe central canal stenosis due to spondylotic changes and developmental narrowing, greatest at L2–3 and L4–5. At L2–3, a 2.0-cm left dorsal-lateral epidural mass contributed to the stenosis. At the operation, left L2–3 disc material (pathologically confirmed) was visualized dorsally, resected, and followed to the ventral aspect of the disc. No rent in the annular fibers was visualized. Postoperatively, the patient had resolution of pain and recovery of motor deficits. He was discharged on postoperative day 3.

In case 4, MR imaging (Fig 6) demonstrated spondylotic changes causing multilevel severe central stenosis from L1 to S1, most notable at L3–4 due to a 1.3-cm left dorsal-lateral epidural mass. At the operation, an L3–4 left disc fragment (pathologically confirmed) was resected. This fragment had a tail that wrapped

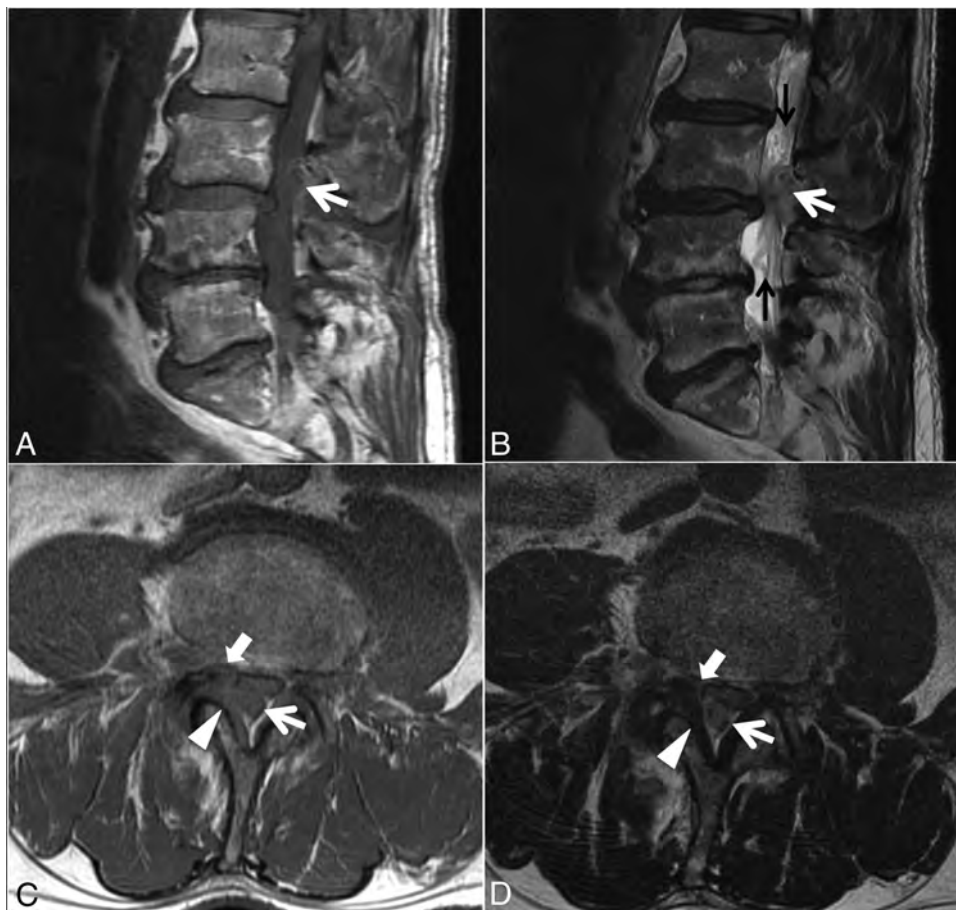


**FIG 4.** Case 2. A 77-year-old man with 4 months of low back pain and intermittent radiation into the right-more-than-left lower extremities, as well as weakness and an acute inability to ambulate. Sagittal T1- (A) and T2-weighted (B) and L3 inferior endplate-level axial T1- (C) and T2-weighted (D) images. A heterogeneous predominantly T1-isointense, mildly T2-hyperintense, 1.9-cm maximal-dimension mass (white arrows, A–D) in the dorsal and right lateral epidural fat abutting the right ligamentum flavum (arrowheads, C–D) contributes to severe L3–4 spinal stenosis, with leftward displacement and effacement of the thecal sac. There is no definite connection to the right L3–4 facet joint. The right lateral epidural fat is effaced, and the dorsal mass is contiguous with the dorsal margin of the L3–4 disc (white block arrow in C–D). Differential considerations in the radiologist’s interpretation included focal epidural hematoma (particularly given the acute clinical presentation), dorsal migration of a disc fragment, an unusual-appearing synovial cyst or other degenerative cyst, and sequela of the recent epidural injection. At the operation, the dorsal disc herniation was indeed traced back to a large annular defect at the right lateral margin of the L3–4 disc. Also contributing to the L3–4 stenosis are slight retrolisthesis of L3 on L4, a disc bulge, and ligamentum flavum redundancy. Tortuosity of the cauda equina (black arrows, B) is compatible with the high-grade stenosis. An L1–2 left subarticular disc extrusion causing advanced lateral recess narrowing is also present at the superior aspect of the sagittal images (A and B).

toward the disc at this level. This was followed ventrally, with no additional fragment identified. The patient was discharged on postoperative day 2 with resolution of pain and ongoing weakness in the ankle dorsiflexors of his right foot.

In case 5, MR imaging (not shown) demonstrated severe central stenosis at L4–5 due primarily to a 2.9-cm peripherally enhancing left dorsal epidural mass, extending from the mid-L4 to the upper L5 body levels. At surgery, a large left dorsal mass of disc material (pathologically confirmed) compressing the thecal sac was resected. This was traced back to an L4–5 annular defect. At a 6-week follow-up, the patient described marked improvement in back and leg symptoms and demonstrated considerably greater lower extremity strength.

In case 6, MR imaging (not shown; images from this case are included in a pictorial review of unusual manifestations of disc pathologic conditions<sup>8</sup>) demonstrated severe spinal stenosis at L4–5 due primarily to a 4.0-cm peripherally enhancing large right ventrolateral-through-foraminal and dorsal epidural soft-tissue

mass, extending from L4–5 to L3–4. At the operation, densely fibrous disc material (pathologically confirmed) was resected, with complete decompression of the thecal sac and right foramen. The patient was discharged on postoperative day 2 and was completely pain-free at a 3-week follow-up.

#### **Analysis of Images from Published Cases**

In addition to our 6 cases, 52 cases from 22 articles on dorsolumbar disc herniation dating back to 2000 were identified.<sup>5-7,9-27</sup> Note that a unique case describing sequestered fragments migrating into facet joints was not included among these 52 cases and was excluded.<sup>28</sup> Among the 52 cases, MR images were available in 29 cases (56%) from 19 articles.<sup>5-7,9-15,17-19,21,23-27</sup> One case was eliminated due to poor image quality (case 1 from Sengoz et al<sup>11</sup>). At least 1 axial MR image was included in 24 of the remaining 28 cases (86%). Thirteen of the published cases included a single axial image, and 11 had at least 2 axial images, with 8 of the latter containing >1 MR imaging sequence type.

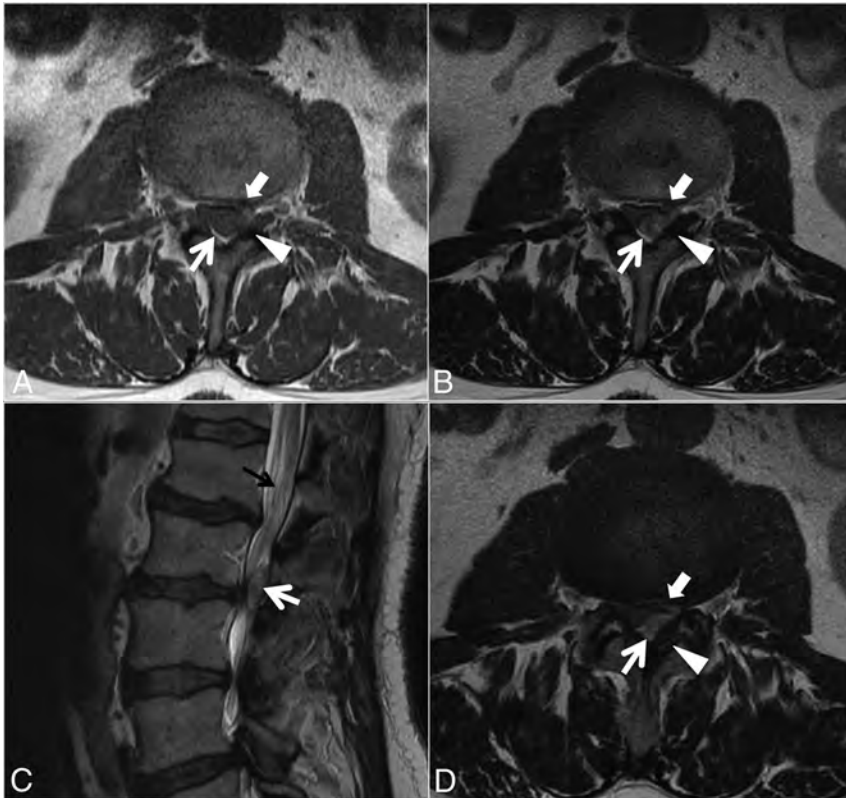


**FIG 5.** Case 3. A 69-year-old man with 2 weeks of low back pain radiating into the thighs and progressive right lower extremity weakness. Axial T1- (A) and T2-weighted (B and D; D is 1 section below A and B) and sagittal T2-weighted (C) images. A heterogeneous predominantly T1-isointense, T2-hyperintense, 2.0-cm maximal-dimension mass (white arrows, A–D) in the dorsal and left lateral epidural fat abutting the left ligamentum flavum (arrowheads, A, B, and D) contributes to severe L2–3 spinal stenosis, with rightward displacement and effacement of the thecal sac. There is no definite connection to the left L2–3 facet joint. The left lateral epidural fat is effaced, and the dorsal mass is contiguous with the dorsal margin of the L2–3 disc (white block arrows in A, B, and D, best seen in D). The radiologist’s diagnosis was a synovial cyst. At surgery, the dorsal disc herniation was traced back to the ventral aspect of the canal, and the disc was probed without other fragments identified. Also contributing to the L2–3 stenosis are a developmentally narrow canal, a disc bulge, and ligamentum flavum redundancy. Mild tortuosity of the cauda equina (black arrow, C) is compatible with the high-grade stenosis.

Twenty-three of these 24 (96%) published dorsally migrated disc herniations had at least 1 axial MR image showing an epidural soft-tissue abnormality wrapping laterally around the thecal sac, as independently noted by electronic review by all 3 aforementioned reviewing neuroradiologists (F.E.D., A.L.K., and J.T.W.). One case from the literature without consensus had a disc herniation localized to the median dorsal epidural space by the authors (their case 3 in their Fig 1A).<sup>10</sup> When disc level axial images were available (18 cases from 15 articles),<sup>5–7,9,10,12–14,18,19,21,24–27</sup> 17 (94%) demonstrated the epidural soft-tissue abnormality abutting the parent disc, as independently noted by all 3 reviewing neuroradiologists. For the 1 case from the literature without consensus for this morphologic feature, 2 of the 3 readers graded it present.<sup>24</sup> In these 17 cases with abutment of the parent disc, the lateral epidural soft-tissue abnormality was also present.

## DISCUSSION

The current clinical report shows that in both a small case series and a larger series of previously published cases of dorsal lumbar disc herniation, 2 morphologic features on axial MR imaging are seen in most (>90%) cases: 1) asymmetric epidural soft tissue

lateral to the thecal sac, and 2) on disc-level axial images, epidural soft tissue ventrally, abutting the parent disc. Indeed, the lesion typically spans from ventral/ventrolateral to dorsolateral/dorsal, rather than being purely dorsal (such as in Figs 2A, -C; 4C, -D; 5B, -D; and 6A, -B, and -D). These findings may help radiologists to more confidently suggest this relatively rare phenomenon in appropriate cases of a dorsolateral-dorsal epidural soft-tissue lesion.

Although the lateral-ventrolateral epidural component may seem intuitive, it is not widely recognized. This scenario is suggested by several of the reviewed reference articles not actually stating the side of the dorsal disc herniation, simply referring to it as posterior.<sup>11,12,19,25,27</sup> Lack of radiologists’ confidence in diagnosing dorsal disc herniation, even by fellowship-trained neuroradiologists as seen in our series, is further evidence for the lack of awareness of the axial morphology we describe herein. As for the apparent contact with the parent disc, it is often not possible to distinguish whether this represents disc material remaining in contiguity or granulation tissue between sequestered material and the parent disc, particularly if postcontrast MR imaging has not been performed. Chen et al<sup>6</sup> described this phenomenon on postgadolinium imaging in their case report of a dorsally migrated disc fragment. They noted, “A tractlike structure with enhancement

from the site of the ruptured disk to the posterior epidural space was identified, suggesting the route of the sequestered disk migration.” On the basis of histopathology and existing literature, these authors attributed the contrast enhancement to granulation tissue (“increased vascularized epidural tissue wrapping the disk contents”).

Suggesting the diagnosis on MR imaging is important because the frequently atypical clinical presentation of dorsal disc herniations can render the diagnosis difficult. Atypical features seen in these types of herniation include a relatively short duration of symptoms, often acute, as seen, for instance, in cases 4 and 5 of our series. Although it was not seen in our patients, there is a high occurrence of cauda equina syndrome<sup>7</sup> compared with more typical ventral herniations.<sup>29,30</sup> Moreover, a number of more common entities with different management approaches to surgical resection are in the differential diagnoses on MR imaging. Dorsal disc herniations are often mistaken for nondiscal lesions, such as abscess, hematoma, synovial cyst, or neoplasm on MR imaging.<sup>6,28</sup> In our series, the interpreting radiologist favored epidural

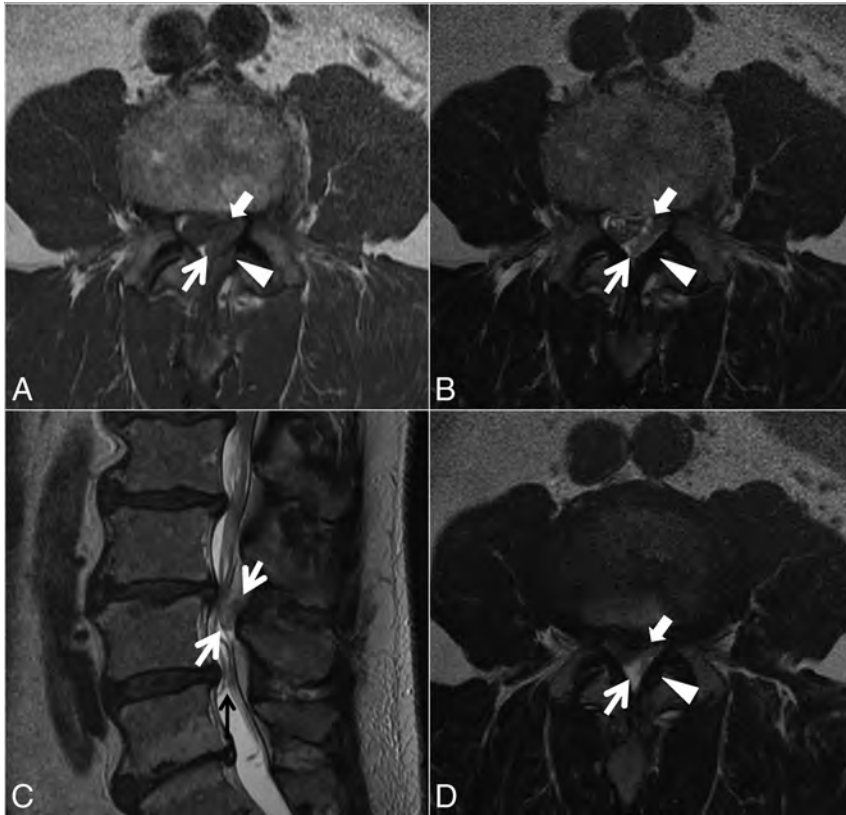


**FIG 6.** Case 4. A 61-year-old man with 5 days of low back pain and 2 days of progressive right lower extremity weakness. Axial T1- (A) and T2-weighted (B and D; D is 1 section above A and B) and sagittal T2-weighted (C) images. A heterogeneous predominantly T1-isointense, mildly T2-hypointense, 1.3-cm maximal-dimension mass (white arrows, A–D) in the dorsal and left lateral epidural fat abutting the left ligamentum flavum (arrowheads, A, B, and D) contributes to severe L3–4 spinal stenosis, with rightward displacement and effacement of the thecal sac. There is no definite connection to the left L3–4 facet joint. The left lateral epidural fat is effaced, and the dorsal mass is contiguous with the dorsal margin of the L3–4 disc (white block arrows in A, B, and D, best seen in D). The radiologist’s favored diagnosis was a small epidural hematoma, with differential considerations of a sequestered disc fragment or degenerative facet-related lesion. At the operation, the dorsal disc herniation was followed back to the ventral aspect of the canal and no other fragments were identified. Also contributing to the L3–4 stenosis are a disc bulge and ligamentum flavum redundancy. Mild tortuosity of the cauda equina (black arrow, C) is compatible with the high-grade stenosis.

hematoma in 2 cases, epidural abscess in 2, and synovial cyst in 1. Indeed, the MR imaging features of these differential considerations have considerable overlap.

Disc herniations are usually isointense on T1-weighted imaging and often are hyperintense on T2-weighted imaging, but these features are variable and nonspecific.<sup>5,7,9</sup> In addition, they often show a variable degree of rim enhancement with gadolinium, depending on the degree of vascularity and granulation tissue formation, which also is nonspecific.<sup>5,9</sup> Dorsal epidural disc migrations are typically treated with surgery. Epidural abscesses are typically isointense or hypointense on T1; hyperintense on T2; typically with a rim pattern of enhancement; often having signal changes at the adjacent infected osseous spinal column/disc; and having associated inflammatory changes in the adjacent paraspinal regions.<sup>31</sup> Treatment options include systemic antibiotics, percutaneous aspiration/drainage, or an operation. Hematomas have variable signal intensities due to the heterogeneous nature and age of blood products; they may be hyperintense on T1 and may show ring enhancement during the resolution phase.<sup>32</sup> De-

pending on the clinical status of the patient, hematomas may be observed rather than evacuated. Imaging features of synovial cysts depend on the content, but they are usually adjacent to degenerative facets and often have a visible connection to them, which helps in their identification. However, dorsal disc herniations may also abut the ligamentum flavum, as in our series. Synovial cysts often have a rim of T2-hypointensity and may peripherally enhance.<sup>33</sup> Synovial cysts may be observed, treated percutaneously, or resected surgically. Solid enhancement can be a clue for a neoplasm, but gadolinium is often not routinely administered for typical lumbar spine MR imaging indications.

Limitations of our clinical report include its retrospective nature. The supplementation of our case series with a separate analysis of published images is not ideal but allows evaluation (albeit imperfect) of considerably more cases of a rare condition. Because our design was based on anecdotal observation, we may have had an expectation bias while reviewing the images. However, the analysis was conducted independently by 3 different board-certified neuroradiologists, with complete agreement needed for the findings to be considered present. Our clinical report does not allow further characterization of how often the ventrolateral abnormal soft tissue represents granulation tissue versus contiguous disc material from the ventral to the dorsal epidural space. We did not conduct a formal analysis of the im-

age quality of the published cases. We acknowledge that other entities on the differential diagnosis described above could (especially if large) have soft-tissue abnormalities present from the ventral-through-dorsal epidural space; thus, this morphology does remain a nonspecific finding. We did not seek to directly compare our series of dorsal disc herniations with a series of epidural hematomas, abscesses, or synovial cysts; thus, the reviewing radiologists were not blinded to the diagnosis of dorsal disc herniation for this clinical report.

In summary, rarity, atypical clinical presentation, and nonspecific MR imaging features cause difficulty in the diagnosis of dorsal lumbar disc herniation. Ventral and lateral epidural soft-tissue abnormalities are typically present on axial MR images and may help radiologists suggest this uncommon diagnosis in appropriate cases or at least include it in the differential diagnosis.

#### ACKNOWLEDGMENTS

The authors thank Sonia Watson, PhD, and Andrea Moran for assistance with manuscript preparation and submission.

Disclosures: Elizabeth Yu—UNRELATED: Travel/Accommodations/Meeting Expenses Unrelated to Activities Listed: Depuy Synthes (Minimally Invasive Surgery Summit meeting); Other: practical reviews by Oakstone Publishing, Comments: summary of medical journal articles for Continuing Medical Education credit. Ahmad Nassr—UNRELATED: Grants/Grants Pending: Pfizer\*; Payment for Lectures (including service on Speakers Bureaus): Magnifi Group; Stock/Stock Options: diversified mutual funds as part of retirement.\* \*Money paid to the institution.

## REFERENCES

- Fardon DF, Williams AL, Dohring EJ, et al. **Lumbar disc nomenclature: version 2.0—recommendations of the combined task forces of the North American Spine Society, the American Society of Spine Radiology and the American Society of Neuroradiology.** *Spine J* 2014;14:2525–45 CrossRef Medline
- Bonaroti EA, Welch WC. **Posterior epidural migration of an extruded lumbar disc fragment causing cauda equina syndrome: clinical and magnetic resonance imaging evaluation.** *Spine (Phila Pa 1976)* 1998;23:378–81 CrossRef Medline
- Lombardi V. **Lumbar spinal block by posterior rotation of anulus fibrosus: case report.** *J Neurosurg* 1973;39:642–47 CrossRef Medline
- Schellinger D, Manz HJ, Vidic B, et al. **Disk fragment migration.** *Radiology* 1990;175:831–36 CrossRef Medline
- Tarukado K, Tono O, Doi T. **Ordinary disc herniation changing into posterior epidural migration of lumbar disc fragments confirmed by magnetic resonance imaging: a case report of a successful endoscopic treatment.** *Asian Spine J* 2014;8:69–73 CrossRef Medline
- Chen CY, Chuang YL, Yao MS, et al. **Posterior epidural migration of a sequestered lumbar disc fragment: MR imaging findings.** *AJNR Am J Neuroradiol* 2006;27:1592–94 Medline
- Tarukado K, Ikuta K, Fukutoku Y, et al. **Spontaneous regression of posterior epidural migrated lumbar disc fragments: case series.** *Spine J* 2015;15:e57–62 CrossRef Medline
- Diehn FE, Maus TP, Morris JM, et al. **Uncommon manifestations of intervertebral disk pathologic conditions.** *Radiographics* 2016;36:801–23 CrossRef Medline
- Derincek A, Ozalay M, Sen O, et al. **Posterior epidural mass: can a posteriorly migrated lumbar disc fragment mimic tumour, haematoma or abscess?** *Acta Orthop Belg* 2009;75:423–27 Medline
- Akhaddar A, El-Asri A, Boucetta M. **Posterior epidural migration of a lumbar disc fragment: a series of 6 cases.** *J Neurosurg Spine* 2011;15:117–28 CrossRef Medline
- Sengoz A, Kotil K, Tasdemiroglu E. **Posterior epidural migration of herniated lumbar disc fragment.** *J Neurosurg Spine* 2011;14:313–17 CrossRef Medline
- Teufack SG, Singh H, Harrop J, et al. **Dorsal epidural intervertebral disk herniation with atypical radiographic findings: case report and literature review.** *J Spinal Cord Med* 2010;33:268–71 CrossRef Medline
- Eksi MS, Yener U, Akakin A, et al. **Posterior epidural disc herniation at L3–L4 mimicking a spinal tumor: a case report.** *J Neurosurg Sci* 2010;54:71–76 Medline
- Kim JS, Lee SH, Arbatti NJ. **Dorsal extradural lumbar disc herniation causing cauda equina syndrome: a case report and review of literature.** *J Korean Neurosurg Soc* 2010;47:217–20 CrossRef Medline
- Carvi y Nieves MN, Hoellerhage HG. **Unusual sequestered disc fragments simulating spinal tumors and other space-occupying lesions: clinical article.** *J Neurosurg Spine* 2009;11:42–48 CrossRef Medline
- El Asri AC, Naama O, Akhaddar A, et al. **Posterior epidural migration of lumbar disk fragments: report of two cases and review of the literature.** *Surg Neurol* 2008;70:668–71; discussion 671 CrossRef Medline
- Lakshmanan P, Ahuja S, Lyons K, et al. **Sequestered lumbar intervertebral disc in the posterior epidural space: a report on two cases and review of the literature.** *Spine J* 2006;6:583–86 CrossRef Medline
- Tatli M, Güzel A, Ceviz A, et al. **Posterior epidural migration of sequestered lumbar disc fragment causing cauda equina syndrome.** *Br J Neurosurg* 2005;19:257–59 CrossRef Medline
- Walsh AJ, Martin Z, McCormack D. **Cauda equina syndrome secondary to posterior epidural migration of a lumbar disc fragment: a rare phenomenon.** *Eur J Orthop Surg Traumatol* 2004;14:30–31 CrossRef
- Kim JH, Kong MH, Lee SK, et al. **A case of posterior epidural migration of an extruded lumbar disc fragment causing cauda equina syndrome.** *J Korean Neurosurg Soc* 2004;35:442–44
- Kuzeyli K, Cakir E, Usul H, et al. **Posterior epidural migration of lumbar disc fragments: report of three cases.** *Spine (Phila Pa 1976)* 2003;28:E64–E67 CrossRef Medline
- Şenel A, Çokluk C, Çelik F. **Posterior epidural migration of extruded lumbar disc mimicking epidural mass: case report.** *Turk Neurosurg* 2003;13:115–17
- Kim MS, Hur JW, Lee JW, et al. **Posterior and lateral epidural migration of extruded lumbar disc fragments: case report.** *J Korean Neurosurg Soc* 2003;33:297–98
- Dösoğlu M, Is M, Gezen F, et al. **Posterior epidural migration of a lumbar disc fragment causing cauda equina syndrome: case report and review of the relevant literature.** *Eur Spine J* 2001;10:348–51 CrossRef Medline
- Eysel P, Herbsthofer B. **Dorsal compression of the epidural cord due to free sequestral lumbar prolapse: diagnostic problems in magnetic resonance imaging and computed tomography.** *Arch Orthop Trauma Surg* 2001;121:238–40 CrossRef Medline
- Şen O, Aydın MV, Erdoğan B, et al. **Cauda equina syndrome caused by posterior epidural migration of an extruded lumbar disc fragment.** *Turk Neurosurg* 2001;11:108–10
- Lisai P, Doria C, Crissantu L, et al. **Posterior epidural migration of an extruded free fragment from a lumbar disc herniation.** *J Orthopaed Traumatol* 2000;2:103–05 CrossRef
- Huang TY, Lee KS, Tsai TH, et al. **Posterior epidural migration of sequestered lumbar disc fragments into the bilateral facet joints: case report.** *Neurosurgery* 2011;69:E1148–E51 CrossRef Medline
- Jennett WB. **A study of 25 cases of compression of the cauda equina by prolapsed intervertebral discs.** *J Neurol Neurosurg Psychiatry* 1956;19:109–16 CrossRef Medline
- Shephard RH. **Diagnosis and prognosis of cauda equina syndrome produced by protrusion of lumbar disk.** *BMJ* 1959;2:1434–39 CrossRef Medline
- Diehn FE. **Imaging of spine infection.** *Radiol Clin North Am* 2012;50:777–98 CrossRef Medline
- Braun P, Kazmi K, Nogués-Meléndez P, et al. **MRI findings in spinal subdural and epidural hematomas.** *Eur J Radiol* 2007;64:119–25 CrossRef Medline
- Apostolaki E, Davies AM, Evans N, et al. **MR imaging of lumbar facet joint synovial cysts.** *Eur Radiol* 2000;10:615–23 CrossRef Medline





## Embryologic Anatomic Variations: Challenges in Intra-Arterial Chemotherapy for Intraocular Retinoblastoma

We read the article on intraocular chemotherapy for retinoblastoma by Bertelli et al,<sup>1</sup> e-published in February 2016, with considerable interest. It gives excellent insight into the adaptable approaches of the procedure described. The authors have mainly described 3 patterns of drug delivery in their patients: a fixed pattern through the ophthalmic artery, a fixed pattern through branches of the external carotid artery (ECA), and a variable pattern via either of these. They have also mentioned the “Japanese technique.”<sup>2</sup> The authors have also highlighted difficulties in direct ophthalmic artery catheterization due to its acute takeoff from the internal carotid artery, where primary shaping of the catheter can be attempted. In cases in which the choroid blush via the ophthalmic artery was not seen, catheterization of the ECA branches was also performed.

In our experience, sometimes even shaping the microcatheter does not allow ophthalmic artery catheterization. In such cases, if a choroid blush is seen only via the ophthalmic artery and not through the middle meningeal artery, the Japanese technique might be helpful. However, sometimes even this may be challenging due to presence of embryologic vascular variations. The case in point was an 11-month-old female child with grade D retinoblastoma in the left eye, refractory to systemic chemotherapy. A left internal carotid artery angiogram revealed a type 1 persistent trigeminal artery (PTA) arising from the vertical portion of the cavernous segment, with an approximate 4-mm caliber (Fig 1A). The left ophthalmic artery had an acute angled takeoff from the ICA (Fig 1A), and attempts to cannulate it with straight and angled microcatheters were unsuccessful. Tumor blush and choroid blush were, however, seen only via the ophthalmic artery on the left ICA injection. Left ECA and selective left middle meningeal artery runs did not show any choroid blush or reformation of the ophthalmic artery. Therefore, a 4 × 7 mm hypercompliant bal-

loon was inflated in the left ICA, distal to the ophthalmic artery origin. A microcatheter run with its tip in the ICA at the level of left ophthalmic artery origin revealed no opacification of the ophthalmic artery due to preferential retrograde flow across the PTA into the posterior circulation (Fig 1B). Ophthalmic artery flow was re-established on restoration of forward flow after balloon deflation. The only option left was using 2 balloons, one at the former position and the other at the PTA origin, followed by injection of the drug in the segment between these 2 balloons. However, due to the excessive complication risk anticipated due to the presence of 2 balloons in a single artery of an infant,<sup>3</sup> this was not attempted. The patient was thus referred for surgical management.

Although the authors have highlighted different approaches to successfully treating intraocular retinoblastomas via the endovascular route, knowledge of embryologic variations in the involved vascular territory and their hemodynamic effects is also essential to prevent failure.

### REFERENCES

1. Bertelli E, Leonini S, Galimberti D, et al. **Hemodynamic and anatomic variations require an adaptable approach during intra-arterial chemotherapy for intraocular retinoblastoma: alternative routes, strategies, and follow-up.** *AJNR Am J Neuroradiol* 2016;37:1289–95 CrossRef Medline
2. Yamane T, Kaneko A, Mohri M. **The technique of ophthalmic arterial infusion therapy for patients with intraocular retinoblastoma.** *Int J Clin Oncol* 2004;9:69–73 CrossRef Medline
3. Suzuki S, Yamane T, Mohri M. **Selective ophthalmic arterial injection therapy for intraocular retinoblastoma: the long-term prognosis.** *Ophthalmology* 2011;118:2081–87 CrossRef Medline

✉ C. Paruthi

✉ V. Gupta

✉ N. Khandelwal

Department of Radio-Diagnosis  
Postgraduate Institute of Medical Education and Research  
Chandigarh, India

<http://dx.doi.org/10.3174/ajnr.A4905>



**FIG 1.** A, Left internal carotid artery run showing ophthalmic artery takeoff at an acute angle (*arrow*) and a type 1 persistent trigeminal artery (*arrowhead*). B, Left internal carotid artery microcatheter run after inflation of a hypercompliant balloon within its lumen distal to the origin of ophthalmic artery (*star*), showing no opacification of the ophthalmic artery and preferential flow across the persistent trigeminal artery (*arrowhead*).

## Regarding “Endovascular Treatment of Very Small Intracranial Aneurysms: Meta-Analysis”

**W**e thank Yamaki et al<sup>1</sup> for updating their review of the outcome of endovascular treatment in patients with very small (<3 mm) intracranial aneurysms (IAs). However, we have a few concerns regarding the “Results”/“Conclusions.”

The conclusion that coil embolization in very small aneurysms can be performed safely and effectively should be reserved for ruptured IAs. The authors themselves discuss the very low rupture rates in very small IAs as reported in the literature. The meta-analysis results show the high rate of complications and poor neurologic outcome in almost 21% of patients overall. One should also note from the study the high rate at which these previously unruptured IAs had been treated (261/1105 treated aneurysms), despite their not-well-understood natural history and likely very low rupture rates. In a recent study by Murayama et al,<sup>2</sup> 301 IAs measuring 2–4 mm were treated, while 1717 were observed; these results show the high rates of treatment in these small IAs. It is disappointing that most of the studies in this meta-analysis do not mention the long-term neurologic outcomes in patients with unruptured IAs, but the high rate of complications, as shown in this meta-analysis, is clearly a reason for concern. In this era of patient-centered decision-making, it would be interesting to see how many patients with unruptured aneurysms are told that the procedure-related mortality rate is roughly 3% and the morbidity rate is 2%, with poor neurologic outcome in a large number of patients. It is also disappointing but important to note that despite advances in treatment, though procedure-related rupture is lower, long-term angiographic occlusion rates are similar and rates of good neurologic outcome are actually worse after 2010. The authors’ conclusion regarding the safety and efficacy of coiling, given all these findings, should be restricted to ruptured IAs.

Table 1 of the article shows that many included studies are unbalanced in terms of ruptured and unruptured IAs. The authors also noted that 9 studies included only ruptured IAs and 2 included unruptured IAs (from Table 1, the study of Pierot et al<sup>3</sup> seems to be the only one reporting only unruptured IAs). The extent of bias in these studies in terms of patient selection is not clear. In addition, there were many more ruptured-than-unrup-

tured IAs. The distribution is not likely to be representative of the patient population with very small IAs, rendering the outcome rates of limited statistical power.

Careful review of the included studies also shows that follow-up was not reported in all the 1105 aneurysms included in the study. For example, Lu et al<sup>4</sup> reported repeat angiographic results in only 21/52 patients, and mean angiographic follow-up was only around 11 months though they said they followed the patients for a mean of 46.7 months (range, 10–105 months). Van Rooij et al,<sup>5</sup> who had the largest series in this meta-analysis of 196 patients, had angiographic follow-up at 6 months in only 158 patients. Hwang et al<sup>6</sup> had follow-up MRA and/or DSA in 33/43 patients.

Although  $I^2$  for procedural rupture for previously unruptured aneurysms is reported to be zero, results from individual studies vary widely, with Hwang et al<sup>6</sup> reporting none, Pierot et al<sup>3</sup> reporting rupture in 3.9% of 51 patients, and Brinjikji et al<sup>7</sup> reporting rupture in 8.5% in their respective studies.

We thank the authors for summarizing and highlighting the results of treatment in very small aneurysms. Hopefully, this will lead to more objective decision-making and discussions with patients, especially those with previously unruptured aneurysms.

### REFERENCES

1. Yamaki VN, Brinjikji W, Murad MH, et al. **Endovascular treatment of very small intracranial aneurysms: meta-analysis.** *AJNR Am J Neuroradiol* 2016;37:862–67 CrossRef Medline
2. Murayama Y, Takao H, Ishibashi T, et al. **Risk analysis of unruptured intracranial aneurysms: prospective 10-year cohort study.** *Stroke* 2016;47:365–71 CrossRef Medline
3. Pierot L, Barbe C, Spelle L. **Endovascular treatment of very small unruptured aneurysms: rate of procedural complications, clinical outcome, and anatomical results.** *Stroke* 2010;41:2855–59 CrossRef Medline
4. Lu J, Liu JC, Wang LJ, et al. **Tiny intracranial aneurysms: endovascular treatment by coil embolisation or sole stent deployment.** *Eur J Radiol* 2012;81:1276–81 CrossRef Medline
5. van Rooij WJ, Keeren GJ, Peluso JP, et al. **Clinical and angiographic results of coiling of 196 very small (< or = 3 mm) intracranial aneurysms.** *AJNR Am J Neuroradiol* 2009;30:835–39 CrossRef Medline
6. Hwang JH, Roh HG, Chun YI, et al. **Endovascular coil embolization**

of very small intracranial aneurysms. *Neuroradiology* 2011;53:349–57 CrossRef Medline

7. Brinjikji W, Lanzino G, Cloft HJ, et al. Endovascular treatment of very small (3 mm or smaller) intracranial aneurysms: report of a consecutive series and a meta-analysis. *Stroke* 2010;41:116–21 CrossRef Medline

● X. Wu

● V.B. Kalra

● D. Durand

● A. Malhotra

Department of Radiology and Biomedical Imaging  
Yale School of Medicine  
New Haven, Connecticut

## REPLY:

**W**e thank Wu et al for their interest and commentary on our article “Endovascular Treatment of Very Small Intracranial Aneurysms: Meta-Analysis.”<sup>1</sup> The authors bring up a number of valid points regarding the treatment of small intracranial aneurysms. Overall, we agree with the authors that treatment of very small intracranial aneurysms should be reserved for those that are ruptured because the natural history of unruptured aneurysms measuring 3 mm or smaller is generally benign. Given the nature of the literature, it is difficult to determine the patient risk factors that led to the decision to treat the 261 very small unruptured aneurysms in our series.

As the authors aptly point out, the limitations to our meta-analysis are largely reflective of the lack of high-quality studies on the treatment of very small aneurysms. In general, studies had heterogeneous patient populations, lacked sufficient follow-up to

study long-term outcomes, and lacked independent assessment of angiographic and clinical outcomes as mentioned in the “Limitations” section of our study.

The purpose of our meta-analysis was to inform the interventional community of the risks and benefits of treating very small intracranial aneurysms. We hope that the information obtained from this study will be used in discussing the risks of treating such aneurysms with patients and their families.

## REFERENCE

1. Yamaki VN, Brinjikji W, Murad MH, et al. **Endovascular treatment of very small intracranial aneurysms: meta-analysis.** *AJNR Am J Neuroradiol* 2016;37:862–67 CrossRef Medline

● **W. Brinjikji**

● **V. Yamaki**

● **G. Lanzino**

Department of Radiology

Mayo Clinic

Rochester, Minnesota

<http://dx.doi.org/10.3174/ajnr.A4909>

## The Utility of Molecular Imaging for Investigating Patients with Visual Hallucinations

We read with interest the recent article entitled “Distinguishing Neuroimaging Features in Patients Presenting with Visual Hallucinations” by Winton-Brown et al.<sup>1</sup> They described the features of dementia with Lewy bodies (DLB) on multiplanar T1-weighted MR imaging.<sup>1</sup> In our practice, we find the diagnosis of DLB challenging with anatomic imaging alone. Molecular imaging can be helpful for differentiating DLB from other causes of visual hallucinations and dementia.<sup>2–4</sup> We present examples of the imaging findings of DLB by using nigrostriatal dopamine terminal imaging with dopamine-transporter single-photon emission CT (DaTscan) with the radioligand [<sup>123</sup>I]FP-CIT (GE Healthcare, Buckinghamshire, United Kingdom) and FDG-PET. These imaging techniques may be considered in addition to anatomic imaging in cases in which a diagnosis of DLB is suspected but remains unclear.

DaTscan is used for the early detection of Parkinson disease, to differentiate essential tremor and psychogenic-/neuroleptic-induced parkinsonism from presynaptic parkinsonian syndromes and to distinguish DLB from other forms of dementia. Nigrostriatal dopaminergic denervation is a crucial feature in Parkinson disease, parkinsonian disorders and DLB. [<sup>123</sup>I]FP-CIT has a high affinity for the dopamine transporter (DaT) and is used to visualize dopaminergic nerve terminals. DaTscan involves the acquisition of SPECT images 3–6 hours after a single injection of [<sup>123</sup>I]FP-CIT at a recommended dose of 111–185 MBq by using a dual-headed (or greater) gamma camera. In a normal DaTscan, the striatum is visible as symmetric, comma-shaped regions. Both the caudate and putamen show high uptake compared with the background (Fig 1A). In DLB, there is typically bilateral loss of DaT binding, predominantly in the putamen and caudate, more symmetric than in Parkinson disease (Fig 1B). A Phase III study by McKeith et al<sup>2</sup> showed that DaTscan has a mean sensitivity of 77.7% for detecting clinically probable DLB and a specificity of 90.4% for excluding other causes of dementia, principally Alzheimer disease (AD).

FDG-PET is a useful imaging technique in differentiating

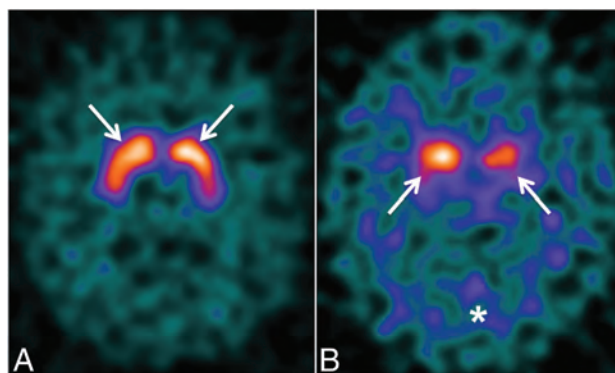


**FIG 1.** A, Normal DaTscan findings with normal background activity. The *arrows* show normal radiotracer uptake within the caudate nuclei and putamen bilaterally. B, Abnormal DaTscan findings in a 68-year-old woman with visual hallucinations and cognitive impairment. There is reduced uptake within the caudate nuclei and putamina (*arrows*) bilaterally with increased background activity (*asterisk*). In the clinical context, these findings are consistent with DLB.

primary neurodegenerative disorders. The FDG metabolic signature of DLB is bilateral parietal and posterior temporal hypometabolism, posterior cingulate gyral hypometabolism, and involvement of the occipital lobes, which are spared in AD (Fig 2).<sup>3</sup> Medial occipital lobe hypometabolism is a key feature of DLB that discriminates it from AD,<sup>4</sup> with a reported sensitivity and specificity of 92%. If the occipital cortex is not involved, DLB and AD cannot be distinguished on the basis of their FDG metabolic pattern.<sup>3</sup> When clinical and FDG-PET findings are indeterminate, DaTscan is complementary.

In conclusion, the integration of molecular imaging, including DaTscan and FDG-PET, can be useful in establishing a diagnosis of dementia with Lewy bodies in patients presenting with visual hallucinations.

Disclosures: Ronan P. Killeen—UNRELATED: Consultancy: Novartis, Comments: consultancy related to review of software for atrophy measures in multiple sclerosis; single fee under \$1000; Royalties: Springer, Comments: FDG PET/CT in *Clinical Oncology* (book) by Jasna Mihailovic, Ronan P. Killeen, and Stanley J. Goldsmith, 2012; *Stock/Stock Options*: Dublin CyberKnife Financing Limited, Comments: owns shares in this company; it runs a CyberKnife for treatment of primarily brain tumors in Hermitage Medical Clinic, Dublin, Ireland.

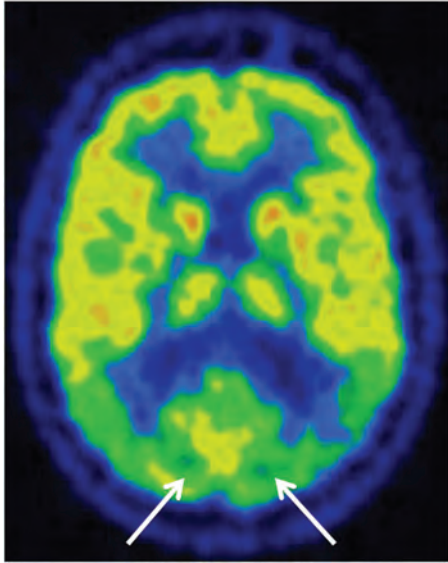


**FIG 2.** FDG-PET in the same patient as Fig 1B shows marked bilateral hypometabolism in the medial occipital lobes, which is a typical finding in DLB.<sup>3</sup> These features distinguish DLB from AD; AD typically shows hypometabolism in the temporal-parietal regions and posterior cingulate gyrus but with normal medial occipital metabolism.

## REFERENCES

1. Winton-Brown TT, Ting A, Mocellin R, et al. **Distinguishing neuroimaging features in patients presenting with visual hallucinations.** *AJNR Am J Neuroradiol* 2016;37:774–81 CrossRef Medline
2. McKeith I, O'Brien J, Walker Z, et al; DLB Study Group. **Sensitivity and specificity of dopamine transporter imaging with <sup>123</sup>I-FP-CIT SPECT in dementia with Lewy bodies: a phase III, multicentre study.** *Lancet Neurol* 2007;6:305–13 CrossRef Medline
3. Brown KJ, Bohnen NI, Wong KK, et al. **Brain PET in suspected dementia: patterns of altered FDG metabolism.** *Radiographics* 2014; 34:684–701 CrossRef Medline
4. Ishii K. **PET approaches for diagnosis of dementia.** *AJNR Am J Neuroradiol* 2014;35:2030–38 CrossRef Medline

● S. Clifford

● Y.M. Purcell

Department of Radiology  
St. Vincent's University Hospital  
Dublin, Ireland

● R.P. Killeen

Department of Radiology  
St. Vincent's University Hospital  
Dublin, Ireland  
Department of Radiology  
Royal Victoria Eye and Ear Hospital  
Dublin, Ireland



**REPLY:**

**W**e read with great interest the letter by Drs Clifford, Purcell, and Killeen concerning our article “Distinguishing Neuroimaging Features in Patients Presenting with Visual Hallucinations,”<sup>1</sup> and we are very grateful for their interest in our work.

The authors make an important point about the difficulty of making the diagnosis of dementia with Lewy bodies (DLB) and other neurodegenerative conditions solely on the basis of anatomic imaging, and they stress the importance of molecular imaging. Much of diagnostic imaging, and perhaps particularly the assessment of neurodegenerative conditions, will be greatly enhanced by these advanced imaging techniques. This advantage may be similar, in some respects, to how greatly imaging benefits from gene testing and histology in other settings.

Unfortunately molecular imaging is still not widely available, and when it is available, it is an additional procedure, usually performed after more conventional anatomic MR imaging. Thus, an understanding of the clinical and MR imaging features of neurodegenerative conditions, even if imaging findings are largely negative, is helpful in guiding the next investigative step because many molecular techniques are far more targeted to 1 clinical question, and thus the correct next test must be chosen.

<http://dx.doi.org/10.3174/ajnr.A4940>

In summary, although we certainly agree with, and are grateful for, the authors’ insights into the benefits of molecular imaging, we believe that a neuroradiologist armed with a good knowledge of the anatomic imaging features of neurodegenerative diseases has a great deal to offer.

**REFERENCE**

1. Winton-Brown TT, Ting A, Mocellin R, et al. **Distinguishing neuroimaging features in patients presenting with visual hallucinations.** *AJNR Am J Neuroradiol* 2016;37:774–81 CrossRef Medline

● **T.T. Winton-Brown**

Department of Neuropsychiatry

● **A. Ting**

Department of Radiology

● **R. Mocellin**

Department of Neuropsychiatry

Royal Melbourne Hospital

Parkville, Victoria, Australia

● **D. Velakoulis**

Department of Neuropsychiatry

Royal Melbourne Hospital

Parkville, Victoria, Australia

Melbourne Neuropsychiatry Centre

National Neuroscience Facility

Carlton, Victoria, Australia

● **F. Gaillard**

Department of Radiology

Royal Melbourne Hospital

Parkville, Victoria, Australia